

The Influence of Intra- and Intermolecular Interactions on the
Magnetic and Optical Properties of Lanthanide and Transition
Metal Complexes

Zur Erlangung des akademischen Grades eines

DOKTORS DER NATURWISSENSCHAFTEN

(Dr. rer. nat.)

von der KIT-Fakultät für Chemie- und Biowissenschaften

des Karlsruher Instituts für Technologie (KIT)

genehmigte

DISSERTATION

von

Jonas Braun

1. Referent/Referentin: Prof. Dr. Annie K. Powell

2. Referent/Referentin: Prof. Dr. Horst Geckeis

Tag der mündlichen Prüfung: 19.07.2023



This document is licensed under a Creative Commons Attribution-NonCommercial-ShareAlike 4.0 International License (CC BY-NC-SA 4.0):
<https://creativecommons.org/licenses/by-nc-sa/4.0/deed.en>

I. Eidestattliche Erklärung

Bei der eingereichten Dissertation zu dem Thema

The Influence of Intra- and Intermolecular Interactions on the Magnetic and Optical Properties of Lanthanide and Transition Metal Complexes

handelt es sich um meine eigenständig erbrachte Leistung.

Ich habe nur die angegebenen Quellen und Hilfsmittel benutzt und mich keiner unzulässigen Hilfe Dritter bedient. Insbesondere habe ich wörtlich oder sinngemäß aus anderen Werken übernommene Inhalte als solche kenntlich gemacht.

Die, Arbeit oder Teile, davon habe ich bislang nicht an einer Hochschule des In- oder Auslands als Bestandteil einer Prüfungs- oder Qualifikationsleistung vorgelegt.

Die Richtigkeit der vorstehenden Erklärungen bestätige ich.

Die Bedeutung der eidestattlichen Versicherung und die strafrechtlichen Folgen einer unrichtigen oder unvollständigen eidestattlichen Versicherung sind mir bekannt.

Ich versichere an Eides statt, dass ich nach bestem Wissen die reine Wahrheit erklärt und nichts verschwiegen habe.

.....
Ort und Datum

.....
Unterschrift

II. Note

The ions shown in the illustrations are not to scale. Organic hydrogen atoms are usually omitted for clarity. Atoms and ions are shown in the following colours in all illustrations:

Element	Colour
Br	Pale orange
C	Grey
Ce ^{III}	Orange
Ce ^{IV} and Zn	Pale yellow
Cl	Pale green
Cu	Cyan
Dy	Lilac
Er	Pink
Eu	Pale red
Gd	Plum
H	White
I	Purple
La and S	Yellow
Nd	Turquoise
N	Dark blue
O	Red
Tb	Gold
Tm	Pale blue

Numerical quantities such as bond lengths and angles are given with their standard uncertainties in round brackets after the respective values and refer to last digits.

This thesis was prepared from 1st of January 2020 to 14th of June 2023 at the Institute of Inorganic Chemistry (AOC), Faculty of Chemistry and Biosciences of the Karlsruhe Institute of Technology (KIT) under the supervision of Prof. Dr. Annie K. Powell.

III. List of Abbreviations

χ_M	molar magnetic susceptibility
χ'_M	molar in-phase magnetic susceptibility
χ''_M	molar out-of-phase magnetic susceptibility
μ_B	Bohr magneton
δ	chemical shift
λ	wavelength
τ	lifetime
ϵ	extinction coefficient
θ	Weiss constant
B	magnetic flux density
M	magnetisation
T	temperature
T_B	blocking temperature
C	Curie constant
U	energy barrier
S	spin
D	anisotropy
J	magnetic exchange coupling
Z	numbers of molecules in a unit cell
Z'	numbers of molecules in an asymmetric unit
$-\Delta S_M$	molar entropy change
SMM	single molecule magnet
QTM	quantum tunnelling of magnetisation
ZFQTM	zero-field quantum tunnelling of magnetisation
Ln	lanthanide (including Y ^{III} as diamagnetic substitute)
TM	transition metal
SOC	spin orbit coupling
CT	charge transfer
IVCT	intervalence charge transfer
ILCT	interligand charge transfer
HB	hydrogen bond
XB	halogen bond
BVS	bond valence sum
VdW	van der Waals
ET	electron transfer
MCE	magnetocaloric effect
Cp^-	cyclopentadienyl anion
RT	room temperature
A	fitting parameter describing direct relaxation
B	fitting parameter describing ZFQTM
V	preexponential fitting parameter for Raman relaxation
w	fitting parameter for the energy barrier to Raman relaxation
T_0	preexponential fitting parameter for Orbach relaxation
MeOH	methanol
EtOH	ethanol
$iPrOH$	<i>iso</i> -propanol
DCM	dichloromethane
THF	tetrahydrofuran

MeCN	acetonitrile
DMF	N,N'-dimethylformamide
PXRD	powder X-ray diffraction
SC-XRD	single crystal X-ray diffraction
UVVis	absorption spectroscopy in the UV and visible spectral region
IR	infrared vibrational spectroscopy
NMR	nuclear magnetic resonance
EPR	electron paramagnetic resonance
SQUID	superconducting quantum interference device

Table of Contents

1. Kurzzusammenfassung/Abstract	1
2. Introduction and Motivation	4
3. General Theoretical Background	6
3.1 Optical Properties of 3d- and 4f Metal Ions and Complexes	6
3.2 Magnetic Properties of 3d- and 4f Metal Ion-containing Complexes	11
3.3 Intermolecular Interactions	16
3.4 Single Molecule Magnets (SMMs) and Relaxation Dynamics	23
4. The Biquinoxen Platform	36
4.1 Introduction	36
4.2 Fluorescent Adducts	41
4.2.1 Solid State Analysis on Luminescent Methylbiquinoxen-Adducts	44
4.2.1.1 Crystallography	44
4.2.1.2 Infrared Spectroscopy (ATR-IR)	51
4.2.1.3 Optical Properties	51
4.2.2 Solution State Analysis	54
4.2.2.1 UVVis Absorption and Emission Spectroscopy	54
4.2.2.2 Quantum Yields and Decomposition in Solution	59
4.3 Transition Metal Radical Complexes	61
4.3.1 Crystallography	61
4.3.1.1 Molecular Structure of $[M^{II}X_2(MbqnO)]$	61
4.3.1.2 Supramolecular Packing of $[M^{II}X_2(MbqnO)]$	65
4.3.2 Magnetic Properties of $[Zn^{II}Cl_2(MbqnO)]$ (12-Zn)	68
4.4 Transition Metal Complex using the Mbqn-(acetone)₂ Adduct – A Proof of Concept	69
4.5 Conclusions and Summary on the Biquinoxen Platform	72
5. H₂opch – A Family of Complexes Designed to Gauge Intermolecular Interactions using Halogen Bonding	76
5.1 Introduction	76
5.2 H₂opch-Lanthanide Complexes - A Story about Lanthanide Contraction	80
5.2.1 The Six Different and New Structures	81
5.2.1.1 A Planar La₅ Disc	81
5.2.1.2 A Mixed-Valence Tetranuclear Cerium Complex	84
5.2.1.3 $[Eu^{III}_5(CO_3)(H_2O)_3(mdeaH)_2(NO_3)(opch)_5]$	89
5.2.1.4 $[Dy^{III}_6(H_2O)(mdeaH_2)_2(NO_3)(\mu_3-OH)_4(\mu_2-OH)_2(opch)_5](NO_3)$	92
5.2.1.5 Two Different Structures of $[Ln^{III}_8(CO_3)_4(H_2O)_8(opch)_8]$	95

5.2.2 Comparison of Optical Properties	100
5.2.3 Magnetic Properties of H₂opch-Lanthanide Complexes	105
5.2.3.1 Magnetic Properties of the Mixed Valence Ce₄ Complex (15-Ce).....	105
5.2.3.2 Comparison of Different Ln₈ Complexes	107
5.2.3.3 The Influence of Packing on Magnetic Properties in Dy₈.....	112
5.2.3.4 Magnetocaloric Effect (MCE) of the Gd₈ Complex.....	114
5.3 Using Modified Ligands to Introduce Halogen Bonds.....	116
5.3.1 Ligand Modifications	116
5.3.2 Different Cluster Types using the H₂opch Ligand Family	120
5.3.3 Carbonate-Bridged Clusters using Modified H₂opch Ligands (Structure Type I)	121
5.3.3.1 Trigonal Prismatic Complexes using Modified H₂opch Ligands	122
5.3.3.2 The Influence of a Bromine Atom	126
5.3.3.3 Possible Intermediate in Trigonal Prism-Formation – A Proposed Mechanism	137
5.3.4 Hydroxo-Clusters using Modified H₂opch Ligands (Structure Type II).....	142
5.3.4.1 Modified Ce₄-Clusters	142
5.3.4.2 A Nd₇ Cluster Resembling Mineral Structures	146
5.3.4.3 The Formation of Supramolecular Dimers and Chains of Ln₇ Clusters <i>via</i> Halogen Interactions	150
5.3.5 Dimeric Ln-Complexes Using Modified H₂opch Ligands (Structure Type III) ..	158
5.3.5.1 Influence of Electrostatic Field (Crystal Field) on Magnetic Properties	160
5.3.5.2 Gauging the Strength of Halogen-Halogen Interactions	179
5.4 Summary and Conclusion on Complexes using H₂opch and Modified Ligands	188
6. Systematic Study on Dimeric Semiquinonate Radical Complexes to Investigate Role of Intra- and Intermolecular Interactions on the Magnetic Relaxation Dynamics	193
6.1 Introduction	193
6.2 Further Analysis of the Archetype Complexes [Ln₂(phsq)₄(NO₃)₂(MeOH)₂]	199
6.2.1 Magnetic Measurements on Further Ln^{III} Analogues	199
6.2.2 Solution State Behaviour of [Ln₂(phsq)₄(NO₃)₂(MeOH)₂]	202
6.3 Changing the Neutral Co-Ligand	211
6.3.1 [Ln₂(phsq)₄(NO₃)₂(EtOH)₂]	211
6.3.2 [Ln₂(phsq)₄(NO₃)₂(iPrOH)]	223
6.4 Varying the Anionic Co-Ligand	232
6.4.1 [Ln₂(phsq)₄(Cl)₂(MeOH)₂].....	233
6.4.2 Further Attempts to Vary the Anionic Co-Ligand	240
6.5 Changing the Radical Ligand	243
6.5.1 Pyrene-4,5-dione	243

6.5.2 Further Attempts to Vary the Radical Ligand	252
6.6 Comparison of Optical and Magnetic Properties	253
6.7 Summary and Conclusions on Semiquinonate Radical Complexes.....	258
7. General Conclusion and Outlook	262
8. Experimental	271
8.1 Biquinoxen.....	273
8.2 The H₂opch Family	282
8.3 Lanthanide-Radical Dimers.....	303
9. References	324
10. Curriculum Vitae	343
11. List of Publications	345
12. Acknowledgements.....	346
13. Appendices.....	348
13.1 Table of Figures	348
13.2 Table of Tables	362
13.3 Crystallographic Tables.....	364

1. Kurzzusammenfassung/Abstract

Kurzzusammenfassung

Die nachfolgende Arbeit ist unterteilt in drei Teilprojekte, in deren näherer Beschreibung 71 neuartige Koordinationsverbindungen, sowie 11 neue organische Verbindungen vorgestellt werden.

Das erste Teilprojekt befasst sich mit der fortgeführten Untersuchung des vielseitigen Biquinoxen Systems, welches dem vielerforschten System der Viologene ähnelt. Das Biquinoxen System besticht durch seine facettenreichen Eigenschaften wie reversiblen Redoxzuständen, Lumineszenz und Koordination an Metallzentren. In der folgenden Arbeit wird die Möglichkeit des Tunens der Emissionswellenlänge der Biquinoxenderivate untersucht und im Zuge dessen werden 7 neue Verbindungen mit Emissionswellenlängen über einen Bereich von 63 nm, von grün-gelbem bis rotem Licht, vorgestellt. Zusätzlich wurde das Biquinoxen System in Reaktionen mit Übergangsmetallsalzen eingesetzt. Dabei wird *in-situ* eine Radikalligandspezies erzeugt, die durch die Koordination an Co^{II}, Cu^{II} und Zn^{II} Ionen stabilisiert wird. Die Co^{II} Komplexe wurden bereits im Rahmen meiner Bachelorarbeit beschrieben, allerdings hier reproduziert, die supramolekularen Netzwerke genauer untersucht und mit den 4 neuen Cu^{II} und Zn^{II} Übergangsmetallkomplexen verglichen.

Die Kapitel zum zweiten Teilprojekt beschreiben die Exploration der Komplexierungseigenschaften der H₂opch ((2-Hydroxy-3-Methoxybenzyliden)pyrazin-2-Carbohydrazide) Ligandenfamilie mit Lanthanoidionen. Zuerst wird der Einfluss der unterschiedlichen Ionenradien der Lanthanoide, aufgrund der Lanthanoidenkontraktion, in Reaktionen mit identischen Reaktionsbedingungen, aber immer anderen Lanthanoidnitraten auf die Komplexbildung untersucht. Dies führte zu 11 neuen vier bis acht-kernigen Komplexen, unter anderem ein gemischt valenter Ce₄ Komplex und eine Gd₈, Verbindung welche einen exzellenten magnetokalorischen Effekt zeigt. Des Weiteren wurde der Ligand modifiziert, um den Einfluss von intra- und vor allem intermolekularen Wechselwirkungen zu untersuchen. Dabei wurde der Fokus auf die Verwendung von Halogen-Wechselwirkungen gelegt, welche den Vorteil haben in ihrer Stärke variiert werden zu können. Dies führte zu 18 neuen Komplexen, in welchen die Einflüsse jener neu eingeführten Wechselwirkungen auf die

Kristallstruktur sowie die magnetischen und optischen Eigenschaften untersucht wurden.

Das dritte Teilprojekt befasst sich mit der Erweiterung eines Radikal-Lanthanoid-Dimer-Systems, welches bereits seit einigen Jahren in der Arbeitsgruppe Powell untersucht wird. Hierbei wurden bekannte Komplexe reproduziert und deren Eigenschaften in Lösung sowie die magnetischen Eigenschaften bisher unerforschter Lanthanoidvariationen gemessen. Des Weiteren wurden alle vier Komponenten des ursprünglichen Komplexes (Lanthanoidion, neutraler Co-Ligand, anionischer Co-Ligand und Radikalligand) systematisch variiert und magnetische Messungen an den Dy^{III} Verbindungen durchgeführt. Dabei wurden 38 neue Komplexe hergestellt, darunter eine Verbindung welche eine thermische Energiebarriere von 475 K aufweist und langsame magnetische Relaxation bis zu einer Temperatur von 30 K im untersuchbaren Messfenster zeigt. Die Relaxationsdynamiken in dieser systematisch variierten Reihe von Einzelmolekülmagneten wurde untersucht und miteinander verglichen, um eine allgemeine Regel aufstellen zu können, wie das Einzelmolekülmagnetverhalten dieser Verbindungen, vor allem durch die Unterdrückung von Phonon-basierten Relaxationsprozessen, verbessert werden kann.

Abstract

The following work is divided into three topics, in which 71 new coordination compounds and 11 new organic compounds are presented.

The first project describes the continuation of the investigation of the versatile biquinoxen system, where biquinoxens are similar to the well-known viologens. The biquinoxen system exhibits multifaceted properties such as reversible redox states, luminescence and coordination to metal centres. In this work, the possibility of tuning the emission wavelength of the biquinoxen derivatives was investigated and in the course of this, 7 new compounds with emission wavelengths over a range of 63 nm, from green-yellow to red light, were produced. In addition, the biquinoxen system was used in reactions with transition metal salts. This involves the *in-situ* generation of a radical ligand species that is stabilised by coordination to Co^{II} , Cu^{II} and Zn^{II} ions. The Co^{II} complexes were already described in my bachelor thesis, but were reproduced

here and their supramolecular networks investigated in more detail and compared with the 4 new Cu^{II} and Zn^{II} containing complexes.

The chapter on the second project describes the exploration of the complexation properties of the H₂opch ((2-hydroxy-3-methoxybenzylidene)pyrazine-2-carbohydrazide) ligand family with lanthanide ions. Firstly, the influence of the different ionic radii of the lanthanides, resulting from the lanthanide contraction, was investigated in reactions with different lanthanide nitrates but with identical reaction conditions. This led to 11 new tetra- to octa-nuclear complexes. Amongst others, a mixed-valent Ce₄ complex and a Gd₈ compound which shows an excellent magnetocaloric effect could be isolated. Furthermore, the ligand was modified to investigate the influence of intra- and especially intermolecular interactions. The focus here was to investigate the effect of halogen interactions which have the advantage of being easily varied in strength, on the resulting optical and magnetic properties. This led to 18 new complexes.

The third project deals with the expansion of a radical-lanthanide dimer system which has been under study for several years in the Powell group. Here, the already known complexes were reproduced and their properties in solution investigated. Furthermore, the magnetic properties of previously unexplored lanthanide variations were measured. All four components of the original complex (lanthanide ion, neutral co-ligand, anionic co-ligand and radical ligand) were systematically varied and magnetic measurements performed on the Dy^{III} analogues. In this investigation, 38 new complexes were prepared, amongst which one compound was identified exhibiting slow relaxation of magnetisation up to a temperature of 30 K and a thermal energy barrier of 475 K. In this systematically varied series of single molecule magnets the relaxation dynamics were investigated and compared in order to establish a strategy on how to improve the single molecule magnetic behaviour of these compounds, in particular by suppressing phonon-based relaxation processes.

2. Introduction and Motivation

Ever since the discovery of magnetic bistability in a Mn_{12} cluster in 1993,^[1] the field of single molecule magnets (SMMs) has been an attractive interdisciplinary research field. SMMs are a class of materials that once magnetised by an external magnetic field retain their magnetisation even when the external magnetic field is switched off. This occurs below a certain temperature, known as blocking temperature T_B and SMMs therefore can show magnetic hysteresis.^[2] This promises applications in the areas of molecular high-density data storage^[3-4] and a variety of spintronic devices^[5-9] such as single-molecule transistors^[10-11] and spin valves.^[9, 12-13] Furthermore, control over the spin states in molecules promises potential application in quantum computing.^[14-20]

However, as of now the magnetisation cannot be retained indefinitely. Current systems show a decay of magnetisation returning to the unmagnetised state, known as slow relaxation of magnetisation. In order to do this, the system has to overcome an energy barrier, the height of which is determined by the spin of the complex as well as its anisotropy. However, in addition to the classical pathway over the top of the barrier (Orbach relaxation) there are through-barrier processes such as quantum tunnelling of the magnetisation (QTM) and phonon-based direct and Raman relaxation processes that are especially prevalent in lanthanide SMMs.^[21-25]

Over the last decades, significant progress was made in terms of quenching these processes, especially zero field quantum tunnelling (ZFQTM). Strategies to stop ZFQTM involve strong superexchange interactions between 3d and 4f metal ions in mixed metal complexes, controlling the molecular symmetry in 4f ion containing SMMs and using radicals to induce strong interactions between two metal ions. These strategies have resulted in SMMs with impressive barriers of more than 1500 cm^{-1} and magnetic hysteresis observed up to 80K and thus above the temperature of liquid nitrogen.^[26-27] However, these organometallic compounds are highly air sensitive which limits their applicability. Thus, the next step in the development of molecules for the applications mentioned above has to focus on the development of more stable compounds and combining the strategies to eliminate ZFQTM along with tackling the next hurdle which is phonon-based relaxation.

This thesis focuses on three projects. The first is a continued investigation on the versatile viologen-like biquinoxen system. The other two of these develop strategies for improving SMM behaviour.

Since the biquinoxen system can be modified to show luminescence, the potential to tune the emission wavelength in order to use the system as a luminescent dye with emission of the desired colour is part of the following investigation. It was already shown that biquinoxens can generate air stable radical species that coordinate to metal ions. This can lead to coordination compounds in which the radicals mediate very strong magnetic interactions.^[28-30] Furthermore, the possibility for supramolecular interactions in complexes using this ligand system are investigated.

The second project explores the coordination chemistry of a Schiff base ligand system, that can be easily tuned and is therefore perfect for detailed investigation of the influences on the magnetic and optical properties through changes to the coordination environments of Ln^{III} ions as well as changes to the interactions between the complexes in a crystal. It is not the goal to produce the most impressive SMMs, but rather to study the variation of intra- and intermolecular interactions in terms of SMM behaviour. The latter are often overlooked in SMM systems. This allows for the development of a general rule on how to improve SMM behaviour.

The third project uses a lanthanide-radical system $[\text{Ln}_2(\text{L})_4(\text{NO}_3)_2(\text{MeOH})_2]$ that was shown by previous PhD students in the Powell group to quench ZFQTM *via* strong intramolecular dipolar interactions.^[31-33] The archetypal air stable radical-Dy^{III} complex furthermore exhibits slow relaxation of magnetisation up to 18 K and can therefore be considered a good SMM. The goal here is to study the systematic variation of the four components to the complex and to evaluate the respective relaxation dynamics, in particular to find a way to reduce phonon-based relaxation mechanisms.

3. General Theoretical Background

In the following chapter the underlying basic principles to the topics covered in this thesis will be elucidated. This includes the optical and magnetic properties of 3d and 4f metal ions as well as the intramolecular influences in complexes governing these. Furthermore, having established the intramolecular influences, different types of intermolecular interactions and their impact on the optical and magnetic properties of coordination clusters will be discussed. Additionally, the class of compounds known as single molecule magnets (SMMs) will be introduced with an emphasis on the relaxation dynamics to the magnetisation reversal.

An introduction framing the results of this thesis within the literature can be found at the beginning of each respective chapter.

3.1 Optical Properties of 3d- and 4f Metal Ions and Complexes

The interaction of electromagnetic radiation with molecules leads to absorption of photons resulting in electronic excitation. These excitations can be followed using spectroscopy with ultraviolet and visible light (UVVis absorption spectroscopy) often in the range between 200 and 800 nm in which most complexes exhibit transitions with corresponding energies. Sometimes transitions also occur in the near-infrared region. In UVVis measurements the molecules are irradiated with a certain intensity I_0 , some of the radiation is absorbed and the transmitted intensity is detected. In solution these electronic excitations can be described using the Beer-Lambert law^[34-35]

$$A = \log_{10} \frac{I_0}{I} = \varepsilon \cdot c \cdot d \quad \text{equation 1}$$

where A = absorbance, ε = extinction coefficient, c = concentration and d = thickness of the medium. In this thesis 10 mm quartz cuvettes were used for all optical absorption measurements.

Excited molecules have a number of processes which can lead to relaxation of the system recovering the electronic ground state. Some of these are shown in the

Jablonski diagram^[36] in figure 1. These processes such as internal conversion (IC) which is the interaction with a vibrational excited state of another electronic state can be non-radiative. In figure 1 this process is shown in yellow from the second excited singlet state S_2 to an excited vibrational level of the S_1 state. After absorption into an excited vibrational state of an excited electronic state, the system can go into the vibrational ground state of the excited electronic state via vibrational relaxation (VR) shown in blue. This is possible intermolecularly by energy transfer to the surrounding solvent or intramolecularly involving adjacent vibrational degrees of freedom. From the vibrational ground state of the electronic excited state the radiating relaxation to the electronic ground state is possible via emission of a photon. This is called fluorescence (green in figure 1). The system can also undergo processes changing spin multiplicity which is usually forbidden and results in slow rates. This so-called intersystem crossing (ISC) is shown in purple from the singlet S_1 state to the triplet T_1 state in figure 1. After VR into the vibrational ground state of the T_1 electronic state, phosphorescence can occur as another radiative relaxation mechanism. The timescale for this can be as long as seconds since another forbidden change in multiplicity is necessary.

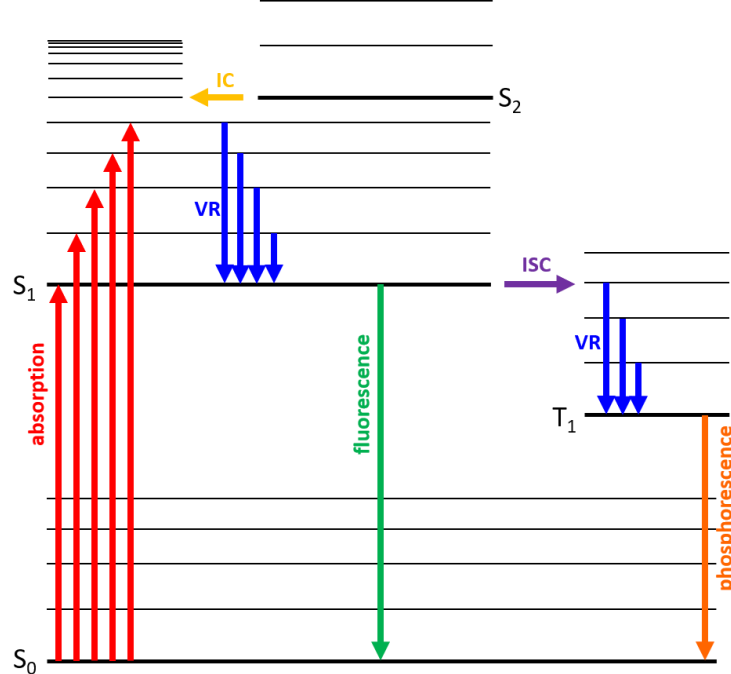


Figure 1. Jablonski diagram showing some of the possible processes upon irradiation of molecules with light.

The Franck-Condon principle states that electronic excitation is vertical, *i.e.* happens on a timescale faster than nuclear vibrations, therefore the electronic excitation is often accompanied by a vibrational excitation. After VR the system can emit a photon from

the vibrational ground state of the electronic excited state. The emission wavelength is then larger than the absorption wavelength. This difference in energy is called the Stokes shift.^[37]

As mentioned above, some transitions are forbidden. There are three selection rules that apply: $\Delta l = \pm 1$ which means that d-d and f-f transitions for example are forbidden, $\Delta j = 0, \pm 1$ as well as $\Delta s = 0$. The latter means that a change in spin such as in the event of an ISC from a singlet to a triplet state is forbidden. Coupling to antisymmetric vibrations as well as spin-orbit coupling nevertheless lead to the observation of such forbidden transitions.^[38-39]

Using emission spectroscopy, the emission wavelength, so the energy of the emitted photon, the Stokes shift as well as quantum yields can be determined. The quantum yield describes the proportion of photons emitted to photons absorbed and therefore is a measure of how effective the radiating relaxation mechanisms are compared to the non-radiating. The fluorescence quantum yield is defined as:^[37]

$$\Phi_f = \frac{\text{number of photons emitted}}{\text{number of photons absorbed}} \quad \text{equation 2}$$

Quantum yields can be determined in two ways: 1) as absolute quantum yields using an integration sphere or 2) as relative quantum yields by comparison of the emission intensity to a suitable reference dye. "Suitable" in this case means that absorption and emission can occur at the same wavelength as in the sample and the quantum yield of the dye in the respective solvent is known. A commonly used reference dye for red emitters is [Ru(bpy)₃]X₂.^[40-41]

The optical properties of 3d metal ions are highly dependent on their ligands and their arrangement since they determine the ligand field splitting and therefore the energy gap between the highest occupied molecular orbital (HOMO) and the lowest unoccupied molecular orbital (LUMO) in ions that do not have a d¹⁰ electron configuration. Additionally, for electron configurations between d⁴ and d⁷ the ligand field determines the spin state of the complex. For example, in contrast to high-spin (HS) octahedral Mn^{II} which only has spin forbidden d-d transitions (in addition to being forbidden by the Laporte rule) and is therefore only very pale in colour, low-spin d⁵ ions have d-d transitions that although Laporte-forbidden are spin allowed and are therefore more intensely coloured (higher extinction coefficients) (see figure 2). Additionally, the coordination geometry has a huge impact on the optical properties of 3d ions.

Tetrahedral complexes are generally more intensely coloured than their octahedral counterparts since the Laporte rule that applies in octahedral O_h symmetry does not in tetrahedral T_d symmetry due to the lack of an inversion centre leading to loss of the parity selection rule.^[38]

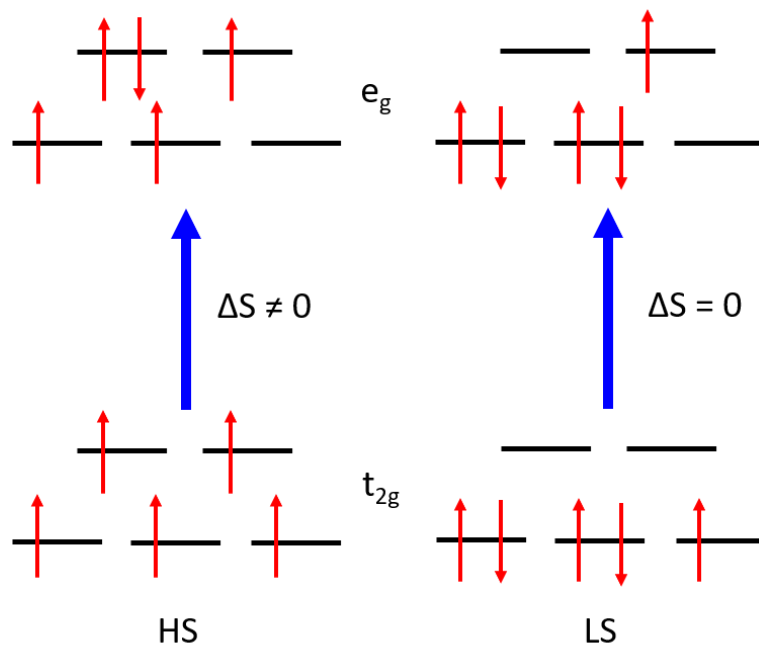


Figure 2. The difference between the d-d transitions in the HS and LS spin state for a $3d^5$ ion.

For trivalent lanthanide (Ln) ions the ligand field is generally less important and the absorption and emission properties are therefore more intrinsic to the respective ion. The f-f transitions, although nominally forbidden, can occur with much higher intensities than their d-d counterparts since the spin-orbit coupling (SOC) perturbs the system, thus allowing such transitions. The characteristic emission wavelengths of the series of Ln^{III} ions span the whole visible region reaching into the NIR as shown in figure 3.^[42-43]

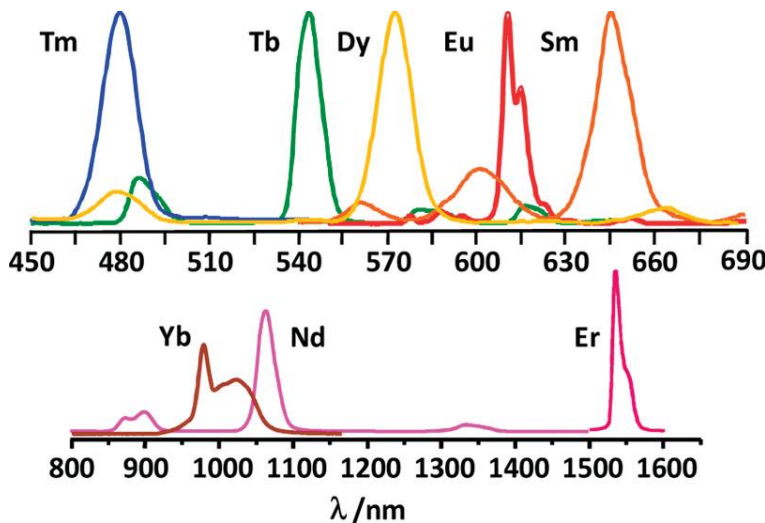


Figure 3. Characteristic emission wavelengths of Ln^{III} ions. Reprinted with permission from reference^[42] [American Chemical Society] copyright [2010].

In addition to d-d and f-f transitions charge transfer (CT) transitions can occur in complexes. As these are not forbidden they are usually a lot more intense as for example seen by the strong purple colour of MnO_4^- . CT transitions can occur between two metals ions (metal to metal charge transfer MMCT), which if they are of the same element but different valency, can be called intervalence charge transfer (IVCT). This occurs in Prussian Blue, for example, with electrons being transferred between the Fe^{II} and Fe^{III} centres. Most charge transfer processes involve an anionic ligand and a cationic metal ion showing either ligand to metal charge transfer (LMCT) or metal to ligand charge transfer (MLCT). Another possibility is inter-ligand charge transfer (ILCT) processes.^[38, 43-44]

Both transition metal and lanthanide complexes are used in the development of novel emitting materials. Often organic chromophores with extended π systems or other conjugated systems are used in order to induce MLCT and LMCT transitions that can lead to the emission of a photon.^[43, 45-49] Moreover, also complexes can be used as chromophore with a subsequent energy transfer to another metal ion as shown using $\text{Re}(\text{CO})_3\text{Cl}$ and $\text{Ru}(\text{bpy})_3$ chromophores coupled to Ln -porphyrin units leading to absorption at the Re^{I} or Ru^{II} centre, followed by an energy transfer to and emission at the Ln^{III} centre.^[50]

3.2 Magnetic Properties of 3d- and 4f Metal Ion-containing Complexes

In order to understand the magnetic properties of complexes a few physical quantities need to be defined that will be used throughout this thesis.

The magnetic field H in vacuum is connected to the magnetic flux density B via the magnetic permeability in vacuum. In matter, the magnetisation of the material needs to be accounted for:

$$B = \mu_0 \cdot H \quad \text{equation 3}$$

where μ_0 = Bohr magneton. As most magnetic measurements, and certainly the ones presented in this thesis, are not performed in vacuum, B in units of Tesla (T) is used to describe the magnetic field applied to the respective samples.

Another important quantity often used in magnetism is the magnetic susceptibility χ . It is defined as:

$$\chi = \frac{dM}{dH} \quad \text{equation 4}$$

During the analysis of the magnetic measurements presented below the molar susceptibilities of the respective compounds are used to enable a comparison of the values to the literature.

There are two basic forms of magnetism, diamagnetism which is present in all elements but hydrogen and stems from paired electrons, and paramagnetism which originates from unpaired electrons. Diamagnetism is not temperature dependent. Diamagnetic materials expel field lines of the applied external magnetic field, while paramagnetism is generally temperature dependent and concentrates field lines of applied external magnetic fields. The susceptibility in vacuum is zero, for diamagnetic samples it becomes negative and for paramagnetic samples it becomes positive. Data obtained from magnetic measurements is corrected for diamagnetic components such as the sample holder, the eicosane used to immobilise powder samples as well as the intrinsic diamagnetic contribution of paired electrons in ligands.

The temperature dependence of a paramagnet can be described using the Curie law:^[51-52]

$$\chi = \frac{C}{T} \quad \text{equation 5}$$

where C, the Curie constant is defined as:

$$C = \mu_0 N_A \frac{g_j^2 J(J+1) \mu_B^2}{3k_B} \quad \text{equation 6}$$

where N_A is the Avogadro constant, J is the total angular momentum, k_B is the Boltzmann constant and g_j is the Landé factor obtained the following way:

$$g_j = 1 + \frac{J(J+1) + S(S+1) - L(L+1)}{2J(J+1)} \quad \text{equation 7}$$

where S is the total spin moment and L the total orbital angular momentum.

Few compounds show Curie paramagnetism, for example $\text{Gd}_2(\text{SO}_4)_3 \cdot 8\text{H}_2\text{O}$ which only deviates from Curie behaviour below 0.182 K.^[52] The good agreement of the temperature dependence of χ with the Curie law in this compound is a result of the separation between the Gd^{III} centres through the large counterions and lattice water.

When (para)magnetic centres are close together, magnetic coupling leads to collective magnetism. This means, depending on the type of coupling, the spins align either parallel or antiparallel to each other below a characteristic temperature. Ferromagnetism describes the parallel alignment of spins below the so-called Curie temperature (T_C). This means in unmagnetised ferromagnetic materials the spins are randomly oriented at $T > T_C$ resulting in no observable magnetisation. However, below T_C they start to align parallelly resulting in magnetisation of the material. Correspondingly, antiferromagnetism describes antiparallel alignment of spins below the so-called Néel temperature (T_N) leading to zero magnetic moment at low temperatures as all spins are aligned in the ground state. Above T_N antiferromagnets, as seen for ferromagnets above T_C , behave like a Curie paramagnet (see figure 4). In a ferrimagnet the spins align antiparallel but have different magnitudes leading to an overall magnetic moment. A naturally occurring example for a ferrimagnet is magnetite (Fe_3O_4). The structure of magnetite was reported to be a spinel type by Bragg in 1915^[53] and found to in fact be an inverse spinel structure by Verwey and de Boer in 1936.^[54] In this structure Fe_3O_4 ($\text{Fe}^{II}\text{Fe}^{III}_2\text{O}_4$), half of the trivalent iron ions are tetrahedrally coordinated by the oxygens while the divalent and the rest of the trivalent iron ions are octahedrally surrounded by oxygens. Magnetically the two sub-lattices

are aligning antiparallel to each other. As the Fe^{III} ions in the tetrahedral and octahedral positions compensate each other a saturation magnetisation of 4 μ_B from the Fe^{II} ions is the result.

The most common depiction of the temperature dependence is $\chi_M T$ vs T diagrams, which are shown for ferromagnetism and antiferromagnetism in figure 4.

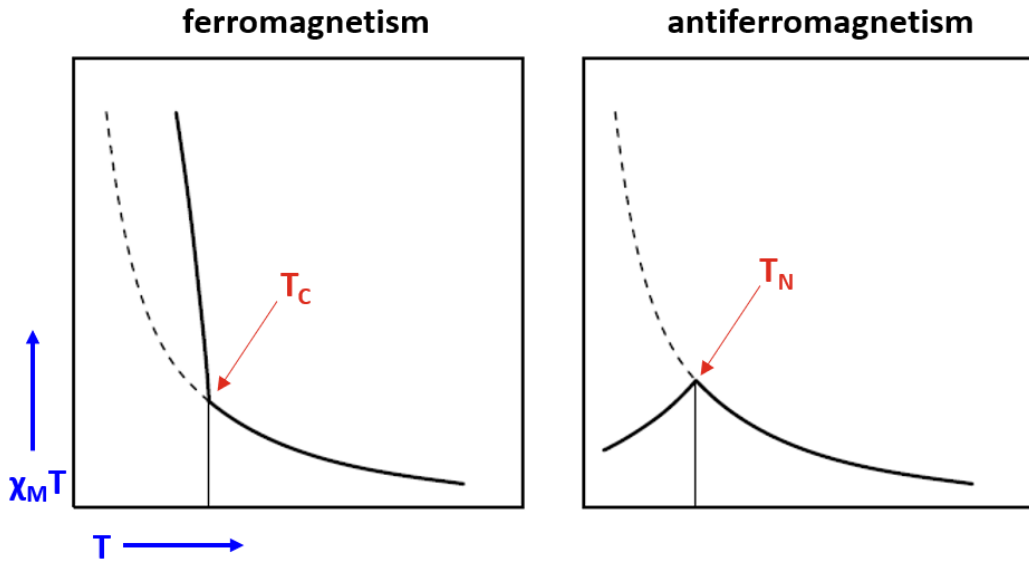


Figure 4. $\chi_M T$ vs T curves for a ferro- and an antiferromagnet (left and right, respectively) highlighting the Curie and Néel temperatures adapted from reference^[38]. The dashed lines correspond to the $\chi_M T$ vs T curve of a Curie paramagnet.

As shown in figure 4 above, materials showing collective magnetism no longer follow the Curie law below T_C or T_N and have to be described using the Curie-Weiss law which introduces the Weiss constant θ accounting for the effect of the magnetic coupling between the ions:

$$\chi = \frac{C}{T-\theta} \quad \text{equation 8}$$

The Weiss constant, which is the x-axis intercept of χ_M^{-1} vs T curves is negative for antiferromagnetically coupled materials and positive for ferromagnetically coupled ones (and zero for Curie paramagnets regaining the Curie law for $\theta = 0$).

Therefore, the Curie-Weiss law can also be used to analyse magnetic data to confirm the presence and sign of the magnetic coupling by plotting the inverse susceptibility vs temperature and fitting the data to the Curie-Weiss law (see figure 5).

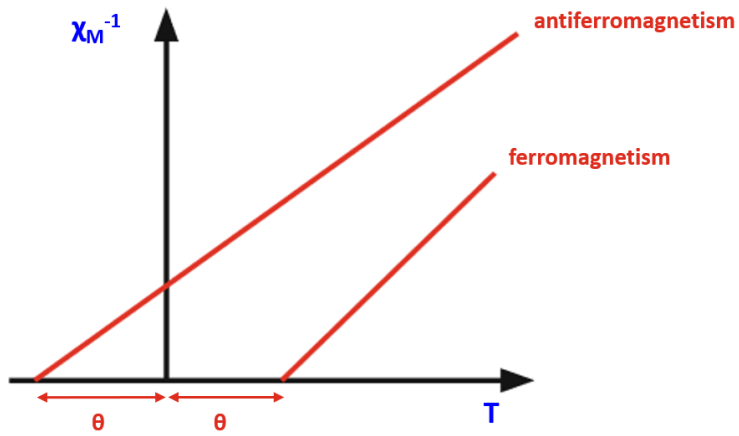


Figure 5. Curie-Weiss plot for a ferro- and an antiferromagnet showing the positive and negative Weiss constants of the respective interaction. Adapted from reference^[39].

In unmagnetised ferromagnets the spins are aligned randomly therefore there is no magnetisation observable. When an external magnetic field is applied increasing in strength, the spins in their respective Weiss domains start aligning in the direction of that field creating the initial curve. The magnetisation keeps increasing until reaching the saturation field H_s at which all spins are parallel to the external field leading to the maximal magnetisation of the material, M_s the saturation magnetisation. After turning off the magnetic field the magnetisation does not return to zero, instead a proportion of the magnetisation is retained, the so-called remanence M_R . In order to de-magnetise the ferromagnet a magnetic field has to be applied in the opposite direction. The field it takes to reduce the magnetisation to zero again is called the coercive field H_C . An example for a magnetic hysteresis is shown in figure 6.

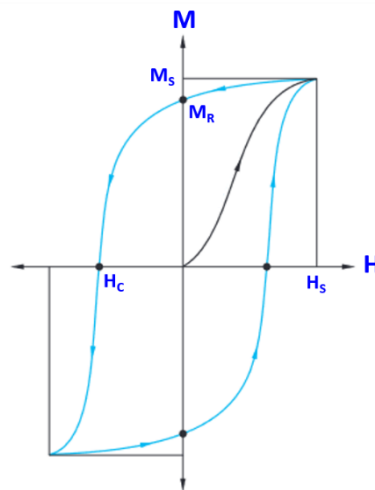


Figure 6. Depiction of a magnetic hysteresis showing the saturation magnetisation and field (M_s and H_s) as well as the remanence M_R and the coercive field H_C . Adapted from reference^[38].

But how does magnetic coupling lead to collective behaviour? When magnetic ions are too far apart to interact *via* direct orbital overlap, exchange interactions can occur using the superexchange mechanism which takes place between neighbouring magnetic ions *via* a diamagnetic bridging ligand. When the M-O-M angle is 180° this leads to antiferromagnetic coupling, but if the M-O-M angle is 90° the interaction results in ferromagnetic coupling as shown in figure 7. This is also described by the Goodenough-Kanamori-Anderson rules.^[55-57]

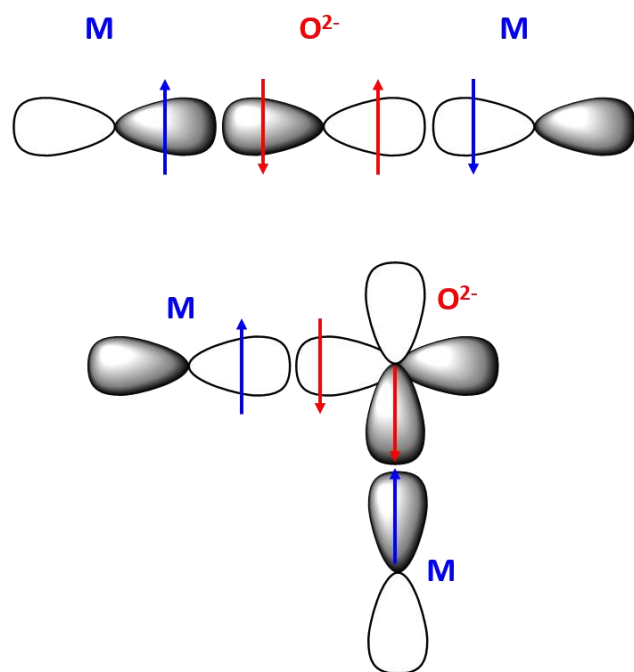


Figure 7. 180° and 90° superexchange respectively leading to antiferro- and ferromagnetic interactions.

Another mechanism for magnetic exchange interactions, double exchange, is observed in mixed-valent systems such as perovskite manganites.^[58] Here, the interaction takes place transferring an electron from a Mn^{III} to a bridging O²⁻ which in turn transfers an electron to the neighbouring Mn^{IV} ion. As for the Pauli principle these two electrons (as the one on the oxygen is simply replaced) must have the same spin quantum number. Therefore, the magnetic interaction resulting between the two manganese ions is ferromagnetic. This was also observed in a mixed-valent V^{II}/V^{III} compound by Long *et al.* in 2010.^[59-60] Additionally, the double exchange mechanism effectively results in the two manganese ions in the perovskite manganites swapping valency, the Mn^{IV} ion is reduced to Mn^{III} since it accepts the oxygen electron, while the Mn^{III} ion is oxidised to Mn^{IV} by replacing the oxygen electron (see figure 8).

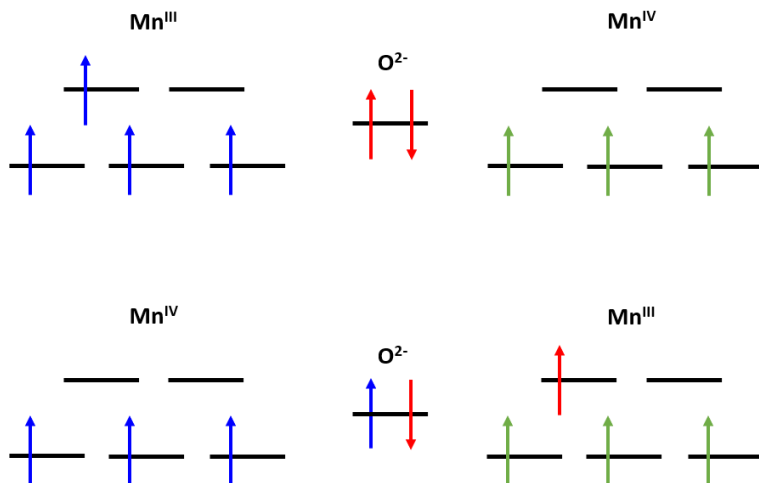


Figure 8. Illustration of the situation before (top) and after (bottom) the double exchange in mixed-valent manganites showing the ferromagnetically coupled manganese ions.

In addition to exchange interactions which require orbital overlap, magnetic centres interact through space *via* dipolar coupling. In dimeric complexes with well-defined parallel anisotropy axes as in centrosymmetric Dy^{III} dimers, which is very relevant for this work, the sign of the dipolar interaction can simply be determined by the angle of the anisotropy axes to the Dy-Dy vector. If the angle is more obtuse than the magic angle (54.74°), at which the dipolar coupling is exactly zero, the resulting interaction is antiferromagnetic.^[61-62] If the angle between anisotropy axes and Dy-Dy vector is more acute than the magic angle, the resulting interaction will be ferromagnetic. Especially in lanthanide based systems intramolecular dipolar coupling is often magnitudes stronger than exchange coupling due to the diffuse nature of the f-orbitals leading to less orbital overlap necessary for the latter. Dipolar coupling can also occur intermolecularly but since the strength of the interaction scales with r^{-3} (see equation 9), with r being the intermolecular M-M distance, this is often negligible.^[61-63]

$$E_{dip} = \frac{-\mu_0 \mu_a \mu_b}{4\pi r^3} (3\cos^2\theta - 1) \quad \text{equation 9}$$

3.3 Intermolecular Interactions

In addition to molecular properties that influence the magnetic and optical behaviour of complexes, such as the ligand field as described above, there are intermolecular interactions between these complexes. Since it is very rarely possible to study isolated molecules of complexes on their own and most analysis is done on randomly oriented

powder samples, the investigation of these intermolecular interactions is essential for understanding the experimentally observed behaviour. This is also true for single crystal measurements which may provide further insight due to elimination of the effect of random orientation. However, these are still affected by the intermolecular interactions within the crystal. There are many types of intermolecular interactions that determine the packing of clusters, therefore only the ones most relevant to the results presented here are discussed.^[64]

The most common, and therefore well-studied interaction, is hydrogen bonding which can occur intra- as well as inter-molecularly. Hydrogen bonds (HBs) are prevalent in all of nature most famously in water and also in a large percentage of complexes. Another example that proves the vital importance of this type of intermolecular interaction is the involvement of HBs in the stabilisation of our DNA, as the nucleobase pairs are connected *via* two or three HBs in the adenine-thymine and guanine and cytosine pair, respectively.^[65] HBs are an interaction between a hydrogen atom that is covalently bound to a more electronegative HB donor and interacts with the lone pair of a close-by neighbouring atom of another molecule (HB acceptor) (see figure 9). The angle between the HB donor (HB_D) the hydrogen atom covalently bound to it and the HB acceptor (HB_A) is preferably close to 180° to ensure maximum interaction. This may not be the case when a hydrogen forms HBs to multiple HB_A atoms.

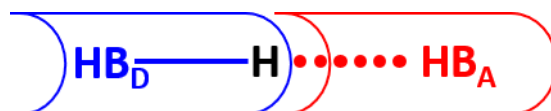


Figure 9. Schematic visualisation of a hydrogen bond HB highlighting the hydrogen atom (black) which is covalently bound to the hydrogen bond donor HB_D in blue and interacts with a lone pair of the hydrogen bond acceptor HB_A in red.

The strength of HBs spans a large range of energies. Commonly observed HBs lie in the range of 4-50 kJ/mol with those with strengths above 15 kJ/mol considered strong. However, there are extreme examples such as bihalide anions where the strength of the interaction can reach up to 161.5 kJ/mol.^[66-67] HBs on the weak end of the energy spectrum are essentially electrostatic in nature while stronger HBs result from additional charge transfer components and/or are resonance assisted.^[68] Resonance assisted hydrogen bonding occurs when the HB is involved in electron delocalisation as part of conjugation in $\text{O}=\text{CR}-\text{CR}=\text{CROH}\dots\text{HB}_A$ type situations.^[69-70] This has also been supported by computational studies.^[71]

Another type of interaction that provides intra- and/or intermolecular stability is so-called π stacking or π - π interactions. There are multiple possible arrangements for such interactions. Contrary to a common belief it was shown that for small aromatic molecules (below 10 Cs) a perfect face-face overlap of aromatic π systems is unfavourable (see figure 10, left).^[72-74] Instead, especially for electron rich aromatics, an edge-face arrangement (figure 10, middle) or an offset or parallel displaced π - π interaction aligning the electropositive region around the outside of the aromatic system with the electronegative centre of another (figure 10, right) are favoured.

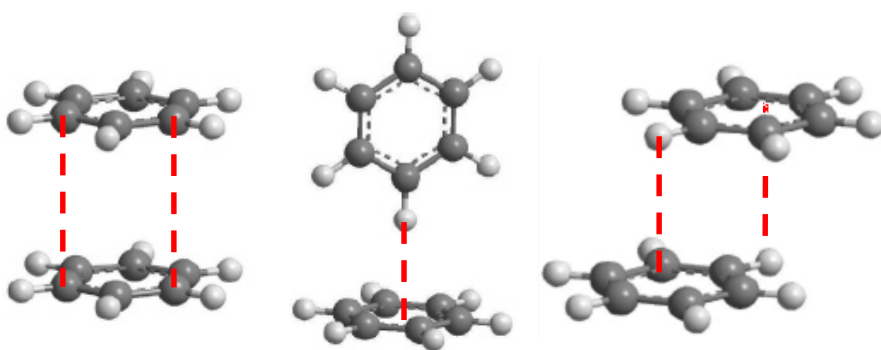


Figure 10. Different possibilities for the stacking of benzene dimers, face-face (left), edge-face (middle) and offset face-face (right). Adapted with permission from reference^[74] [American Chemical Society] copyright [2005].

Therefore, the π stacking interactions are not based on the maximum overlap of π electron clouds instead quite the contrary was proposed by Hunter and Sanders who demonstrate that overall attractive π - π interactions are actually a result of π - σ interaction outweighing the repulsion between two π systems.^[75] It therefore also relies on the efficient alignment of electropositive areas on the system with electronegative ones on another π system. This also implies a significant electrostatic contribution to this interaction in addition to dispersion effects which only become relevant at very short distances. This was also concluded in investigations studying adsorption of larger aromatic systems on graphene that arranged in an A-B sheet layered structure.^[76] From all the results presented above it can be concluded that π - π interactions preferably will occur in edge-face or offset face-face arrangements of the aromatic systems while face-face interactions between aromatics need an additional attractive component to achieve this geometry of the interaction. This is also shown in a series of mononuclear lanthanide complexes in which the Tb^{III} and Dy^{III} complexes form offset π - π stacks while the Er^{III} compound with the same molecular structure shows an edge-face arrangement of π systems.^[77]

Further intermolecular interactions which are relevant to this work are halogen-interactions. The key to understand this type of interaction is to take a closer look at the distribution of electron density around halogen atoms. If one considers an isolated halogen atom the electron distribution is spherical. When the halogen is covalently bound to another atom, for example a carbon atom belonging to an organic ligand, this leads to an electrophilic region of low electron density on the elongation of the covalent bond where the antibonding σ^* -orbital is located. This region is called the σ -hole. Instead, the electron density of the three unpaired electrons of the halogen is distributed in a belt orthogonal to the C-X bond creating a nucleophilic region of high electron density. A halogen bond is an interaction of the electrophilic σ -hole on the halogen atom X which is called the halogen bond donor XB_D (Lewis acid) with the lone pair/electron density on an atom of the neighbouring molecule, the halogen bond acceptor XB_A (Lewis base). This definition can sometimes be confusing and is therefore reiterated here: The electron density donor to this interaction is the XB_A and the electron density acceptor is the XB_D (see figure 11).^[78-79]

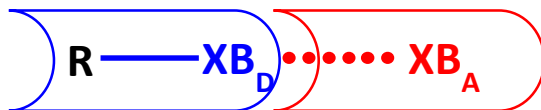


Figure 11. Schematic visualisation of a halogen bond. The halogen atom acts as the XB_D and an atom on the neighbouring molecule with a lone electron pair, that can interact with the σ -hole on the halogen, acts as XB_A . R often is an organic carbon that is covalently bound to the halogen.

In addition to the electrostatic component to the interaction between the lone pair and the σ -hole, there are further effects adding to this attractive interaction leading to distances between XB_A and XB_D being shorter than their combined VdW radii. Due to the intense colour of halogen bonded complexes, such as amylose-iodine, the interaction was originally thought to be exclusively CT-based before the discovery of the electrostatic interaction involving the σ -hole.^[78, 80] Nowadays, it is known that CT from the XB_A to the σ^* -orbital of the XB_D is one contribution to the XB among several others.^[78, 81-82] Furthermore, polarisation effects contribute to XBs. Since XB_A and XB_D are highly polarisable atoms which are closer to each other than their combined VdW radii, this leads to significant polarisation effects. For example, in CH_3Cl the entire electrostatic surface is negative *i.e.* there is no observable σ -hole. Nevertheless, the organic complex chloromethane-formaldehyde complex $\text{CH}_3\text{Cl}...\text{O}=\text{CH}_2$ was shown to exhibit an attractive interaction, due to the polarisation of the chlorine atom by the

electron density on the formaldehyde carbonyl.^[83] The influence of the polarisability of the XB_D has also been studied by Politzer and co-workers who investigated the size of the σ -hole of CF_3X with $\text{X} = \text{F}, \text{Cl}, \text{Br}$ and I . They found that the σ -hole got successively larger, the larger the halogen atom, with the fluorine version not having a σ -hole at all (see figure 12, left).^[84] Furthermore, comparing the σ -holes of CH_3Br , CH_2FBr , CHF_2Br and CF_3Br , it becomes clear that electron-withdrawing groups like fluorine enlarge the σ -hole on X and therefore lead to stronger XB donor properties (figure 12, right).^[85] The interaction strength of halogen bonds can vary over a broad range from 5 kJ/mol between $\text{Cl}\dots\text{Cl}$ in chlorocarbons to 180 kJ/mol between $\text{I}^-\dots\text{I}_2^-$ in I_3^- .^[83, 86] This exemplifies the tunability of halogen interactions by the use of differently polarisable XB_D atoms as well as stronger or weaker electron-withdrawing groups. Thus, in this work effective tuning of intermolecular interactions between metal clusters, that in turn affect the optical and magnetic properties, was explored.

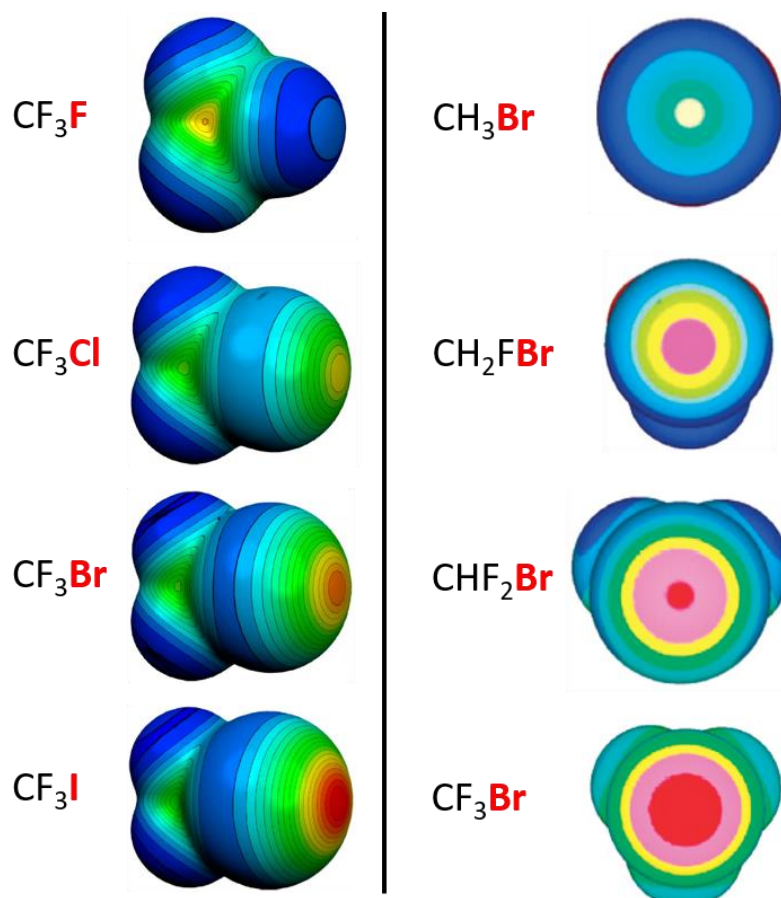


Figure 12. Electrostatic potential surfaces revealing the existence and comparing the relative size of the σ -hole upon variation of the XB_D (left), and upon variation of the electron-withdrawing groups (right). Adapted with permission from reference^[84] [Springer] copyright [2007] and reference^[85], respectively.

The XB_A atom is often a nitrogen atom interacting using its lone electron pair, such as was seen in the first identified halogen bond complex, $I_2...NH_3$, reported by Guthrie in 1863.^[87] Also other atoms such as oxygen act as XB_A , as reported by Hassel in 1954 where 1,4-dioxanate moieties use the lone electron pairs of the oxygens to interact with the σ -holes on bridging Br_2 molecules.^[88] It was also shown that π systems can act as XB_A as seen in a benzene- Br_2 adduct held together by halogen bonds.^[89]

Another special case is when halogen atoms act as both XB_D with their σ -hole and XB_A using their unpaired electrons. These halogen-halogen interactions are classified into two types according to the two $R-X...X$ angles θ_1 and θ_2 (see figure 13).^[90] The more obvious case is the type II interaction in which the σ -hole on one halogen atom is aligned with the electron density belt around the elongation of the $R-X$ bond on the other. Therefore, θ_1 has to be close to 180° in order to align the σ -hole and θ_2 is close to 90° in order to provide the electron density (see figure 13, right). Type II interactions are also called halogen-halogen bonds. In contrast in type I interactions θ_1 and θ_2 are equal and the interaction was previously often described to be a short contact due to packing requirements (figure 13, left). Therefore, short contacts between halogen atoms in type I geometry are not called halogen-halogen bonds, but only halogen-halogen interactions.

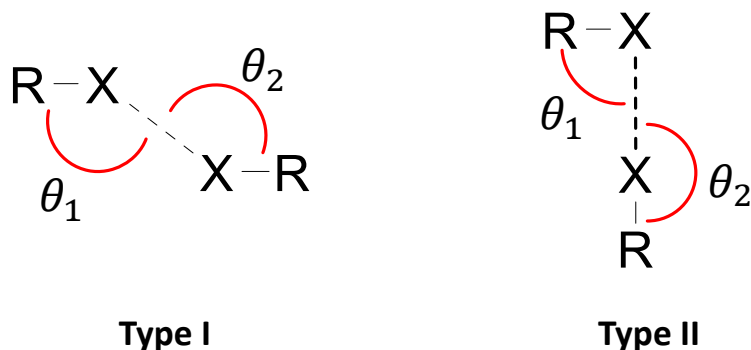


Figure 13. The classification into two types of halogen-halogen interactions according to the $R-X...X$ angles.

However, in a recent publication Scheiner calculated the principal forces holding together type I and type II dimers and found that the two types not only share the same forces to give rise to the interaction but also the interaction is only a slightly stronger for type II than type I geometries. He concluded the reason for this is that while type II interactions have a clear interaction direction (one donor, one acceptor), type I interactions have weaker interactions but in both directions. Therefore, in type I halogen-halogen interactions both halogen atoms act as XB_D and XB_A simultaneously.

This is because the angles between 90° and 180° allow the interaction of both σ -holes with the electron density of the other halogen. These two interactions amount to almost the same stabilisation energy as obtained from type II interactions. He further concluded that although the stabilisation energy of type I vs type II interactions may not differ much, type I interactions still do not represent a true minimum to the potential energy surface. Instead, type I geometries can be understood as the energetically most favoured pathway between two equal type II geometries (see figure 14), which would mostly result in spontaneous reversion to a type II interaction.^[91]

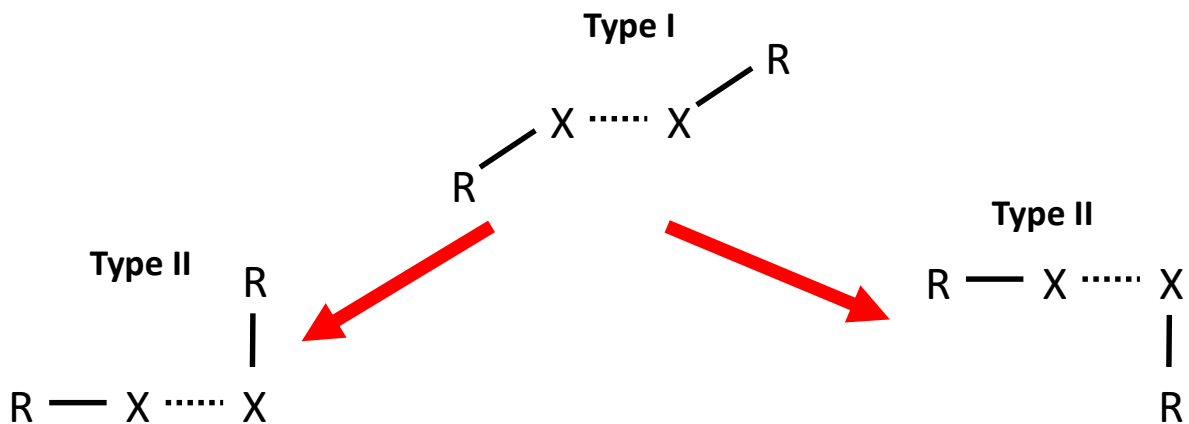


Figure 14. Type I halogen-halogen interactions as intermediate between two energetically degenerate type II halogen-halogen bond geometries as proposed by Scheiner.^[91]

Indeed, asymmetric halogen-halogen interactions were nearly always found to be of or close to type II geometry as illustrated by the scatter plot of iodine-iodine contacts (figure 15). Here, type I interactions are found on the diagonal and type II interactions are found near the values for θ_1 and θ_2 of 180° and 90° .^[92] This directionality is also one of the biggest advantages of using halogen-halogen interactions in crystal engineering and can help to rationally design structures exhibiting tailored properties.

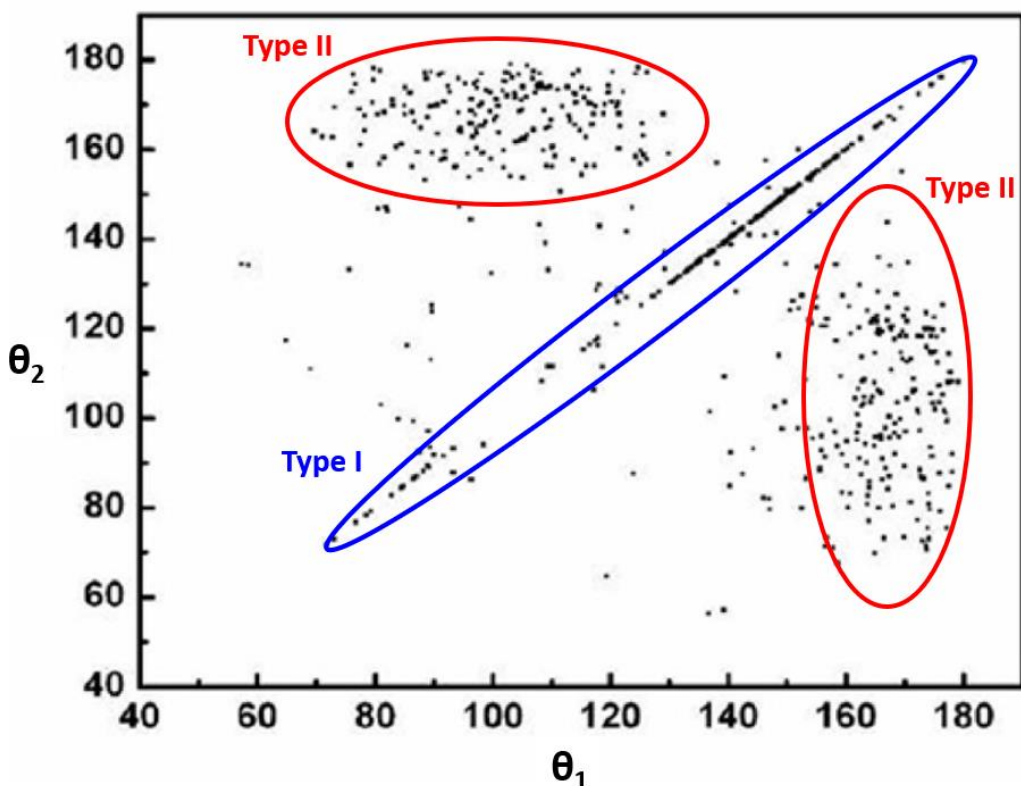


Figure 15. Scatter plot of short iodine-iodine contacts in the literature showing that if an iodine-iodine contact is asymmetric and therefore not type I, it will arrange close to type II geometry forming a halogen-halogen bond. Adapted from reference^[92] [American Chemical Society] copyright [2014].

3.4 Single Molecule Magnets (SMMs) and Relaxation Dynamics

SMMs are a class of materials that show slow relaxation of magnetisation which can lead to magnetic hysteresis similar to an extended solid state ferromagnet. Here, the hysteresis is not a result of long range order and direct interactions between paramagnetic ions, but instead of molecular origin. Therefore, when an SMM is magnetised by an external magnetic field and the field is turned off the molecules retain a proportion of their magnetisation for a certain length of time up to a temperature known as the blocking temperature T_B . This could enable the use of SMMs as molecular high-density data storage devices.^[3-4]

The first identified SMM is a mixed valence Mn_{12} cluster $[Mn_{12}(OAc)_{16}(H_2O)_4O_{12}]$ ($Mn_{12}ac$) which was first synthesised in 1980 by Lis *et al.*^[93] and identified to block magnetisation reversal over a decade later in 1993 by Prof. Dr. Roberta Sessoli during

her PhD work under Prof. Dr. Dante Gatteschi.^[1] The core structure of Mn₁₂ac is shown in figure 16 with the four Mn^{IV} ions in pink and the eight Mn^{III} ions in purple.

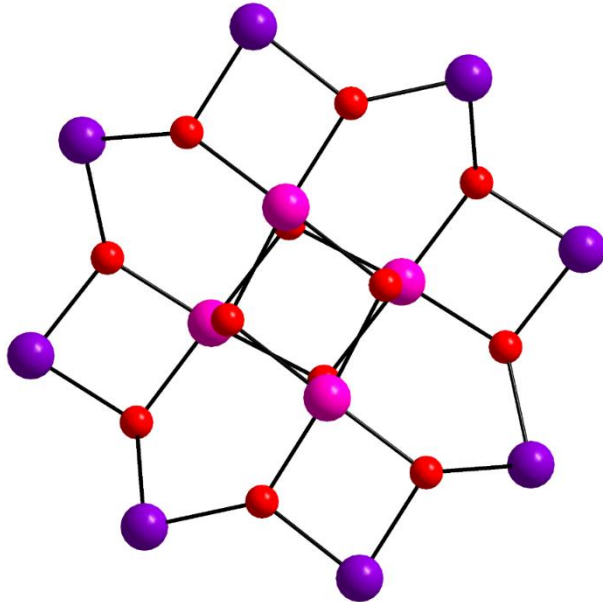


Figure 16. Core structure of Mn₁₂ac. The Mn^{IV} ions are shown in pink and the Mn^{III} ions in purple.

They identified that the thermal energy barrier that slows down the relaxation of magnetisation in Mn₁₂ac (see figure 17) depends on two parameters: Spin and anisotropy. The thermal energy barrier is defined for integer spin systems as^[2]

$$U = S^2 \cdot |D| \quad \text{equation 10}$$

and for half-integer spin as

$$U = \left(S^2 - \frac{1}{4}\right) \cdot |D| \quad \text{equation 11}$$

Where U is the energy barrier, S is the spin ground state and D is the anisotropy. This is where the mixed-valent nature of Mn₁₂ac is important. The molecular structure contains four ferromagnetically coupled Mn^{IV} ions (S = 6) in a tetrahedral arrangement in the centre, which are surrounded by a ring of eight ferromagnetically coupled Mn^{III} ions (S = 16). These two units are antiferromagnetically coupled leading to an overall spin ground state of S = 10. This leads to m_J states from -10 to 10 as shown in the depiction of the thermal energy barrier (figure 17).

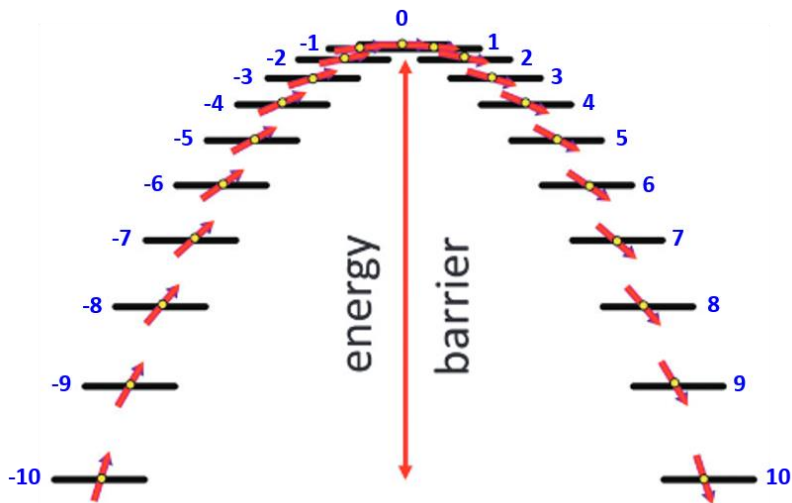


Figure 17. Energy barrier to magnetisation reversal in Mn_{12}ac with the m_J states indicated in blue. Adapted from reference^[21].

Looking at equation 10, there are two obvious ways to improve the energy barrier to magnetisation reversal. Firstly, as the barrier height scales quadratically with the spin ground state, clusters were synthesised with large ground states culminating in the record spin ground state of $83/2$ in a Mn_{19} cluster by Powell *et al.*^[94] However, this compound although containing anisotropic Mn^{III} ions, was found to have no molecular anisotropy due to the arrangements of the Jahn-Teller axes on these Mn^{III} centres. The resulting extremely small D value found from EPR by Waldmann *et al.* explains the lack of SMM behaviour. As Waldmann explained, this is a consequence of the fact that the energy barrier in a real system does not increase quadratically with S , since $|D|$ is inversely proportional to S^2 , therefore compensating the effect of a large spin ground state. For this reason he proposed that it would be better to focus on the second approach, the development of highly anisotropic low nuclearity systems.^[95] Indeed this led to successive improvements in barrier height and in turn SMM performance as exemplified by a pentanuclear mixed-valent $\text{Mn}^{\text{II}}_2\text{Mn}^{\text{III}}_3$ cluster with an energy barrier of 28.0 cm^{-1} ,^[96] a linear Fe^{I} compound with an energy barrier of 226 cm^{-1} ^[97] as well as a linear Co^{II} complex raising the bar to 450 cm^{-1} in 2018.^[98]

In order to further improve the barrier height, working groups all over the world shifted their focus towards lanthanide ions, some of which show strong single ion anisotropy due to spin-orbit coupling. Kramers ions in the series of Ln^{III} ions such as Dy^{III} also come with a degenerate doublet ground state which makes it predestined to be magnetically bistable.^[25] Non-Kramers ions such as Tb^{III} however need ligand fields of

certain symmetries to exhibit a degenerate ground state (so-called Ising doublet).^[25] This is exemplified by a Tb^{III}-phthalocyanine double-decker complex with D_{4d} symmetry reported by Ishikawa *et al.* which shows SMM properties.^[99-101]

The thermal pathway to relaxation of magnetisation, over the top of the energy barrier, is not the only relaxation mechanism. Quantum tunnelling of magnetisation QTM can occur either from the ground state (zero-field quantum tunnelling abbreviated as ZFQTM) or from an excited state (thermally assisted quantum tunnelling TAQTM). These also provide pathways to magnetic relaxation which become dominant especially at low temperatures. QTM occurs due to interactions between degenerate states, therefore magnetic dc fields which further split the m_J microstates can quench this pathway. Ideally, only the small internal field in the crystal would be needed to achieve this,^[25] but in reality it is often necessary to apply an external dc magnetic field. SMMs which show significant ZFQTM need such an external dc field in order to show slow relaxation of the magnetisation and are called field-induced SMMs.^[102-103] QTM due to transverse anisotropy (E) is forbidden in Kramers doublet systems (half-integer spin) with negative axial zero field splitting (D), giving another reason for the frequent use of Co^{II} (S = 3/2) and Dy^{III} (S = 5/2) ions in the attempt to produce compounds showing slow relaxation of magnetisation.^[2, 104-106]

Furthermore, there are direct and Raman processes which can provide pathways through instead of over the thermal energy barrier. The direct process is a two phonon relaxation mechanism, which is a consequence of direct spin-phonon coupling with one transition absorbing a phonon going into an excited state (± 2 in figure 18, bottom) and an emission of another leading to relaxation from the excited state back to the ground state with opposite spin direction (1 state in figure 18, bottom).^[21, 24-25] The Raman process works in the same way, the difference being that the Raman mechanism uses an intermediate virtual state instead of a real one.^[21, 24-25]

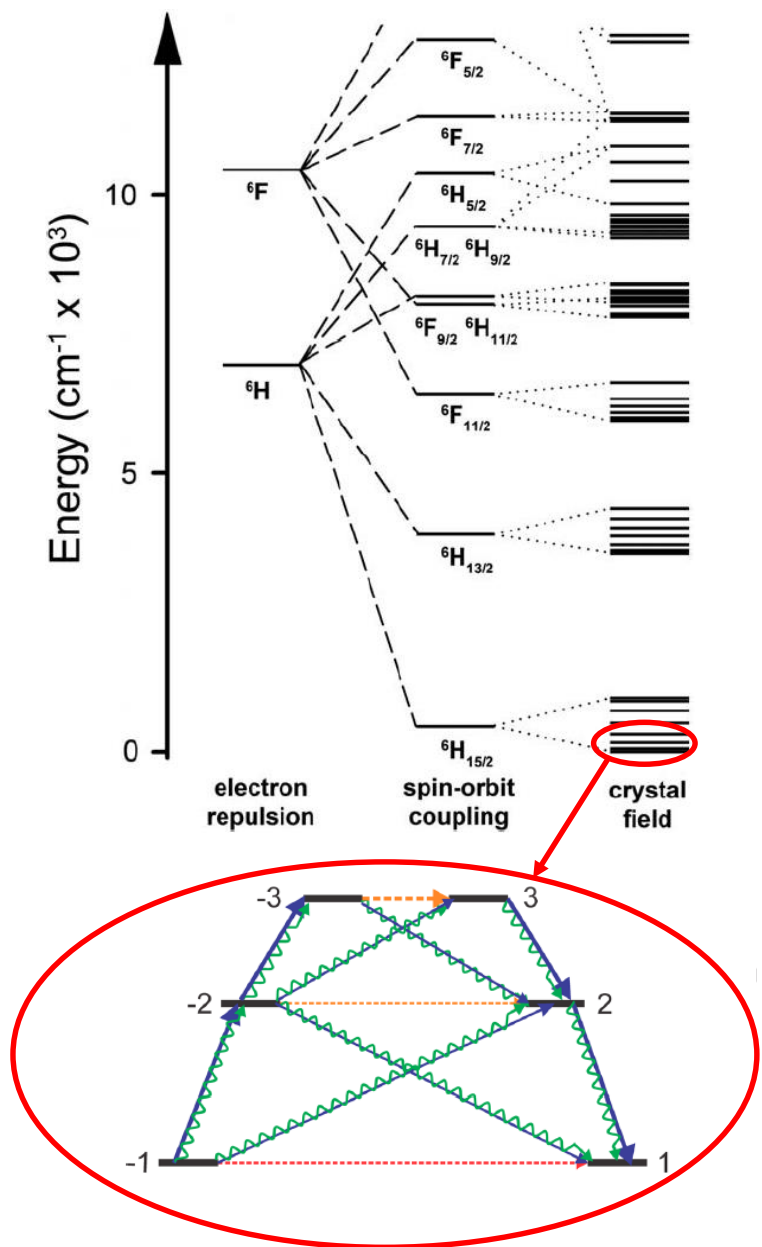


Figure 18. State splitting in a Dy^{III} ion due to electronic repulsion, SOC and crystal field (top). Adapted from reference^[107]. Possible relaxation mechanisms (bottom) with the red dashed line representing ZFQTM, the orange dashed lines representing TAQTM, the blue arrows showing relaxation via direct spin-phonon coupling and the green arrows showing Raman processes. Adapted with permission from reference^[25] [American Chemical Society] copyright [2016].

These additional pathways to relaxation are especially important in Ln^{III} ion containing SMMs which regularly show higher thermal energy barriers than their 3d transition metal containing counterparts but suffer from such through-barrier relaxation mechanisms. However, these do certainly also occur in 3d metal complexes as exemplified by the hysteresis plot for Mn₁₂ac in figure 19, in which QTM is visible as vertical jumps in magnetisation.

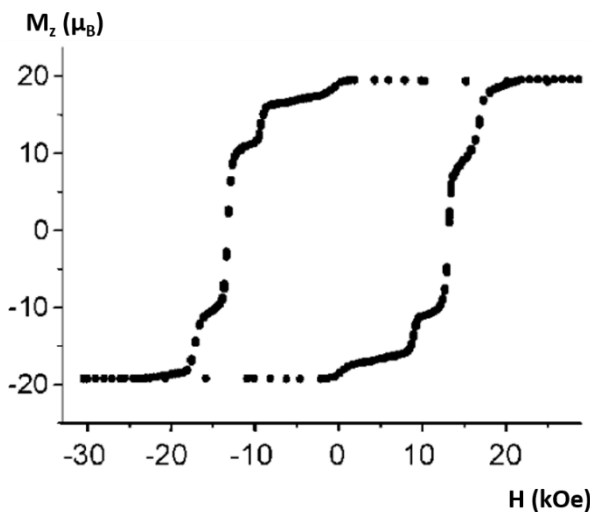


Figure 19. Hysteresis of Mn_{12}ac showing the vertical steps due to QTM. Adapted with permission from reference^[105] [John Wiley & Sons] copyright [2003].

Another advantage of using 4f ions is that Ln^{III} ions of similar size tend to form isostructural complexes. The single ion anisotropy of Ln^{III} ions changes throughout the series (see figure 20) and therefore provides an additional handle to tune the desired properties. Since Dy^{III} is a Kramers ion and exhibits both a high spin ground state with $S = 5/2$ and $J = 15/2$ as well as strong single ion anisotropy it has become the 4f ion of choice in the endeavour to improve SMM behaviour.

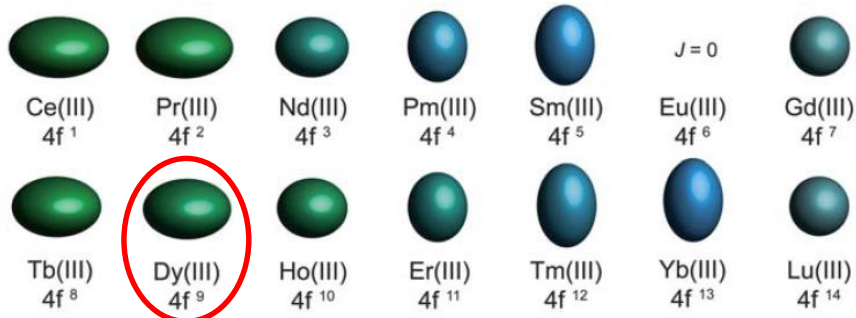


Figure 20. Visualisation of the single ion anisotropy ellipsoids of the series of Ln^{III} ions highlighting Dy^{III} . Adapted from reference.^[107]

There are multiple approaches to improve SMM behaviour using Dy^{III} ions: 1) Employing them in mixed 3d-4f complexes in order to benefit from the advantages of both transition metal and lanthanide ions. 2) Using radical ligands in order to enhance magnetic interactions. 3) Exploiting the specific shape of the single ion anisotropy ellipsoids of 4f ions in low nuclearity clusters through careful variation of the coordination environment.

The first mixed 3d-4f complex exhibiting SMM behaviour was reported by Osa *et al.* in 2003.^[108] Since then the field of 3d-4f complexes in the context of improving magnetic properties grew rapidly, developing in parallel to the investigation of purely 4f ion-containing compounds.^[109-111] One reason to combine 3d and 4f ions is the enhancement of magnetic exchange interactions, for example *via* a proposed mechanism involving higher Ln-based 5d, 6s and 6p orbitals, in order to quench QTM (see figure 21).^[24, 112-113] Strong superexchange in 3d-4f compounds can be exemplified by a series of compounds with the same overall core structure but different bridging ligands. In these Cr^{III}-Dy^{III} compound the exchange coupling was found to be as strong as 1.6 cm⁻¹ which is higher than most Ln^{III}-Ln^{III} exchange couplings.^[114] Another highlight was the synthesis of a Mn₁₈Dy cluster which shows the same core structure as the Mn₁₉ cluster discussed above with the central eight coordinate Mn^{II} ion exchanged for a Dy^{III} ion. This Mn₁₈Dy cluster now shows SMM behaviour exemplifying the synergistic effect the mixture of 3d and 4f ions can have.^[94, 115] Furthermore, the ability to control spins using the combination of 3d and 4f metal ions led to more exotic quantum chemical-/physical properties such as exciton formation and intermolecular charge hopping in Fe₁₀Ln₁₀ clusters,^[116] proximity to a quantum critical point that would lead to infinite ground states in the Fe₁₀Gd₁₀ analogue^[117] as well as toroidal systems such as a CrDy₆^[118] and Fe₁₈Dy₆ cluster.^[119] This makes 3d-4f clusters a research area that continues to expand.

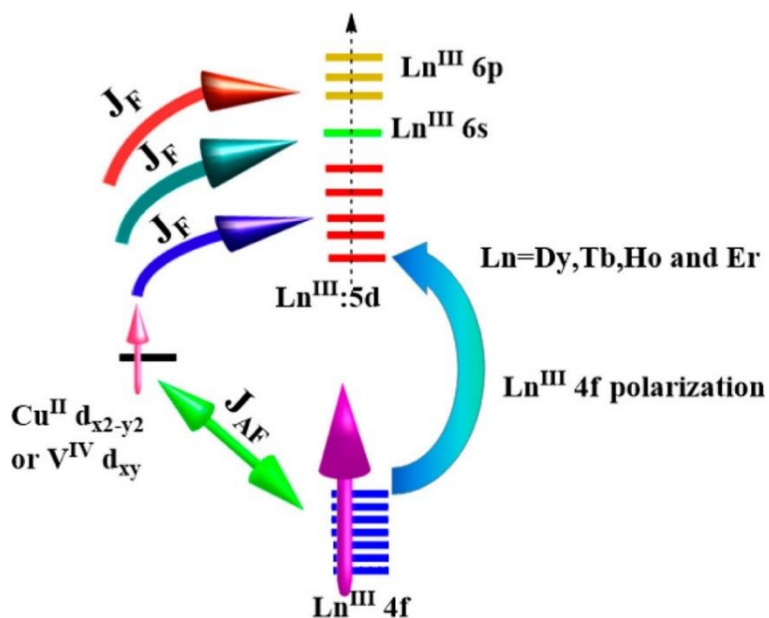


Figure 21. Proposed mechanism for the strong exchange interactions in 3d-4f compounds responsible for the quenching of QTM. Reprinted with permission from reference^[112] [American Chemical Society] copyright [2016].

The second approach employing radicals that was mentioned above also takes advantage of exchange interactions to quench quantum tunnelling and produce high performing SMMs. Using radical bridged Ln^{III} ions leads to extremely strong direct exchange interactions due to the diffuse spin orbitals of anionic radical ligands being able to interact with the 4f electrons that are located relatively close to the core and therefore rarely show strong exchange interactions.^[120] The success of this approach in molecules was first reported by Long *et al.* with a dinuclear $\text{N}_2^{\text{3-}}$ radical bridged complex (see figure 22) the Dy^{III} analogue of which showed an open magnetic hysteresis up to 8.3 K setting the record at the time.^[121] The use of radical ligands for enhanced magnetic coupling to quench QTM was then applied to more examples that were able to further validate this approach.^[120, 122-127] All of these examples exhibit extreme air sensitivity limiting their applicability. However, in 2017 Dunbar *et al.* reported the first air stable example, opening the door to a new class of radical bridged compounds.^[128]

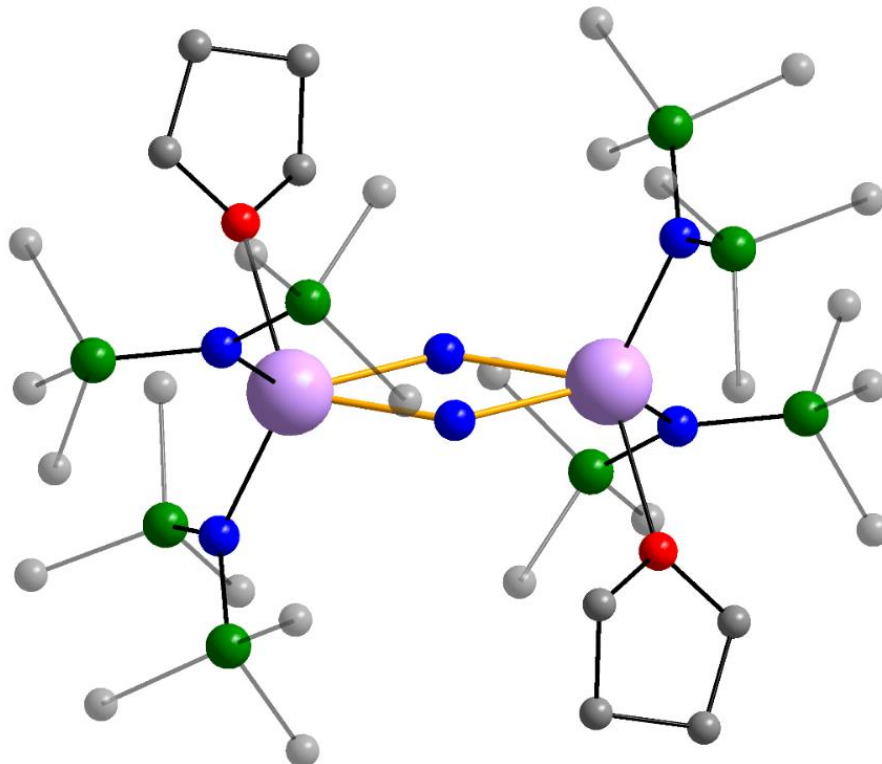


Figure 22. Molecular structure of the first example of a radical bridged SMM, the $\text{N}_2^{\text{3-}}$ -radical bridged $[\text{K}(18\text{-crown-6})][\text{Dy}_2(\mu_2\text{-N}_2)(\text{N}(\text{SiMe}_3)_2)_4(\text{THF})_2]$.^[121]

The radical bridging approach was carried to the extreme by the encapsulation of two Ln^{III} ions into a C_{80} fullerene. The Ln^{III} ions are bridged by a single electron creating a Ln-Ln bond with a bond order of 0.5 (see figure 23). The resulting $[\text{Tb}_2@\text{C}_{80}(\text{CH}_2\text{Ph})]$

analogue is not only air stable but was also shown to exhibit open hysteresis at 27 K and therefore is among the best SMMs as of today. Additionally, Popov *et al.* were able to show that while the fullerene cage isolates the Ln_2 pairs from each other, excluding intermolecular interactions, it remains permeable for electrons enabling further tuning of the magnetic properties by electrochemical means.^[129]

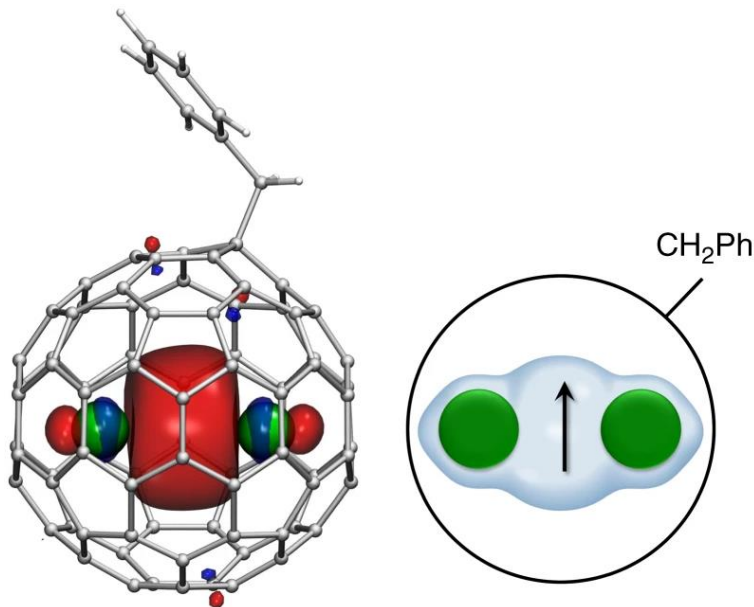


Figure 23. Structure of $[\text{Ln}_2@\text{C}_{80}(\text{CH}_2\text{Ph})]$ showing the singly occupied molecular orbital (left) and schematic representation on the right highlighting the unpaired electron. Reprinted from reference^[129].

The third approach mentioned above seeks to improve the single ion anisotropies of Ln^{III} ions by variation of the ligand environment. A Dy^{III} ion with its oblate anisotropy ellipsoid was predicted to benefit from coordination spheres with completely axial ligand fields, since this would further “squash” the ellipsoid and therefore enhance the anisotropy.^[24, 101, 107, 130-131] In contrast Er^{III} and Tm^{III} ions with their prolate anisotropy ellipsoids will benefit from an equatorial ligand field as shown by complexes employing Er^{III} with the aromatic cyclooctatetraene dianion COT^{2-} as ligand. This ligand with its hoop-like coordination sphere stabilises prolate anisotropy ellipsoids.^[132-135]

Indeed, Dy^{III} containing complexes with strongly axial ligand fields such as organometallic dysprosoceneum complexes (see figure 24) led to an increase in energy barrier above 1000 cm^{-1} . The first such reported cations, $[\text{Dy}(\text{Cp}^{\text{ttt}})_2][\text{B}(\text{C}_6\text{F}_5)_4]$ by Goodwin *et al.*, using two Cp^- ligands decorated with three *tert*-butyl groups each, also exhibited open hysteresis up to a then unprecedented temperature of 60 K.^[136] Variation of the Cp^- ligands to Cp^{iPr4H} , $\text{Cp}^{\text{iPr4Me}}$, $\text{Cp}^{\text{iPr4Et}}$ and Cp^{iPr5} led to a further increase in the temperature at which magnetic hysteresis is observed.^[137] The record

is held by a dysprosocenium complex $[\text{Dy}(\text{Cp}^*)(\text{Cp}^{\text{iPr}5})][\text{B}(\text{C}_6\text{F}_5)_4]$ with open hysteresis at 80 K and therefore above the magic barrier of liquid nitrogen (77 K).^[27] The molecular structures of these six dysprosocenium compounds are shown in figure 24. Additionally, their energy barriers as well as the Cp-Dy-Cp angles and Dy-Cp_{centroid} distances responsible for the difference in magnetic behaviour between them are listed in table 1. All six crystallise with a $\text{B}(\text{C}_6\text{F}_5)_4^-$ counteranion. These are omitted for clarity in figure 24. The reason for the higher performance of $[\text{Dy}(\text{Cp}^*)(\text{Cp}^{\text{iPr}5})][\text{B}(\text{C}_6\text{F}_5)_4]$ is its asymmetric nature. The Cp ligand with five *iso*-propyl residues promotes Cp-Dy-Cp angles closer to 180° and the less sterically hindered Cp* ligand is responsible for the shorter Dy-Cp_{centroid} distance increasing the donor strength of the axial ligands.^[27] This, as predicted, leads to some of the best-performing SMMs as of today. However, these organometallic compounds have one disadvantage that makes their application incredibly challenging, their severe air sensitivity.

Table 1. Energy barriers, Cp-Dy-Cp angles and Dy-Cp_{centroid} distances for the six dysprosocenium SMMs mentioned above.

Ligands	$(\text{Cp}^{\text{ttt}})_2$	$(\text{Cp}^{\text{iPr}4\text{H}})_2$	$(\text{Cp}^{\text{iPr}4\text{Me}})_2$	$(\text{Cp}^{\text{iPr}4\text{Et}})_2$	$(\text{Cp}^{\text{iPr}5})_2$	$(\text{Cp}^*)-(\text{Cp}^{\text{iPr}5})^-$
Reference	107	108	108	108	108	109
$U_{\text{eff}} (\text{cm}^{-1})$	1223	1285	1468	1380	1334	1541
Cp-Dy-Cp angle (°)	152.7(1)	147.2(8)	156.6(3)	161.1(2)	162.1(7)	162.507(1)
Dy-Cp_{centroid} distance (Å)	2.316(3)	2.29(1)	2.298(5)	2.302(6)	2.340(7)	Cp*: 2.296(1) Cp ^{iPr5} : 2.284(1)

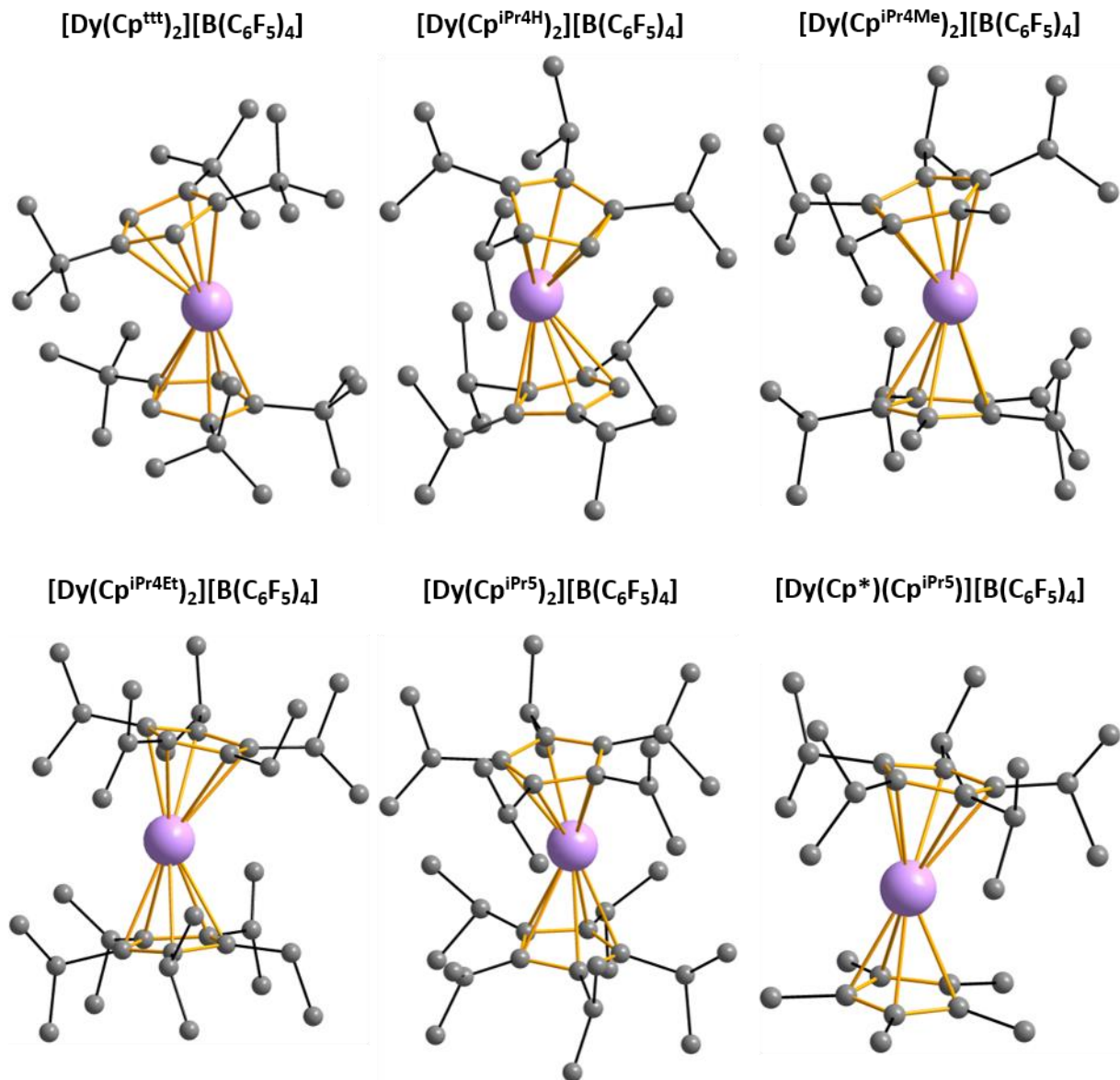


Figure 24. Molecular structures of the high temperature dysprosocene SMMs. Counteranions and hydrogens are omitted for clarity.^[27, 136-137]

Recently, the approach used by Popov *et al.*, to bridge Ln^{III} ions with a single electron, was combined with the approach seeking to maximise axiality, resulting in mixed-valent [Ln₂(Cp^{iPr5})₂I₃] compounds.^[26] The molecular structure of this complex is shown in figure 25. It forms a Ln-Ln bond with a bond order of 0.5 with an unpaired electron in a σ molecular orbital of Ln-based 5d_{z²} parentage. This drastically increases the interaction strength (J_{exchange} of the gadolinium analogue = +387 cm⁻¹) as emphasised by theoretical calculations^[26, 138] and leads to a record energy barrier of 1631 cm⁻¹ in the dysprosium analogue. The reason for this is that all spins, the ones of the dysprosium ions as well as the single unpaired electron, are collinear in this system as also evident by the positive value for the exchange coupling.^[26] The magnetic

hysteresis closes at 80 K matching the $[\text{Dy}(\text{Cp}^*)(\text{Cp}^{\text{iPr}5})][\text{B}(\text{C}_6\text{F}_5)_4]$ compound mentioned above but relaxation times are much longer in the compound employing the Ln-Ln bond with τ about 1000 s at over 60 K while the compound by Layfield *et al.* reaches $\tau = 1000$ s only at about 30 K.^[26-27]

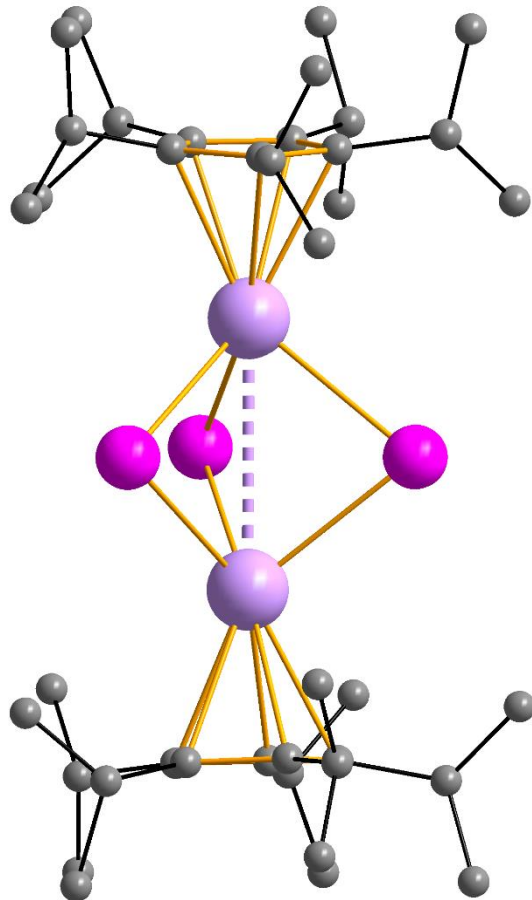


Figure 25. Molecular structure of $[\text{Ln}_2(\text{Cp}^{\text{iPr}5})_2\text{I}_3]$ highlighting the central metal-metal bond using one unpaired electron.^[26]

Having established how to effectively quench QTM as a relaxation pathway, as evidenced by the high temperature SMMs presented above, the next challenge requires the quenching of phonon-based relaxation processes such as the Raman process. The quenching of Raman processes in the dysprosium compound shown in figure 25 above appears to be the reason for the longer relaxation times at higher temperatures compared to the dysprosocenium compounds. This emphasises the importance of rationalising the design options that quench such phonon-based processes.^[26]

The role of phonons in spin relaxation and how to treat magnetic data to accommodate for this is currently under hot discussion in the SMM community.^[22, 139-144] The

previously favoured equation to fit the Arrhenius plot ($\ln(\tau)$ vs $1/T$), used to extract relaxation rates of different mechanisms to relaxation of the magnetisation (see equation 12), has more and more become viewed as overparameterised. In addition, the physical sense of describing the Raman exponent n with a power law is criticised. The reason for this is that the description of Raman exponents between 2 and 7 as a superposition of optical and acoustic phonons, may not be valid in molecular systems (in contrast to extended solid state structures) as elaborated by Gu and Wu.^[140-141]

$$\tau(T)^{-1} = AT + B + CT^n + \tau_0^{-1} \exp\left(-\frac{U}{k_B T}\right) \quad \text{equation 12}$$

where A is the parameter describing the direct process, B the parameter describing the ZFQTM, C being the prefactor for the Raman term with the Raman exponent n , τ_0 is the preexponential factor of the Orbach term, U the thermal energy barrier and k_B the Boltzmann constant.

Two working groups independently came forward with alternative equations both employing exponential laws to describe Raman-type relaxation.^[139-141] Equation 13 as seen below was proposed by Lunghi *et al.* and is the fitting function that was used to fit relaxation data in the present work.^[139]

$$\tau(T)^{-1} = AT + B + V \frac{\exp\left(-\frac{w}{k_B T}\right)}{\left(\exp\left(-\frac{w}{k_B T}\right) - 1\right)^2} + \tau_0^{-1} \exp\left(-\frac{U}{k_B T}\right) \quad \text{equation 13}$$

Where A is the parameter describing the direct process, B the parameter describing the ZFQTM, V the preexponential factor for the Raman term, w the energy barrier associated with Raman relaxation, τ_0 being the preexponential factor of the Arrhenius law-like Orbach term and U the associated energy barrier.

To avoid overparameterisation using this equation, the Arrhenius-law type Orbach term can be left out (set to 0) when fitting data obtained at low temperatures. Significant contribution of Orbach type relaxation only plays a role at temperatures of above at least 10 K for the systems presented in this thesis.

4. The Biquinoxen Platform

4.1 Introduction

One aspect of the biquinoxen system that is central to this chapter is its redox non-innocence and the ability to stabilise radical species. There are many examples of molecules able to form stable radical species such as nitronyl nitroxides,^[145-149] verdazyls,^[150] thiazyls^[151] and quinones^[152] (see figure 26) that are attractive to use for a wide variety of applications.^[153] Quinones are especially important to chapter 6 and are therefore introduced in more detail there.

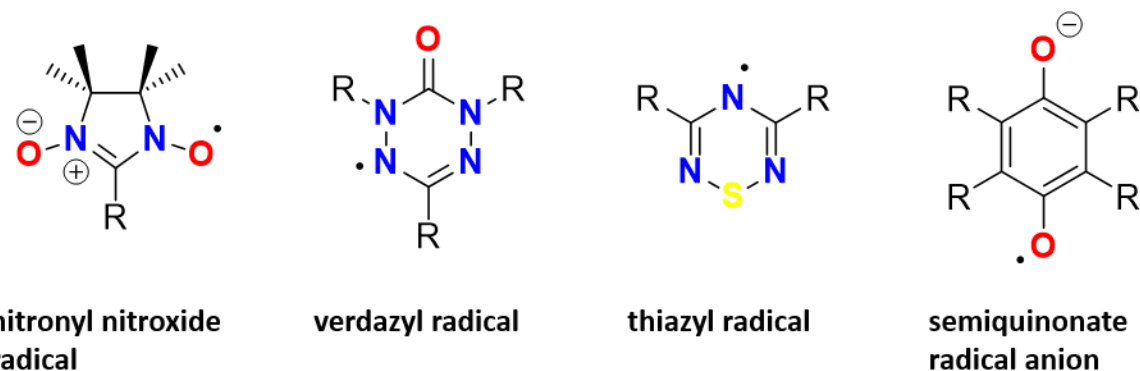


Figure 26. Examples for four types of stable radicals.

Stable radicals can for example be used in polymer synthesis,^[154] as fluorescent dyes^[155] or as spin carriers in magnetic molecules.^[156] The use of radicals to design molecules with enhanced magnetic exchange interactions leading to high-performant SMMs was previously discussed in chapter 3.4.^[121] However, redox non-innocence and availability of stabilised radical species of ligands can also be used to tune such exchange interactions. This was shown for a dinuclear Ni^{II} containing complex that exhibits switchable magnetic exchange ranging from weakly antiferromagnetic to very strongly ferromagnetic through control of the redox state of the pyrazine-based ligand.^[157] Even purely organic radicals were shown to be able to exhibit interesting magnetic properties such as magnetic bistability and room temperature ferromagnetism.^[148, 158-160]

Instead of using radicals for molecular design, they can also be used for crystal design since radicals in delocalised π -systems tend to form so-called pancake bonds (see figure 27).^[151, 161-162] Pancake bonds are radical-radical interactions between neighbouring π systems through overlap of their singly occupied molecular orbitals

(SOMO),^[163] that can lead to distances between the π systems that are shorter than double the VdW radius of carbon of 3.4 Å.^[164] In purely organic radicals or complexes using diamagnetic metal ions this often leads to an overall diamagnetic material,^[165] while in complexes employing paramagnetic metal ions it can be used to bring magnetic centres into close proximity which has a significant impact on the magnetic properties.^[166-167]

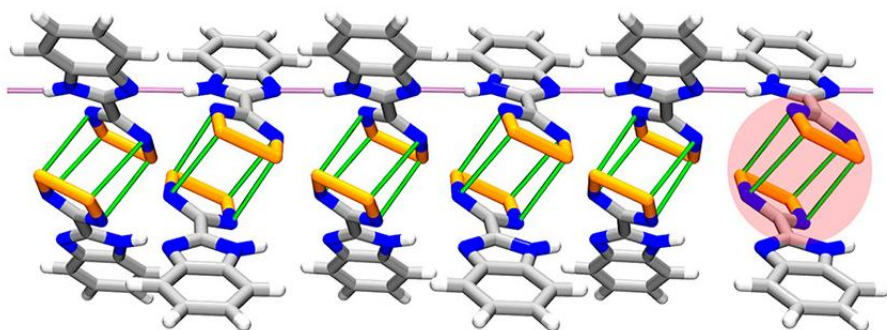


Figure 27. Pancake bonding used for crystal design on the example of the 4-(2'-benzimidazolyl)-1,2,3,5-dithiadiazolyl radical, crystals of which exhibit magnetic bistability. Reproduced from reference^[159] with permission [American Chemical Society], copyright [2018].

Another class of naturally occurring non-innocent ligands that can stabilise radicals and which are amongst the most stable radical species are viologens (1,1'-disubstituted-4,4'-bipyridinium ions).^[168-171] These undergo reversible redox processes between a dication, a radical cation and a neutral form. In addition to the reversible redox states of viologens, modifications of the 1,1'-residue (see figure 28) allow for a plethora of applications, for example as herbicides,^[172] fluorescent dyes,^[173-174] electrochromic displays^[175-179] or molecular machines.^[178-182] Kaim *et al.* have shown that by altering the π system of viologens and introducing further N-heteroatoms, such molecules can also be used as ligands similar to 2,2'-bipyridine.^[183] With a similar goal in mind and keeping the non-innocent redox properties of viologen-like molecules intact while providing the possibility to coordinate to metal ions, investigation of the biquinoxen system began in the Powell group in 2016.^[30] The system was not only shown to be able to stabilise radical species, but its coordinative properties were exemplified by the successful synthesis of a Cd^{II} complex employing the methylbiquinoxen dication (see figure 28) as ligand.

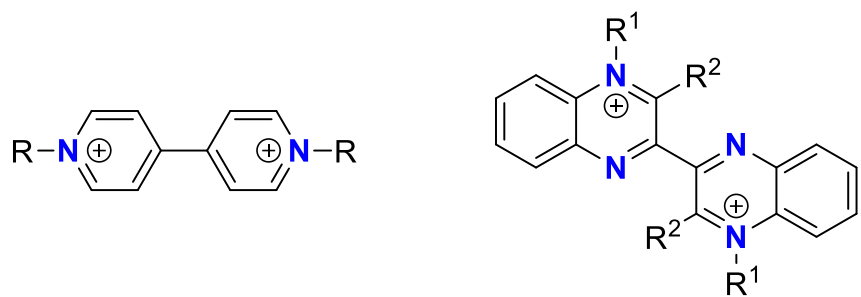


Figure 28. The viologen dication (left) and the biquinoxen dication (right) showing the similarities between the two systems.

Furthermore, it was shown that the biquinoxen system exhibits the same possibility for modification of the N-residue (R^1 in figure 28 above) by the synthesis of the methyl, ethyl, propyl and benzyl versions,^[184] in addition to the synthesis of the methylbiquinoxen dipseudobase as well as adducts that vary R^2 .^[29] This shows the versatility of this new viologen-like ligand system that promises the potential for plentiful applications. It was also found that the dication, strongly luminescent alcohol-based adducts as well as the dipseudobase form a pH dependent equilibrium (see figure 29).

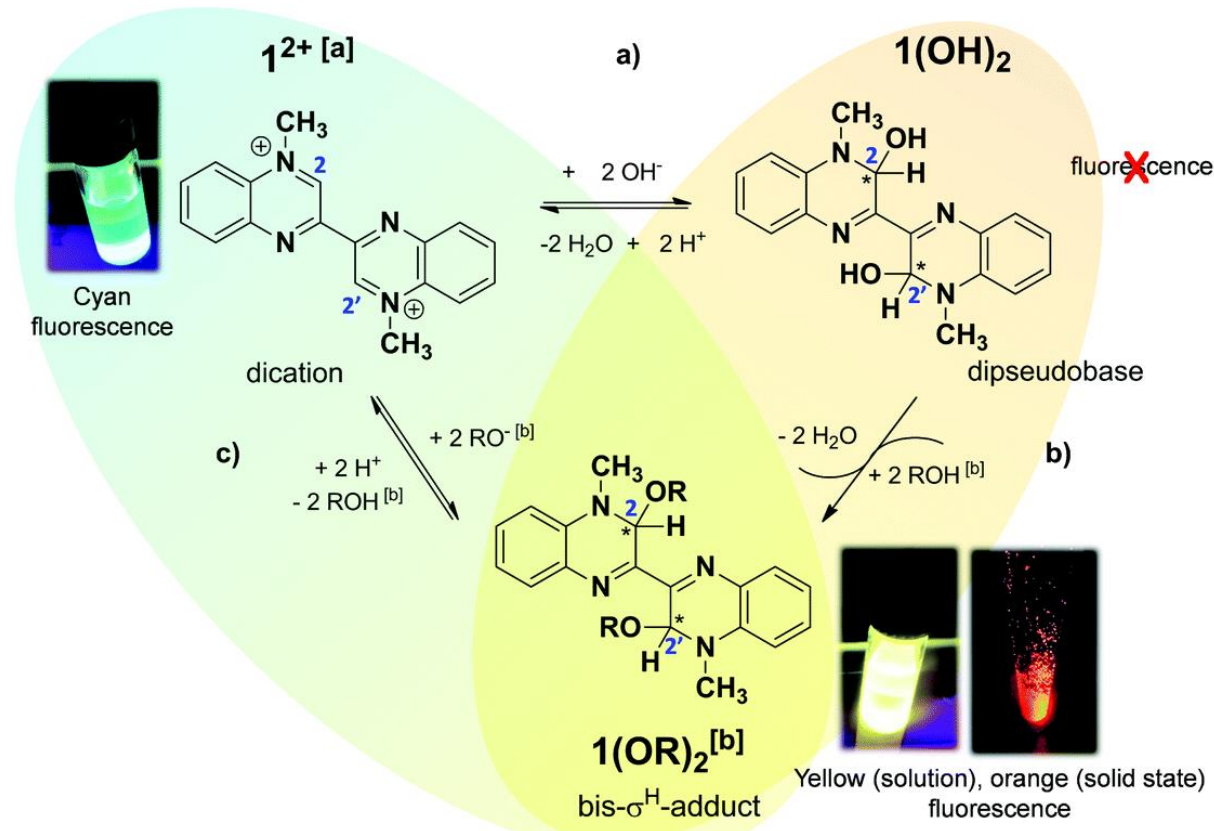


Figure 29. Equilibrium process between the methylbiquinoxen dication, the alcohol-based adducts as well as the methylbiquinoxen dipseudobase. Reprinted from reference.^[29]

In the work which is presented in the following sections the methylbiquinoxen dipseudobase ($(\text{Mbqn-OH})_2$) was used as a starting material. Therefore, the compound was reproduced using the literature procedure. The four reaction steps are shown schematically in figure 30 and further details concerning the synthesis can be found in chapter 8.1.^[29-30]

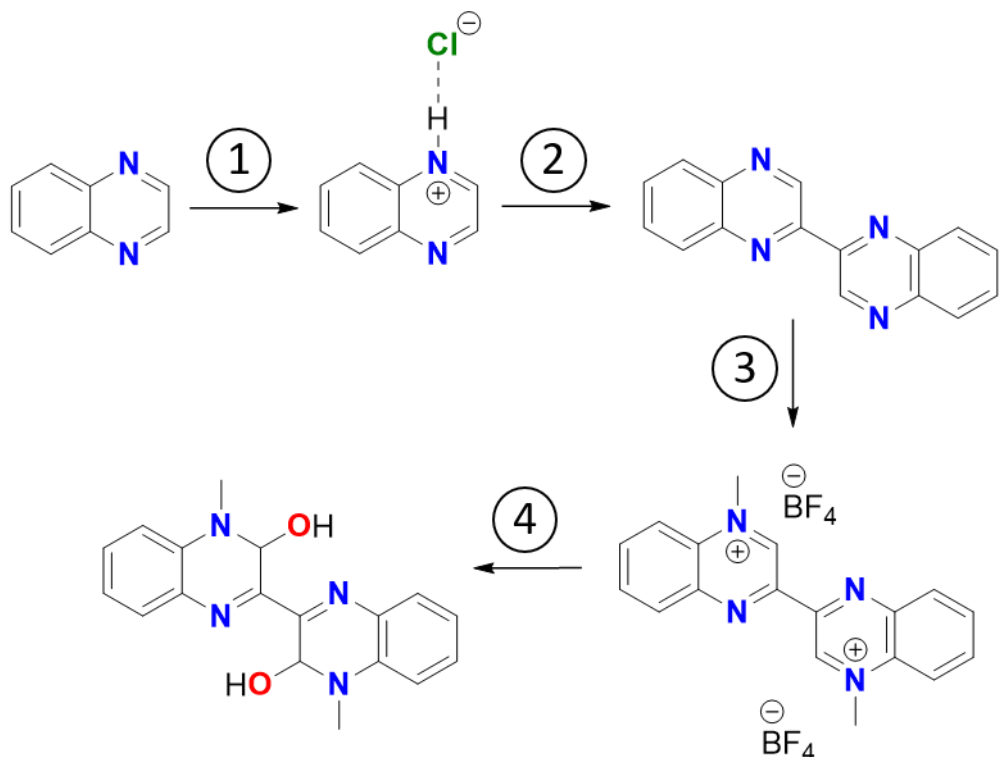


Figure 30. Reaction steps in the synthesis of the methylbiquinoxen dipseudobase ($(\text{Mbqn-OH})_2$).

Quinoxaline is first reacted with HCl to give the hydrochloride salt (step 1), which is then coupled to a second quinoxaline hydrochloride in the presence of dimethylaniline (step 2). The methylation is subsequently carried out using trimethyloxonium tetrafluoroborate (Meerwein's salt) as methylating agent and the dication is obtained in pure form by recrystallisation from water (step 3). In a last step the uncharged Mbqn-OH_2 is obtained by sonicating the dication for 2 h in a basic aqueous solution of K_2CO_3 (step 4). The organic synthesis was followed and the purity of the final product confirmed using $^1\text{H-NMR}$ spectroscopy (details can be found in chapter 8.1).

Preliminary results show the possibility of Mbqn-OH_2 forming brightly fluorescent adducts with the OH-based nucleophiles MeOH, EtOH and EtOEtOH (figure 31, top). It was also shown that the adduct formation also works using polymers with OH end groups such as PEG 350 leading to similar fluorescence (figure 31, bottom).^[29] This was the starting point to the work conducted here in order to further investigate and

tune the emission exhibited by methylbiquinoxen adducts which is described in section 4.2.



Figure 31. Reaction resulting in fluorescent methylbiquinoxen-adducts using alcohol-based nucleophiles (top) and luminescence indicating the same reaction to be possible using polymers with OH end groups (bottom). Reprinted from reference.^[29]

Furthermore, the coordination properties of Mbqn-(OH)₂ to Co^{II} ions were investigated in 2017 and are reported in my Bachelors thesis, which was conducted under the supervision of Dr. Nicolas Leblanc and Dr. Yan Peng.^[28] It was found that complexation reactions carried out by dissolving the ligand in DMF and adding Co^{II} salts with various anions led to a rapid colour change (see figure 32). The resulting dark purple crystals were determined to be complexes of the formula [CoX₂(MbqnO)] with X = Cl and Br, similar to the published Cd^{II} complex which used the dication as ligand. From the crystal structure it was apparent that the dipseudobase was oxidised during the complexation since one of the OH groups was removed while the other shows bond lengths characteristic of a carbonyl C-O bond. In magnetic measurements antiferromagnetic coupling was observed. However, since the individual Co^{II} ions are more than 9 Å apart, it was concluded that the organic ligand must be paramagnetic *i.e.* has formed a radical species which is abbreviated as MbqnO in the following.^[28]



Figure 32. Visual appearance of Mbqn-(OH)₂ (left) and [CoCl₂(MbqnO)] (right) in DMF solution as well as solid state highlighting the colour change characteristic for the complexation reaction in which the ligand reacts to a radical species.^[28]

This marks the start of work conducted on transition metal complexes presented here. This aimed to expand the family of (MbqnO)-radical complexes and perform further analysis to help understand the radical ligand and how it impacts the magnetic properties.

4.2 Fluorescent Adducts

Given these preliminary results the idea was then to investigate the influence of different residues on the luminescence properties of the methylbiquinoxen-adducts.

During attempts on reacting Mbqn-(OH)₂ with various potential adducts as well as metal salts (see chapter 8.1) a crystal structure of the pure starting material was obtained (see figure 33). The ligand crystallises in the monoclinic space group P2₁/c and the unit cell obtained during the work on this thesis is close to the one reported in the literature in terms of cell volume, but with some subtle differences in cell dimensions.

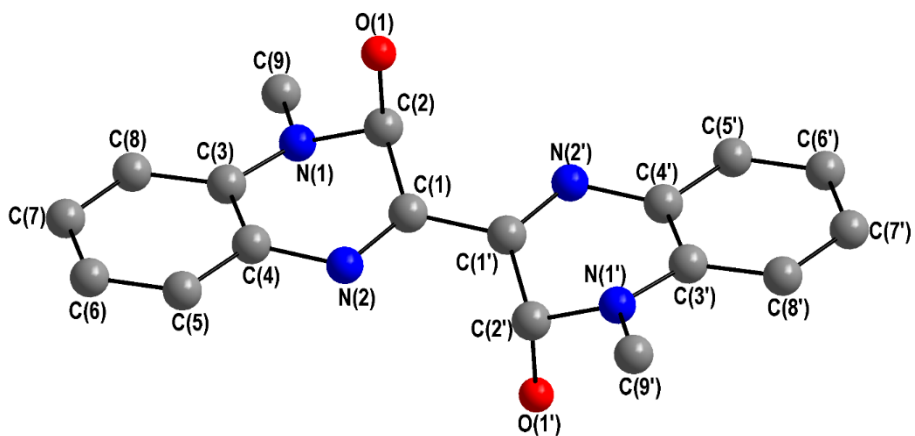


Figure 33. Molecular structure of the starting material Mbqn-(OH)₂. Hydrogens omitted for clarity.

The investigation of fluorescent adducts began with the reproduction of the already known Mbqn-(OMe)₂ and Mbqn-(OEt)₂ compounds.^[29] The success of the reactions was immediately visible from the strong luminescence when irradiated with UV light as soon as the starting material is dissolved in MeOH or EtOH, respectively. To extend the library of compounds, first multiple alternative alcohols were tested. Some examples are shown in figure 34.

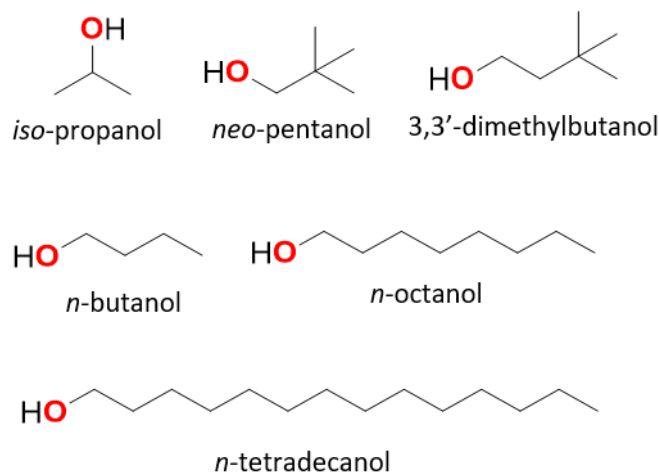


Figure 34. Alcohol-based reactants that yielded fluorescent products when used in attempted syntheses of luminescent methylbiquinoxen-adducts.

For the *iso*-propyl (**Mbqn-(OⁱPr)₂**), 3,3'-dimethylbutyl (**Mbqn-(O-Bu(Me)₂)₂**) and *n*-butyl (**Mbqn-(OⁿBu)₂**) adducts the product was obtained as crystals suitable for single crystal X-ray diffraction (SC-XRD). The *n*-octanyl (**Mbqn-(OⁿOct)₂**) adduct was confirmed to be present by comparison of IR and UVVis absorption spectra. Fluorescent adducts of the alcohols that have melting points above RT (neo-pentanol and *n*-tetradecanol) could not be obtained as pure solids of the respective adduct. This is a result of the lack in stability of the adducts in solution (as further discussed in section 4.2.2.2 below) making column chromatography impossible. Therefore, the luminescent product could not be separated from solidified alcohol after the reaction. Additionally, further alcohols which were tested such as *tert*-butanol, *iso*-butanol and 1,3-dichloro-*iso*-propanol gave fluorescent solutions when reacted with Mbqn-(OH)₂ but no solid adducts could be obtained.

NMR spectroscopy, normally the standard way of confirming the structure and purity of organic compounds was not possible for most of the adducts due to solubility issues leading to very low intensities as well as the decomposition discussed in section 4.2.2.2. The ¹H-NMR spectra of **Mbqn-(OⁱPr)₂** and **Mbqn-(OⁿBu)₂** which are shown in figure 35, were recorded by dissolving the solid compounds in the fume hood of the NMR lab and immediately measured to obtain useful spectra.

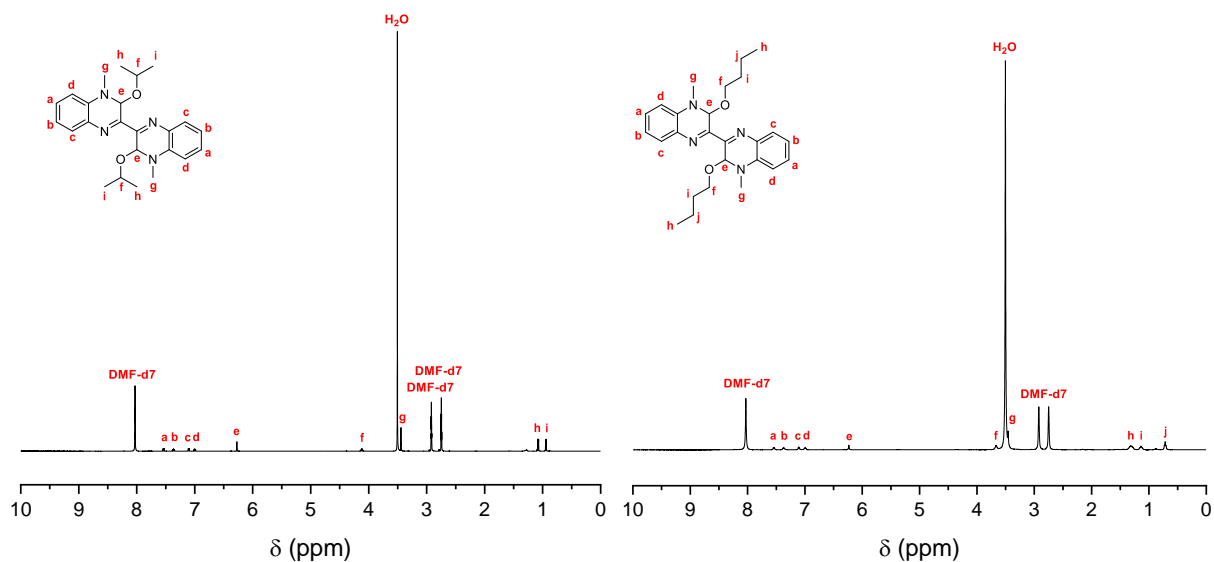


Figure 35. ^1H -NMR of **Mbqn-(OⁱPr)₂** and **Mbqn-(OⁿBu)₂** measured in DMF-d₇.

To gain more insight into the luminescence properties of the adducts and the possibility to fine-tune the emission wavelength. For this, sulfur-based analogues in the form of *iso*-thiopropyl (**Mbqn-(SⁱPr)₂**) and *n*-thiobutyl (**Mbqn-(SⁿBu)₂**) adducts were synthesised (see figure 36, left). Both compounds were obtained as deep red crystals and the purity performed by X-ray based techniques.

Fluorescent solutions were often obtained serendipitously. For example, dissolving the starting material in CHCl_3 led to a bright yellow fluorescent solution (see figure 36, right). Also, dissolving Mbqn-(OH)₂ in acetone in the process of cleaning glassware led to fluorescent solutions. This inspired a reaction using freshly distilled acetone, in which the reaction procedure for O-based adducts was used. This indeed yielded crystals of **Mbqn-(acetone)₂** suitable for SC-XRD.

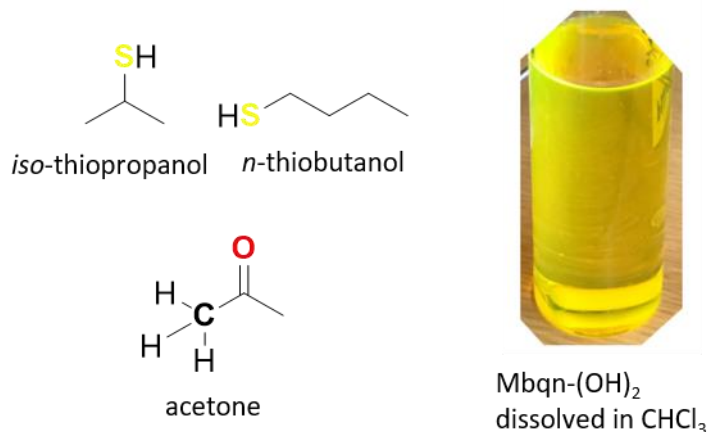


Figure 36. Starting materials for further methylbiquinoxen adducts (left) and a photograph of the luminescent solution of starting material Mbqn-(OH)₂ in CHCl_3 courtesy of Yannik Schneider.

These compounds were selected for an in-depth investigation of their optical properties: **Mbqn-(OⁱPr)₂** (1), **Mbqn-(OⁿBu)₂** (2), **Mbqn-(SⁱPr)₂** (3), **Mbqn-(SⁿBu)₂** (4), **Mbqn-(OⁿOct)₂** (5), **Mbqn-(O-Bu(Me)₂)₂** (6) and **Mbqn-(acetone)₂** (7) although for (7) only a crystal structure could be obtained due to the very low yield of the synthesis (see figure 37).

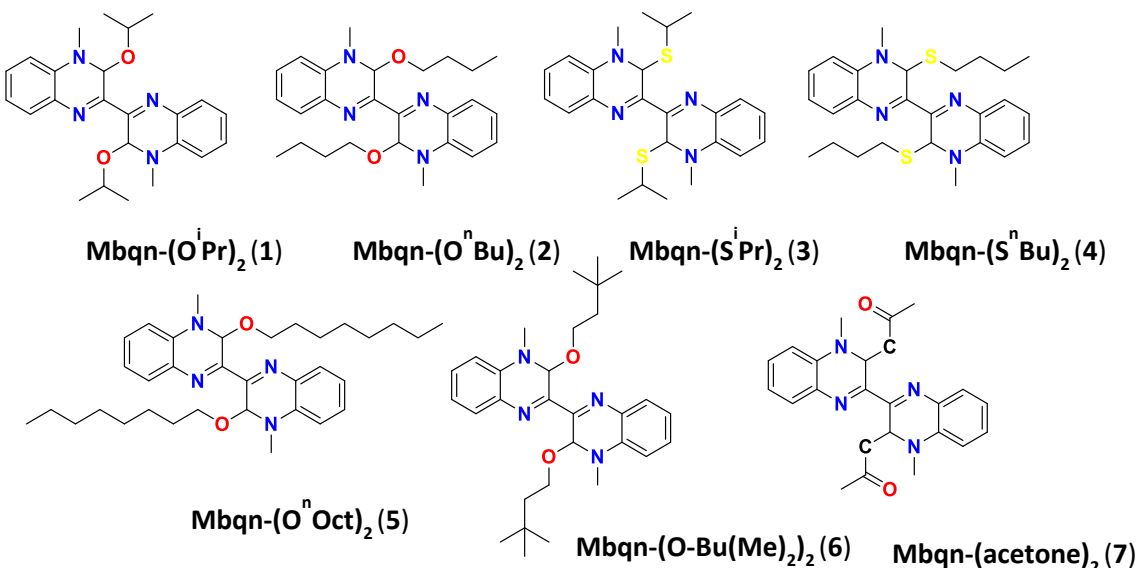


Figure 37. The methylbiquinoxen adducts studied to shine light on the tuning of luminescent properties.

4.2.1 Solid State Analysis on Luminescent Methylbiquinoxen-Adducts

Where possible the crystals were analysed via SC-XRD. In order to gain insights into the contents of the bulk sample, powder X-ray diffraction (PXRD), ATR-IR, elemental analysis as well as solid state UVVis absorption experiments were performed.

4.2.1.1 Crystallography

Single Crystal X-Ray Diffraction

Compound (1) crystallises in well-formed orange rhombic crystals from a bright yellow luminescent solution after 2 days of slow evaporation (see figure 38, left). It crystallises in the triclinic space group $P\bar{1}$ with $Z = 2$. The molecular structure is shown in figure 38, right. The molecule is essentially planar either side of the central C-C bond. Only

the central carbon atoms (C(1) and C(1')) and the carbon atoms linked to the *iso*-propyl residues (C(2) and C(2')) as well as the methyl carbons (C(9) and C(9')) are out of the plane of the rest of the molecule.

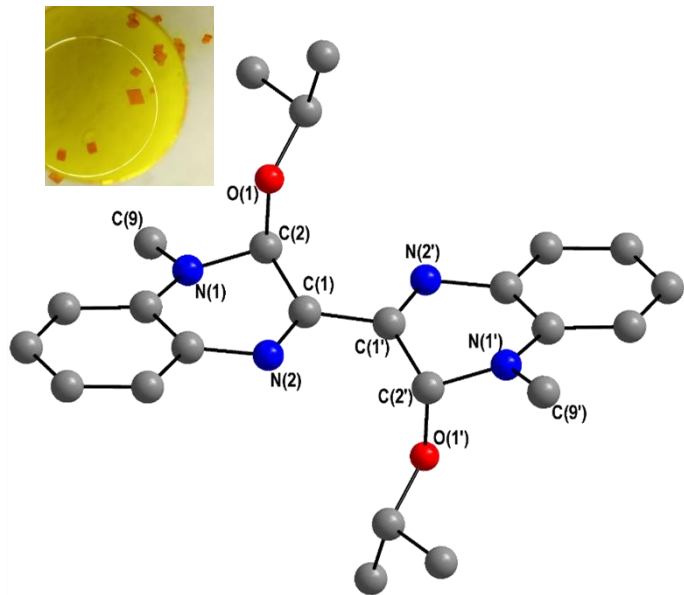


Figure 38. Molecular structure of (1) and visual appearance of crystals of (1) under a microscope.

As seen in figure 39 compound (1) forms stacks of molecules along the crystallographic *a* axis which are held together by offset π - π stacking between the biquinoxen π systems. The shortest C-C distance between molecules of (1) is 3.979(2) Å which is in line with distances observed in the literature.^[185]

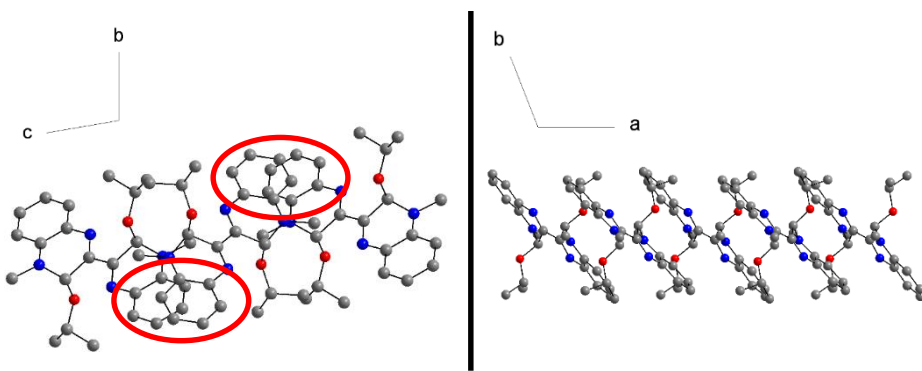


Figure 39. Two views on the packing of (1) along the crystallographic *a*- and *c*-axis (left and right, respectively). The offset π stacking is highlighted with red circles.

For all the other methylbiquinoxen adducts apart from (5) which forms as an amorphous powder, crystal structures were also obtained. The amorphous nature of (5) is hardly surprising given that the long alkyl chain impedes crystallisation. Compounds (2), (3), (4), (6) and (7) all crystallise in a variation of the monoclinic space group 14 ($P2_1/c$, $P2_1/n$ or $P2_1/a$). The crystal structure of (4) was obtained by another

group member, Dr. Nicolas Leblanc, who had left the group before the start of the work on this thesis. Compound (4) was however reproduced during the present work as a result of careful reaction optimisation. As the sample obtained of (4) here was successfully reproduced and confirmed to be isostructural to the one previously obtained by powder X-ray diffraction (PXRD) (see section on PXRD below), the full crystal structure was not measured again. Therefore, the molecular structure of (4) is not included in figure 40 below showing the molecular structures of the other obtained adducts, since the structure falls in line with the other structures obtained here. The cif file from the extant measurement was used here in order to compare structural aspects of compound (4) to the other adducts.

All molecules have identical halves on either side of the central C-C bond, apart from (2) in which the symmetry is broken by the different spatial arrangements of the *n*-butyl residue on both sides as highlighted in figure 40, top left. However, with R-factors of at least 20% the crystal structure of (2) is the worst of the biquinoxen adducts but gives an idea of the molecular structure.

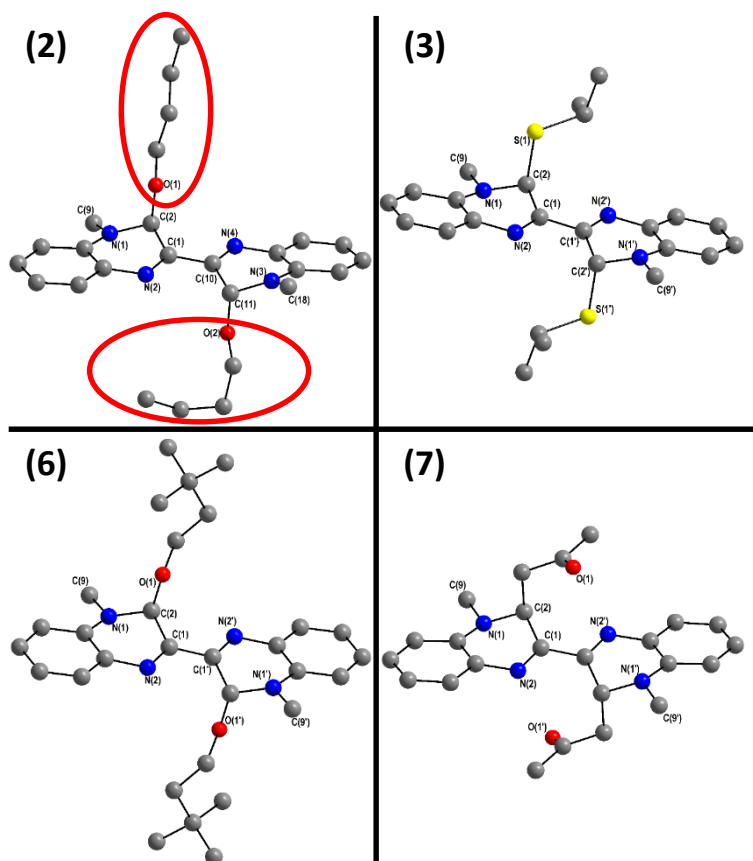


Figure 40. Molecular structures of (2), (3), (6) and (7). The different arrangements of the *n*-butyl residues in (2) leading to an asymmetric molecule are highlighted with red circles.

The packing of (3) is shown in figure 41 as an example for the packing of the adducts that crystallise in a variation of the monoclinic space group 14. As observed for (1), the packing is dominated by π - π stacking between offset phenyl rings with the shortest C-C distance of 3.938(7) Å. This creates stacks of molecules along the crystallographic c axis.

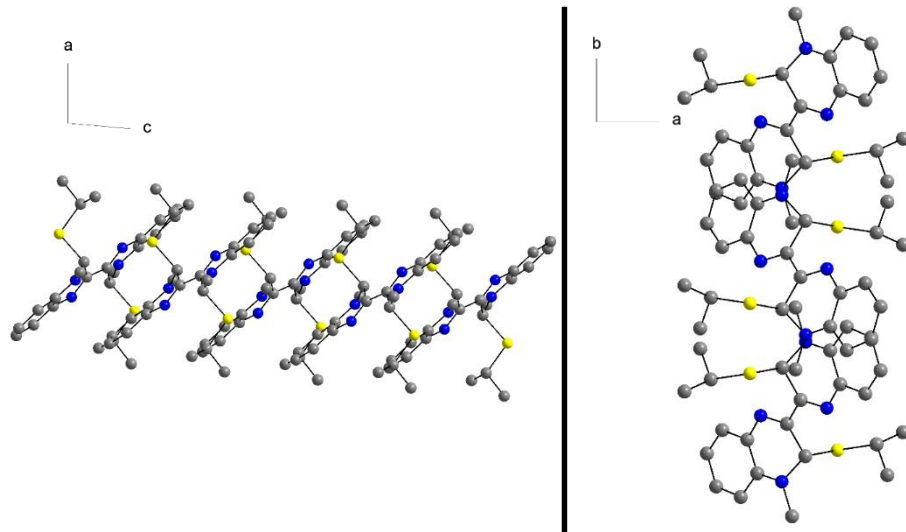


Figure 41. Two views on the packing (3), along the crystallographic b and c axes (left and right, respectively) showing the π stacked arrangement.

In the following, the planarity of the different adducts will be investigated. Generally, it can be expected that the more planar these molecules are, the stronger the aromaticity and in turn the stability of the adduct will be. To explain the comparison of the planarities of the different adducts, the molecular structure of (1) is shown again in figure 42. For clarity hydrogens as well as the *iso*-propyl residues have been omitted. The carbon atoms that are out of plane (central carbon, carbon connected to the omitted residue and methyl carbon) are labelled and a mean plane was put through the two nitrogens and the six remaining unlabelled carbon atoms on either side of the molecule. The distance of the out-of-plane carbons to this plane as well as the distance between the two planes on either side of the ligands are summarised in table 2. This procedure was repeated for (2), (3), (4), (6) and (7). For (2) both sides of the molecule had to be treated separately due to the asymmetry.

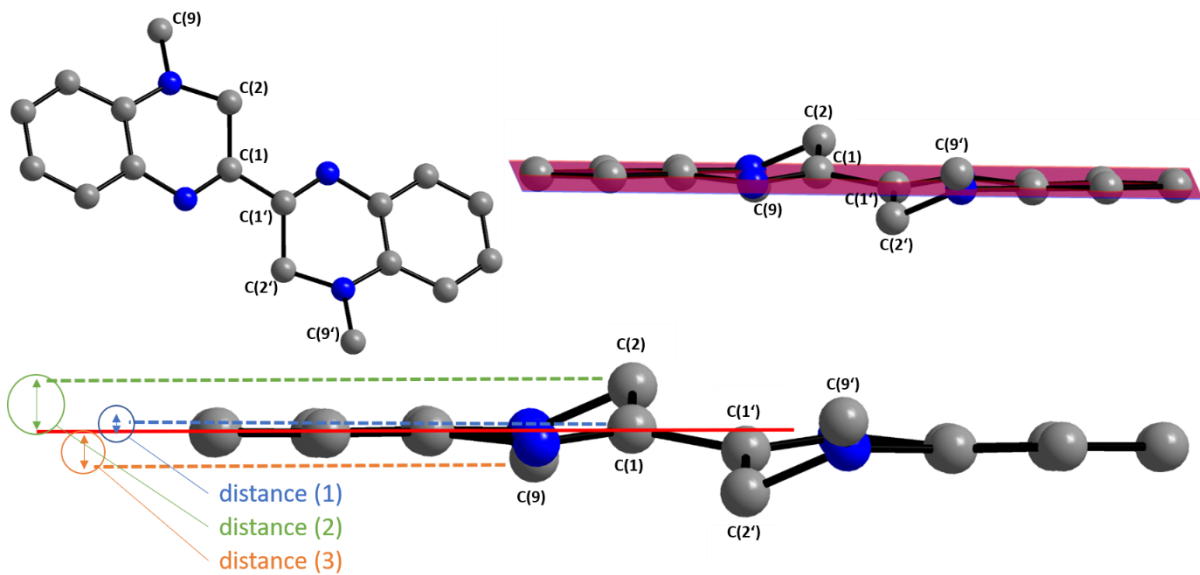


Figure 42. Deviation from planarity shown for the example of (1) in two views (top) and scheme explaining the distances used in the following table to describe the deviation from planarity.

Table 2. Deviation from planarity analysed for the luminescent methylbiquinoxen adducts.

Name	Distance between planes (Å)	Distance of central carbon C2 to plane (Å) (distance 1)	Distance of C1 to plane (Å) (distance 2)	Distance of methyl carbon to plane (Å) (distance 3)
Mbqn-(OⁱPr)₂ (1)	0.0226	0.1144	0.5553	0.3229
Mbqn-(SⁱPr)₂ (3)	0.2168	0.1750	0.5969	0.0832
Mbqn-(SⁿBu)₂ (4)	0.1838	0.1593	0.5373	0.0617
Mbqn-(O-Bu(Me)₂)₂ (6)	0.1295	0.1155	0.5011	0.2199
Mbqn-(acetone)₂ (7)	0.0540	0.1450	0.6584	0.0417
	Dihedral angle between planes (°)	Distance 1 (Å)	Distance 2 (Å)	Distance 3 (Å)
Mbqn-(OⁿBu)₂-A (2)	6.771	0.1104	0.5185	0.3757
Mbqn-(OⁿBu)₂-B (2)	6.771	0.1819	0.6224	0.3820

Looking at the symmetric adducts, it can be noted that the distance between planes is generally lower for the acetone-adduct as well as for the O-based adducts compared to the S-based ones. The distances of C1 and C2 are comparable amongst all structures. The methyl carbon atom is further out of plane for the O-based adducts

than for the S-based ones. However, since the methyl group does not contribute to conjugation in the system it is therefore less relevant for the stability of the molecules. All this indicates a generally higher stability of the O-based adducts. The dihedral angles of the two planes in the asymmetric compound (**2**) is 6.8° . As a result of this, the methyl carbons are twisted further out of plane compared to the other O-based adducts. The other carbon to plane distances are in line with the ones observed for the other compounds. It can also be seen that one half of the molecule in (**2**) is less planar than the other. This is likely a consequence of the different spatial arrangements of the *n*-butyl residues. While the residue on one side is essentially straight, the residue on the other is bent making it sterically unfavourable. This is reflected in the greater deviation from planarity in the biquinoxen molecule in this half (as shown above in figure 40).

Powder X-Ray Diffraction

Four compounds which are particularly closely related (**1-4**) were selected for checking their crystallinity and phase purity by PXRD and comparison to the powder patterns simulated with the software Mercury using the SC-XRD crystal structures.^[186]

Compounds (**1**) and (**2**) both lose crystallinity immediately after removal from the mother liquor. This is also reflected in the powder pattern of (**1**) (see figure 43) that does not match the simulated ones at higher angles. Given that three different samples of (**1**), that were synthesised over the course of three years using three different batches of starting material, give the same powder pattern (see figure 43) and that elemental analyses as well as $^1\text{H-NMR}$ match the expected compound, further experiments were conducted with these solids.

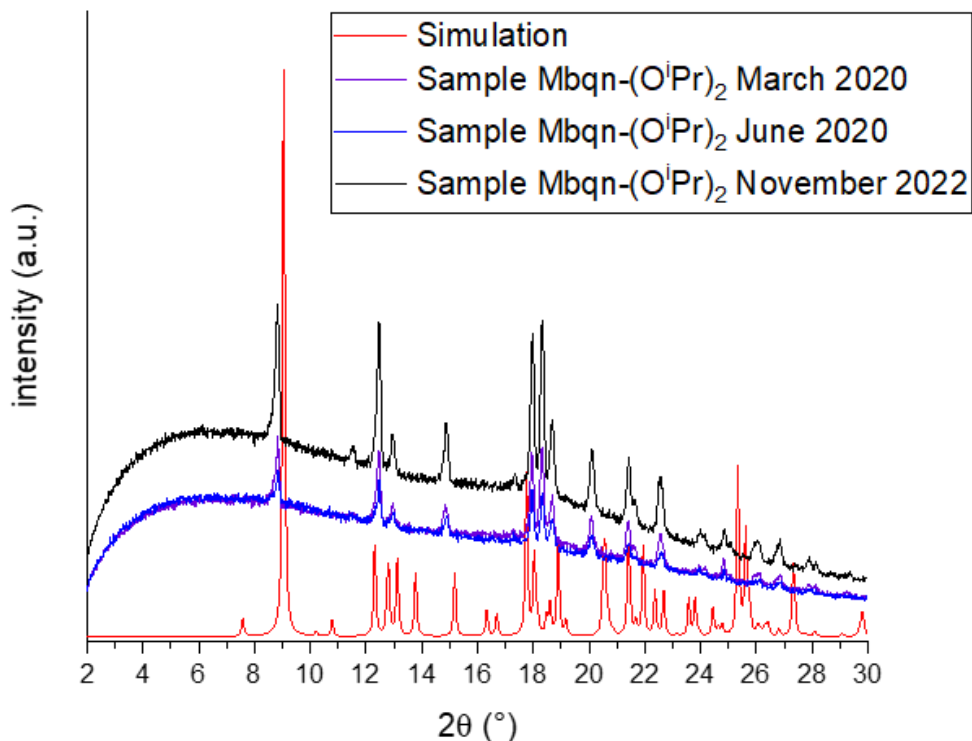


Figure 43. Experimental and simulated powder patterns of (1), comparing the different samples prepared throughout the work on this thesis.

Both S-based adducts remain crystalline in a dried state which results from the different synthetic procedure in which the S-based compounds are obtained by evaporating the THF to dryness before washing the deep red crystals. The powder patterns of both (3) and (4) show good agreement with the simulated ones (figure 44 left and right, respectively).

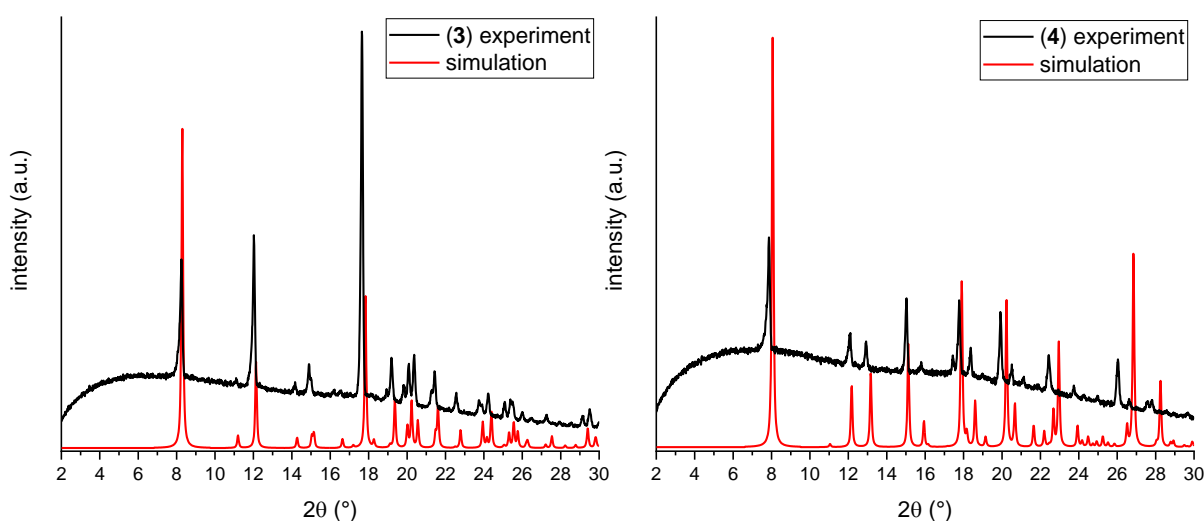


Figure 44. Experimental and simulated PXRDs of (3) (left) and (4) (right).

4.2.1.2 Infrared Spectroscopy (ATR-IR)

By comparison of the IR spectra, adducts that did not crystallise well enough to obtain a crystal structure were analysed. The spectra of (2), (4), (5) and (6) show peaks at 2910 cm^{-1} , 2850 cm^{-1} as well as 1465 cm^{-1} that are absent in (1) and (3). These can be assigned to characteristic vibrations originating from CH_2 stretching and scissor vibrations, confirming the formation of the desired adducts (see figure 45, left).^[187] In (3) and (4) IR bands at 685 cm^{-1} and 674 cm^{-1} are characteristic of thioether moieties (see figure 45, right).^[188]

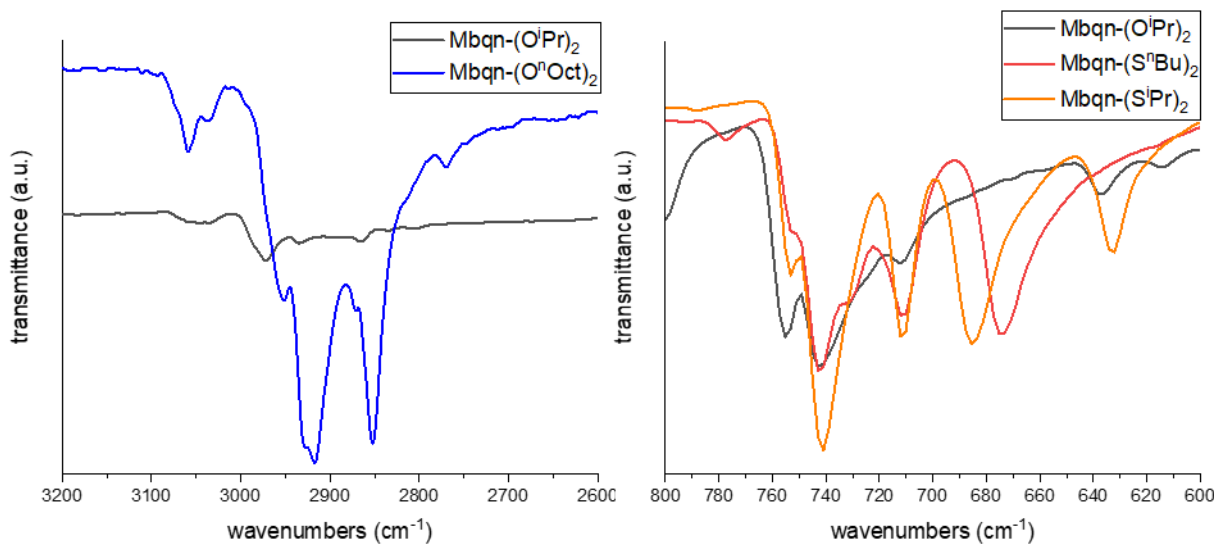


Figure 45. Comparison of the IR spectra of (1) and (5) in the range $3200\text{-}2600\text{ cm}^{-1}$, exemplifying the CH_2 -based vibrations at 2916 cm^{-1} and 2853 cm^{-1} (left); Comparison of the IR spectra of (1), (3) and (4) in the range of $800\text{-}600\text{ cm}^{-1}$ showing the thioether vibrations at 685 cm^{-1} and 674 cm^{-1} , respectively.

4.2.1.3 Optical Properties

The O-based adducts all form orange, crystalline powders (figure 46, top left) and show luminescence in the solid state as crystals and ground powders (figure 46, middle and right). The S-based adducts are obtained as red crystals (figure 46, bottom left) and irradiation with UV light shows that the S-based ones are not luminescent when in their crystalline form, but only when ground (figure 46, bottom right).

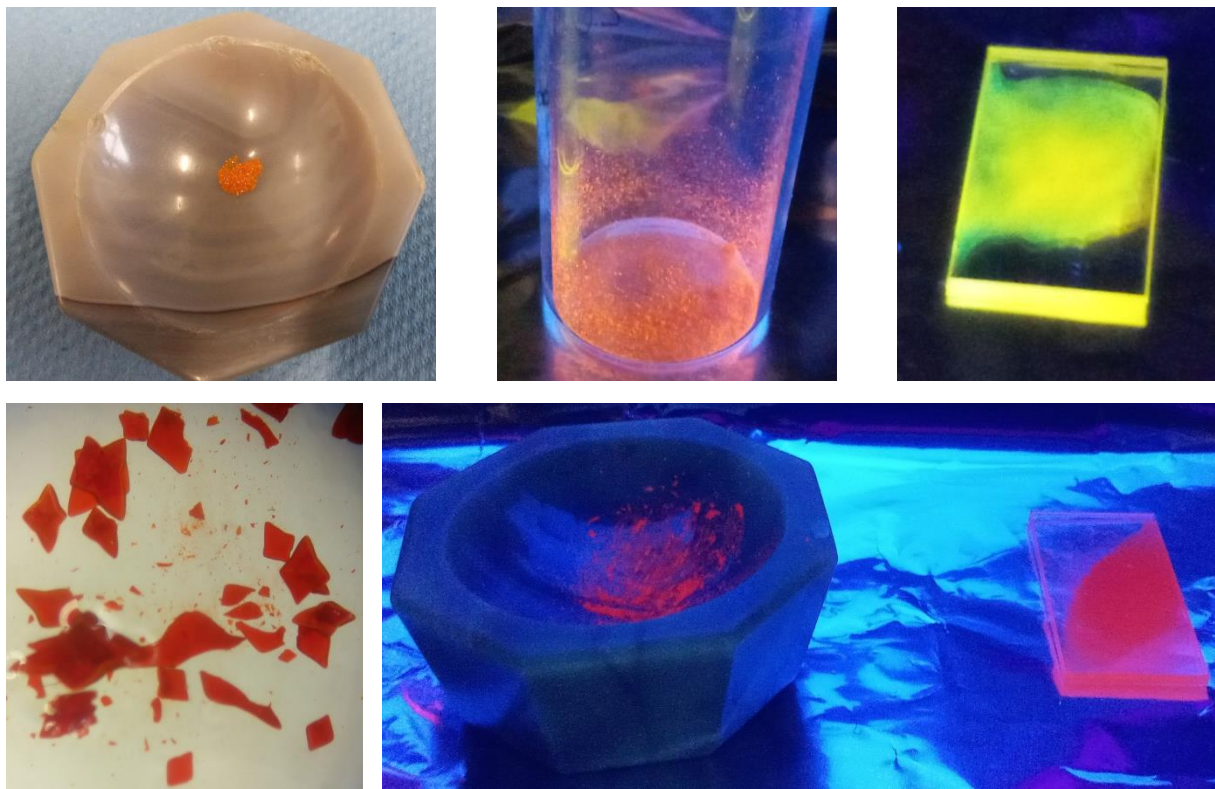


Figure 46. Appearance of O-based adducts exemplified using (5) as crystalline solid under normal white light (left), under UV light (365 nm) (middle) and between two quartz plates for solid state absorption spectroscopy under UV light of the same wavelength (right). Crystals of (3) under a microscope showing the appearance of the S-based adducts (bottom left) and ground powder of (3) under UV irradiation (bottom right).

UVVis absorption spectroscopy was performed using ground powders with an added drop of mineral oil pressed between two quartz plates. The spectra of O- and S-based adducts differ from each other. However, the absorption spectra of the O- and S-based adducts are essentially independent of their different residues (figure 47).

For the O-based adducts four bands are visible in the UV region at 205, 224, 265 and 317 nm as well as a band and shoulder in the visible region at 442 and 465 nm. The two S-based adducts differ from each other in the UV region but show the same behaviour above 300 nm. For (3) one band is visible at 240 nm with two shoulders at lower energies at 266 and 289 nm, while for (4) one band is visible in the UV region at 253 nm with a shoulder at higher energy at 220 nm. Above 300 nm both spectra show bands occurring at 333, 487 and 537 nm which explains the deep red colour of the compounds.

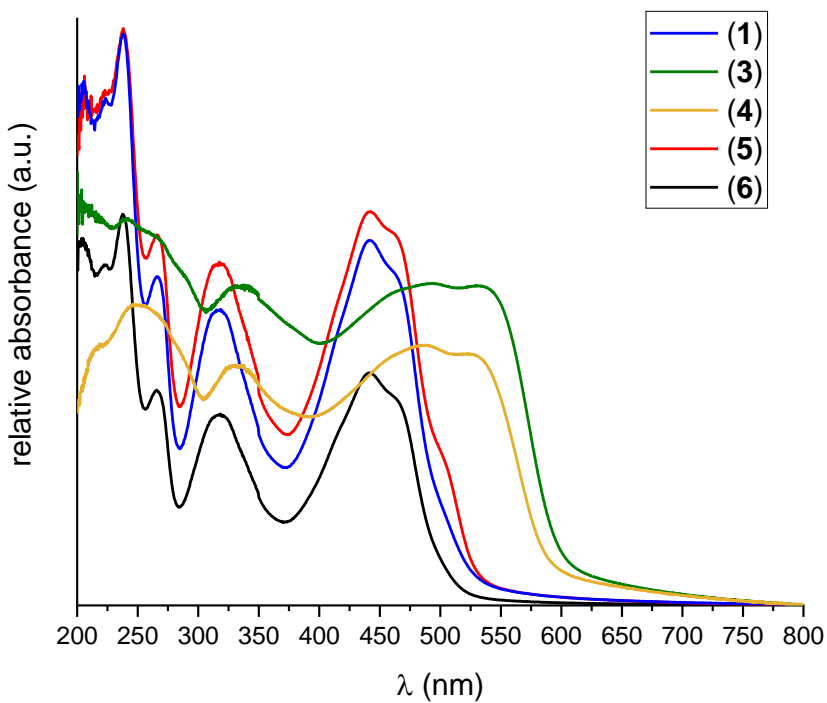


Figure 47. Solid state UVVis absorption spectra of (1-6) in the range of 200 to 800 nm.

Furthermore, a solid state emission and excitation spectrum was recorded of (1) in collaboration with Dr. Mikhail Khorenko in the group of Prof. Dr. Claus Feldmann (KIT, AOC). For this the sample was excited at 365 nm and an orange emission with a wavelength of 615 nm was obtained (figure 48). The absolute quantum yield was obtained as 13% which is comparable to the previously reported luminescent biquinoxen adducts.^[29]

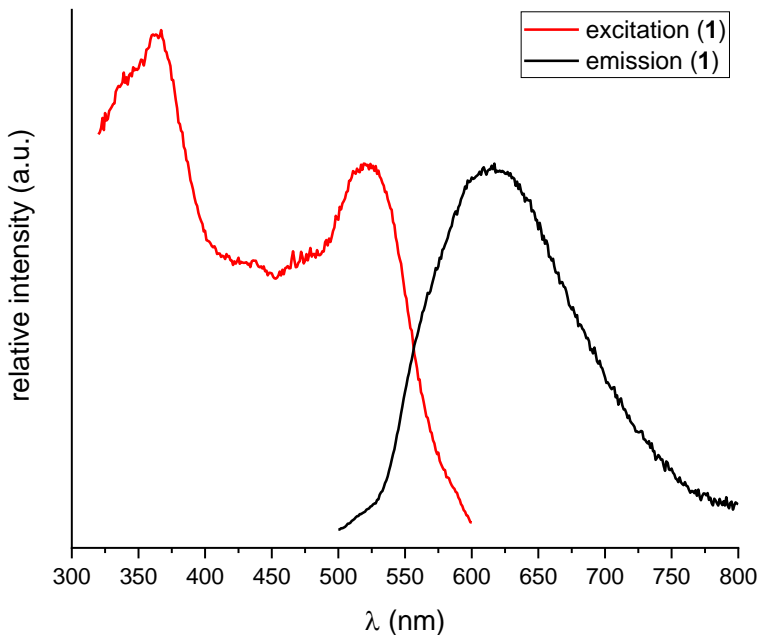


Figure 48. Solid state excitation and emission spectrum of compound (1), by excitation at 365 nm. The excitation spectrum was recorded for the emission at 615 nm.

4.2.2 Solution State Analysis

Although the O-based adducts show luminescence in the solid state, the light emission clearly becomes stronger in solution and can also be observed for the S-based adducts. As the starting material Mbqn-(OH)₂ reacts with a plethora of solvents to form adducts in solution as evidenced by their luminescence, the solvent used in order to investigate the optical properties of the adducts had to be chosen carefully to avoid possible equilibrium reactions distorting the results. Also, a solvent had to be chosen in which all adducts are soluble in order to be able to compare the results. DMF was chosen since it fulfils the aforementioned criteria of not reacting with the starting material and dissolving all adducts. The only disadvantage of DMF in the context of UVVis spectroscopy is the solvent cut-off at 260 nm limiting the full typical UV region. Therefore, as (1) is soluble in other solvents UVVis spectra were also recorded in MeCN and DCM solution and compared to the spectrum in DMF and solid state (see figure 49). In addition to UVVis spectroscopy and luminescence spectroscopy (absolute quantum yield determination performed by Dr. Mikhail Khorenko in the group of Prof. Dr. Claus Feldmann (KIT AOC)), further emission spectroscopy as well as femtosecond spectroscopic measurements were performed to gain insights into the decomposition of the adducts in solution by Dr. Julia Leier in the group of Prof. Dr. Andreas-Neil Unterreiner (KIT, IPC).^[189] All experiments in solution had to be performed with freshly prepared solutions as even in DMF the adducts slowly decompose, possibly due to an equilibrium with the methylbiquinoxen dipseudobase starting material. This is further discussed in section 4.2.2.2.

4.2.2.1 UVVis Absorption and Emission Spectroscopy

For UVVis absorption spectroscopy all samples were prepared in the following way. 5 mg of powder sample were dissolved in 1 ml solvent to produce a stock solution which was diluted further to give solutions with concentrations between 1 and 50 µmol/l. These diluted solutions were measured in 10 mm quartz cuvettes. For each sample four different concentrations were measured in order to determine extinction coefficients.

Firstly, the UVVis absorption spectrum of (1) was tested for possible solvent dependence by comparison of the spectra in DMF, MeCN, DCM and solid state (see figure 49). The spectra are essentially solvent independent with bands occurring around 236, 266, 313 and 440 nm with a shoulder at 459 nm. The peaks further into the UV region are only visible in the MeCN and DCM spectra due to the solvent cut-off of DMF at 260 nm. Subtle differences between the spectra are that the MeCN sample is slightly blue shifted (2-3 nm), while the DCM sample is slightly red-shifted (2-3 nm) in regard to the DMF sample. These solution spectra compare well to the solid state spectrum which has a slightly broader band in the visible region with an additional small shoulder at 506 nm. As the absorption spectrum of (1) is essentially solvent independent the other adducts were analysed in DMF solution in order to allow comparison between them, as especially the S-based adducts are only very sparingly soluble in other solvents.

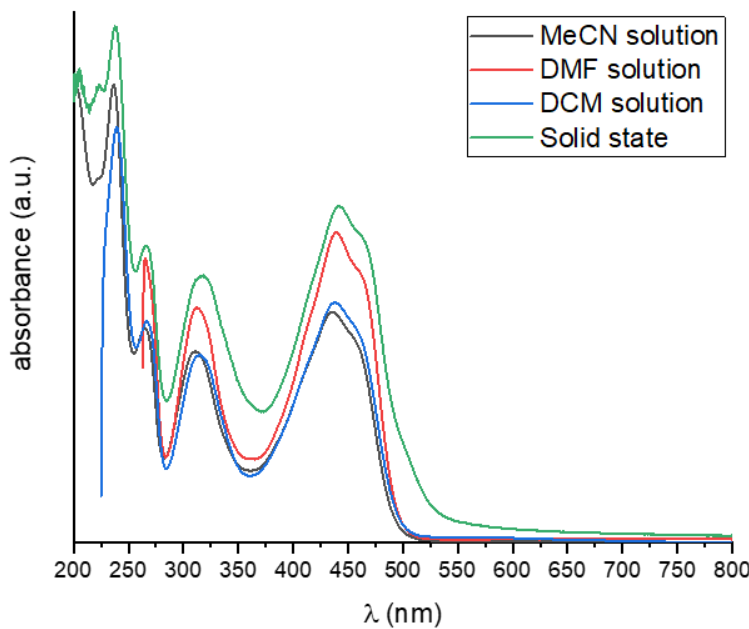


Figure 49. UVVis absorption spectra of (1) in MeCN, DMF, DCM as well as in solid state between 200 and 800 nm.

The absorption spectrum of (1) in DMF shows three peaks and a shoulder above 260 nm (figure 50 A). The determination of extinction coefficients with a linear fit to a plot of the maximal absorbance at λ_{\max} of each peak against the concentration, is shown for (1) as an example (figure 50 B-D). The extinction coefficient can be determined as the slope of the respective linear fits. This was done for peaks 2-4 only as peak 1 is too close to the solvent cut-off. The same was done for the other compounds and the results are listed and compared in table 3.

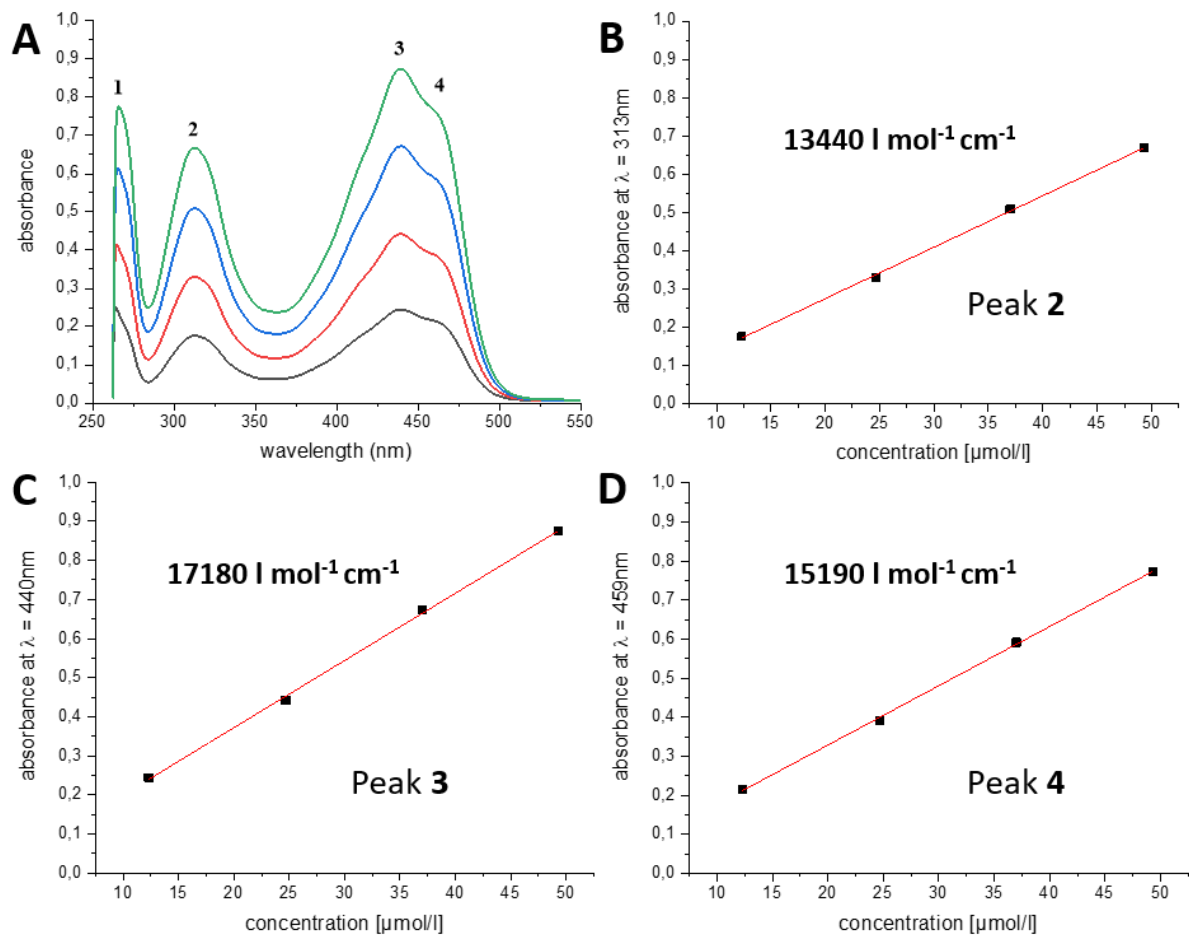


Figure 50. A: UVVis absorption spectrum of (1) at four different concentrations between 10 and 50 $\mu\text{mol/l}$. B-D: Linear fit for extraction of extinction coefficients for peaks 2-4, respectively.

Table 3. Comparison of extinction coefficients of compounds (1-6).

Compound	λ (nm)	ϵ (l mol $^{-1}$ cm $^{-1}$)
(1)	313	13440
	440	17180
	459	15190
(2)	313	7875
	440	9958
	459	8553
(3)	330	2507
	470	2173
(4)	330	8323
	470	8617
(5)	313	7475
	440	9556
	459	8431
(6)	313	13960
	440	19170
	459	16987

In figure 51 the DMF solution spectra of (1-6) are compared. As observed for the solid state UVVis absorption spectra, the absorption spectra of the O- and S-based adducts in DMF solution are essentially independent of the residues in terms of the position of the absorption bands. For the O-based adducts the maximum absorption can be observed at 440 nm while the strongest absorption of the S-based adducts appears to be the band starting at *circa* 280 nm which gets cut off by the spectral limit of DMF at 260 nm. The extinction coefficients of (1) and (6) are highest, while the O-based adducts with long carbon chain residues (2) and (5) show reduced extinction coefficients at 440 nm. The S-based adducts show bands at 260, 330 and 470 nm and while the extinction observed for (3) is in the range of (2) and (5), the extinction of (4) is only about a third of these values. The UVVis absorption spectra and extinction coefficients are in line with the behaviour previously reported for the MeOH and EtOH adducts in which the absorption bands in the visible region could be assigned to HOMO-LUMO π - π^* transitions.^[29]

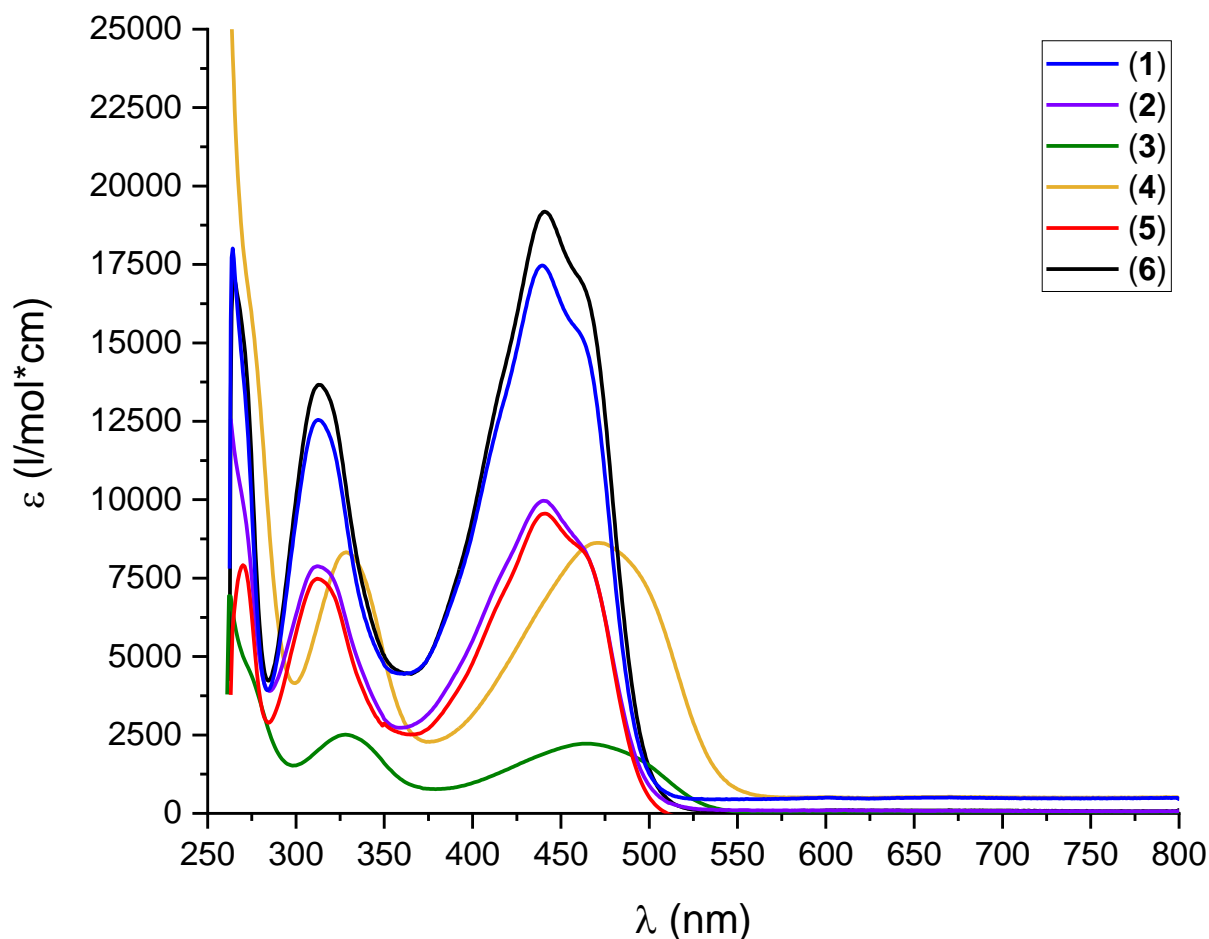


Figure 51. UVVis absorption spectra of (1-6) in DMF solutions in the range of 260 to 800 nm.

Subsequently, the emission spectra of (1-6) in DMF solution were measured and are compared in figure 52. O-based adducts were excited at 440 nm leading to green/yellow light emission and S-based adducts were excited at 465 nm leading to red/orange emission. The emission wavelengths for (1-6) are listed in table 4 showing the shift of the emission wavelengths from 548 nm in (5) and (6) to 611 nm in (4). Therefore, it is shown that the strength and colour of the emitted light in this system is easily tunable by the reaction of Mbqn-(OH)₂ with different nucleophiles.

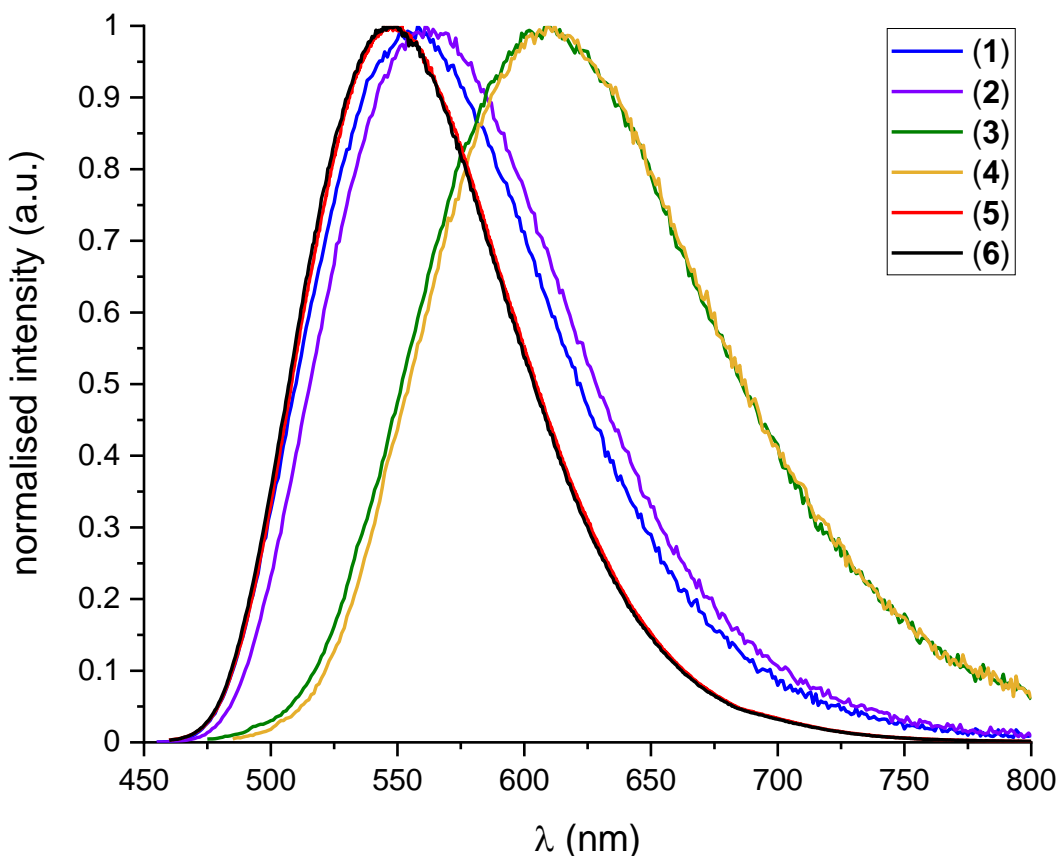


Figure 52. Normalised emission spectra of (1-6). The O-based adducts were excited at 440 nm, the S-based adducts at 465 nm.

Table 4. Tuning of the emission wavelength in (1-6).

Compound	Emission wavelength (nm)
(1)	558
(2)	561
(3)	610
(4)	611
(5)	548
(6)	548

4.2.2.2 Quantum Yields and Decomposition in Solution

The determination of quantum yields was complicated by a decomposition of the adducts in solution which was first observed by NMR spectroscopy where the measured spectrum changes over time. In figure 53 an excerpt of the ^1H -NMR spectrum of (1) is shown. This was recorded from the same DMF-d7 solution of Mbqn-(OⁱPr)₂, that yielded the clean NMR spectrum shown in figure 35 above but measured 12 h later. The *iso*-propyl C-H septet that was previously obtained centred at 4.13 ppm is split into multiple sets of septets after 12 h suggesting more than one intermediate species forms during the decomposition of (1).

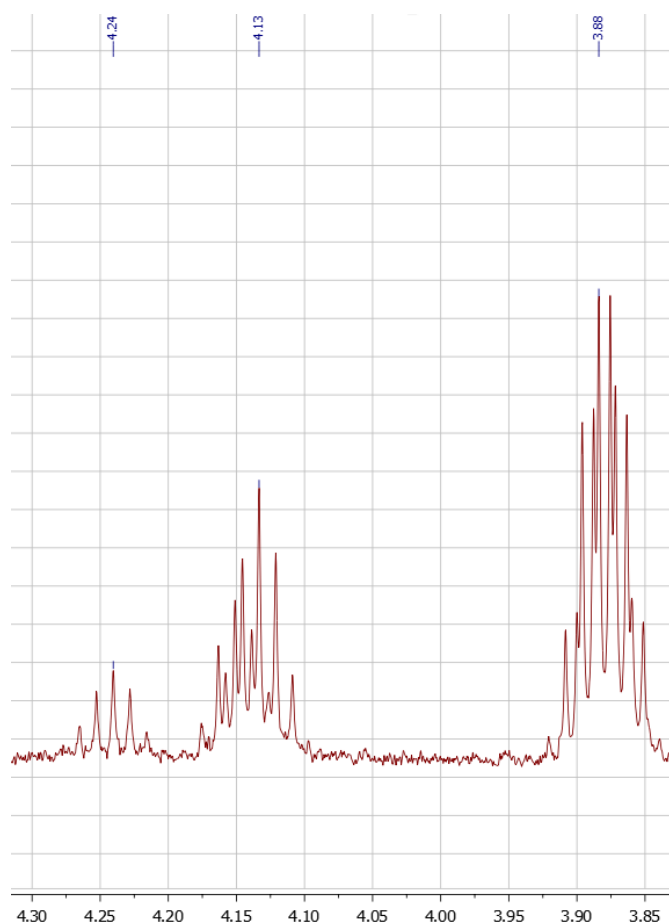


Figure 53. Excerpt of the ^1H -NMR spectrum of (1) showing the decomposition in solution after 12 h.

The decomposition was further investigated in collaboration with Dr. Julia Leier in the group of Prof. Dr. Andreas-Neil Unterreiner (KIT, IPC) and is also described in her dissertation.^[189] For this, the quantum yield of (1) in DMF was determined in fresh solutions and the measurements repeated at certain time intervals. While freshly prepared solutions exhibit quantum yields of 97%, the quantum yield reduces drastically after a couple of hours (see table 5), reaching 6.2% after 24 h, further

continuing to decrease indicating that the final product is non-luminescent. This was also seen in femtosecond spectroscopic investigations performed by Dr. Julia Leier, exciting **(1)** to the S_1 state at 490 nm and recording the time-dependence. While in fresh solutions a long-lived dynamic (>2 ns) was observed, this was absent in solutions that were stored for up to many days. Therefore, it can be concluded that the reason for the quenching of fluorescence is a process that takes place on the timescale of hours.

With 97% the quantum yield of the freshly prepared solution of **(1)** is higher than the ones obtained in the literature, further emphasising the possibility to fine-tune the chemical and photophysical properties of this system.

Table 5. Quantum yields of DMF solutions of **(1)** after different times after sample preparation.^[189]

time after dissolution of (1) in DMF (h)	quantum yield (%)
fresh	97
2	64
3	52
5	47
24	6.2
>24	1.1
>>24	0.4

The quantum yields of of **(2)**, **(3)** and **(4)** were also determined in freshly prepared solutions. While the quantum yield for **(2)** is also high at 90%, it is lower than the one obtained for **(1)**. The S-based adducts are weaker emitters as shown by the quantum yields of 7% and 6% for **(3)** and **(4)**, respectively.^[189]

A reason for the decrease in quantum yield could be an equilibrium favouring the reaction of **(1)** back to the non-luminescent starting material Mbqn-(OH)₂ in solution, similar to the reversible reaction pathways described for the biquinoxen adducts in the literature.^[29] This is in line with the UVVis absorption spectrum of **(1)** not changing over time since the non-luminescent dipseudobase shows the same spectrum. This theory is further strengthened by removing the solvent after decomposition for several days and dissolution of the obtained powder in hot *iso*-propanol thereby regaining higher quantum yields. The decomposition for the S-based adducts is observed to be much faster and is accompanied by a shift in the absorption spectrum indicating decomposition *via* different mechanism.^[189]

4.3 Transition Metal Radical Complexes

As described in section 4.1, the reaction of Mbqn-(OH)₂ with transition metal halides in DMF leads to an immediate colour change from deep red to dark purple (see figure 32 above). During the complexation reaction the ligand reacts to the neutral radical species MbqnO. This radical species could not be isolated as a purely organic compound since it can only be stabilised by the presence of a metal ion. The Co^{II} complexes [Co^{II}Cl₂(MbqnO)] (**8-Co**) and [Co^{II}Br₂(MbqnO)] (**9-Co**) that resulted from the work done during my Bachelor thesis in 2017 were reproduced during the work on this doctoral thesis and analysed further. Additionally, the new transition metal-radical complexes [Cu^{II}Cl₂(MbqnO)] (**10-Cu**), [Cu^{II}Br₂(MbqnO)] (**11-Cu**) and [Zn^{II}Cl₂(MbqnO)] (**12-Zn**) were synthesised using the methylbiquinoxen dispeudobase as starting material. This was supported by the efforts of the student Yannik Schneider who conducted his Bachelor thesis under my supervision.^[28, 190]

4.3.1 Crystallography

4.3.1.1 Molecular Structure of [M^{II}X₂(MbqnO)]

Crystals suitable for SC-XRD of the five compounds (**8/9-Co**, **10/11-Cu** and **12-Zn**) were obtained after layering a DMF solution of ligand and transition metal salt with MeCN and leaving the vials undisturbed for 4 d (for further details see chapter 8.1). The compounds are essentially isostructural crystallising in the monoclinic space group P2₁/c. Additionally, a second polymorph was found for (**12-Zn**) with a different packing crystallising in P2₁/n. The Zn^{II} compound that is isostructural to the others is abbreviated as (**12-Zn A**) and the polymorph with the same molecular structure but different packing as (**12-Zn B**) in the following. In terms of the molecular structure all complexes are very closely related. The metal ions are coordinated to N(1) and N(3) of the essentially planar MbqnO radical ligand with two halides (Cl⁻ or Br⁻) completing the coordination sphere. The molecular structure of (**10-Cu**) is shown in figure 54 as a representative for these biquinoxen-radical transition metal complexes. The molecular structure of the polymorph (**12-Zn B**) is fully ordered while the other complexes show varying amounts of disorder of the carbonyl oxygen O(1) with the vicinal H(10). The different occupancies of the oxygen atoms are listed in table 6. It can be observed that

the compounds with Br^- ligands (**9-Co**) and (**11-Cu**) show less disorder than their Cl^- counterparts. Furthermore, the Cu^{II} containing complexes are better ordered than the Co^{II} versions. The two versions of the Zn^{II} complex show both extremes with (**12-Zn A**) essentially statistically disordered and (**12-Zn B**) fully ordered suggesting the packing has a strong influence on the molecular disorder in these compounds.

Table 6. Disorder on O(1) in (**8/9-Co**, **10/11-Cu** and **12-Zn A** and **B**).

	(8-Co)	(9-Co)	(10-Cu)	(11-Cu)	(12-Zn A)	(12-Zn B)
O(1A)	0.54	0.63	0.74	0.84	0.51	1.00
O(1B)	0.46	0.37	0.26	0.16	0.49	0.00

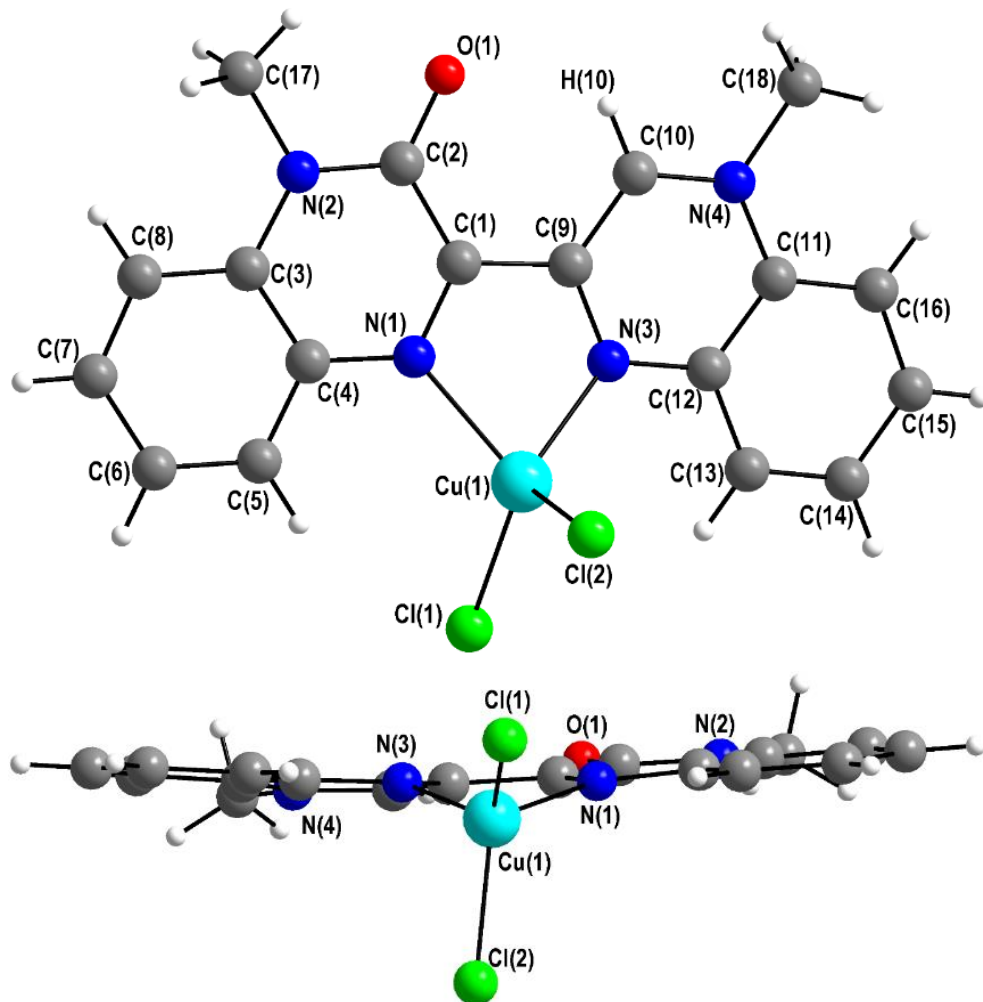


Figure 54. Molecular structure of (**10-Cu**) as representative for the biquinoxen-radical complexes. The disorder of the carbonyl O(1) and the neighbouring vicinal H(10) was removed in favour of the atoms with higher occupancy.

The bond length between $\text{C}(2)\text{-C}(1) = 1.456(2)$ Å is longer than its counterpart on the other side of the central C-C bond of $\text{C}(9)\text{-C}(10) = 1.418(2)$ Å. This as well as the shorter $\text{C}(1)\text{-N}(1) = 1.323(2)$ Å bond compared to the $\text{C}(9)\text{-N}(3) = 1.338(2)$ Å, leads to

the suggested structure of the complex shown below (see figure 55). Judging by the dark colour of all the complexes the radical appears to be delocalised. This is further supported by the central C-C bond length of 1.464(2) which is between what would be expected of a carbon-carbon single and double bond.

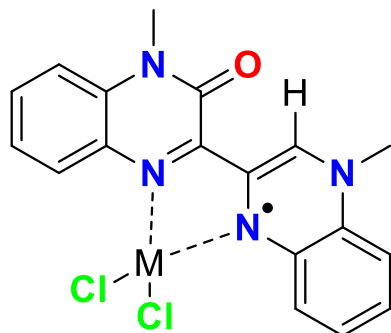


Figure 55. Proposed structure of the complexes in terms of the location of single and double bonds.

The radical ligand is very slightly bent out of planarity as shown by the distance of only 0.31 Å and 0.28 Å of the outmost carbon atoms C(7) and C(15) to a mean plane through N(1), C(1), C(9) and N(3), respectively. The metal ion lies slightly out of the same radical ligand mean plane (0.47 Å) with the geometry around the metal ion significantly distorted from tetrahedral. This becomes apparent from Cu(1)-Cl(1) and Cu(1)-Cl(2) bond lengths of 2.235(1) Å and 2.233(1) Å being longer than the Cu(1)-N(1) and Cu(1)-N(3) bond length of 2.087(1) Å and 2.016(1) Å as well as an acute N(1)-Cu(1)-N(3) angle of 78.4(1)°. Furthermore, the different distance of the two halide ligands to the radical ligand mean plane is another regarding the distortion from tetrahedral symmetry around the Cu^{II} ion. One of the halide ligands Cl(1) is only slightly out of the plane of the radical ligand with a distance of 0.60 Å, while Cl(2) is much further away from this plane with a distance of 2.63 Å. This enables Cl(2) to help stabilise the supramolecular structure as discussed in the following section. These bond lengths are compared for all the structures in table 7. Unsurprisingly, the difference between the two sides of the molecules reduces when the disorder approximates 50:50 as in (8-Co) and (12-Zn A).

Table 7. Important distances and angles in (8/9-Co, 10/11-Cu as well as 12-Zn A and B).

bond distances (Å)	(8-Co)	(9-Co)	(10-Cu)	(11-Cu)	(12-Zn A)	(12-Zn B)
C(1)-C(9)	1.445(3)	1.432(6)	1.464(2)	1.471(5)	1.455(2)	1.460(4)
C(1)-C(2)	1.431(3)	1.425(6)	1.456(2)	1.466(5)	1.431(2)	1.470(4)
C(9)-C(10)	1.429(3)	1.425(6)	1.418(2)	1.404(5)	1.437(2)	1.393(4)
C(1)-N(1)	1.348(3)	1.347(5)	1.323(2)	1.317(4)	1.346(2)	1.320(3)
C(9)-N(3)	1.348(3)	1.361(6)	1.338(2)	1.348(4)	1.337(2)	1.365(4)
N(1)-M(1)	1.992(2)	1.998(4)	2.087(1)	2.093(3)	2.049(1)	2.078(2)
N(3)-M(1)	1.994(2)	1.982(3)	2.016(1)	2.024(3)	2.061(2)	2.028(2)
X(1)-M(1)	2.221(1)	2.363(1)	2.235(1)	2.376(1)	2.203(1)	2.188(1)
X(2)-M(1)	2.221(1)	2.356(1)	2.233(1)	2.365(1)	2.220(1)	2.221(1)
angle (°)	(8-Co)	(9-Co)	(10-Cu)	(11-Cu)	(12-Zn A)	(12-Zn B)
N(1)-M(1)-N(3)	80.8(1)	81.3(1)	78.4(1)	78.4(1)	79.3(1)	79.7(1)
Distances to mean plane defined by N(1), N(3), C(1) and C(9) (Å)	(8-Co)	(9-Co)	(10-Cu)	(11-Cu)	(12-Zn A)	(12-Zn B)
M(1)-plane	0.38	0.38	0.47	0.48	0.42	0.38
X(1)-plane	0.96	1.02	0.60	0.63	0.91	0.87
X(2)-plane	2.49	2.62	2.63	2.79	2.56	2.56

The oxidation state, albeit fairly obvious in the case of (**12-Zn A** and **B**) was confirmed to be 2+ for all compounds using bond valence sum (BVS) analysis with the following formula:

$$BVS = \sum \exp\left(\frac{(R_0 - R)}{B}\right) \quad \text{equation 14}$$

where R = bond length between metal ion and ligand donor atom and R₀ as well as B being empirical parameters that are tabulated on the website of the International Union of Crystallography (IUCr).

The parameters used for the different metal ions and the results of the BVS analyses are listed in table 8.^[191-194]

Table 8. Parameters used for and the results of the BVS analyses.^[191-194]

Compound	$R_0(M-N)$ (Å)	$R_0(M-X)$ (Å)	BVS
(8-Co)	1.65	2.033	1.99
(9-Co)	1.65	2.18	2.03
(10-Cu)	1.751	2.00	1.95
(11-Cu)	1.751	2.134	1.93
(12-Zn A)	1.77	2.01	2.09
(12-Zn B)	1.77	2.01	2.12

This, by looking at the overall charge balance, confirms the radical ligand to be neutral since there are no further ions present in the lattice.

4.3.1.2 Supramolecular Packing of $[M^{II}X_2(MbqnO)]$

The packing of the isomorphous complexes (**8/9-Co**, **10/11-Cu** and **12-Zn A**) shows supramolecular chain formation using offset π stacking between the radical ligands of neighbouring molecules with shortest C-C stack distances in the range between 3.314(6) Å in (**11-Cu**) and 3.389(6) Å in (**9-Co**). These distances indicate a rather strong attractive π - π interaction since they are shorter than double the VdW radius of carbon (3.4 Å^[164]). This could be a result of an enhancement of interaction strength through an involvement of neighbouring radicals. Interactions between π stacked radicals with C-C distances smaller than double the VdW radius of carbon are often referred to as pancake bonds.^[161-162] Usually such pancake bonds are observed between overlapping face to face π systems that are not offset (centroid to centroid interaction).^[195] In the case of the complexes presented here, a superposition of common offset π stacking interactions and an additional contribution from the delocalised radicals seems feasible. This π stacking leads to chain formation and is assisted by non-classical hydrogen bonding *via* the halogen ligand which lies furthest out of the ligand plane in each molecule (see figure 56). Hydrogen bond distances lie between 2.7342(4) Å in (**12-Zn A**) and 2.8781(4) Å in (**11-Cu**). There are two orientations of chains throughout the crystal, one in the a-b plane diagonally between the crystallographic a and b axes and one tipped out of the a-b plane by 70.9°.

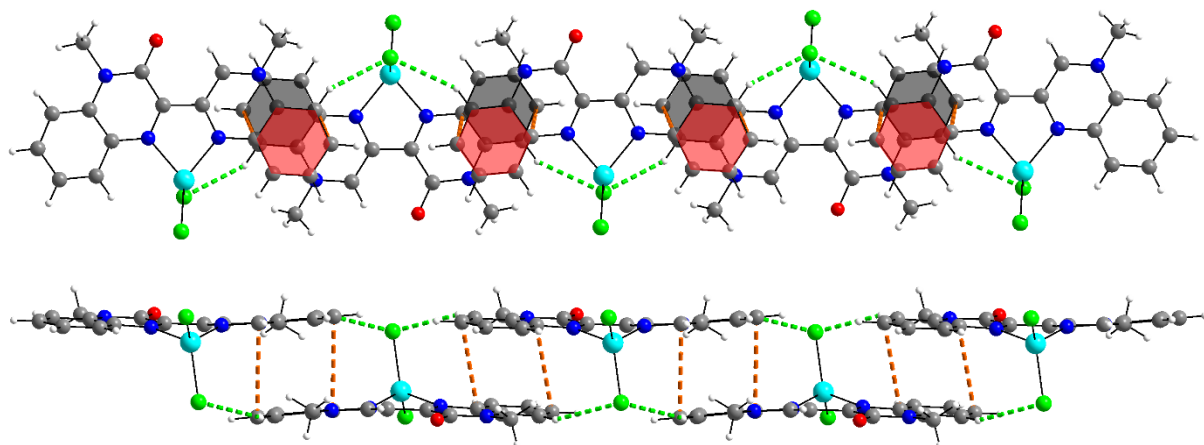


Figure 56. Supramolecular chain formation dominating the packing of **(8/9-Co, 10/11-Cu and 12-Zn A)**. Chains are held together by a mixture of offset π stacking (top view) and non-classical HBs shown in green (side view). This is illustrated here using the crystal structure of **(10-Cu)** as a representative.

Instead of supramolecular chains, the polymorph of the Zn^{II} complex (**Zn-12 B**) forms intermolecular π stacked dimers with shortest C-C distances of 3.378(5) Å which therefore also can be referred to as pancake bonds. These are additionally connected to neighbouring dimers *via* HBs between H(18B), which is one of the protons of the methyl groups and the carbonyl O(1). The distance between C(18)-H(18B)...O(1) is 2.459(3) Å with an angle of 130.0(2) $^{\circ}$.(see figure 57)

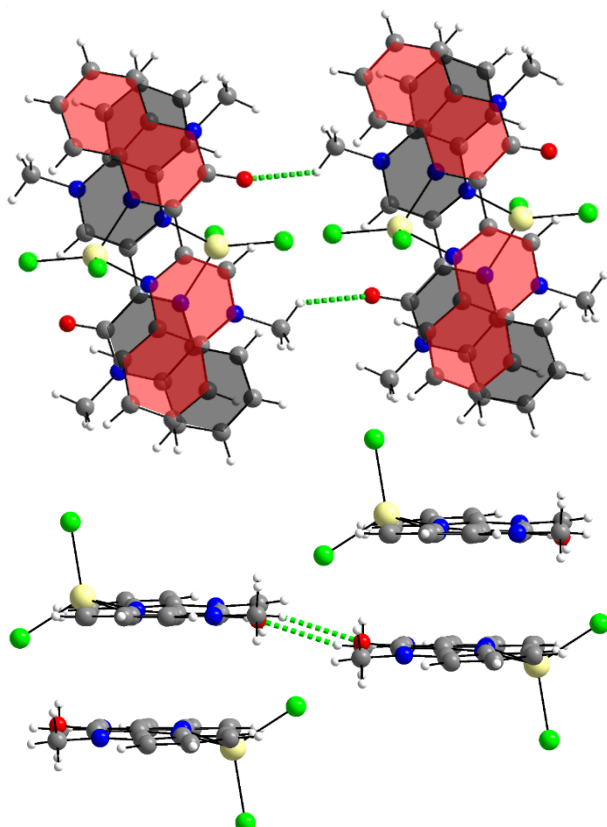


Figure 57. Packing interactions in **(12-Zn B)** showing the pancake bonded dimers that are interconnected *via* HBs.

Phase purity of the isostructural complexes (**9-Co**, **10/11-Cu**) was confirmed from PXRD measurements with a small amount of crystalline impurity visible in the (**8-Co**) sample (see figure 58).

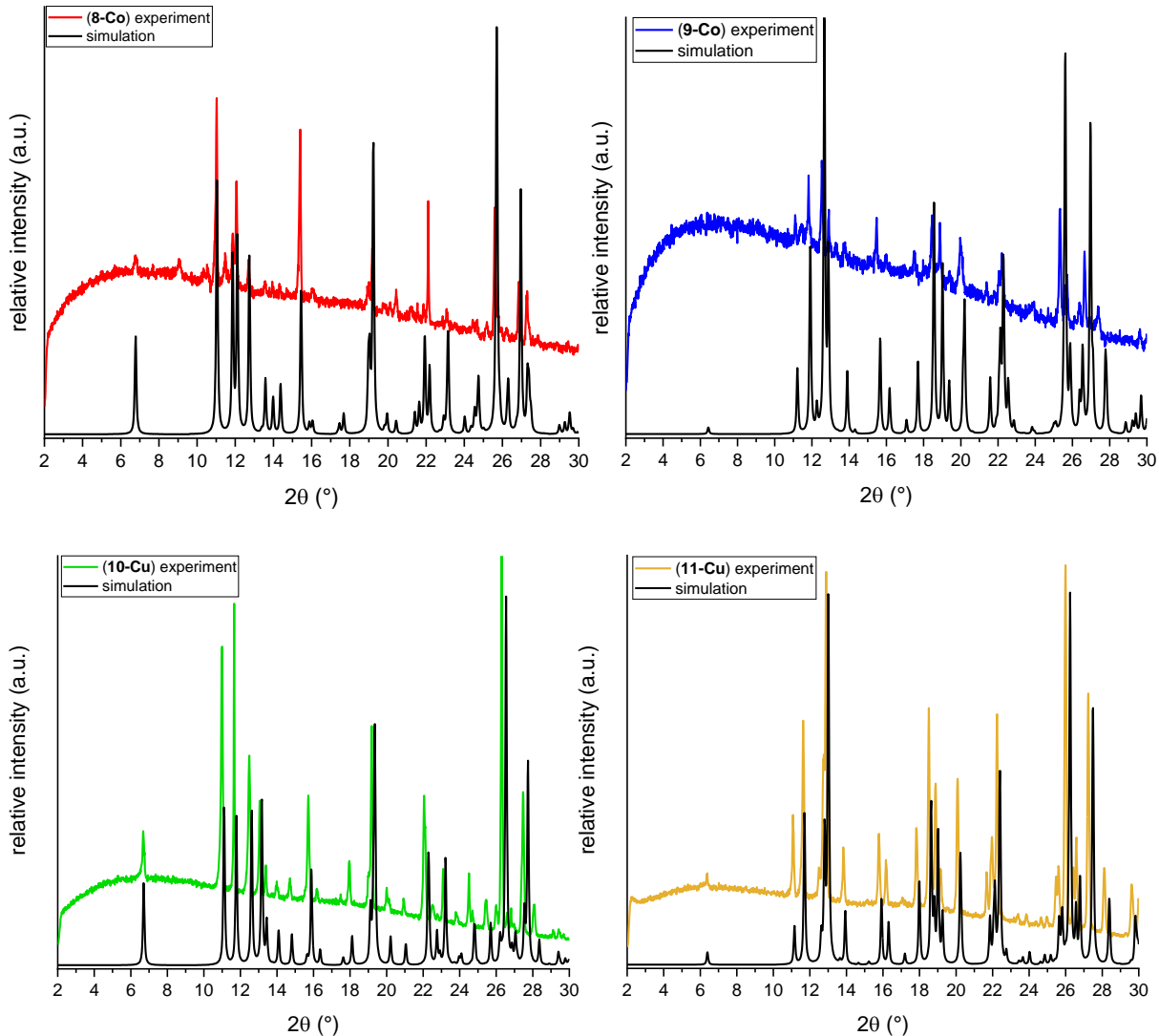


Figure 58. Experimental and simulated powder patterns of (**8- and 9-Co**) (top) as well as (**10- and 11-Cu**) (bottom) confirming phase purity of all samples but (**8-Co**) in which small amounts of crystalline impurity can be observed.

The PXRD measurement on batches of (**12-Zn**) additionally proved that both polymorphs are present in the bulk sample (see figure 59), peaks at higher angles are slightly shifted.

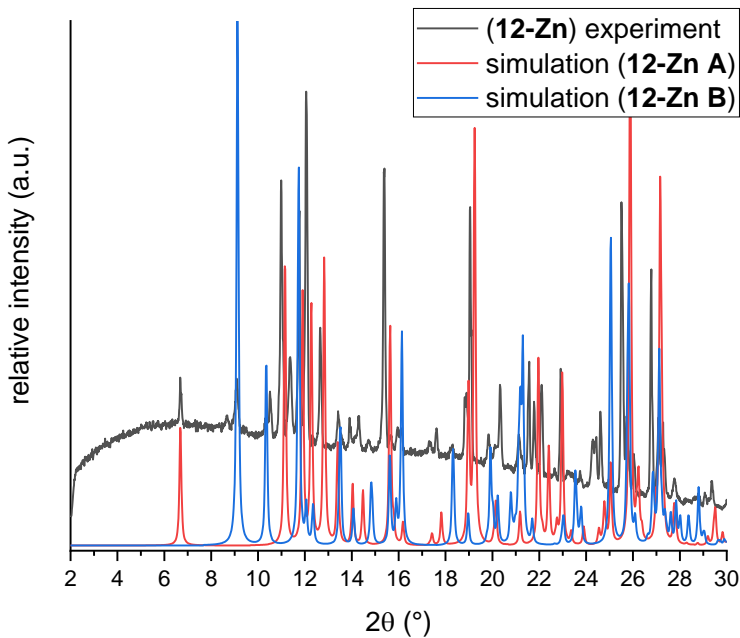


Figure 59. PXRD of the bulk sample of **(12-Zn)** compared to the simulated powder patterns of both polymorphs **(12-Zn A)** and **(12-Zn B)** in the region between 2 and 20°, revealing both polymorphs to be present.

4.3.2 Magnetic Properties of $[\text{Zn}^{\text{II}}\text{Cl}_2(\text{MbqnO})]$ (**12-Zn**)

In addition to the magnetic measurements performed previously on **(8- and 9-Co)** reported in my Bachelor thesis,^[28] magnetic measurements using dc fields were performed on a powder sample of **(12-Zn)** containing both polymorphs. The first observation is that the **(12-Zn)** complex could be centred in the SQUID magnetometer and shows a paramagnetic signal. This is further proof of the radical nature of the ligand since the metal ion, Zn^{II} in this case, is diamagnetic. The magnetic susceptibility was measured for this mixed powder sample of the two polymorphs of **(12-Zn)** in the temperature range between 1.8 and 300 K and the $\chi_{\text{M}}\text{T}$ vs T plot and the Curie-Weiss plot are shown in figure 60 left and right, respectively. Compound **(12-Zn)** does not reach the expected $\chi_{\text{M}}\text{T}$ value of $0.375 \text{ cm}^3\text{Kmol}^{-1}$ with the maximum value of $0.311 \text{ cm}^3\text{Kmol}^{-1}$ at 300 K. However, near RT a significant slope is still observed, which could indicate that antiferromagnetic coupling is present in this compound which still persists up to this temperature. Indeed, the χ_{M}^{-1} vs T curve which follows the Curie-Weiss law between 100 and 300 K, can be fitted with a Weiss constant θ of -257.7 K indicating not only an antiferromagnetic coupling but a very strong one. This suggests that radicals of neighbouring molecules in both the chain-like and dimer-like supramolecular motifs interact antiferromagnetically with each other. This is

reasonable since strong intermolecular magnetic coupling interactions have been previously reported for organic radicals.^[196-197]

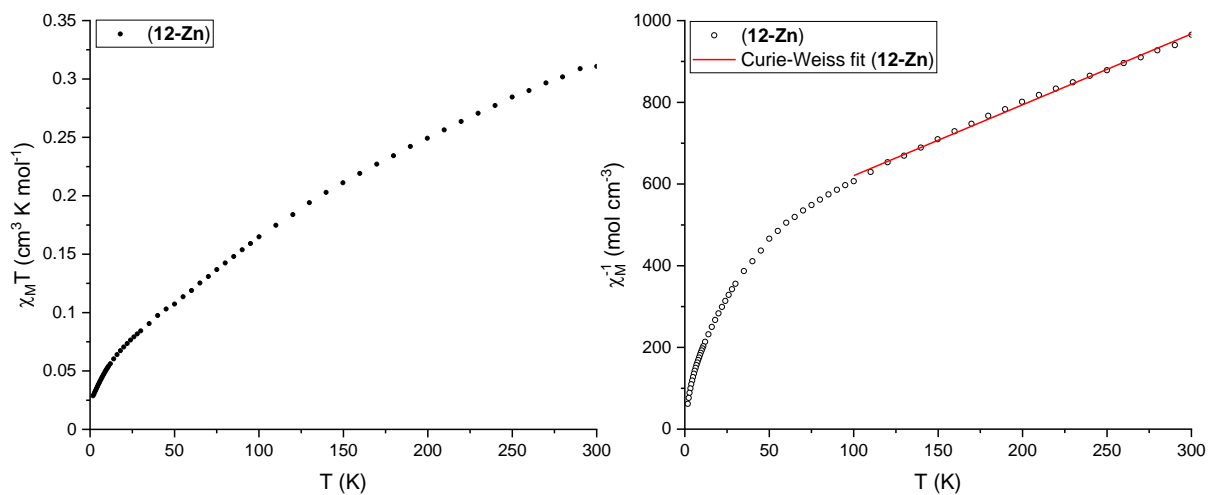


Figure 60. $\chi_M T$ vs T plot (left) and Curie-Weiss plot and fit of (12-Zn) (right) confirming not only the radical nature of the ligand but also a strong antiferromagnetic interaction to be present between neighbouring molecules.

No hysteresis could be observed in field dependent measurements from -7 to 7 T and no out-of-phase maxima were observed at 2 K and 1000 Hz in ac measurements.

4.4 Transition Metal Complex using the Mbqn-(acetone)₂ Adduct – A Proof of Concept

Using the procedure to synthesise the fluorescent acetone adduct (7) described in chapter 8.1 but adding $ZnCl_2$ instead of waiting for the fluorescent adduct to crystallise, resulted in a dark solution which yielded crystals that were suitable for SC-XRD of the desired complex isostructural to the ones described in the previous section. The molecular structure of $[ZnCl_2(Mbqn\text{-}(acetone)_2)]$ (13-Zn) is shown in figure 61 providing a proof-of-principle that the adducts presented in section 4.2 can be used as ligands to coordinate transition metal ions allowing for further tuning of the optical and magnetic properties.

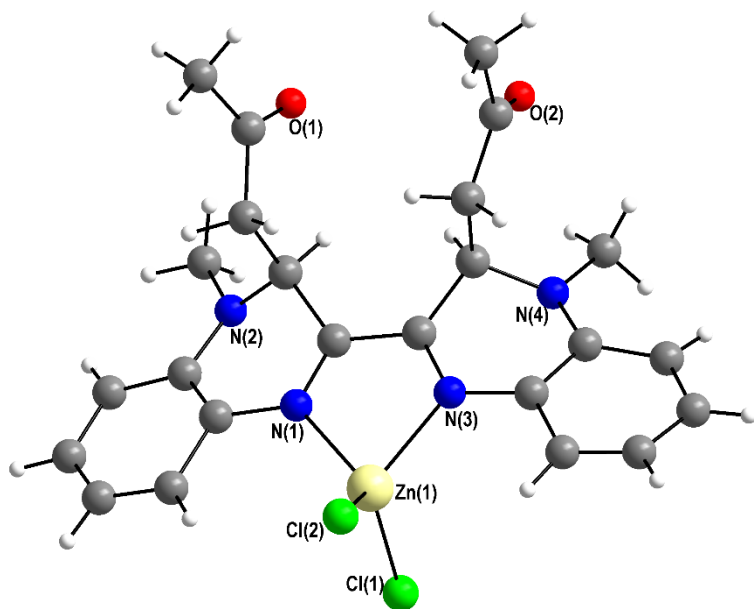


Figure 61. Molecular structure of (13-Zn) providing a proof of principle for the extension of complexes in this ligand system using the adducts presented in section 4.2.

Compound (13-Zn) crystallises in the monoclinic space group $P2_1/n$ with $Z = 4$ and forms supramolecular chains that appear similar to the ones observed in section 4.3 above. In (13-Zn) these chains form along the crystallographic a axis and create channels along this axis (see figure 62).

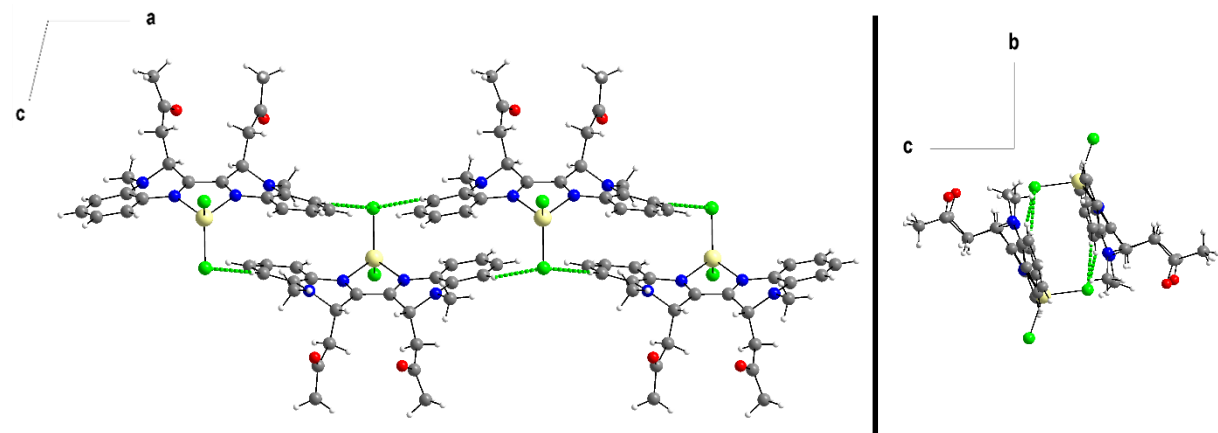


Figure 62. Two views on the packing of four molecules of (13-Zn) showing the formation of supramolecular chains along the crystallographic a axis.

While the previously discussed chain structures were formed due to pancake bonding between radical ligands assisted by non-classical HBs, the π - π overlap between neighbouring molecules in (13-Zn) is minimal. This is also reflected by the shortest C-C distance of $3.65(2)$ Å which is longer than double the VdW radius of carbon. This leads to the conclusion that since only distinctly weaker π - π interactions appear to be present in (13-Zn), another interaction seems to help in determining the packing. The

weaker π - π interaction may also be related to the likely absence of a radical in (**13-Zn**). The non-classical HBs that are assisting the chain formation are also present in (**13-Zn**). However, with distances of 2.845(3) Å and 3.024(3) Å between C(8)-H(8)...Cl(1) and C(20)-H(20)...Cl(1), respectively, they are also slightly weaker than the ones that were observed for (**8/9-Co**, **10/11-Cu** and **12-Zn A**). Instead, there are additional HBs between the Mbqn-(acetone)₂ ligands of molecules that belong to two different chains forming something that can best be described as a molecular zipper (see figure 63). These then form a 3-dimensional network with the known chain structure connecting molecules along the a axis and the new HBs, enabled by the ligand substitution, now further interconnecting these chains along the b and c axes (see figure 63). The HB distances of 2.50(1) and 2.53(3) Å indicate that the intermolecular acetone-O to acetone-H HBs are stronger than the non-classical ones described previously and therefore influence the packing of (**13-Zn**).

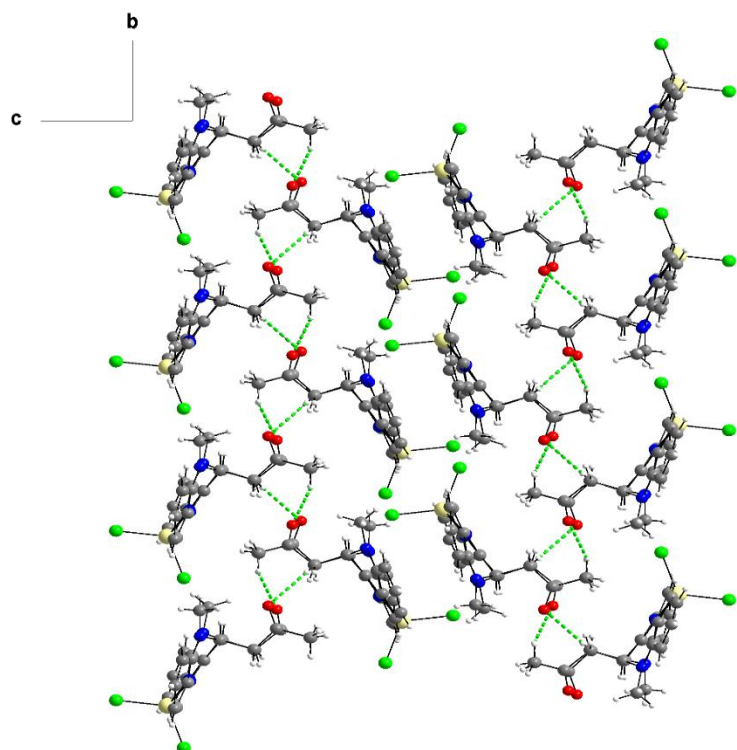


Figure 63. Packing of (**13-Zn**) along the crystallographic a axis, showing the interconnection of the previously observed chain structures by zipper-like HBs (green dashed lines) forming a 3-dimensional network.

Since the yield of this compound was only a couple of crystals, although it made it possible to identify (**13-Zn**), no further characterisation could be conducted. Reproduction and reaction optimisation of this type of synthesis will be the next step in order to help understand the magnetic, optical and redox properties of this ligand system.

4.5 Conclusions and Summary on the Biquinoxen Platform

Fluorescent adducts

The fluorescent methylbiquinoxen adducts using MeOH and EtOH that were previously reported,^[29] were reproduced. The use of further alcohols as nucleophile resulted in four new compounds Mbqn-(OⁱPr)₂ (**1**), Mbqn-(OⁿBu)₂ (**2**), Mbqn-(OⁿOct)₂ (**5**) and Mbqn-(O-Bu(Me)₂)₂ (**6**). Furthermore, the synthesis of adducts using different heteroatoms was successful as shown by the isolation of Mbqn-(SⁱPr)₂ (**3**) and Mbqn-(SⁿBu)₂ (**4**) as well as Mbqn-(acetone)₂ (**7**). All new adducts apart from (**5**) yielded crystals suitable for X-ray diffraction. In the case of (**5**) the floppy n-octanyl residues inhibited crystallisation. The molecular structures lead to the conclusion that the O-based adducts are generally more planar than the S-based ones, leading to stronger aromaticity in the former. This was an indication of the higher stability of these compared to their S-based counterparts.

The optical properties of compounds (**1**)-(**6**) were investigated using UVVis absorption spectroscopy in solid state and solution. In solid state measurements it was observed that while O- and S-based adducts show different absorption spectra, the individual residues have no effect for the O series and also for the S series. For compound (**1**) it was shown that the solution state UVVis spectra are essentially solvent independent and that the spectra of freshly prepared solutions match the solid state spectrum. This indicates stability, at least in freshly prepared solutions, and validates the other experiments that were performed. The solution state UVVis spectra of (**1**)-(**6**) were compared in DMF led to the same conclusion regarding the lack of influence of the residue on the absorption spectra.

All six compounds were further investigated using emission spectroscopy in DMF solutions. Despite the UVVis absorption spectra showing that the transitions in the O-based adducts all occur at the same energy, the emission wavelength is red-shifted by 13 nm between (**5**) and (**1**). Thus, it was shown that by changing the carbon chain on the O-based residue it is possible to fine-tune the emission wavelength from yellow light to a more greenish colour. This possibility to tune the colour of the emitted light is further shown by the emission of the S-based adducts being red shifted into the red

spectral region to 610 and 611 nm for (3) and (4), respectively. This means by variation of the residue on the biquinoxen core of the molecule it was possible to shift the emission wavelength by 63 nm covering the spectral region from yellow to red light.

Compound (1) was additionally shown to be fluorescent in solid state with a quantum yield of 13% which were measured in collaboration with Dr. Mikhail Khorenko from the group of Prof. Dr. Claus Feldmann.

Quantum yields of compounds (1)-(4) were also determined in solution. In freshly prepared solutions the quantum yields of the O-based adducts (1) and (2) surpass 90% and therefore show excellent efficiency, while the S-based compounds (3) and (4) show significantly lower quantum yields of 7% and 6%, respectively. However, it was also shown using successive quantum yield measurements as well as femtosecond spectroscopic experiments in collaboration with Dr. Juli Leier from the group of Prof. Dr. Andreas-Neil Unterreiner, that all adducts decompose in solution. The O-based adducts were shown to decompose to a non-emitting product over the course of a few days, likely reacting back to the non-fluorescent Mbqn-(OH)₂ starting material *via* the equilibrium shown in figure 29. This equilibrium, which was previously reported to be present in this system,^[29] was found to be pH sensitive, therefore, experiments changing the basicity of the solutions could result in stabilisation of the desired fluorescent dyes. The S-based adducts decompose within hours and therefore much faster than the O-based ones. This is in line with the weaker aromaticity observed in the crystal structures of (3) and (4). The product of the decomposition is as yet unknown but carefully following the decomposition process *via* NMR spectroscopy may yield further insights in future work.

All these investigations lead to the conclusion that by carefully choosing the residue on the biquinoxen core, emitters with tailored emission wavelengths can be designed. Possibilities for improving the performance of these emitters, enhancing the stability in solution of all adducts and increasing the quantum yield, especially of the non-O-based adducts are discussed in the outlook in chapter 7.

Transition metal-radical complexes

During the work presented in this chapter the Co^{II} complexes (**8**- and **9-Co**), which are also reported in my Bachelors thesis were reproduced for further analysis.

Furthermore, the family of complexes using the MbqnO ligand, which is formed *in-situ* and stabilised by the coordination to a metal ion, was expanded by the successful synthesis of the Cu^{II} analogues (**10- and 11-Cu**) as well as the Zn^{II} analogue (**12-Zn**). The packing in the crystal structures was subjected to a closer analysis and the formation of supramolecular chains *via* a mixture of π - π interactions, which seem to be superposed with radical-radical interactions similar to pancake bonds, and non-classical HBs, was recognised in the isomorphous structures of compounds (**8-9-Co** and **10-11-Cu**). For the Zn^{II} containing complex, two polymorphs were identified using SC-XRD. Compound (**12-Zn A**) is isomorphous to the other complexes forming supramolecular chains. Compound (**12-Zn B**) instead forms supramolecular dimers which are further connected to the neighbouring dimer pair *via* HBs. From PXRD measurements it can be concluded that in the bulk sample of (**12-Zn**) both polymorphs are present. Magnetic measurements were performed on such a bulk sample of (**12-Zn**) containing both polymorphs. The fact that during the process of centering the sample a paramagnetic signal was obtained, provides further proof for the radical nature of the ligand. The $\chi_M T$ vs T plot which is shown in figure 60 above suggests significant antiferromagnetic interactions at RT are still present in the system. Since Zn^{II} is diamagnetic this means that through the formation of supramolecular structures throughout the crystal, extremely strong intermolecular magnetic interactions between neighbouring radicals are enabled.

Transition metal complex using biquinoxen adduct as ligand

The synthesis of a Zn^{II} complex (**13-Zn**), using one of the fluorescent adducts as ligand was successful yielding crystals suitable for X-ray diffraction. A closer look at the packing interactions in (**13-Zn**) revealed that supramolecular chains not unlike the ones observed in (**8/9-Co**, **10/11-Cu** and **12-Zn A**) are present. The longer intermolecular C-C distances between the π systems of neighbouring molecules as well as the less significant overlap of these, indicate much weaker interactions within these chains. This may be the result of the absence of a radical on the organic ligand in this compound. The acetone residue on the ligand does, however, interact intermolecularly by forming HBs with acetone residues of neighbouring complexes belonging to a different supramolecular chain. This creates a well-connected 3-dimensional network of supramolecular interactions within this system.

The synthesis of **(13-Zn)** can be regarded as a proof-of-concept that further modification of this system is possible through the use of biquinoxen adducts as ligands. This could provide an opportunity for the rational design of crystals controlled by the steric demand and the chemical nature (here the ability to act as HB donor and acceptor simultaneously) of the adduct residue. Such modifications could provide an additional tuning handle in order to steer the magnetic and optical properties of transition metal complexes within this system.

5. H₂opch – A Family of Complexes Designed to Gauge Intermolecular Interactions using Halogen Bonding

5.1 Introduction

The goal of the following chapter is to use one ligand system and investigate the influence of subtle changes to the intra- and intermolecular interactions in terms of the properties of lanthanide complexes. Schiff base ligands are an excellent choice for this, since their synthesis allows for easy modification through the use of differently substituted aldehydes. A pyrazine and *ortho*-vanillin-based ligand system was chosen as a testbed here given the possibility for enhanced intermolecular interactions through the heteroatoms on the pyrazine ring, in addition to the availability of many substituted *ortho*-vanillin modifications (see figure 64).

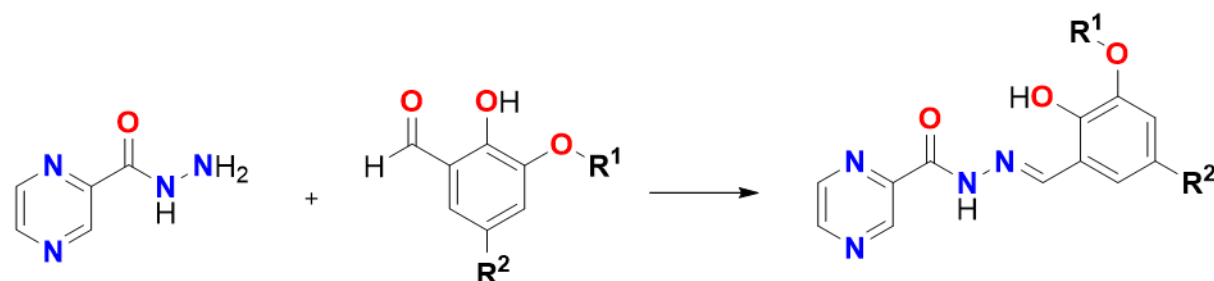


Figure 64. Molecular components to prepare the chosen ligand system.

The simplest form of this ligand is 2-hydroxy-3-methoxybenzylideneypyrazine-2-carbohydrazide abbreviated as H₂opch with R¹ = Me and R² = H. This ligand was previously used to produce many lanthanide clusters by the group of Prof. Dr. Jinkui Tang.^[198-201] It was shown that the multiple possible coordination sites of H₂opch make the system flexible concerning its coordination modes. The ligand is therefore able to accommodate ions of different sizes as exemplified by the isolation of a dinuclear 3d-4f complex employing an eight coordinate Dy^{III} and a seven coordinate Mn^{II} ion. The ligand was also shown to be able to form complexes of different nuclearities under varied reaction conditions as proved by the synthesis of di-, penta-, hexa- and octanuclear Dy^{III} containing complexes, all of which exhibit SMM behaviour.^[198-201] Since similar structures were obtained during the work for this thesis, the reported

molecular structures of the dimeric, the hexanuclear as well as the octanuclear Dy^{III} compound are shown in figure 65.

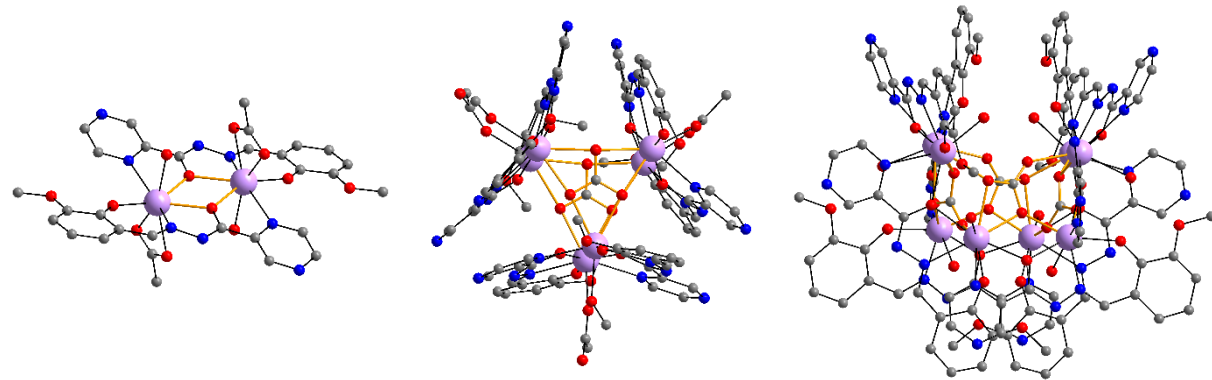


Figure 65. The molecular structures of a Dy^{III} dinuclear, hexanuclear and octanuclear complex employing the $H_2\text{opch}$ ligand reported by Tang *et al.* highlighting the versatility of this Schiff base ligand.^[198-200]

The trigonal prismatic hexanuclear and the octanuclear clusters are held together by two and four bridging carbonate ligands, respectively. Since carbonate anions can coordinate in many bridging modes (some of which are shown in figure 66) they can be used to template the formation of larger clusters.^[202-206]

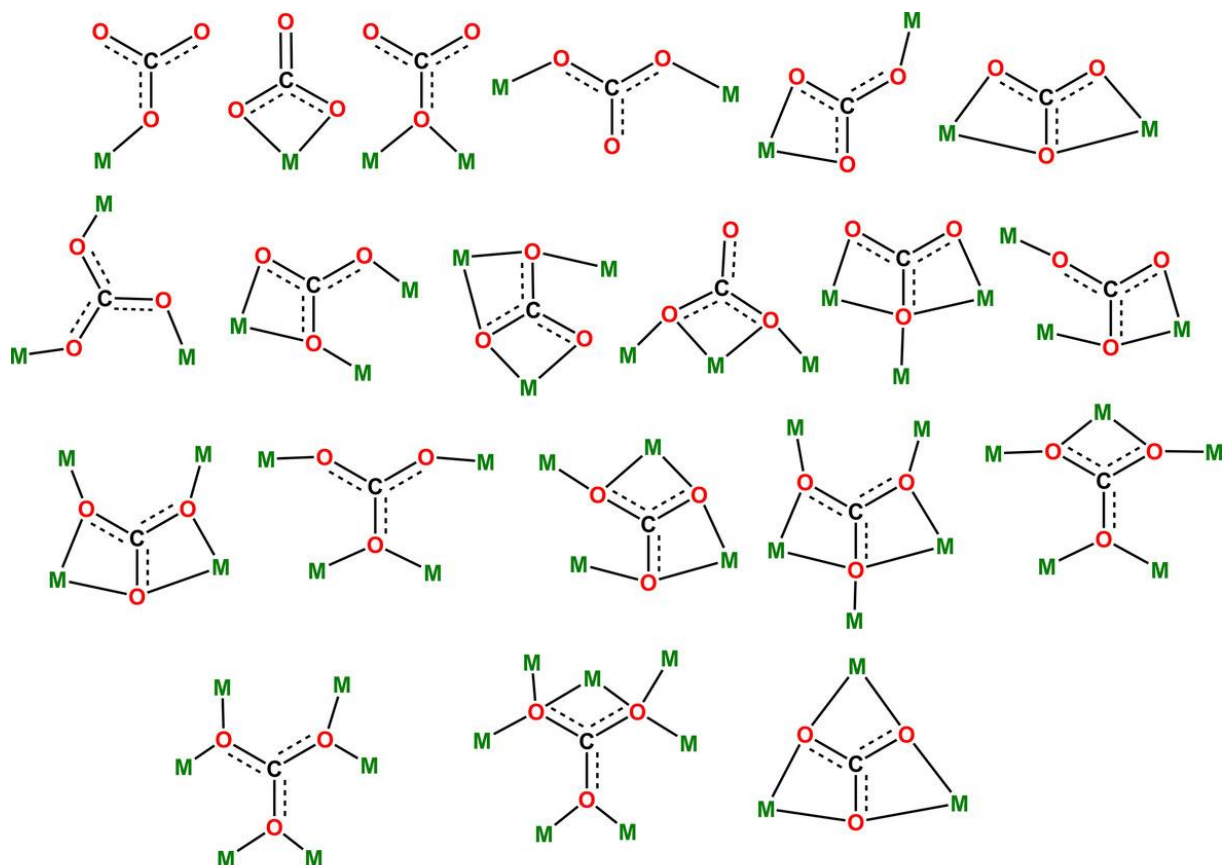


Figure 66. Flexible coordination modes of CO_3^{2-} . Adapted from reference^[207] with permission [John Wiley and Sons] copyright [2017].

Carbonate can be introduced into reaction mixtures in several ways. In the case of the aforementioned Dy_6 and Dy_8 clusters, adventitious fixation of aerial CO_2 was responsible for the formation of the respective cluster.^[199-200] This was also reported in other instances in which CO_2 from air led to the formation of lanthanide clusters.^[207-224]

Alternatively, CO_2 can be bubbled through the reaction mixture,^[225-227] carbonate sources such as carbonate and bicarbonate salts can be added^[228-231] or the carbonate anions can be generated by ligand decomposition and decomposition of DMF under solvothermal conditions.^[232-233]

By combining the possibility of varying the Ln^{III} ions in the syntheses of new clusters, with the exhibited ability to form carbonate bridges by CO_2 fixation and the tolerance of the system to a wide variety of anions as well as solvents, there are many ways in which intramolecular interactions can be tailored. In order to tune the intermolecular interactions, R^1 and R^2 of the *ortho*-vanillin component of the H_2opch ligand system can be varied without effecting the coordination pockets. In other words, the goal was to produce complexes having the same molecular structure in terms of coordination modes, but to vary the intermolecular interactions. For this reason, halogen interactions were chosen since they provide directionality that can be used to engineer symmetric arrangements of clusters in the crystal packing.^[78, 234-235] This directionality was introduced and discussed in chapter 3.3 in the context of organic molecules and was visualised by imaging self-assembled halobenzenes on silver surfaces using an inelastic tunnelling probe.^[236] However, the same directionality can also be used as a synthon in order to control the supramolecular interaction between metal complexes.^[237-238] This was, for example, shown in a series of halogen bonded lanthanide complexes by Cahill *et al.*^[239-241]

Intermolecular halogen interactions have also been shown to have a direct effect on the magnetic behaviour of complexes as found in the case of a Cr^{III} iodoanilate complex. In this complex, antiferromagnetic interactions can be observed in the χ_M vs T curve at temperatures below 4.1 K. These are reported to stem from halogen bonds between iodoanilate I and O atoms. This leads to supramolecular dimer formation enabling these antiferromagnetic exchange interactions between otherwise non-interacting Cr^{III} ions *via* the extended iodine orbitals (see figure 67).^[242]

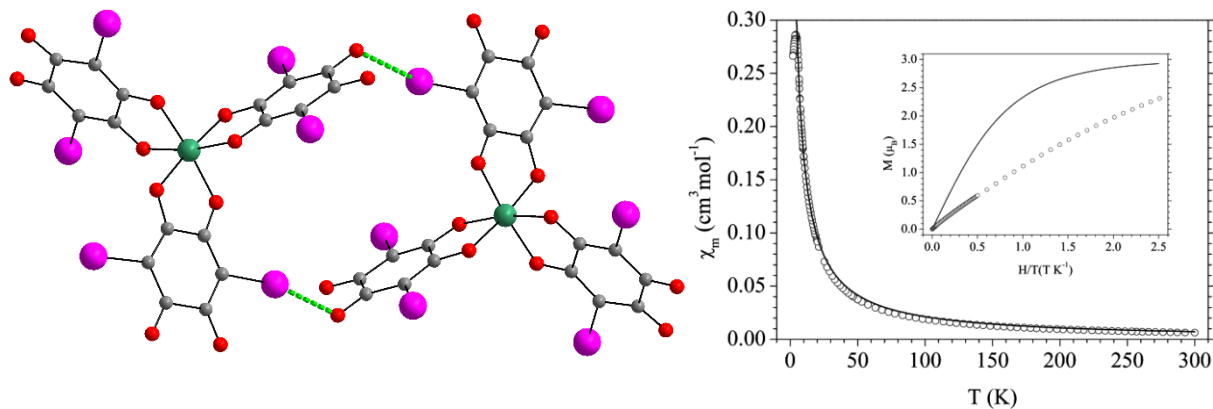


Figure 67. Halogen bound supramolecular dimers of $(\text{PPh}_3)_3[\text{Cr}^{\text{III}}(\text{I}_2\text{An})_3]$ (left) and χ_M vs T plot showing the induced antiferromagnetic interaction below 4.1 K (right). Reprinted from reference.^[242]

Mediation of magnetic interactions through halogen bonds was also shown by Turnbull and Schlueter and co-workers in Cu^{II} pyrazine-based complexes.^[243-244] Magnetic exchange interactions through Br-Br contacts between chains of a Cu^{II} -dimethylpyrazine coordination polymer were shown to reach extremely high values of $2J = -234$ K, which exemplifies the significant impact halogen bonds can have on the magnetic properties of complexes.^[243]

Moreover, halogen bonds have been described as “spin-couplers” by Jin *et al.*, who have shown that by variation of the XB_D , which form co-crystals with a modified TEMPO radical, it was not only possible to use the directionality of halogen bonds to determine the crystal packing, but also enhance antiferromagnetic interactions between these radicals.^[245]

Similarly, halogen bonds have been used to form well-defined 2-dimensional spin arrays of perchloro-triphenyl-methyl radicals with terminal bromines deposited on gold surfaces. Using atomic force microscopy (AFM) it was shown that the radicals form arrays using either linear, triangular or hexagonal Br-Br halogen-halogen interactions.^[246]

Therefore, the work conducted here, using H_{opch} , started with the reproduction of the ligand as well as the synthesis of the modifications employing halogen atoms in order to systematically gauge the influence of intra- and intermolecular interactions on the properties of lanthanide complexes.

5.2 H₂opch-Lanthanide Complexes - A Story about Lanthanide Contraction

Using the same reaction procedure employing the Schiff base ligand E-N'-(2-hydroxy-3-methoxybenzylidene)pyrazine-2-carbohydrazide (H₂opch) with the whole series of lanthanide nitrates as well as Y^{III}(NO₃)₃·6H₂O led to 6 unique structures depending on the size of the corresponding Ln^{III} ion (see figure 68). The work on this section was supported by the synthetic efforts of the student Daniel Seufert who conducted his Master project under my supervision in the lab.^[247]

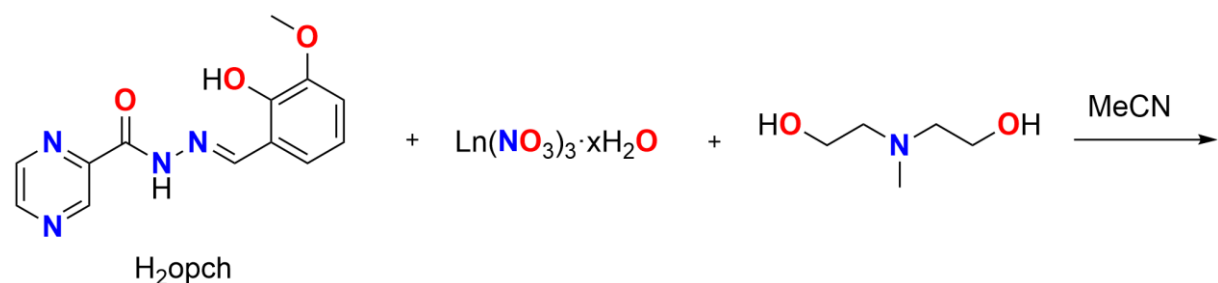


Figure 68. Using the same reaction conditions with the Schiff base ligand H₂opch, mdeaH₂ as base and potential co-ligand as well as the corresponding lanthanide nitrate salt, six unique structures could be obtained depending on the Ln³⁺ ion used (Ln = La-Lu and Y).

Reaction of the Ln-nitrates with the H₂opch ligand in MeCN with N-methyldiethanolamine (mdeaH₂) led to yellow solutions with one exception (see figure 69). The reaction using Ce^{III}(NO₃)₃·6H₂O produced a dark brown solution after only a few minutes of stirring which can be attributed to partial oxidation of the Ce^{III} ions to Ce^{IV} (discussed further below). Most of the complexes produced by this method include bridging carbonate anions resulting from absorption of CO₂ from the atmosphere, therefore the reaction vials were stirred open to air for at least one hour before they were closed and left to stir further overnight.

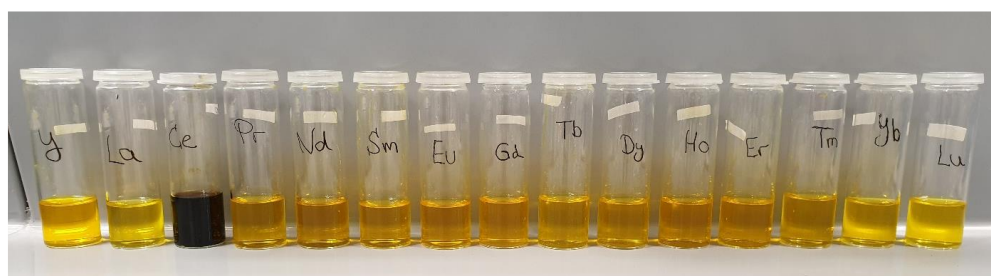


Figure 69. Visual appearance of the reaction mixtures using all Ln³⁺ ions in combination with H₂opch (picture courtesy of Daniel Seufert).

5.2.1 The Six Different and New Structures

5.2.1.1 A Planar La₅ Disc

The reaction using the largest of the employed metal ions, La^{III}, with an effective ionic radius of 121.6 pm (for nine-coordinate La^{III})^[248] resulted in yellow crystals of a pentanuclear La complex [La^{III}₅(CO₃)(mdeaH)₂(NO₃)₃(opch)₄]·4.5MeCN (**14-La**) (see figure 70).

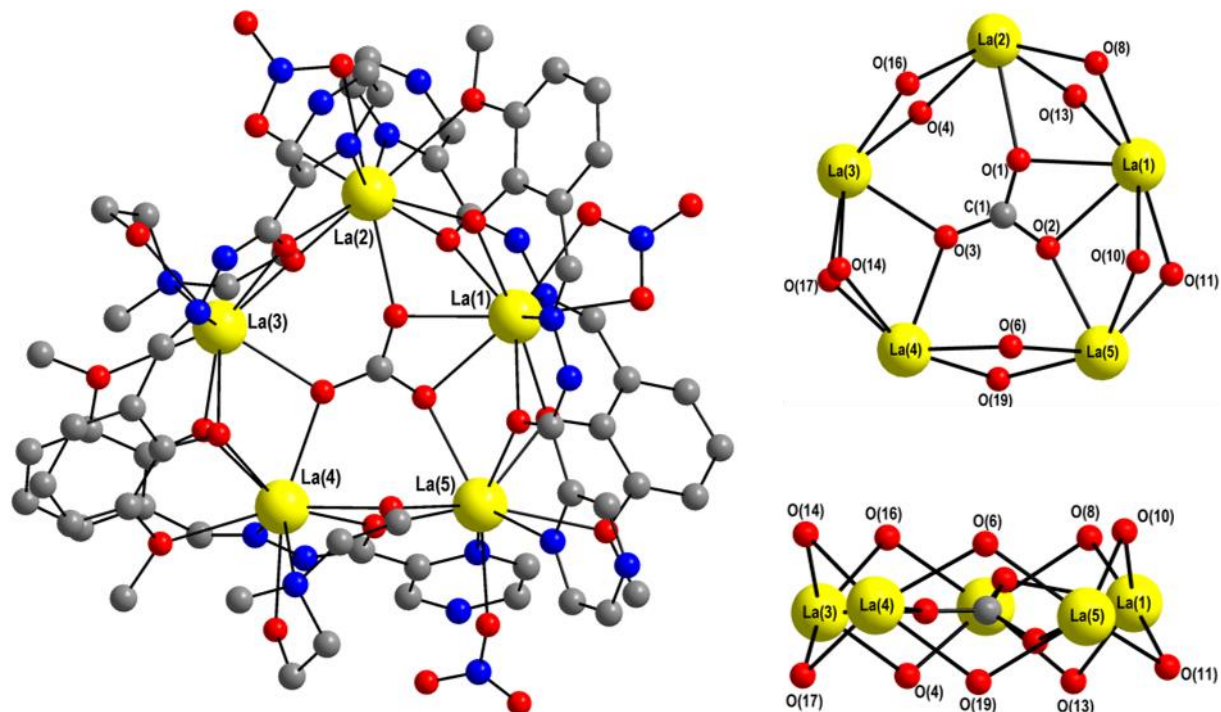


Figure 70. Molecular structure of (**14-La**) (left) and top and side view of the essentially planar core (right).

(**14-La**) crystallises in *P*̄*I* with *Z* = 2. The nine- and ten-coordinate La^{III} ions are arranged in a near planar pentagon held together by a central bridging carbonate anion that is coordinated to all five La^{III} ions with one oxygen coordinating to each of La(2)-La(5) but chelating La(1). The intramolecular La-La distances are fairly regular with lengths between 3.9058(4) and 4.1136(4) Å. The La₅ pentagon is also close to planar, with La(5) showing the greatest displacement (0.1179(2) Å) out of the mean plane defined by the five La centres. The slight distortion of the pentagonal arrangement can be seen most clearly by looking at the La-La-La angles. La(5)-La(1)-La(2), 119.56(1)° is significantly larger than the others, which have values between 98.22(1)° and 112.59(1)° (and are thus closer to the perfect pentagon internal angle = 108°), mainly due to the chelation of La(1) by the carbonate. The coordination spheres of La(3) and La(4) are the same as both are three times coordinated by one of the two singly

deprotonated mdeaH co-ligands. The coordination spheres of La(2) and La(5) are also nearly the same only differing in the coordination modes of the nitrate ligands as La(2) is chelated by a nitrate while the nitrate on La(5) only coordinates with one oxygen atom. The unique coordination sphere of La(1) consists of two opch^{2-} ligands chelating three times each, a chelating nitrate and the chelating central carbonate. Apart from the different bonding modes of the nitrates on La(2) and La(5), and a slight tipping of the carbonate relative to the La_5 plane, the molecule approximates to twofold symmetry.

Intermolecular hydrogen bond interactions (highlighted in green in figure 71) lead to the packing of **(14-La)** in stacks of La_5 -discs with lattice MeCN filling voids in the structure. The HBs involve the protonated mdeaH alcohol arms O(5)/H(5) and O(7)/H(7) that interact with pyrazine sites of the opch^{2-} ligand N(13) and N(17). The distances between HB donor and acceptor with $d(\text{O}(5)\text{-H}(5)\dots\text{N}(13)) = 2.665(5)\text{\AA}$ and $d(\text{O}(7)\text{-H}(7)\dots\text{N}(17)) = 2.754(5)\text{\AA}$ as well as the angles of $177(7)^\circ$ and $169(6)^\circ$, respectively, reveal that the HB involving O(5) is slightly stronger (interaction between the middle two La_5 complexes in figure 71).

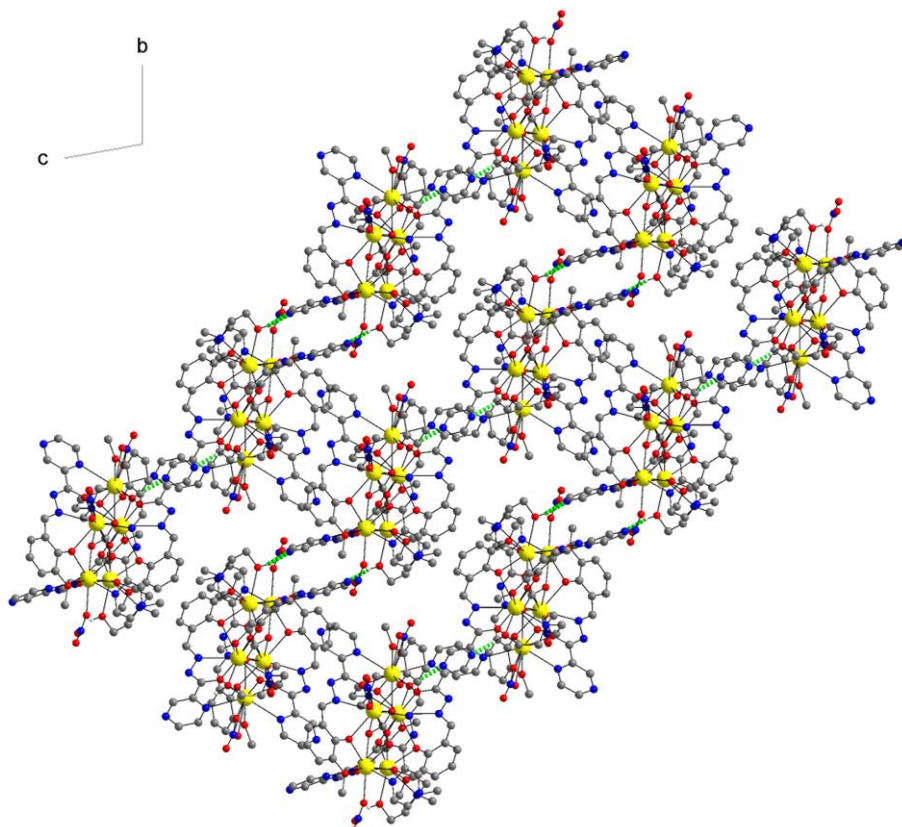


Figure 71. View along the a-axis highlighting the hydrogen bonds responsible for the stacking of the La_5 discs in green.

The planar La_5 discs stack almost in parallel to the a-b-plane as seen in figure 72 with an angle between a mean plane through all the La^{III} ions to the a-b-plane of 20° .

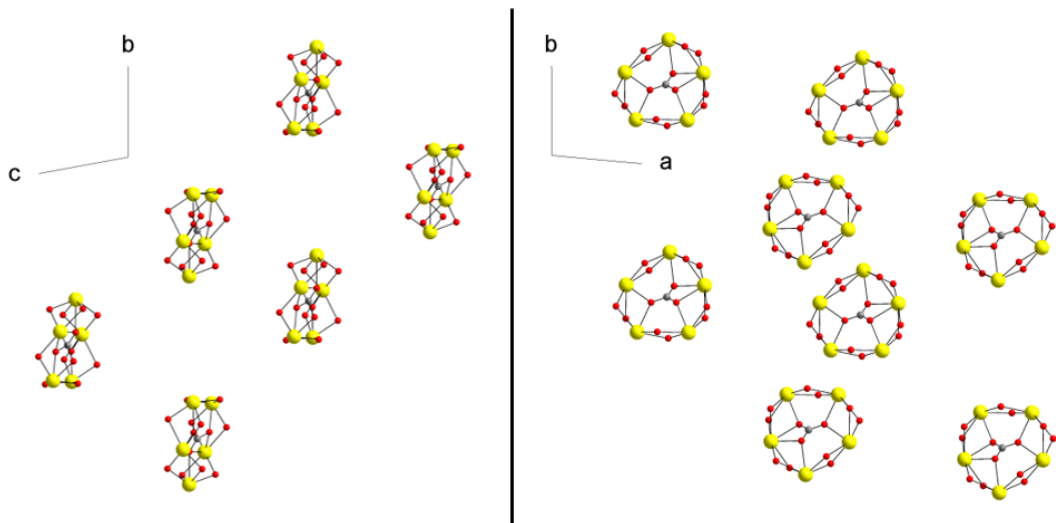


Figure 72. Two views on the packing of (14-La), along the a-axis (left) and along the c-axis (right). Everything but the core was omitted for clarity.

The bulk sample was confirmed to be phase pure by PXRD (Figure 73, left) as well as elemental analysis which is consistent with the replacement of the lattice MeCN by six water molecules. This exchange of lattice solvent could also explain the partial loss of crystallinity seen by some amorphous component in the PXRD.

In the IR spectrum (Figure 73, right) the antisymmetric CO stretch band at 1430 cm^{-1} can be identified consistent with IR spectra of multidentate CO_3^{2-} anions in metal complexes in the literature.^[221, 249]

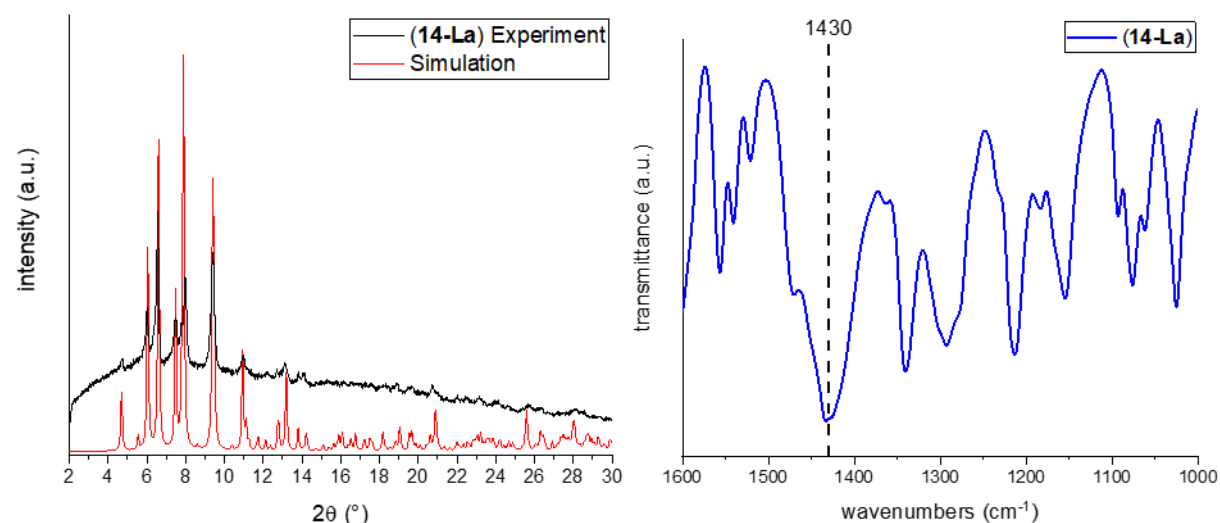


Figure 73. PXRD confirming the phase purity of (14-La) (left) and excerpt of the IR spectrum of (14-La) between 1600 and 1000 cm^{-1} highlighting the asymmetric CO stretch vibration of the multidentate CO_3^{2-} ligand at 1430 cm^{-1} (right).^[249]

A potential application of this La_5 compound could lie in catalysis. It was shown in the literature that La-clusters have the ability to homogeneously and heterogeneously catalyse hydroboration reductions of amides to tertiary, secondary and, most importantly, primary amines as well as the reduction of esters in the presence of pinacolborane (HBpin). HBpin acts as a mild reductant that is easily handled and is tolerant towards a great variety of functional groups and heteroatoms.^[250-251] Furthermore, Hessen *et al.* were able to show catalytic activity of La-clusters in hydroamination/cyclisation reactions as well as in Z-selective dimerisation reactions of phenylacetylenes.^[252-253]

Therefore, the catalytic activity of (**14-La**) towards multiple types of organic reactions including a wide variety of substrates will be investigated in the future. The planar arrangement of five La^{III} ions in close proximity in compound (**14-La**) would make an involvement of multiple La^{III} ions in a catalytic cycle possible. This could further be enabled by the versatile coordination modes of the bridging carbonate ligand which could provide vacant coordination sites needed for the catalytic reaction while providing stability to the La_5 -cluster during the catalytic cycle.

5.2.1.2 A Mixed-Valence Tetranuclear Cerium Complex

Using $\text{Ce}^{\text{III}}(\text{NO}_3)_3 \cdot 6\text{H}_2\text{O}$ in the same reaction led to a surprising colour change to dark brown given that the reactions with all other Ln^{III} ions gave yellow solutions. Therefore, it was clear from the start that something different is happening here. The resulting crystals were measured to reveal the tetranuclear cerium compound $[\text{Ce}^{\text{III}}_2\text{Ce}^{\text{IV}}_2(\text{H}_2\text{O})_3(\text{NO}_3)_2(\mu_2\text{-OH})_4(\text{opch})_4] \cdot 4\text{MeCN}\cdot\text{H}_2\text{O}$ (**15-Ce**) with a square planar core connected via bridging opch^{2-} ligands as well as bridging hydroxy groups (see figure 74).

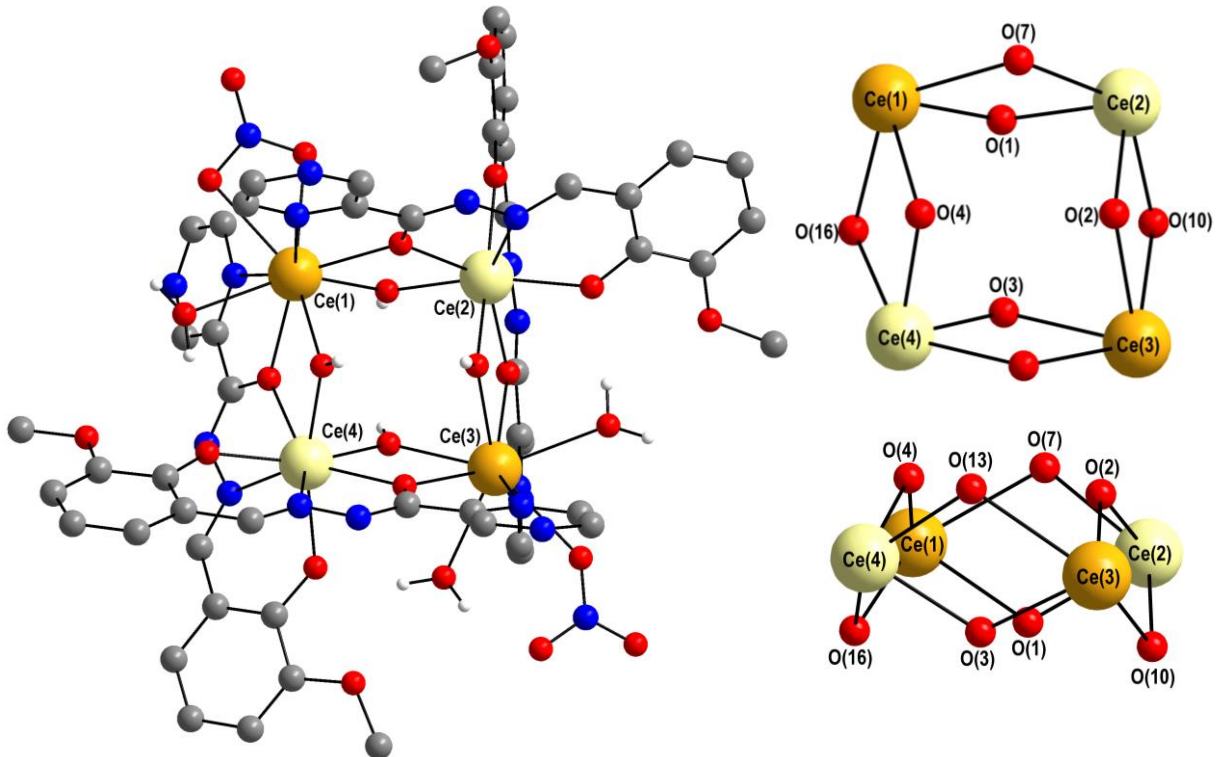


Figure 74. Molecular structure (left) and two views of the square planar tetranuclear core of (15-Ce) (right).

The four cerium ions are arranged in a square with side lengths between 3.9463(3) Å and 4.0052(3) Å internal angles between 86.247(7)° and 94.331(7)°. The deviation from planarity of the square is also only very small with the distance of Ce(4) from a plane through the other three cerium ions is only 0.11 Å. The ions are held together by four bridging hydroxy groups O(1), O(2), O(3) and O(4) and bridging oxygen atoms of the opch²⁻ ligands O(7), O(10), O(13) and O(16), that correspond to the carbonyl O in the isolated ligand. The elongated C-O (d = 1.306(4) Å) and shortened adjacent C-N (d = 1.296(5) Å) bond lengths in the complex suggest the amide moiety mostly to be in its enol form. This is consistent with the deprotonation of the hydrazine nitrogen and the proximity of the oxygen to the positively charged lanthanide ion. While the coordination spheres of the eight-coordinate Ce(2) and Ce(4) are identical there is a minor difference between the environments of the nine-coordinate Ce(1) and Ce(3). Ce(1) is chelated by a nitrate co-ligand with one additional H₂O ligand completing the coordination sphere while Ce(3) is coordinated by a monodentate nitrate ligand with two additional H₂O ligands.

By examining the charge of the compound, it was found that the complex must be mixed-valence with two Ce^{III} ions shown in orange and two Ce^{IV} ions shown in yellow to balance the charge (4x -1 from the μ_2 -OH + 4x -2 from the opch ligand + 2x -1 from

nitrate = a total charge of -14). This is supported by the coordination spheres around the cerium ions. Ce(2) and Ce(4) are eight-coordinate and the ligand sphere involves both negatively charged sites of the opch_2^- ligand, while Ce(1) and Ce(3) are nine-coordinate involving softer co-ligands. This is in line with the demand for a higher coordination number for Ce^{III} ions due to the ionic radii of eight-coordinate Ce^{IV} ($R_{\text{eff}} = 97 \text{ pm}$) and nine-coordinate Ce^{III} ($R_{\text{eff}} = 120 \text{ pm}$).^[248] It is also supported by the HSAB principle as the softer pyrazine ligand sites coordinate the larger less charged Ce^{III} ions and the hard phenoxy sites coordinate the smaller more charged Ce^{IV} ions.

To further strengthen the hypothesis of a mixed-valence cluster the charges of the cerium ions were also analysed by BVS analysis.

The parameters used for the BVS analysis and the results supporting the assignation of the charges above are shown in tables 9 and 10.

Table 9. Parameters used for the BVS analysis on (15-Ce).

	Ce^{III} O- donor ^[254]	Ce^{III} N- donor ^[191]	Ce^{IV} O- donor ^[254]	Ce^{IV} N- donor ^[255]
B [Å]	0.37	0.37	0.37	0.37
R_0 [Å]	2.121	2.34	2.068	2.179

Table 10. Results of the BVS analysis highlighting the closest result for each of the four cerium ions in (15-Ce).

	$\text{Ce}(1)$	$\text{Ce}(2)$	$\text{Ce}(3)$	$\text{Ce}(4)$
BVS(Ce^{III})	3.18	4.86	3.20	4.94
BVS(Ce^{IV})	2.61	3.99	2.63	4.05

The question that arises concerns the oxidation mechanism to produce (15-Ce). Ce^{IV} is known to be the only easily accessible tetravalent lanthanide ion and Ce^{IV} -containing substances such as ceric ammonium nitrate (CAN) are widely used as oxidising agents^[256] or in catalysis for water oxidation for example.^[257] Oxidation reactions yielding Ce^{IV} compounds have therefore been intensively investigated in particular for the last two decades. Besides electrochemical means, oxidation via aerial oxygen was observed before, when the ions were coordinated to hard ligand donor atoms.^[258-260] Additionally, especially basic CO_3^{2-} rich solutions are known to stabilise the Ce^{IV} oxidation state.^[261-262] Alternative oxidation routes under inert atmosphere were proposed by Hayton *et al.* using $[\text{NO}_3]^-$ as an oxygen donor to produce Ce^{IV} -oxo

clusters either by inner-sphere nitrate reduction or photolytic cleavage under elimination of NO_2 .^[263-264]

The partial oxidation of Ce^{III} to Ce^{IV} to form mixed-valence clusters has only been reported in a handful of examples to date. The first reported example was a trinuclear $\text{Ce}^{\text{IV}}_2\text{Ce}^{\text{III}}$ complex reported by Lappert and co-workers in 2002 followed by 3d-4f clusters containing Mn as well as $\text{Ce}^{\text{IV}/\text{III}}$ reported by Christou and co-workers as well as Powell and co-workers.^[265-267] As mentioned before, the oxidation of Ce^{III} to Ce^{IV} in solution by aerial oxygen was observed before when the ions are coordinated to hard donor atoms, but only in scarce cases such as reported by Mondal and co-workers this led to a partial oxidation and a hexanuclear mixed-valence $\text{Ce}^{\text{IV}}_2\text{Ce}^{\text{III}}_4$ compound.^[268]

As the reaction to synthesise (**15-Ce**) is performed at ambient conditions and open to air and the Ce^{IV} ions in (**15-Ce**) are coordinated to the hard donor atoms of the opch^{2-} the oxidising agent indeed appears to be aerial oxygen. Especially considering, that the H_2opch ligand system discussed here, in combination with mdeaH_2 , which can act as a base, is shown in this work to be prone to fix CO_2 from air, this seems to be a plausible explanation. Therefore, the conditions seem ideal for a complete oxidation of the ions to Ce^{IV} , which means the key in order to obtain a mixed-valence compound instead of a purely Ce^{IV} -containing complex in the reaction towards (**15-Ce**) is the presence of both hard and soft donor sites on H_2opch making the Ce^{IV} and Ce^{III} state preferable, respectively. This is further aided by the readily available and small water ligands completing the coordination spheres and therefore stabilising the larger Ce^{III} ions.

Compound (**15-Ce**) crystallises in the monoclinic space group $\text{P}2_1/n$ as shown in figure 75 with the screw axis close to parallel to the crystallographic b-axis. The packing is dominated by the steric demand of the ligands without any obvious intermolecular interactions. Lattice MeCN and H_2O fill the voids between the Ce_4 clusters.

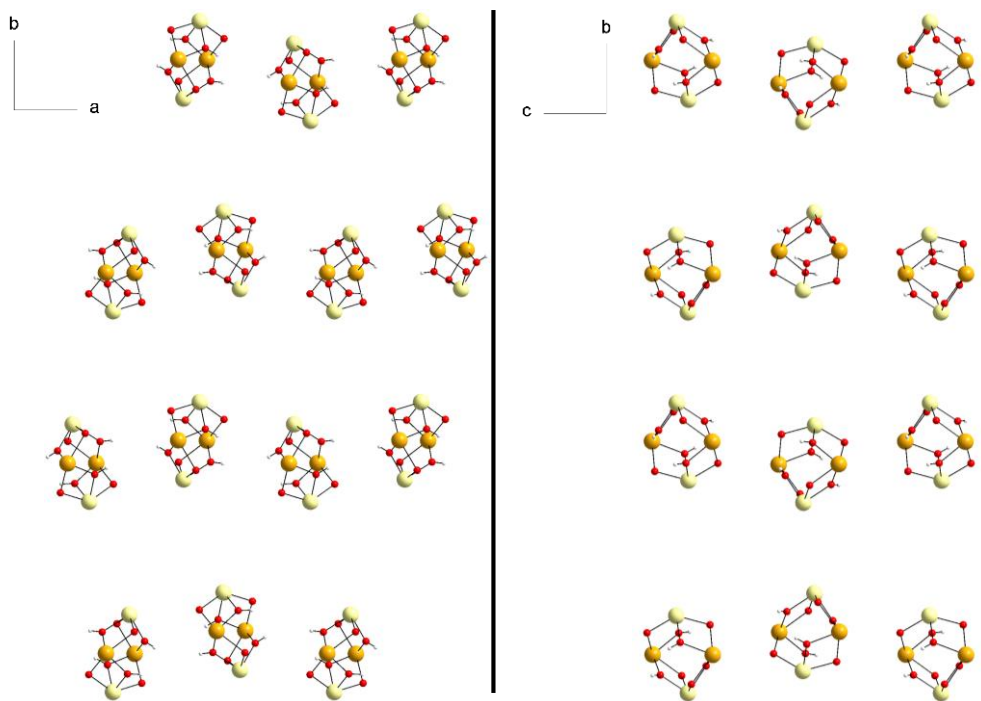


Figure 75. View of the packing of (15-Ce) along the a-axis (left) and along the c-axis (right).

The PXRD of (15-Ce) (see figure 76, left) shows that the crystalline part of the bulk sample is the expected Ce₄ cluster, fitting the simulated pattern well at angles below 12° 2θ. At higher angles the recorded diffractogram barely shows any reflections as a result of the bad signal to noise ratio. The simulated reflections at 18° and 20° 2θ are visible though slightly shifted in the experiment, confirming the purity albeit poor crystallinity of (15-Ce). In the IR spectrum of (15-Ce) the O-H stretch vibrations of the bridging hydroxy groups can be seen around 3350 cm⁻¹ (see figure 76, right).

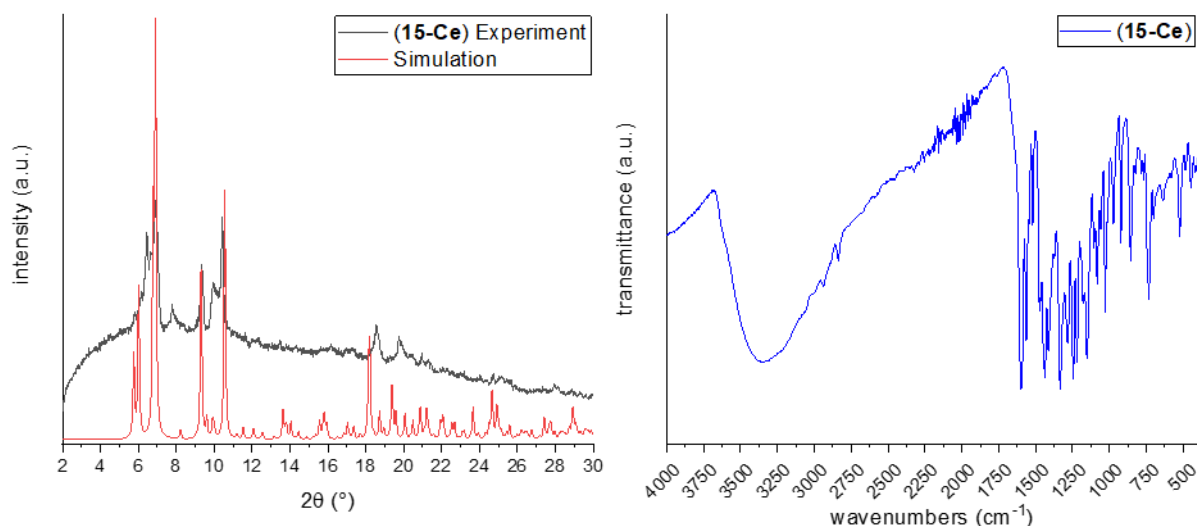


Figure 76. Experimental and simulated PXRD (left) and ATR-IR spectrum between 4000 and 400 cm⁻¹ (right) of (15-Ce).

5.2.1.3 $[\text{Eu}^{\text{III}}_5(\text{CO}_3)(\text{H}_2\text{O})_3(\text{mdeaH})_2(\text{NO}_3)(\text{opch})_5]$

Using $\text{Eu}^{\text{III}}(\text{NO}_3)_3 \cdot 6\text{H}_2\text{O}$ orange hexagonal prismatic crystals of $[\text{Eu}_5(\text{CO}_3)(\text{H}_2\text{O})_3(\text{mdeaH})_2(\text{NO}_3)(\text{opch})_5] \cdot 17.33\text{MeCN} \cdot \text{H}_2\text{O}$ (**16-Eu**) grew from the reaction mixture (see figure 77).

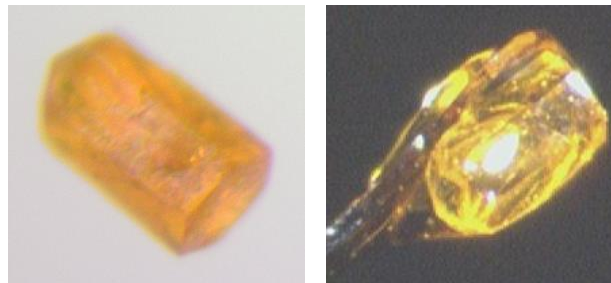


Figure 77. Hexagonal prismatic crystal of (**16-Eu**) in perfluoroether oil (left) and on the goniometer head (right).

At a first glance the molecular structure of (**16-Eu**) seems similar to the one of (**14-La**) with the central carbonate showing the same bridging coordination mode. The main difference between the two compounds lies in the number of opch^{2-} ligands. Whereas (**14-La**) had only four, the Eu^{III} compound (**16-Eu**) has five Schiff base ligands. To accommodate this extra ligand with its increased steric demand the Eu^{III} ions are forced out of planarity. The distance of $\text{Eu}(3)$ and $\text{Eu}(4)$ from a plane defined by $\text{Eu}(1)$, $\text{Eu}(2)$ and $\text{Eu}(5)$ are 1.03\AA and 0.52\AA , respectively (see figure 78).

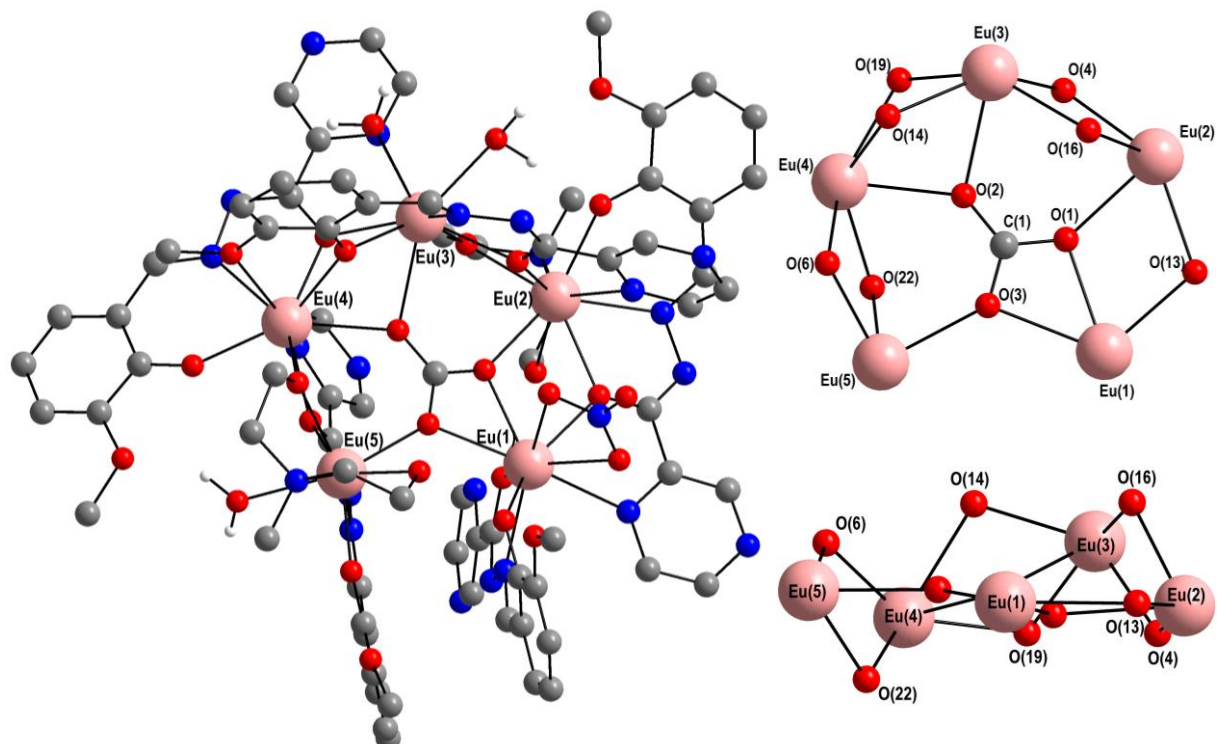


Figure 78. Molecular structure (left) and two views of the core of (**16-Eu**) (right).

All Eu^{III} ions except Eu(5) are nine coordinate all with different coordination spheres that are summarised in the table 11 below.

Table 11. Type and number of ligands forming the coordination spheres around Eu(1)-Eu(5) in (16-Eu). Opch-N stands for the hydrazine-N, O-CH₃ for the methoxy-O, phen-O for the phenoxy-O, carb for the carbonyl-O and pyz for the pyrazine-N of the H₂opch ligand. The number of strokes indicates the number each Eu^{III} ion is coordinated to each type of ligand site.

	opch-N	O-CH ₃	phen-O	carb	pyz	mdeaH ₂ -N	mdeaH ₂ -O	CO ₃	NO ₃	H ₂ O
Eu(1)										
Eu(2)										
Eu(3)										
Eu(4)										
Eu(5)										

All ions are surrounded by different ligands/ opch²⁻donor atoms and there are some things that need to be highlighted. Eu(1) is coordinated to the two nitrates as well as chelated by the central carbonate that render the complex neutral. The main bridging donor sites keeping the five ions together are the carbonyl-O of the opch²⁻ ligands as shown by the fact that all Eu^{III} ions but Eu(5) are coordinated to two of them (see table 11 above). The two mdeaH₂ co-ligands are fully protonated in (16-Eu), unlike the mdeaH co-ligands on (14-La), and chelate one Eu^{III} ion each (Eu(2) and Eu(5)) with one alcohol arm bridging to the neighbouring Eu^{III} ion. The coordination sphere of the out-of-plane Eu(3) is completed by two H₂O ligands. The other donor sites of opch²⁻ are fairly equally distributed over the five Eu^{III} ions.

Despite the unsymmetrical molecular structure, the complexes are organised very symmetrically in the crystal. (16-Eu) crystallises in the high-symmetry trigonal space group $P\bar{3}$ with six molecules in the unit cell. The water ligands on Eu(3) and Eu(5) form intermolecular and intramolecular hydrogen bonds with one of their protons, respectively. The three molecules that can be seen in figure 79 interact via the hydrogen bond of O(27)-H(27A)...N(17) with the donor-acceptor distance measured at 2.926(6) Å and an angle of 167(6)° (highlighted in green in figure 79).

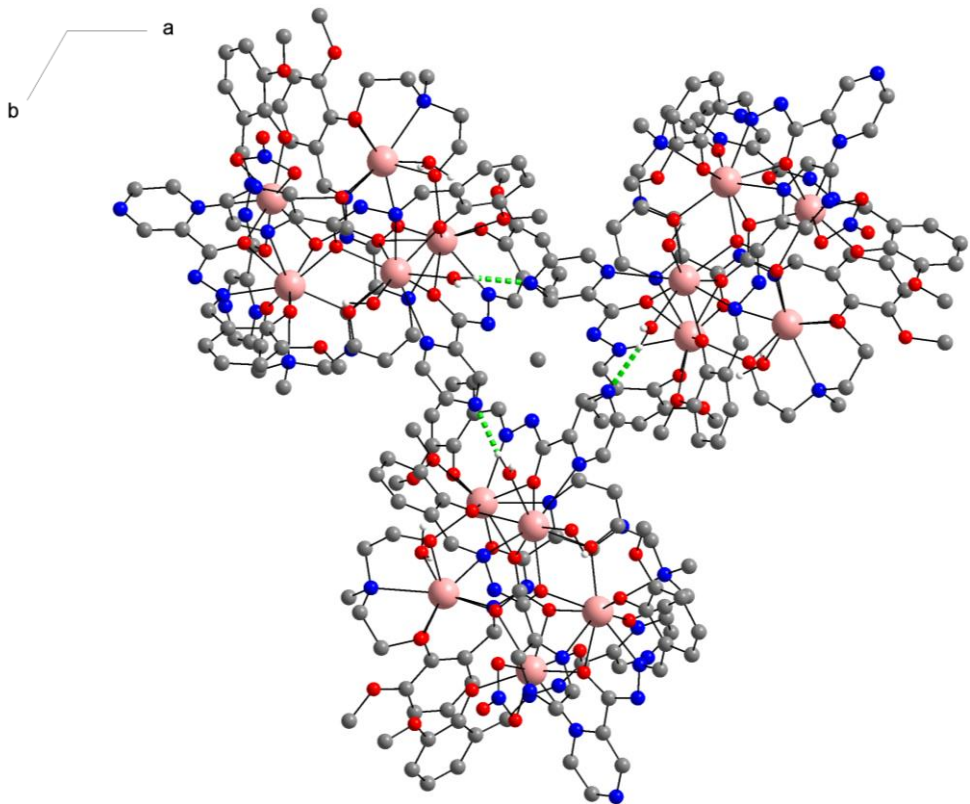


Figure 79. View of the packing of **(16-Eu)** along the c-axis highlighting the threefold axis with a lattice MeCN molecule lying on it as well as the hydrogen bonds (green). Other lattice solvent molecules were omitted for clarity.

The PXRD of **(16-Eu)** corresponds well to the simulation with the peaks only slightly shifted to the left, therefore confirming phase purity of the bulk sample (figure 80 left). In the excerpt of the IR spectrum (figure 80 right) the carbonate antisymmetric CO stretch vibration is highlighted. As the bridging mode of the central carbonate in **(16-Eu)** is identical to the one in **(14-La)**, the energy of this vibration can be compared. A shift of 12 cm^{-1} to higher energies with the vibration occurring at 1442 cm^{-1} in **(16-Eu)** compared to at 1430 cm^{-1} in **(14-La)** can be attributed to shorter bond lengths of the carbonate oxygens to the metal ions which range from 2.41\AA to 2.56\AA in **(16-Eu)** and from 2.50\AA to 2.60\AA in **(14-La)**. This is a further consequence of the reduced size of the Eu^{III} ions compared to La^{III} ions.

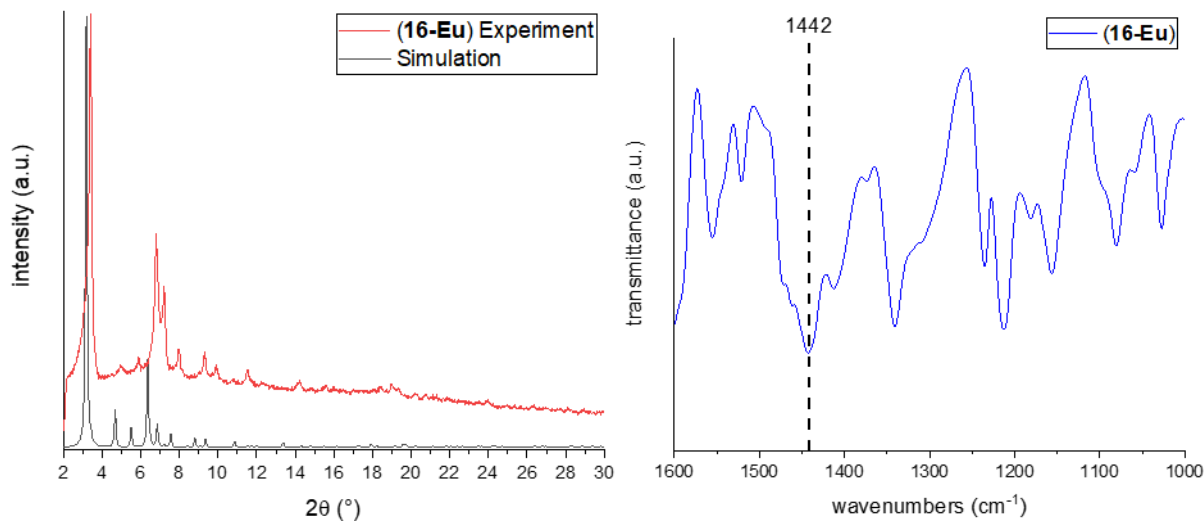


Figure 80. PXRD (left) and excerpt of the IR spectrum of **(16-Eu)** highlighting the asymmetric CO stretch vibration of the multidentate bridging carbonate ligand (right).

5.2.1.4 $[\text{Dy}^{\text{III}}_6(\text{H}_2\text{O})(\text{mdeaH}_2)_2(\text{NO}_3)(\mu_3\text{-OH})_4(\mu_2\text{-OH})_2(\text{opch})_5](\text{NO}_3)$

Using $\text{Dy}(\text{NO}_3)_3 \cdot 6\text{H}_2\text{O}$ in this reaction gave two products that were separable by crystal picking as the Dy_6 compound presented here crystallises as small yellow crystals, while the Dy_8 compound presented in section 5.2.1.5 crystallises as big red blocks. The Dy_6 compound $[\text{Dy}^{\text{III}}_6(\text{H}_2\text{O})(\text{mdeaH}_2)_2(\text{NO}_3)(\mu_3\text{-OH})_4(\mu_2\text{-OH})_2(\text{opch})_5](\text{NO}_3)$ (**17-Dy**) appears to be a side product in this reaction as in multiple attempts only pure red Dy_8 samples or mixtures of the two could be obtained.

The arrangement of the Dy^{III} ions in **(17-Dy)** seems similar to the one seen in a Ln_7 compound with a tripodal ligand reported by Sharples *et al.* in which six Ln^{III} ions form an essentially planar hexagon with a central ion shifted slightly out of plane and connected to the surrounding hexagon by six $\mu_3\text{-OH}$ groups.^[269-270] In the case of **(17-Dy)** the same motif can be seen as five of the six Dy^{III} ions in **(17-Dy)** are arranged in the shape of a hexagon that lacks one of its corners with $\text{Dy}(1)$ in the middle (see figure 81 with vacant site highlighted by a green arrow). This becomes obvious by examining the internal angles on $\text{Dy}(3)$, $\text{Dy}(4)$ and $\text{Dy}(5)$ (the Dy^{III} ions not neighbouring the vacant site) which with 115.1° - 117.4° are closer to the 120° you would expect for a hexagon than to the 108° expected for a pentagon, but also shows that the hexagon is quite distorted because of the vacant site. The outer Dy^{III} ions are also not in one plane. $\text{Dy}(6)$ is 0.77\AA below a plane defined by $\text{Dy}(3)$, $\text{Dy}(4)$ and $\text{Dy}(5)$ while $\text{Dy}(2)$ is 0.33\AA above the same plane. The charge of **(17-Dy)** is balanced by a non-coordinated nitrate

in the lattice. Similar to the reported Ln_7 structure the outer ions are coordinated by chelating opch^{2-} ligands. Instead of a sixth opch^{2-} that would coordinate to the Dy^{III} ion missing from the hexagon, two mdeaH_2 ligands complete the coordination sphere of $\text{Dy}(2)$ and $\text{Dy}(6)$. While the other Dy^{III} ions are coordinated eight (in the case of $\text{Dy}(2)$, $\text{Dy}(5)$ and $\text{Dy}(6)$) or nine times (in the case of $\text{Dy}(3)$ and $\text{Dy}(4)$), the central $\text{Dy}(1)$ only has a coordination number of seven being coordinated by six bridging hydroxy groups and a nitrate co-ligand. Four of the bridging hydroxy groups are $\mu_3\text{-OH}$ as for the ones in the published structure but two hydroxy groups only bridge between two ions as a result of the vacant site in the hexagon.

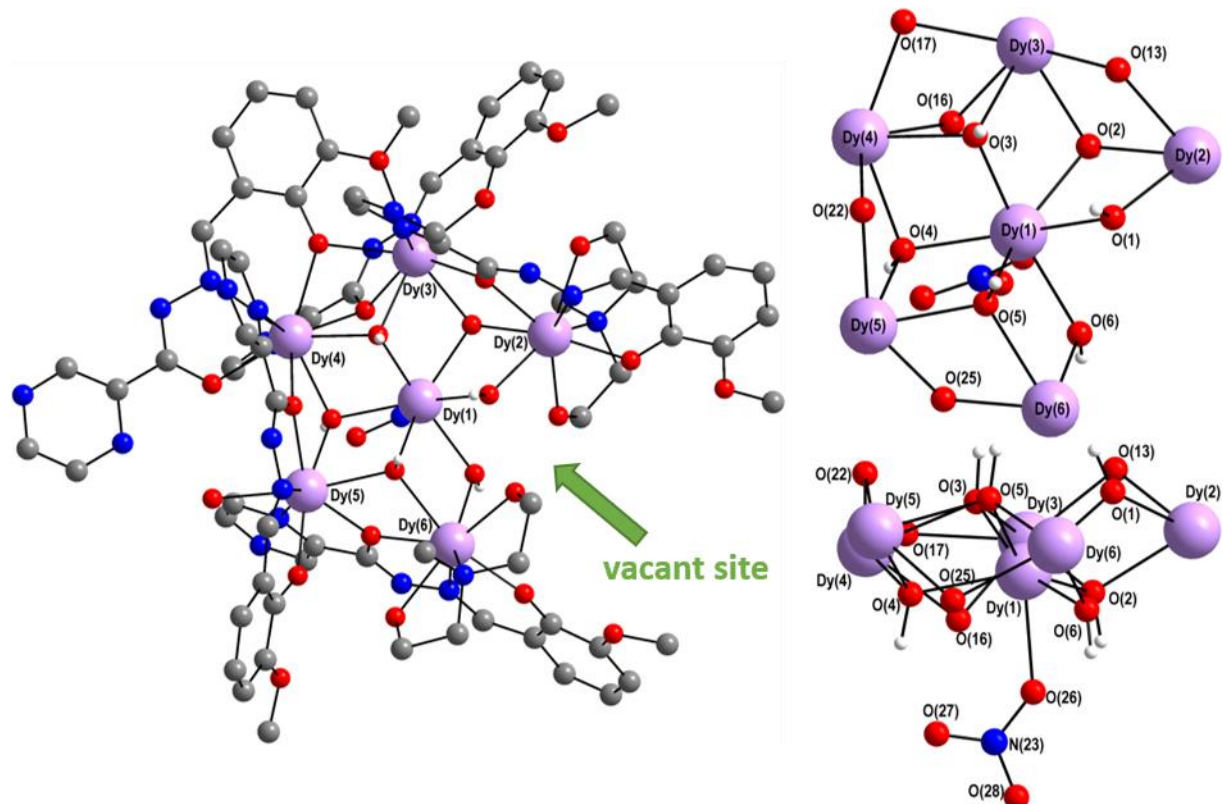


Figure 81. The molecular structure of (17-Dy) (left) with two views on its core structure (right). The vacant site is highlighted with a green arrow.

(17-Dy) crystallises in the triclinic space group $P\bar{1}$ with $Z = 2$. The nitrate that is coordinated to the central $\text{Dy}(1)$ acts as an HB-acceptor and forms two HBs, one to lattice MeCN and the other to the non-aromatic C-H proton H(30) of the opch^{2-} ligand bridging between $\text{Dy}(3)$ and $\text{Dy}(4)$ on the neighbouring molecule (see figure 82).

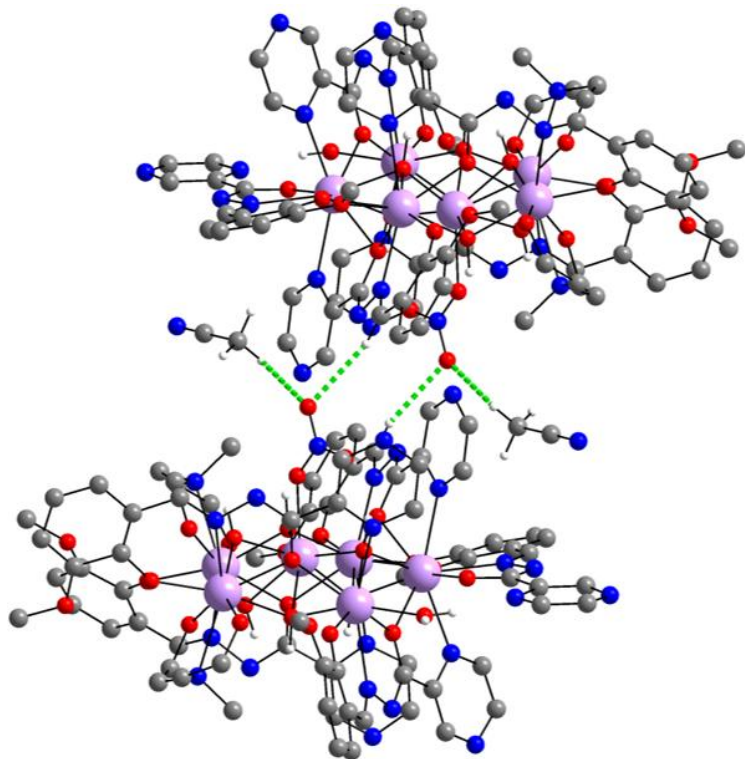


Figure 82. Packing of **(17-Dy)** highlighting the intermolecular HBs in green.

The molecules stack nearly parallel to the a-b-plane at an angle of 22.3° between the mean plane through all six Dy^{III} ions and the a-b-plane (see figure 83).

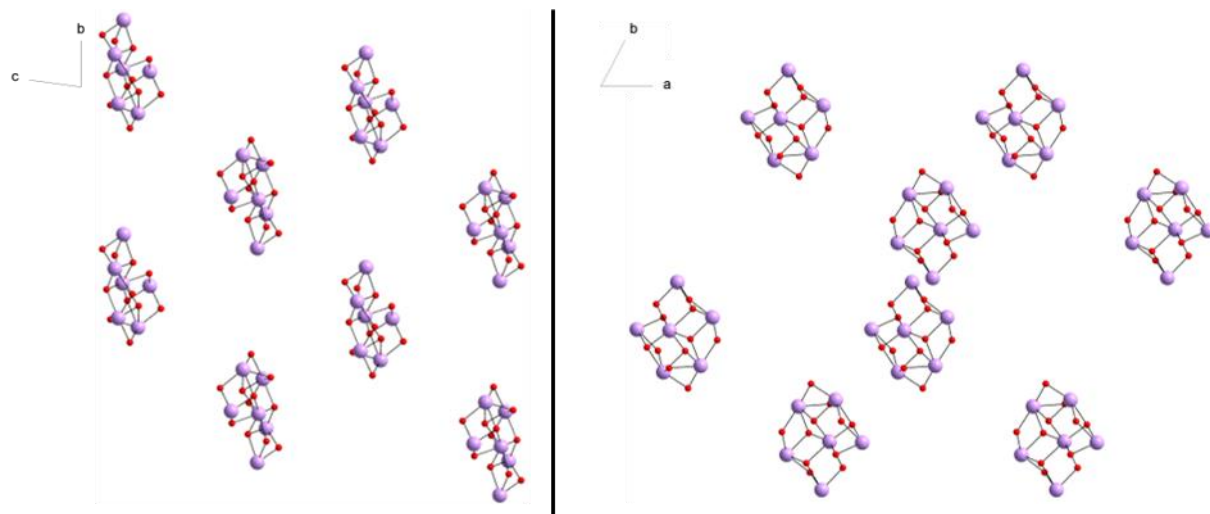


Figure 83. Two views of the packing of the cores of **(17-Dy)**, along the a-axis (left) and along the c-axis (right) showing the orientation of the cores towards in the lattice.

The PXRD reveals the phase purity of the bulk sample of compound **(17-Dy)** manually separated from the co-crystallising Dy₈ with only minor amorphous components. In the IR spectrum the OH stretch vibrations can be assigned to the broad peak at 3380 cm⁻¹ (see figure 84).

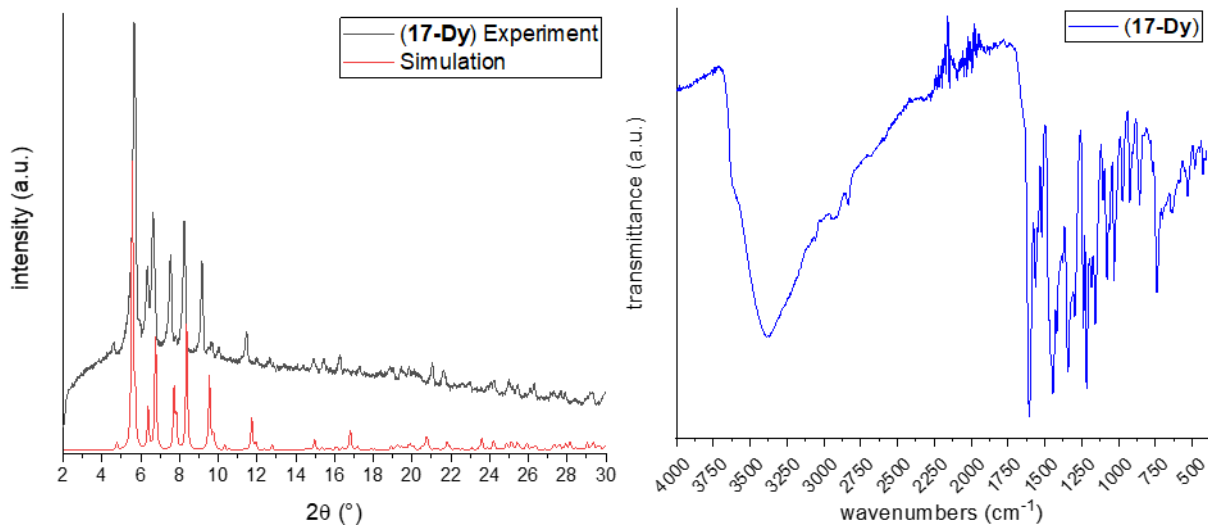


Figure 84. PXRD (left) and IR spectrum of (17-Dy) (right).

5.2.1.5 Two Different Structures of $[\text{Ln}^{\text{III}}_8(\text{CO}_3)_4(\text{H}_2\text{O})_8(\text{opch})_8]$

The same reaction with the Ln^{III} -nitrates from Sm^{III} to Er^{III} (with the exception of Eu^{III} the result of which was already discussed in chapter 5.2.1.3) led to octanuclear complexes. The molecular structure is essentially the same for all seven compounds $[\text{Sm}^{\text{III}}_8(\text{CO}_3)_4(\text{H}_2\text{O})_8(\text{opch})_8] \cdot 12\text{MeCN} \cdot 4\text{H}_2\text{O}$ (18-Sm), $[\text{Gd}^{\text{III}}_8(\text{CO}_3)_4(\text{H}_2\text{O})_8(\text{opch})_8] \cdot 10\text{MeCN} \cdot 4\text{H}_2\text{O}$ (19-Gd), $[\text{Tb}^{\text{III}}_8(\text{CO}_3)_4(\text{H}_2\text{O})_8(\text{opch})_8]$ (20-Tb), $[\text{Dy}^{\text{III}}_8(\text{CO}_3)_4(\text{H}_2\text{O})_8(\text{opch})_8] \cdot 11\text{MeCN}$ (21-Dy), $[\text{Ho}^{\text{III}}_8(\text{CO}_3)_4(\text{H}_2\text{O})_8(\text{opch})_8] \cdot 7\text{MeCN}$ (22-Ho), $[\text{Er}^{\text{III}}_8(\text{CO}_3)_4(\text{H}_2\text{O})_8(\text{opch})_8] \cdot 7\text{MeCN}$ (23-Er) and $[\text{Y}^{\text{III}}_8(\text{CO}_3)_4(\text{H}_2\text{O})_8(\text{opch})_8]$ (24-Y). The core of the eight Ln^{III} ions is arranged in a distorted antiprism and held together by four bridging carbonate ligands. Each of the Ln^{III} ions is eight-coordinate, connected to two of the bridging carbonates, chelated by two opch^{2-} ligands and bears an additional water ligand to complete the coordination sphere. One of the two opch^{2-} ligands that chelate each Ln^{III} ion coordinates with the pyrazine-N while the other coordinates with the hydrazine-N as well as the phenoxy-O. Both opch^{2-} ligands have a carbonyl-O bridging between two Ln^{III} ions (see figure 85). This molecular structure is the same as for a Dy_8 cluster reported by Tang *et al.* in 2012 using the same ligand but a different synthetic procedure.^[200]

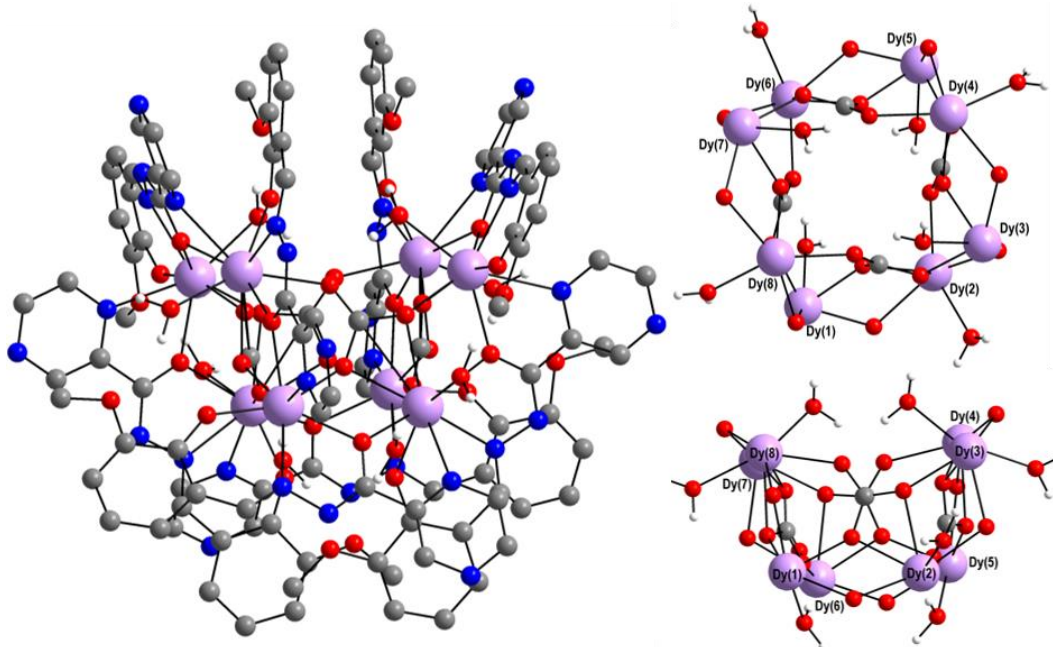


Figure 85. Molecular structure of (21-Dy) representative for the other Ln_8 compounds (left) and two views on the carbonate bridged core structure (right).

Although all seven compounds reported here have an essentially identical molecular structure, the crystal structures obtained on (18-Sm), (19-Gd) and (21-Dy) were measured in the triclinic space group $P\bar{1}$ while the other four ((20-Tb), (22-Ho), (23-Er) and (24-Y)) were measured in the monoclinic space group $C2/c$, with the major difference being amount and the distribution of lattice solvent. It has to be noted that the Dy_8 cluster by Tang and co-workers crystallised in the monoclinic structure type.^[200] The higher symmetry space group with symmetrically distributed lattice solvent results in $Z' = 0.5$ while the asymmetric unit of clusters crystallising in $P\bar{1}$ contains one full molecule. The two obtained unit cells are quite similar to each other with the triclinic cell being transformable into a monoclinic *c*-centred cell that almost resembles the monoclinic cells obtained for (20-Tb), (22-Ho), (23-Er) and (24-Y) as well as the reported Dy_8 .

To crystallise in the triclinic structure type such as (21-Dy) the hydrogens on the water ligands that coordinate Dy(2) and Dy(8) form HBs with the pyrazine-N opch²⁻ ligands on one of the neighbouring Dy_8 clusters. This forms a zig-zag chain along the *b*-axis (see figure 86). In the monoclinic structure type the packing is different with each Ln_8 cluster being linked via intermolecular HBs to four neighbouring ones as shown in figure 87.

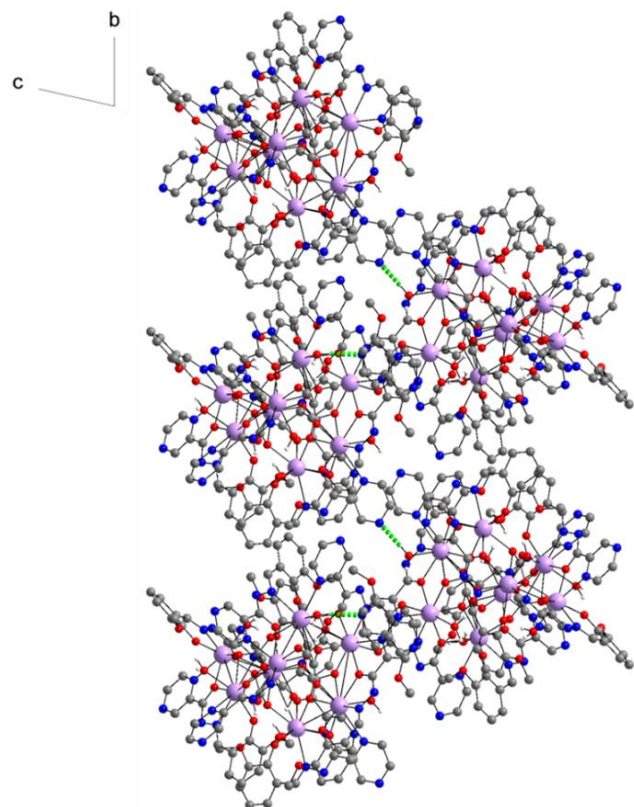


Figure 86. Packing of the triclinic structure of (21-Dy), view along the a-axis highlighting the intermolecular HBs in green.

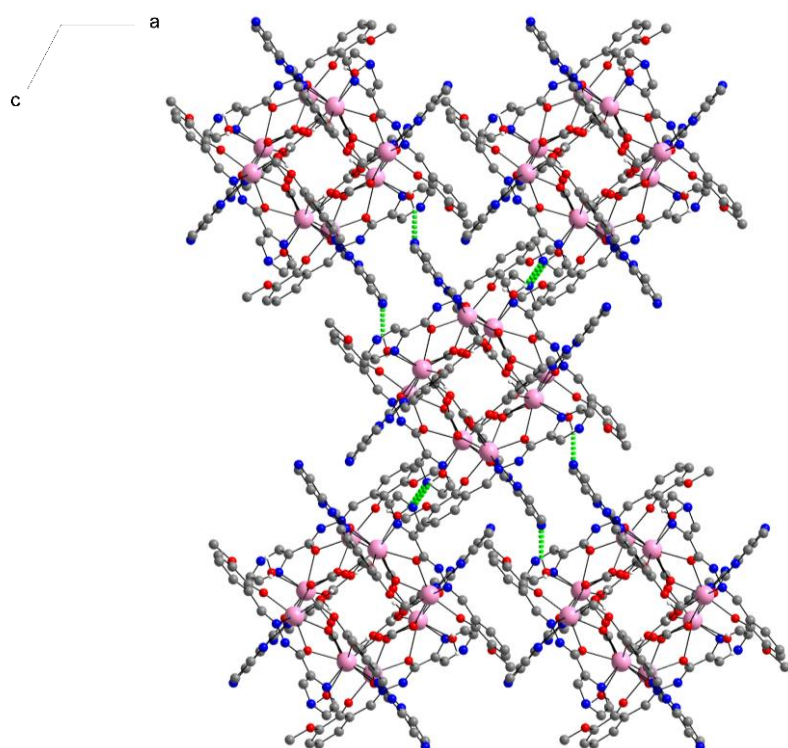


Figure 87. Packing of the monoclinic structure type using the measurement of (23-Er). View along the b-axis with the intermolecular HBs shown in green.

The tendency points towards the larger Ln^{III} ions preferring more lattice solvent to fill the gaps in the crystal structure leading to a decrease in symmetry with **(20-Tb)** being an exception to that. From the crystal structure which was measured on the best-looking crystal of a sample no conclusion can be drawn regarding the phase purity of the compound in one or the other crystal structure. Therefore, PXRD was measured on all samples revealing that all of the powders correspond well to the simulated powder pattern of the monoclinic structure (figure 88). The three compounds that were measured in $P\bar{1}$ show a small peak at 7° 2θ that corresponds well to the predicted powder pattern of the triclinic crystal structure of **(21-Dy)** indicating that they crystallise in a mixture of the two structural types. The ratio of triclinic to monoclinic component increases the larger the Ln^{III} ions are as the peak indicating the triclinic structure type increases in intensity (inset of figure 88).

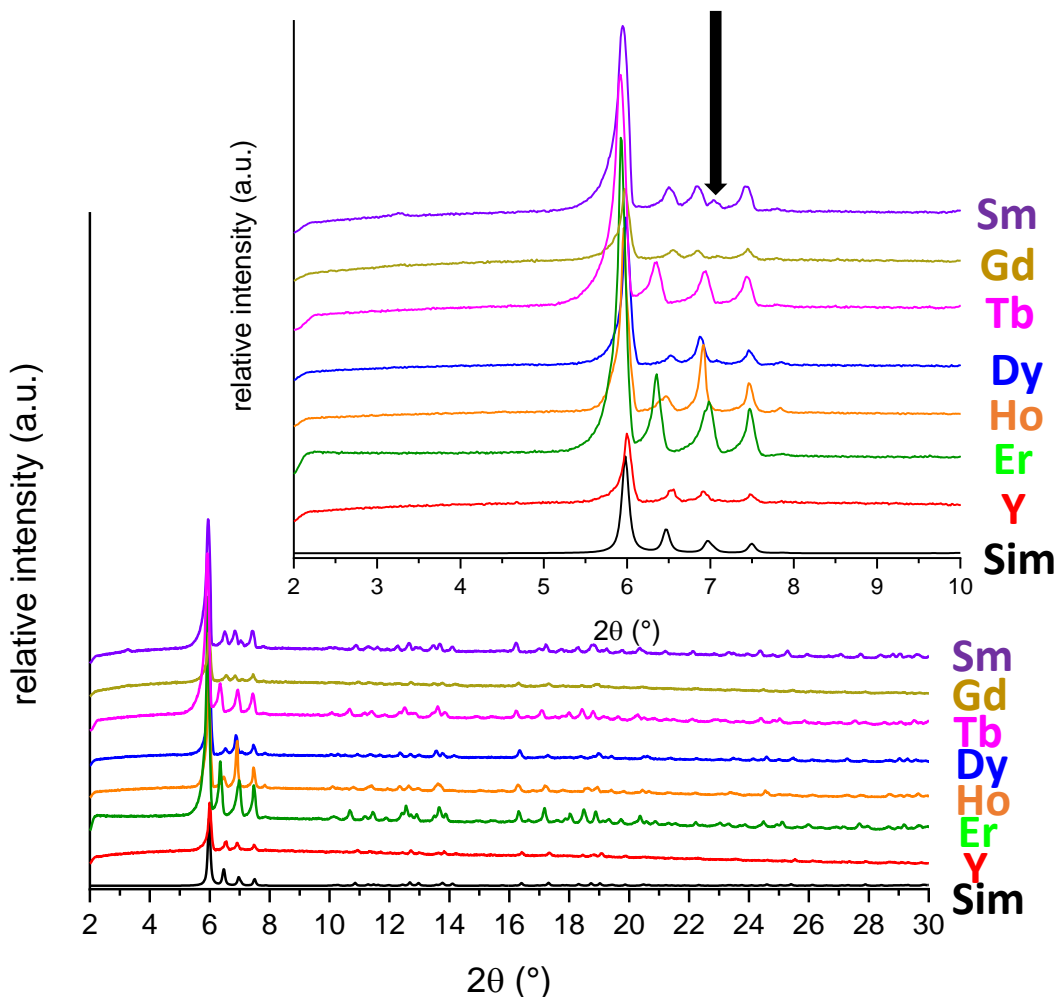


Figure 88. Comparison of the PXRDs of the Ln_8 complexes with the predicted powder pattern of the monoclinic crystal structure of **(23-Er)**. The inset highlights the peak characteristic for the triclinic crystal structure obtained for larger Ln^{III} ions with a black arrow.

It should also be noted that these reactions were repeated multiple times during the work on this thesis and while all the aforementioned compounds were obtained pure, at times they co-crystallised with some side products as exemplified by the co-crystallisation of **(17-Dy)** and **(21-Dy)** in one of the batches. One batch of the reaction with $\text{Tb}(\text{NO}_3)_3 \cdot 6\text{H}_2\text{O}$ yielded orange crystals in addition to the red main product **(20-Tb)**. These could be identified as a Tb_5 cluster isostructural to **(16-Eu)** by PXRD (see figure 89). Something similar happened in one batch using $\text{Sm}(\text{NO}_3)_3 \cdot 6\text{H}_2\text{O}$ where next to the red **(18-Sm)** a few yellow crystals could be obtained that were measured using single crystal XRD. As a result of the poor quality of the crystals the resulting data set could not be refined, but it was possible to identify six heavy atom sites suggesting it might be something similar to **(17-Dy)**. Due to the poor crystallinity and the small amount no further experiments were conducted on these yellow crystals.

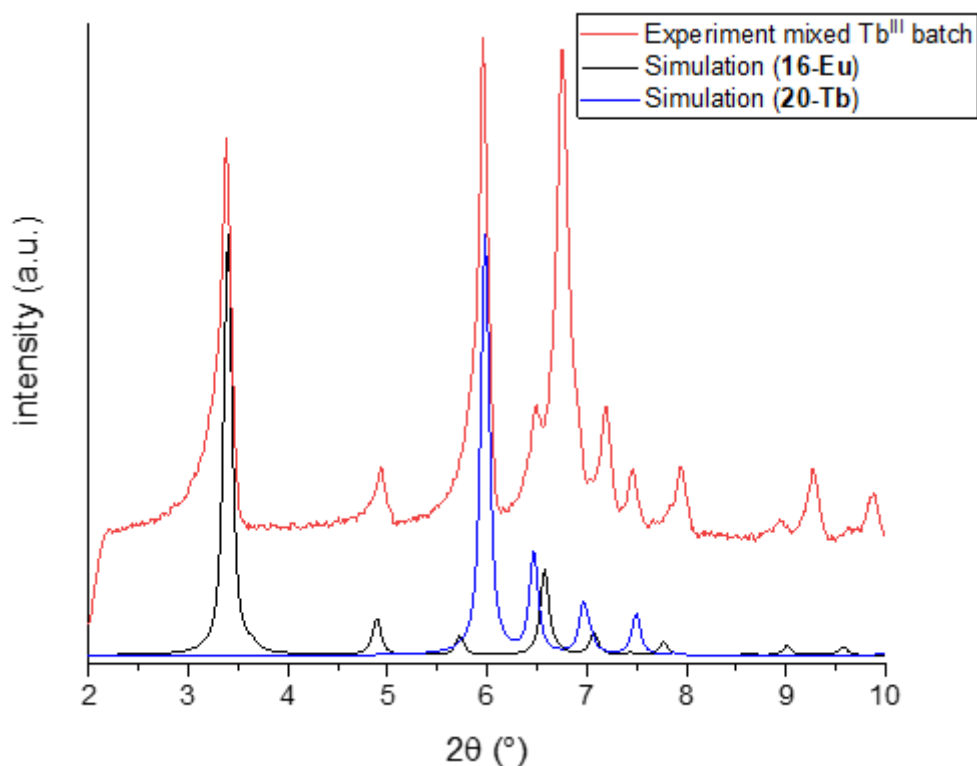


Figure 89. Identification of the side product of the reaction towards **(20-Tb)** as a Tb_5 complex, isostructural to **(16-Eu)**.

The smallest Ln^{III} ions Tm^{III} , Yb^{III} and Lu^{III} only yielded amorphous powders suggesting another type of complex formation is present here. This is also indicated by looking at the reaction using $\text{Er}(\text{NO}_3)_3 \cdot 5\text{H}_2\text{O}$. Although it was possible to grow single crystals of **(23-Er)** from the reaction, after a few hours the solution turns cloudy with yellow

precipitate similar to the one obtained with Tm^{III} - Lu^{III} (see figure 90). This shows that Er^{III} seems to be the size at which the reaction begins to yield another different product.



Figure 90. Appearance of the vials containing the same reaction mixture once using $Ho(NO_3)_3 \cdot 5H_2O$ (left) and once using $Er(NO_3)_3 \cdot 5H_2O$ as lanthanide source (right). Picture courtesy of Daniel Seufert.

Similarly, Pr^{III} and Nd^{III} did not yield any measurable crystals. The yellow product obtained from reaction with those ions is visually remarkably similar to the appearance of the yellow Sm^{III} -by-product as well as (17-Dy), suggesting it can be speculated to be a hexanuclear compound as well.

5.2.2 Comparison of Optical Properties

To investigate the optical properties of the aforementioned complexes solid state absorption spectra were recorded for all structure types (but (17-Dy) of which there was not enough sample) and are shown in figure 91. All complexes show similar behaviour between 200 and 450 nm with two bands in the UV region, one near 200 nm and the other at 238 nm and two bands in the visible region with maxima at 348 nm and 433 nm. In (15-Ce) the two bands in the visible range overlap significantly, hardly distinguishable from each other. It has to be said that generally data after the lamp change to the UV lamp and the simultaneous detector change (so data points below 350 nm) have a larger error than the ones that are measured with the visible light lamp. The reason for this could not be found during the work on this thesis. Comparing the spectra between 200 and 450 nm with the ligand spectrum (black in figure 91) it can be proposed that the bands in the UV region can be attributed to ligand-centred excitations. The band in the ligand spectrum at 317 nm seems to be red-shifted about 30 nm in the complexes which can be explained by the fact that the ligand is present in its doubly deprotonated form in the complexes. Deprotonation is usually associated with a red-shift of absorption bands. The complexes show an additional band at 433 nm which does not show up in the ligand spectrum and therefore appears to be an

excitation involving atoms strongly interacting with the metal ions. Generally, the complexes although different structurally do not differ much from each other in terms of their optical behaviour with **(15-Ce)** being the exception to that, whose dark colour can be explained by the broad band that spans the whole visible region suggesting electronic delocalisation in this compound.

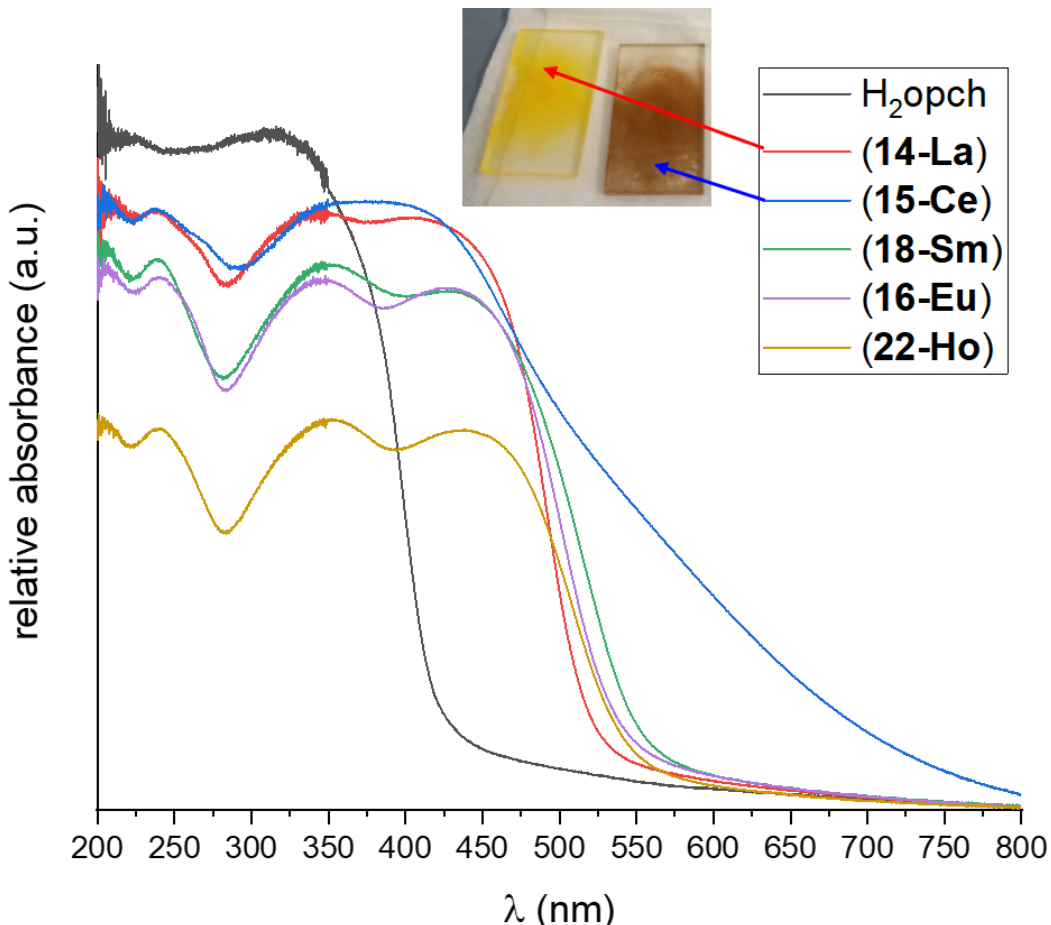


Figure 91. Solid state absorption spectra in the spectral range between 200 and 800 nm comparing the H_2opch ligand (black) with the different structure types obtained using the same reaction conditions only changing the lanthanide ion. At the top the visual appearance of the samples prepared of **(14-La)** and **(15-Ce)** highlighting the colour difference.

Due to the mixed-valent nature of **(15-Ce)** the broad band is attributed to an intervalence charge transfer (IVCT) transition.^[271-272]

Work on mixed-valence materials and their electron transfer reactions was pioneered by Allen and Hush^[273] as well as Robin and Day^[274] and the associated IVCT transitions are classically described by the Hush model which is derived from Marcus theory.^[275-277] A crucial factor in the analysis of IVCT bands in mixed-valence complexes is the extent of electronic coupling between the metal ions and the classical treatment of

IVCT bands is only valid if there is strong localisation (class II in the Robin and Day classification) or delocalisation (class III) present in the system. [271, 274]

The results of the bond valence sum analysis for **(15-Ce)** (see chapter 5.2.1.2) yields values suggesting the oxidation state of the cerium ions all to be between III and IV with a tendency towards either oxidation state as a result of the different coordination spheres discussed in the same chapter. This indicates that neither a localised nor delocalised limit is present in **(15-Ce)** which can therefore not be treated classically. This is a challenge often associated with the theoretical treatment of mixed-valence clusters and tailor made quantum chemical calculations are needed to treat such systems. [271, 278-279]

The analysis of the band shape in order to obtain information on the mechanism and the rates of the electron transfer is further complicated by significant overlap with other, in part, ligand-based transitions seen in the absorption spectra of all the complexes. Additionally, **(15-Ce)** is tetranuclear (not dinuclear, as most of the complexes studied in the literature such as the famous Creutz-Taube ion^[280]) which means each Ce^{III} ion has two neighbouring Ce^{IV} ions and vice versa. This likely results in an overlap of multiple IVCT processes, which could explain the extreme width of the band.

The whole electron transfer situation in this system could further be complicated by an electron transfer mechanism introduced by Creutz, Newton and Sutin in which the metal-to-metal charge transfer is mediated by MLCT and/or LMCT to or from the bridging ligand. [271, 281-282]

Additionally, as parameters such as concentration and thickness of the investigated sample are not easily obtainable in the solid state absorption spectroscopy measurements performed here (ground up powder sample pressed between two quartz plates with some mineral oil), parameters such as the extinction cannot be used in the analysis of the IVCT band.

Therefore, solution state measurements were performed on the family of complexes as well. In order to compare the results of all the complexes the solvent was chosen to be DMF due to solubility issues in some cases (figure 92). Even in DMF not everything dissolved for certain compounds making the determination of concentrations and extinction coefficients impossible. Therefore, the relative absorbances of the compounds are shown. It can be seen that the spectrum of the complexes all show

two bands observable in DMF that are red-shifted when compared to the pure ligand. The first band can be seen at wavelengths between 332 nm for **(15-Ce)** and 442 nm for **(21-Dy)** and **(22-Ho)**. In the second band the difference between the metal complexes is more pronounced with wavelengths of 397 nm for **(15-Ce)** and 426 nm for the Ln_8 clusters. The IVCT band of **(15-Ce)** can also be seen as the absorbance does not reach 0 before 725 nm. The difference between the solution and solid state spectra of **(15-Ce)** can be explained by decomposition in DMF solution.

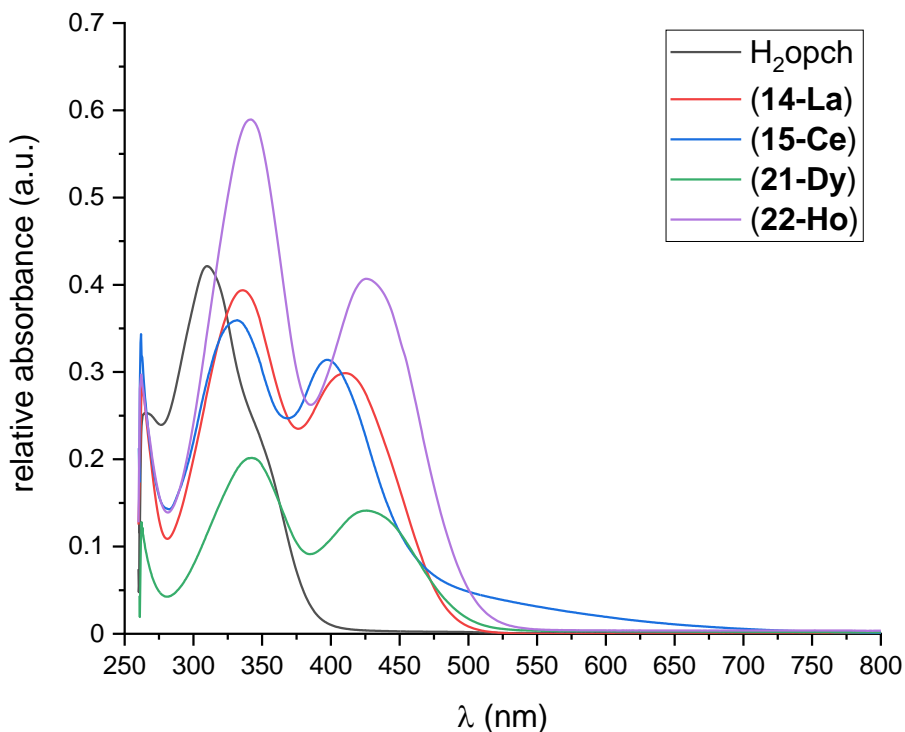


Figure 92. Absorption spectra of different structure types discussed in this chapter.

When measuring **(15-Ce)** in DMF solution a rapid change of the absorption spectrum was observed over time. In figure 93 below the successive measurements of three different concentrations of **(15-Ce)** in DMF are shown (black, red and blue curves), that were measured directly after diluting the freshly prepared stock solution. It is estimated that between dissolution of **(15-Ce)** to prepare the stock solution and the first measurement (black curve) five minutes have passed (preparation of diluted solutions, walking to the instrument and measuring background). Even within the short time frame between these first three measurements there are significant differences between the spectra. The first measurement shows two bands, one at 332 nm and a second at 403 nm. It can also be noted that the first sample is still absorbing at 800 nm similar to the behaviour observed in the solid state measurement. In the second and third measurement (red and blue curves) a significant increase in intensity of the first band

can be observed, while the second band is slightly decreasing in intensity and is blue-shifted by 7 nm towards 396 nm. This blue-shift could be the result of ligand rearrangement in solution having the opch^{2-} ligands less strongly interacting with the metal ions. These two measurements also do not absorb at higher wavelengths anymore indicating the electron transfer between the Ce^{III} and Ce^{IV} ions does not take place anymore after less than ten minutes in solution. The stock solution was kept in a screw top vial and diluted solutions were remeasured after one and five days respectively (green and purple curves). It can be seen that the first band at 332 nm continues to increase in intensity while the second band continues decreasing in intensity and is merely a shoulder in the last measurement. The change of the spectrum in DMF can be explained by ligand rearrangement in solution. The spectrum after 5 days is remarkably similar to that of the free ligand qualitatively, but is still red-shifted confirming that the H_2opch ligand is still interacting with the metal ions.

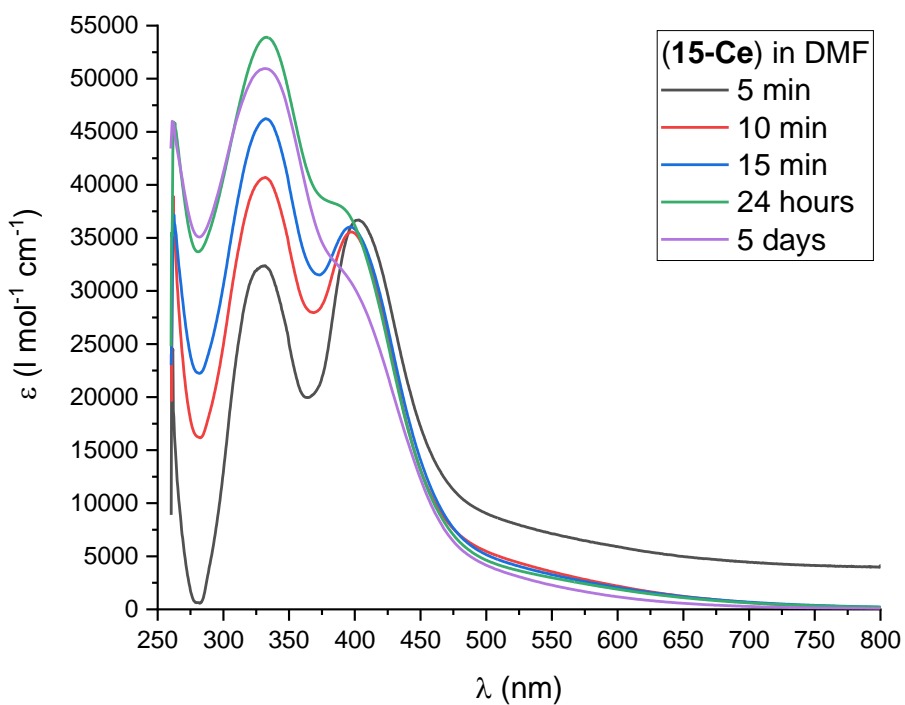


Figure 93. Absorption spectra of (15-Ce) in DMF solution. The first three samples were measured directly after dilution of the freshly prepared stock solution (black, red and blue). The same stock solution was used after 24 hours and after 5d resulting in the green and purple spectra.

5.2.3 Magnetic Properties of H₂opch-Lanthanide Complexes

SQUID measurements were performed on (**15-Ce**), (**19-Gd**), (**20-Tb**), (**21-Dy**) and (**22-Ho**) and are compared here. Additionally, the magnetic properties of (**21-Dy**) are compared to the Dy₈ compound reported by Tang *et al.*^[200] that was also mentioned in section 5.1 above.

As a general comment it has to be said that due to the restrictions associated with the Covid-19 pandemic and the renovation of the inorganic chemistry institute at KIT where our own in-house SQUID instrument is located, magnetic measurements have been performed on several different SQUIDs in collaboration with the groups of Prof. Dr. Mario Ruben (MPMS-XL-1 at KIT, INT), Prof. Dr. Jinkui Tang (MPMS-XL-7 Changchun Institute of Applied Chemistry) and Prof. Dr. Ruediger Klingeler (MPMS-3 at the University of Heidelberg, KIP). Therefore, the amount of data points of the individual measurements can vary. Also, it was not always possible to get magnetisation M(B) data.

5.2.3.1 Magnetic Properties of the Mixed Valence Ce₄ Complex (**15-Ce**)

The mixed-valent nature of (**15-Ce**) means that there are two Ce^{III} ions that have one unpaired electron while the two Ce^{IV} ions only have paired electrons. In $\chi_M T$ vs T plots obtained with an applied dc field of 0.1 T (**15-Ce**) reaches a $\chi_M T$ value of 1.28 cm³Kmol⁻¹ at RT which is lower than the expected value for two uncoupled Ce^{III} ions of 1.6 cm³Kmol⁻¹.^[283] This might be the result of thermally activated delocalisation of the two unpaired electrons over the four possible sites, leading to magnetic interactions via superexchange and possibly double exchange.

On lowering the temperature $\chi_M T$ remains constant until reaching 200 K when it begins to decrease monotonically reaching a minimum value of 0.61 cm³Kmol⁻¹ at 1.8 K (see black curve in figure 94). The inverse susceptibility vs T curve (red in figure 94) only follows the Curie-Weiss law between 130 and 300 K indicating that the magnetic behaviour may not be possible to be rationalised easily. The data could be fitted in this temperature region (blue in figure 94). The Weiss constant $\theta = -22.6$ K suggests antiferromagnetic coupling. The Curie constant extracted from the linear fit is

$1.39 \text{ cm}^3 \text{Kmol}^{-1}$. At low temperatures there seems to be no antiferromagnetic interaction present anymore which may suggest localisation of the electrons at the Ce^{III} sites identified above. This would make exchange interactions impossible as the Ce^{III} ions are located on opposite corners of the square complex.

The assumptions made above could be validated by performing an experiment that measures the susceptibility, especially at low temperatures where it is suggested that no thermal activation of the delocalisation process takes place, while irradiating the sample with visible light. From the IVCT band in the UVVis measurements presented above it can be assumed that electron delocalisation would be possible again via optical excitation thereby switching the antiferromagnetic coupling back on. Unfortunately, this experiment could not be performed during the work on this thesis as a glass fibre component could not be delivered. This will clearly be a priority in the further investigation of the properties of (15-Ce).

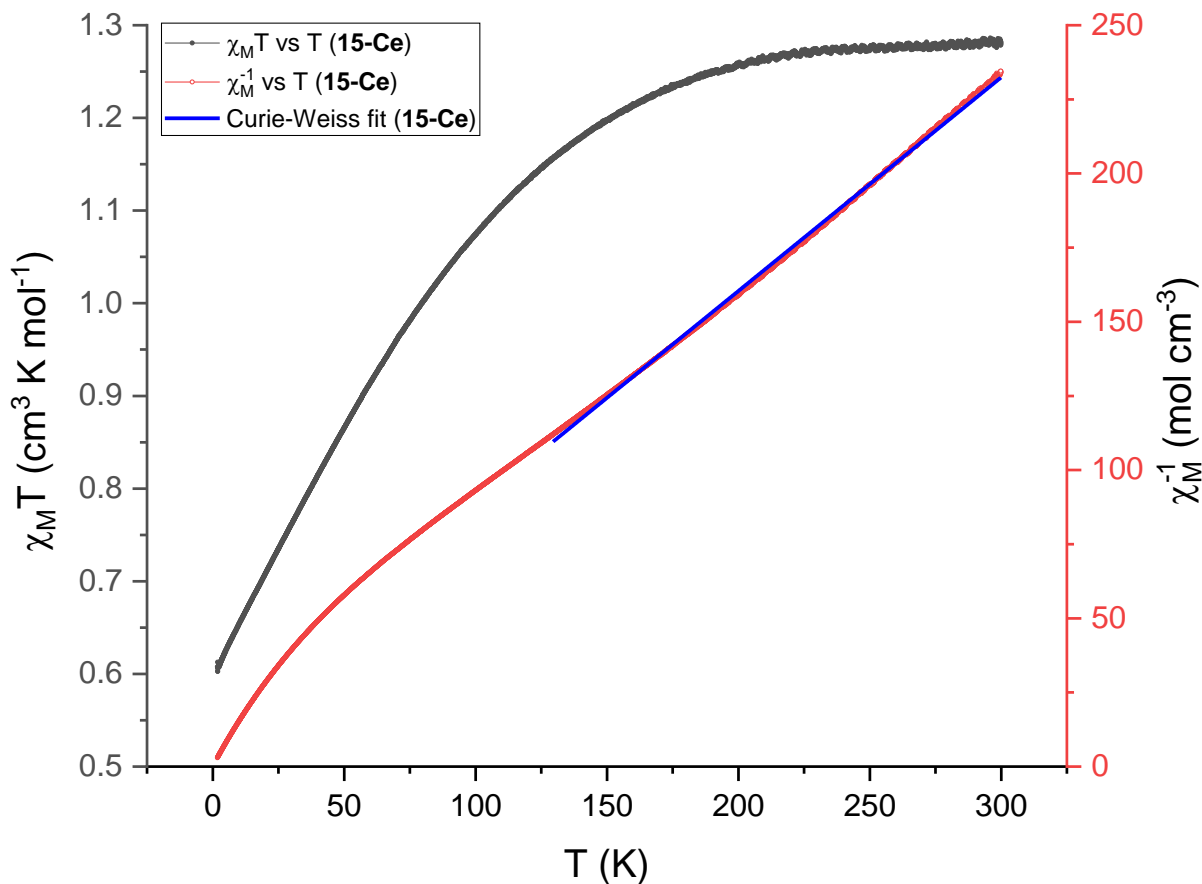


Figure 94. Magnetic measurement of (15-Ce) performed at an applied dc field of 0.1 T at temperatures between 1.8 and 300 K. $\chi_M T$ vs T curve in black, χ_M^{-1} vs T curve in red and Curie-Weiss fit of the latter in the temperature range between 130 and 300 K in blue.

Magnetisation of **(15-Ce)** was also measured at dc fields between 0 and 7 T (figure 95). Saturation is not reached by the system at 7 T with an observed maximum value of $1.7 \mu_B$. From the reduced magnetisation in which the curves at 1.8, 3 and 5 K superpose essentially perfectly it can be concluded that there is no significant anisotropy present in **(15-Ce)**. Therefore, it is not surprising that no slow relaxation was observed in measurements using ac fields.

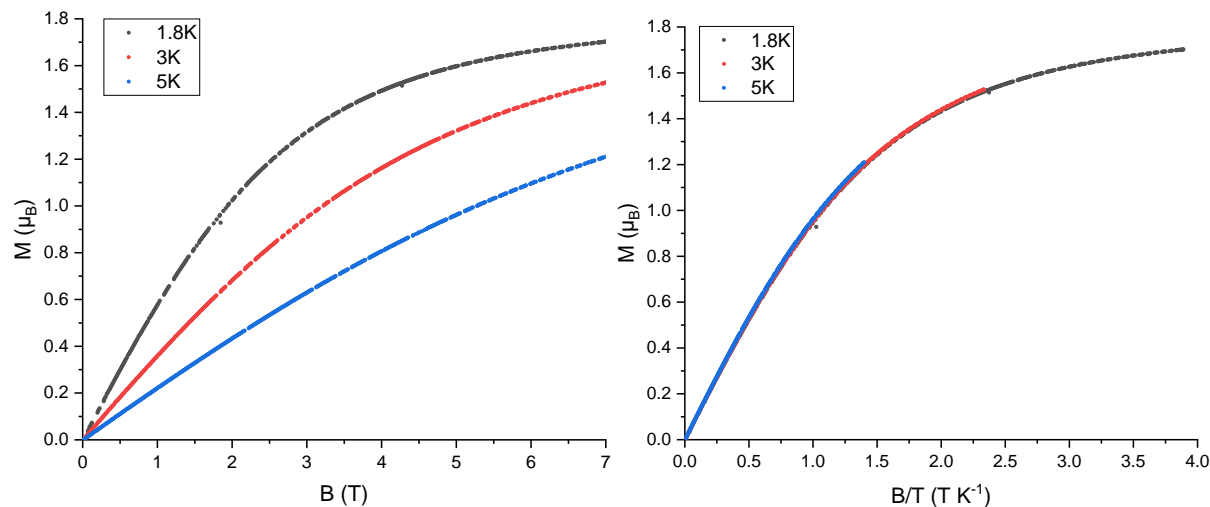


Figure 95. Magnetisation (left) and reduced magnetisation plots (right) of **(15-Ce)** at dc fields between 0 and 7 T at 1.8, 3 and 5 K.

5.2.3.2 Comparison of Different Ln_8 Complexes

Magnetic measurements were performed on the Ln_8 compounds most likely to show SMM behaviour (**20-Tb**), (**21-Dy**) and (**22-Ho**). Measurements were also performed on the isotropic (**19-Gd**) to gauge the strength of the magnetic interactions. There was not enough sample of (**23-Er**) available to obtain magnetic data.

Magnetic susceptibilities were measured for the four compounds named above at temperatures between 2 and 300 K with an applied dc field of 0.1 T (figure 96). At RT the experimental values fit the expected values for eight uncoupled trivalent ions of the respective lanthanide very well. For (**19-Gd**) the $\chi_M T$ values remain essentially constant until reaching 16 K below which a small decrease is observed leading to a minimum value of $60.5 \text{ cm}^3 \text{Kmol}^{-1}$ at 2 K. Similarly, the $\chi_M T$ values for (**20-Tb**) remain constant at high temperatures before starting a gradual decrease at 90 K that becomes much steeper below 25 K reaching a minimum value of $64.8 \text{ cm}^3 \text{Kmol}^{-1}$ at 2 K. (**21-Dy**)

and **(22-Ho)** show similar behaviour with decreasing $\chi_M T$ values over the whole temperature range. This decrease starts gradually, increasing its slope at about 80 K and becoming steep below 12 K reaching minimum values of $85.9 \text{ cm}^3 \text{Kmol}^{-1}$ and $73.0 \text{ cm}^3 \text{Kmol}^{-1}$ at 2 K, respectively. The decrease of $\chi_M T$ observed for all four samples may stem from the depopulation of excited states and potential antiferromagnetic interactions.

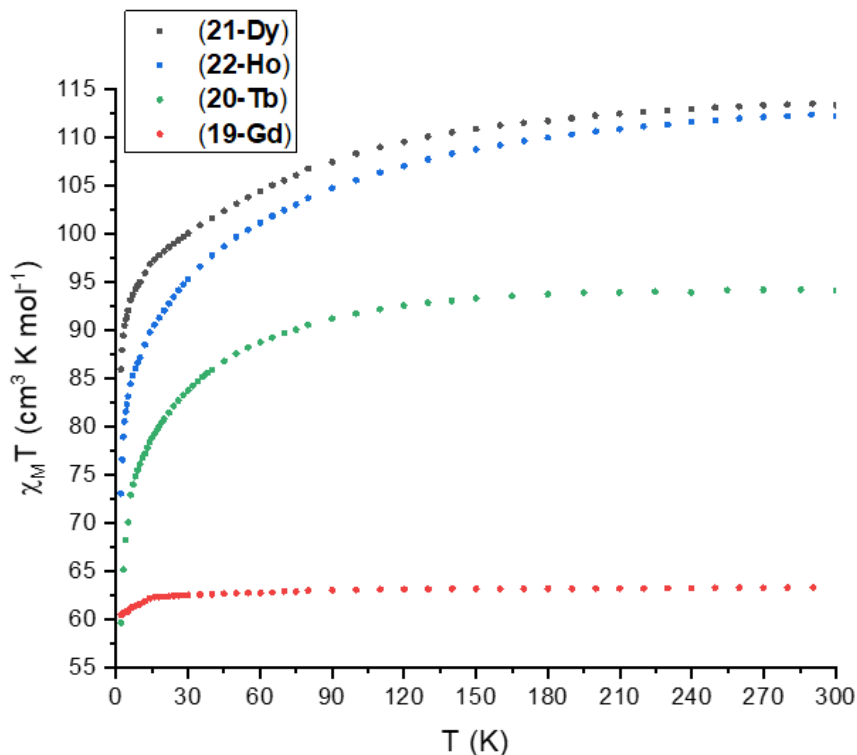


Figure 96. $\chi_M T$ vs T plots for **(19-Gd)** in red, **(20-Tb)** in green, **(21-Dy)** in black and **(22-Ho)** in blue at temperatures between 2 and 300 K measured with an applied dc field of 0.1 T.

In order to investigate the possibility of antiferromagnetic interactions in these four compounds, the inverse magnetic susceptibility was plotted against temperature and fitted to a Curie-Weiss law (figure 97). The results of the linear fits as well as the respective temperature region in which the curves followed the Curie-Weiss law are shown in table 12. From the negative Weiss constants, it can be concluded that there are indeed weak to very weak antiferromagnetic interactions present in these four clusters. For **(19-Gd)** containing isotropic Gd^{III} this value is considerably smaller than for the compounds containing anisotropic Ln^{III} ions. This suggests a very small antiferromagnetic exchange interaction present in **(19-Gd)** and a considerably stronger albeit still weak antiferromagnetic dipolar interaction for the others.

Table 12. Weiss constants θ , Curie constants C extracted from the linear fit and the temperature ranges in which the curves follow the Curie-Weiss law for (19-Gd), (20-Tb), (21-Dy) and (22-Ho).

	(19-Gd)	(20-Tb)	(21-Dy)	(22-Ho)
T (K)	2-300	10-300	10-300	10-300
θ (K)	-0.03	-3.8	-4.0	-6.3
C (cm³Kmol⁻¹)	63.3	95.2	114.9	113.6

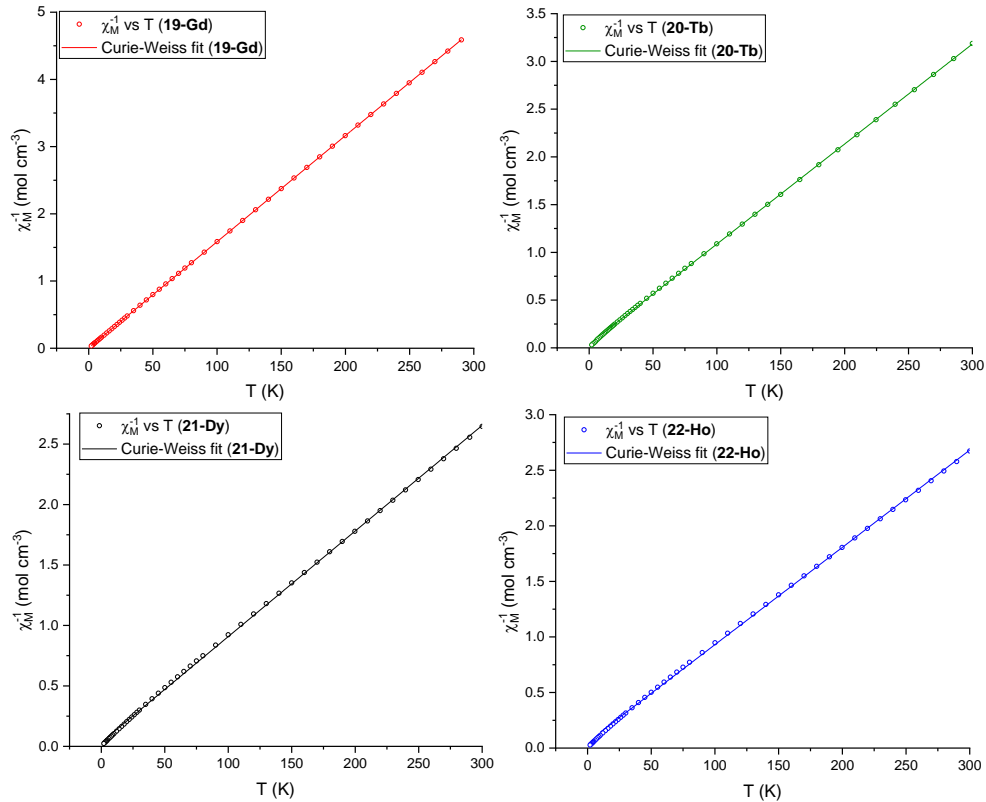


Figure 97. Curie-Weiss plots and fits for (19-Gd) in red, (20-Tb) in green, (21-Dy) in black and (22-Ho) in blue confirming weak to very weak antiferromagnetic interactions to be present.

Magnetisation measurements at applied dc fields between 0 and 7 T were performed on (19-Gd), (21-Dy) and (22-Ho) and can be seen in figure 98 as well as the respective reduced magnetisation plots. (20-Tb) was measured on a different SQUID magnetometer only equipped with a 1 T magnet, therefore no M vs B data was collected for (20-Tb). For (19-Gd) the magnetisation was recorded at more temperatures in order to calculate the magnetocaloric effect as further discussed in section 5.2.3.4. At 2 K (19-Gd) saturates at about 5 T at a value of 54.4 μ_B which is close to the expected value of 56 μ_B for eight Gd^{III} ions. The reduced magnetisation curves for (19-Gd) superpose essentially perfectly in the temperature range between 2 and 10 K as expected given the isotropic nature of Gd^{III}. The magnetisation of (21-Dy) saturates at a value of 44.2 μ_B at 7 T while (22-Ho) does not saturate as indicated by the still significant slope reaching a maximum value of 44.0 μ_B at 7 T. The reduced

magnetisation curves of **(21-Dy)** superpose fairly well considering the strong single ion anisotropy of Dy^{III} . This might be a result of the anisotropy axes of the Dy^{III} ions being oriented in “random” directions leading to very little overall anisotropy of the Dy_8 cluster or it could result from the fact that there are very little low-lying excited states that can be populated in this temperature and field range. For **(22-Ho)** the reduced magnetisation curves do not superpose indicating the opposite effect, either suggesting the involvement of excited states or stronger overall anisotropy. As the single ion anisotropy of Ho^{III} is oblate as in Dy^{III} , but of a lesser magnitude, the difference observed in the reduced magnetisation of **(22-Ho)** compared to **(21-Dy)** can most likely be explained by the higher density of low-lying excited states in **(22-Ho)**.

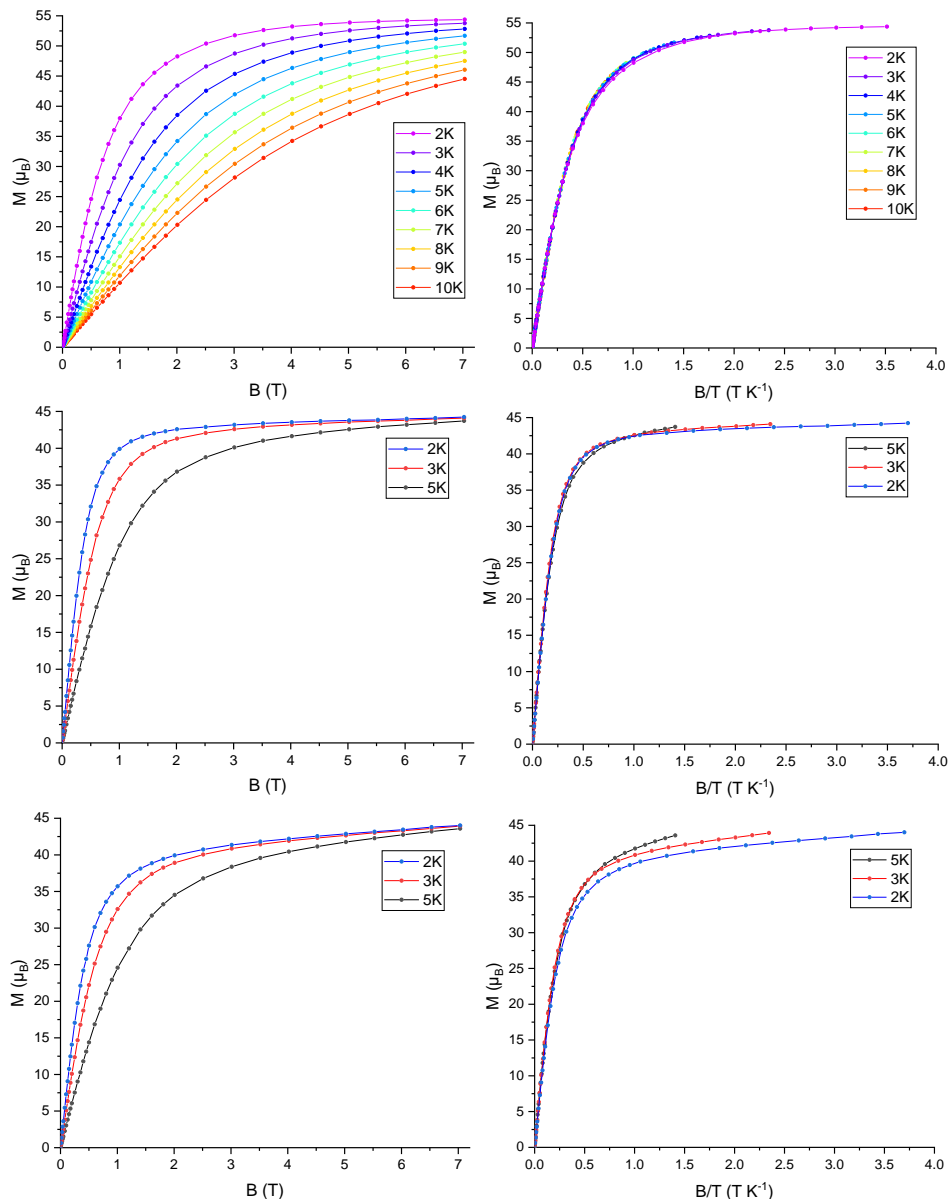


Figure 98. Magnetisation measurements at dc fields between 0 and 7 T (left) and reduced magnetisation plot (right) for **(19-Gd)** (top), **(21-Dy)** (middle) and **(22-Ho)** (bottom). Lines are a guide to the eye.

No ac signals could be observed for **(19-Gd)** as might be expected since Gd^{III} is isotropic. The same is true for **(22-Ho)** which can also be attributed to the lack of sufficient anisotropy in Ho^{III} as well as the fact that it is not a Kramers ion and therefore does not have a doubly degenerate ground state *per se*. The other tested non-Kramers ion containing compound **(20-Tb)** does show slow relaxation but only under an applied dc field of 0.3 T and with very low susceptibility (see figure 99). In the χ'' vs frequency plot it becomes obvious from the twin maxima at each temperature that there are two mechanisms to spin relaxation with similar rates present in this compound. The lines in figure 99 correspond to the best fits of the experimental data to the generalised Debye model using equation 15 and 16:

$$\chi'_M(f) = \chi_S + \left(\frac{(\chi_T - \chi_S) \cdot (1 + (2\pi f \tau)^{1-\alpha} \cdot \sin(\frac{\pi \alpha}{2}))}{1 + 2 \cdot (2\pi f \tau)^{1-\alpha} \cdot \sin(\frac{\pi \alpha}{2}) + (2\pi f \tau)^{2-2\alpha}} \right) \quad \text{equation 15}$$

$$\chi''_M(f) = \chi_S + \left(\frac{(\chi_T - \chi_S) \cdot (1 + (2\pi f \tau)^{1-\alpha} \cdot \cos(\frac{\pi \alpha}{2}))}{1 + 2 \cdot (2\pi f \tau)^{1-\alpha} \cdot \sin(\frac{\pi \alpha}{2}) + (2\pi f \tau)^{2-2\alpha}} \right) \quad \text{equation 16}$$

where χ_S = isothermal susceptibility, χ_T = adiabatic susceptibility, the thermal equilibrium takes the time τ to settle and α is a parameter describing a distribution of relaxation processes with large values for α indicating multiple relaxation processes present for the specific temperature and frequency.

The ac data of **(21-Dy)** will be compared to the literature known Dy₈ compound with the identical molecular structure but different crystal packing in the following section 5.2.3.3.^[200]

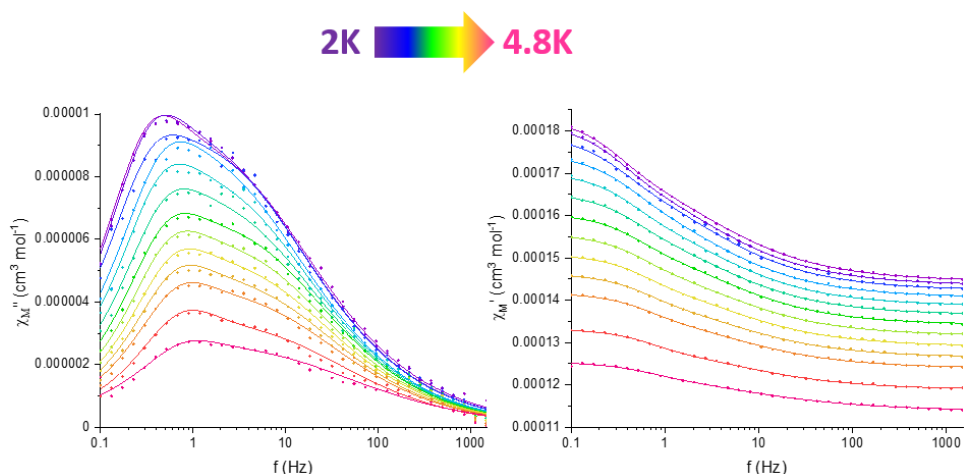


Figure 99. Ac magnetic data for **(20-Tb)** with an applied dc field of 3000 Oe. Out-of-phase magnetic susceptibility (left) and in-phase magnetic susceptibility (right) against frequency at temperatures between 2.0 K and 4.8 K. Points are the experimental data and solid lines are best fits to these using the Debye model.

Although τ values for both sets of maxima can be extracted from the fit to the Debye model, the small intensity of the signal and the lack of a sufficient amount of data points (only 13) make it impossible to fit the relaxation data.

5.2.3.3 The Influence of Packing on Magnetic Properties in Dy_8

As mentioned above, Tang *et al.* have reported a Dy_8 cluster that crystallises in the monoclinic structure version of the Ln_8 clusters presented above. This exhibits a different packing from (21-Dy). Although the bulk sample of (21-Dy) appears to have both monoclinic and triclinic structural versions present as seen in the PXRD, the magnetic behaviour is different as can be immediately seen from ac measurements. While the reported Dy_8 is an SMM in zero applied dc field, (21-Dy) shows the best response with an applied field of 0.175 T (see figure 100, left).

The Debye fit was used to extract the τ values for both sets of maxima, but only one could be fit using a variation of the equation proposed by Lunghi *et al.*^[142] (equation 13) in order to evaluate the relaxation processes (see figure 100, right). In this variation the Orbach process is left out due to not being relevant at such low temperatures, instead the parameters V_a and w_a help in accounting for vibrational relaxation which seems to be responsible for the slower of the relaxation processes visible for (21-Dy). The other set of maxima shows long lifetimes at high temperatures going through a minimum at 3 K and increasing again at lower temperatures. This is most likely an overlap of multiple relaxation processes with very similar rates that could not be fit using equation 13. The parameters to the best fit that can be seen in figure 100, right can be found in table 13. The ZFQTM parameter B was set to 0 since the measurement is done at 0.175 T while the other parameters were allowed to converge freely. This resulted in a very low parameter A which describes direct processes, indicating vibronic relaxation processes to be dominant here which could be influenced by the amount and the distribution of lattice solvents.

Table 13. Fitting parameters of the best fit to the relaxation processes relevant in (21-Dy) using equation 13.

A (s⁻¹ K⁻¹)	B (s⁻¹)	V_a (s⁻¹)	w_a (K)	V_b (s⁻¹)	w_b (K)
5.89E-17	0	69.5	25.7	17902	25.8

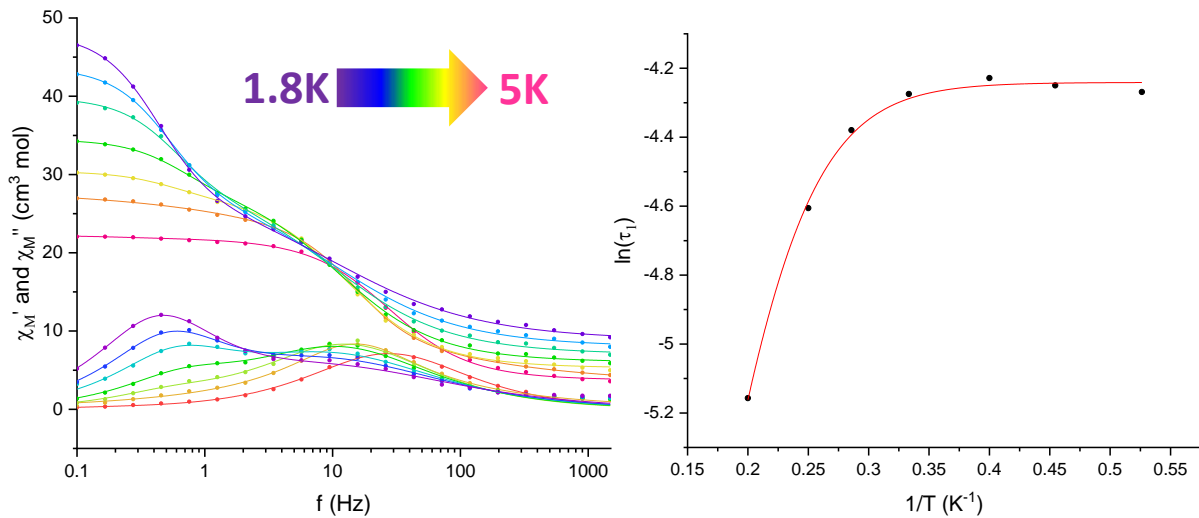


Figure 100. In- and out-of-phase ac magnetic susceptibilities of **(21-Dy)** measured between 1.8 and 5 K and frequencies between 0.1 and 1500 Hz showing slow relaxation of magnetisation. Solid lines are the best fit to experimental data using the Debye model (left) and Arrhenius plot of the first set of maxima (right, black dots) and the best fit to equation 13 (right, red line).

Since the ac susceptibility data of the two Dy_8 compounds are not directly comparable as a result of the need to apply field for the measurement of **(21-Dy)**, microSQUID measurements were conducted on single crystals of both compounds in collaboration with Dr. Haiquan Tian and Prof. Dr. Jinkui Tang (Changchun Institute of Applied Chemistry), who provided a sample of the literature known Dy_8 compound, and Dr. Michael Schulze in the group of Prof. Dr. Wolfgang Wernsdorfer (KIT, PHI) who conducted the experiment. The results that are shown in figure 101 clearly show a difference in the low temperature magnetic behaviour of the two samples. **(21-Dy)** barely shows any hysteresis and very strong ZFQTM as indicated by the vertical increase in magnetisation around zero field, which is in line with the ac susceptibility measurements demanding an applied dc field of 0.175 T. In the literature known Dy_8 the hysteresis is clearly open at low temperatures and the increase of magnetisation more gradual leading to a rounded shape of the curve. This difference may be the result of low-lying excited states in the reported Dy_8 with slightly different energies which would explain the gradual increase in M with increasing B and also the absence of significant ZFQTM. In **(21-Dy)**, the states seem to overlap more, leading to the increased probability of ZFQTM. Whether this is a result of additional phonons because of different lattice vibrations due to lattice solvent in **(21-Dy)** needs an in depth study of the relaxation processes by also measuring the ac out-of-phase magnetic susceptibility of the literature known Dy_8 cluster in a SQUID magnetometer with an applied field of 0.175 T. This will be the next step in the investigation of this system.

Furthermore, additional variations employing another different lattice solvent might prove helpful.

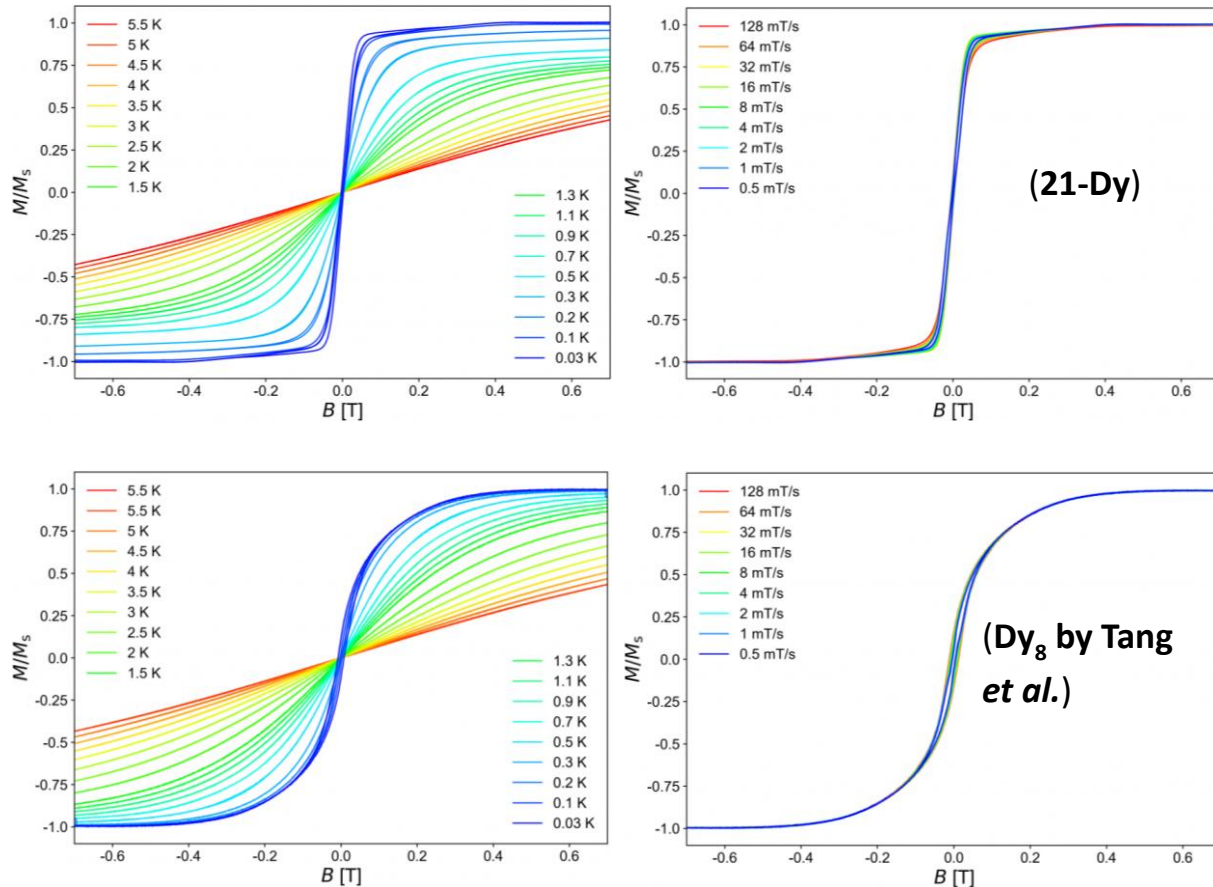


Figure 101. MicroSQUID measurements on single crystals of **(21-Dy)** (top) and the literature known $\text{Dy}_8^{[200]}$ (bottom). On the left the temperature dependence is shown between 0.03 K and 5.5 K and on the right the sweep rate dependence between 0.5 T/s and 128 T/s.

5.2.3.4 Magnetocaloric Effect (MCE) of the Gd_8 Complex

Since isotropic Gd^{III} ions are generally considered good candidates for magnetic refrigerants utilising the magnetocaloric effect, the entropy change of **(19-Gd)** was calculated using Maxwell's equation (equation 17) from isothermal magnetisation measurements at fields between 0 and 7 T and temperatures between 2 and 10 K that are shown above in section 5.2.3.2.

$$\Delta S(T)_{\Delta H} = \int [\partial M(T, H)/\partial H]_H dH \quad \text{equation 17}$$

The temperature and field dependence of the entropy change (figure 102) increases with increasing magnetic field and decreasing temperature reaching a maximum value

of $30.22 \text{ J kg}^{-1}\text{K}^{-1}$ at 2 K and 7 T. This is amongst the highest reported values for entropy changes in Gd_8 clusters in the literature^[284-286] and very close (86.5%) to the maximum theoretical value of $34.94 \text{ J kg}^{-1}\text{K}^{-1}$ for eight uncoupled Gd^{III} ions that can be calculated using the following equation:

$$-\Delta S_M = \frac{nR \ln(2S+1)}{M_w} \quad \text{equation 18}$$

Where n is the number of Gd atoms, R is the gas constant, $S = 7/2$ for Gd^{III} ions and M_w is the molecular weight of the cluster.

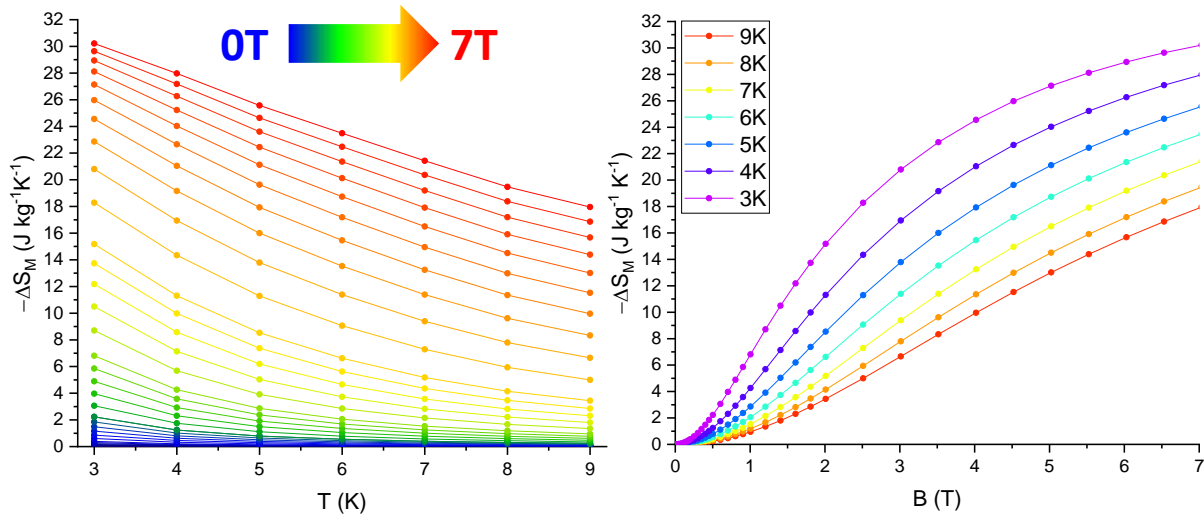


Figure 102. Temperature dependence (left) and magnetic field dependence of the molar entropy change of (19-Gd) calculated using the Maxwell relation (equation 17). Lines are guide to the eyes.

5.3 Using Modified Ligands to Introduce Halogen Bonds

5.3.1 Ligand Modifications

Five modifications of the H₂opch ligand were prepared using the following reaction using differently substituted *ortho*-vanillin components (see figure 103). While H₂opch is obtained with R¹ = Me and R² = H, modifications were synthesised here which increase the steric demand of R¹ and introduce functional groups as R² that can influence the electronic properties and therefore the intramolecular interactions in a compound, but also can engage in intermolecular interactions such as halogen interactions. The five modified ligands that were used are shown in figure 104.

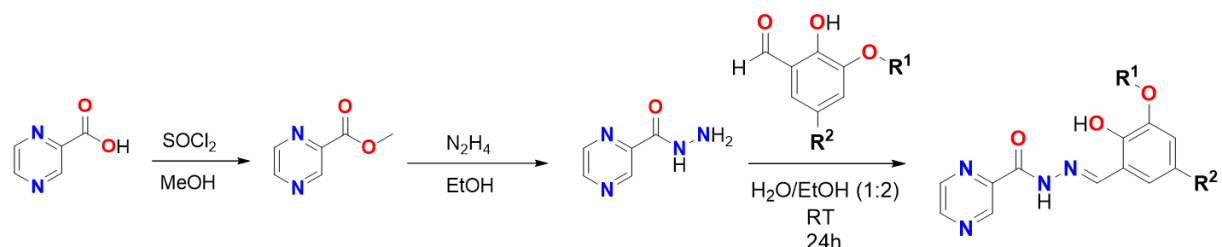


Figure 103. Synthesis of further members of the H₂opch ligand family. In the last step functional groups can be introduced that can alter the ligand and therefore complex properties. R¹ = methyl or ethyl and R² = H, Br, I, NO₂.

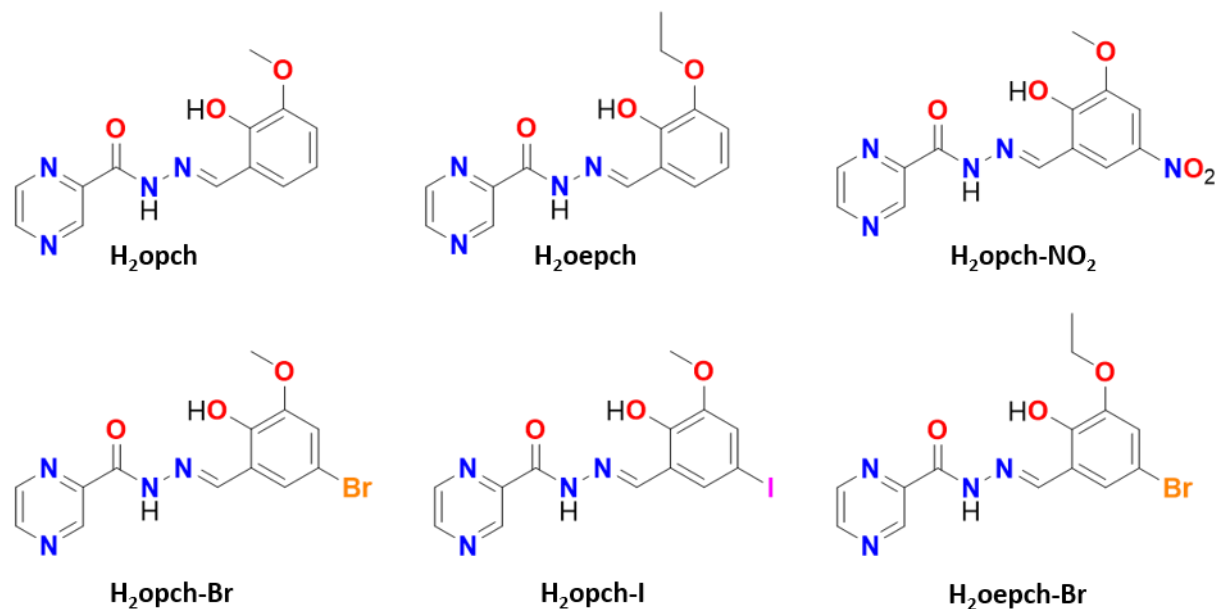


Figure 104. H₂opch and the five modified ligands that were used during this work.

The purity of the ligands was confirmed by ^1H -NMR spectroscopy (see figure 105). After drying under reduced pressure (water is not an issue as for following complexation reactions metal salt hydrates are used), they were used to produce lanthanide complexes without any further purification necessary.

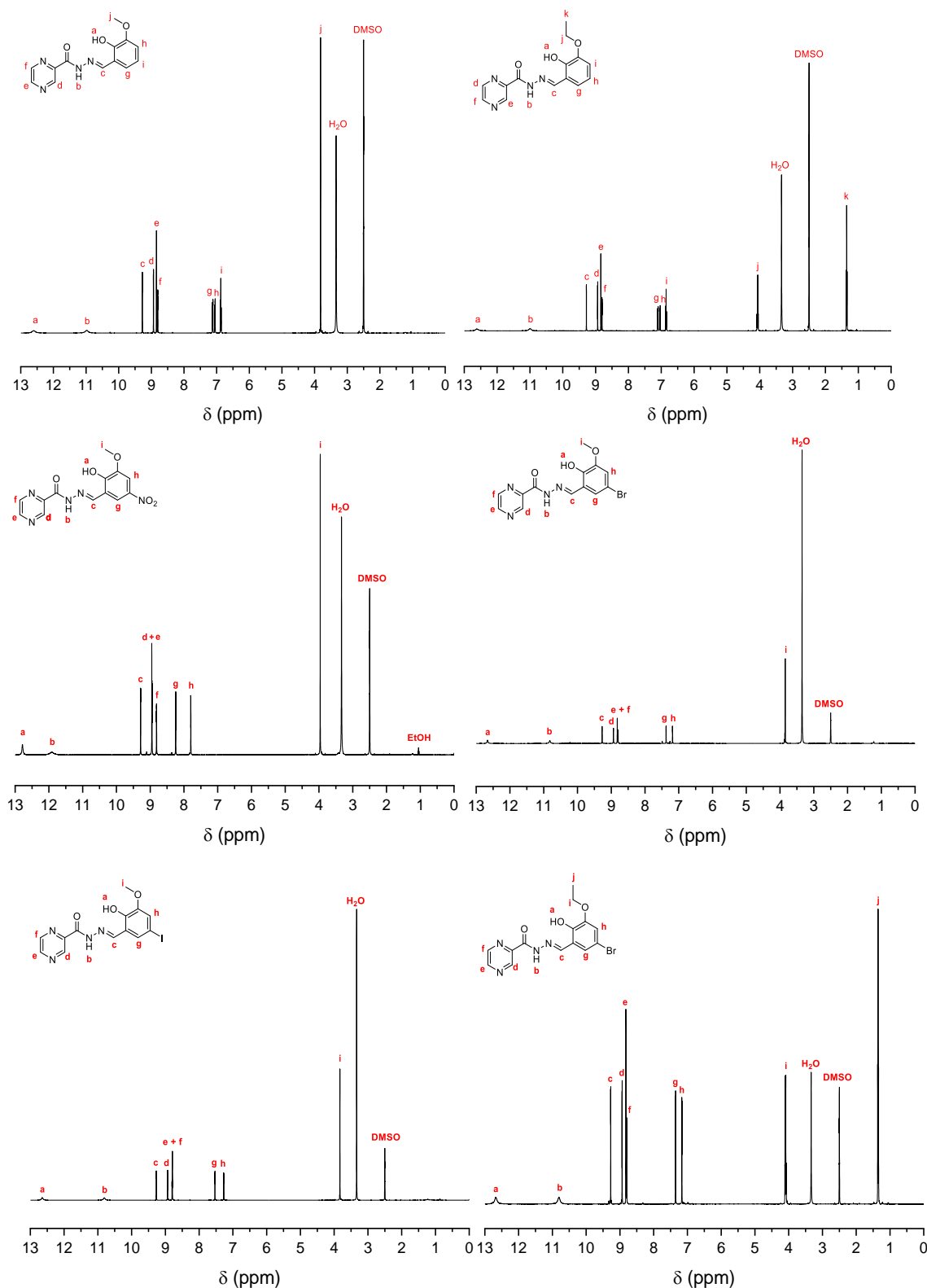


Figure 105. ^1H -NMR spectra of the ligand modifications recorded in DMSO-d6.

In order to better understand the optical properties of the Ln-complexes, absorption spectra of the ligands were recorded in solution as well as in solid state. The solid state absorption spectra of the ligands are compared in figure 106. The large error in the UV region between 200 and 350 nm is likely to be a problem with the solid state accessories of the UV-Vis machine. This issue grew worse over time. This can be seen by comparing the red spectrum of H₂oepch that was recorded in 2022 with the other five which were recorded in March 2023. Nevertheless, it can be seen that in the best resolved spectra three distinct peaks are visible with maxima at 235 nm, 271 nm and 325 nm.

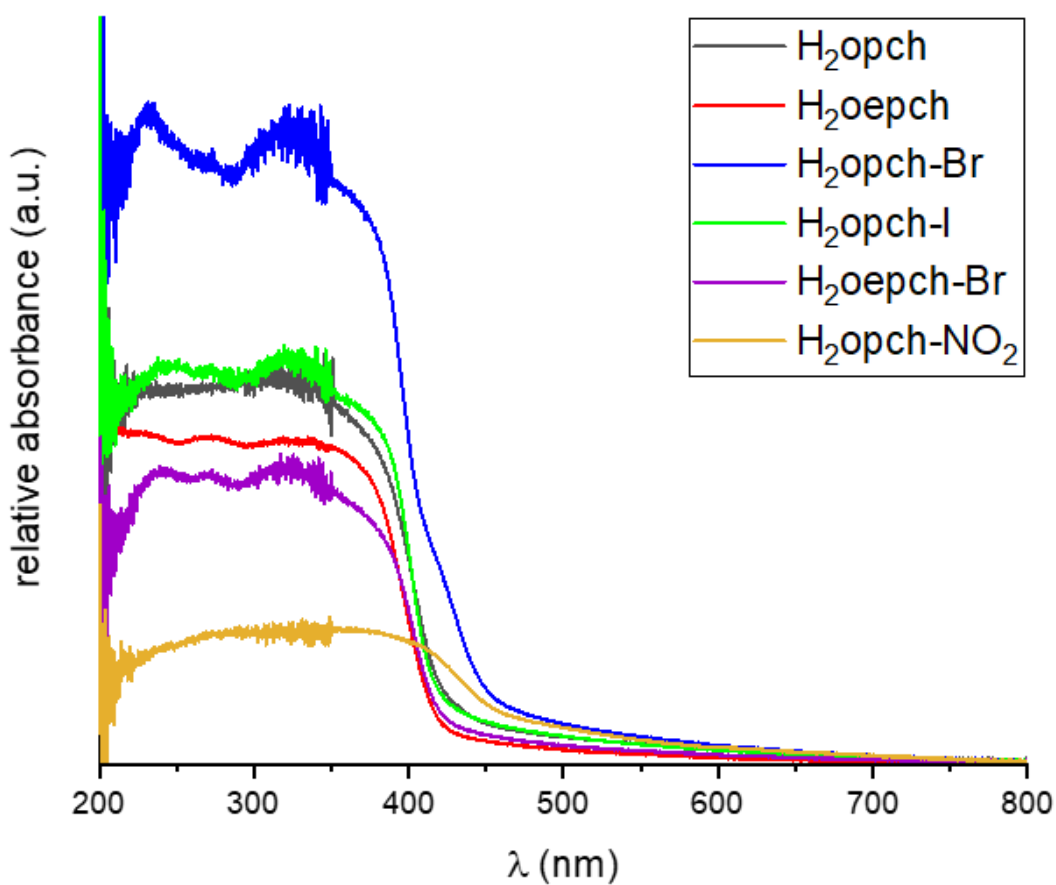


Figure 106. Solid state UVVis spectra of the modified H₂opch ligands between 200 and 800 nm.

The optical properties were also measured in solution. The organic ligands are all soluble in MeCN and the absorption spectra in MeCN solution are compared in figure 107. From the visual appearance of the ligands as powders it could be expected that H₂opch and H₂oepch would show almost no absorption in the visible region as they are both white powders with an only very light yellow tint (the left of the three powders in figure 107). This is confirmed by the absorption spectra which only show a slight shoulder in the visible range at 350 nm for these two compounds. H₂opch-Br, H₂oepch-

Br and H₂opch-I are obtained as light yellow powders (middle powder in figure 107) which can be attributed to the more pronounced shoulder at 350 nm for these three ligands. The last modified ligand discussed here, H₂opch-NO₂, is an ochre powder (right powder in figure 107), as confirmed by an additional absorption band at 440 nm which only appears in this ligand and therefore seems to involve the nitro group that is used in the R² substitute position.

While the general form of the absorption spectra is the same for all the ligands, apart the additional band in H₂opch-NO₂, there are subtle differences. There are three bands in the UV region that appear in all the spectra and the previously mentioned shoulder at 350 nm. The first band is shifted between all spectra indicating that this transition involves the phenyl ring bearing the R¹ and R² substituents. The other two bands appear consistently at 264 nm and 307 nm as well as the shoulder at 350 nm.

The shifting first band appears at 215 nm for H₂opch-NO₂, for H₂oepch at 221 nm, for H₂opch at 223 nm, for H₂oepch-Br and H₂opch-Br at 229 and 230 nm, respectively and at 237 nm for H₂opch-I. The shift can be explained by the different mesomeric and inductive effects of the R¹ and R² substituents. NO₂ has a -I and +M effect decreasing the electron density at the phenyl ring shifting the first excitation band towards higher energies in H₂opch-NO₂ compared to the other ligands. The bands of H₂opch and H₂oepch are the second highest in energy, as the R² substituents are H not altering the electron density on the phenyl ring. The slight difference between them arises from the small difference in R¹ substitution. The bromine containing compounds H₂opch-Br and H₂oepch-Br have their first band at 230 and 229 nm, respectively. The rather weak -I effect of the bromine is outweighed by its +M effect resulting in an increased electron density at the phenyl ring compared to the previous examples. The slight energy difference between the two first bands again occurs as a result of the different R¹ substituents (methyl and ethyl). The ligand with its band at 237 nm and therefore the lowest energy is H₂opch-I in which the iodine atom has an even weaker -I effect when compared to the bromine atom previously discussed leading to even higher electron density at the ring facilitating electronic excitation.

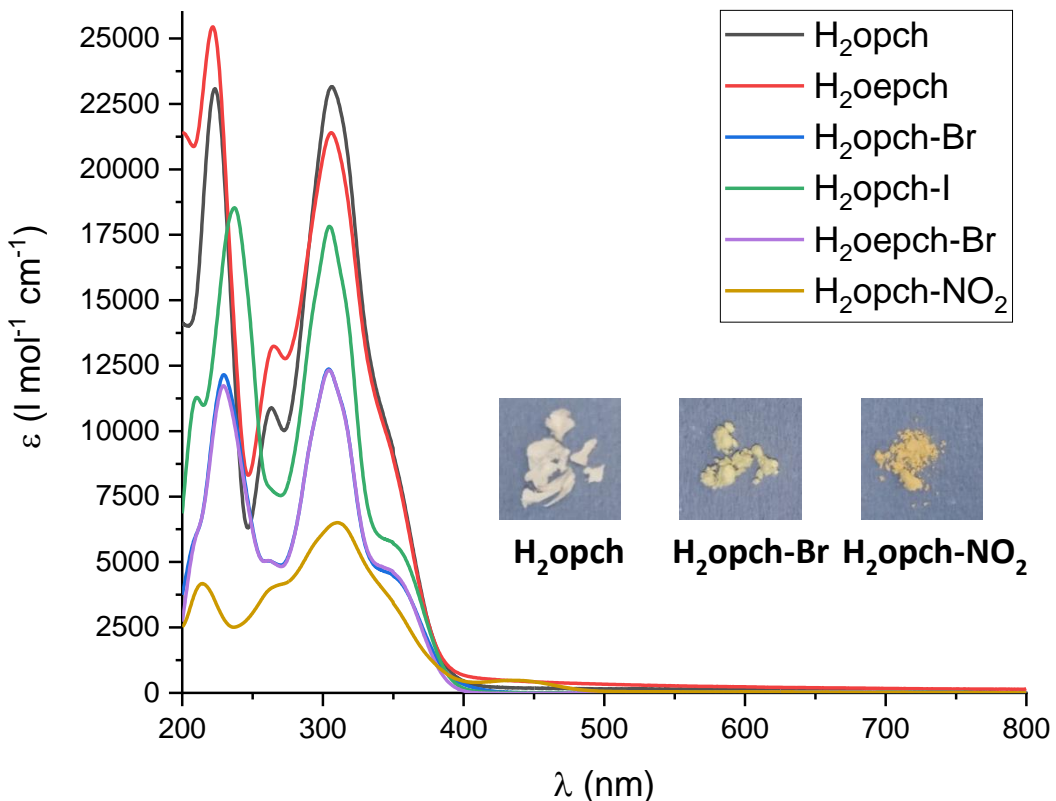


Figure 107. Absorption spectra of the modified ligands in MeCN between 200 and 800 nm.

5.3.2 Different Cluster Types using the H₂opch Ligand Family

In the following chapters various lanthanide salts were used in reactions with the modified ligands in various reaction conditions such as different solvents, bases and reaction times to produce compounds that can be classified as one of three types. 1) Carbonate-bridged clusters, 2) hydroxo-clusters and 3) dimers. All complexes that will be presented in greater detail in the following chapter are listed with their respective ligand and compound identifier in table 14 in order to provide an overview over the produced complexes.

Table 14. Overview of the complexes presented in this chapter and their classification into the three different structure types.

Complex	Ligand	Compound Identifier
Type I: Carbonate bridged clusters		
$[\text{Ln}_6(\text{Cl})_2(\text{CO}_3)_2(\text{H}_2\text{O})(\text{MeOH})_3(\text{oepch})_6]$ (Ln = Tb-Er)	H_2oepch	(25-Tb), (26-Dy), (27-Ho) and (28-Er)
$[\text{Er}_6(\text{Cl})_2(\text{CO}_3)_2(\text{H}_2\text{O})_3(\text{MeOH})(\text{opch-Br})_6]$	$\text{H}_2\text{opch-Br}$	(29-Er)
$[\text{Er}_4(\text{CO}_3)_2(\text{H}_2\text{O})_4(\text{opch-I})_4]$	$\text{H}_2\text{opch-I}$	(30-Er)
Type II: Hydroxo clusters		
$[\text{Ce}_4(\text{H}_2\text{O})_2(\text{NO}_3)_2(\mu_2\text{-OH})_4(\text{oepch})_4]$	H_2oepch	(31-Ce)
$[\text{Ce}_4(\text{H}_2\text{O})_2(\text{NO}_3)_2(\mu_2\text{-OH})_4(\text{opch-Br})_4]$	$\text{H}_2\text{opch-Br}$	(32-Ce)
$[\text{Ce}_4(\text{H}_2\text{O})_2(\text{NO}_3)_2(\mu_2\text{-OH})_4(\text{opch-I})_4]$	$\text{H}_2\text{opch-I}$	(33-Ce)
$[\text{Nd}_7(\text{H}_2\text{O})_2(\text{MeCN})(\text{NO}_3)_3(\mu_3\text{-OH})_6(\text{oepch})_6]$	H_2oepch	(34-Nd)
$[\text{Ln}_7(\text{NO}_3)_4(\mu_3\text{-OH})_6(\text{Hopch-I})(\text{opch-I})_5]$ (Ln = Gd and Dy)	$\text{H}_2\text{opch-I}$	(35-Gd A), (35-Gd B) and (36-Dy)
Type III: Dimers		
$[\text{Tb}_2(\text{H}_2\text{O})_2(\text{OAc})_2(\text{opch})_2]$	H_2opch	(37-Tb)
$[\text{Dy}_2(\text{MeOH})_2(\text{OAc})_2(\text{opch-Br})_2]$	$\text{H}_2\text{opch-Br}$	(38-Dy)
$[\text{Dy}_2(\text{DMF})_4(\text{NO}_3)_2(\text{opch-NO}_2)_2]$	$\text{H}_2\text{opch-NO}_2$	(39-Dy)
$[\text{Dy}_2(\text{Cl})_4(\text{Hopch-Br})_2]$	$\text{H}_2\text{opch-Br}$	(40-Dy)
$[\text{Dy}_2(\text{acetone})_2(\text{NO}_3)_2(\text{opch-Br})_2]$	$\text{H}_2\text{opch-Br}$	(41-Dy)
$[\text{Dy}_2(\text{acetone})_2(\text{NO}_3)_2(\text{opch-I})_2]$	$\text{H}_2\text{opch-I}$	(42-Dy)

The influence of the subtle changes in electronic structure of the modified ligands on formation and properties of the three types of structures, as well as the possibility for additional intermolecular interactions through the R¹ and R² substituents and their influence, will be discussed in the following sections.

5.3.3 Carbonate-Bridged Clusters using Modified H₂opch Ligands (Structure Type I)

As for the previously presented complexes (14-La), (16-Eu) and the variations on Ln₈ clusters, the carbonate-bridged complexes shown in this chapter form by binding CO₂

from air. This fixation of CO_2 from air to form CO_3^{2-} in basic media is well-known and was reported to be responsible for the formation of a plethora of carbonate bridged lanthanide clusters in the literature. Indeed, the templating effect of CO_3^{2-} was deliberately used to assist self-assembly of highly symmetric and/or high nuclearity lanthanide clusters. Key for this are the variable coordination modes of carbonate as discussed in section 5.1.^[199-200, 207, 209-211, 213-219, 221-224, 287-290]

Besides the Dy_8 cluster using H_2opch by Tang *et al.*, a Dy_6 cluster with the same ligand and bridging carbonates was reported by the same group.^[199-200] In a later publication they suggest to have identified the anion of the used Dy salt being responsible for directing the structural type obtained.^[198] This could not be confirmed by this work on modified H_2opch complexes, therefore the search for a mechanism began.

5.3.3.1 Trigonal Prismatic Complexes using Modified H_2opch Ligands

In attempts to produce more variations on the Ln_8 motif, reactions using the procedure used to obtain **(18-Sm)** to **(24-Y)**, were performed with H_2opch as ligand. These did not yield the desired compounds. As an alternative, the reaction procedure that led to the Dy_8 compound by Tang *et al.*,^[200] which uses lanthanide chlorides instead of nitrates and a solvent mixture of MeOH/DCM (1:2) instead of MeCN, was tested with the newly synthesised H_2opch ligand. This resulted in a series of hexanuclear complexes. These show the same core structure as the trigonal prismatic Dy_6 compound mentioned before.^[199] Four new compounds $[\text{Tb}_6(\text{Cl})_2(\text{CO}_3)_2(\text{H}_2\text{O})(\text{MeOH})_3(\text{oepch})_6]$ (**25-Tb**), $[\text{Dy}_6(\text{Cl})_2(\text{CO}_3)_2(\text{H}_2\text{O})(\text{MeOH})_3(\text{oepch})_6]$ (**26-Dy**), $[\text{Ho}_6(\text{Cl})_2(\text{CO}_3)_2(\text{H}_2\text{O})(\text{MeOH})_3(\text{oepch})_6]$ (**27-Ho**) and $[\text{Er}_6(\text{Cl})_2(\text{CO}_3)_2(\text{H}_2\text{O})(\text{MeOH})_3(\text{oepch})_6]$ (**28-Er**) involving the H_2opch ligand could be crystallised and were confirmed to be isostructural from single crystal X-ray diffraction (for **25-Tb**) and **(27-Ho)** only the unit cells were determined). The molecular structure of **(28-Er)** is shown in figure 108.

The structure consists of two Er triangles that are held together by a bridging carbonate anion each. Both triangles (Er(1)-Er(2)-Er(3) and Er(4)-Er(5)-Er(6)) are close to equilateral with angles of 59°, 60° and 61°, respectively, as well as Er-Er distances between 4.7602(6) Å and 4.8924(6) Å. The two triangles are connected to form a

compressed trigonal prism by two bridging oepch²⁻ ligands along each of these connecting edges with Er-Er distances of 3.8480(6) Å between Er(1) and Er(4), 3.8420(6) Å between Er(2) and Er(5) and 3.8481(6) Å between Er(3) and Er(6). Therefore, the core is an essentially perfect trigonal prism with one triangle only very slightly twisted from the other (see figure 108 showing the top view of the core). The coordination mode of the oepch²⁻ ligands can best be explained by looking at two Er^{III} ions from different triangles that are on top of each other, for example Er(1) and Er(4). They are chelated by the same two oepch²⁻ ligands both bridging between Er(1) and Er(4) with their carbonyl oxygen O(9) and O(12), respectively. Furthermore, now only looking at the oepch²⁻ ligand containing O(9) it additionally coordinates to Er(1) with a pyrazine nitrogen while it chelates Er(4) with its phenoxy oxygen and hydrazine nitrogen atom. The other oepch²⁻ ligand bridging Er(1) and Er(4) coordinates exactly the other way around (pyrazine at Er(4) and phenoxy as well as hydrazine at Er(1)). The coordination spheres of the six eight-coordinate Er^{III} ions is completed by one additional co-ligand each. To balance the overall charge, two anionic co-ligands, in this case chlorides are necessary which coordinate to Er(2) and Er(4). Er(1), Er(5) and Er(6) are coordinated by MeOH ligands and Er(3) is coordinated by a water ligand that is responsible for the intermolecular hydrogen bonding determining the packing as further described below.

The molecular structure is therefore strikingly similar to the situation in the reported Dy₆ compound using the H₂opch ligand with the only difference being the anionic co-ligands. For the reported Dy₆ the charge is balanced by two acetate ligands from the Dy(OAc)₃ starting material. For the new Ln₆ complexes LnCl₃ was used and therefore the charge is balanced by two coordinating chlorides.^[199] Using a very similar ligand H₂opvh, which has a pyridine ring instead the pyrazine in H₂opch, Tang and co-workers were also able to report this trigonal prismatic structure as well as the Dy₈ motif described above in section 5.1.^[226]

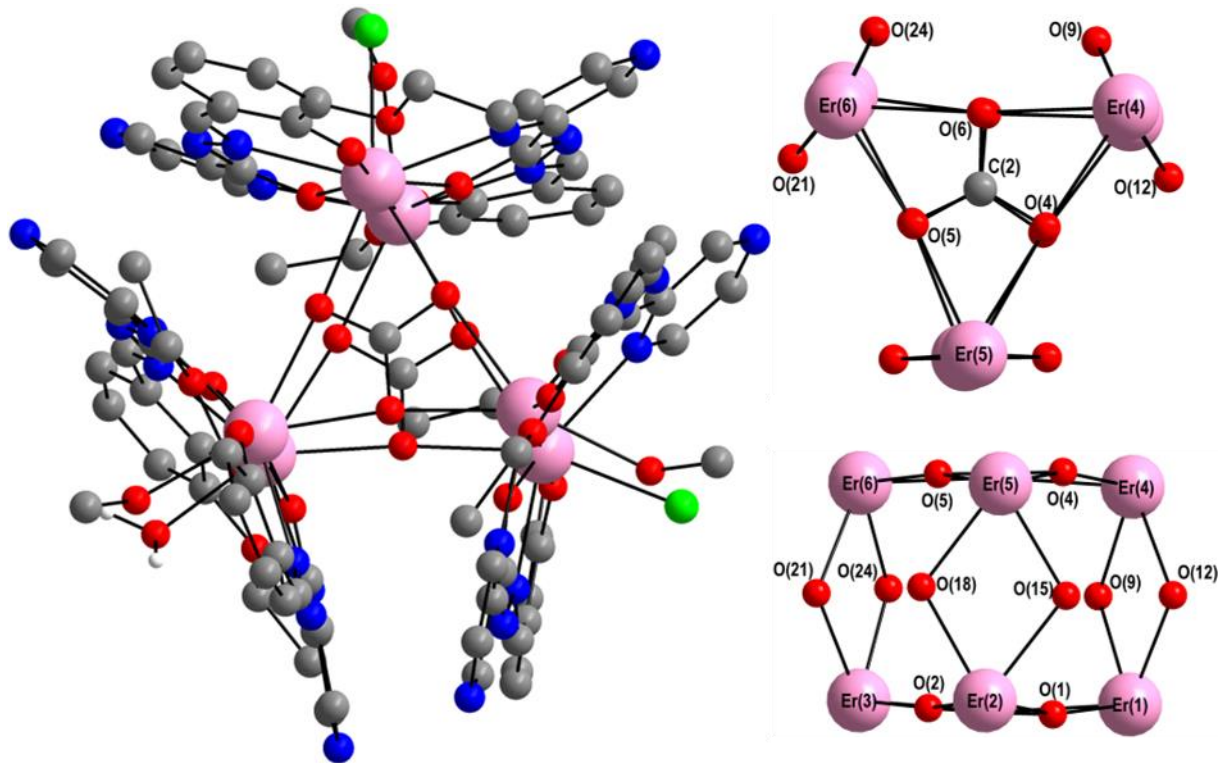


Figure 108. Molecular structure of (28-Er) showing the trigonal prismatic arrangement of Er^{III} ions (left) and a top and side view of the core structure (right).

There are further examples in the literature in which this particular $\mu_3\text{-}\eta^3\text{:}\eta^3\text{:}\eta^3$ coordination mode of the CO_3^{2-} ligand is observed. This coordination mode especially favours triangular arrangements of lanthanide ions as can be seen from discrete tri-lanthanide complexes^[209] that can show intriguing magnetic properties such as toroidicity,^[207, 217] but can also show the opposite behaviour as observed in a Dy_3^{III} triangle with almost perfectly frustrated Ising spins.^[291] The carbonate-bridged triangular structures have also been reported to be part of a bigger design.^[211, 221, 225, 292]

Strong bands at around 1450 cm^{-1} were observed for all of these examples and assigned to coordinated carbonate vibrations which is consistent with the IR spectra of carbonate-bridged transition metal complexes.^[293] This is also observed for (25-28-Ln) with a peak at 1444 cm^{-1} as highlighted in figure 109.

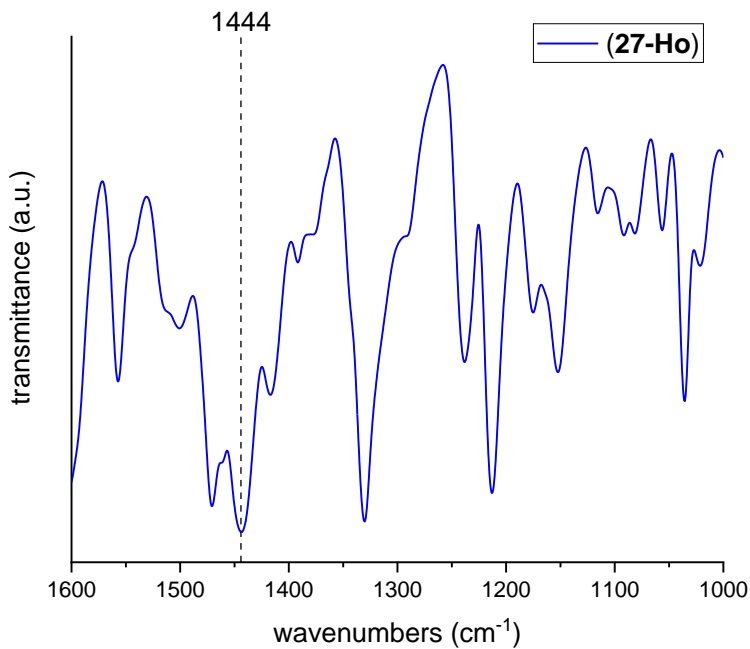


Figure 109. Excerpt of the solid state ATR-IR spectrum of (27-Ho) highlighting the carbonate based vibration at 1444 cm^{-1} .

Compounds (25-Tb), (26-Dy), (27-Ho) and (28-Er) crystallise in $P\bar{1}$ with two molecules in the unit cell. The single coordinating water molecule now has an important role in the packing of the structure since it forms a HB to a pyrazine-N on the neighbouring molecule via one of its protons. The distance between O26-H26A...N23 is $2.722(7)\text{\AA}$ with an angle of $169(6)^\circ$. Other than this hydrogen bond between the two molecules in the unit cell there are no other obvious intermolecular interactions (see figure 110). In the Dy₆ compound by Tang *et al.*^[199] which crystallises in the monoclinic space group P2₁c, hydrogen bonds form zig-zag chains of Dy₆ clusters throughout the crystal. The PXRD of (28-Er) confirms the phase purity of the sample (figure 111) and the magnetic and optical properties were investigated in the following.

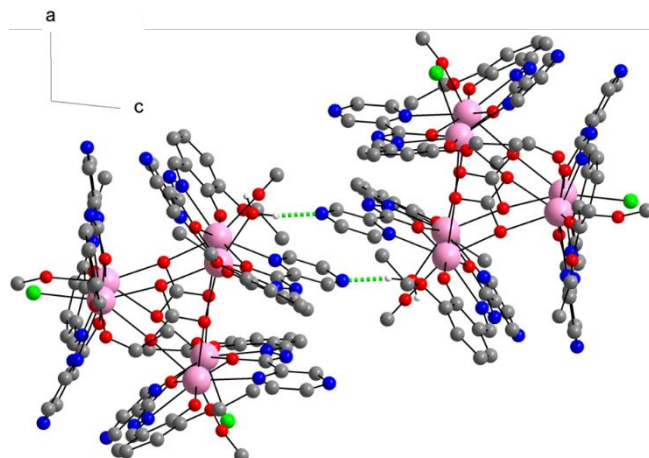


Figure 110. Packing view of (28-Er) along the b-axis highlighting intermolecular HBs in green.

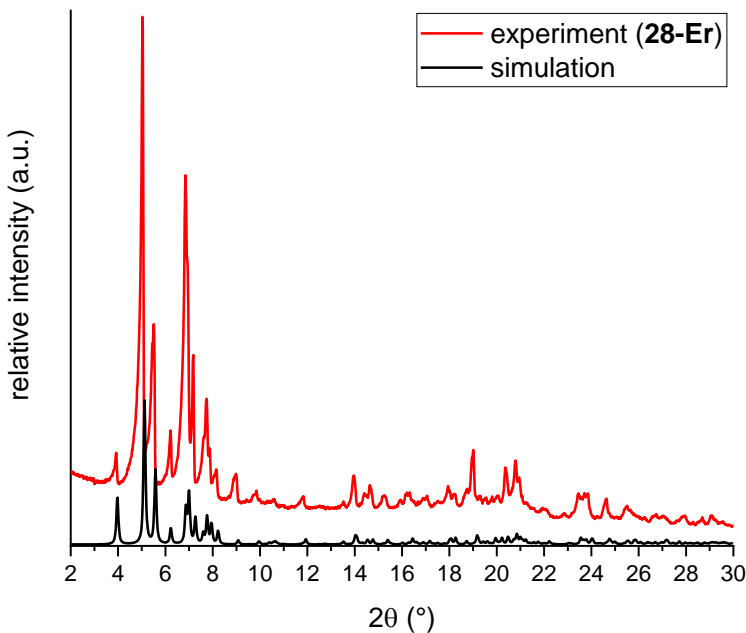


Figure 111. Powder pattern (28-Er) compared to the simulation.

5.3.3.2 The Influence of a Bromine Atom

The same reaction procedure that led to the trigonal prismatic clusters with H₂oepch was performed using H₂opch-Br in order to introduce halogen interactions to the system and probe the effect of additional interactions on the crystal design as well as the physical properties. Indeed, the reaction resulted in an Er^{III} complex with the same basic core structure as in (25-28-Ln) (see figure 112).

As in (25-Tb), (26-Dy), (27-Ho) and (28-Er) the total charge of the clusters is balanced by two coordinating chlorides. In (29-Er) now one of them is localised at Er(1) while the other is disordered roughly equally over three sites (occupancy at Er(2) = 0.35, at Er(3) = 0.30 and at Er(5) = 0.35). The other 65/70% of these sites are occupied by water ligands whose protons are not refinable due to the overlap with the residual electron density of the chlorides.

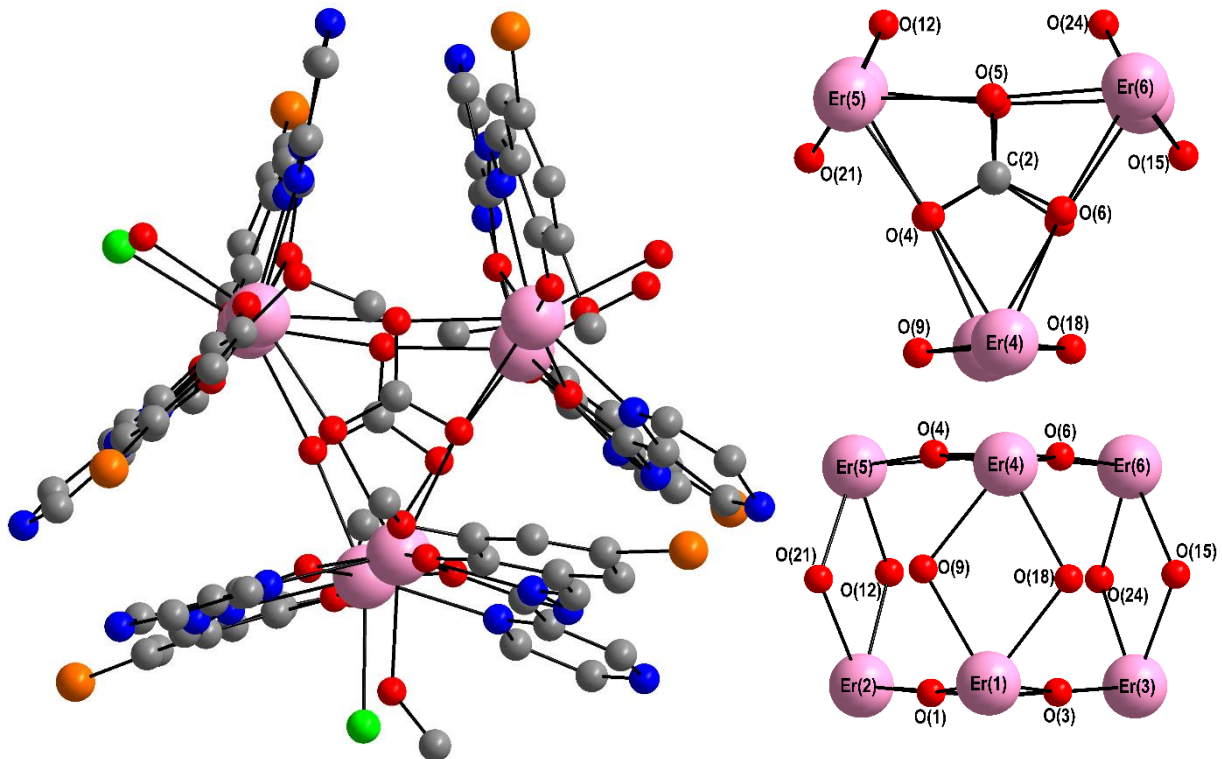


Figure 112. Molecular structure (left) and two views on the Er₆ core of (29-Er) (right). The disorder has been removed for clarity and the Cl ligand assigned to the site coordinating Er(2) for the graphics.

The phase purity was confirmed by PXRD and the carbonate vibration highlighted in the excerpt of the IR spectrum which can both be seen in figure 113.

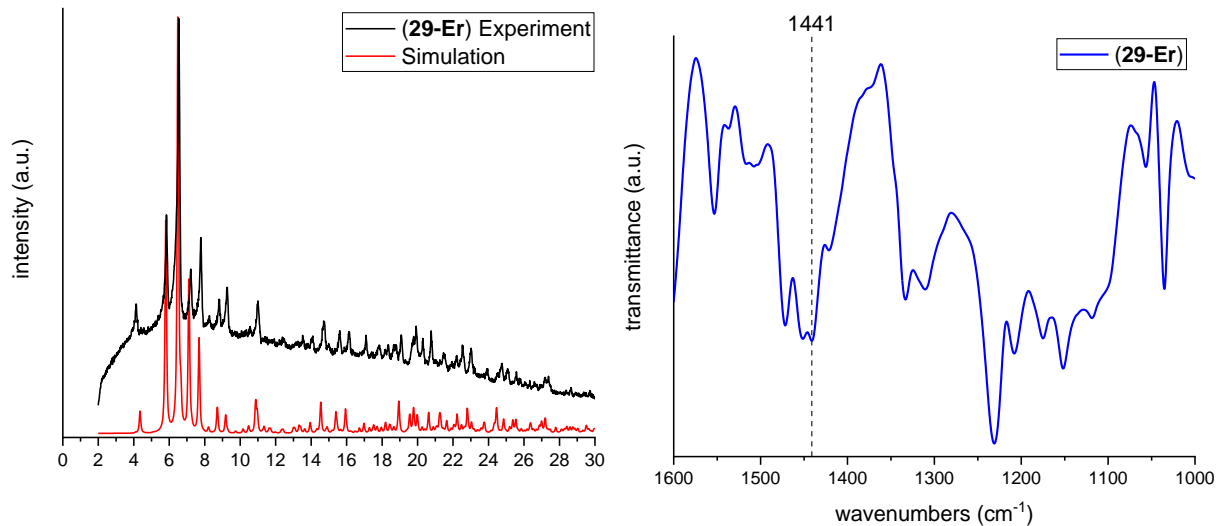


Figure 113. Powder pattern confirming the phase purity of (29-Er) (left) and excerpt of the IR spectrum of (29-Er) between 1600 and 1000 cm⁻¹ with the carbonate peak highlighted at 1441 cm⁻¹ (right).

To show the similarities of the slightly distorted trigonal prismatic core structures of the complex with the H₂oepch ligand (**28-Er**) compared to the one with the H₂opch-Br ligand (**29-Er**) both are shown in figure 114 on the left and right respectively.

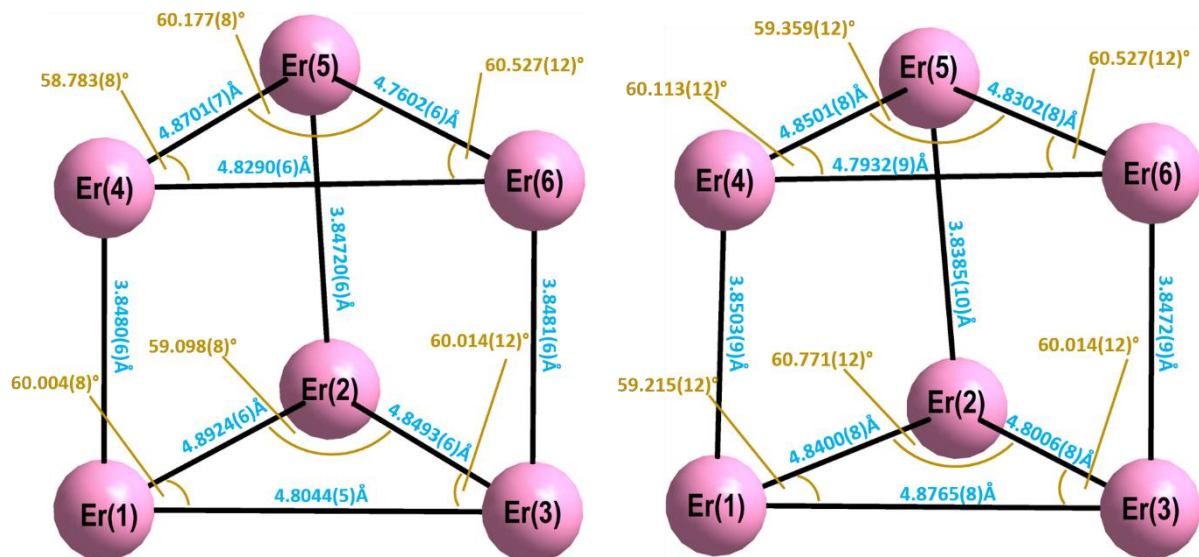


Figure 114. Core structures of **(28-Er)** (left) and **(29-Er)** (right) highlighting the distortion of the trigonal prism and the high level of similarity between them.

In both trigonal prismatic Ln_6 complexes with H_2oepch and $\text{H}_2\text{opch-Br}$, the molecular structure exhibits a *pseudo*-threefold axis through the carbon atoms of the central carbonates. The symmetry is broken by the slight distortion of the core as well as the two anionic co-ligands that must be distributed equally over six sites if they are to retain threefold symmetry. Although the molecular structure is therefore not very symmetric the introduction of a bromine atom to the ligand in (**Er-29**) still leads to arrangement of the trigonal prisms in a highly symmetric way (see figure 115). (**29-Er**) crystallises in the tetragonal space group $P\bar{4}2_1c$ with $Z = 8$. In figure 115 half of the molecules in the unit cell can be seen with a view along the fourfold axis that coincides with the crystallographic c axis. The bromine-bromine distances of $3.604(3)\text{\AA}$ that are highlighted in figure 115, are shorter than twice the VdW radius of bromine which amounts to 3.70\AA .^[164] This indicates an attractive interaction between them. Such a dramatic increase in symmetry from triclinic to tetragonal by the introduction of a single bromine atom to the ligand emphasises the crucial role halogen interactions can play in the crystal design of coordination clusters while leaving the molecular structure intact.

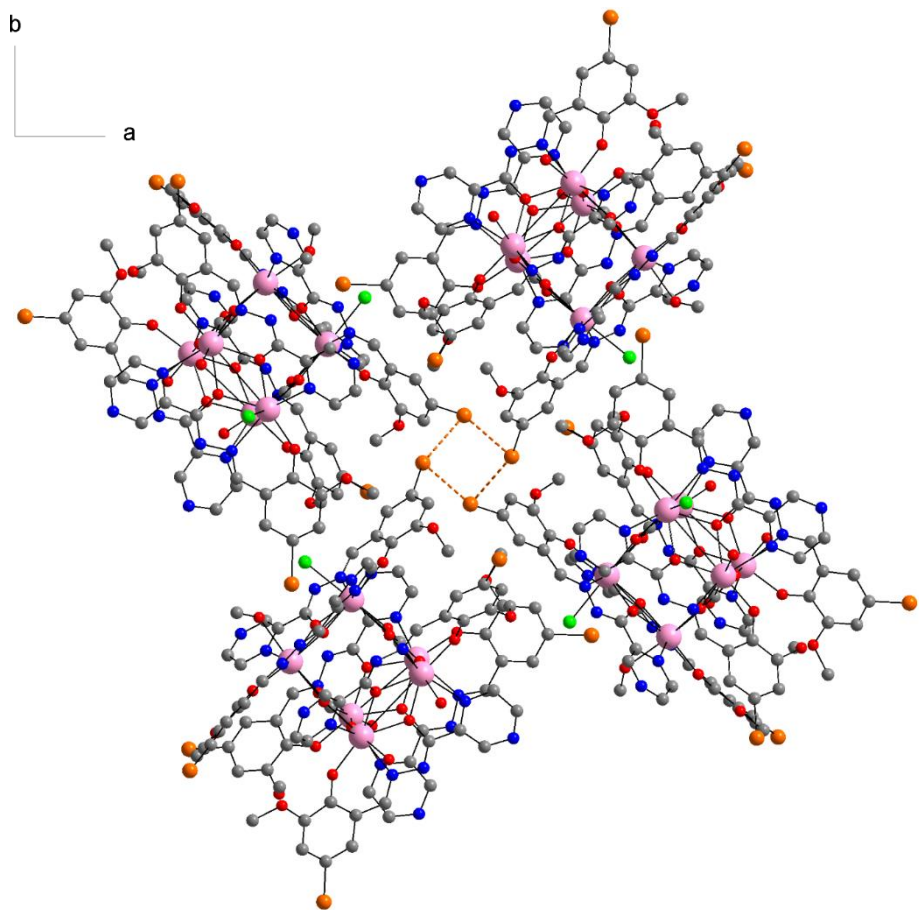


Figure 115. Packing view along the fourfold axis (crystallographic c axis). Short bromine-bromine contacts are highlighted by the orange dotted lines.

Looking at the crystal structure from another angle it becomes obvious that the four bromine atoms, and along with them the four trigonal prismatic clusters, form a giant tetrahedron as shown in figure 116. The halogen interactions in **(29-Er)** can be classified as type II (halogen bonds). This is shown by the angles highlighted in blue in figure 116. As explained in chapter 3.3 the electron density around a covalently bound halogen atom is anisotropic. At the elongation of the covalent bond is a region of low electron density as the antibonding σ^* orbital is located there. This electrophilic region on the surface of a halogen atom is called σ -hole. The electron density of the three free electron pairs form a belt around the halogen atom. This makes the areas orthogonal to the σ -hole nucleophilic. The angle between C(6A)-Br(1A)...Br(1B) is $162.3(6)^\circ$, essentially aligning the σ -hole on Br(1A) with Br(1B). This, in combination with the angle between C(6B)-Br(1B)...Br(1A) of $98.6(6)^\circ$ being close to 90° makes the nucleophilic area around Br(1B) align with the electrophilic area of Br(1A) and enables an attractive interaction resulting in short Br-Br contacts.

Here, the convention for halogen bonds has to be briefly mentioned again in order to avoid confusion. The electron donor in a halogen bond (in this case Br(1B)) is the XB acceptor and vice versa. All four bromine atoms act as XB donor and acceptor simultaneously resulting in the overall tetrahedral arrangement.

This tetrahedral arrangement arising through halogen bonds has apparently not been reported in the literature especially in terms of connecting Ln-clusters. This provides an example for a novel bonding mode which significantly increases the symmetry of a system.

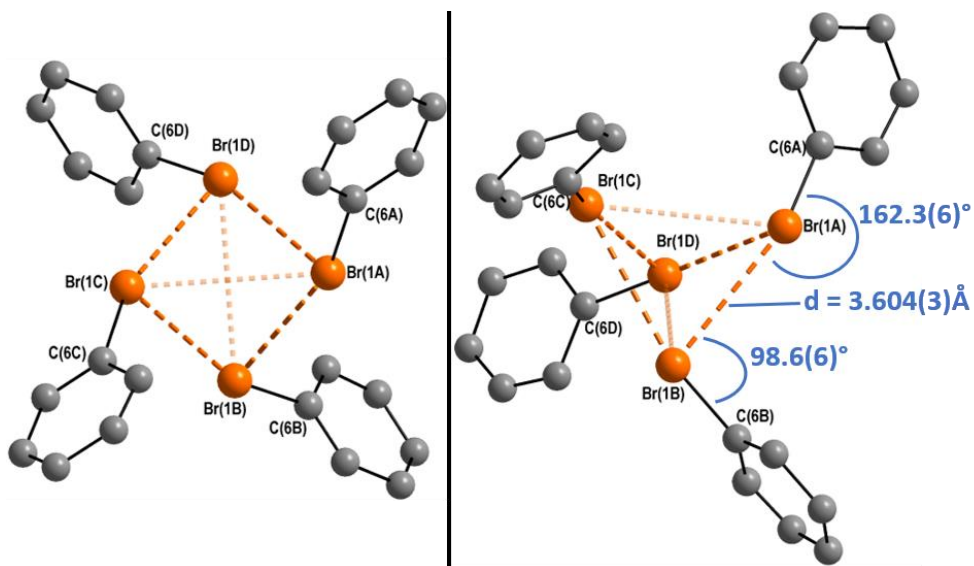


Figure 116. Enlarged view of the halogen-halogen interactions dominating the packing of (29-Er) looking along the c axis (left) and from a different angle demonstrating the tetrahedral arrangement (right). The shortest distance between the tetrahedrally arranged bromine atoms (each Br(1) of one Er_6 -cluster) is smaller than the combined VdW-radii indicating an attractive interaction. The angles highlighted in blue classify the interaction as a type II halogen interaction also known as a halogen bond.

If one considers only Br-Br contacts that are shorter than twice the VdW radius of Br (2x VdW radius of Br = 3.70 \AA) Br(1A) as an example is only directly connected to Br(1B) and Br(1D) in the tetrahedron shown above. The distance between Br(1A) and Br(1C) is too long with 3.9308(34) \AA which is not surprising as there is no direct attractive interaction between the two. These distances are therefore shown paler in figure 116. Nevertheless, each Er_6 cluster is connected to six others in total by Br-Br halogen bonding as Br(1) on each Er_6 cluster does not only connect to the two other Br(1)s in the tetrahedron but also to Br(4) of another neighbouring cluster. Additionally, Br(6) is connected to Br(2), Br(4) to Br(1) and Br(2) to Br(6) of neighbouring clusters, respectively.

The topology of the three dimensional supramolecular network resulting from this was analysed in collaboration with Dr. George Kostakis (University of Sussex) and this variation of the 6/4/t8 topologycal type was found not to be reported before. In figure 117 the result of the topological analysis is visualised. Each orange dot represents an Er_6 cluster that is connected via blue halogen-halogen bonds to six of its neighbours. The point symbol of this network is $(4^9.6^6)$ with the vertex symbol $[4.4.4.4.4.4.4(3).4(3).6(2).6(2).6(4).6(4).6(6).6(6)]$.^[294-295]

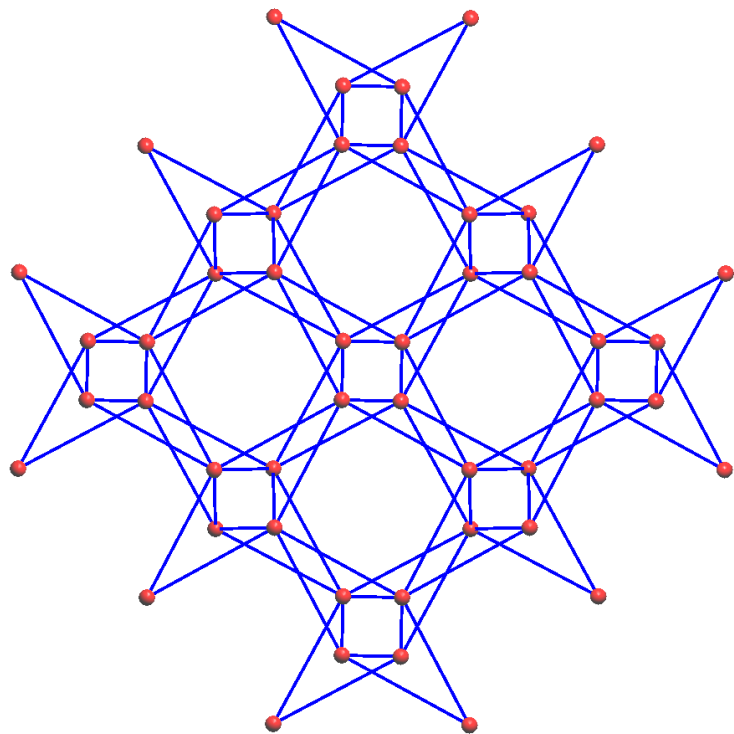


Figure 117. Result of the topological analysis on **(29-Er)** in collaboration with Dr. George Kostakis (University of Sussex). Orange dots each represent one Er_6 complex, blue lines indicate the pattern in which each cluster is halogen bonded to six others.

UVVis absorption spectra of **(29-Er)** were recorded as powder and in DMF solution and are compared to the spectra of **(27-Ho)** in figure 118. **(Er-29)** shows maxima at 208 nm, 240 nm, 333 nm and a band in the visible region at 420 nm in the solution spectrum that is red-shifted to 443 nm in the solid state spectrum. From the comparison of the solid state and DMF solution spectra of **(29-Er)** it can be concluded that the complex remains stable in solution. By comparison with the spectra of **(27-Ho)** it can further be concluded that the halogen bonded network does not influence the absorption spectrum in solution excluding the possibility of ET reactions via the Br-Br orbital overlap.

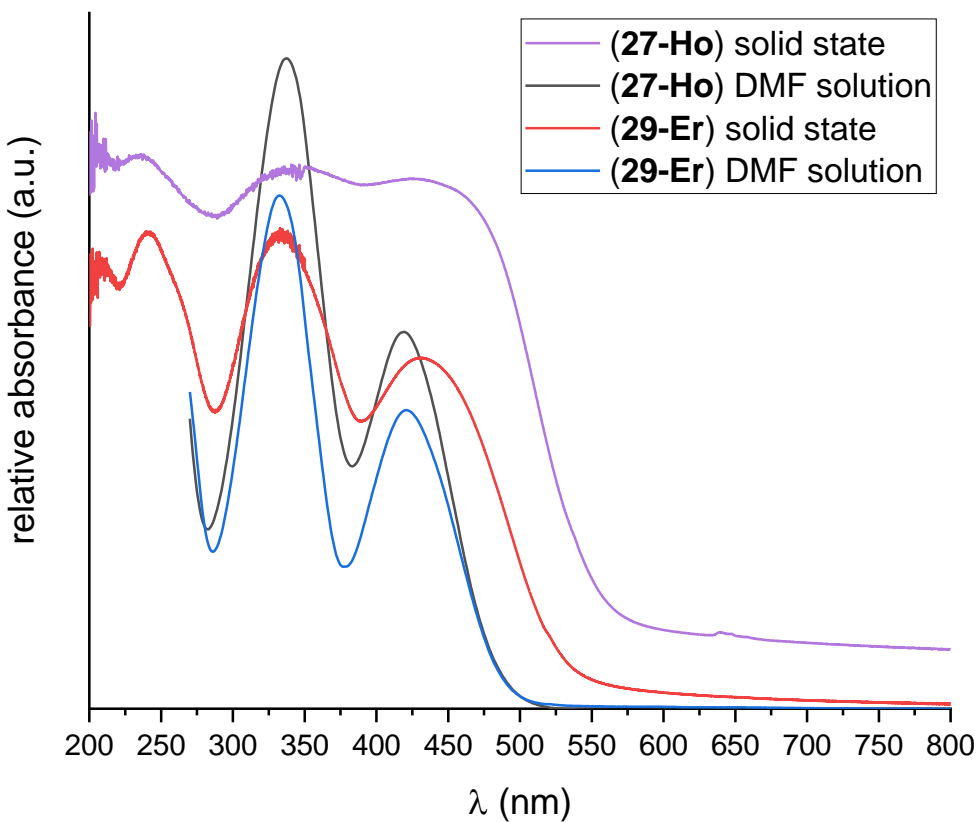


Figure 118. UVVis absorption spectra of (27-Ho) and (29-Er) in solid state and DMF solution.

Magnetic measurements were performed on both (28-Er) and (29-Er) to gauge whether the significant increase in symmetry in addition to the intermolecular interaction pathway provided by halogen-halogen bonding has an influence on the magnetic signatures.

The magnetic moment was measured at variable temperatures between 1.8 K and 300 K with an applied dc field of 0.1 T (1000 Oe). The results can be seen in the $\chi_{\text{M}}\text{T}$ vs T plots in figure 119. Both compounds behave essentially identical with a RT $\chi_{\text{M}}\text{T}$ value of 67.7 and $67.5 \text{ cm}^3\text{Kmol}^{-1}$ for (28-Er) and (29-Er), respectively. This comes very close to the expected value of $68.88 \text{ cm}^3\text{Kmol}^{-1}$ for six uncoupled Er^{III} ions. With decreasing temperature, the $\chi_{\text{M}}\text{T}$ values of both compounds show a gradual decrease which at temperatures below 40 K becomes much steeper. At 1.8 K (28-Er) reaches a $\chi_{\text{M}}\text{T}$ value of $30.78 \text{ cm}^3\text{Kmol}^{-1}$ and (29-Er) reaches a $\chi_{\text{M}}\text{T}$ value of $29.08 \text{ cm}^3\text{Kmol}^{-1}$. The constant decrease in $\chi_{\text{M}}\text{T}$ with decreasing temperature is a result of the depopulation of excited Stark-levels that might be super positioned with antiferromagnetic coupling between the Er^{III} ions.

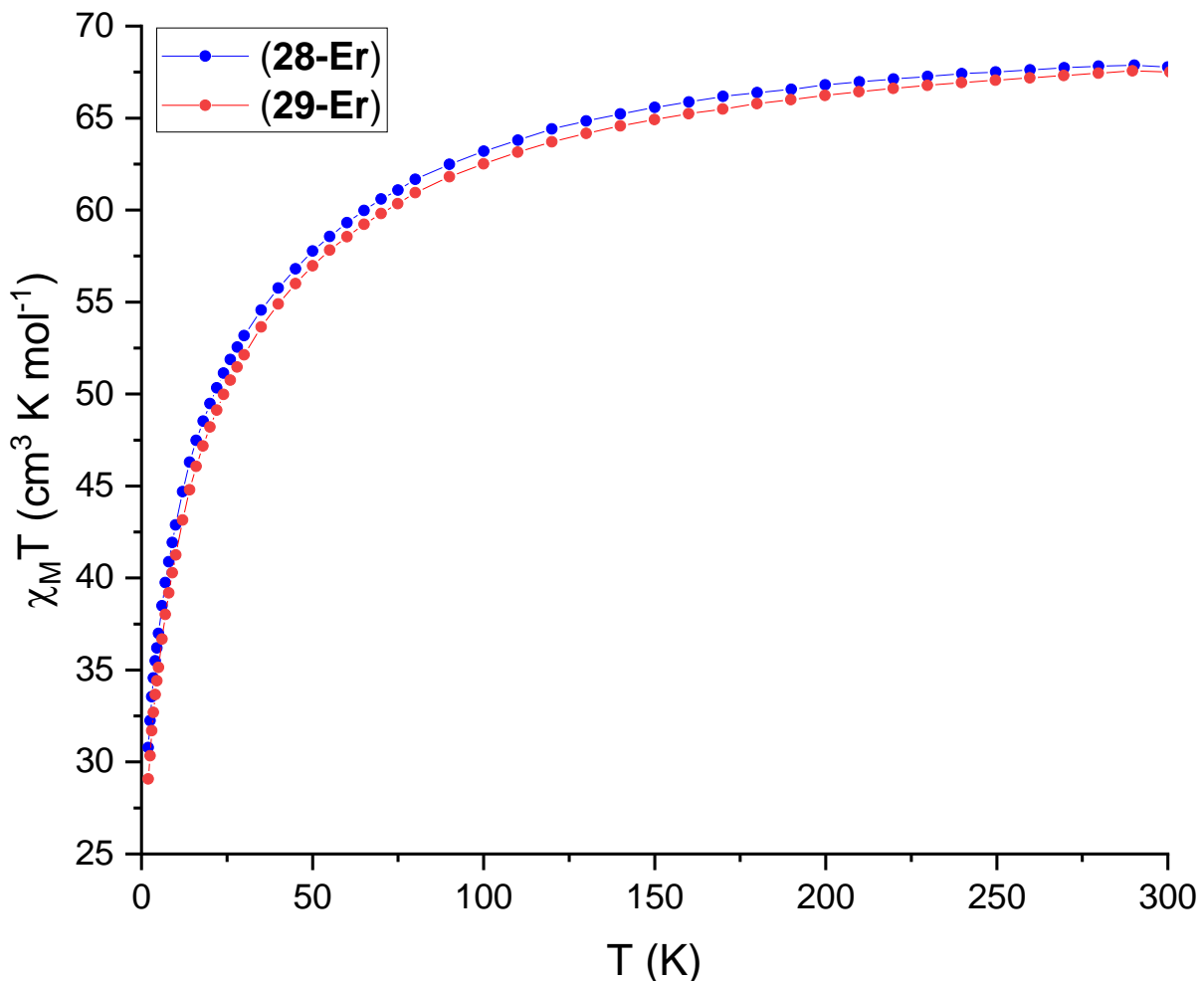


Figure 119. Magnetic M vs T measurements performed on (28-Er) (blue) and (29-Er) (red) between 1.8 K and 300 K with an applied dc field of 0.1 T. Solid lines are a guide to the eye.

By plotting the inverse magnetic susceptibility against temperature, it can be identified whether there is any antiferromagnetic interaction present in the system. The curves for both compounds (see figure 120) follow the Curie-Weiss law in the temperature range between 30 K and 300 K and can be fit with Curie constants C of $70.4 \text{ cm}^3 \text{Kmol}^{-1}$ for (28-Er) and $69.9 \text{ cm}^3 \text{Kmol}^{-1}$ for (29-Er) as well as Weiss constants θ of -11.0 K for (28-Er) and -11.7 K for (29-Er). Therefore, it can be concluded that there is indeed an effective antiferromagnetic interaction present between either set of six Er^{III} ions.

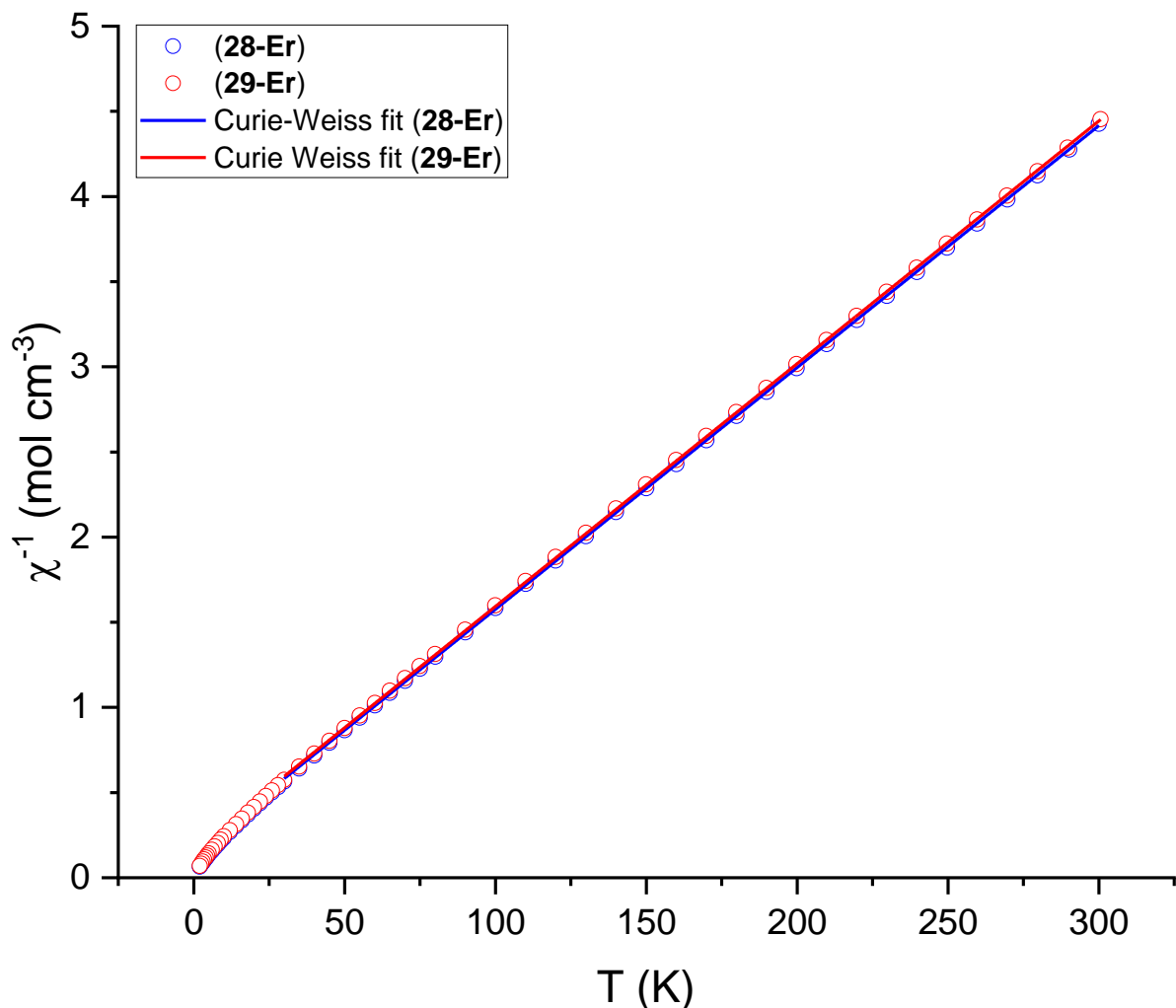


Figure 120. Curie-Weiss plots for (28-Er) and (29-Er) in blue and red, respectively. Linear fits between 30 and 300 K reveal a negative Weiss constant indicating antiferromagnetic interactions.

The behaviour of the magnetic moment with variable applied dc fields between 0 and 7 T was probed at 2, 3 and 5 K and the results can be seen in figure 121 (top). Saturation is not seen for either compound as shown by the still significant slope at 7 T reaching a maximum value of $32 \mu_B$. In figure 121 (bottom) the reduced magnetisation is plotted. The non-superposition of the plots as well as not reaching the expected saturation value of $57.5 \mu_B$ for six uncoupled Er^{III} ions^[52] hints at significant anisotropy and crystal field effects lifting the degeneracy of the 16 sub states of the $^4I_{15/2}$ ground state.^[108]

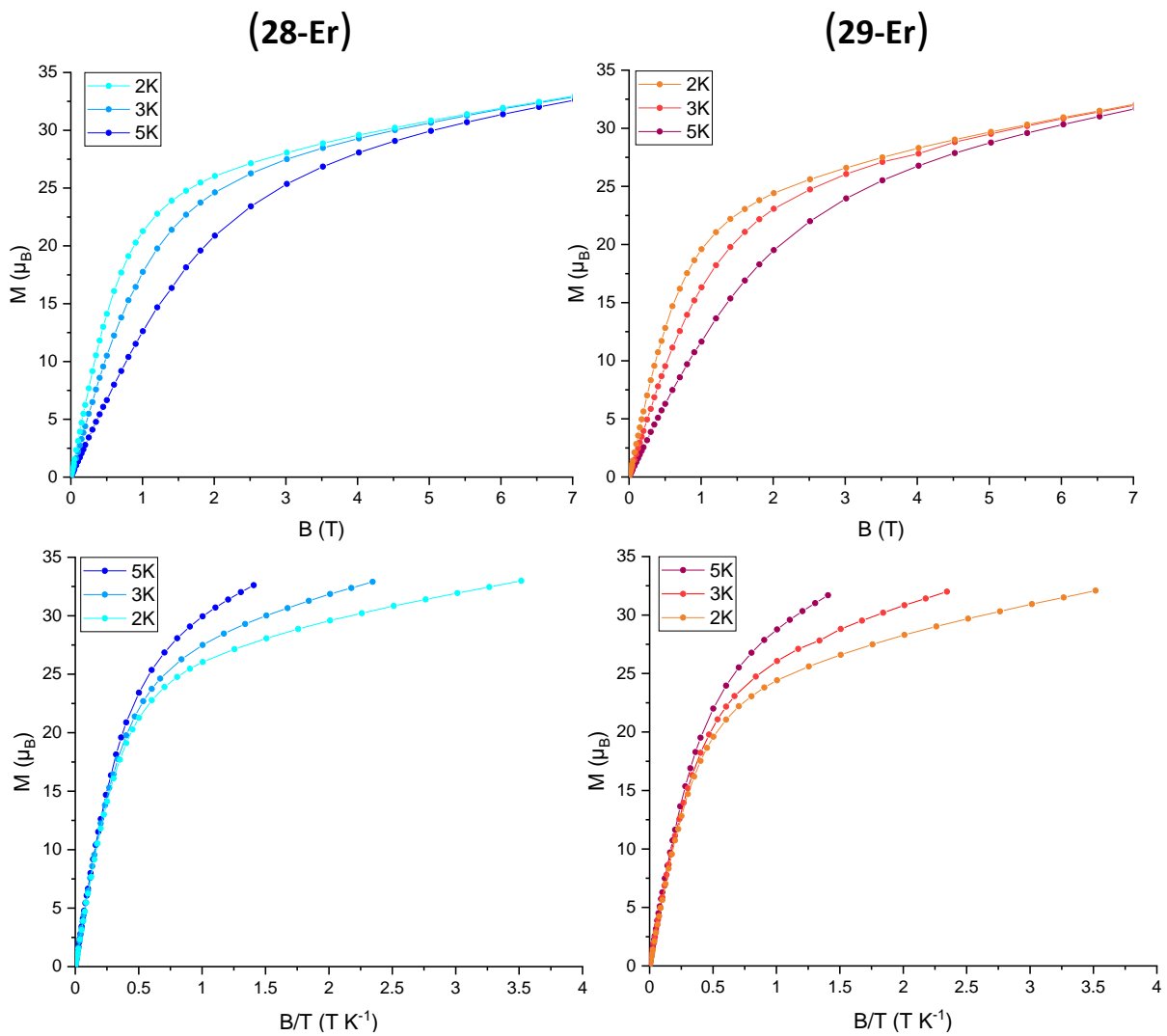


Figure 121. Magnetisation measurements were performed with applied dc fields between 0 and 7 T at 2, 3 and 5 K. Both compounds (28-Er) and (29-Er) do not reach saturation at 7 T (top). Reduced magnetisation plots (bottom) showing the anisotropy of the system. Lines are guide to the eye.

In ac measurements no out-of-phase signals and therefore no slow relaxation of the magnetisation was seen for either compound. This is not totally surprising as although Er^{III} ions are strongly spin-orbit coupled Kramers ions, they do however possess oppositely shaped single ion anisotropy compared to Dy^{III} . As the literature known Dy_6 clusters^[199, 222] show SMM behaviour it is somewhat expected that Er^{III} in the same coordination environment does not show slow relaxation of the magnetisation. Er^{III} SMMs in the literature are often sandwich complexes using ligands that coordinate non-axially supporting the prolate anisotropy of Er^{III} such as COT^{2-} .^[132]

The essentially identical curves above lead to the conclusion that at least for static magnetic fields the halogen-halogen bonds in (29-Er) do not influence the magnetic behaviour, hence do not provide an additional pathway for intermolecular magnetic

interactions as observed in some instances in the literature.^[242, 296] The reason for this appears to be the lack of direct orbital overlap between the halogens and the lanthanide ions which was discussed to be the reason for the intermolecular interactions in reference^[242].

While the Dy analogue (**26-Dy**) was obtained for the trigonal prisms with the H₂oepch ligand, the analogous compound with H₂opch-Br could not be synthesised. It can be speculated that while there may be no direct intermolecular interaction possible via the halogen-halogen bonds, the increase in symmetry would alter the relaxation dynamics. Slow relaxation might be expected for (**26-Dy**) given the behaviour of the H₂opch and H₂opvh trigonal prisms in the literature.^[199, 222]

The question that as of now remains unanswered is how the increase in symmetry through the introduction of halogens would impact upon this behaviour.

Although the yield of the Dy analogue (**26-Dy**) was too low to perform magnetic measurements on this compound, the anisotropy axes of the axial Dy^{III} were calculated from the crystal structure using the MAGELLAN software^[297] mentioned before. MAGELLAN uses a purely electrostatic model for its calculations, but in our working group we found empirically, that in the absence of certain co-ligands such as nitrates that seem to sometimes perturb the calculation, the direction of the axes from MAGELLAN coincides well with those obtained from state-of-the-art *ab initio* calculations.

The directions of the axes for (**26-Dy**) can be seen in figure 122 below. They align essentially orthogonal to the triangles in the trigonal prisms which would result in a high S ground state for the case of ferromagnetic coupling as observed in the literature known Dy₆^[199] and in a very low S ground state in the case of antiferromagnetic coupling.

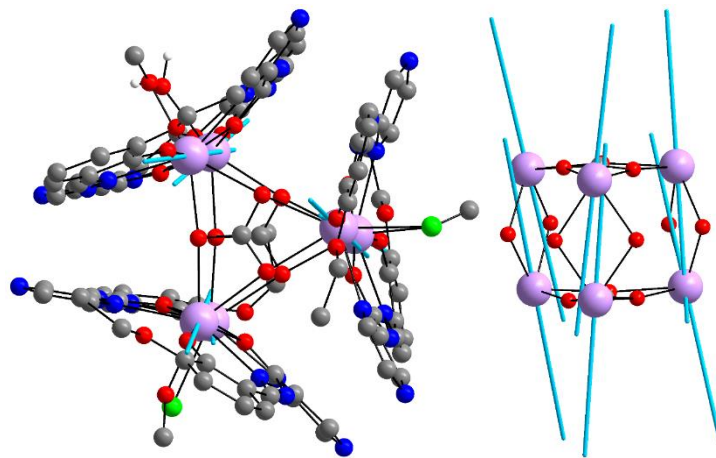


Figure 122. Anisotropy axes (in light blue) of (26-Dy) calculated using MAGELLAN.^[297]

5.3.3.3 Possible Intermediate in Trigonal Prism-Formation – A Proposed Mechanism

Repeating the reaction with other modified ligands did not yield the respective trigonal prismatic complexes. Therefore, other reaction conditions were altered. Using $\text{ErCl}_3 \cdot 6\text{H}_2\text{O}$ with the $\text{H}_2\text{opch-I}$ ligand in acetone with triethylamine as base resulted in a product that might shed light on how the trigonal prismatic compounds are formed. $[\text{Er}_4(\text{CO}_3)_2(\text{H}_2\text{O})_4(\text{opch-I})_4] \cdot 10\text{acetone}$ (**30-Er**) is a tetranuclear complex that is coordinated by two bridging carbonate ions and resembles an incomplete trigonal prismatic complex (see figure 123).

(**30-Er**) crystallises with half of the molecule in the asymmetric unit with the coordination modes of the modified H_2opch ligands ($\text{H}_2\text{opch-I}$ in this case) being identical to the ones observed in (**28-Er**) and (**29-Er**). The distances between $\text{Er}(1)$ and $\text{Er}(2)$ with $3.8675(13)\text{\AA}$ and between $\text{Er}(1)$ and $\text{Er}(2')$ with $4.7002(13)\text{\AA}$ are also close to the ones observed in the two trigonal prismatic Er clusters presented before. This strengthens the suspicion of (**30-Er**) resembling an incomplete trigonal prismatic cluster. The molecular symmetry here is made possible by the lack of two further trivalent Er^{III} cations. These then do not have to be compensated by two doubly deprotonated opch-I^{2-} ligands as well as two additional coordination anionic co-ligands distributed over six possible sites which was the main reason for the asymmetric molecular structure of (**28-Er**) and (**29-Er**). Instead, in (**30-Er**) the co-ligands

completing the coordination sphere are four water ligands allowing for the possibility for an inversion centre to be present within the molecule.

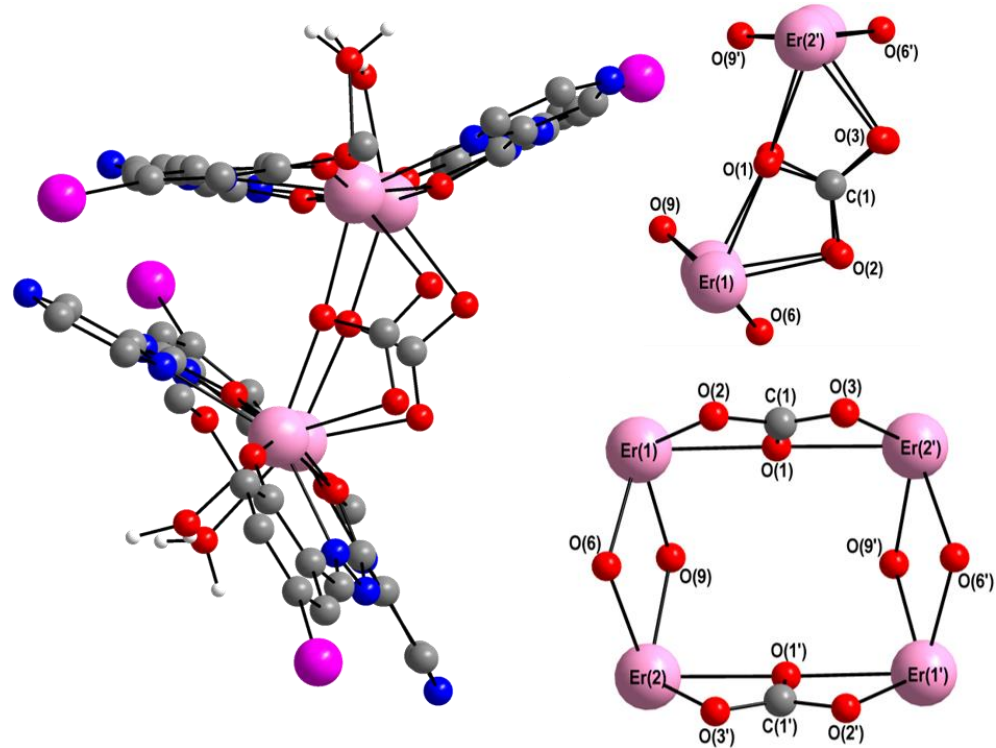


Figure 123. Molecular structure (left) and two views on the core of (30-Er) (right).

Phase purity of (30-Er) was confirmed using PXRD and the carbonate vibration is highlighted in the excerpt of the IR spectrum in figure 124.

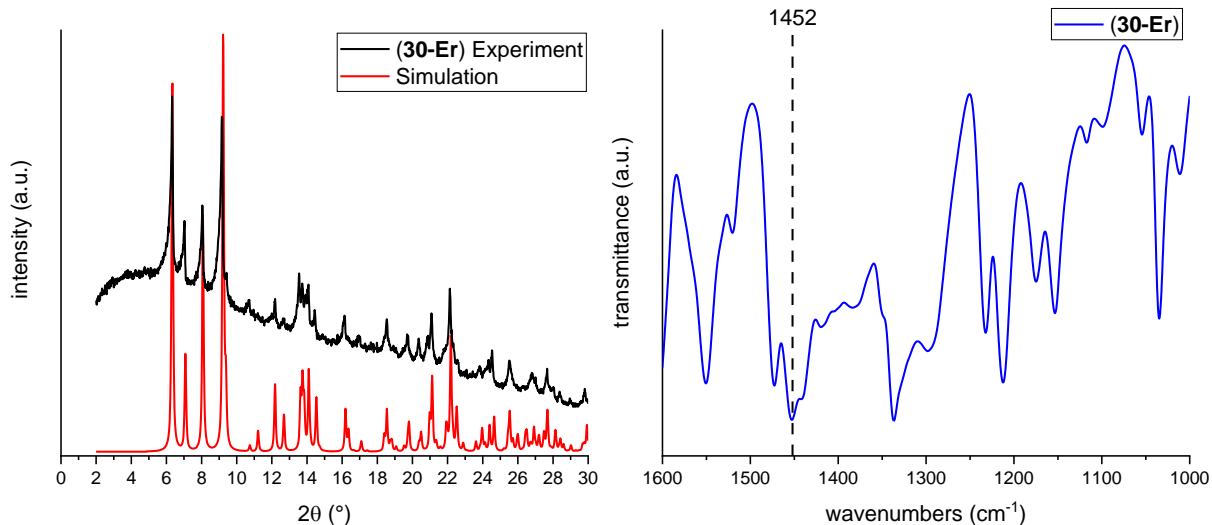


Figure 124. Powder pattern confirming the phase purity of (30-Er) (left) and excerpt of the IR spectrum that highlights the carbonate related vibration at 1452 cm^{-1} (right).

A similar formation of two thirds of the compound was also observed by Nag *et al.*^[209] who reported a series of carbonate-bridged trinuclear complexes with $\text{Ln} = \text{La}^{\text{III}}$, Nd^{III} ,

Sm^{III}, Gd^{III}, Tb^{III} and Lu^{III}. Surprisingly, the synthesis of the Y^{III} version, which has about the same ionic radius as Ho^{III} and therefore sits in between the ions that formed the triangular clusters, resulted in a dinuclear complex. The mechanism for the formation of these different products could therefore not be attributed to the influence of the lanthanide contraction on the ionic radii such as for the complexes described in chapter 5.2 and also could not be explained by the authors. The formation of triangular and dinuclear complexes in the literature corresponds to half of the ones presented here, (**28/29-Er**) and (**30-Er**), respectively. These authors do however discuss a mechanism for the self-assembly of their complexes which seems to be triggered by the formation of the bridging carbonate from aerial CO₂ by hydrolytic reactions. They also observe a faster CO₂ absorption by smaller lanthanide ions which could explain the formation of the CO₃²⁻-bridged clusters in this chapter only with ions heavier than Gd^{III}.^[209]

The invocation of hydrolytic reactions to give carbonate-bridged clusters using CO₂ from air as widely accepted in the literature, makes the suggestion of a mechanism for the formation of (**28-30-Er**) possible (see figure 125).^[209] The first step in the reaction towards trigonal prismatic complexes as opposed to the triangular ones described in the literature,^[207, 209, 217, 291] in this proposed mechanism, appears to be the formation of a dimeric Ln₂ species (A). The existence of dimeric compounds using H₂opch as ligand is exemplified by the work of Tang *et al.*^[198, 298] The same is true for modified H₂opch complexes as will be further elaborated on in section 5.3.5. It is important to note the +2 charge on the dimeric species in figure 125 suggests the importance of the counterion which can be controlled by the lanthanide salt used as starting material. It appears strongly coordinating counterions such as nitrate and acetate tend to result in the dimeric species crystallising (see section 5.3.5). When chloride as a weaker coordinating ligand was used in the reactions to prepare (**28-30-Er**) the system tends to react further. As the reaction is performed in a basic solution the formation of bigger aggregates such as the tetranuclear species (B) seen in the scheme below via formation of hydroxo-bridges seems feasible. This is further validated by the crystallisation of hydroxo-bridged clusters such as (**15-Ce**) and additional ones presented in section 5.3.4 from this system. The next step in this proposed mechanism is the formation of bicarbonate bridges. This has been discussed to be possible in two ways. Firstly, the bound hydroxy group could perform a nucleophilic attack on the electrophilic carbon atom of atmospheric CO₂ resulting in a bicarbonate bridged species (C) similar to the mechanism of carbonic anhydrase.^[299] The same result could

be obtained by the substitution of the OH^- with a HCO_3^- that is known to form in basic (aqueous) solutions.^[214, 300-301] This could be facilitated by water present due to the use of lanthanide chloride hydrates as well as wet solvents. By deprotonation of the bicarbonate hydrogens a species with a -2 charge (D) results, that could electrostatically attract a doubly positive charged dimeric species (A) present in solution to form a trigonal prismatic cluster (E) by dissociation of the hydroxo groups and chelation of the carbonate ligand. The two positive charges are then compensated by terminal co-ligands during crystallisation (in this case chlorides) as seen for (**28-Er** and **29-Er**). Alternatively, (D) could react to (F) by dissociation of the OH-groups and completion of the coordination sphere by omnipresent water ligands to form tetranuclear complexes such as (**30-Er**).

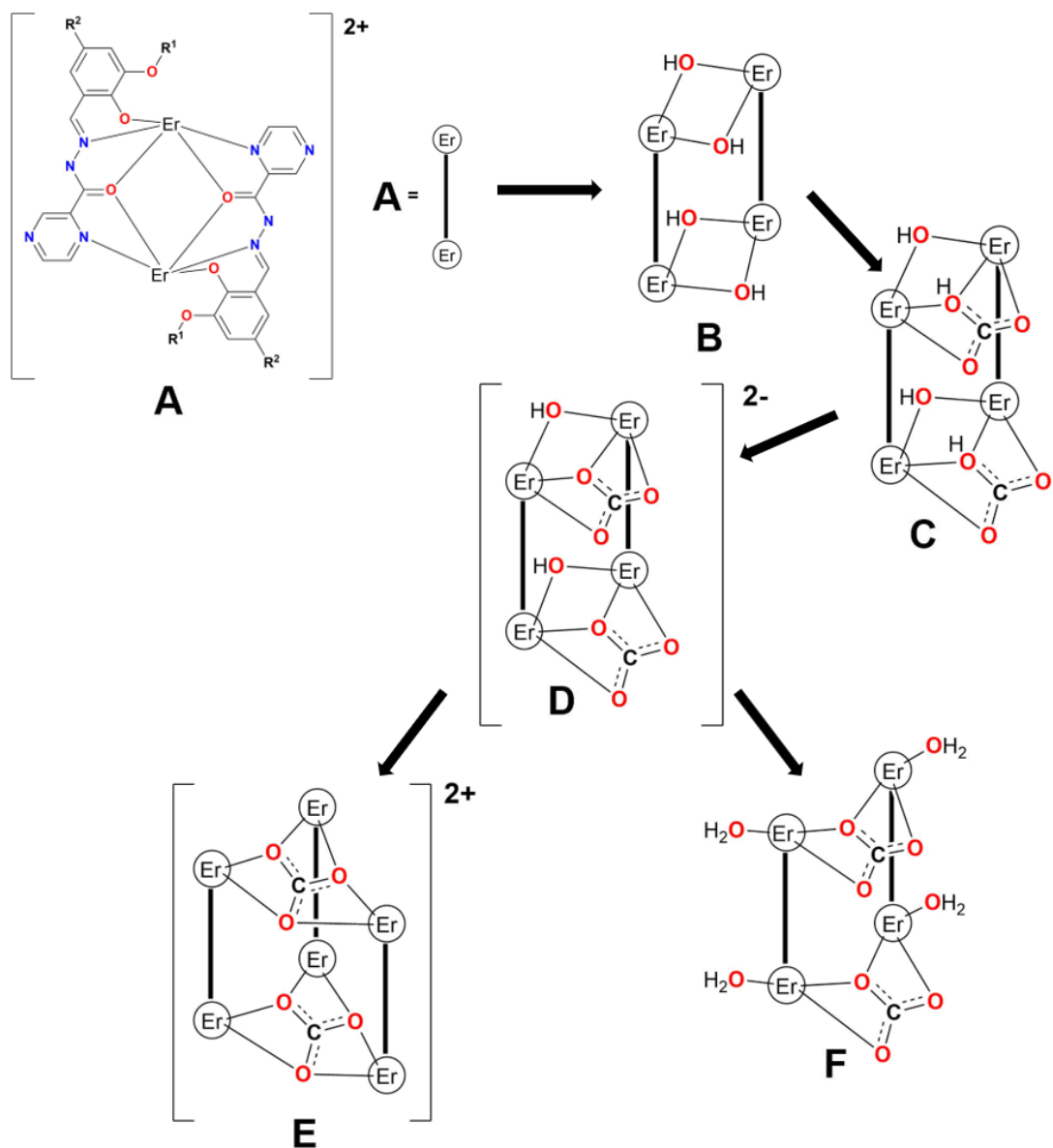


Figure 125. Proposed mechanism for the self-assembly of (**28-30-Er**).

The reason that the reaction with H₂opch-I results in (**30-Er**) instead of the trigonal prismatic core structure might lie in the crystal packing which is strongly dominated by halogen interactions between the iodine atoms as XB donor and the lone pair at the pyrazine nitrogens as XB acceptor. This becomes obvious when looking at the I...N distances which with 3.291(14) Å are much shorter than the combined VdW radii of I and N that amount to 3.53 Å.^[164] These interactions appear to be more favourable than the ones in a hypothetical iodine analogue of (**29-Er**). In other words, the corresponding I₄-tetrahedron would give less stability than the packing actually observed in (**30-Er**). The reason for this seems to be the greater polarisability of iodine compared to bromine which makes it a stronger XB donor. The larger size and the resulting stronger delocalisation of the electrons in iodine also makes it a much weaker XB acceptor (electron donor). In the halogen-halogen interactions in (**29-Er**) each of the Br(1) atoms acts as XB donor and acceptor simultaneously which makes bromine ideal for the crystal structure of (**29-Er**). Due to the much bigger polarisability of iodine, the analogous iodine-iodine interaction would be much weaker, which could be the reason for the formation of this Er₄ cluster instead of another trigonal prismatic compound. The pyrazine-N to iodine interactions in (**Er-30**) result in crystallisation in the highly symmetric orthorhombic space group Fdd2 which might be an additional explanation, why the Er₄ core is favoured in this case.

The Er₄ clusters are stacked all parallel as shown in figure 126 below. The Flack parameter is essentially 0 meaning that basically all Er₄ clusters are arranged in the same direction throughout the crystal explaining why compound (**30-Er**) crystallises in an acentric space group.

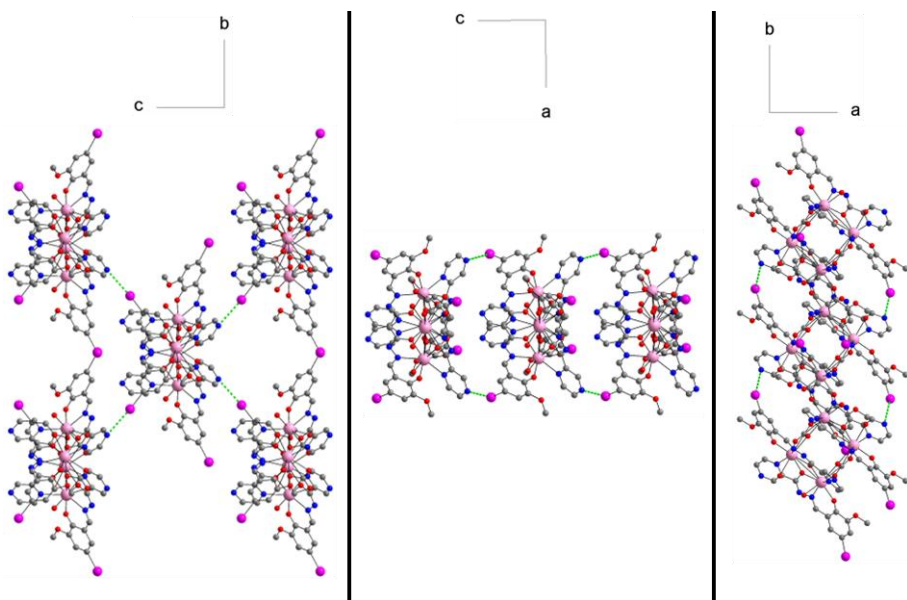


Figure 126. View along all three crystallographic axes of the packing of (30-Er). Intermolecular interactions between the lone electron pair of the pyrazine-N and the σ -hole of the iodine are highlighted in green.

5.3.4 Hydroxo-Clusters using Modified H₂opch Ligands (Structure Type II)

Some reactions discussed here did not follow the mechanism presented above as shown by the formation of hydroxo bridged clusters instead of carbonate bridged clusters or dimers. The structures of the compounds described in this section appear to provide an alternative thermodynamic sink in the energy landscape of the reaction which favours these structures over those which incorporate aerial CO₂ into the clusters resulting in carbonate ligands. The reason for this in the case of (15-Ce) (and other Ce₄ clusters presented in the following) may be the soft and hard coordination pockets accommodating the differently sized Ce^{III} and Ce^{IV} ions.

5.3.4.1 Modified Ce₄-Clusters

Indeed, the reaction of Ce(NO₃)₃·6H₂O with the modified H₂opch ligands resulted in the same colour change towards dark brown after a few minutes of stirring the mixture in air (see figure 127). This is a strong indication for the presence of the mixed-valence compound in solution.

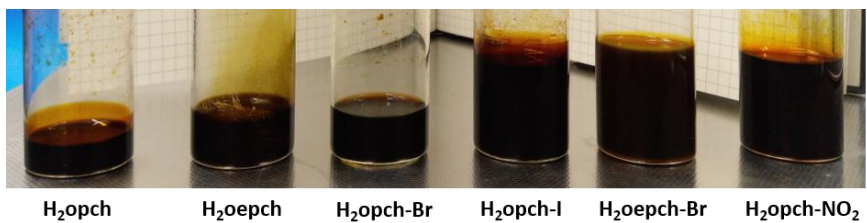


Figure 127. Visual appearance of the reactions with the goal to produce modified Ce_4 clusters.

The reaction with H_2oepch resulted in dark brown crystals of $[\text{Ce}_4(\text{H}_2\text{O})_2(\text{NO}_3)_2(\mu_2\text{-OH})_4(\text{oepch})_4]\cdot 8\text{MeCN}$ (**31-Ce**) suitable for SC-XRD. The molecular structure shown in figure 128 confirms that the cerium ions in (**31-Ce**) forms essentially the same almost square core structure as observed for (**15-Ce**). $\text{Ce}(1)$ and $\text{Ce}(3)$ are coordinated by the soft ligand sites such as pyrazine nitrogen atoms whereas $\text{Ce}(2)$ and $\text{Ce}(4)$ are coordinated by the harder ligand sites such as the phenolate oxygens. The sole difference is that in (**31-Ce**) both $\text{Ce}(1)$ and $\text{Ce}(3)$ have the same coordination sphere with one additional coordinating water and a chelating nitrate, whereas in (**15-Ce**) one of them instead has two coordinating waters and the nitrate only coordinating with one of its oxygen atoms.

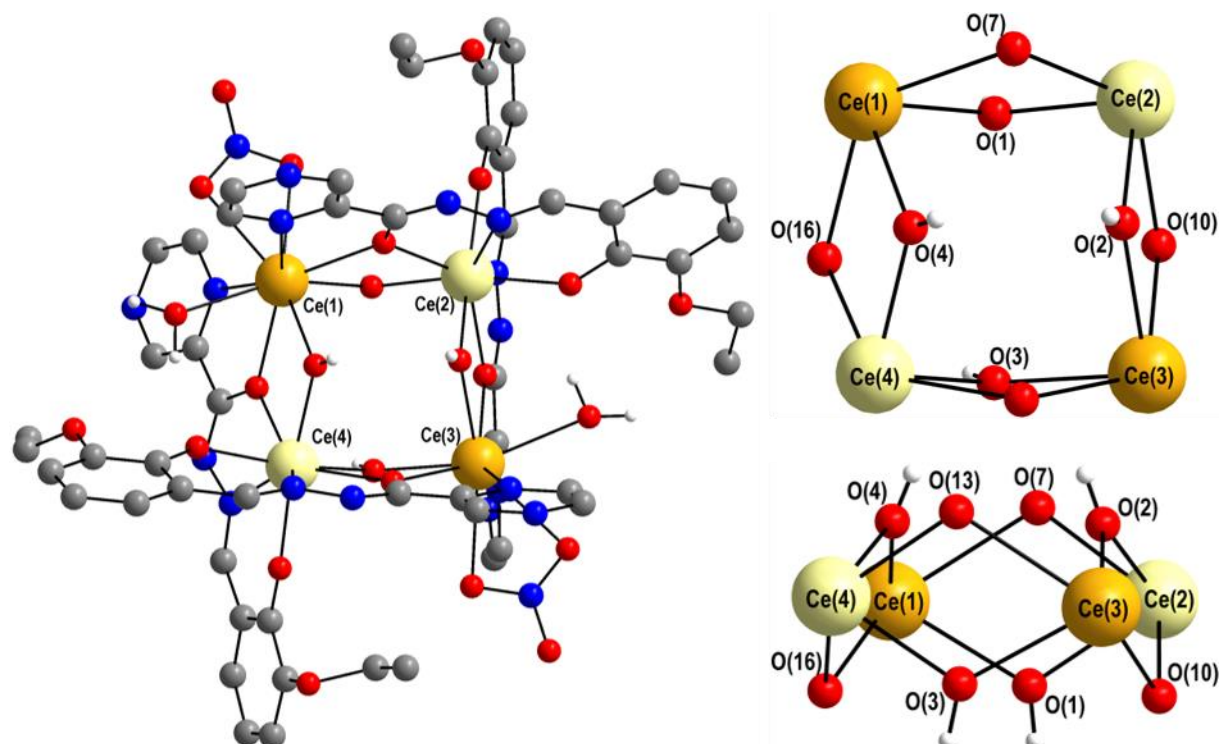


Figure 128. Molecular structure (left) and two views on the core of (**31-Ce**) (right).

The core structures of **(31-Ce)** and **(15-Ce)** are compared in figure 129 emphasising the similarity between them as well as the closeness to a perfect square shape. As expected from the identical coordination spheres of Ce(1) and Ce(3) in **(31-Ce)** the core structure with angles between 88.8° and 91.0° as well as distances between 3.95 \AA and 3.99 \AA is even closer to a perfect square than that of **(15-Ce)**.

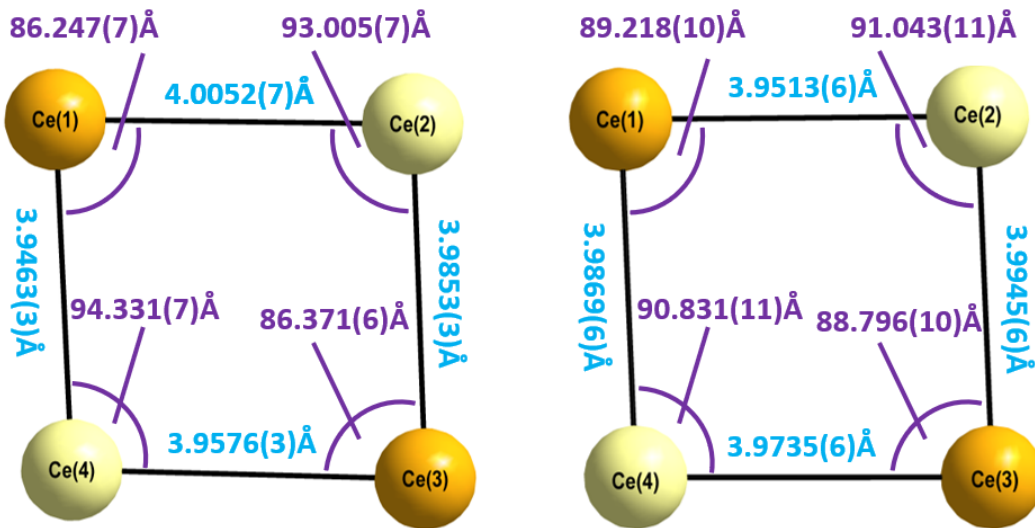


Figure 129. Comparison of the angles and distances of the essentially square core structures of **(15-Ce)** (left) and **(31-Ce)** (right).

The oxidation states of the cerium ions were again confirmed by looking at the overall charge balance as well as a BVS analysis (see table 15) which resulted in the same situation as described for **(15-Ce)** above with Ce(1) and Ce(3) in +3 oxidation state and Ce(2) and Ce(4) as +4.

Table 15. BVS analysis on the cerium ions in **(31-Ce)** using the same parameters as for the BVS analysis on **(15-Ce)** described in section 5.2.1.2. The best results are highlighted in red.^[191, 254-255]

	Ce(1)	Ce(2)	Ce(3)	Ce(4)
BVS Ce ^{III}	3.32	5.01	3.29	4.99
BVS Ce ^{IV}	2.73	4.12	2.70	4.09

While the molecular structure is nearly identical, the packing of **(31-Ce)**, which can be seen in figure 130, is different. **(31-Ce)** crystallises in the triclinic space group $P\bar{1}$ with two molecules in the unit cell that are connected via four hydrogen bonds between the protons of the bridging hydroxy groups O(2) and O(4) of one molecule with the pyrazine nitrogen N(3) of the other and vice versa. Additionally, these two clusters are connected to the next pair via hydrogen bonds between the proton on another bridging hydroxy group O(3) and another pyrazine nitrogen N(7) forming strands of Ce₄ cluster pairs in the a-c plane. The strands are further connected via hydrogen bonds between

the proton on the remaining bridging hydroxy group to the MeCN lattice solvent which act as HB donor and acceptor simultaneously. This last set of interactions connecting the strands is omitted for reasons of clarity.

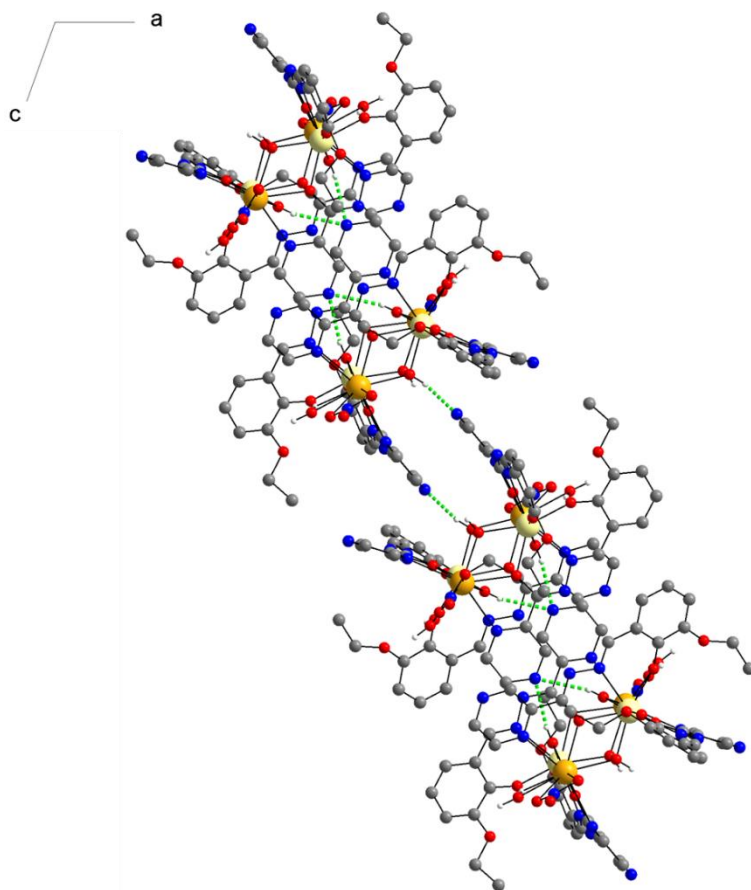


Figure 130. Packing of (31-Ce) highlighting the hydrogen bonded stacks. View along the crystallographic b axis.

The reaction with H₂opch-Br and H₂opch-I also gave a dark product that was confirmed to be the respective analogous Ce₄ cluster (**32-Ce** and **33-Ce**) via comparison of the IR spectra.

In figure 131 the comparison of the solid state UVVis absorption spectra of three of the different Ce₄ clusters is shown. The low yield of the analogues using H₂opch-Br (**32-Ce**) and H₂opch-I (**33-Ce**) meant that the latter could not be included in this comparison, whilst the former only gave very low intensities (all of the remaining sample was used) and had to be multiplied by 5 in order to be compared to the others. This process also amplifies the noise in this spectrum explaining the poor quality of the data.

The same overall trend can be observed for all three samples confirming the IVCT band spanning the whole visible range and explaining the dark colour of the

compounds also present in the modified Ce₄ clusters. However, there are subtle differences that may indicate the influence of the modification of the organic ligand. For example, the IVCT band in (32-Ce) is broader than in the other two samples and does not reach zero absorbance at 800 nm. Also, in (31-Ce) the shoulder of the IVCT band is particularly pronounced, although this might be a result of the data handling for obtaining this spectrum.

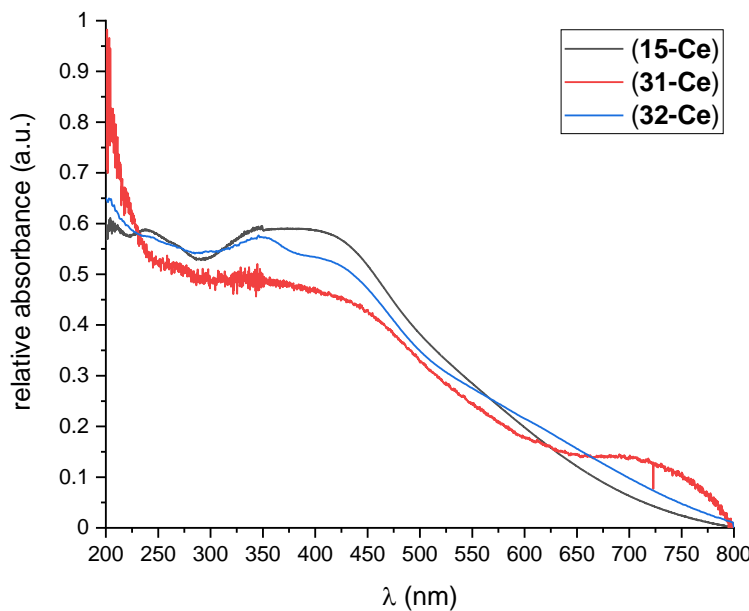


Figure 131. Solid state UVVis absorption spectra of (15-Ce), (31-Ce) and (32-Ce) compared between 200 and 800 nm.

5.3.4.2 A Nd₇ Cluster Resembling Mineral Structures

Using Nd(NO₃)₃·6H₂O in a reaction with H₂oepch resulted in well-formed orange rhombic crystals of [Nd₇(H₂O)₂(MeCN)(NO₃)₃(μ₃-OH)₆(oepch)₆] (34-Nd). The molecular structure has the seven Nd^{III} ions arranged in an essentially planar hexagon with the central Nd(1) sitting above the plane. This motif was seen before in (17-Dy) although the vacant site in that compound is now filled by another Nd^{III} in (34-Nd) (see figure 132). This core structure motif was also observed before in the literature where the Gd-versions were used as a magnetic cooler utilising the magnetocaloric effect (MCE)^[269-270, 302] and the Dy-versions show SMM behaviour.^[270, 303] It is also observed as part of larger clusters such as Ln₁₆ clusters and structures with nuclearities up to 48.^[302-304] The μ₃-OH bridged core also resembles the structure of the naturally occurring minerals brucite (Mg(OH)₂) and hydrotalcite (Mg₆Al₂CO₃(OH)₁₆).^[303, 305] This

might be part of the reason for the formation of a hydroxy bridged cluster instead of a carbonate bridged one after the proposed mechanism in section 5.3.3.3, as it exemplifies the stability of this core structure. Another reason might be the slower reactions leading to carbonate bridged clusters by the fixation of atmospheric CO_2 exhibited by larger Ln^{III} ions as observed in the literature.^[209]

In the case of **(34-Nd)** the central $\text{Nd}(1)$ is the only one being eight-coordinate with the six $\mu_3\text{-OH}$ groups as well as one of three nitrates that balance the overall charge. The six outer Nd^{III} ions are all 9-coordinate with three bridging oepch^{2-} ligands above and three below the plane. Two of these provide five coordination sites to $\text{Nd}(2)$, $\text{Nd}(4)$ and $\text{Nd}(6)$ whose coordination sphere is completed by two bridging hydroxy groups as well as co-ligands which include the other two nitrates needed to balance the charge. $\text{Nd}(3)$, $\text{Nd}(5)$ and $\text{Nd}(7)$ are also coordinated by two bridging OH groups as well as three of the bridging Schiff base ligands which provide seven further ligands.

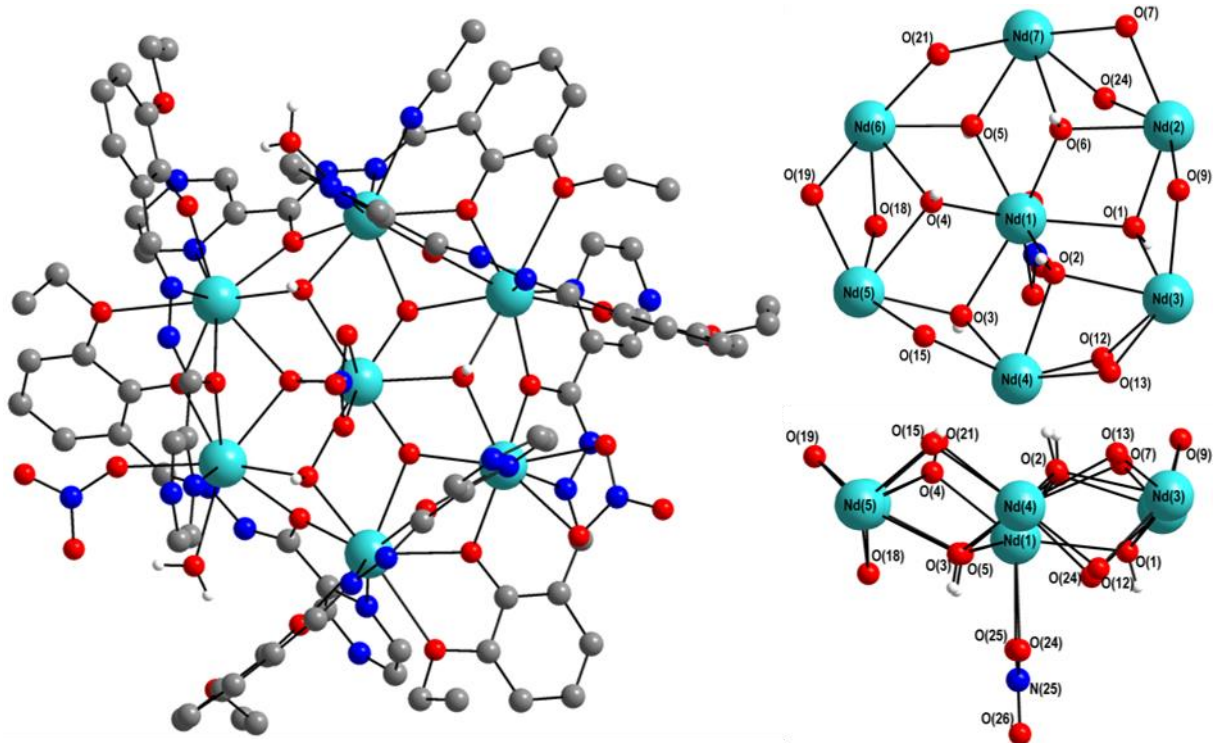


Figure 132. Molecular structure of **(34-Nd)** (left) and a top and side view on the heptanuclear core (right).

The outer hexagon is essentially regular with internal angles alternating between about 116° and 123° close to the 120° expected for a perfect hexagon and Nd-Nd distances alternating between 3.75 \AA and 4.0 \AA (see figure 133 for the exact values including standard deviation).

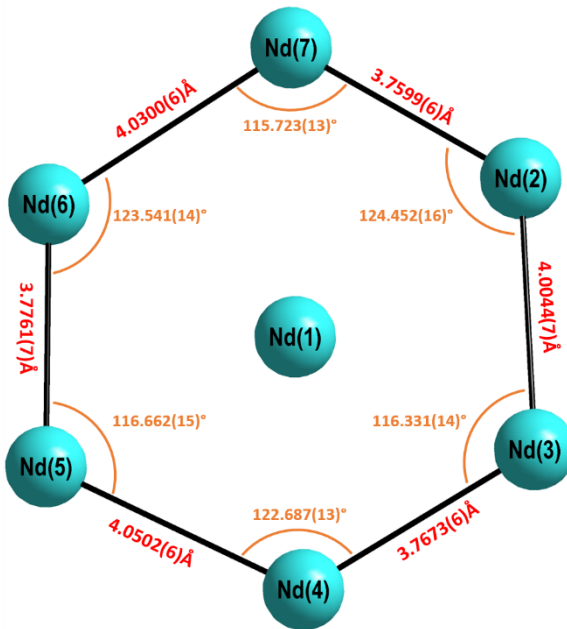


Figure 133. Core structure of (34-Nd) showing the essentially perfect hexagon around the central Nd(1).

(34-Nd) crystallises in the monoclinic space group $P2_1/n$ with four molecules in the unit cell. The molecules form dyads that are connected via HBs between the proton of the hydroxy group O(6)-H(6) with the pyrazine nitrogen N(3) on the neighbouring molecule and vice versa with the O(6)-H(6)...N(3) distance of 3.003(4) Å and an angle of 161(4)°. Each dyad is further connected to their next-nearest neighbours via further HBs involving the water hydrogen H(33B) and another pyrazine nitrogen N(15) (see figure 134).

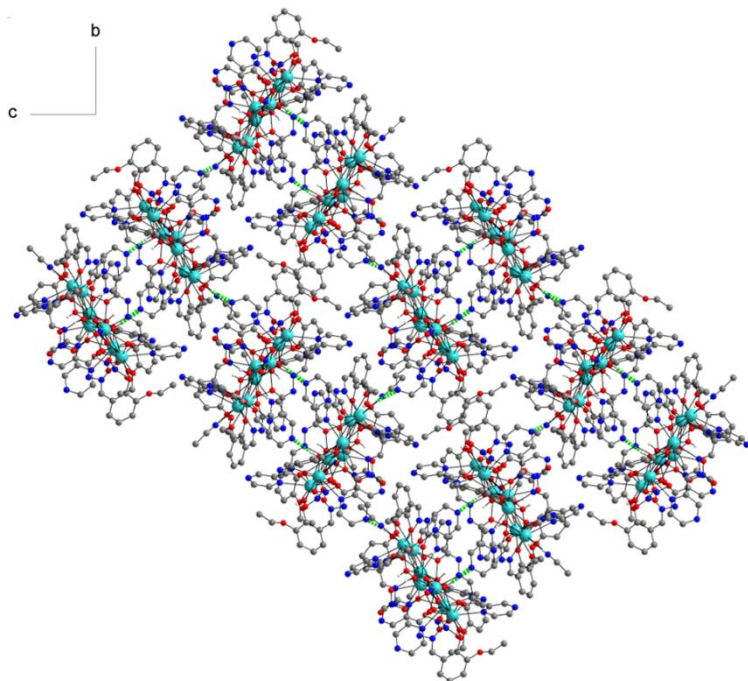


Figure 134. Packing of (34-Nd), view along the crystallographic a axis with the hydrogen bonds highlighted in green.

The phase purity of (**34-Nd**) was confirmed by PXRD and the IR spectrum shows the very broad OH vibrations at energies around 3300 cm^{-1} (figure 135).

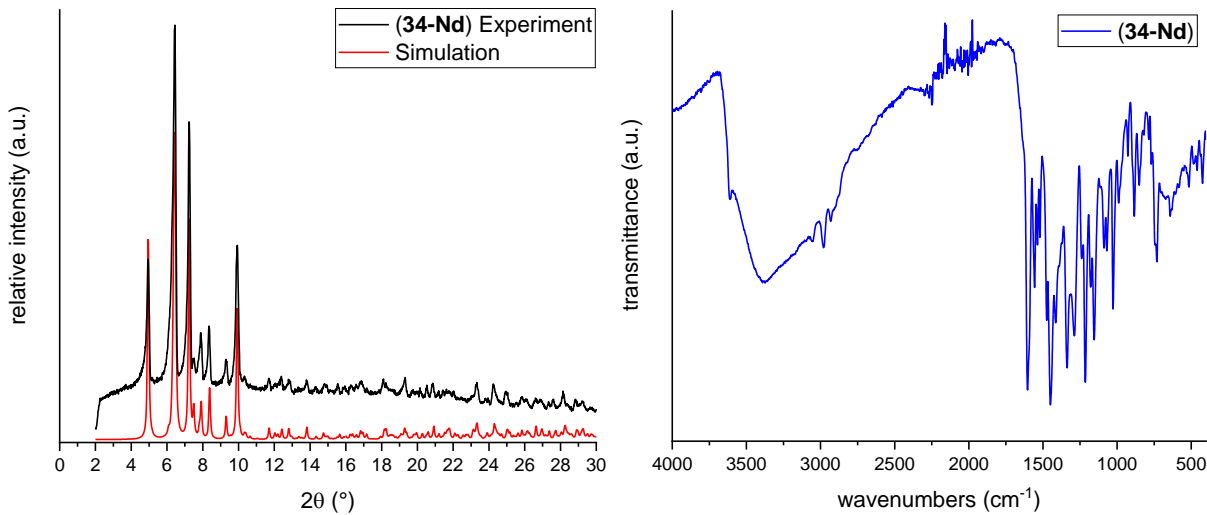


Figure 135. PXRD confirming the phase purity of (**34-Nd**) (left) and IR spectrum of (**34-Nd**) (right) showing the OH-vibrations at around 3300 cm^{-1} .

Four sets of usually forbidden f-f transitions can be seen in the solid state UVVis spectrum of (**34-Nd**) (figure 136). Generally disruption of the centre of symmetry through asymmetric vibrations can weakly allow such transitions.^[306] The f-f transitions are all excitations from the $^4\text{I}_{9/2}$ ground state and the final states as indicated in figure 136 are in line with those reported in the literature.^[307-309]

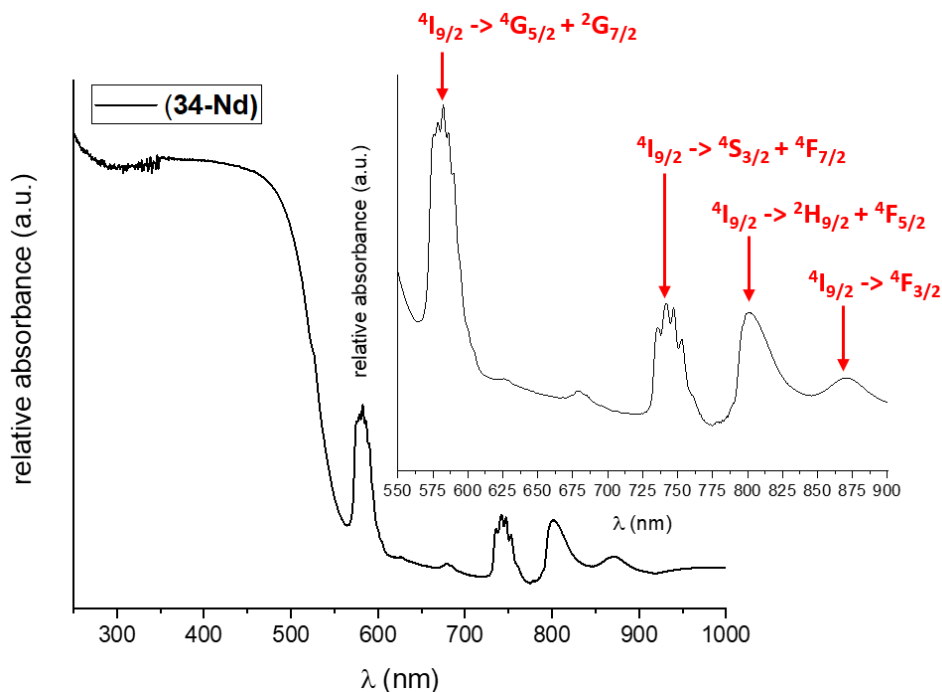


Figure 136. Solid state UVVis absorption spectrum of (**34-Nd**) between 200 and 1000 nm. The states of the f-f transitions from the $^4\text{I}_{9/2}$ ground state.

The single ion anisotropy of Nd^{III} although not nearly as strong as that for Dy^{III} also has an oblate character. Therefore, the magnetic properties of (34-Nd) at low temperatures could show exotic behaviours such as a non-magnetic ground state due to a non-Ising arrangement of spins such as in toroidal dysprosium systems. These were investigated using microSQUID measurements in collaboration with Dr. Michael Schulze in the group of Prof. Dr. Wolfgang Wernsdorfer (KIT, PHI). The results can be seen in figure 137 which show no hysteresis nor the more exotic properties described above. Instead, the measurement shows a gradual increase of magnetisation with increasing magnetic field which may be the result of a high number of low-lying excited sub-states. The reason for this may lie in the fact that the Nd^{III} ions (even the ones forming the outer hexagon) are not identical. Therefore, their excited states are at very similar but slightly different energies leading to a gradual increase in magnetic moment along the field direction, instead of well-defined jumps.

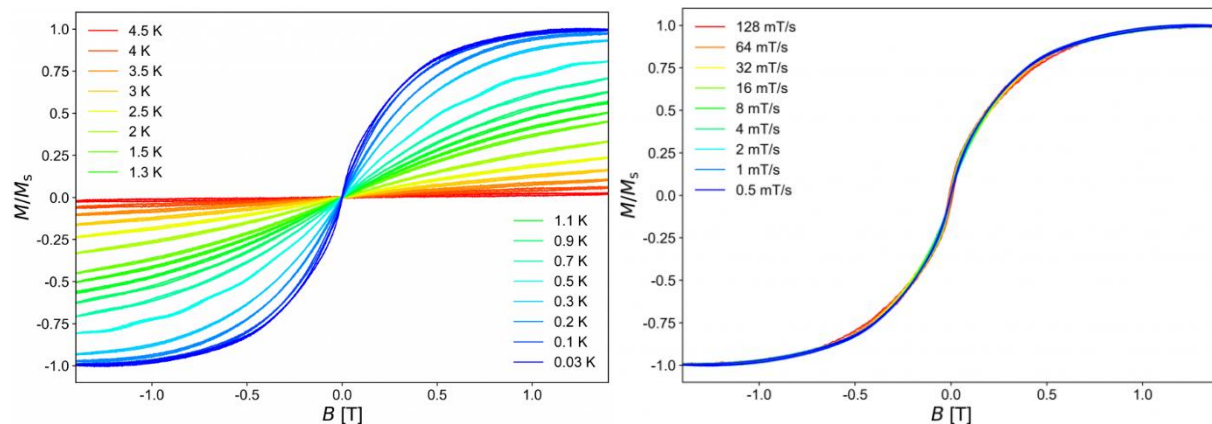


Figure 137. MicroSQUID measurements performed on single crystals of (34-Nd). Temperature dependence measured between 30 mK and 4.5 K (left) and sweep rate dependence measured for sweep rates between 0.5 mT/s and 128 mT/s (right).

5.3.4.3 The Formation of Supramolecular Dimers and Chains of Ln₇ Clusters *via* Halogen Interactions

To produce crystals suitable for SC-XRD using H₂opch-I proved a challenge as the usual recipes that use MeCN or MeOH/DCM did not yield anything. Changing the solvent to freshly distilled acetone as for (30-Er) was successful, working with other Ln^{III} ions as well. In this case orange block crystals of two gadolinium compounds with

the same molecular structure $[\text{Gd}_7(\text{NO}_3)_4(\mu_3\text{-OH})_6(\text{Hopch-I})(\text{opch-I})_5]\cdot7\text{acetone}$ (**35-Gd A**) and $[\text{Gd}_7(\text{NO}_3)_4(\mu_3\text{-OH})_6(\text{Hopch-I})(\text{opch-I})_5]\cdot12\text{acetone}$ (**35-Gd B**) but different amounts of lattice solvent leading to different intermolecular interactions determining the packing were obtained. In addition, the dysprosium analogue of (**35-Gd B**) $[\text{Dy}_7(\text{NO}_3)_4(\mu_3\text{-OH})_6(\text{Hopch-I})(\text{opch-I})_5]\cdot12\text{acetone}$ (**36-Dy**) was obtained. The molecular structure of (**35-Gd B**) is shown in figure 138 as a representative.

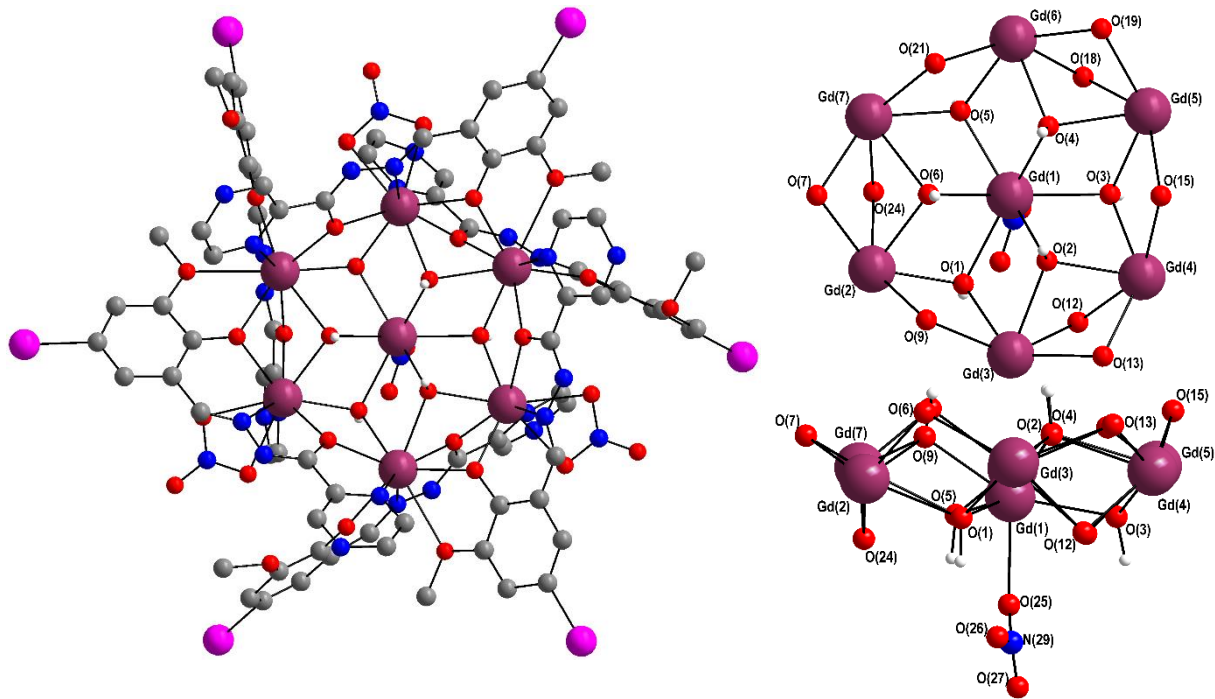


Figure 138. Molecular structure (left) and two views on the core structure (right) of (**35-Gd B**) as a representative for the Ln_7 clusters obtained using $\text{H}_2\text{opch-I}$.

The molecular structure for all three compounds (molecular structure of (**35-Gd B**) shown as a representative) is very similar to the one of (**34-Nd**) described above (see figure 132). Six Ln^{III} ions form an essentially regular planar hexagon around a central ion that is shifted slightly out of plane. In table 16 important angles and distances that make up the outer hexagon in the four Ln_7 clusters are compared as well as the shift of the central ion out of the mean plane formed by the six outer ones.

Table 16. Comparison of the six Ln-Ln bond lengths and the internal Ln-Ln-Ln angles (labelled with the central Ln^{III} ion of the angle) forming the outer hexagon as well as the distance of the central Ln^{III} ion from a mean plane through the outer six in (34-Nd), (35-Gd A), (35-Gd B) and (36-Dy).

	(34-Nd)	(35-Gd A)	(35-Gd B)	(36-Dy)
Ln-Ln distances [Å]				
Ln(2)-Ln(3)	4.0044(7)	3.9244(10)	3.6532(9)	3.8852(6)
Ln(3)-Ln(4)	3.7673(6)	3.6736(10)	3.9346(7)	3.6211(6)
Ln(4)-Ln(5)	4.0502(6)	3.9499(13)	3.6652(7)	3.8986(6)
Ln(5)-Ln(6)	3.7761(7)	3.6675(8)	3.9626(9)	3.6016(6)
Ln(6)-Ln(7)	4.0300(6)	3.9195(12)	3.6687(9)	3.8929(6)
Ln(7)-Ln(2)	3.7599(6)	3.6432(13)	3.9421(8)	3.5987(6)
Internal Ln-Ln-Ln angles [°]				
Ln(7)-Ln(2)-Ln(3)	124.45(2)	122.45(2)	122.31(2)	122.46(1)
Ln(2)-Ln(3)-Ln(4)	116.31(1)	117.05(3)	117.06(2)	116.71(1)
Ln(3)-Ln(4)-Ln(5)	122.69(1)	122.05(3)	123.35(2)	123.10(2)
Ln(4)-Ln(5)-Ln(6)	116.66(2)	116.76(3)	116.30(2)	116.05(1)
Ln(5)-Ln(6)-Ln(7)	123.52(1)	123.15(2)	122.76(2)	123.68(1)
Ln(6)-Ln(7)-Ln(2)	115.72(1)	117.07(3)	116.77(2)	116.85(1)
Distance between the central Ln(1) and mean plane through the outer six [Å]				
Ln(1)-plane	0.7691(5)	0.6116(7)	0.6325(6)	0.5569(4)

The distance of the central Ln(1) to the mean plane of the six outer ones decreases, consistent with decreasing ionic radius of the respective Ln^{III} ion due to the lanthanide contraction. Additionally, it can be seen from the alternating longer and shorter Ln-Ln distances as well as Ln-Ln-Ln angles, going around the hexagon, that the molecules possess *pseudo* threefold symmetry in all four cases. In (34-Nd) threefold symmetry is broken as there are only three nitrates present one of which chelates the central Nd^{III} leaving only two nitrates for the six outer Nd^{III} ions. This also highlights the major difference between the molecular structures of (35-Gd A), (35-Gd B) and (36-Dy), which is the presence of a fourth nitrate co-ligand. Therefore, one more negative charge has to be compensated in these compounds. Schiff base ligands with similar structures have been shown to have two possible forms: A doubly deprotonated form in which the ligand undergoes keto-enol tautomerism leading to an enolate oxygen to carbon bond length of around 1.3 Å and a mono deprotonated form with carbonyl

oxygen to carbon bond lengths about 1.25 Å.^[310] By looking at the C-O bond lengths of the carbonyl function of the ligands present here it can be concluded that one of the six ligands per cluster is in its N-protonated form Hopch-I⁻ with the possibility of this protonation being disordered in the molecule. In the molecular structure of (**35-Gd B**) shown above this is revealed by the bond lengths between O(12)-C(22) = 1.266(16) Å and O(18)-C(48) = 1.261(13) Å. The threefold symmetry in (**35-Gd A**), (**35-Gd B**) and (**36-Dy**) is broken by the orientation of the nitrate ligand coordinating the central Ln(1) ion which forms an intramolecular HB with one of the μ_3 -OH groups.

All three compounds crystallise in the triclinic space group $P\bar{1}$ with $Z = 2$ with the difference between the two different structure types being the amount of lattice acetone. In the case of (**35-Gd A**) which crystallises with seven lattice acetone molecules this leads to a smaller unit cell volume of 6846.6(4) Å³ compared to the 7662.3(4) Å³ and 7528.1(9) Å³ observed for the isostructural (**35-Gd B**) and (**36-Dy**), respectively, which crystallise with twelve acetone molecules in the lattice. This lattice acetone evaporates very quickly upon removal of the crystals from the mother liquor leading to loss of crystallinity as indicated by the clear orange block crystals turning opaque within seconds in air. This made structural determination via SC-XRD challenging and PXRD essentially impossible.

There appears to be a fine energy balance between the two structure types associated to the different amounts of lattice solvent that has an immense impact on the packing of the compounds. Both structures form intermolecular halogen-halogen networks with (**35-Gd A**) forming supramolecular dimers and (**35-Gd B**) and (**36-Dy**) forming chains. The interactions between I(4) and I(6) of neighbouring Gd₇ clusters forming dimers in (**35-Gd A**) (see figure 139) can be classified as halogen-halogen bonds with an I(4)-I(6) distance of 3.927(2) Å which is shorter than twice the VdW radius of iodine which add up to 3.96 Å^[164] as well as angles between C(69)-I(6)...I(4) and C(43)-I(4)...I(6) of 105.6(5)° and 157.2(4)°, respectively.

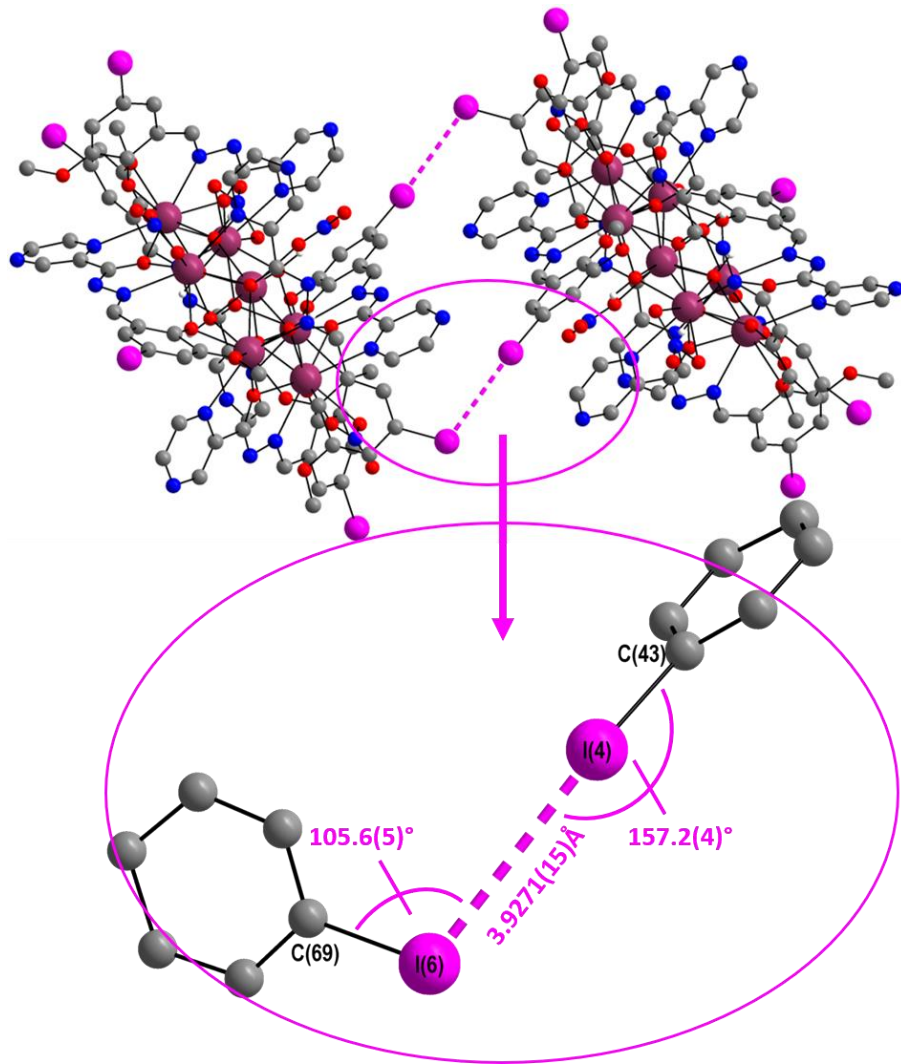


Figure 139. Packing of **(35-Gd A)** showing the supramolecular dimer formed by halogen-halogen bonds as indicated by the highlighted I-I distance as well as C-I...I angles.

In **(35-Gd B)** and **(36-Dy)** the interactions forming the supramolecular chains (see figure 140) will only be described for **(35-Gd B)** as the compounds are isostructural. Each Gd₇ cluster interacts with two of its neighbours with two iodine atoms at opposite sides of the hexagon (I(3) and I(6)). The I(3)-I(6) distance between neighbouring clusters is 3.867(1) Å and therefore significantly shorter than double the VdW radius of iodine (3.96 Å^[164]). The angles between C(30)-I(3)...I(6) and C(69)-I(6)...I(3) are essentially equal with 145.6(4)° and 146.1(3)°, respectively, defining this interaction as a type I halogen-halogen interaction.

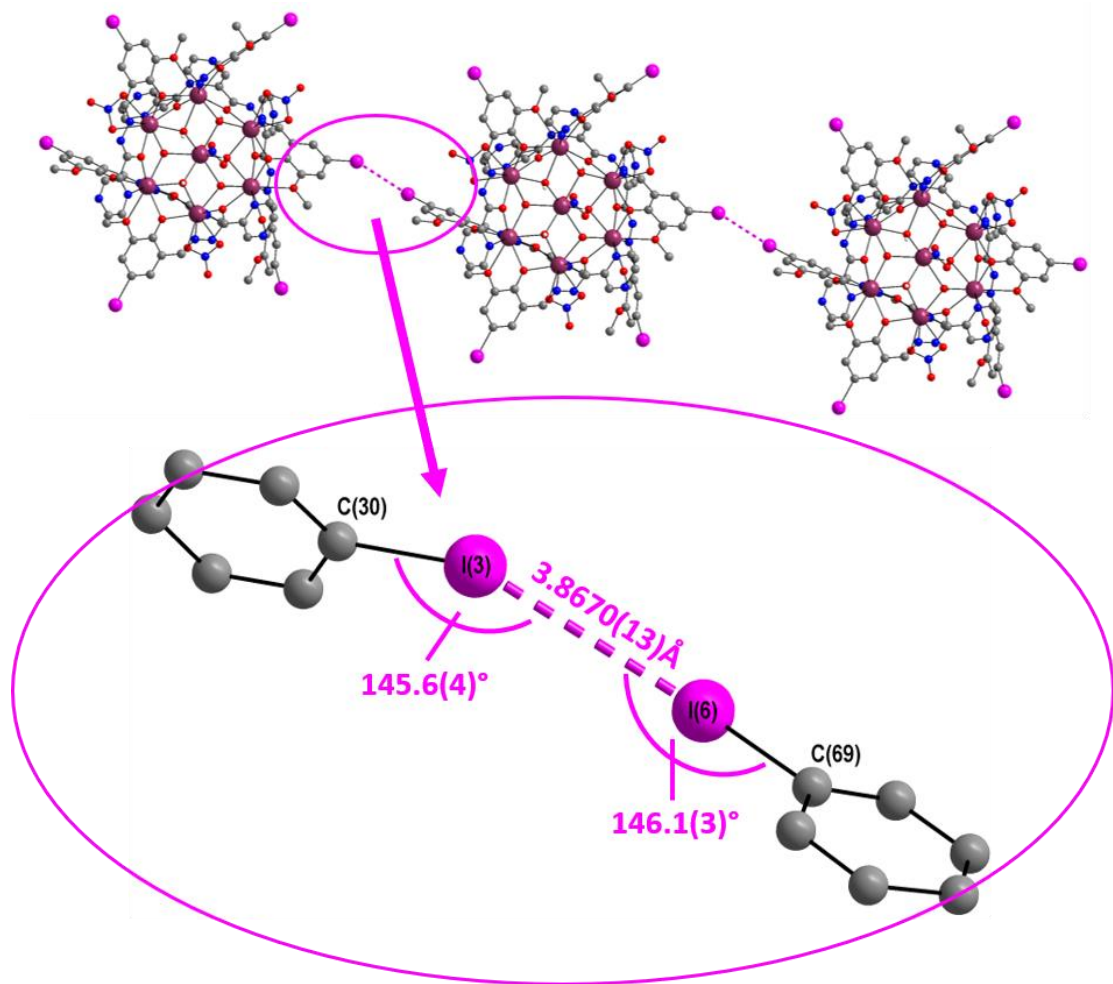


Figure 140. Packing of (35-Gd B) showing the supramolecular chain formation also found in (36-Dy). Halogen-halogen interactions are of type I as indicated by the highlighted I-I distance as well as C-I...I angles.

Magnetic measurements on (36-Dy) under an applied dc field 0.1 T at temperatures between 2 and 300 K were performed and the $\chi_M T$ vs T as well as χ_M^{-1} vs T plots are shown in figure 141 in red and blue, respectively. The $\chi_M T$ values at RT with $97.1 \text{ cm}^3 \text{Kmol}^{-1}$ are slightly lower than the expected value for seven uncoupled Dy^{III} ions of $99.2 \text{ cm}^3 \text{Kmol}^{-1}$ but in an acceptable range. With decreasing temperature, a gradual decrease in $\chi_M T$ that becomes steeper below 75 K is observed likely due to the depopulation of excited states overlapped with a possible antiferromagnetic interaction. At temperatures below 4.5 K a jump in $\chi_M T$ can be seen that may be a result of temperature-stabilising issues of the SQUID magnetometer during the measurement and is therefore not further discussed. The χ_M^{-1} vs T plot follows the Curie-Weiss law over the whole temperature range and leads to a Weiss constant $\theta = -3.6 \text{ K}$ and a Curie constant $C = 98.03 \text{ cm}^3 \text{Kmol}^{-1}$ confirming a small antiferromagnetic interaction present in the system. This is in line with the behaviour reported for a compound with a very similar $\mu_3\text{-OH}$ bridged core structure.^[270]

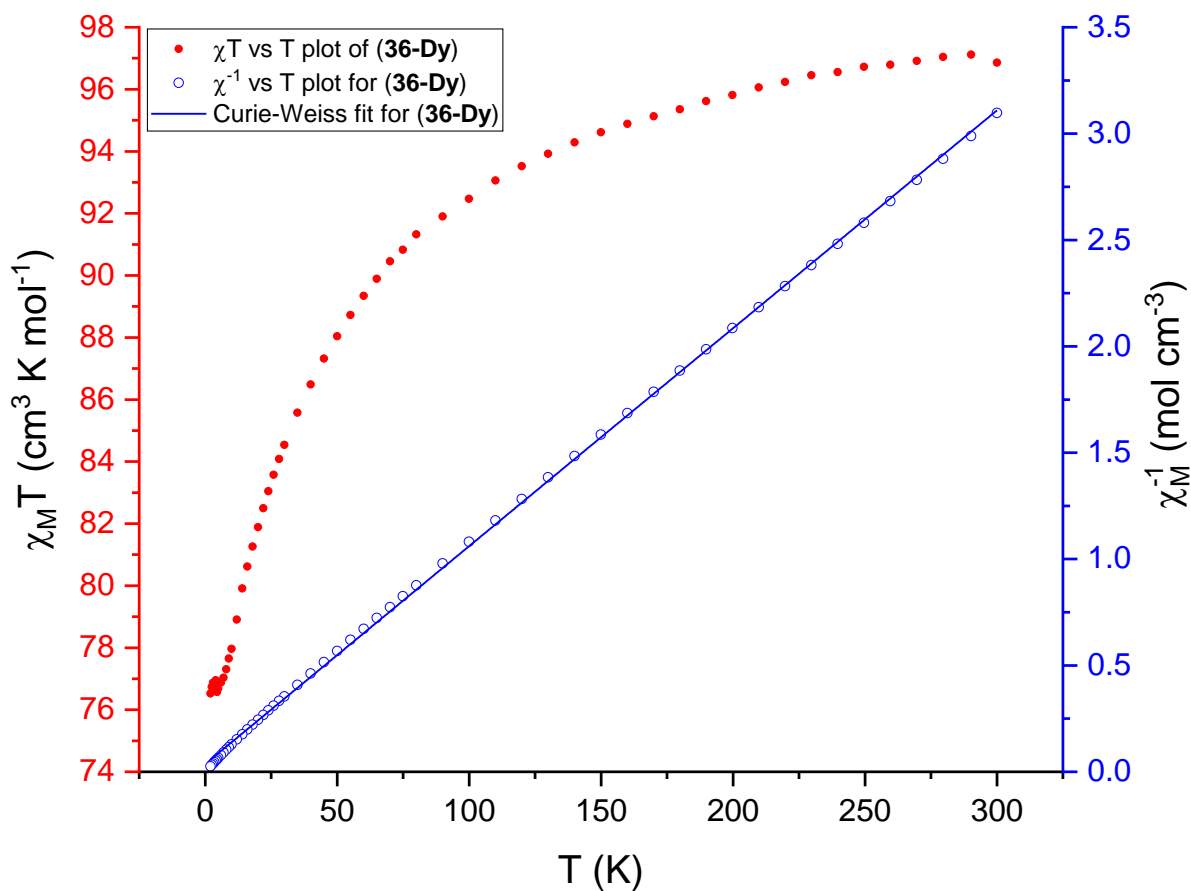


Figure 141. $\chi_M T$ vs T plot of (36-Dy) (red) and χ_M^{-1} vs T plot (hollow points) with the corresponding Curie-Weiss fit in blue.

The magnetisation of (36-Dy) was measured at fields between 0 and 7 T (see figure 142). The system approaches saturation at $38 \mu_B$ and the reduced magnetisation curves at 2, 3 and 5 K do not superpose which could be attributed magnetic anisotropy and low-lying excited states. These results are again in line with the behaviour reported by Sharples *et al.*,^[270] confirming that the halogen-halogen interactions in the H₂opch cluster family do not act as an intermolecular pathway for exchange interactions.

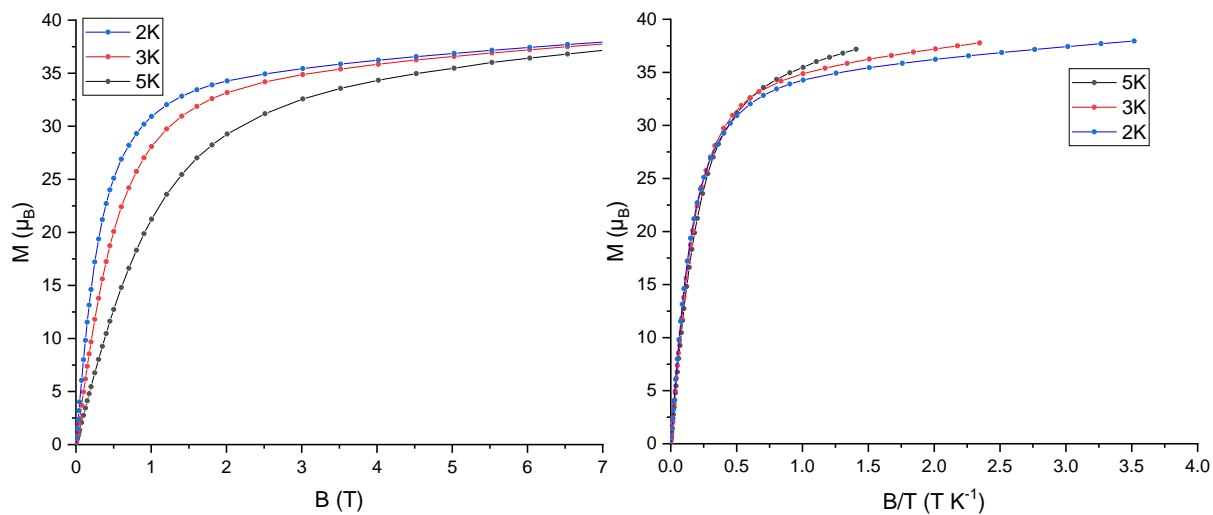


Figure 142. M vs B plot (left) and reduced magnetisation (right) of **(36-Dy)** at 2, 3 and 5 K. Lines are a guide to the eye.

Unlike in the published compound^[270] no maxima were detected in ac out-of-phase measurements for **(36-Dy)**. The reason for this appears to be the lower *pseudo* threefold symmetry in **(36-Dy)** when compared to the literature known compound which lies on an inversion centre. This means that the published compound consists of two sets of three identical Dy^{III} ions and a central Dy^{III} that is disordered to lie above and below the plane of the others. As the anisotropy axes of crystallographically identical Dy^{III} ions are parallel to each other, the reported Dy_7 contains four distinct orientations of axes. Comparing this to the situation in **(36-Dy)**, which shows seven uniquely oriented anisotropy axes from the MAGELLAN analysis,^[297] (see figure 143) gives a possible explanation for the absence of slow relaxation of magnetisation at 2 K here. The absence of SMM behaviour for compounds with poorly aligned anisotropy is known for over a decade and was sufficiently discussed in the literature.^[311-312] Furthermore, the possibility for additional relaxation pathways involving phonons due to the halogen-halogen bound chains of clusters throughout the crystal should be considered a possible contributor to a lack of observable slow relaxation.

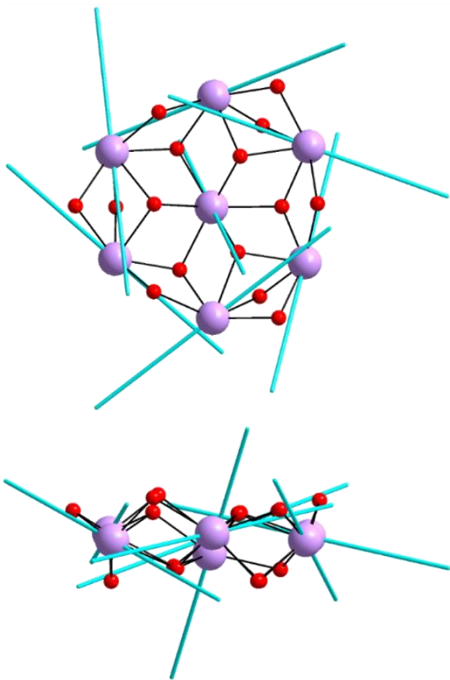


Figure 143. Anisotropy axes calculated using MAGELLAN^[297] showing the poor alignment likely responsible for the absence of slow relaxation of magnetisation.

5.3.5 Dimeric Ln-Complexes Using Modified H₂opch Ligands (Structure Type III)

Using $\text{Tb(OAc)}_3 \cdot x\text{H}_2\text{O}$ with the unmodified H₂opch ligand in MeCN led to single crystals of $[\text{Tb}_2(\text{H}_2\text{O})_2(\text{OAc})_2(\text{opch})_2]$ (**37-Tb**) that were analysed using SC-XRD. The molecular structure of the dimeric Tb^{III} complex is shown in figure 144. It consists of two Tb^{III} ions that are linked by two bridging opch²⁻ ligands in the same coordination mode that was described for the trigonal prismatic complexes (**28/29-Er**) with a bridging oxygen O(3) which comes from the carbonyl group but is better described as an enolate oxygen as evidenced by the C-O bond length of 1.286(7) Å. One of the Tb^{III} ions is then chelated by the phenolate oxygen O(1) and the hydrazine nitrogen N(1) of one opch²⁻ ligand and additionally coordinated by the pyrazine nitrogen N(4) of the other Schiff base ligand. This resembles species (A) in the proposed mechanism for the formation of the carbonate-bridged clusters shown in figure 125 in section 5.3.3.3. The two remaining positive charges are balanced by two acetate ligands that chelate either Tb^{III} ion. As mentioned before, the strongly coordinating properties of the co-ligand, here acetate, appear to be responsible for stabilising this dimeric species instead of allowing further reaction to give larger clusters. The coordination sphere of both eight coordinate Tb^{III}

ions is completed by one water ligand, which is also responsible for the intermolecular hydrogen bonding network dominating the packing. The molecular structure is therefore remarkably similar to the previously reported H_2opch -dysprosium dimer with the sole difference lying in the neutral co-ligands which are MeOH in the reported structure but are replaced by water here.^[222]

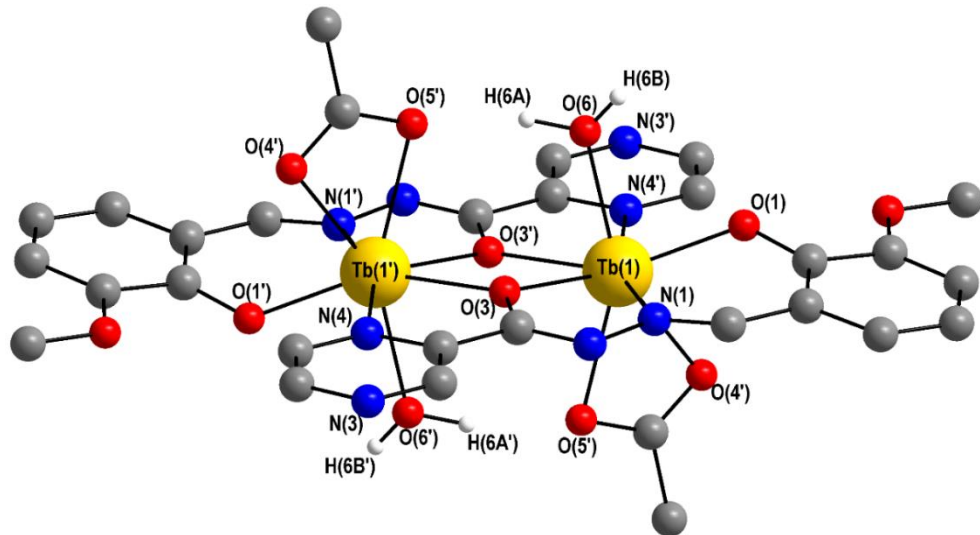


Figure 144. Molecular structure of (37-Tb) as an example for dimeric compounds with the original H_2opch ligand.

As shown in figure 145 each dimer is surrounded by six lattice water molecules which connect a central Tb^{III} dimer to six surrounding Tb^{III} dimers creating an extensive hydrogen bonding network. The lattice waters act as HB acceptors towards the coordinated water ligands $\text{O}(6)$ and HB donors towards one acetate oxygen $\text{O}(4)$ as well as a hydrazine nitrogen $\text{N}(2)$ of the opch^{2-} ligand.

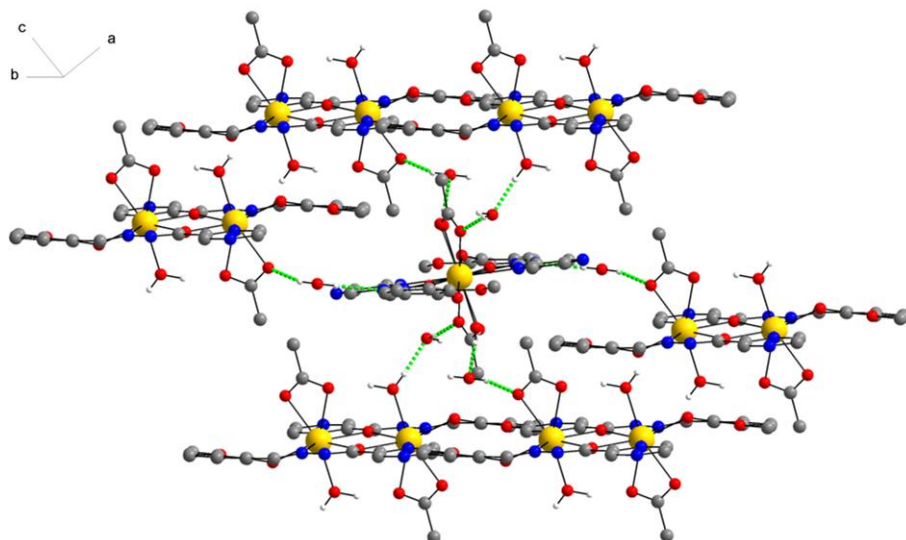


Figure 145. Packing of (37-Tb). Hydrogen bonding to lattice water molecules stabilising the crystal structure highlighted in green.

Only a few crystals of (**37-Tb**) were obtained therefore no further analysis was possible. Nevertheless, this establishes the generic structure of most dimeric complexes obtained here with two doubly deprotonated ligands from the H₂opch family, two anionic co-ligands that are derived from the lanthanide salt used in the synthesis as well as two neutral co-ligands which originate from the solvent. There are two exceptions to this generic structure which are amongst the compounds described in the next section and show how the magnetic properties of dimeric Dy^{III} complexes can be tuned.

5.3.5.1 Influence of Electrostatic Field (Crystal Field) on Magnetic Properties

In this section three Dy^{III} dimers are compared that introduce subtle changes especially to the intramolecular interactions. First the structures of these complexes and their unique features will be described. Then the magnetic anisotropy axes obtained from MAGELLAN^[297] will be compared with axes obtained from *ab initio* calculations and related to some magnetic data.

The molecular structure of the first of the presented complexes [Dy₂(MeOH)₂(OAc)₂(opch-Br)₂] (**38-Dy**) is shown in figure 146. It is very similar both to (**37-Tb**) as well as the literature known Dy₂ that use the unmodified H₂opch ligand.^[222] As seen for the other two, the anionic co-ligand in (**38-Dy**) is acetate and as in the literature known compound the neutral co-ligand is MeOH. The main Schiff base ligand H₂opch-Br is modified to by the additional bromine atom on the *o*-vanillin precursor.

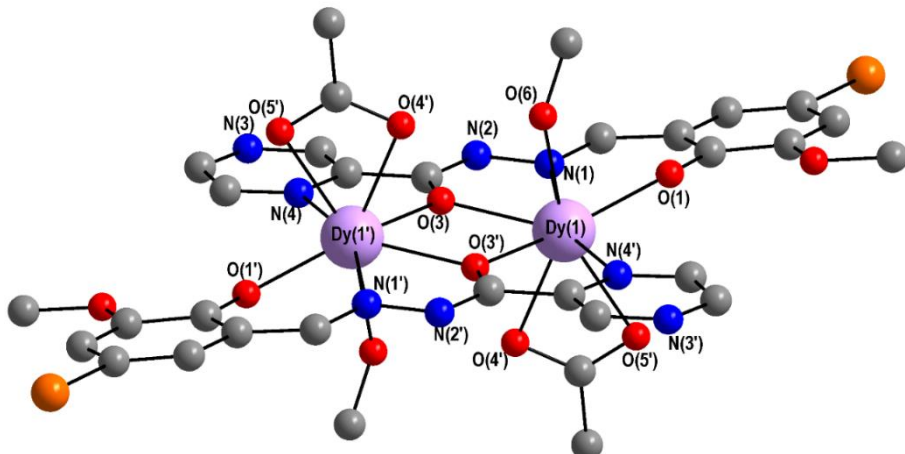


Figure 146. Molecular structure of (**38-Dy**).

The packing is dominated by offset π - π interactions forming stacks throughout the crystal. The overlap between the π -systems of neighbouring molecules are shown in figure 147. These π - π -stacks are angled alternately to form the zig-zag stacks of the packing shown in figure 148.

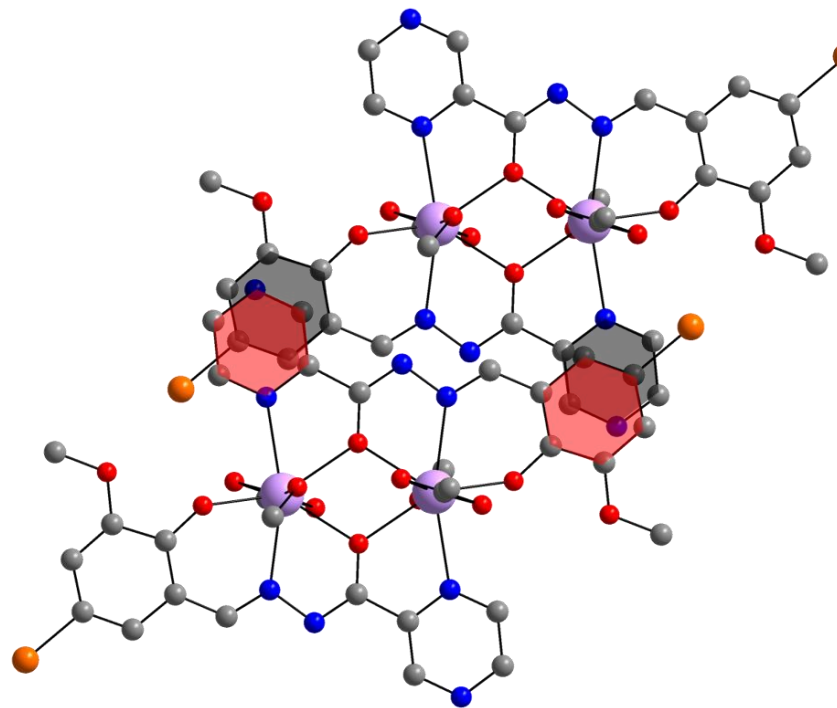


Figure 147. Red and black hexagons highlight the overlap of the π -systems resulting in offset π - π stacking responsible for the packing of (38-Dy).

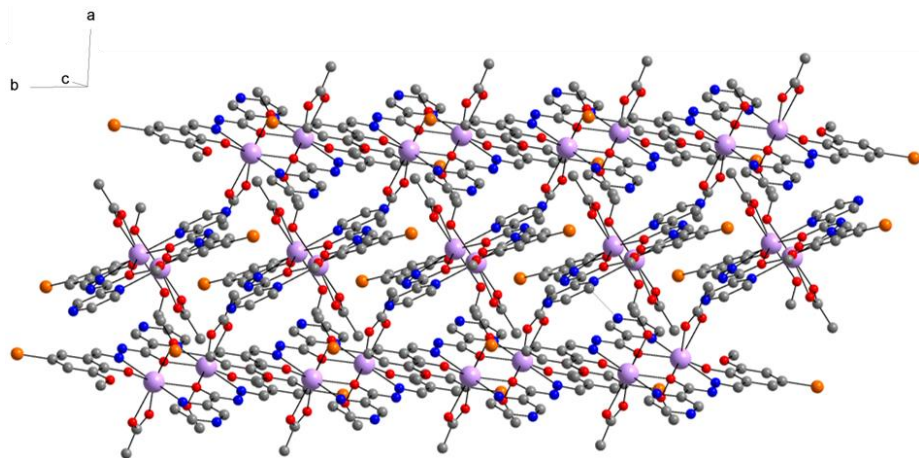


Figure 148. View on the packing of (38-Dy) showing the zig-zag stacks.

After 6 days of slow evaporation yellow needle crystals of (38-Dy) had formed and were measured using SC-XRD. After an additional week a yellow microcrystalline powder formed on the bottom of the vial. Both crystals harvested before the

precipitation of yellow powder as well as the yellow powder were investigated using PXRD. It can clearly be seen (figure 149) that the crystals pre-powder-precipitation are phase pure, while the yellow microcrystalline powder contains another crystalline compound besides (38-Dy).

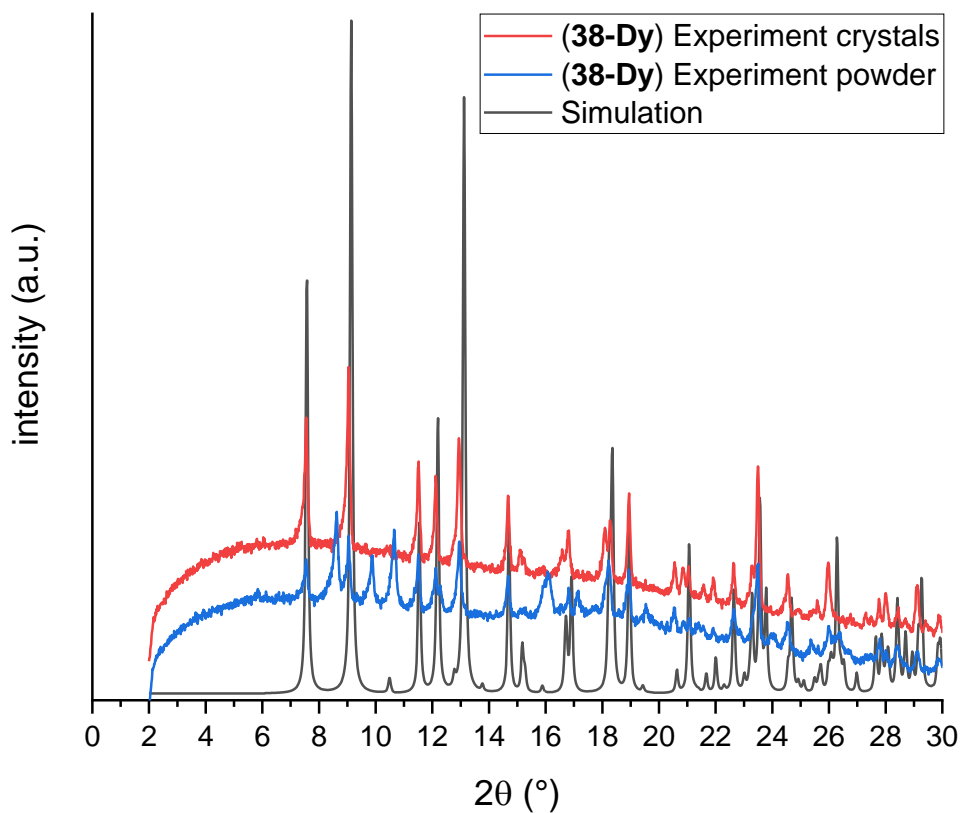


Figure 149. PXRD of (38-Dy) confirming the phase purity of the crystals, while confirming the presence of another crystalline material in the bulk powder sample.

The second compound presented here $[\text{Dy}_2(\text{DMF})_4(\text{NO}_3)_2(\text{opch-NO}_2)_2]$ (39-Dy) which is one of the exceptions to the generic structure of H_2opch -family dimers as the Dy^{III} ions are coordinated by an additional neutral co-ligand derived from the solvent, DMF in this case, each. The molecular structure with the two nine-coordinate Dy^{III} ions is shown in figure 150. The crystallisation of this compound took 4 weeks which may be a result of the presence of the nitro group in the R^2 position decreasing the electron density on the phenyl ring significantly. As a result of this the phenolate oxygen to dysprosium distance $\text{O}(1)\text{-Dy}(1)$ with $2.2080(19)\text{\AA}$ is longer than the ones in the other dimers presented here. This might also be the explanation for the additional DMF co-ligand as it provides additional electron density to compensate the trivalent Dy^{III} ion.

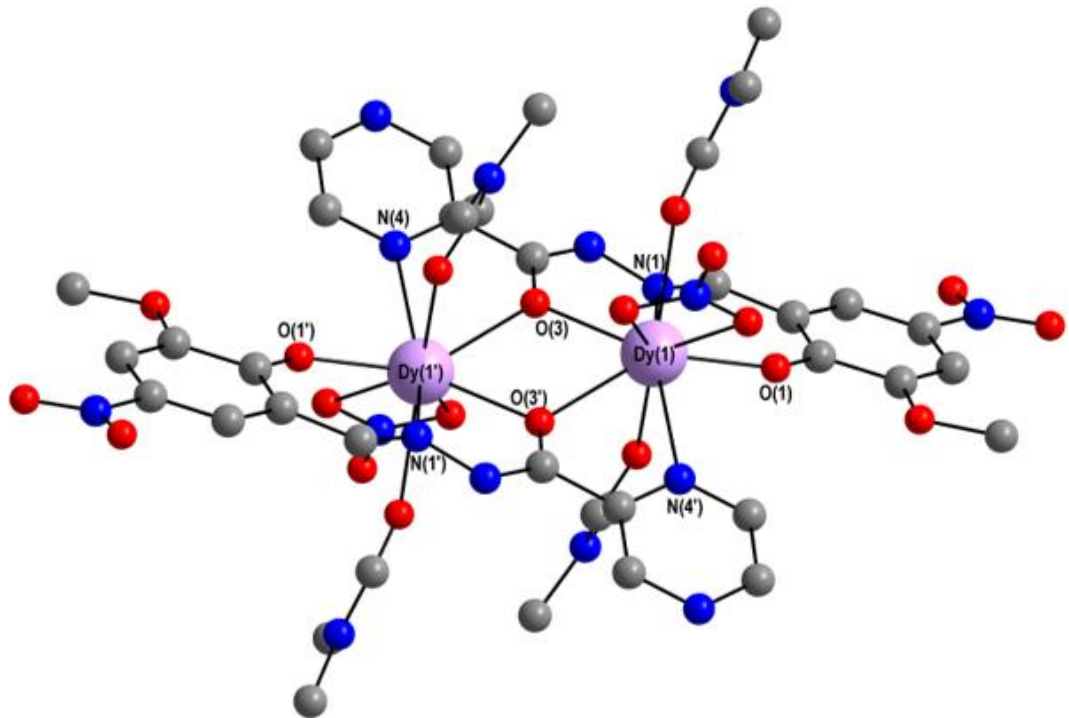


Figure 150. Molecular structure of (39-Dy).

There are no obvious intermolecular interactions in the packing of (39-Dy) which crystallises in $P\bar{1}$ with only one molecule in the unit cell (figure 151).

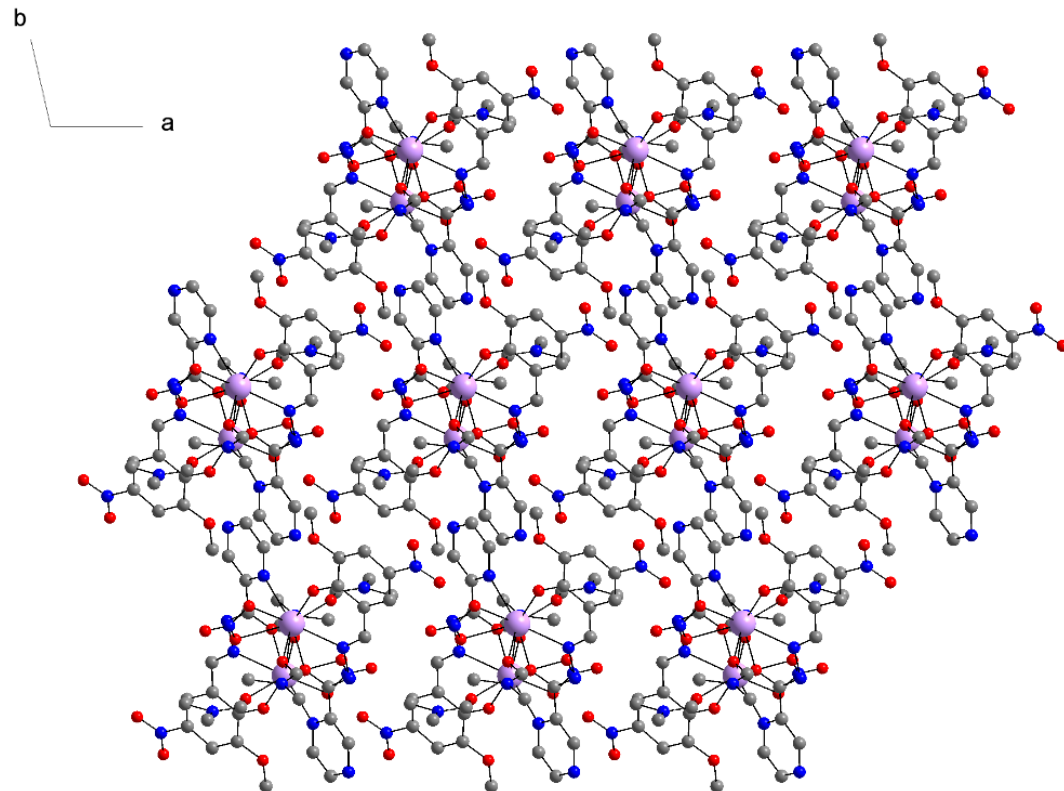


Figure 151. Packing of (39-Dy) along the c axis showing that all molecules are oriented in the same direction as for crystallisation in $P\bar{1}$ with $Z = 1$.

The sample of (**39-Dy**) was confirmed to be phase pure by PXRD shown in figure 152.

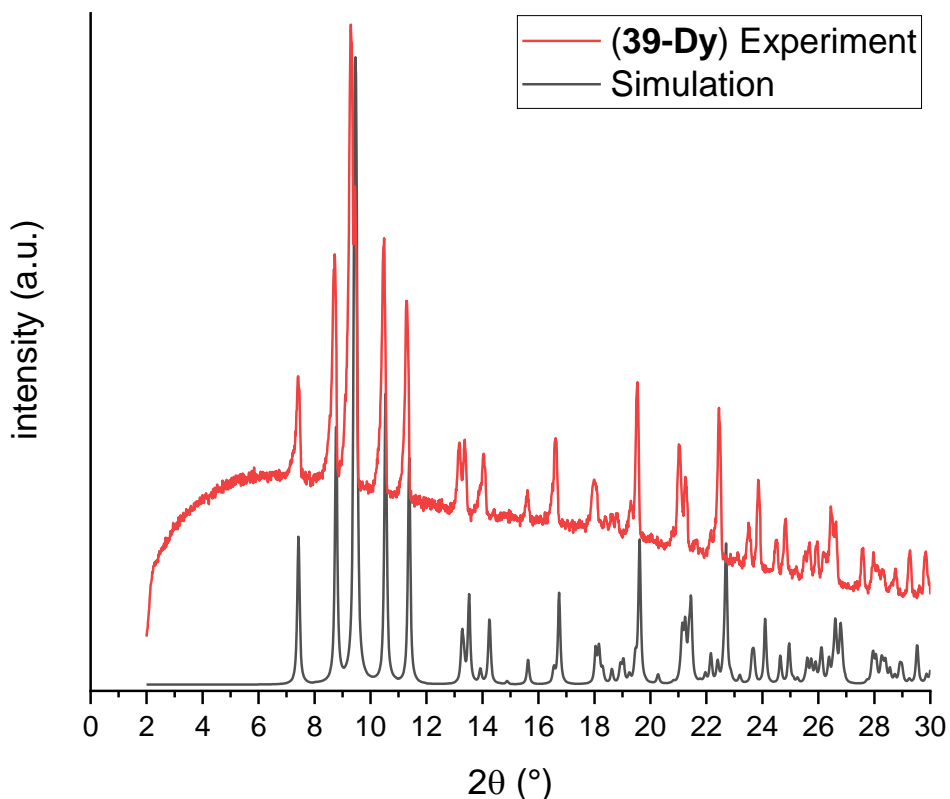


Figure 152. Powder pattern of (**39-Dy**) showing the phase purity of the compound.

The third dimer presented here is the one that is most different to the others as the Schiff base ligand is only singly deprotonated leading to a different coordination mode involving a bridging phenolate oxygen (see figure 153). As can be seen in figure 154 which shows the molecular structure of $[\text{Dy}_2\text{Cl}_4(\text{Hopch-Br})_2]$ (**40-Dy**) the hydrazine nitrogen N(2) is still protonated leading to O(3) to be present in its keto form as indicated by the corresponding C-O bond length of $1.251(7)\text{\AA}$. Instead, the overall charge is balanced by the coordination of four anionic co-ligands. In contrast to the other dimers presented here the anionic co-ligands are chlorides. This as well as the different coordination mode of the Hopch-Br⁻ ligand suggest that (**40-Dy**) is formed via a different mechanism than the one proposed in section 5.3.3.3. The different reaction mechanism leading to different resulting structures can be rationalised by the different synthetic method used here, which is using solvothermal conditions. A further factor was that the glass autoclave that was used did not seal tightly leading to a simultaneous increase in concentration as *circa* 80% of the solvent/base mixture evaporated over the course of 1 day. This might also explain the monodeprotonated form of Hopch-Br⁻ found here, since significant amounts of base apparently evaporated

during the process. Similarly, it was observed in the literature that the use of weaker bases can result in monodeprotonated forms of similar Schiff base ligands. These then also tend to favour the coordination mode involving the phenolate oxygen bridging between the Dy^{III} ions.^[310] Due to these structural differences, it is useful to compare (**40-Dy**) to the other dimers as it exemplifies how small changes in the molecular structure can have a dramatic impact on the magnetic properties as discussed further below.

As mentioned before the Hopch-Br⁻ ligand in (**40-Dy**) is bridging with the phenolate oxygen O(1) instead of the enolate oxygen as observed for the other dimers. This is shown in figure 153 which compares the coordination modes of the H₂opch-type ligands in (**38-** and **39-Dy**) with the ligand doubly deprotonated and mostly in its enolate form - negative charge delocalised between C and N but due to the cationic nature of the Dy^{III} ion drawn towards the oxygen site - to the one in (**40-Dy**) being only deprotonated once resulting in the keto form as evidenced by the C-O bond length. The different coordination modes lead to small but significant changes in the central Dy-O-Dy angles as the enolate form results in Dy-O-Dy angles of 113.1(1)[°] and 114.5(1)[°] for (**38-Dy**) and (**39-Dy**), respectively, while the keto form results in a Dy-O-Dy angle of 103.8(1)[°] in (**40-Dy**). This also influences the Dy-Dy distances which are 3.9154(5)Å and 3.9525(4)Å for (**38-Dy**) and (**39-Dy**), respectively, and 3.6708(6)Å for (**40-Dy**). The changes in Dy-O-Dy angles might influence the orbital overlap and therefore the effectiveness of magnetic exchange interactions. Additionally, the Dy-Dy distances influence the magnetic properties of compounds by changing the strength of dipolar Dy-Dy interactions.

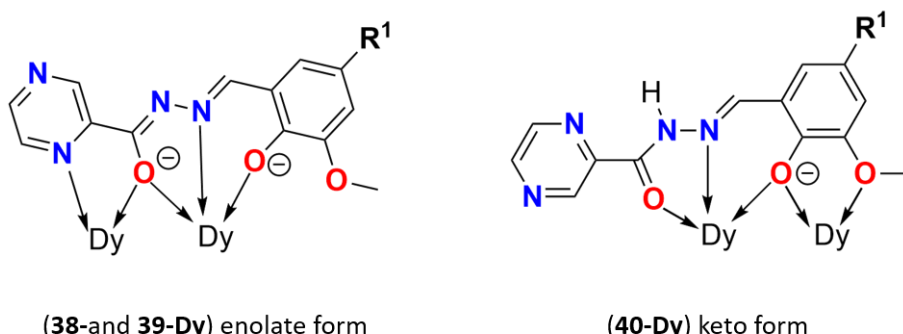


Figure 153. The two different coordination modes displayed by the opch-family ligands in (**38-40-Dy**).

In (**40-Dy**) the carbonyl oxygen O(3) as well as the hydrazine nitrogen N(1) are additionally chelating one Dy^{III} ion while the methoxy oxygen O(2) coordinates to the

other. The Schiff base ligands are essentially planar which can be attributed to the same co-ligands coordinating above and below the ligand plane, unlike in the other dimers in which an anionic co-ligand is on one side and a neutral co-ligand on the other side of the Dy_2O_2 plane. This induced planarity of the Hopch-Br ligand leads to coordination environments close to pentagonal bipyramidal of the seven coordinate Dy^{III} ions (see figure 154).

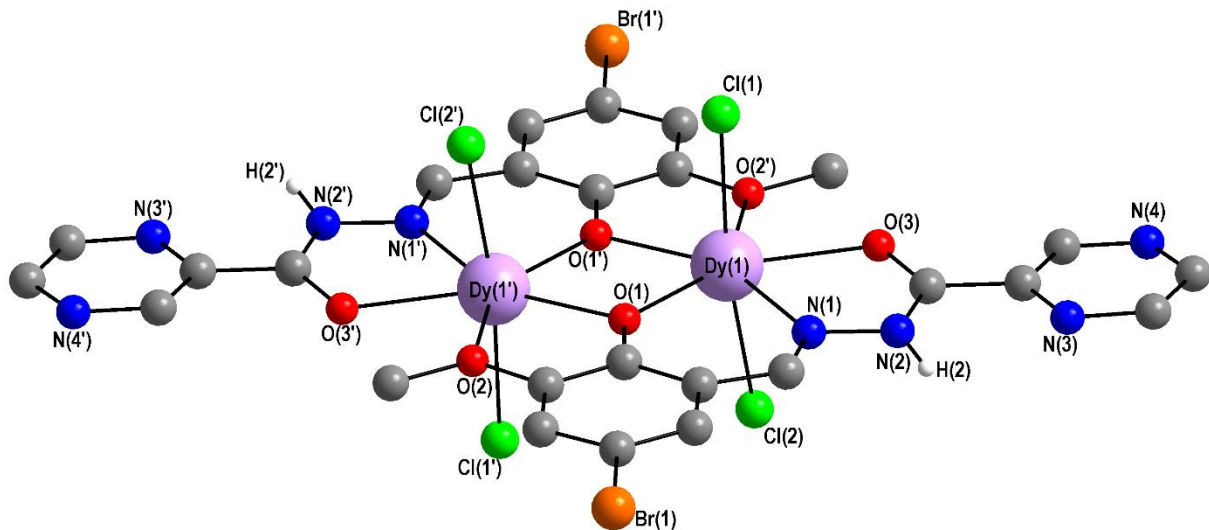


Figure 154. Molecular structure of (40-Dy).

(40-Dy) crystallises in the tetragonal space group $\text{P}4/n$ with $Z = 4$. This is another example in which the high symmetry of the crystal structure is resulting from the involvement of halogen interactions as well as a high number of intermolecular hydrogen bonds. Since the ligand is only singly deprotonated in (40-Dy) $\text{H}(2)$ present on the hydrazine nitrogen engages in extensive hydrogen bonding with the pyrazine nitrogens $\text{N}(4)$ of neighbouring molecules. This gives $\text{N}(2)\text{-H}(2)\dots\text{N}(4)$ distances of $2.870(7)\text{\AA}$ and $\text{N}(2)\text{-H}(2)\text{-N}(4)$ angles of $156(6)^\circ$. These HBs are shown in yellow in figure 155. Additionally, the disorder of the lattice CCl_4 molecules is shown in figure 155. This stems from the halogen-halogen interactions with the coordinating chlorides. There are two sorts of lattice CCl_4 in the crystal structure. One is disordered four times placing it in the middle of four bromine atoms from the Schiff base ligand in an attempt to form halogen-halogen interactions. The shortest Cl-Br distances are still longer than their combined VdW radii which formally means they are not halogen bonds. The second sort of disordered lattice CCl_4 has one of its C-Cl bonds on the fourfold axis leading to a situation in which the other three chlorine atoms interact with four coordinated chlorides in an attempt to align with the coordinated chlorides to maximise

the strength of the halogen-halogen interactions. This is shown in figure 156 in which the disorder was removed to show the halogen-halogen interactions between the two chlorine atoms (one coordinated, the other from lattice solvent) which are 3.121(30) Å and 3.388(7) Å apart from each other and therefore a distance shorter than double the VdW radius of Cl (3.5 Å).^[164] which puts them within the range where they can be described as hal-hal bonds. The angles of 106.3(1)° and 114.1(6)° being relatively close to 90° and the angles of 178.3(5)° and 157.3(13)° being relatively close to 180° confirm the interaction to be a type II halogen interaction, although the angles are not ideal due to the disorder of the lattice CCl_4 chlorines.

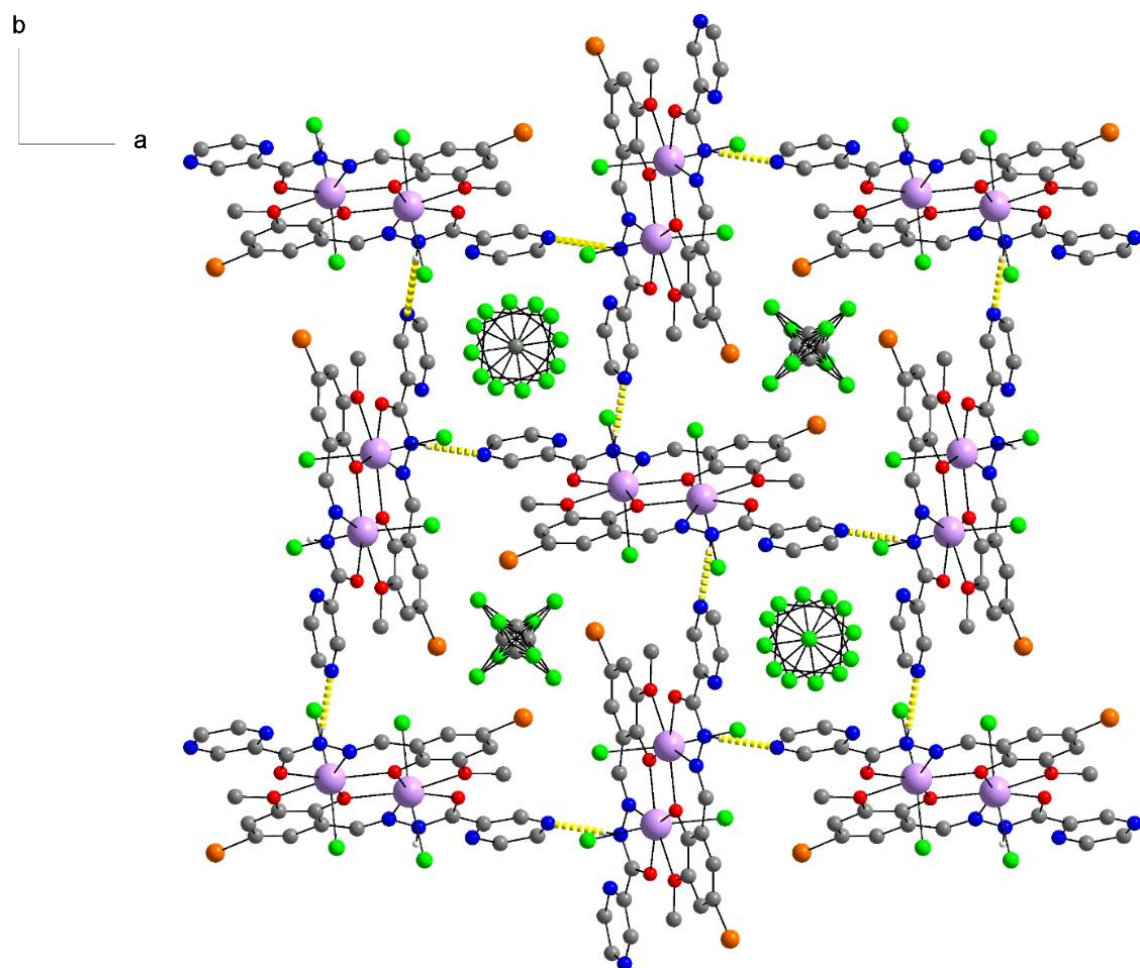


Figure 155. View on the packing of **(40-Dy)** along the c-axis highlighting the high symmetry of the crystal structure and the disorder of the lattice CCl_4 molecules. Hydrogen bonds can be seen in yellow.

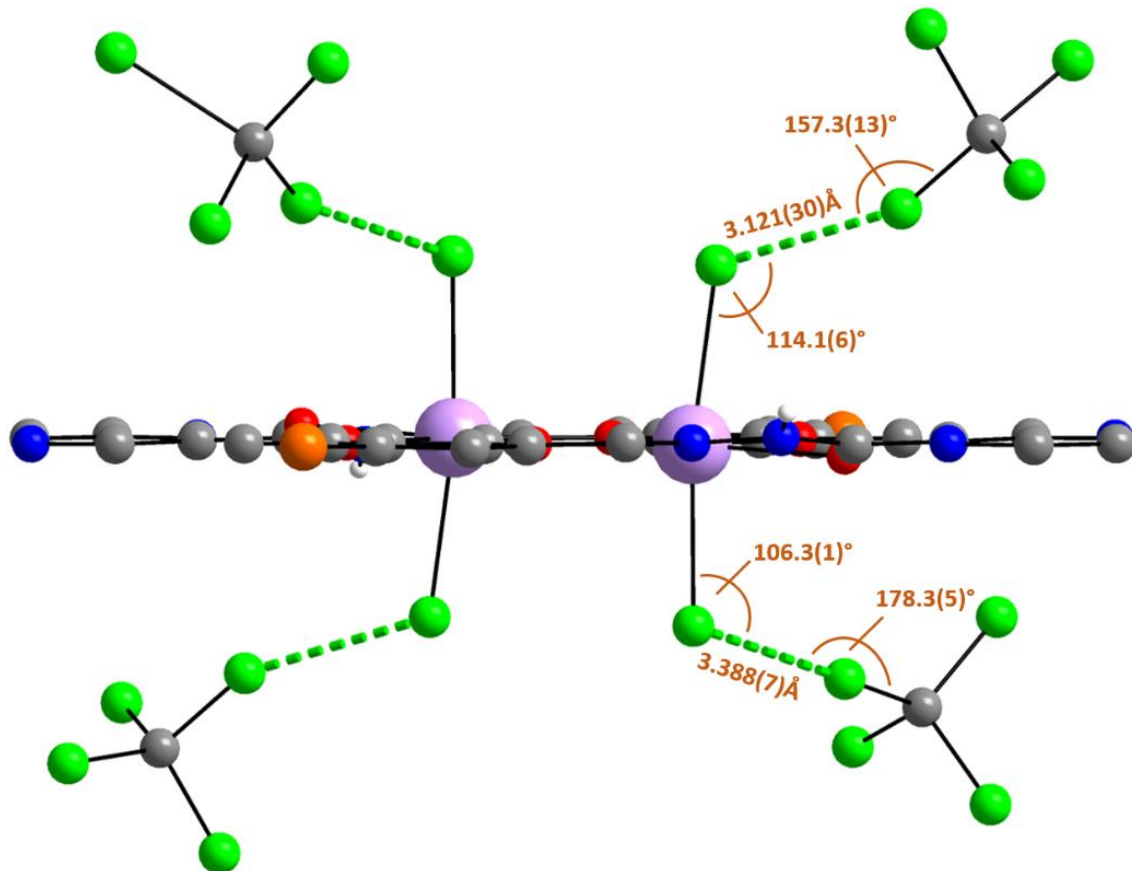


Figure 156. Halogen-halogen bonds in **(40-Dy)** between coordinated chlorides and lattice CCl_4 shown as green dotted lines. Relevant distances and angles are given in orange.

In order to evaluate the effect the different coordination environments and the resulting Dy-Dy distances have on the magnetic behaviour, the anisotropy axes for the three dimers (**38-40-Dy**) were calculated using MAGELLAN.^[297] The results of the calculations are shown in figure 157. Both axes in each dimer are parallel to each other as expected considering the asymmetric unit only contains half the molecule. The axes for the Dy^{III} ions in (**38-** and **39-Dy**), so Dy^{III} ions bridged by the enolate oxygen of the doubly deprotonated Schiff base ligands point towards the phenolate oxygen of the ligand as was previously shown in the literature.^[62] The short distance defines the direction of the anisotropy according to the electrostatic model of MAGELLAN. This is also observed for dinuclear dysprosium complexes with similar coordination environments and Dy-Dy distances in the literature.^[62, 198, 213, 298, 313-314]

In **(40-Dy)** the axes are roughly pointing along the $\text{Cl}-\text{Dy}-\text{Cl}$ vectors, nearly orthogonal to the Dy-Dy vector (85.3°), in contrast to the angle between the axes and the Dy-Dy vectors in **(38-Dy)** and **(39-Dy)** which are 20.4° and 11.8° , respectively. This can be explained using the same arguments of reducing electrostatic repulsion between the

Dy^{III} ions and the negatively charged ligands and is also consistent with similar compounds in the literature.^[315-316]

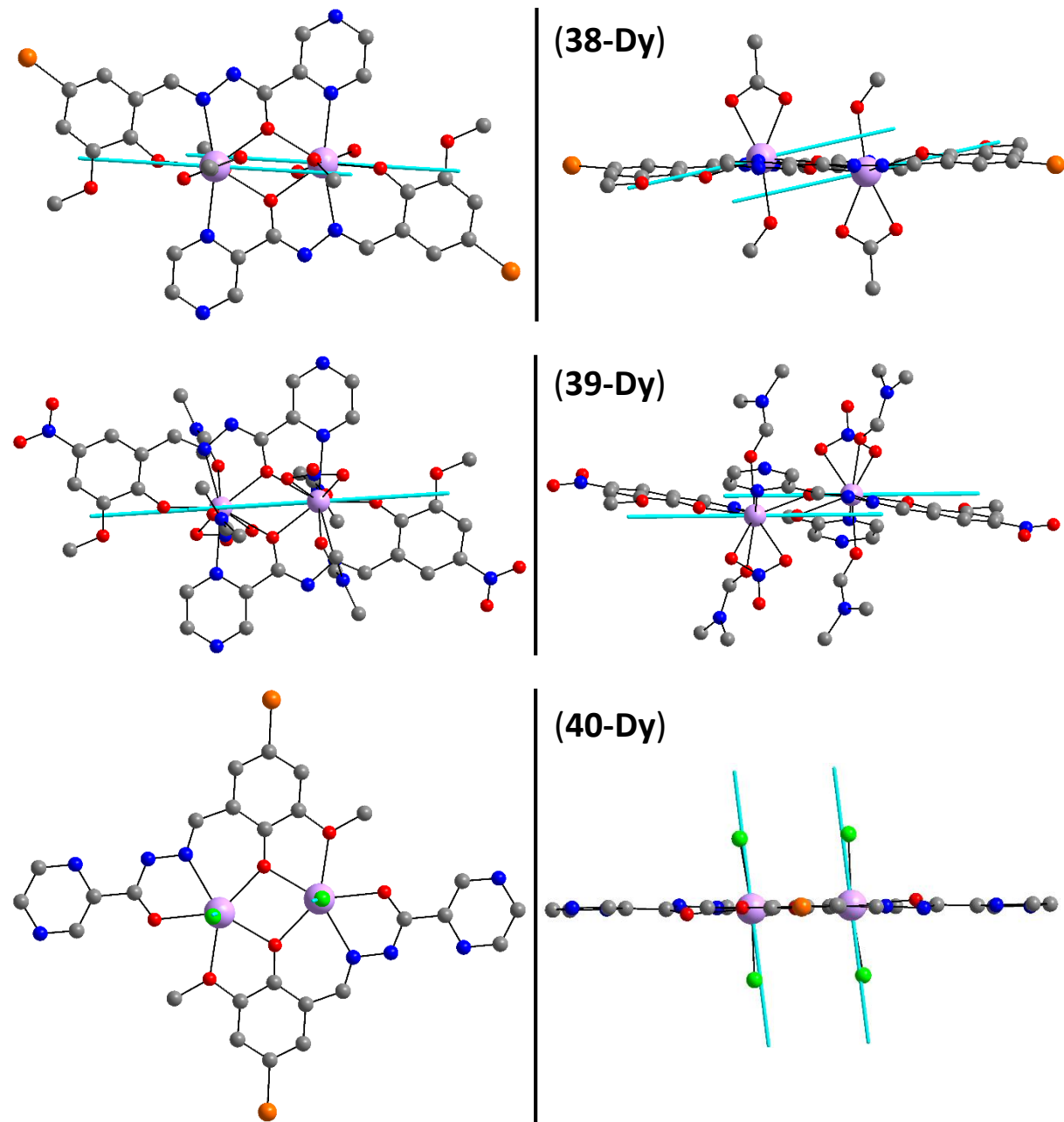


Figure 157. Two views on the anisotropy axes in (38-40-Dy) calculated using MAGELLAN^[297] showing that the axes are essentially parallel to the Dy-Dy vector in (38/39-Dy) and essentially orthogonal to the Dy-Dy vector in (39-Dy), highlighting the difference the coordination mode makes to the anisotropy in dimers.

However, no conclusion can be drawn regarding the sign of the magnetic interactions from MAGELLAN calculations. Therefore, magnetic measurements were performed on (39- and 40-Dy). (38-Dy) was not measured due to the precipitation of an additional compound after a week as described above.

The $\chi_{\text{M}}T$ vs T plots of (39-Dy) and (40-Dy) are shown in figure 158. The room temperature $\chi_{\text{M}}T$ values of $31.01 \text{ cm}^3 \text{Kmol}^{-1}$ in (39-Dy) and $28.24 \text{ cm}^3 \text{Kmol}^{-1}$ in (40-Dy) are in good agreement with the theoretical value of $28.34 \text{ cm}^3 \text{Kmol}^{-1}$ for two uncoupled Dy^{III} ions. For (39-Dy) shown in red the $\chi_{\text{M}}T$ value steadily increases with decreasing temperature indicating ferromagnetic interaction. At 60 K the slope of the increase flattens out before a second sharper increase at 12 K resulting in a maximum $\chi_{\text{M}}T$ value of $70.42 \text{ cm}^3 \text{Kmol}^{-1}$ at 1.8 K. While ferromagnetic interaction is clearly indicated here, there appears to be another reason such as an overlap of the ferromagnetic coupling with the depopulation of excited states or a structural/magnetic phase change responsible for the additional features in this graph. The $\chi_{\text{M}}T$ values of (40-Dy) shown in blue decrease monotonically with decreasing temperature until reaching 25 K, then a sharp decrease of $\chi_{\text{M}}T$ can be observed likely due to the depopulation of excited Stark-levels as well as a potential additional antiferromagnetic interaction. At 1.8 K a $\chi_{\text{M}}T$ value of $13.51 \text{ cm}^3 \text{Kmol}^{-1}$ is reached by (40-Dy).

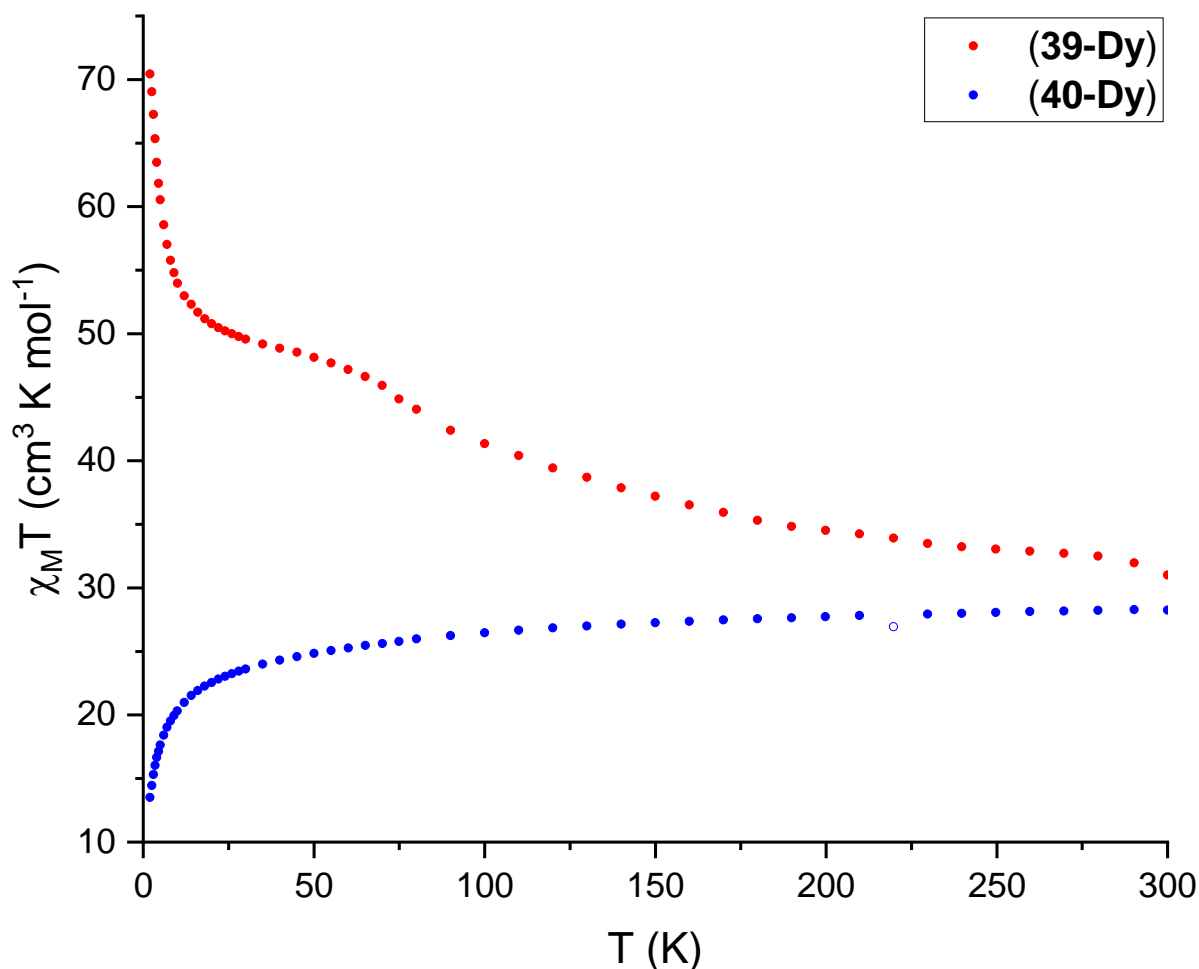


Figure 158. $\chi_{\text{M}}T$ vs T plots for (39-Dy) (red) and (40-Dy) (blue) revealing ferromagnetic interaction between the Dy^{III} centres in (38-Dy) and a potential antiferromagnetic interaction in (40-Dy).

The $1/\chi$ versus temperature plots of both compounds are shown in figure 159. Fitting the data of **(40-Dy)** between 10 K and 300 K to a Curie-Weiss law proves the existence of an antiferromagnetic interaction. The curve can be fitted with a Weiss constant θ of -7.1 K and a Curie constant C of $28.57 \text{ cm}^3 \text{Kmol}^{-1}$. The point not lying on the linear fit was not used to obtain the fit as indicated in both figures 158 and 159 by an unfilled sphere in figure 158 and a blue cross in figure 159. Due to the additional features displayed by **(39-Dy)** the curve follows the Curie-Weiss law only in the temperature range between 100 K and 280 K and can be fit using $\theta = 32.6 \text{ K}$ and $C = 28.57 \text{ cm}^3 \text{Kmol}^{-1}$.

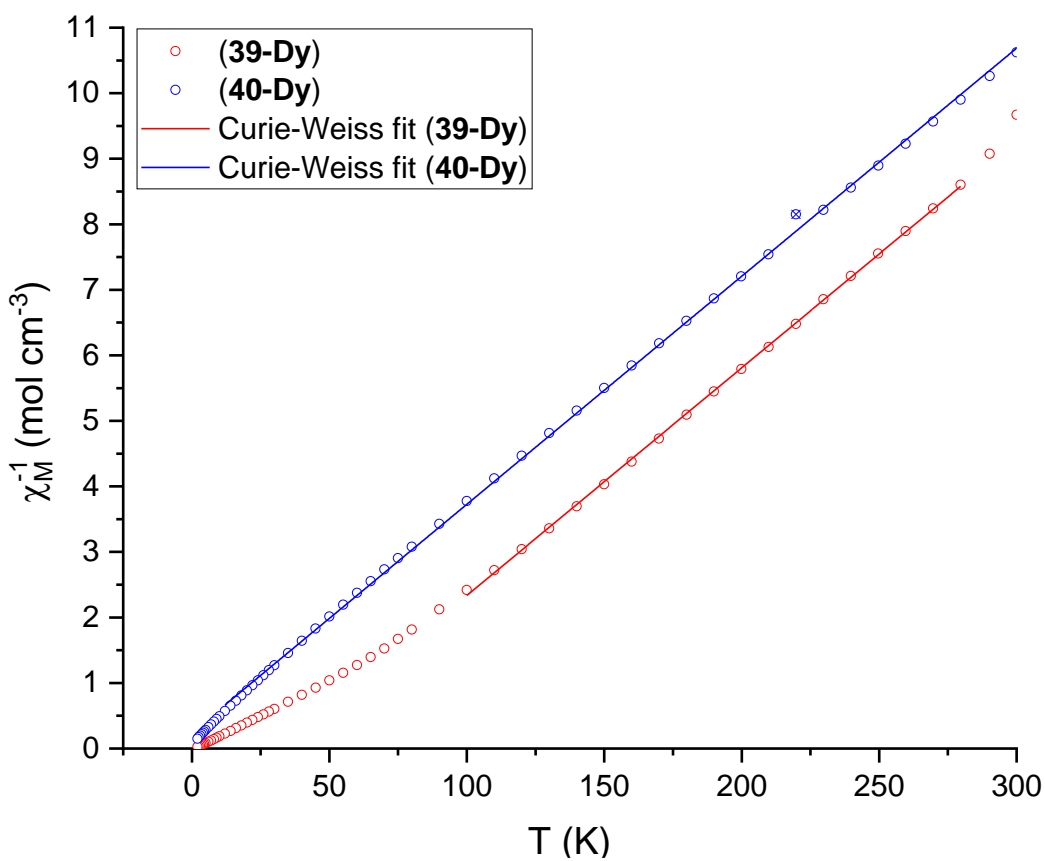


Figure 159. Inverse magnetic susceptibility plots and Curie-Weiss fits for **(39-Dy)** and **(40-Dy)** showing the sign of the magnetic interaction in the respective dimer.

The sign of the resulting magnetic coupling in dimers with similar Schiff base ligands is suggested to be dependent on the Dy-O-Dy angles of the central Dy_2O_2 rhomboid. These determine the orbital overlap between the Dy^{III} ions.^[310, 315] In the following table (table 17) dinuclear dysprosium complexes from the literature with similar ligand systems and coordination environments as well as the dimers presented here are listed

and their Dy-Dy distances and Dy-O-Dy angles compared and related to the direction of anisotropy axes as well as resulting sign of the magnetic coupling.

Table 17. Comparison of compounds (38-40-Dy) with complexes from the literature with Schiff base ligands with similar coordination spheres (both variations, enolate-bridged as well as phenoxy-bridged). In the “sample” column the compound identifiers for compounds produced in this work or molecular formulae for compounds from the literature are listed. Angles are given in degrees and distances in Angstrom with standard deviations if given in the corresponding reference. For compounds in which the direction of the anisotropy axes (abbreviated as AA) was investigated either by MAGELLAN^[297] or *ab initio* methods, the direction is indicated as either “o” for axes (near) orthogonal to the Dy-Dy-vector or as “p” for axes (near) parallel to the Dy-O_{phenoxy} bonds. Additionally, the sign of the experimentally observed overall magnetic interaction is given as either “F” for ferromagnetic interactions or “AF” for antiferromagnetic ones as well as the references of the respective compounds.

Sample	Dy-O-Dy angle [°]	Dy-Dy distance [Å]	AA	Magnetic interaction	Ref
(38-Dy)	113.3(1)	3.9154(5)	p		this work
(39-Dy)	114.5(1)	3.9525(4)	p	F	this work
(40-Dy)	103.8(1)	3.6708(6)	o	AF	this work
[Dy ₂ (ovph) ₂ (NO ₃) ₂ (H ₂ O) ₂]	110.1(2)	3.8258(6)		F	[310]
[Dy ₂ L ₂ (HCOO) ₂ (MeOH) ₂]	113.7	3.900	p	F	[317]
[Dy ₂ (ovph) ₂ Cl ₂ (MeOH) ₃]	111.5 112.4	3.8644	p	F	[318]
(NHEt ₃) ₂ [Dy ₂ (μ ₂ -NO ₃) ₂ (NO ₃) ₂ (HL) ₂] [*]	108.3(1)	3.729(5)	p	AF	[62]
[Dy ₂ (a'povh) ₂ (OAc) ₂ (DMF) ₂] [*]	102.62	3.6768	p	AF	[319]
[Dy ₂ (opch) ₂ (OAc) ₂ (H ₂ O) ₂]	113.1(2)	3.891(1)	p	F	[198]
[Dy ₂ (opch) ₂ Cl ₂ (MeOH) ₂]	111.8(3)	3.851(4)	p	F	[298]
[Dy ₂ (ovgrd) ₂ (acac) ₂ (H ₂ O) ₂]	113.6	3.98	p	F	[313]
[Dy ₂ (Hovph)(ovph)(NO ₃) ₂ (H ₂ O) ₄] ^{**}	113.5(2) 111.1(2)	3.8926(8)		F	[310]
[Dy ₂ (Hovph) ₂ (μ ₂ -OH)(OH)(H ₂ O) ₅] [*]	99.7(2) 100.1(2) 92.1(2)	3.6145(4)		AF	[310]
[Dy ₂ (nb) ₄ (H ₂ L) ₂]	105.3	3.6768	o	AF	[315]
[Dy ₂ L ₂ (DBM) ₂ (DMF) ₂]	106.5(2)	3.727(2)	o	AF	[316]

^{*}Additional bridging ligands other than the Schiff base ligand. ^{**}Complex containing one doubly deprotonated ligand with bridging enolate oxygen and one singly deprotonated ligand with bridging phenoxy oxygen.

It can generally be seen that in complexes with doubly deprotonated ligands bridging with the enolate oxygen the axes all point along the Dy-phenoxy oxygen bond as expected from an electrostatic viewpoint as discussed above. All examples apart from the ones with additional bridging ligands between the two Dy^{III} ions have Dy-Dy

distance longer than 3.82Å and Dy-O-Dy angles larger than 110°. This then results in a ferromagnetic interaction between the Dy^{III} centres. When additional bridging ligands such as nitrate or acetate are present (as indicated by an asterisk in table 17), the Dy^{III} ions are forced into closer proximity as shown by the Dy-Dy distances shorter than 3.73Å as well as Dy-O-Dy angles smaller than 110°. This results in an antiferromagnetic interaction.

For the systems in table 17 which are bridged by the phenolate oxygen atoms of the respective monoprotonated forms of the ligands, the direction of the anisotropy axes was reported to be essentially orthogonal to the Dy-Dy vector.^[315-316] The phenolate bridged coordination mode generally favours short Dy-Dy distances and small Dy-O-Dy angles resulting in antiferromagnetic coupling, which again is in line the electrostatic arguments discussed before. One example in the literature has the two Dy^{III} ions bridged by one monodeprotonated ligand and one doubly deprotonated ligand (indicated by two asterisks in table 17) exhibiting the same trend where longer Dy-Dy distances and larger Dy-O-Dy angles are favourable for resulting ferromagnetic interactions.^[310]

The question now is why the magnetic coupling changes its sign as a result of shorter Dy-Dy distances and smaller Dy-O-Dy angles. In table 18 below the J values obtained by *ab initio* calculations for four selected examples are shown.^[198, 298, 315-316] The exchange coupling is consistently antiferromagnetic and is also smaller than the dipolar coupling in three out of four examples. For the enolate bridged complexes (with the longer Dy-Dy distances), the dipolar coupling is calculated to be ferromagnetic and outweighs the significantly smaller exchange couplings leading to an overall ferromagnetic interaction. In the phenolate bridged complexes (with the shorter Dy-Dy distances) the antiferromagnetic exchange interactions are assisted by antiferromagnetic dipolar interactions resulting in antiferromagnetically coupled Dy^{III} ions. The change in sign of the dipolar coupling can be explained by the angle of the axes to the Dy-Dy vector. In centrosymmetric systems, which therefore have parallel anisotropy axes, for angles smaller than 54.74°, also known as the magic angle at which the dipolar coupling is exactly zero, the interaction is ferromagnetic. For angles larger than the magic angle the interaction is antiferromagnetic.^[62, 320] Therefore, it can be concluded that the bridging mode that determines the direction of the anisotropy axes in this particular system is simultaneously determining the sign of the dipolar

coupling. Thus, the overall magnetic interaction is determined by the details of the bridging mode of the ligands.

Table 18. Comparison of *ab initio* calculations on four compounds representative for both bridging modes shown in scheme 153 as indicated by the bridging oxygen atom in the second column. The related directions of anisotropy axes are also indicated in the same column by “p” for anisotropy axes parallel to the Dy-O_{phenoxy} bond or “o” for axes orthogonal to the Dy-Dy vector.

Compound	Type of bridging mode and orientation of anisotropy axes	J (cm ⁻¹)
[Dy ₂ (opch) ₂ (OAc) ₂ (H ₂ O) ₂] ^[198]	enolate, p	J _{ex} = -0.023, J _{dip} = +0.208, J _{total} = +0.185
[Dy ₂ (opch) ₂ Cl ₂ (MeOH) ₂] ^[298]	enolate, p	J _{ex} = -2.5, J _{dip} = +4.69, J _{total} = +2.19
[Dy ₂ (nb) ₄ (H ₂ L) ₂] ^[315]	phenoxy, o	J _{ex} = -2.75, J _{dip} = -3.12, J _{total} = -5.87
[Dy ₂ L ₂ (DBM) ₂ (DMF) ₂] ^[316]	phenoxy, o	J _{ex} = -2.93, J _{dip} = -2.22, J _{total} = -5.15

Furthermore, measurements of the magnetisation at dc fields between 0 and 7 T were conducted at 2, 3 and 5 K (see figure 160). The magnetisation of (**39-Dy**) increases very sharply at low temperatures and fields which is in line with the ferromagnetic coupling and the fact that there is only a single orientation of anisotropy axes in the system. This leads to alignment of the magnetic moments of the randomly oriented powder sample at low fields. The magnetisation at 2 K is essentially saturated at 0.5 T and reaches a maximum value of 17.8 μ_B . In the reduced magnetisation plot for (**39-Dy**) the curves at 2 and 3 K almost superpose with the curve at 5 K deviating from the others. This may be a result of excited states being significantly separated from the ground state only becoming accessible at temperatures between 3 and 5 K. In the antiferromagnetically coupled compound (**40-Dy**) the magnetisation curves show a more gradual increase reaching a maximum value of 10.5 μ_B without saturating. The non-superposed curves in the reduced magnetisation point towards significant anisotropy in the system and/or low lying excited states.

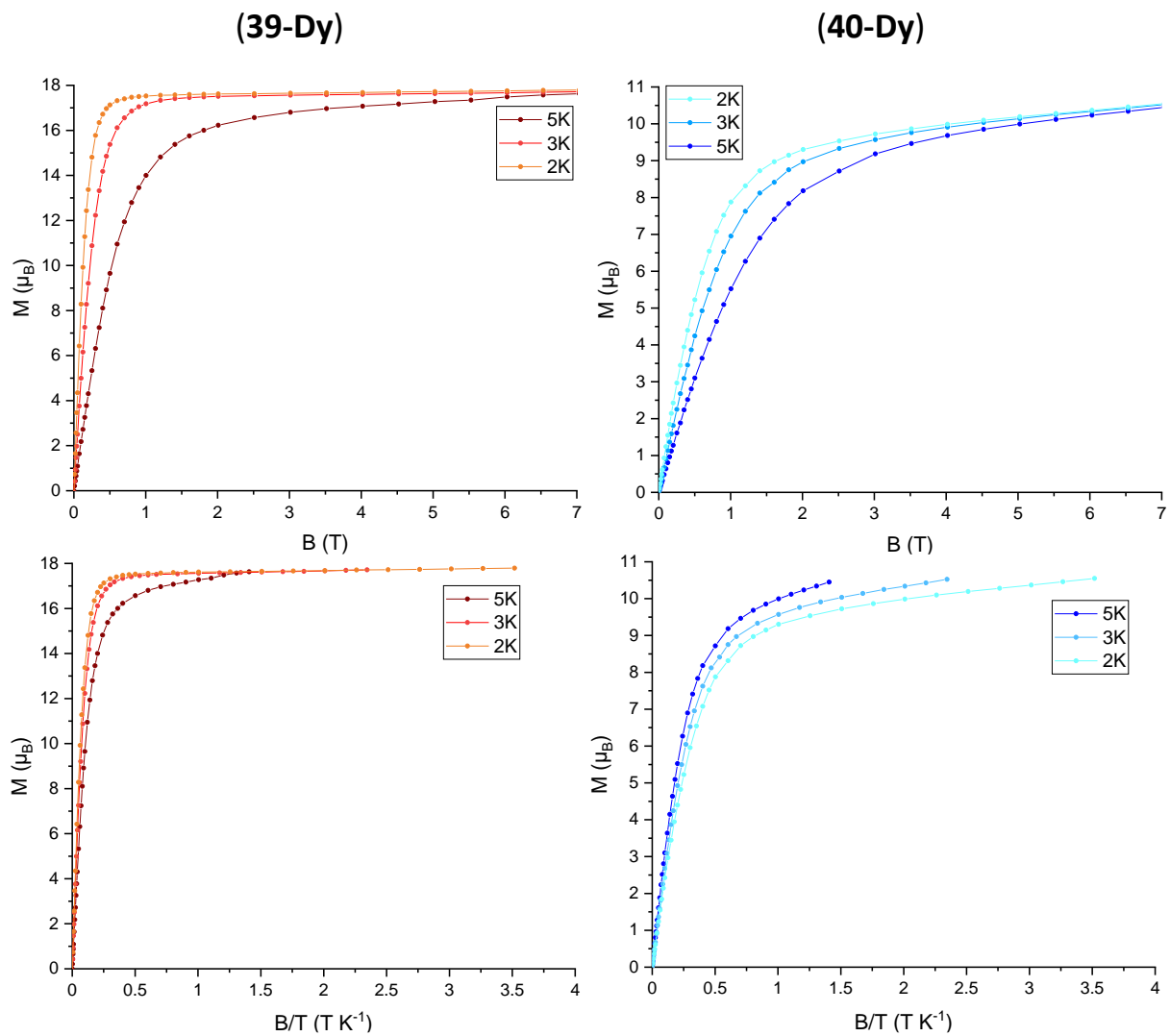


Figure 160. Magnetisation at applied dc fields between 0 and 7 T (top) and reduced magnetisation (bottom) of (39-Dy) (left) and (40-Dy) (right).

Both compounds show maxima in ac out-of-phase susceptibility measurements confirming slow relaxation of magnetisation. While the out-of-phase signal is well resolved for (39-Dy) and could be fitted using the generalised Debye model (see figure 163) thus making it possible to extract more information regarding the relaxation processes, this was not possible for (40-Dy) due to the poor intensity of the out-of-phase signal. This led to many outliers that would reduce the quality of a fit significantly, as shown in figure 161.

Nevertheless, some qualitative information can be extracted. There are multiple relaxation processes present in (40-Dy) which can be seen from the data at low temperatures and high frequencies which in turn suggest an additional faster relaxation present in this system. Multiple relaxation processes are also indicated by the first maximum increasing in intensity between 2 and 3 K before starting to decrease.

Regarding the identification of relaxation processes it can be concluded that the set of maxima that is visible within the range of the measurement does not correspond to ZFQTM as shown by the shift in frequency with changing temperature.

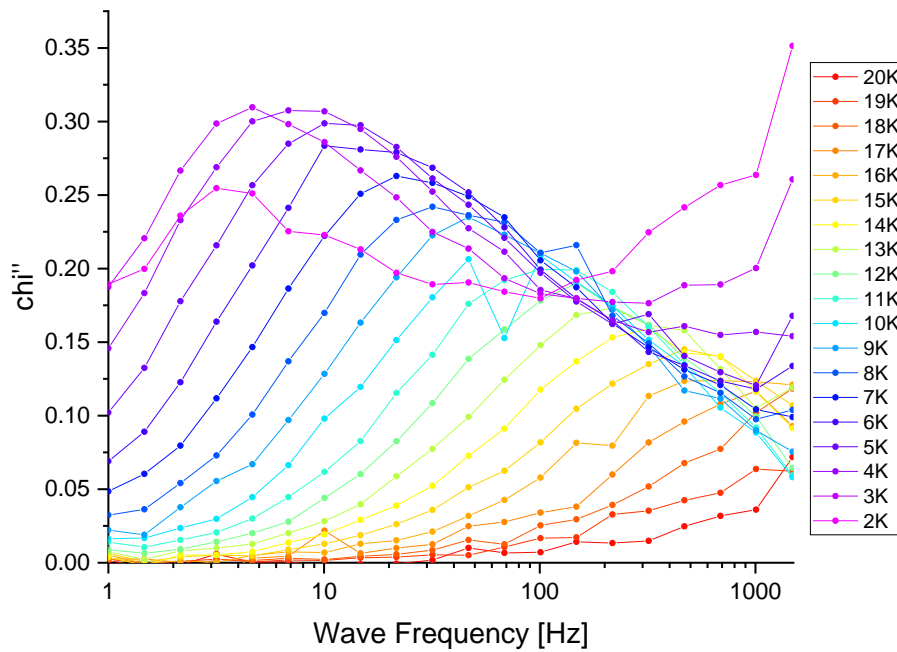


Figure 161. Magnetic ac out-of-phase susceptibility data for **(40-Dy)** showing the poor intensity. Lines are guide to the eye.

The extremely weak SMM behaviour is also apparent from the microSQUID measurements performed on single crystals of **(40-Dy)** by Dr. Michael Schulze in the group of Prof. Dr. Wolfgang Wernsdorfer (PHI, KIT). A very narrow hysteresis around zero-field can be seen at 30 mK in the graph showing the temperature dependence (figure 162, top) which quickly closes upon increasing the temperature. From the small scan rate dependence (see figure 162, bottom), it can be concluded that part of the relaxation happens on a fast time scale usually associated with direct processes. The hysteresis does not close even at the slowest measured scan rate suggesting there is an additional slow process for relaxation. This is in line with the multiple maxima present in the out-of-phase magnetic susceptibility.

Additionally, the microSQUID measurements show a relatively stable antiferromagnetic state that persists up to *circa* 0.5 T. The non-zero magnetisation of the antiferromagnetically coupled state may result from more than one orientation of molecules present in the crystal structure (see figure 155 above).

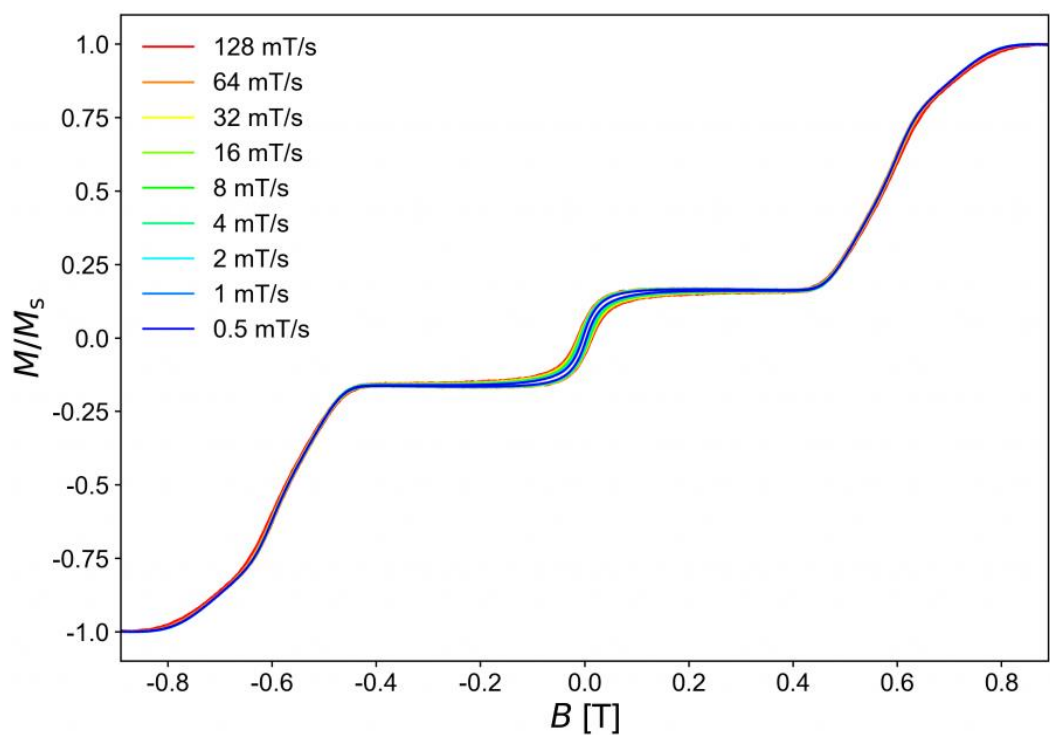
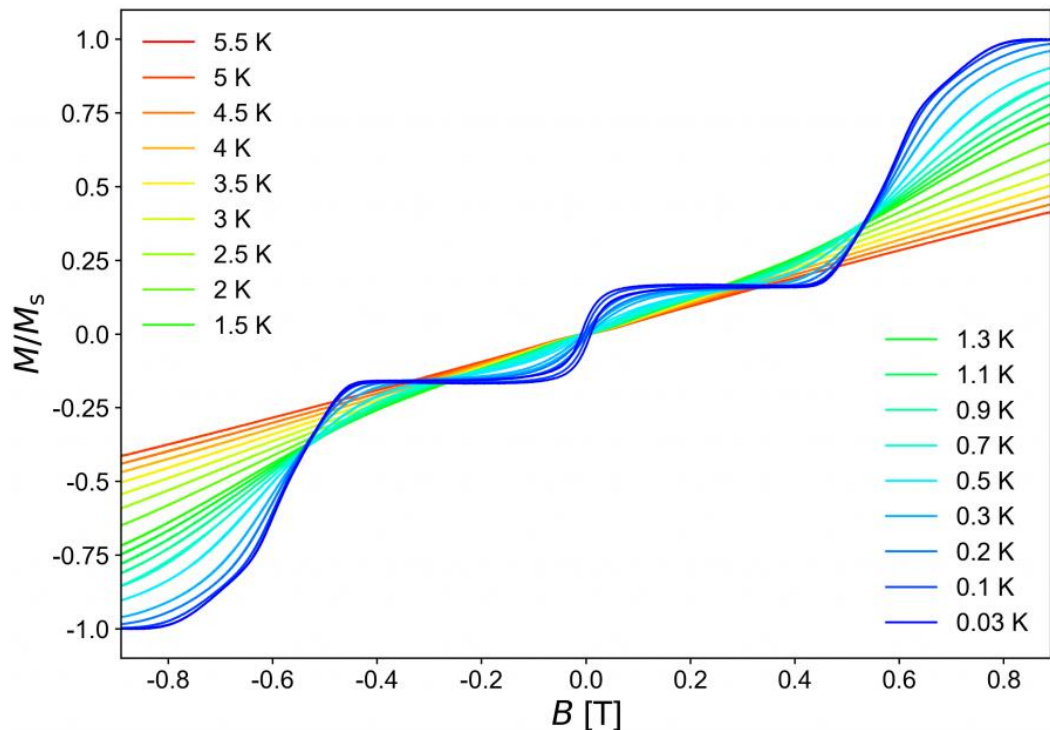


Figure 162. MicroSQUID measurements performed on single crystals of **(40-Dy)** between 30 mK and 5.5 K at a sweep rate of 128 mT/s (top) as well as sweep rates between 0.5 mT/s and 128 mT/s at 0.03 K (bottom).

The situation in **(39-Dy)** is different as is immediately obvious by looking at the out-of-phase susceptibility data presented in figure 163. The intensity is about ten times higher than in **(40-Dy)** making it possible to fit the data to the generalised Debye model.

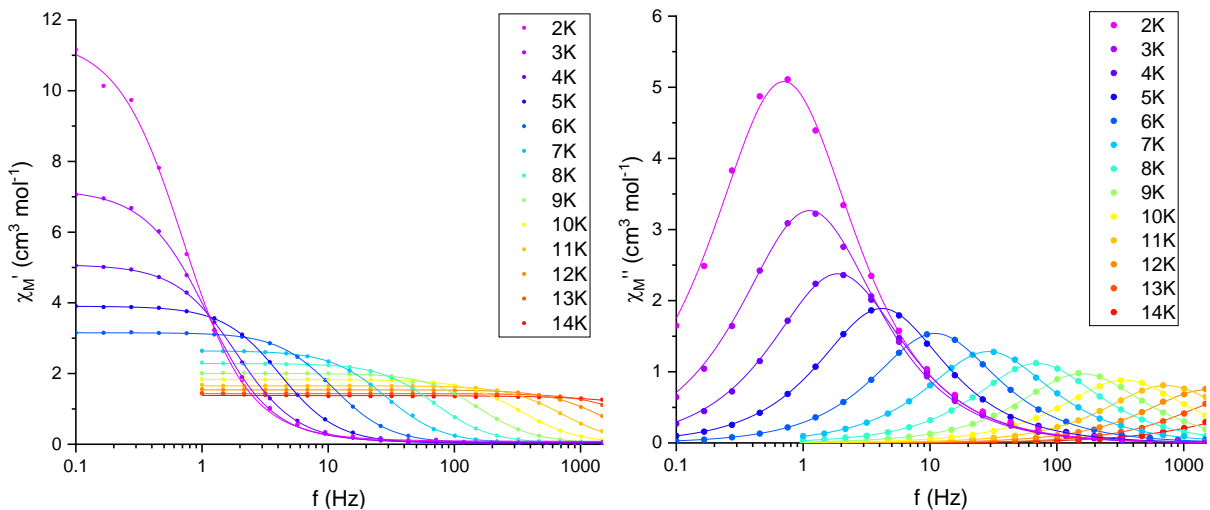


Figure 163. In-phase (left) and out-of-phase (right) ac susceptibility measurements on (39-Dy) in the range between 0.1 and 1500 Hz at 2-6 K and between 1 and 1500 Hz at 7-14 K. Lines are the best fit to the acquired data points using the Debye model.

The τ values extracted from the Debye fit to the out-of-phase susceptibility data were used to produce the Arrhenius plot shown in figure 164 below. The relaxation processes were fitted in two ways. First only assuming an Orbach process, the high temperature data were fitted using a linear function (blue in figure 164). Although it has to be mentioned that this fit is highly dependent on how many data points are considered for (39-Dy), this makes it possible to obtain an approximate energy barrier to this purely thermal relaxation process which due to the presence of additional relaxation processes is higher than the actual effective energy barrier to magnetisation reversal of this system. Additionally, the T_{B100} value which is a universal parameter to compare the performance of SMMs^[129] can be extracted by calculating the temperature at which $\tau = 100$ s. The linear fit led to an $U_{\text{Orbach}} = 106.0$ K and a T_{B100} of 4.8 K.

Additionally, the curve was fitted using the equation proposed by Lunghi *et al.*^[142]. The best fit to equation 13 is shown in red in figure 164. From the fitting parameters it can be concluded that there is no ZFQTM present in (39-Dy) as the parameter B which describes ZFQTM is not needed to obtain the best fit to the Arrhenius plot. This has been tested by allowing the parameter B to be free which resulted in it converging to 0 making it obsolete.

The resulting parameter of the fit to equation 13 are listed in the following table 19.

Table 19. Fitting parameters using equation 13 to fit the lifetime values extracted using the Debye model to fit the ac data of (39-Dy).

A (s ⁻¹ K ⁻¹)	B (s ⁻¹)	V (s ⁻¹)	w (K)	τ ₀ (s)	U (K)
2.389	0	124197	46.0	1.37E-9	138.5

From these parameters it can be concluded that direct and Raman processes provide the favoured relaxation pathways in (39-Dy), while ZFQTM is not observed.

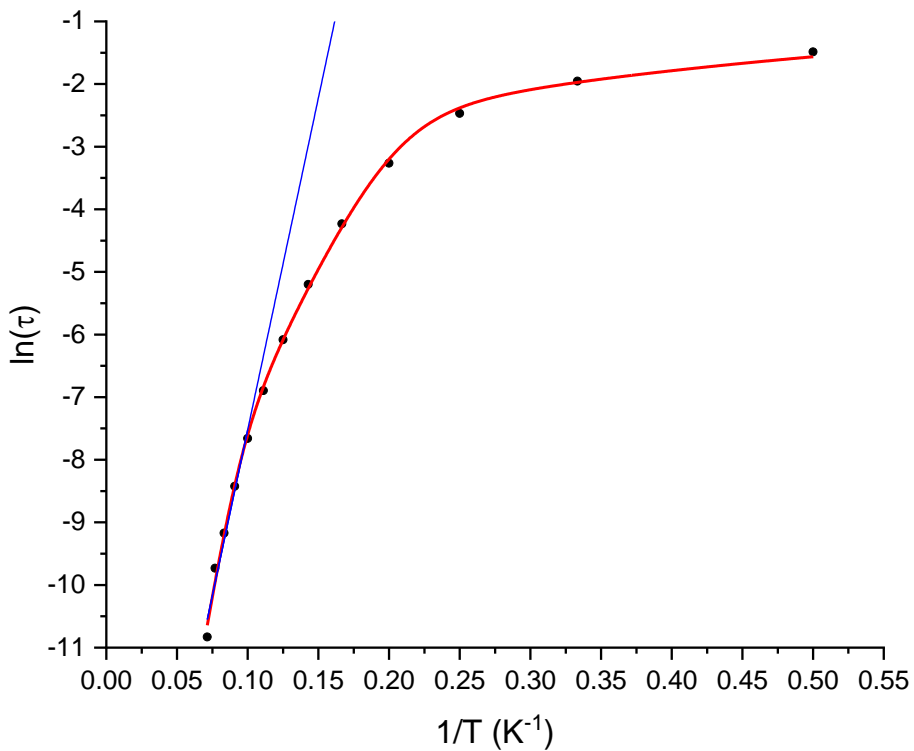


Figure 164. Arrhenius plot of (39-Dy) using the τ values extracted from the Debye fit (black dots). Linear fit corresponding to the Orbach relaxation process (blue) and fit of the relaxation data to equation 13 proposed by Lunghi *et al.*^[142] (red).

5.3.5.2 Gauging the Strength of Halogen-Halogen Interactions

Having established the difference intramolecular interactions can make to the magnetism of relatively simple low-nuclearity systems such as dimers, this section now investigates a way to tune the strength of intermolecular interactions while leaving the molecular structure intact. In fact, halogen bonds provide such an opportunity as the strength of the interaction can be influenced by the variation of the halogen atom. Specifically, the modified H₂opch ligands H₂opch-Br and H₂opch-I seem to be predestined for this as the coordination to the Dy^{III} ions remain the same, whereas the

halogen atoms can be varied in order to modify the packing interactions. This idea was successfully realised in the reactions of $\text{H}_2\text{opch-Br}$ and $\text{H}_2\text{opch-I}$ with $\text{Dy}(\text{NO}_3)_3 \cdot 6\text{H}_2\text{O}$ and Et_3N^+ in acetone resulting in the closely related complexes $[\text{Dy}_2(\text{acetone})_2(\text{NO}_3)_2(\text{opch-Br})_2]$ (**41-Dy**) and $[\text{Dy}_2(\text{acetone})_2(\text{NO}_3)_2(\text{opch-I})_2]$ (**42-Dy**). Both dimers are chelated by their respective Schiff base ligand in the same bridging mode observed for (**38-** and **39-Dy**) with the bridging enolate oxygen atom O(3). The co-ligands in the case of (**41-** and **42-Dy**) are nitrates to balance the charge and acetone as coordinating solvent completing the coordination sphere, resulting in a hula-hoop coordination environment for the Dy^{III} ions (see figure 165).

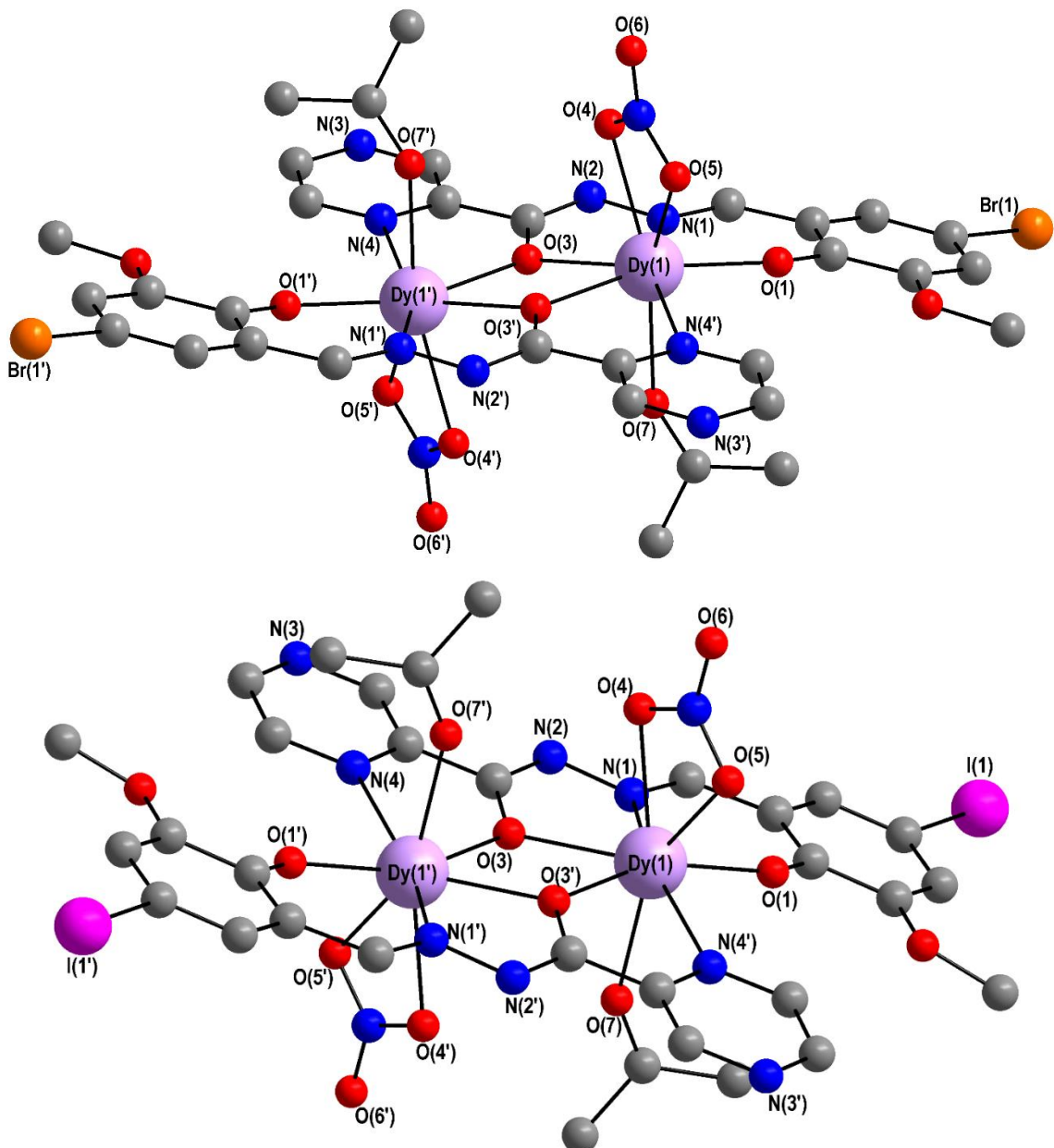


Figure 165. Molecular structures of (41-Dy) (top) and (42-Dy) (bottom).

The packing of both (**41-Dy**) and (**42-Dy**) are shown in figures 166 and 167. Alternating angled stacks of dimers are formed along the crystallographic b axis which are held together by interactions between the lone pair of the uncoordinated oxygen of the nitrate co-ligands and the σ -hole on the halogen atom of a ligand that belongs to a dimer in the neighbouring stack. In (**41-Dy**) the O(6)-Br(1) distances with 4.38(1) \AA are far longer than the combined VdW radii of N and Br (3.4 \AA ^[164]) and it can therefore not be spoken of a halogen bond since any interaction would be incredibly small. Comparing this to the situation in the iodine analogue (**42-Dy**) (see figure 167) in which the O(6)-I(1) distances of 3.199(5) are much shorter than the combined VdW radii of N and I (3.53 \AA ^[164]), it can be concluded that the halogen interactions in (**42-Dy**) are significantly stronger. The angles between C(4)-I(1)...O(6) = 172.0(2) $^\circ$ and N(6)-O(6)...I(1) = 110.9(3) $^\circ$ in (**42-Dy**) classify the interaction as a halogen bond.^[78] As mentioned before the greater polarisability of iodine compared to bromine influences the strength of the interaction present. Although it was shown in previous sections that a direct exchange interaction via halogen bonding is not to be expected, in this particular ligand system because of the lack of direct orbital overlap between the Dy^{III} ions and the halogen bound atoms, the interaction might still change the relaxation behaviour of the two compounds. One way the magnetic properties and particularly the relaxation dynamics may be influenced is by alteration of the vibrational modes responsible for spin-phonon relaxation processes. These combined with tunnelling generally dominate in lanthanide SMMs over thermal relaxation processes. In (**42-Dy**) the vibrational modes are expected to be of higher energy due to the strong intermolecular 3D network. Additionally, the nitrates now form bonds using all three oxygen atoms. This could mitigate the often observed adverse effects of the presence of nitrate on SMM behaviour.

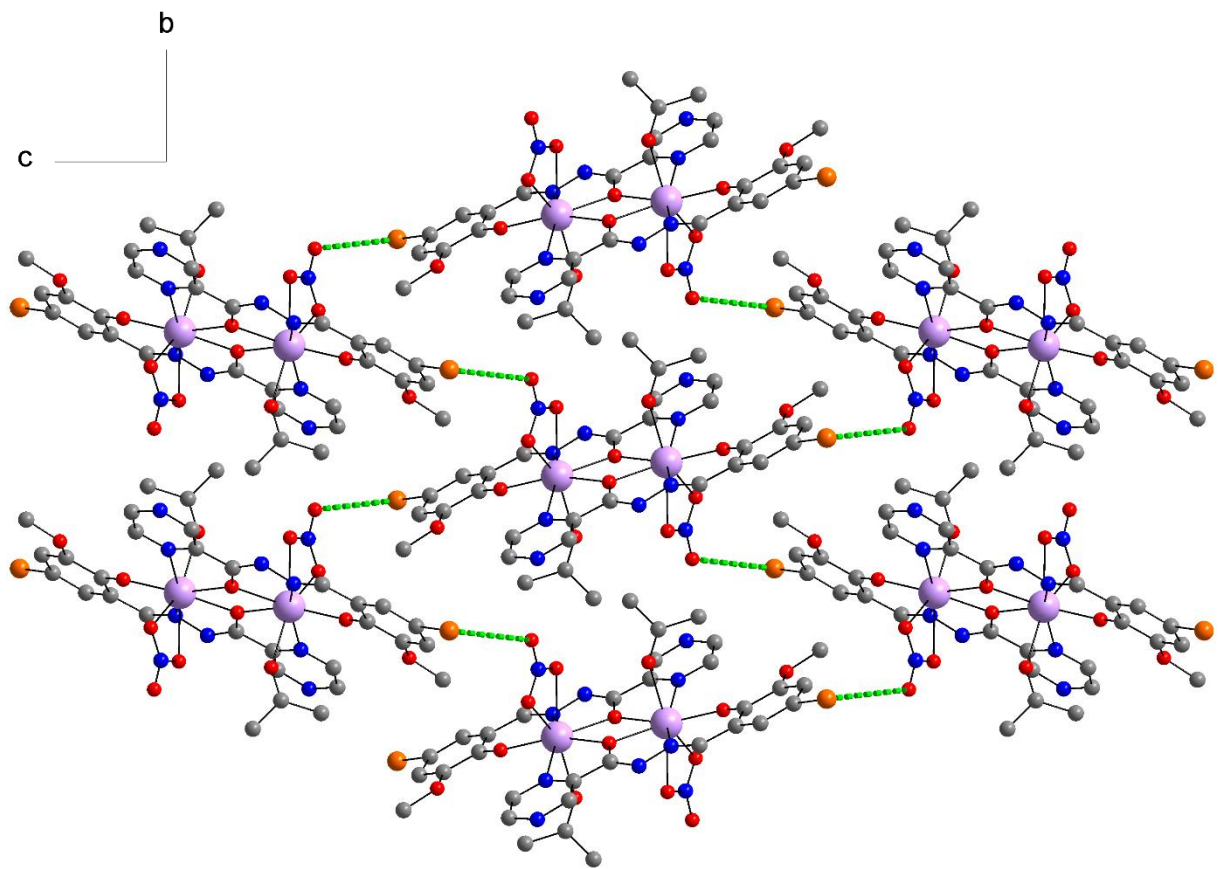


Figure 166. View along the a axis on the packing of (41-Dy) highlighting the weak halogen interactions in green.

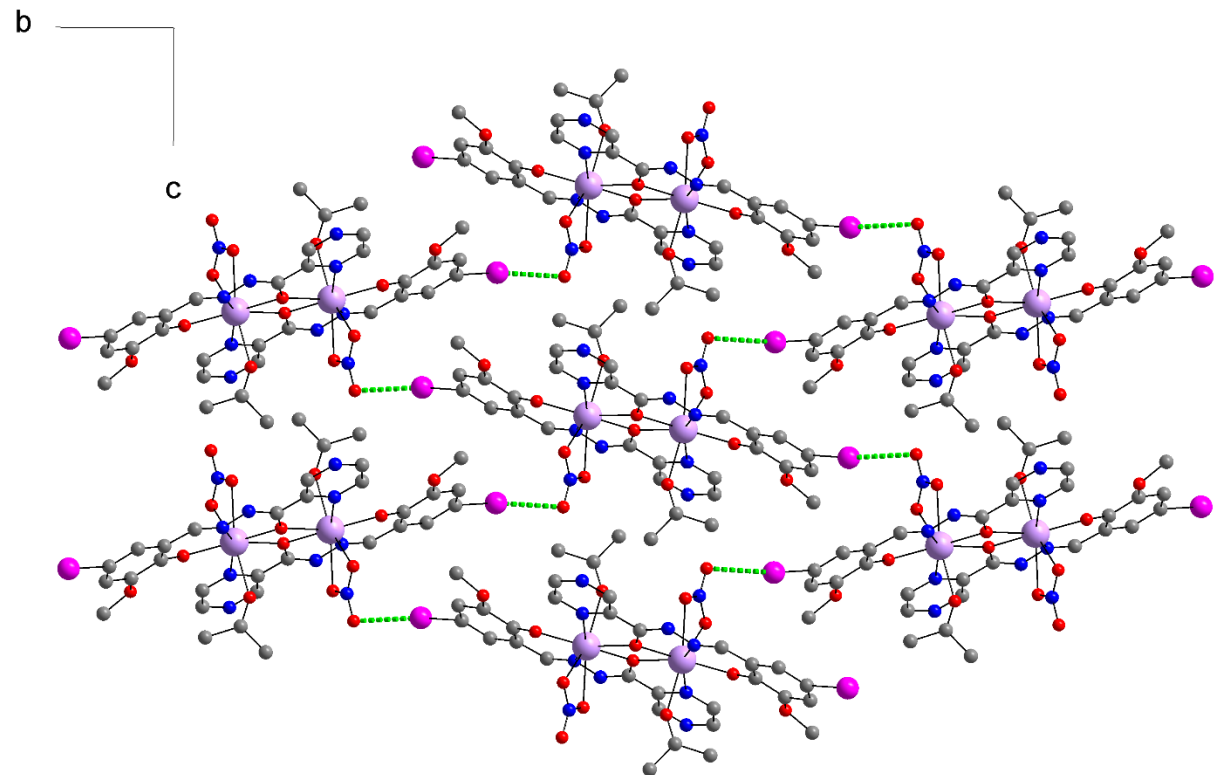


Figure 167. View along the a-axis on the packing of (42-Dy). Strong intermolecular halogen bonds are highlighted in green.

A direct comparison of the magnetic properties of (**41**- and **42-Dy**) is not possible here as the yield of (**42-Dy**) was too low. Nevertheless, the anisotropy axes of both compounds calculated using MAGELLAN (shown in figure 168) and the magnetic behaviour of (**41-Dy**) are comparable with those previously described.

The axes point along the Dy-O_{phenoxy} bond as observed before for dimers with the enolate bridging mode of the opch-type ligands. The Dy-Dy distances of 3.8844(9) Å and 3.8437(8) Å as well as the central Dy-O-Dy angles of 113.9(3)° and 111.9(2)° in (**41-Dy**) and (**42-Dy**), respectively, are in line with the previously presented results. From this a ferromagnetic coupling in both compounds can be expected.

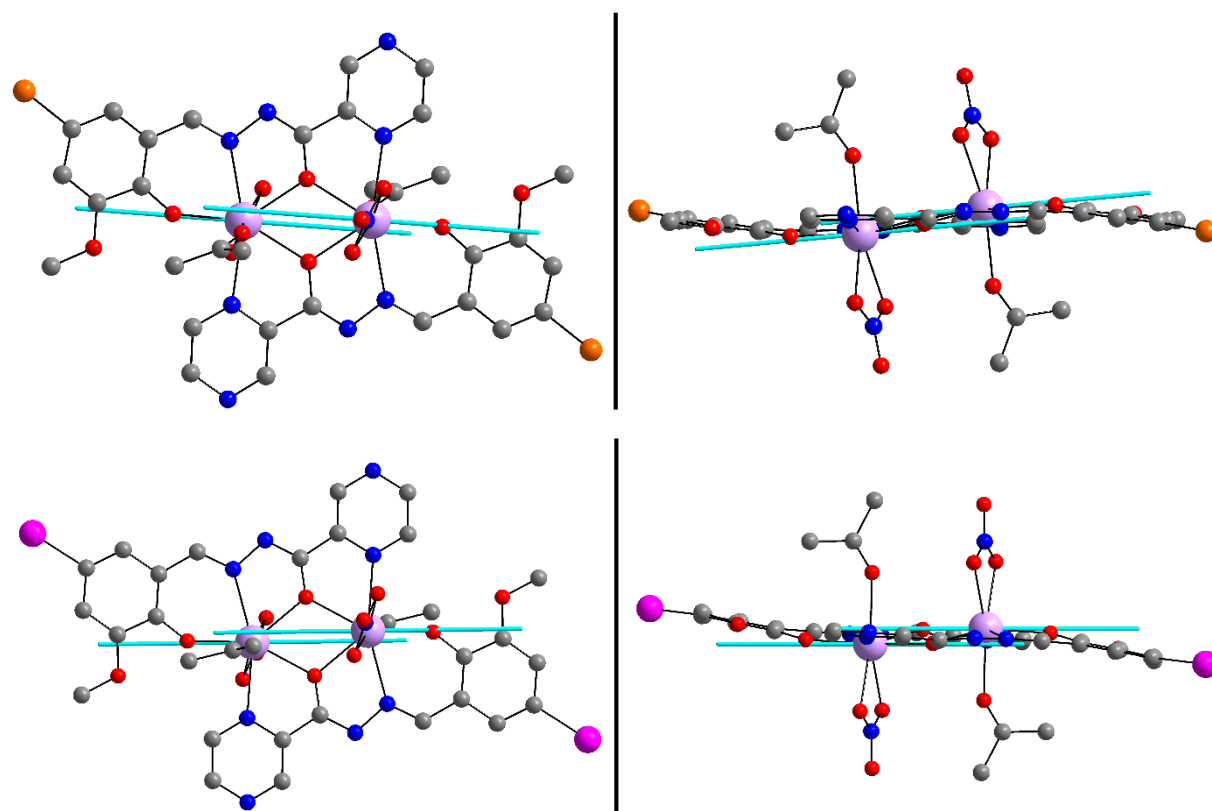


Figure 168. Anisotropy axes calculated with MAGELLAN^[297] for (**41-Dy**) (top) and (**42-Dy**) (bottom).

Indeed, the experimental magnetic data confirm a ferromagnetic interaction for (**41-Dy**) as can be seen from the $\chi_M T$ vs T plot shown in red as well as from the χ_M^{-1} vs T shown in blue in figure 169. The latter follows a Curie-Weiss law in the temperature range between 100 and 280K (as observed before for (**39-Dy**)) and can be fit with a Weiss constant $\theta = 19.4$ K and a Curie constant $C = 30.3 \text{ cm}^3 \text{Kmol}^{-1}$. The $\chi_M T$ curve for (**41-Dy**) roughly follows the same trend as the one for (**39-Dy**) with a RT $\chi_M T$ value of $31.05 \text{ cm}^3 \text{Kmol}^{-1}$ which is in good agreement albeit slightly higher than the theoretical value for two uncoupled Dy^{III} ions, followed by a gradual increase until

reaching a plateau at 100 K. Here, a slight decrease of $\chi_M T$ values with decreasing temperature, which could stem from a superposition of the ferromagnetic coupling with the depopulation of excited states is observed until reaching 35 K where the ferromagnetic coupling appears to outweigh such a depopulation leading to a sharp increase which stops right before the end of the measuring window at 2 K at a $\chi_M T$ value of $49.14 \text{ cm}^3 \text{Kmol}^{-1}$.

These results obtained from the Curie-Weiss fit as well as the $\chi_M T$ curve suggest a weaker ferromagnetic coupling being present in (41-Dy) compared to the one observed in (39-Dy) by comparison of the Weiss constants of 19.4 K and 32.6 K in (41-Dy) and (39-Dy), respectively, as well as the low temperature $\chi_M T$ values of $49.14 \text{ cm}^3 \text{Kmol}^{-1}$ in (41-Dy) and $70.42 \text{ cm}^3 \text{Kmol}^{-1}$ in (39-Dy).

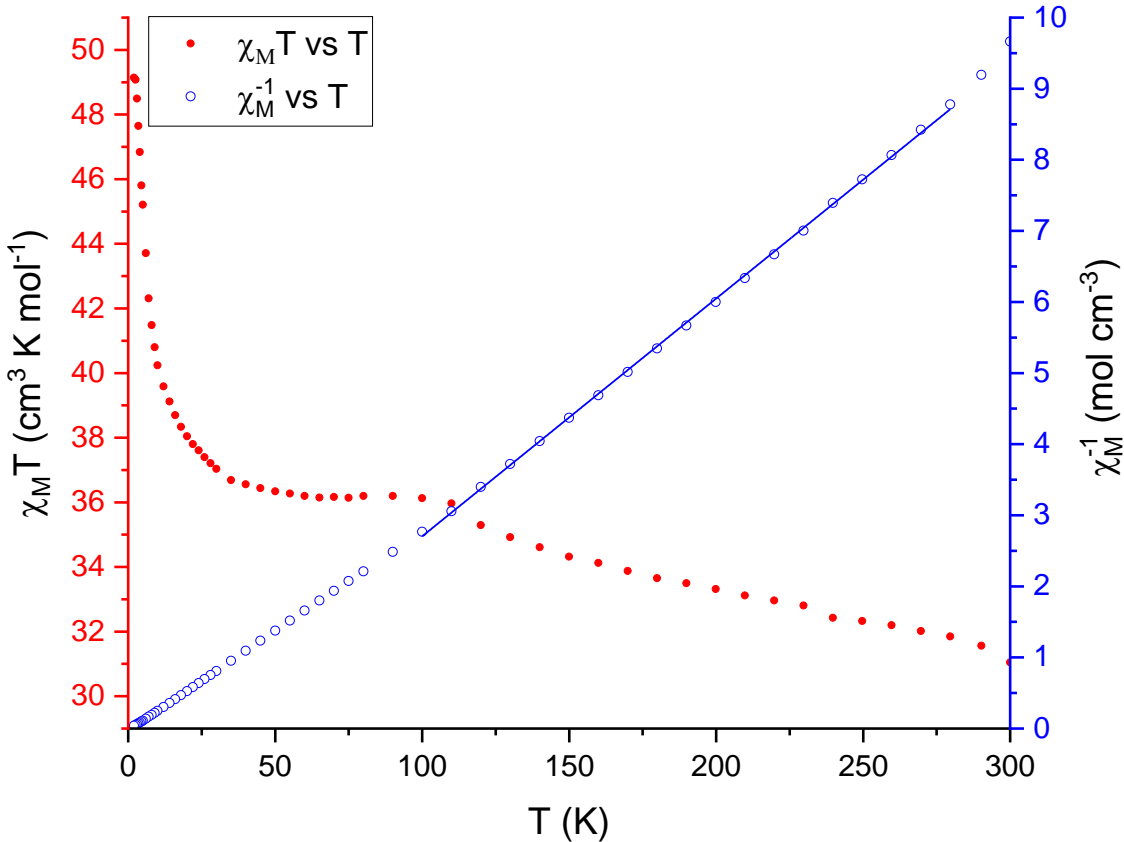


Figure 169. $\chi_M T$ vs T plot (red) and Curie Weiss plot plus fit (blue) of (41-Dy). The $\chi_M T$ vs T plot reveals a ferromagnetic interaction which is confirmed by the linear fit to the χ_M^{-1} vs T plot resulting in a Weiss constant of +19.4K.

The magnetisation measurements at 2, 3 and 5 K on (41-Dy) at dc magnetic fields between 0 and 7 T confirm the similarity of the magnetic behaviour here to the one in (39-Dy) (see figure 170) The same trend with a sharp increase at low fields followed

by an abrupt saturation for the curves at 2 and 3 K at values of $16.3 \mu_B$. At 5 K the saturation happens more gradually and is not completed at 7 T. In the reduced magnetisation the curves at 2 and 3 K superpose very well while the 5 K curve deviates from the others as was observed in (39-Dy). Again, this might be the result of the presence of populated excited states only becoming relevant at temperatures higher than 3 K.

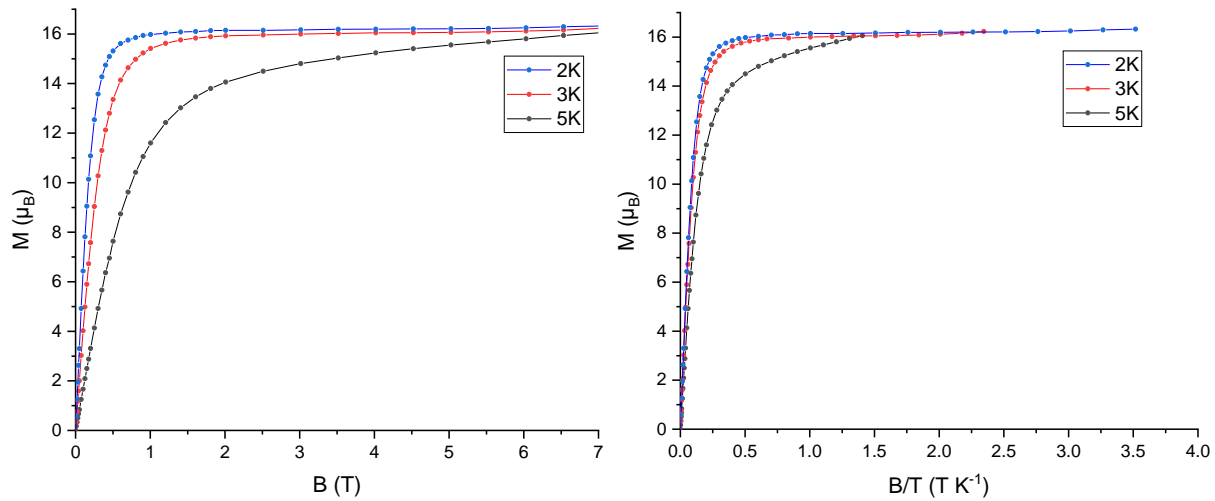


Figure 170. Magnetisation measurements on (41-Dy) at variable fields between 0 and 7 T at 2, 3 and 5 K (left) and reduced magnetisation (right). Lines are guide to the eyes.

Slow relaxation of the magnetisation was observed for (41-Dy) as shown by the ac in- and out-of-phase signals shown in figure 171. χ_M' and χ_M'' were fitted simultaneously using the generalised Debye and the best fits can be seen as lines in figure 171.

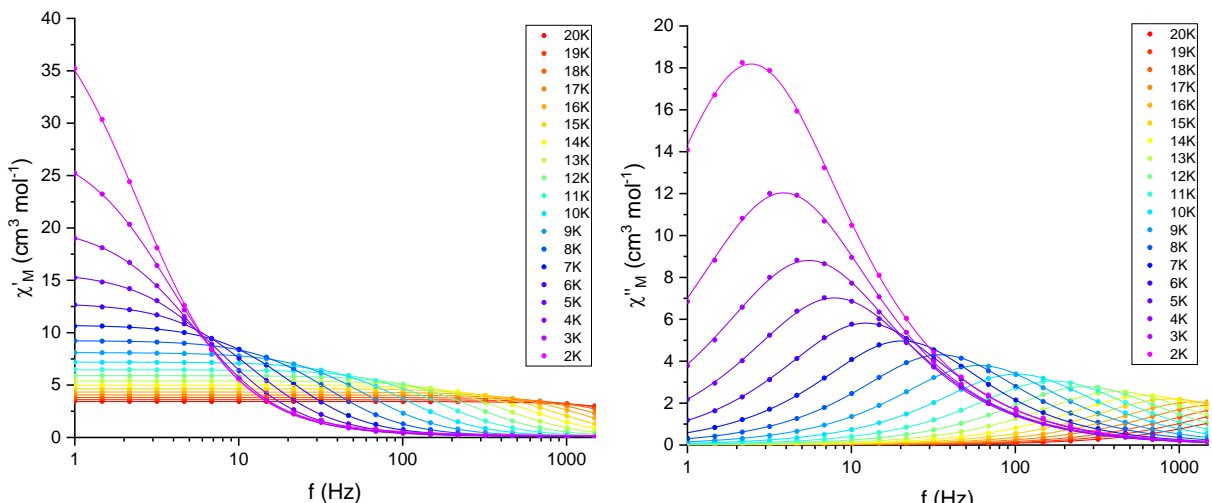


Figure 171. In-phase and out-of-phase ac susceptibility measurements of (41-Dy) between 2 and 20 K and 1 and 1500 Hz. Lines are the best fits to the data points using the Debye model.

The extracted relaxation times were used to produce the Arrhenius plot shown in figure 172. The values for temperatures higher than 15 K were not used as the maxima of these peaks in the out-of-phase susceptibility were not visible leading to the Debye fit being considerably worse. This in turn would affect the fits to the Arrhenius plot. Two fits were done in order to gain insight into the relaxation processes present here. First the high temperature values were linearly fitted corresponding to a pure Orbach process. The energy barrier extracted for the Orbach process $U_{\text{Orbach}} = 64.9$ K and the T_{B100} obtained from calculating the intercept between the linear fit with the value of $\ln(\tau=100\text{s}) = 4.065$ equals 3.8 K. This is consistent with the hysteresis plot at 2 K of (41-Dy) shown in figure 172, in the inset of which, only showing the region near zero-field and zero magnetisation, a weak hysteresis can be seen. This is due to other relaxation processes, that are visible in the Arrhenius plot, resulting in a real T_B below 2 K. Using the fitting function proposed by Lunghi *et al.* (equation 13)^[142] it can be concluded that there is no ZFQTM present in this system as the parameter corresponding to this process converges to zero and is therefore not needed to fit the data. The relaxation processes that dominate in the low temperature region are direct as well as a vibronic Raman relaxation mechanisms. In contrast to (39-Dy) in which Raman was the most relevant rate determining process to relaxation, in (41-Dy) it is the direct processes as indicated by the rather high value of $7.97 \text{ s}^{-1}\text{K}^{-1}$ for A (see table 20). This could be the result of very weak intermolecular Br-NO₃ interactions that increase the energy of acoustic phonons and therefore make them less favoured to provide a relaxation pathway. This also explains why (41-Dy) shows maxima in the ac susceptibility data up to higher temperatures as well as a slightly open hysteresis at 2 K, even though the system has a significantly lower effective energy barrier than that of (39-Dy). This is a result of the direct processes becoming much less relevant at higher temperatures and the Raman process, which takes over in (39-Dy) and provides a fast-track to relaxation, is hindered in (41-Dy).

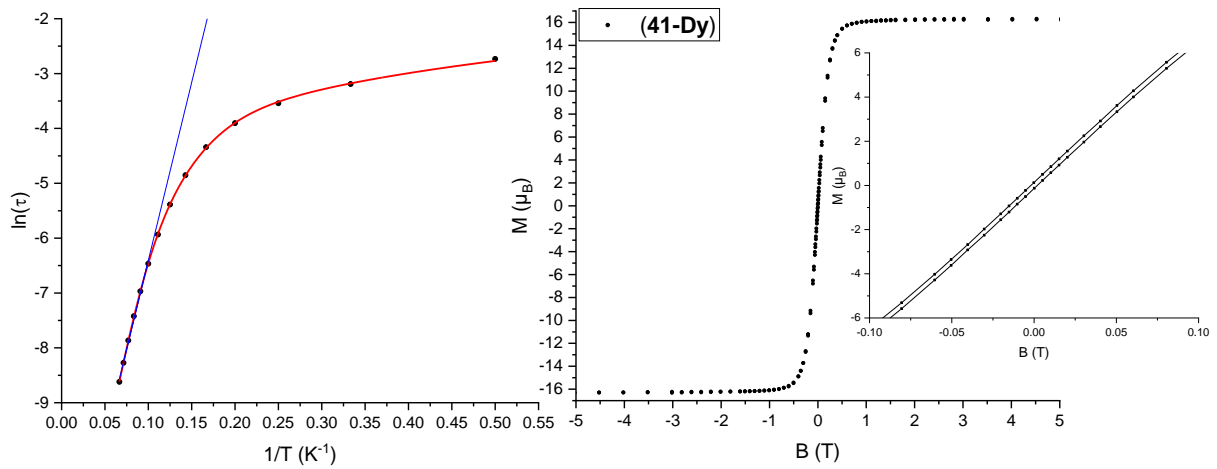


Figure 172. Arrhenius plot (left) (black dots) showing the relaxation dynamics in (41-Dy) between 2 and 15K. Linear fit to the Orbach process shown in blue and the best fit using the more sophisticated fitting method proposed by Lunghi *et al.*^[142] taking other relaxation processes into account shown in red. Hysteresis plot at 2 K for (41-Dy) (right) between -5 and 5 T with the inset showing the very slight hysteresis near zero field. Lines in the inset are guides to the eye.

Table 20. Fitting parameters using equation 13 to fit the relaxation processes in (41-Dy).

A (s$^{-1}$ K$^{-1}$)	B (s$^{-1}$)	V (s$^{-1}$)	w (K)	τ_0 (s)	U (K)
7.97	0	8370	34.0	8.35E-7	84.4

5.4 Summary and Conclusion on Complexes using H₂opch and Modified Ligands

Complexes using H₂opch

Using the same reaction conditions but altering the $\text{Ln}(\text{NO}_3)_3 \cdot x\text{H}_2\text{O}$ salt used as starting material, it was possible to obtain six new structures of complexes with nuclearities between four and eight. Using La^{III}, a carbonate bridged and essentially planar La₅ cluster (**14-La**) was obtained which may have potential application in catalysis. Starting with Ce(NO₃)₃·6H₂O, an almost square Ce₄ cluster (**15-Ce**) was crystallised, which was shown to be mixed valence from SC-XRD, BVS as well as solid state UVVis absorption spectroscopy. It was further shown that (**15-Ce**) is not stable in solution using successive solution state UVVis measurements. In the case of the reaction using Eu^{III} the crystal structure of a carbonate bridged Eu₅ cluster (**16-Eu**) could be identified that, unlike (**14-La**), is not planar as a result of the size difference and the presence of an additional opch²⁻ ligand. A Tb₅ compound isostructural to (**16-Eu**) was observed as a side product in reactions using Tb(NO₃)₃·6H₂O. Similarly, reactions with Dy(NO₃)₃·6H₂O led to two products. As the main product, a carbonate bridged Dy₈ cluster (**21-Dy**) that shows the same structure as one previously reported,^[200] but different packing as well as a Dy₆ cluster (**17-Dy**) as side product. The two clusters can easily be separated mechanically since the former is obtained as red crystals and the latter as yellow crystals.

The magnetic properties of the two Dy₈ clusters, (**21-Dy**) and the one reported by Tang *et al.*,^[200] were compared and it was found that the packing differences, which occur due to the amount and distribution of lattice solvent, do indeed have an effect on the magnetic properties. Whereas the reported compound^[200] shows SMM behaviour without the need to apply a dc field, (**21-Dy**) exhibits more effective zero-field quantum tunnelling and was therefore measured with an applied dc field of 0.175 T. This allows the SMM behaviour to become apparent and the relaxation data could be fitted without the need for an Orbach term. These results were corroborated by microSQUID measurements, performed in collaboration with the group of Prof. Dr. Wolfgang Wernsdorfer, on a fresh sample of the previously reported Dy₈ cluster that was sent from China by Prof. Dr. Jinkui Tang as well as (**21-Dy**). The vertical increase in

magnetisation around zero field that is observed for (**21-Dy**) is proof for the significant ZFQTM present in this compound (see figure 101).

Moreover, carbonate bridged Ln_8 clusters with the same molecular structure as (**21-Dy**) were obtained for Sm^{III} - Er^{III} (with the exception of Eu^{III}). By comparison of the unit cells it was possible to observe a trend in which the triclinic space group obtained for (**21-Dy**) is favoured by larger Ln^{III} ions while the monoclinic space group obtained for the reported Dy_8 ^[200] is favoured by the smaller ions. PXRD measurements, however, revealed that in these samples, in which the triclinic space group was favoured for single crystals, a mixture of both packing versions are present in the bulk sample.

The magnetic properties of the Gd^{III} (**19-Gd**), Tb^{III} (**20-Tb**) and Ho^{III} (**22-Ho**) analogues were investigated using SQUID measurements. While (**22-Ho**) did not show SMM behaviour due to the lack of significant anisotropy, it was possible to obtain maxima in the out-of-phase ac susceptibility measurements on (**20-Tb**) with an applied magnetic dc field of 0.3 T. The Gd_8 cluster (**19-Gd**) exhibits an excellent MCE with a maximum entropy change of $30.22 \text{ J kg}^{-1} \text{ K}^{-1}$, which places it amongst the highest values observed for Gd_8 compounds in the literature. This entropy change, which was calculated using the Maxwell relation, equates to 86.5% of the maximum possible entropy change in this system.

Thus, it can be concluded that the ionic radius of the Ln^{III} ion directs the result of reactions performed under the same conditions. This leads to complexes of nuclearities between four and eight. This also leads to competing reactions, especially in reactions using ions of intermediate size as shown for Tb^{III} which yielded a Tb_5 as well as a Tb_8 compound. This is also observed for Dy^{III} which forms a Dy_6 cluster and two polymorphs of a Dy_8 cluster.

Complexes using Modified Ligands

The successful syntheses of five ligand modifications (H_2oepch , $\text{H}_2\text{opch-NO}_2$, $\text{H}_2\text{opch-Br}$, $\text{H}_2\text{oepch-Br}$ and $\text{H}_2\text{opch-I}$) were confirmed using NMR spectroscopy. Exploration of the complexation behaviour of these modified ligands led to complexes that can be divided into three types. Type I: Carbonate bridged clusters that were formed by the fixation of aerial CO_2 ; Type II: Hydroxo bridged clusters; Type III: dimers.

Structure Type I

Using the sterically more demanding ethoxy version of the H₂opch ligand (H₂oepch) led to the crystallisation of a trigonal prismatic Er^{III} containing complex (**28-Er**) with a core structure very similar to a previously obtained Dy^{III} complex formed with the unmodified H₂opch ligand.^[199] The goal of producing complexes with the same core structure, but inducing intermolecular halogen interactions, was attained in the successful synthesis of (**29-Er**). Using H₂opch-Br, the same trigonal prismatic core structure was obtained, but the addition of a bromine atom to the back of the ligand results in the formation of halogen bonds between Br atoms of neighbouring clusters. These halogen bonds, in which the participating Br atoms act as XB_D and XB_A simultaneously, organise the Er₆ clusters into giant tetrahedral. This increases the symmetry of the obtained space group from P $\bar{1}$ in (**28-Er**) to the tetragonal space group P $\bar{4}2_1c$ in (**29-Er**). This is another example on how the directionality of halogen bonds can be utilised in supramolecular chemistry.

In magnetic measurements on (**28-** and **29-Er**) no difference could be detected between the two clusters and both did not exhibit SMM behaviour. This is likely to be the consequence of a lack of direct orbital overlap between the halogen atoms involved in the halogen bonds and the magnetic Er^{III} centres.^[242] However, the significant difference in symmetry suggests that a difference in SMM behaviour of the Dy^{III} analogues could be expected, since the lattice vibrations responsible for relaxation processes involving phonons would change. In future work, it should be possible to elucidate the connection between intermolecular interactions and phonon-based relaxation mechanisms.

Additionally, the crystal structure of the tetranuclear complex using H₂opch-I (**30-Er**), which resembles an incomplete trigonal prism, led to a proposed mechanism (see figure 125 in section 5.3.3.3) for the formation of such carbonate bridged clusters.

Structure Type II

Dark solutions characteristic of hydroxy bridged mixed-valent cerium complexes, related to the previously mentioned (**15-Ce**), were obtained using all five of the modified ligands. However, it was only possible to obtain solid product for the H₂oepch, H₂opch-Br and H₂opch-I ligands. All of the modified Ce₄ complexes exhibit a broad IVCT band

spanning the whole visible region in solid state UVVis absorption measurements showing subtle differences that will be the subject of future investigations.

Further hydroxy bridged compounds were obtained in the form of the Ln_7 clusters (**34-Nd**) using the ethoxy ligand H_2oepch and (**35-Gd A and B**) as well as (**36-Dy**) using the iodine ligand $\text{H}_2\text{opch-I}$. All show related molecular structures. The packing of the Gd^{III} and Dy^{III} containing compounds is dominated by intermolecular halogen-halogen interactions, whereas (**35-Gd A**) forms supramolecular dimers with halogen-halogen bonds, whilst (**35-Gd B**) and (**36-Dy**) form supramolecular chains *via* type I halogen-halogen interactions. The only difference between the two polymorphs of the Gd_7 cluster is the amount of lattice solvent. This appears to influence the packing of the compounds. Since MCE was observed in similar Gd_7 compounds in the literature,^[269-270] isothermal magnetisation measurements up to temperatures around 10 K will be performed in future in order to gauge whether the halogen bonding has an impact on the entropy change. Magnetic measurements were performed on (**36-Dy**), but no out-of-phase maxima were observed. This is likely due to the lack of symmetry in the compound which results in not well-aligned anisotropy axes of the Dy^{III} ions.

Structure Type III

Through the careful comparison of the structural and magnetic data of the dimeric compounds (**39-Dy**) and (**40-Dy**), which exhibit overall ferro- and antiferromagnetic interactions, respectively, it was possible to propose a simple rule-of-thumb as to when to expect ferromagnetic and when to expect antiferromagnetic dipolar coupling. This is related to the angles made by the parallel anisotropy axes of the Dy^{III} ions to the Dy-Dy vector in such centrosymmetric dimers. When the angle is more obtuse than 54.74° (the magic angle), the dipolar interaction is antiferromagnetic, whereas in the case of a more acute angle the dipolar interaction is ferromagnetic. In the presented dimers this is governed by the bridging mode of the modified H_2opch ligand. In (**39-Dy**) the Dy^{III} ions are bridged by the enolate oxygen of the ligand leading to anisotropy axes which make an acute angle of 11.8° to the Dy-Dy vector, while in (**40-Dy**) the Dy^{III} ions are bridged by the phenoxy oxygens resulting in anisotropy axes almost perpendicular to the Dy-Dy vector (85.6°). Both coordination modes are shown in figure 153. Since the dipolar coupling usually heavily outweighs exchange interactions in such lanthanide dimers, this provides a simple model which can predict the overall observed

magnetic interaction in dimers of the H₂opch ligand family. Comparison with literature known compounds using similar Schiff base ligands having both an enolate as well as phenolate oxygen, confirmed this model to be valid beyond the H₂opch family.

Furthermore, a direct gauging of the strength of halogen interaction is possible shown from the synthesis of two dimers with the same molecular structure and very closely related packing. Compound (**41-Dy**) is formed with the H₂opch-Br ligand while (**42-Dy**) is formed with the H₂opch-I ligand. Halogen interactions using iodine as the XB_D atom instead of bromine are usually expected to provide stronger interaction due to the greater polarisability of iodine (see section 3.3). Indeed, the intermolecular X-N distances in (**42-Dy**) are much shorter than the ones observed for (**41-Dy**). Since the relaxation behaviour of (**41-Dy**) already suggests the inhibition of Raman processes by the formation of an intermolecular halogen-bonded network, the measurement of (**42-Dy**) will be conducted in the future. This could provide a highly sought after pathway to quench Raman processes. This is one of the most pressing current challenges in the development of high-performant SMMs.

6. Systematic Study on Dimeric Semiquinonate Radical Complexes to Investigate Role of Intra- and Intermolecular Interactions on the Magnetic Relaxation Dynamics

6.1 Introduction

Quinones, as mentioned in chapter 4.1, are a class of molecules that can exhibit reversible redox processes and that can stabilise a radical species, the semiquinone radical anion (see figure 173). This property also plays an important role in biological redox processes,^[321-322] such as in photosynthesis in which quinones facilitate redox processes in photosystem II.^[323-325]

Quinones have also been employed in coordination chemistry and were used to produce magnetic materials *via* “the metal-radical approach” as proposed by Gatteschi *et al.* in 1989.^[326] Semiquinone radicals are generally regarded as short-lived organic species that are hard to isolate, but their anionic form was successfully employed in a wide variety of transition metal as well as lanthanide complexes which stabilise the radical redox state.^[327-332] This, as proposed by Gatteschi *et al.* and following the approach of bridging lanthanide centres with a radical, as discussed in chapter 3.4 above, can lead to SMM behaviour and is regarded as one of the routes forward to obtain high-performant SMMs.^[156] This was, for example, shown in a dichlorotetraoxolene-bridged Dy^{III} cluster, which when the ligand is in its closed-shell form does not exhibit SMM behaviour. However, once chemically reduced to the semiquinone radical form, using [CoCp₂] as a one-electron reducing agent, SMM behaviour is switched on.^[333] Similar results were obtained using dibromotetraoxolene as bridging ligand, which in its radical state was shown to reduce ZFQTM and enhance the observed SMM behaviour.^[334]

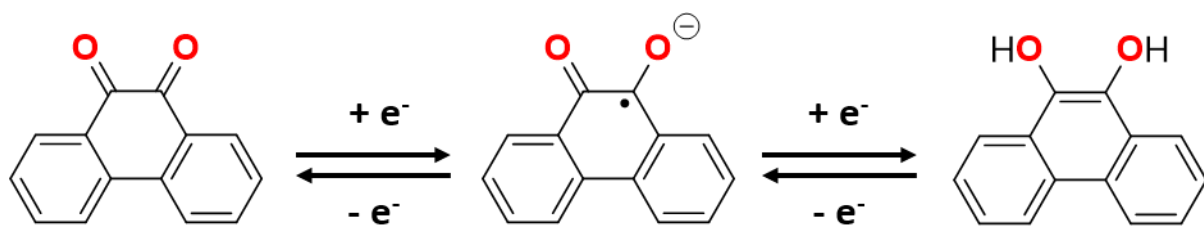


Figure 173. Redox activity of 9,10-phenanthrenequinone (left) showing two possible reversible one-electron reductions to the seqmiquinone radical anion (middle) and the diol form (right).

The three oxidation states of the phenanthrenequinone shown in figure 173 can easily be distinguished from the C-O bond lengths, which are around 1.2 Å for the quinone form,^[335] around 1.3 Å for the semiquinone form^[336] and around 1.4 Å for the diol form.^[335] This useful tool was applied to check the oxidation state of the ligand used in this chapter. 9,10-Phenanthrenequinone was used to form complexes which feature the phenanthrene semiquinonate radical anion which is abbreviated as phsq^{·-} in the following.

This ligand was shown by Eaton to form complexes with transition metals as well as Y^{III} and La^{III} ions using EPR. In the same context, the observation was made that, while the organic radicals decompose quickly in air, once they are coordinated to a metal ion the radical becomes much harder to oxidise.^[337]

Similar results were obtained using optical spectroscopy in order to follow the photochemical properties of phenanthrenequinone. Rennert and co-workers irradiated phenanthredione in ethanol with visible light and observed rapid photoreduction to the diol form, which was shown to be reversible by oxidation with aerial oxygen. Subsequently, they repeated the experiment in the presence of the divalent metal ions Mg^{II}, Ca^{II} and Zn^{II}. This led to the observation of a dark blue-green colour in an intermediate state between the dione and diol forms which could only be observed when these cations were present. This blue-green product was shown to be stable in solution when the irradiation was halted and photoreduction to the diol occurred once it was resumed. Again, this was shown to be a reversible process either by continuous irradiation with light or oxidation by aerial oxygen. They were also able to confirm the blue-green product to be paramagnetic using EPR, thus proving the radical nature of the ligand stabilised by metal ions.^[338] In figure 174 the UVVis absorption spectra of the 9,10-phenanthrenequinone before irradiation (solid line additionally indicated by a red arrow in figure 174), after short irradiation forming the blue-green radical species

(small dashed line and indicated by a blue arrow in figure 174), after complete photoreduction to the diol (bigger dashed line, also indicated by a golden arrow in figure 174) and after re-oxidation in air (biggest dashed line, additionally indicated by a green arrow in figure 174).^[338]

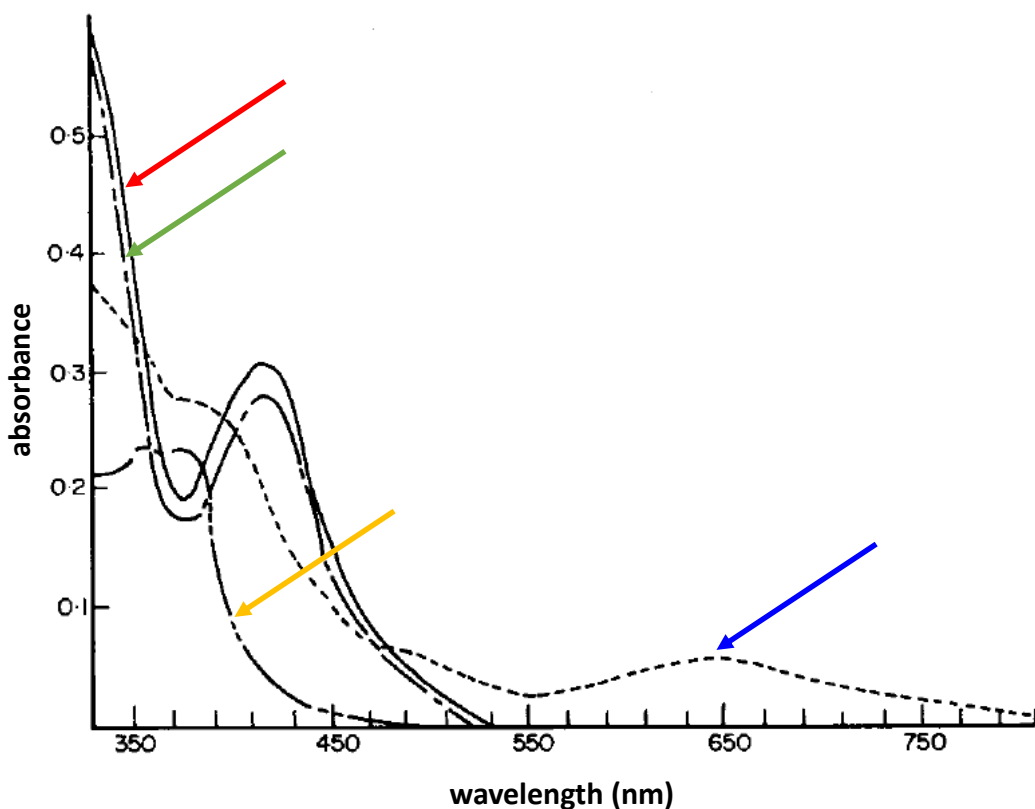


Figure 174. UVVis absorption spectra of 9,10-phenanthrenequinone (red arrow) before irradiation with visible light, after short irradiation with light leading to the blue-green radical intermediate that is stabilised by metal ions (blue arrow), after completed photoreduction to the diol (golden arrow) and after re-oxidation to the 9,10-phenanthrenequinone *via* aerial oxygen (green arrow). Adapted with permission from reference^[338] [John Wiley & Sons] copyright [2008].

In the following sections, complexes that use *in-situ* generated semiquinonate radical anion ligands to coordinate to Ln^{III} ions are discussed. In contrast to the approach presented in section 3.4, which uses radicals to induce strong exchange interactions between Ln^{III} ions, the radicals serve a different purpose here. The archetypal complex (see figure 175 for the molecular structure) $[\text{Dy}_2(\text{phsq})_4(\text{NO}_3)_2(\text{MeOH})_2]$ was first accidentally obtained by the then PhD student Dr. Thomas Kriese in the Powell group in 2015. Since this was almost a decade ago and multiple PhD students have worked on this long-term project, it is important to outline the preliminary results which inspired the further work described in this thesis.

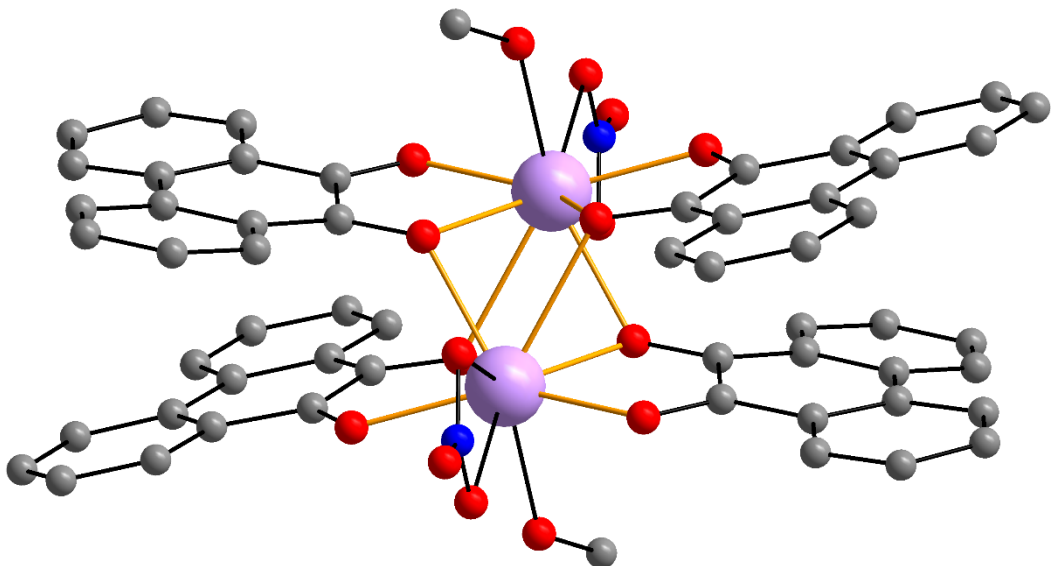


Figure 175. Molecular structure of the archetype complex $[\text{Dy}_2(\text{phsq})_4(\text{NO}_3)_2(\text{MeOH})_2]$.

The complex consists of two Dy^{III} ions that are coordinated by four phenanthrene-based ligands which were shown to be in their semiquinonate radical anion state phsq^- and form what can be described as a “biplane” motif with one bridging and one non-bridging oxygen each. Additionally, the Dy^{III} ions are chelated by one anionic nitrate and one neutral MeOH co-ligand each. The π systems on either side of the two Dy^{III} ions are in close proximity to each other, suggesting strong π - π interactions that might be assisted by radical-radical interactions. This seemingly strong interaction between the radical ligands forces the Dy^{III} ions to be close together as well ($d(\text{Dy-Dy}) = 3.34 \text{ \AA}$).

Dr. Thomas Kriese additionally reported the crystal structures of the Y^{III} , Sm^{III} , Eu^{III} , Gd^{III} , Tb^{III} , Ho^{III} , Er^{III} , Yb^{III} and Lu^{III} analogues of this complex as well as a variation in which the nitrate anion was exchanged for a chloride as well as a further variation which has six radical ligands.^[33]

After the departure of Dr. Thomas Kriese from the working group, the then PhD student Dr. Anthony Blue Carter inherited the project. The synthetic method by which Dr. Thomas Kriese obtained these complexes proved unreliable since it relied on irradiation with sunlight, which naturally is not a constant nor controllable factor. Much of the synthetic work of Dr. Anthony Blue Carter was therefore focussed on the development of a reliable synthetic method. This was successful since reactions performed in Teflon lined steel autoclaves reproducibly led to the desired complex. In-depth magnetic studies were performed especially on the Dy^{III} -, the Gd^{III} - and the Y^{III} -analogue of this complex.^[32] Additionally, theoretical calculations were performed by

Dr. Tilmann Bodenstein from the group of Prof. Dr. Karin Fink (INT, KIT) that revealed an exceedingly strong radical-radical coupling of 76 kJ/mol on either side of the two Dy^{III} ions. Since the radical are so strongly coupled this explained the diamagnetism of the Y^{III} ion containing dimer which persists even at RT. It also explains the virtual lack of coupling between the Ln^{III} ion and the radical. Furthermore, the Ln^{III}-Ln^{III} exchange coupling was obtained as -0.05 cm⁻¹ in the case of the Gd^{III} dimer. This leaves only dipolar coupling as a possible magnetic interaction pathway between the two lanthanide ions.

From the anisotropy axes that were calculated by Dr. Tilmann Bodenstein and Prof. Dr. Karin Fink for the Dy^{III} complex, it can be concluded that the dipolar interaction must be antiferromagnetic, since the axes are essentially orthogonal to the Dy-Dy vector. This is in line with the experimentally observed magnetic behaviour. For the Dy^{III} analogue slow relaxation of magnetisation with maxima in the out-of-phase susceptibility data was observed up to 18 K. Fitting $\ln(\tau)$ vs $1/T$ curve, resulting from the Debye fit, to equation 13, the relaxation processes could be analysed. It was observed that ZFQTM is effectively quenched in this system. In order to investigate the origin of the quenching of ZFQTM an Y-doped sample was produced by Dr. Anthony Blue Carter by using 90% diamagnetic $\text{Y}(\text{NO}_3)_3 \cdot 6\text{H}_2\text{O}$ and 10% paramagnetic $\text{Dy}(\text{NO}_3)_3 \cdot 6\text{H}_2\text{O}$ starting material. This resulted in a bulk material in which the majority consists of the entirely diamagnetic dimer which is silent in magnetic measurements, with an intermediate amount of the desired Dy-Y mixed compound and small amounts of the Dy^{III} dimer. The magnetic signature of the latter is known and could therefore be distinguished from the one of the desired mixed-metal complex. Interestingly, the Dy-Y doped sample did show significant ZFQTM. This leads to the conclusion that the quenching of ZFQTM is a result of a synergetic effect between the two Dy^{III} ions.^[32]

Therefore, in order to gain further insight into this, microSQUID measurements were conducted on the Dy^{III} dimer as well as on the Dy-Y doped sample in collaboration with the group of Prof. Dr. Wolfgang Wernsdorfer. The results are shown in figure 176 and paint the same picture of quenched ZFQTM in the archetype Dy^{III} complex which is “switched” on by removing one of the two Dy^{III} ions. Furthermore, it is observed that the antiferromagnetic ground state of the Dy^{III} dimer persists up to a field of 0.3 T.

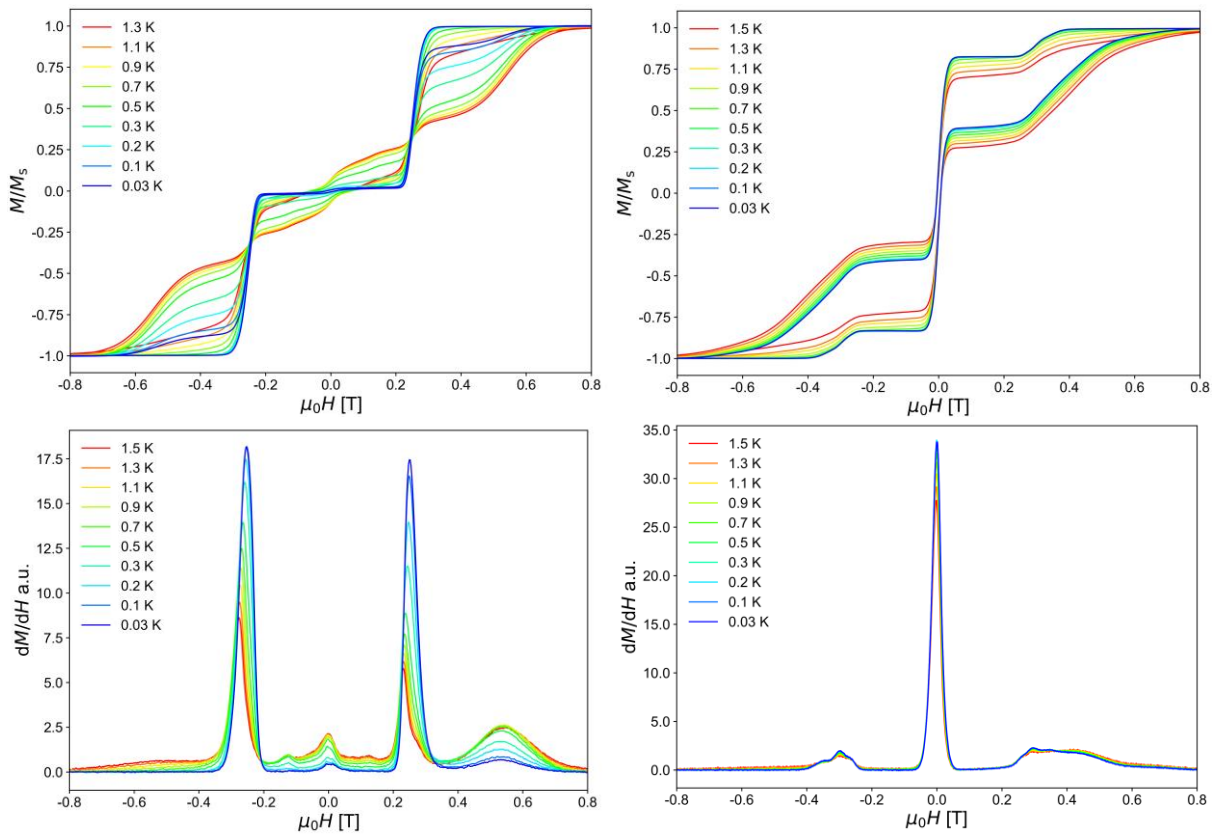


Figure 176. MicroSQUID measurements performed on single crystals of the archetype Dy^{III} dimer (left) as well as on the Y-doped sample (right) prepared by Dr. Anthony Blue Carter^[32] showing the quenching of ZFQTM in the former and the presence of ZFQTM in the latter.

These results are presented in a manuscript that is close to submission to the Journal of the American Chemical Society (JACS), with myself as a co-author, due to my involvement in the project as a Master student under the supervision of Dr. Anthony Blue Carter and my continuation of the project after his departure from the Powell working group.^[339]

The results of my Master thesis, which can also be found in the doctoral thesis of my then supervisor Dr. Anthony Blue Carter, include the optimisation of the reaction conditions of the synthesis of the archetype Dy^{III} dimer as well as the reproduction of other members of the lanthanide series, which were previously obtained by Dr. Thomas Kriese and expanding this series of complexes by further new analogues.

6.2 Further Analysis of the Archetype Complexes [Ln₂(phsq)₄(NO₃)₂(MeOH)₂]

Using the reaction conditions that were optimised in the context of the results presented in my Master thesis [Ln₂(phsq)₄(NO₃)₂(MeOH)₂] with (Ln = Nd^{III}-Lu^{III} and Y^{III}) (**43-Nd**), (**44-Sm**), (**45-Eu**), (**46-Gd**), (**47-Tb**), (**48-Dy**), (**49-Ho**), (**50-Er**), (**51-Tm**), (**52-Yb**), (**53-Lu**) and (**54-Y**) were reproduced as could be confirmed by comparing IR spectra to ones previously obtained of the same compounds. Furthermore, doped versions using 10% Dy(NO₃)₃·6H₂O and 90% Lu(NO₃)₃·6H₂O (**55-DyLu**) or 90% Gd(NO₃)₃·6H₂O (**56-DyGd**) as starting material were synthesised. Additional magnetic measurements on the lanthanide variations (**45-Eu**) and (**47-Tb**) as well as investigation of the properties of these archetypal complexes in solution were carried out and are described in the following sections.

6.2.1 Magnetic Measurements on Further Ln^{III} Analogues

As mentioned above the magnetic properties of (**46-Gd**), (**48-Dy**), (**50-Er**) and (**54-Y**) were already explored during the doctoral work of either Dr. Thomas Kriese or Dr. Anthony Blue Carter. Here, the magnetic behaviours of (**45-Eu**) and (**47-Tb**) were explored.

Eu^{III} is a lanthanide ion that is usually not viewed as particularly magnetically interesting since it has a J = 0 ground state which can be described with the term symbol ⁷F₀. As mentioned above the radicals also appear not to directly contribute to the observed magnetism as shown by the diamagnetic behaviour of the Y^{III}-analogue which persists even to RT. This was explained using theoretical calculations which predict an extremely strong coupling between the two radicals to either side of the two metal ions resulting in diamagnetism. The first excited state of Eu^{III} compounds is usually separated from the ground state by 300 -350 cm⁻¹ [283, 340-342]. Therefore, the only magnetic signal expected for (**45-Eu**) at RT would be the partial thermal population of the magnetic excited ⁷F₁ state.

In figure 177 the $\chi_M T$ vs T and χ_M^{-1} vs T plots for (**45-Eu**) are shown. The RT $\chi_M T$ value of 2.88 cm³Kmol⁻¹ indeed suggests thermal population of the excited ⁷F₁ state and/or

out-of-state mixing of this magnetic state with the ground state. On reducing the temperature, the $\chi_M T$ monotonically decreases essentially reaching 0 at 1.8 K which suggests that the Eu^{III} ions are now in their non-magnetic ground state. This is in line with the magnetic behaviour of other Eu^{III} compounds in the literature.^[340-343]

The χ_M^{-1} vs T plot follows a Curie-Weiss law between 150 and 300 K and can be fitted with a Weiss constant θ of -235.1 K and a Curie constant $C = 5.15 \text{ cm}^3 \text{Kmol}^{-1}$ suggesting significant antiferromagnetic coupling between the magnetic 7F_1 states of both Eu^{III} ions in the dimer at temperatures above 150 K.

Due to the non-magnetic nature of the 7F_0 ground state and the high percentage of population of it, it is not surprising that no out-of-phase signal is observed in ac susceptibility measurements.

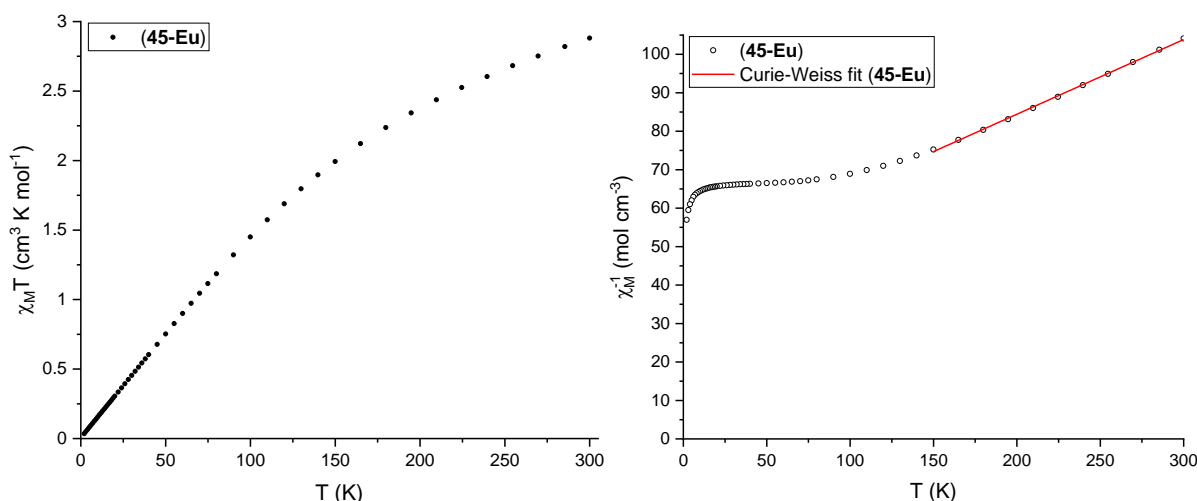


Figure 177. $\chi_M T$ vs T plot of (45-Eu) (left) showing thermal population of the 7F_1 state and Curie-Weiss plot and fit of (45-Eu) (right).

(47-Tb) was subjected to susceptibility measurements at temperatures between 1.8 and 300 K with an applied dc magnetic field of 0.1 T (figure 178). The RT $\chi_M T$ value of $21.63 \text{ cm}^3 \text{Kmol}^{-1}$ is in good agreement with the theoretical value of $23.64 \text{ cm}^3 \text{Kmol}^{-1}$ for two uncoupled Tb^{III} ions.^[283] The $\chi_M T$ value decreases monotonically with decreasing temperature, first slowly until reaching a temperature of 40 K below which the decrease becomes steeper leading to a minimum value of $14.89 \text{ cm}^3 \text{Kmol}^{-1}$ at 1.8 K. The Curie-Weiss plot follows the Curie-Weiss law for the whole measured temperature range and can be fitted with a Weiss constant of -3.5 K indicating antiferromagnetic coupling consistent with other Ln-analogues of this complex as well as a Curie constant of $21.74 \text{ cm}^3 \text{Kmol}^{-1}$.

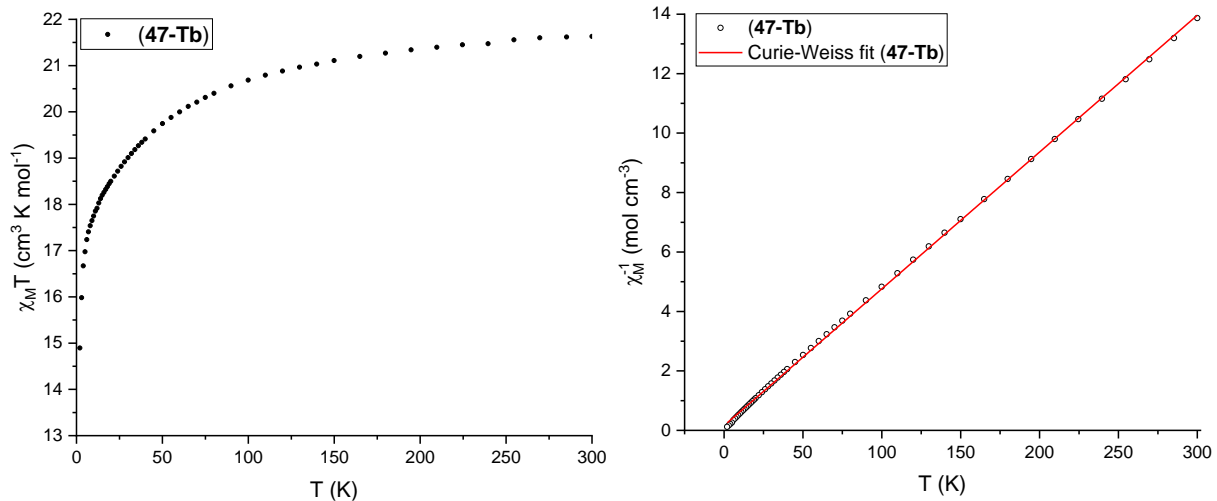


Figure 178. $\chi_M T$ vs T plot of **(47-Tb)** (left) and Curie-Weiss plot and fit (right).

For **(47-Tb)** ac out-of-phase signals could be detected using an applied dc field of 0.28 T to quench ZFQTM (figure 179). This is a significant difference to the Dy^{III} analogue which was investigated in detail by Dr. Anthony Blue Carter [32] in which ZFQTM on one of the Dy^{III} ions was quenched by the dipolar field of the other due to the extraordinarily short Dy-Dy distance.^[339] The fact that ZFQTM is present in **(47-Tb)**, although the Tb-Tb distance of 3.3370(3) Å is comparable to the one in the Dy^{III} analogue,^[31] suggests that the non-degenerate ground states of the non-Kramers ion Tb^{III} allows for tunnelling in this system. At an applied field of 0.28 T there is one set of maxima around 1 Hz and the onset of a second set of maxima can be seen, however with relaxation faster than the measuring window up to 1500 Hz. Therefore, it can be concluded that in addition to the ZFQTM that is removed by application of a dc field there are further relaxation processes with different rates present in this field-induced SMM.

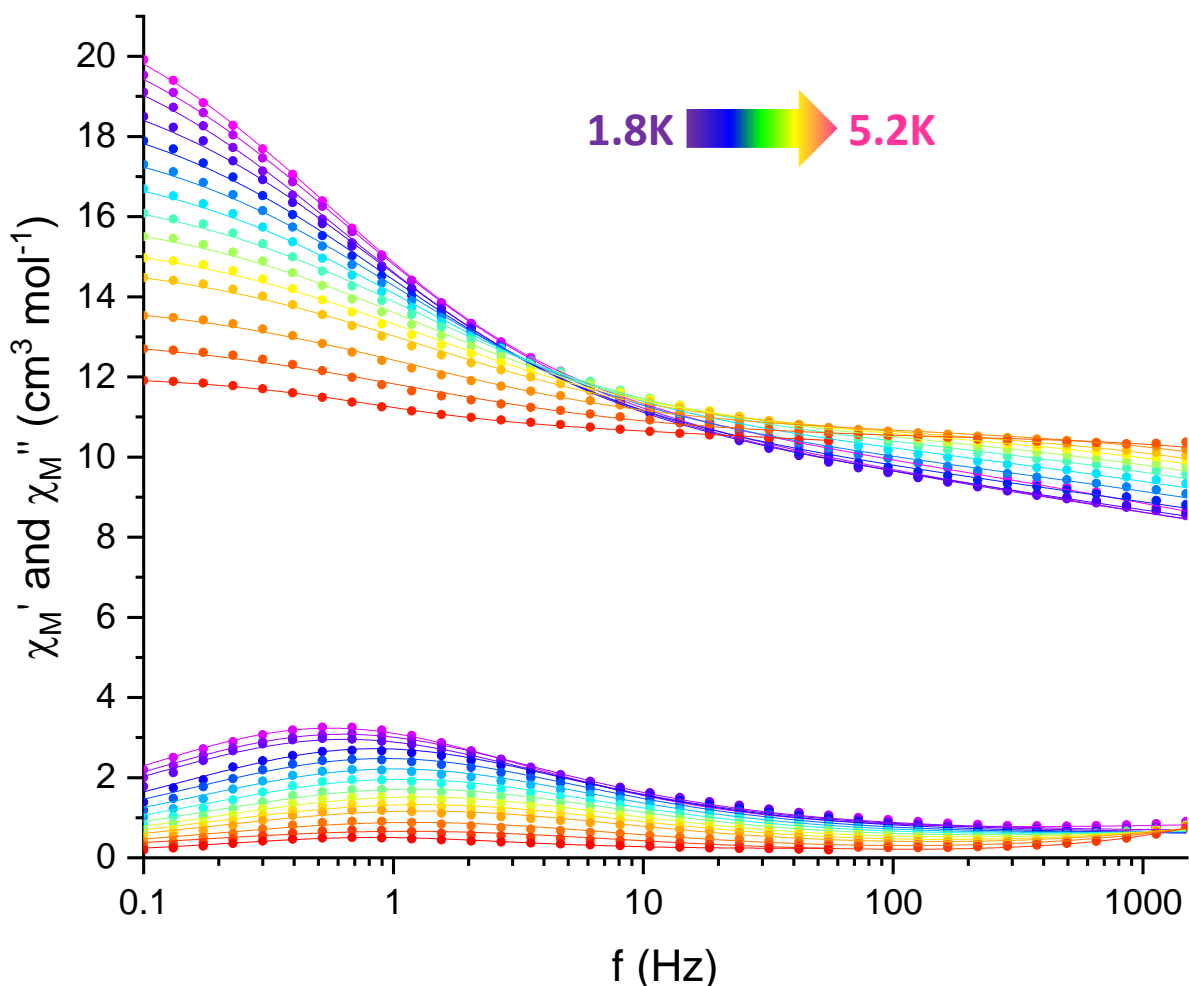


Figure 179. In-phase (top) and out-of-phase (bottom) ac susceptibility vs frequency measured on (47-Tb) at temperatures between 1.8 K and 5.2 K with an applied dc field of 0.28 T. Lines are the best fit to the Debye model accounting for two sets of maxima.

6.2.2 Solution State Behaviour of $[\text{Ln}_2(\text{phsq})_4(\text{NO}_3)_2(\text{MeOH})_2]$

In order to study the behaviour of these complexes in solution, work under meticulous exclusion of oxygen was necessary due to the rapid discolouration of the dark green or blue, depending on the solvent, solutions in air. This is shown in figure 180 with photographs of the same vial before heating the reaction mixture, after completion of the reaction and after opening the vial up to air.^[31] In order to conduct these experiments under inert atmosphere a Networking Grant by the Karlsruhe House of Young Scientists (KHYS) made it possible to finance a two week stay in the labs of Dr. Joy Farnaby (University of Glasgow) who is an expert on optical properties of air sensitive lanthanide compounds and has worked on similar systems in the past.

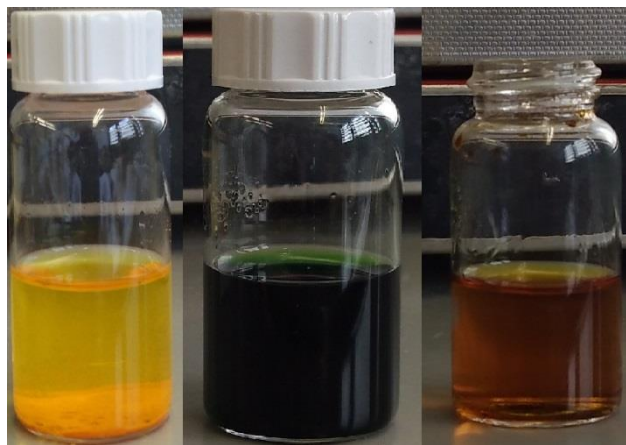


Figure 180. Reaction vials showing the reaction mixture before heating (left), the dark green colour of the methanolic reaction solution after completion of the reaction (middle) as well as the discolouration of the dark solution in air (right).^[31-32]

To understand the optical properties of the complexes in solution and identify the oxidation product after reaction with O₂, the UVVis absorption spectrum of the organic starting material (commercial 9,10-phenanthrenequinone) was recorded in diluted MeCN solution between 210 and 800 nm for later comparison (figure 181). In the UV region a band at 265 nm with a shoulder at 257 nm can be observed. Additionally, two further bands at 319 and 411 nm can be seen in the visible region.

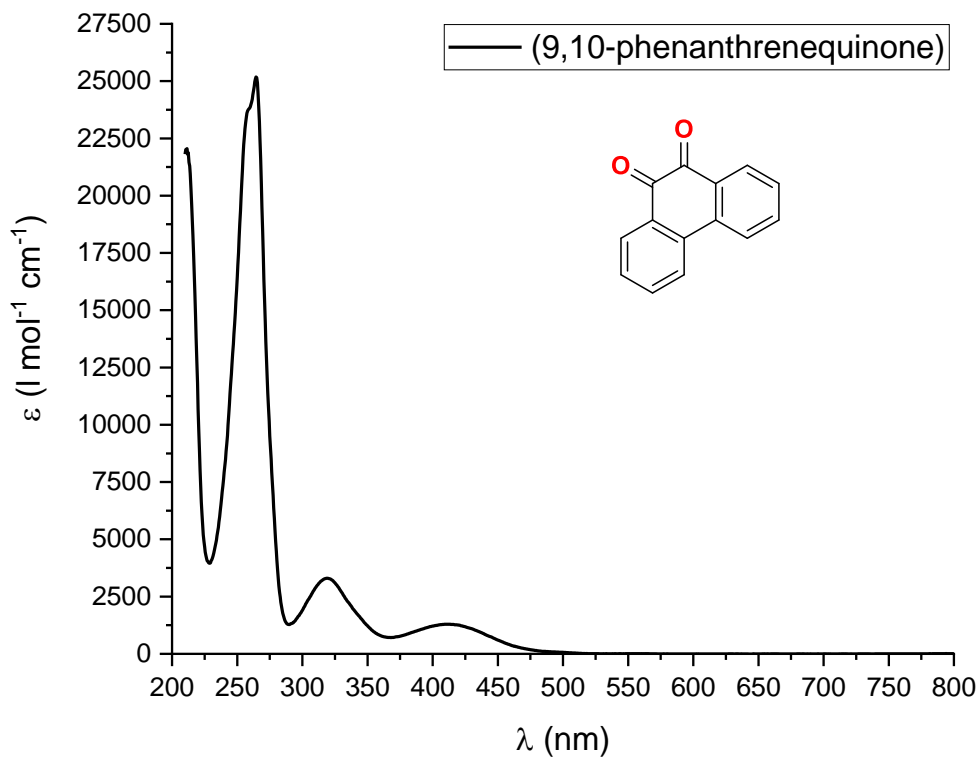


Figure 181. UVVis absorption spectrum of a 10 μM MeCN solution of the commercially obtained starting material 9,10-phenanthrenequinone.

During the reaction the ligand is reduced to give the 9,10-phenanthrenesemiquinonate radical anion. This was confirmed using the C-O bond lengths obtained using SC-XRD measurements. Therefore, a reference UVVis spectrum for this radical species was measured for comparison with the complex spectra as well. In order to obtain this reference spectrum cobaltocene was used as a one electron reductant to produce the cobaltocenium salt of the semiquinone radical $[\text{CoCp}_2^+](\text{phsq}^-)$, a procedure that was used by Farnaby *et al.* to produce the semiquinone radical species of a similar ligand.^[344] The formation of the desired compound was confirmed by a simulation of the spectrum obtained from EPR spectroscopy in collaboration with Dr. Stephen Sproules (University of Glasgow) (see figure 182).

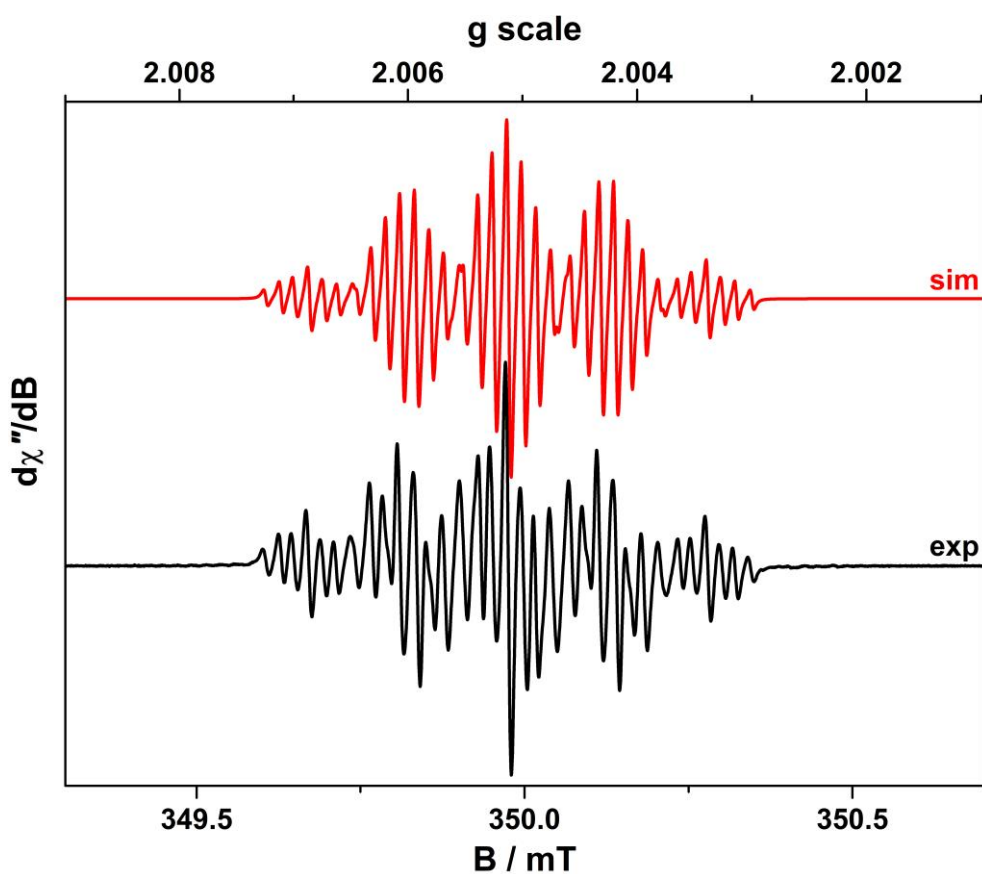


Figure 182. Simulated and experimental EPR spectra confirming the synthesis of $[\text{CoCp}_2](\text{phsq})$.

The UVVis absorption spectrum of the cobaltocenium salt of the radical ligand present in the final complexes was investigated by dissolving $[\text{CoCp}_2](\text{phsq})$ in dry MeCN in a glove box. The dark purple stock solution was diluted to give a 10 μM solution which was filled into an air tight screw top cuvette. Five bands are visible between 200 and 800 nm (see figure 183). The most intense excitation at 263 nm occurs at the same energy as in the oxidised dione-form of the ligand. Additional features are observed in

the region between 300 and 400 nm compared to the starting material which are likely an overlap of excitations of the $[\text{CoCp}_2]^+$ unit and the radical ligand since cobaltocene shows absorption bands at 322 and 370 nm.^[345] A new broad band at lower energies centred around a wavelength of 518 nm is responsible for the dark colour of the solution and can be assigned to $\pi \rightarrow \pi^*$ transitions within the phsq^{·-} as also observed in the literature.^[332, 344, 346]

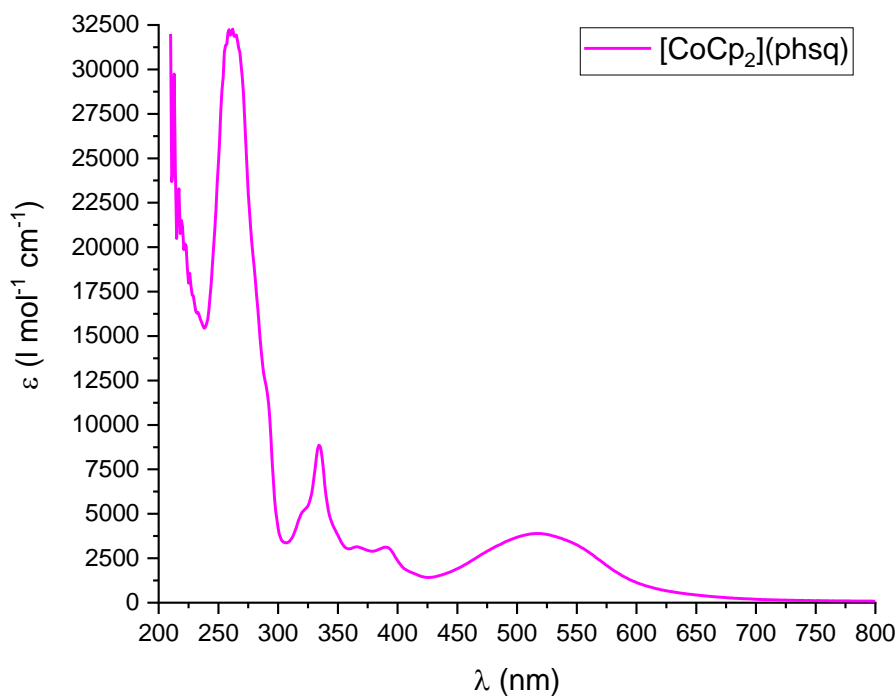


Figure 183. UVVis absorption spectrum of a 10 μM solution of $[\text{CoCp}_2](\text{phsq})$ in MeCN between 200 and 800 nm.

Subsequently, the decomposition of $[\text{CoCp}_2](\text{phsq})$ in air was investigated by measuring the UVVis absorption spectrum of $[\text{CoCp}_2](\text{phsq})$ repeatedly after removing the screw top of the cuvette. One measurement with the parameters that were chosen takes 90 s and the machine takes about 10 s to reset. Therefore, the spectra shown in figure 184 were measured with a time delay of *circa* 100 s. Within about 15 minutes the UVVis spectrum of 9,10-phenanthrenedione is reproduced confirming the oxidation of the radical species back to the dione-form in air.

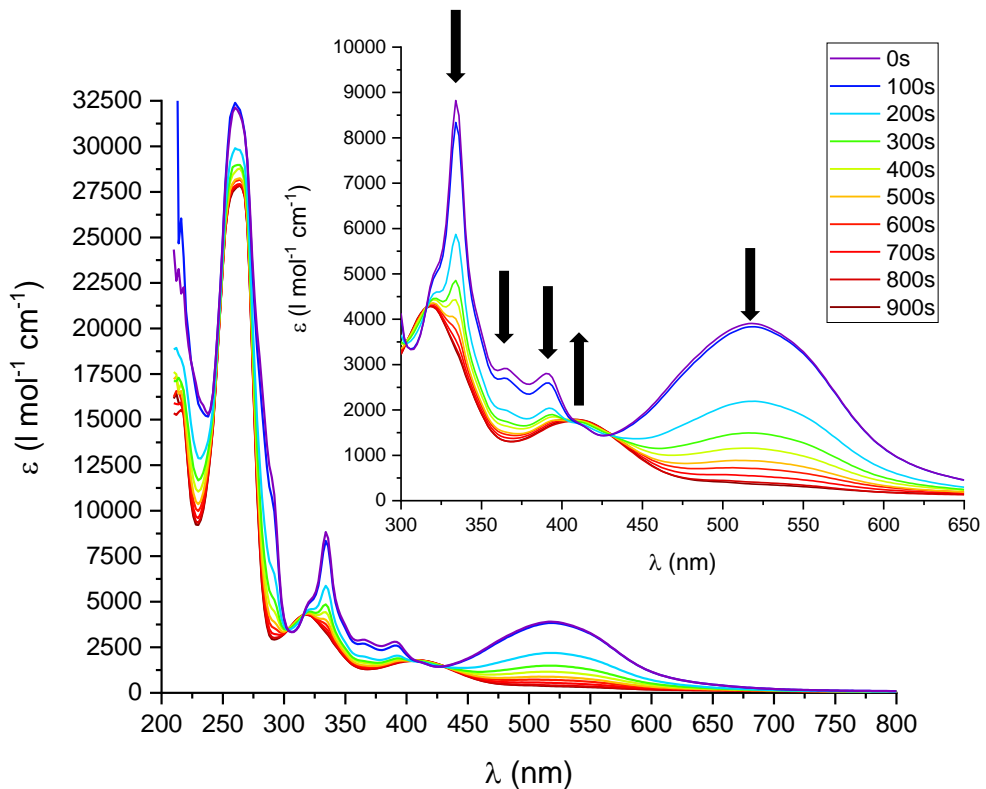


Figure 184. Decomposition of $[\text{CoCp}_2](\text{phsq})$ in air as shown by successive UVVis absorption spectroscopy measurements. After about 15 minutes the spectrum of the dione-starting material is reproduced.

Having established the reference spectra, MeCN solutions of **(48-Dy)** and **(49-Ho)** were produced and diluted in the same way as for $[\text{CoCp}_2](\text{phsq})$. Then the optical properties of the blue solutions (see figure 185) were investigated. Both compounds show five bands in the UVVis absorption spectra with two in the UV region, two between 350 and 400 nm and a broad band at 630 nm which is responsible for the dark colour. This low energy band corresponds to the band at 518 nm observed in $[\text{CoCp}_2](\text{phsq})$ but in the case of **(48-Dy)** and **(49-Ho)**, since the radicals are now coordinated to a metal ion, it is specified as an inter-ligand charge transfer (ILCT) band.^[332, 344, 346]

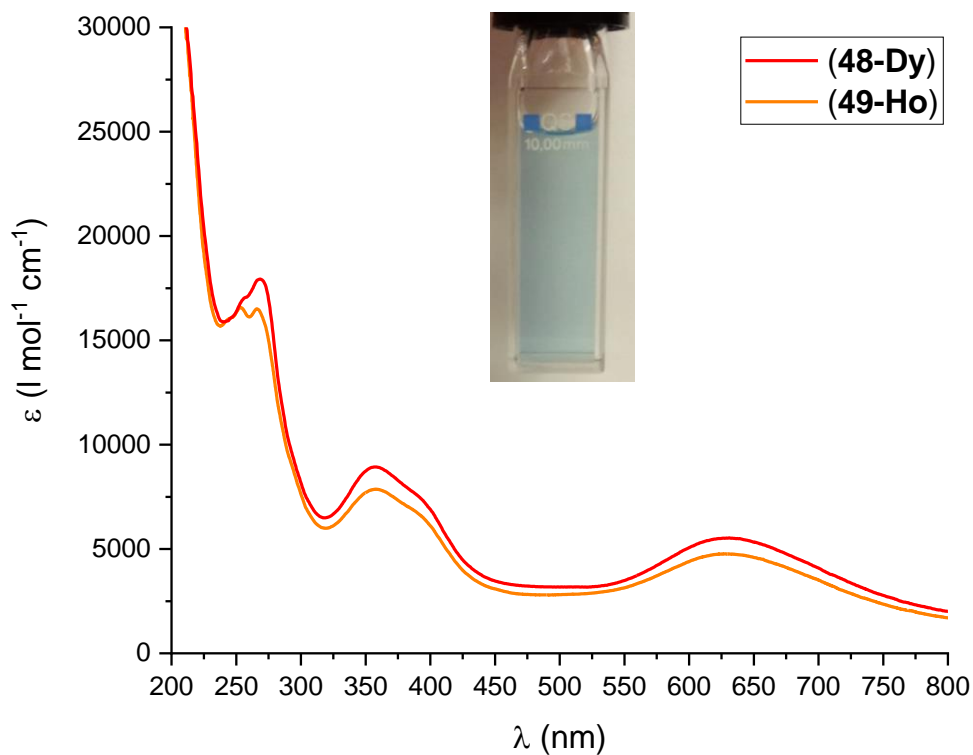


Figure 185. Comparison of the UVVis spectra of **(48-Dy)** and **(49-Ho)** in 10 μM MeCN solutions.

In figure 186 the MeCN solution spectra of **(48-Dy)** and **(49-Ho)** are compared to the solid state spectra of the same compounds that were measured during the work reported in my Master thesis^[31-32] as well as the MeCN solution spectra of the radical ligand and the oxidised starting material that were presented above. The solution spectra of both complexes match their respective solid state spectra indicating that the complex stays intact in freshly prepared solutions. Furthermore, the bands in the UV region are at the same energies as the ones in the dione and the semiquinonate radical forms. The band at 360 nm with a shoulder at 390 nm in the complex spectra matches the twin bands in the spectrum of the cobaltocenium salt of phsq⁻ suggesting that these excitations involve the radical species. The $\pi \rightarrow \pi^*$ band at 518 nm in $[\text{CoCp}_2](\text{phsq})$ is red-shifted by over 110 nm to give the ILCT band at 630 nm in the complexes as mentioned above.

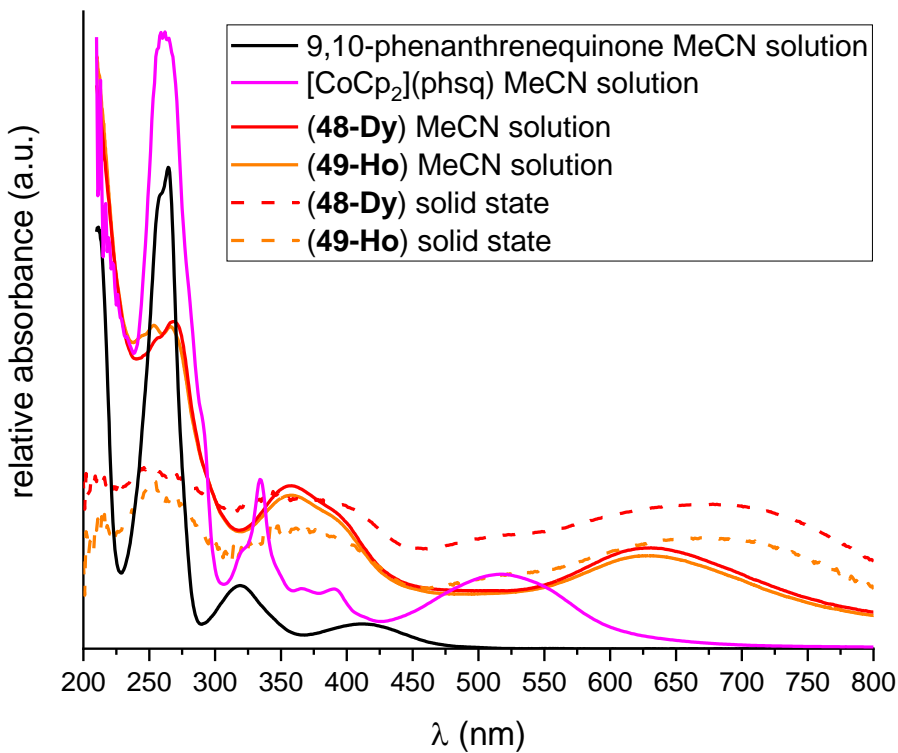


Figure 186. Comparison of the UVVis absorption spectra of (48-Dy) and (49-Ho) in MeCN (blue and red solid lines) to the respective solid state spectra (blue and red dashed lines) as well as the MeCN solution spectra of 9,10-phenanthrenequinone and the cobaltocenium salt of the phenanthrenesemiquinonate radical (green and orange lines, respectively).

As for [CoCp₂](phsq), the screw top cuvette of (49-Ho) was opened to air and the UVVis spectrum recorded every 100 s (see figure 187). After ten minutes the absorption spectrum of 9,10-phenanthrenequinone is obtained, again confirming that the complexes decompose in air due to the oxidation of the radical ligand leading back to the starting material. This is accompanied by the colour change towards orange that was shown above. The band in the UV region does not change significantly and is therefore omitted in figure 187 which shows the changes in the range between 300 and 800 nm.

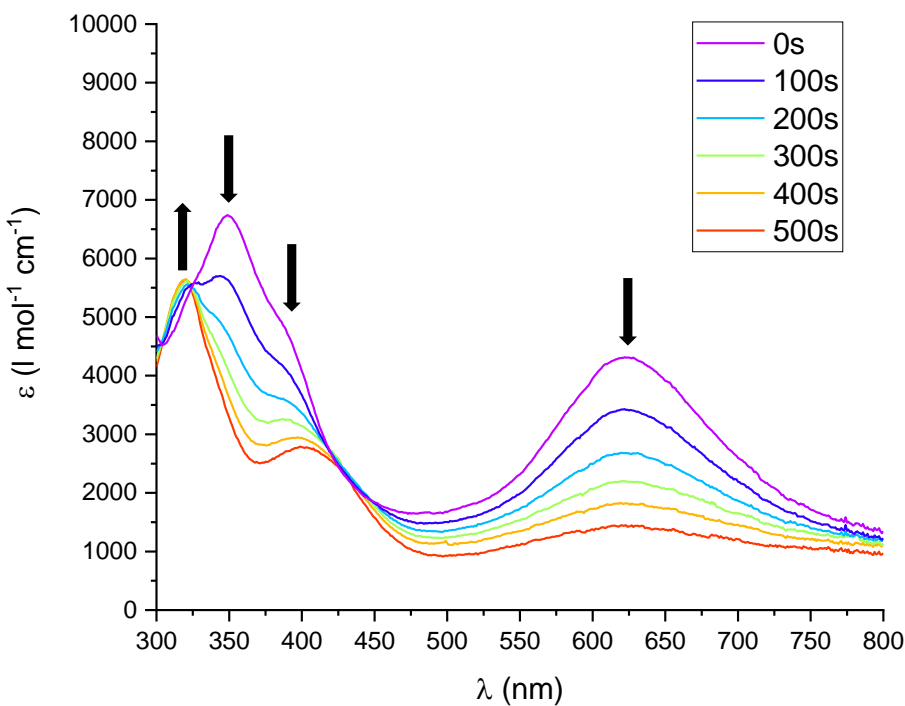


Figure 187. Oxidation of the MeCN solution of **(49-Ho)** within ten minutes when opened to air.

Luminescence properties were investigated using MeCN solutions of **(45-Eu)**, but no emission was observed in the freshly prepared solutions. However, after storing the screw top cuvettes in with **(45-Eu)** solutions for 3 d in the glove box, a colour change was noticed towards cyan (see figure 188). The UVVis absorption spectra recorded after 3 d of storage under inert atmosphere, so ruling out any oxidation from O_2 , are significantly different from those of fresh solutions (figure 188).

The bands in the UV region show a slightly blue shifted additional shoulder, the bands at 350 to 400 nm that are assigned to the radical ligand decrease in intensity and the band at 630 nm becomes very broad and does not attain zero absorbance within the measurement window. Therefore, it can be concluded that the complexes are not only susceptible to oxidation by oxygen but also decompose over time in solution. This is in stark contrast to the solid state in which crystals are stable for at least six months in air.

This decomposition may result from ligand rearrangement in solution and can also be seen in the emission spectra of **(45-Eu)** since samples that were stored for three days now show the characteristic Eu^{III} luminescence (figure 189).

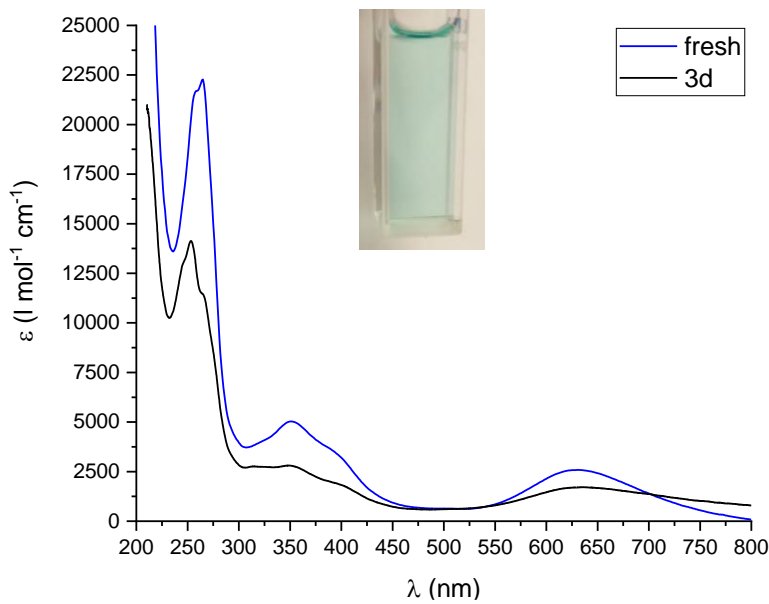


Figure 188. UVVis absorption spectra of the same sample of (45-Eu) measured immediately after preparation (blue) and after storage under inert atmosphere (black).

The strong red emission at 612 nm stems from a so-called hypersensitive transition, named so as a result of its sensitivity to the environment of the metal ion. This transition is from the electronic excited state 5D_0 to the 7F_2 vibronic excited state of the electronic ground state.^[42, 343, 347-348]

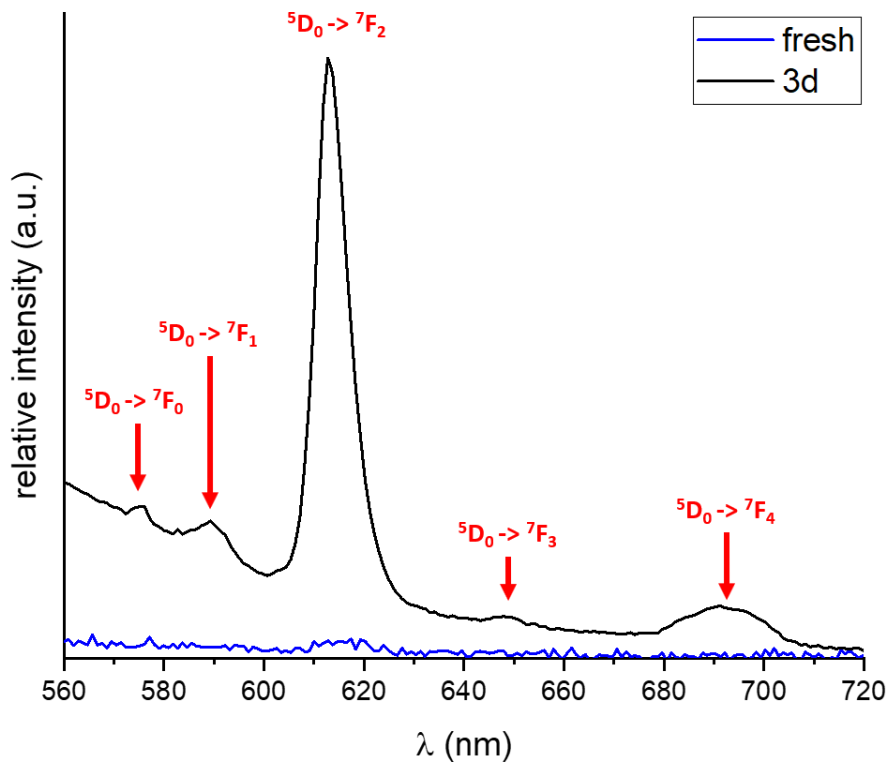


Figure 189. Emission spectra of the same sample of (45-Eu) measured immediately after preparation (blue) and after storage under inert atmosphere for three days (black). The corresponding states of the transitions are shown in red.

6.3 Changing the Neutral Co-Ligand

As mentioned in the introduction to this chapter there are four components to this extended family of complexes that can be varied. In the following section the alteration of the neutral co-ligands from MeOH in the parent compounds towards larger alcohols will be presented. The first example of such complexes, $[\text{Ho}_2(\text{phsq})_4(\text{NO}_3)_2(\text{EtOH})_2]$, was synthesised in low yields as reported in my Master thesis and is also described in the doctoral thesis of my then supervisor in the lab Dr. Anthony Blue Carter.^[31-32] The next step was thus the reproduction of this compound and the optimisation of the reaction procedure in order to expand the systematic study on Ln_2Rad_4 complexes within the scope of this thesis.

6.3.1 $[\text{Ln}_2(\text{phsq})_4(\text{NO}_3)_2(\text{EtOH})_2]$

Repeating the reaction procedure that led to the parent compounds but changing the solvent from MeOH to EtOH resulted in dark crystals in a very low yield that have been identified as the desired compound now bearing EtOH co-ligands. Different parameters of the reaction conditions were then varied. A decrease in reaction temperature from the original 90°C did not yield any product, while an increase in temperature did not improve the yield of the reaction. This is consistent with the results obtained for the optimisation performed on the parent system.^[31-32] However, increasing the reaction time from 5 d to 14 d, which in the parent system did not significantly impacted the yield, leads to a doubling of the yield to around 5 mg (3%) in the EtOH version. The yield was further improved by changing the metal salt to ligand ratio to 2:1 as well as changing the cooling rate after the reaction. Thus, instead of taking the autoclaves out of the oven and letting them cool down on the bench, the oven was turned off but the door left shut for another 24 h ensuring a slower cooling rate. This optimisation improved the yields of $[\text{Ln}_2(\text{phsq})_4(\text{NO}_3)_2(\text{EtOH})_2]$ to 15 to 40 mg (8 to 23%) per reaction depending on the Ln^{III} ion used. Nevertheless, it can be concluded that the EtOH version of the complex does not form as easily as the MeOH version. This may be attributed to the larger size of EtOH as a co-ligand making it react slower than MeOH therefore demanding longer reaction times to obtain acceptable yields. Crystallisation may take longer due to the floppier nature of EtOH compared to rather

rigid MeOH making the cooling rate an important factor in the crystallisation of this series of compounds.

Using this improved synthetic procedure $[\text{Ln}_2(\text{phsq})_4(\text{NO}_3)_2(\text{EtOH})_2]$ was synthesised with $\text{Ln}^{\text{III}} = \text{Eu}^{\text{III}}$ to Tm^{III} (**57-Eu**), (**58-Gd**), (**59-Tb**), (**60-Dy**), (**61-Ho**), (**62-Er**), (**63-Tm**) as well as the Dy-Y-doped version (**64-DyY**). Although, the compounds named above were obtained as dark mostly crystalline material, very few crystals suitable for SC-XRD were obtained. The crystal structure of (**60-Dy**) will be discussed in the following and the molecular structure is shown in figure 190.

(**60-Dy**) shows the same biplane type of structure as observed before for the MeOH version of this compound with two radical ligands on either side chelating one of the Dy^{III} ions with both of their oxygen atoms. One oxygen atom (O(1)/O(3)) of the semiquinonate ligand additionally bridges to the other Dy^{III} ion. The C-O bond lengths of the ligand confirm the semiquinonate radical anion form (phsq^{\cdot}) of the ligand. The C-O bond lengths in semiquinone radicals are expected to be around 1.3 Å as opposed to about 1.2 Å for carbonyls and 1.4 Å for alcohols.^[32, 335-336] The C-O bond lengths to the bridging oxygens are $d(\text{C}(1)-\text{O}(1)) = 1.286(7)$ Å and $d(\text{C}(15)-\text{O}(3)) = 1.302(7)$ Å and the C-O bond lengths to the non-bridging oxygens are $d(\text{C}(2)-\text{O}(2)) = 1.270(7)$ Å and $d(\text{C}(16)-\text{O}(4)) = 1.289(7)$ Å. The strong radical-radical interaction forming a pancake bond on either side of the compound that was calculated for the parent compound^[32-33, 339] appears also to be present in (**60-Dy**). This becomes obvious by looking at the closest inter-ligand C-C and O-O distances of 2.680(9) Å and 2.563(6) Å between C(1) and C(15) as well as O(1) and O(3), respectively. These values are comparable to the distances in the parent compound and are in fact slightly shorter. However, the Dy-Dy distance of 3.3940(5) Å in (**60-Dy**) is slightly longer than the 3.3436(3) Å observed in the original compound.

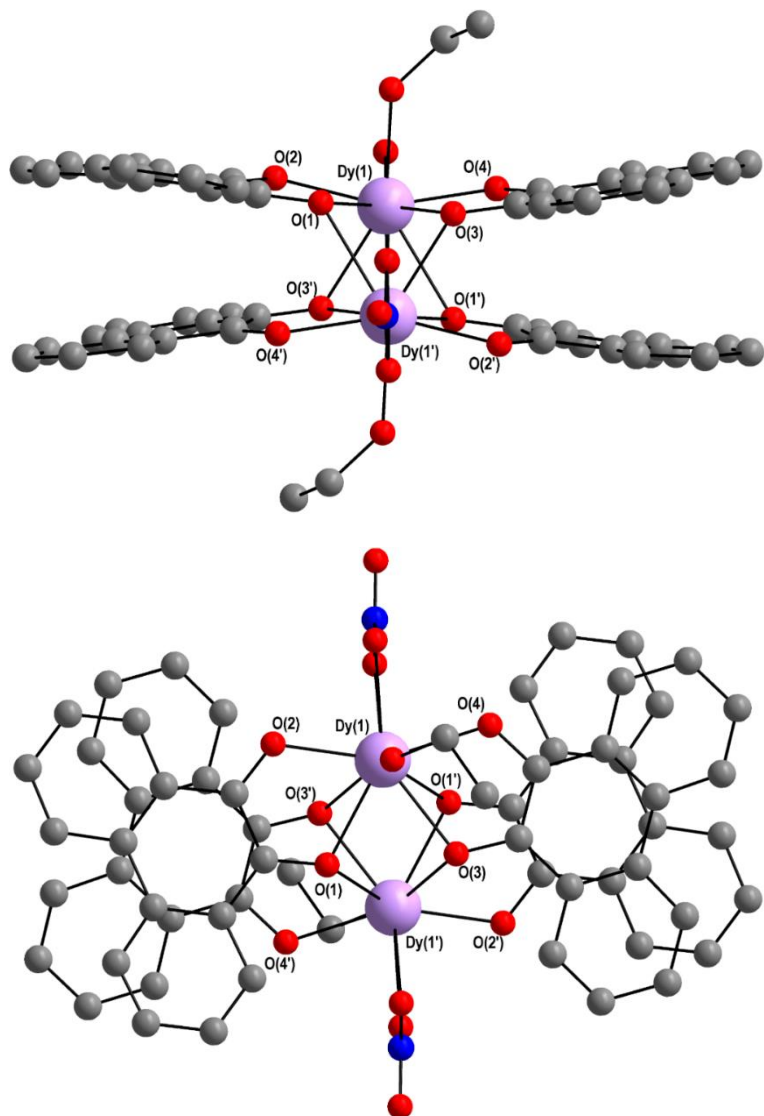


Figure 190. Two views on the molecular structure of **(60-Dy)** as a representative for the $[\text{Ln}_2(\text{phsq})_4(\text{NO}_3)_2(\text{EtOH})_2]$ complexes.

The impact of the larger EtOH co-ligand, which only has minor effects on the molecular structure, influences the packing quite significantly. The MeOH versions of the Ln_2Rad_4 complexes crystallised in the orthorhombic space group *Pbca*. The same unit cell was found for the Ho-EtOH-analogue that was mentioned in the preliminary results section. **(60-Dy)** now crystallises in the monoclinic *P2₁/n* with $Z = 2$ suggesting that there is more than one structure type possible for the EtOH dimers. The packing of the monoclinic structure of **(60-Dy)** is shown in figure 191. The only significant intermolecular interactions are HBs from the coordinated EtOH to a lattice EtOH which is hydrogen bonded to another lattice EtOH which in turn is hydrogen bonded to the non-coordinated nitrate oxygen on the neighbouring molecule. Therefore, it can be concluded that the change of the solvent impacts the way the molecules interact with

each other, which might affect the magnetic behaviour. Although it may seem like there are intermolecular π - π stacking interactions, none are actually observed in (**60-Dy**).

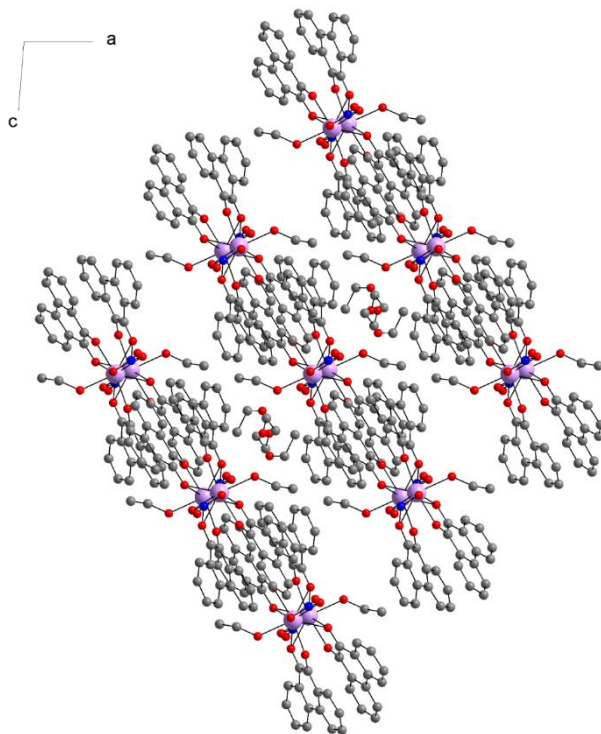


Figure 191. View along the b axis on the packing of (**60-Dy**).

The PXRDs of (**59-Tb**), (**60-Dy**), (**61-Ho**), (**62-Er**) and (**63-Tm**) are compared to the simulated ones of the orthorhombic and the monoclinic unit cells in figure 192. None of the PXRDs match these simulations. The IR as well as the solid state UVVis spectra that are shown in figure 193 however are consistent across the series of compounds, indicating that the molecular structure is indeed the presented EtOH version of Ln_2Rad_4 . Since the system was already shown to be prone to crystallise in multiple space groups, it can be speculated that additional peaks in the PXRD may stem from further 3D structural types that have not yet been discovered via SC-XRD. Additionally, the partial or complete loss of lattice EtOH or the exchange of lattice EtOH with water could induce structural changes that could either shift the PXRD peaks if an axis of the unit cell is compressed more than others or alter the powder pattern altogether. In the case of (**60-Dy**) a loss of lattice EtOH seems likely, reducing crystallinity resulting in a low signal to noise ratio as well as shifting the peaks. In the case of (**63-Tm**) the elemental analysis fits perfectly for one water molecule per cluster (instead of four EtOH molecules) suggesting that the intense peak at $2\theta = 8.7^\circ$ may belong to an unexplored structure type with water in the lattice. Since the IR and UVVis spectra

match each other it was deemed that further analysis of the optical and magnetic properties of **(60-Dy)** is possible.

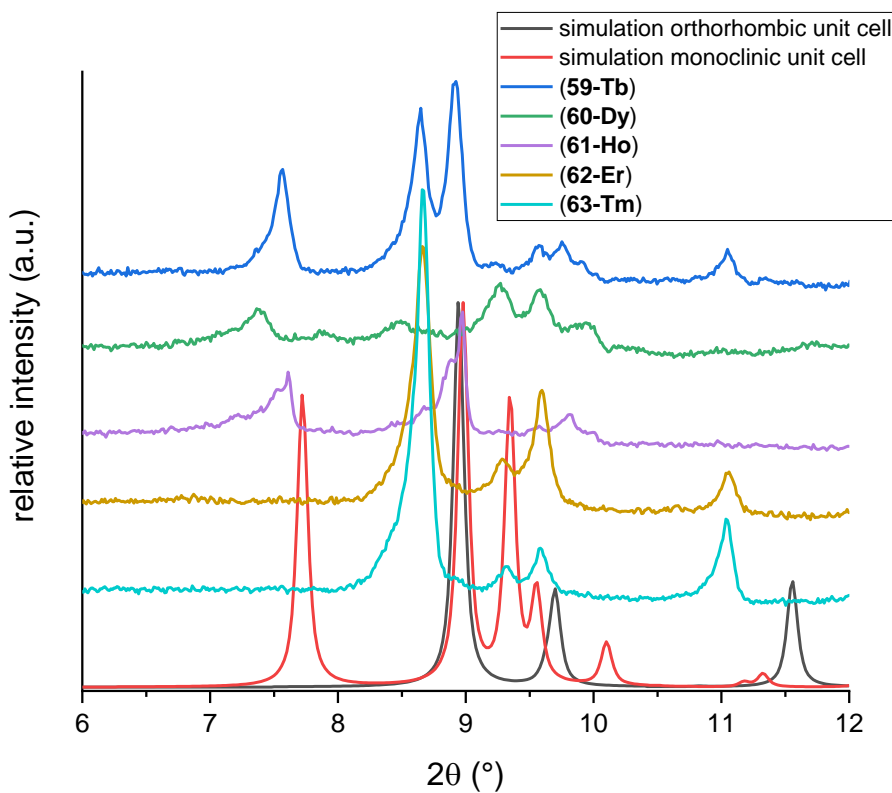


Figure 192. PXRDs of EtOH dimers suggesting the easy loss of lattice solvent potentially leading to the presence of at least one more unexplored crystal structure.

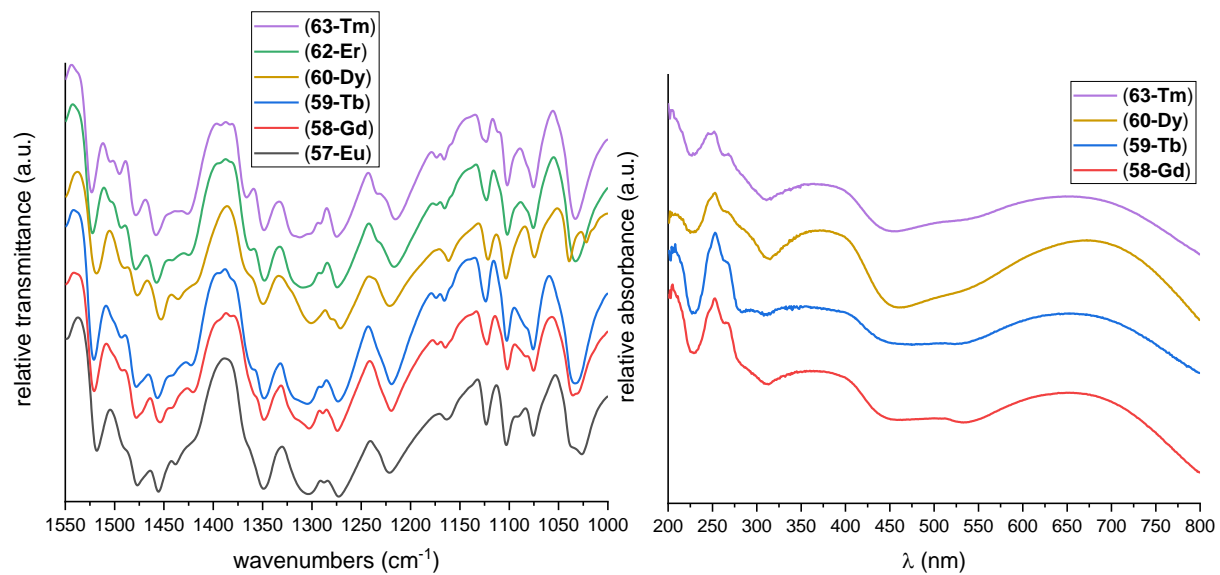


Figure 193. IR and UVVis suggesting identical molecular structures of different members of the $[\text{Ln}_2(\text{phsq})_4(\text{NO}_3)_2(\text{EtOH})_2]$ series.

The UVVis absorption spectrum of (**60-Dy**) was also recorded in MeCN solution which was prepared under inert atmosphere as described in section 6.2.2 and is compared to the solid state spectrum of the same compound as well as the solution and solid state spectra of (**48-Dy**) and the ligand reference spectra in figure 194. The spectrum of (**60-Dy**) in MeCN solution (solid blue line) matches the solid state spectrum (dashed blue line) but comparison with the solution spectrum of (**48-Dy**) (red solid line) reveals subtle differences. Intensities between the two solution spectra are qualitatively comparable since both are roughly the same concentration (*circa* 10 μ M). The band in the UV region is blue-shifted by 8 nm in (**60-Dy**) and much more intense. It additionally matches the same band in the dione starting material. The bands between 350 and 400 nm as well as the ILCT band at 630 nm are much less intense in (**60-Dy**) than in (**48-Dy**). It appears that the solution spectrum of (**60-Dy**) shows the complex during the process of degradation as indicated by the bands corresponding to the radical species (360 nm, 395 nm and 630 nm) becoming reduced in intensity and bands corresponding to the dione species increasing in intensity (260 nm and 320 nm). This would also explain the higher intensity seen in the UV region of the solution spectrum of (**60-Dy**) and the lower intensity in the visible region when compared to the solution spectrum of (**48-Dy**) in addition to the similarity to the spectrum of (**45-Eu**) after storage for 3 d (see section 6.2.2). Since both solutions were prepared freshly just minutes before the respective measurements it can be concluded that the EtOH version (**60-Dy**) decomposes in solution faster than the MeOH version (**48-Dy**). This could be the consequence of the presence of multiple structural types.

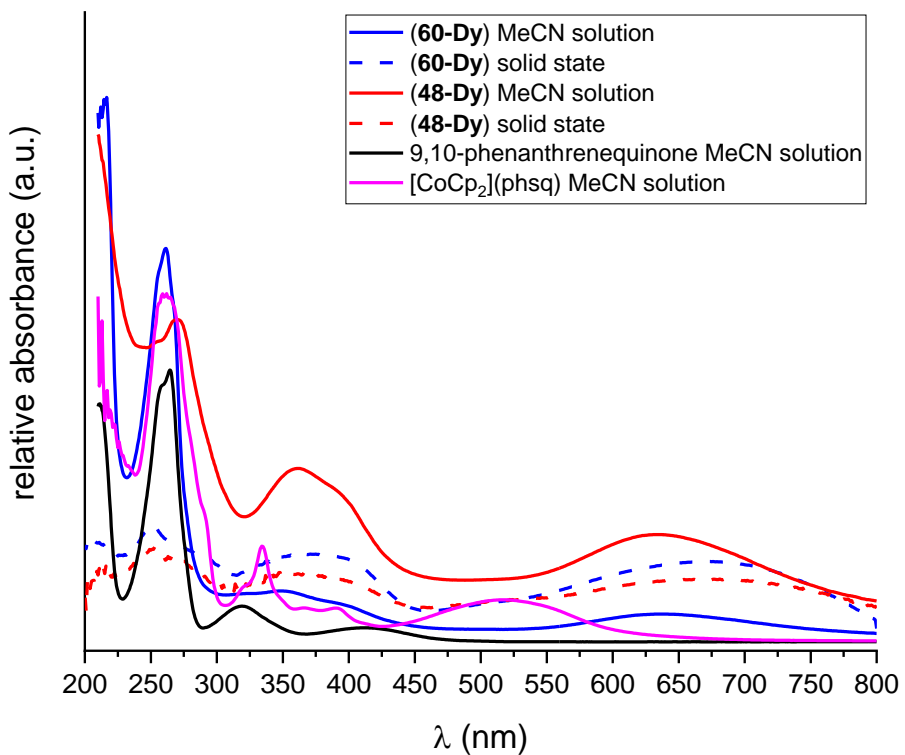


Figure 194. Solid state and solution UVVis absorption spectra in MeCN of **(60-Dy)** compared to the spectra of the MeOH version **(48-Dy)** as well as the ligand reference spectra established above.

The anisotropy axes of **(60-Dy)** were calculated using MAGELLAN^[297] and are oriented the same way as in the parent compound (see figure 195). The axes are essentially orthogonal to the Dy-Dy vector (89.1°) which, as this is a more obtuse angle than the magic angle of 54.74° , means the dipolar interaction will be antiferromagnetic.^[62, 320] Considering that the dipolar interaction between the Dy^{III} ions in the parent compound is magnitudes stronger than the exchange coupling an overall antiferromagnetic interaction can be expected for **(60-Dy)**.

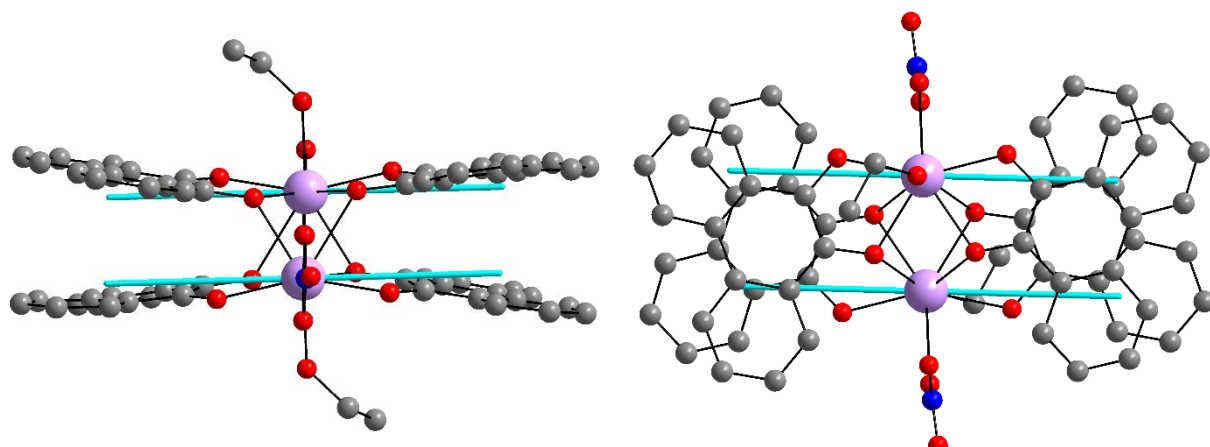


Figure 195. Anisotropy axes of the Dy^{III} ions in **(60-Dy)** calculated using MAGELLAN.^[297]

Susceptibility measurements were performed at temperatures between 1.8 and 300 K with an applied field of 0.1 T. The RT $\chi_M T$ value of $27.96 \text{ cm}^3 \text{Kmol}^{-1}$ of **(60-Dy)** is in very good agreement with the theoretical value of $28.34 \text{ cm}^3 \text{Kmol}^{-1}$. On decreasing the temperature, the $\chi_M T$ values stay essentially constant to 50 K below which a steep decrease can be observed leading to a minimum value of $5.48 \text{ cm}^3 \text{Kmol}^{-1}$ at 1.8 K (see figure 196, left). The χ_M^{-1} vs T plot (figure 196, right) follows the Curie-Weiss law between 4 and 300 K and can be fitted with a Weiss constant $\theta = -5.5 \text{ K}$ confirming overall antiferromagnetic interactions to be present in this compound as well as a Curie constant $C = 28.49 \text{ cm}^3 \text{Kmol}^{-1}$.

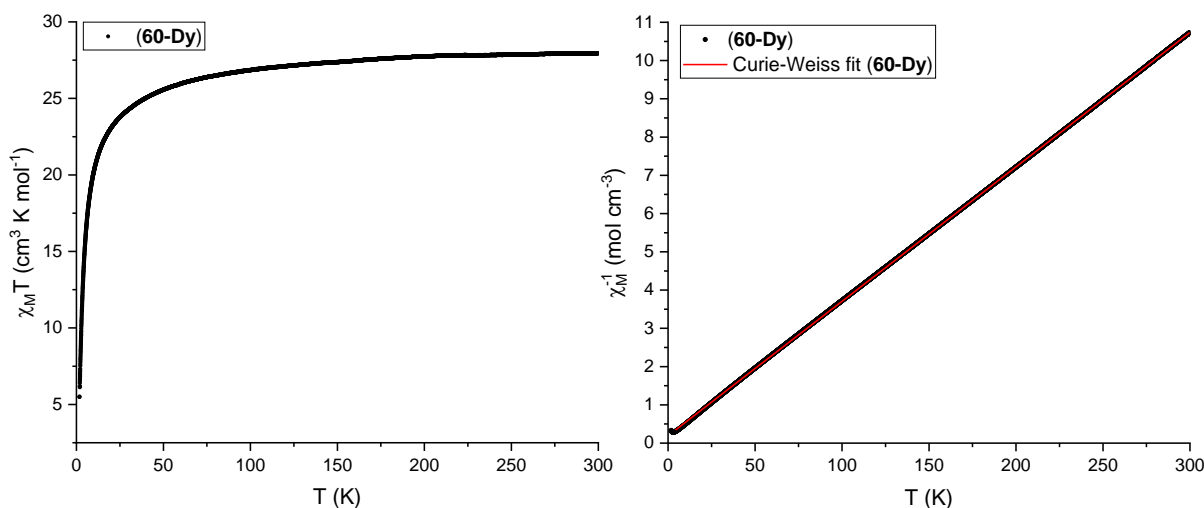


Figure 196. $\chi_M T$ vs T (left) and χ_M^{-1} plot of **(60-Dy)** (right) obtained from susceptibility measurements at temperatures between 1.8 and 300 K and an applied magnetic dc field of 0.1 T.

In magnetisation measurements at 1.8, 3 and 5 K and magnetic fields between 0 and 7 T, the magnetisation curves (figure 197, left) follow each other up to a magnetic field of 0.27 T before deviating from each other. This coincides with an inflection point indicating that there is a level crossing at around 0.27 T. The sample does not reach saturation with a maximum value of $10.7 \mu_B$. In the reduced magnetisation plots the curves do not overlap suggesting significant anisotropy and/or the presence and involvement of low-lying excited states.

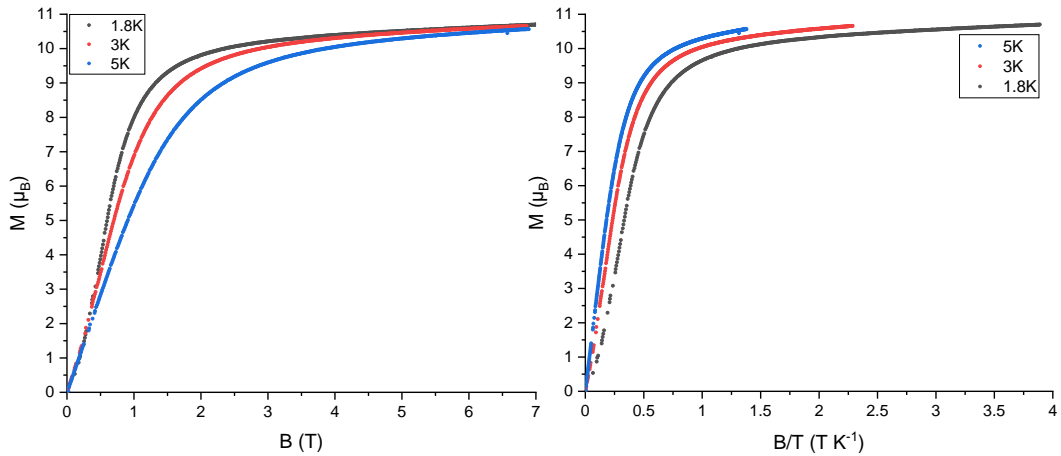


Figure 197. Magnetisation of (60-Dy) measured at 1.8, 3 and 5 K and fields between 0 and 7 T (left) and reduced magnetisation plots (right).

Slow relaxation of magnetisation can be observed with maxima in the out-of-phase susceptibility in measurements with ac fields switching direction at frequencies between 1 and 1000 Hz. The in- and out-of-phase susceptibilities at temperatures between 1.8 and 20 K are shown in figure 198. The experimental data were fitted using the generalised Debye model and τ values extracted in order to evaluate the relaxation mechanisms present.

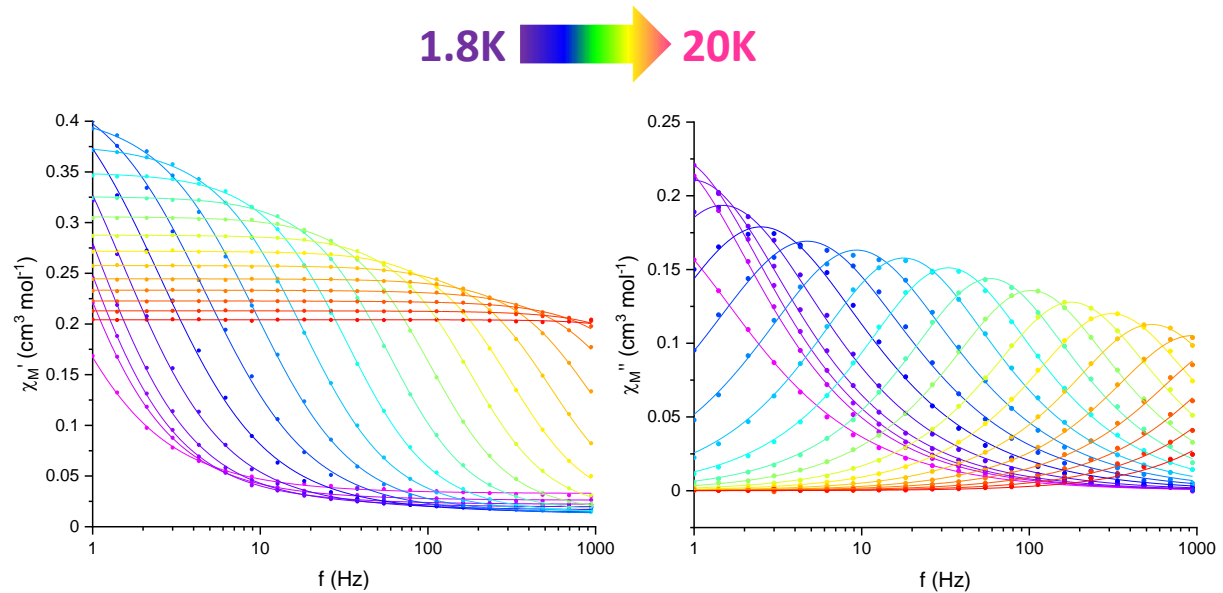


Figure 198. In- and out-of-phase susceptibility at ac field frequencies between 1 and 1000 Hz and temperatures between 1.8 and 20 K of (60-Dy) (left and right, respectively).

The $\ln(\tau)$ vs $1/T$ plot using the τ values extracted from the Debye fit to the ac data shown in figure 199, can be fitted using two approaches. From a linear fit to the high temperature data (blue in figure 199) an energy barrier that only takes the purely thermal Orbach relaxation process into account, and is therefore higher than the

effective energy barrier to relaxation in this system, can be obtained as well as T_{B100} which is a value often used to compare the performance of SMMs. $U_{\text{Orbach}} = 158.3 \text{ K}$ and $T_{B100} = 7.0 \text{ K}$. From the hysteresis plot shown in figure 200 it can be concluded that the real blocking temperature lies between 1.8 and 3 K confirming that through-barrier relaxation processes play a significant role in **(60-Dy)**. This is consistent with what was found for the parent compound as well as many lanthanide complexes in the literature.^[24, 339, 349]

In a second step the data were fitted using equation 13 (red in figure 199) in order to investigate the above-mentioned through-barrier relaxation mechanisms present here. The parameters used to fit the Arrhenius plot are listed in table 21. The parameter B which describes the ZFQTM becomes incredibly small when fitting without restricting any parameters and was therefore set as 0 for the final convergence of the fit. Both direct and Raman processes are favoured in contrast to the parent compound which explains why ac signals are only obtained to slightly lower temperatures than in the original dimer inspite of a higher energy barrier U.

Table 21. Fitting parameters using the equation introduced by Lunghi *et al.*^[142] used to obtain the red fit to the relaxation processes in **(60-Dy)** in figure 199.

A (s⁻¹ K⁻¹)	B (s⁻¹)	V (s⁻¹)	w (K)	τ₀ (s)	U (K)
1.41	0	72000	62.2	2.27E-9	185.3

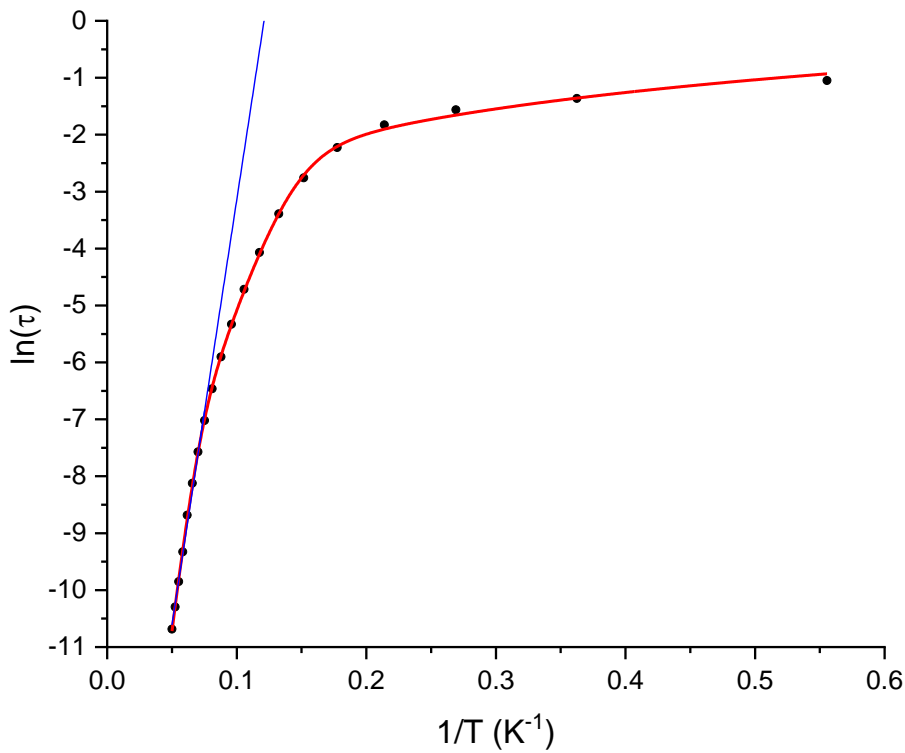


Figure 199. Arrhenius plot of **(60-Dy)** (black dots) using the τ values extracted from the Debye fit to the ac susceptibility data fitted using a linear fit taking the thermal Orbach relaxation mechanism into account (blue) as well as using equation 13 by Lunghi *et al.* (red).^[142]

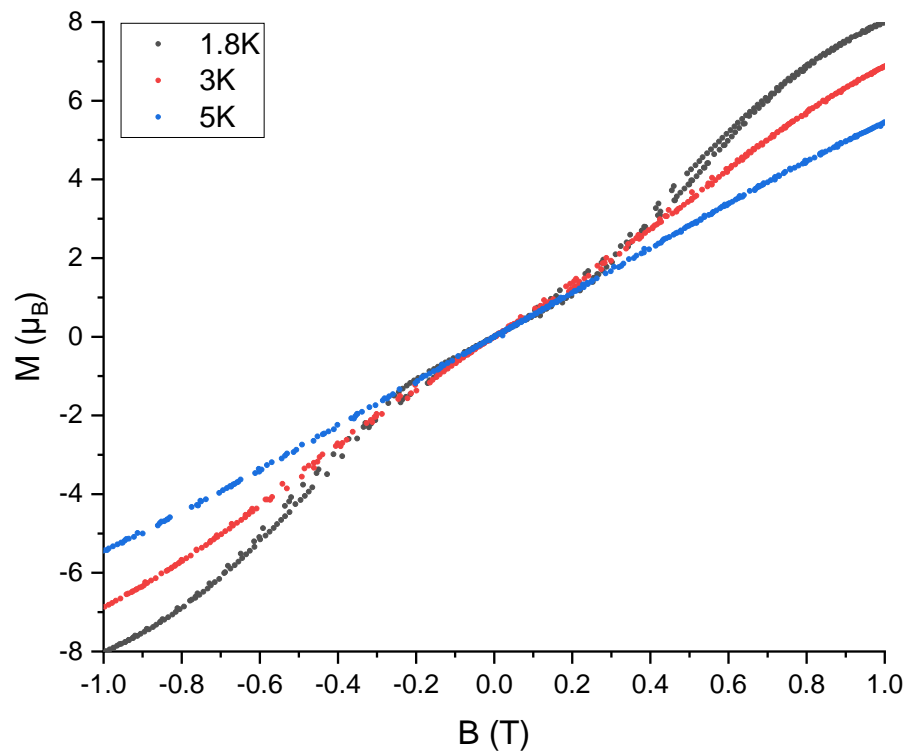


Figure 200. Narrow hysteresis shown by **(60-Dy)** at 1.8 K between fields of -0.6 and -0.3 T as well as 0.3 and 0.6 T indicating SMM behaviour at this temperature.

MicroSQUID measurements on single crystals of **(60-Dy)** were performed in collaboration with Dr. Sagar Paul in the group of Prof. Dr. Wolfgang Wernsdorfer (KIT, PHI) in order to investigate the magnetic behaviour at very low temperatures (see figure 201). At the centre of the plots a hysteresis opens at temperatures between 0.03 and 0.3 K that is sweep rate independent indicating slow relaxation rates and excluding the possibility of ZFQTM in line with the results of the fit to the Arrhenius plot above. This is a major difference to the behaviour exhibited by the parent compound in terms of the microSQUID measurements, in which no hysteresis is observed around zero field and instead a non-magnetic ground state that persists up to 0.3 T is observed. In **(60-Dy)** at 0.269 T a vertical increase in magnetisation is observed indicating a level crossing via quantum tunnelling which is clearly visible in the derivative plots (figure 201 bottom). This is in good agreement with the magnetisation curves at 1.8, 3 and 5 K shown above which showed an inflection point at similar fields and also with the parent compound which exhibits a level crossing at similar fields. The narrow hysteresis at fields between 0.3 and 0.6 T that was observed for **(60-Dy)** shown above can be seen here as well. This suggests that at temperatures even below 0.3 K levels are populated above and below 0.27 T. Magnetisation relaxes slowly from both of these but with very different relaxation mechanisms in place. A measurement using an ac field below 0.3 K is not yet possible but should result in further insight into the intricate relaxation dynamics of **(60-Dy)**.

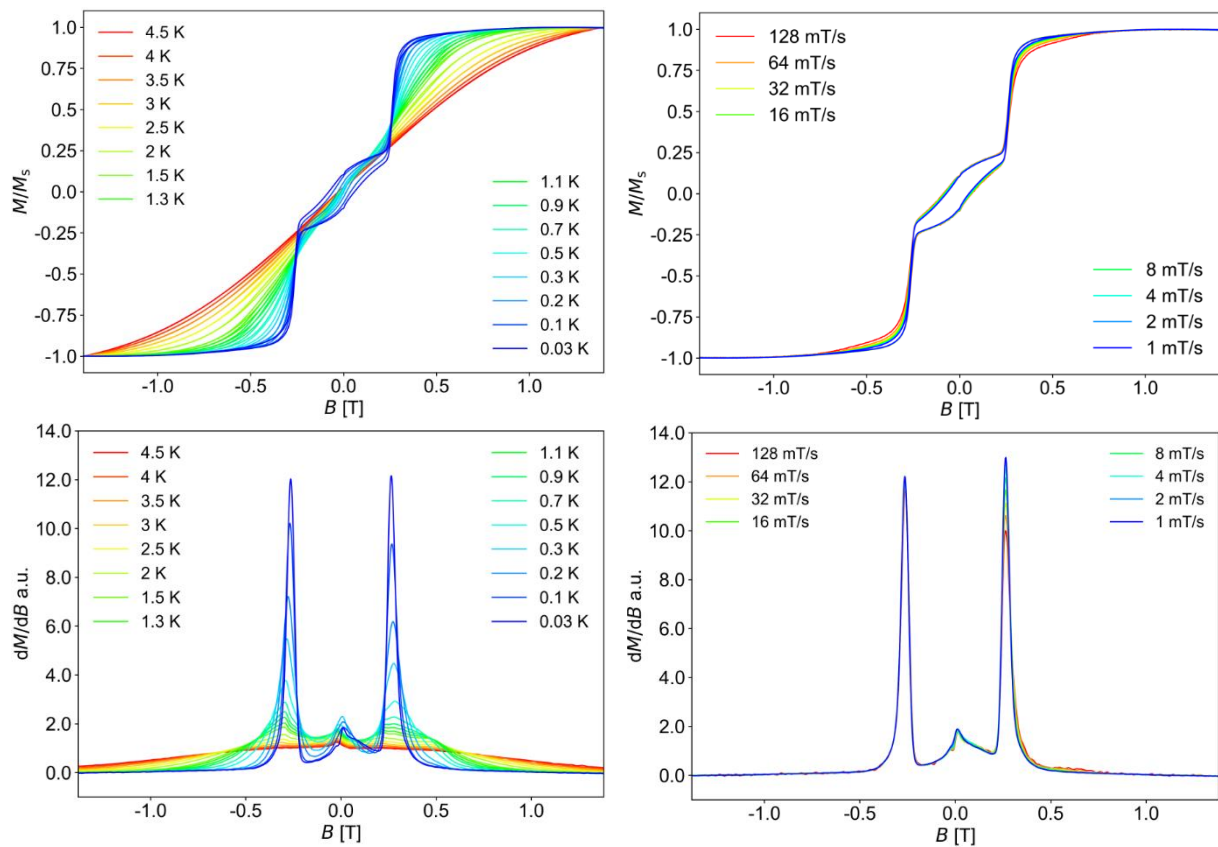


Figure 201. MicroSQUID performed on single crystals of **(60-Dy)**. Temperature dependence at temperatures between 0.03 and 4.5 K (left) and sweep rate dependence between 1 mT/s and 128 mT/s was investigated (right). Derivative plots of the respective measurements show the predominant level crossing at ± 0.27 T (bottom).

6.3.2 $[\text{Ln}_2(\text{phsq})_4(\text{NO}_3)_2(\text{iPrOH})_2]$

Using iPrOH as an even larger alcohol as solvent and employing the same reaction conditions as for the EtOH version yielded black crystals of $[\text{Ln}_2(\text{phsq})_4(\text{NO}_3)_2(\text{iPrOH})_2]$ in good yields. The formation of the compounds with $\text{Ln}^{\text{III}} = \text{Pr}^{\text{III}}\text{-Lu}^{\text{III}} + \text{Y}^{\text{III}}$ (**65-Pr**), (**66-Nd**), (**67-Sm**), (**68-Eu**), (**69-Gd**), (**70-Tb**), (**71-Dy**), (**72-Ho**), (**73-Er**), (**74-Tm**), (**75-Yb**), (**76-Lu**), (**77-Y**) as well as the Dy-Y-doped version (**78-DyY**) was confirmed by PXRD and/or IR as well as UVVis. These compounds have the same molecular structure as the MeOH and EtOH versions shown above (see figure 202). In contrast to the EtOH version, crystals of the iPrOH version of this complex form much more readily as indicated by the higher yield and overall higher crystallinity as well as better formed single crystals. Given the observation of multiple possible space groups for the EtOH version, this is another indication that EtOH might be of a size that does not favour the crystallisation of the desired dimeric compounds. Taking (**74-Tm**) as representative for

in this series of compounds, the ligands can again be confirmed to be the semiquinonate radical by the C-O bond lengths which are 1.275(3) Å C(2)-O(2) as well as C(16)-O(4), 1.287(3) Å for C(15)-O(3) and 1.300(3) Å for C(1)-O(1). The π -systems form a pancake bond of similar strength as the MeOH and EtOH versions with the shortest inter-ligand C-C distance of 2.699(3) Å and the shortest O-O distance of 2.557(2) Å. This forces the Tm^{III} ions into close proximity with the Tm-Tm distance of 3.3120(5) Å even being shorter than the one for the Tm-MeOH analogue (d(Tm-Tm) = 3.2833(5) Å).^[31]

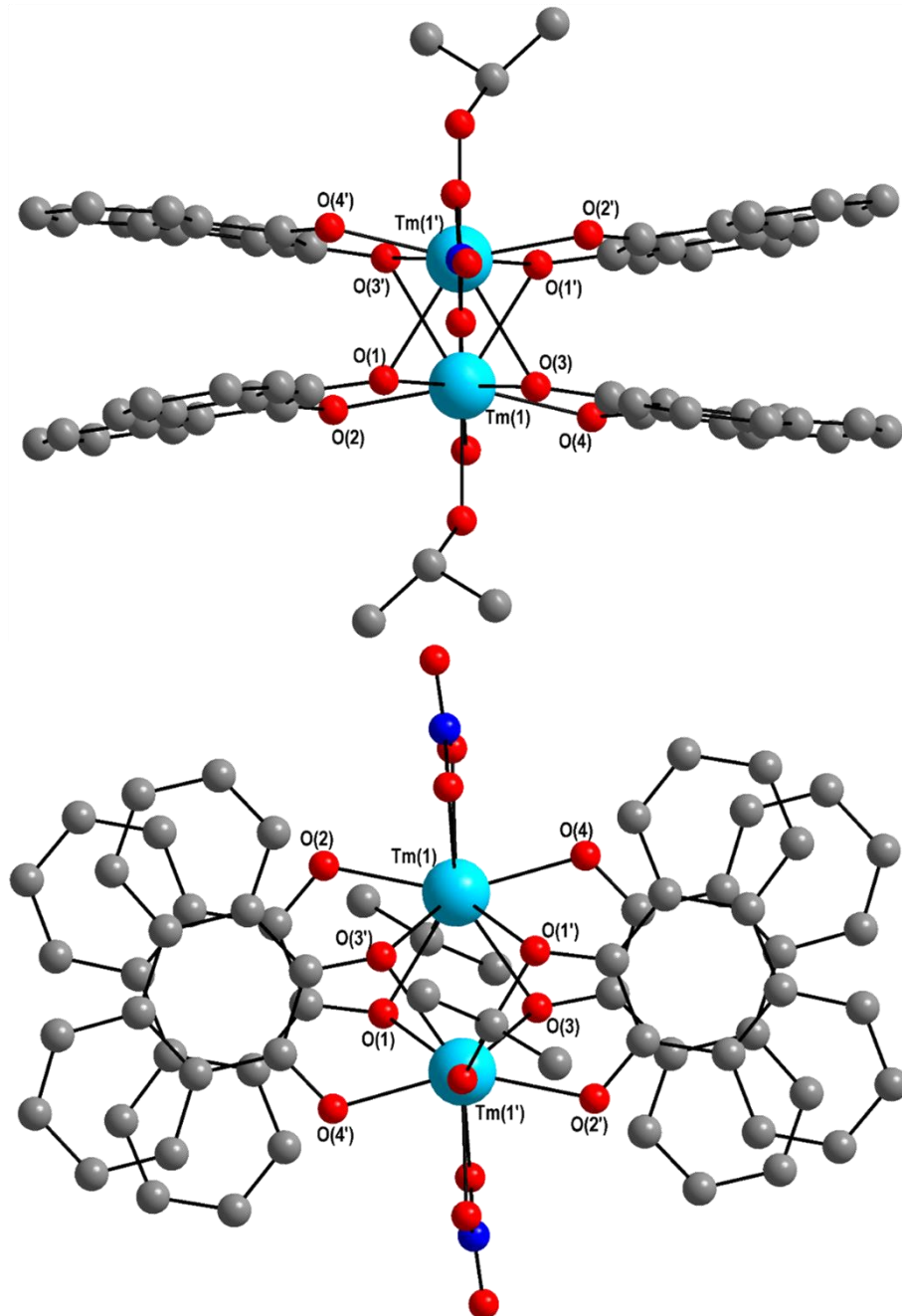


Figure 202. Side and top view on the molecular structure of (74-Tm) as representative for the series of $[\text{Ln}_2(\text{phsq})_4(\text{NO}_3)_2(\text{iPrOH})_2]$ complexes.

(74-Tm) crystallises in the monoclinic $P2_1/n$ space group. The unit cell of **(74-Tm)** is similar to the one for **(60-Dy)** and the packing which is shown in figure 203 is therefore similar as well. There are HBs between the OH proton of the coordinated iso-propanol to the lattice solvent. This is in contrast to the lattice EtOH molecules in **(60-Dy)** which are close to each other in the crystal structure and form further HBs. The two lattice $^i\text{PrOH}$ in **(74-Tm)** are too far apart for further interactions. Instead the OH proton of the lattice $^i\text{PrOH}$ molecules form rather weak HBs with O(4), one of the semiquinone oxygens, as indicated by the O(9)-H(9)...O(4) distance of 2.914(3) Å and the angle of 132(5) $^\circ$. The shortest intermolecular Tm-Tm distances are 10.5967(5) Å which means that any intermolecular coupling would be extremely weak.

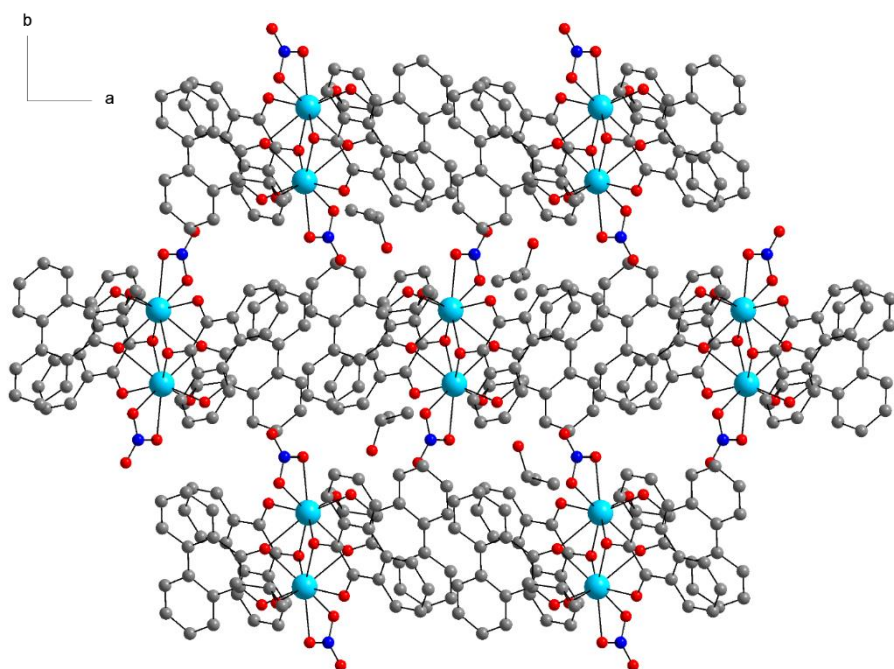


Figure 203. Packing of **(74-Tm)** viewed along the c axis.

In contrast to the EtOH version of the complex, the series of $^i\text{PrOH}$ versions are isostructural. This was confirmed by PXRD for the series of compounds with $\text{Ln}^{\text{III}} = \text{Eu}^{\text{III}}\text{-Lu}^{\text{III}}$ plus Y^{III} and the Dy-Y-doped analogue (figure 204). The yields of the three compounds with the larger Ln^{III} ions **(65-Pr)**, **(66-Nd)** and **(67-Sm)** were too low to do the same experiment.

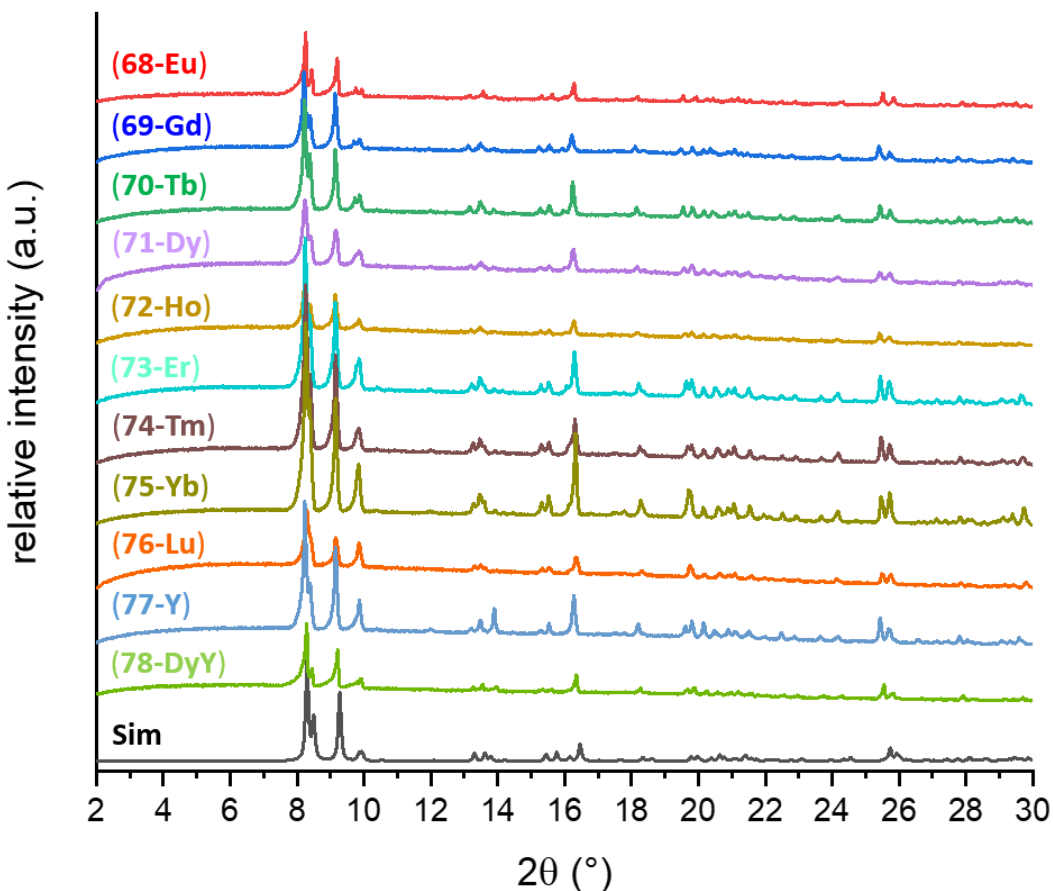


Figure 204. PXRD measurements compared to the simulated pattern using the SC-XRD dataset of (74-Tm) confirming the series of $[\text{Ln}_2(\text{phsq})_4(\text{NO}_3)_2(\text{iPrOH})_2]$ complexes to be isostructural from Eu^{III} to Lu^{III} as well as the Y and Dy-Y-doped versions.

The successful syntheses of the Pr^{III} , Nd^{III} and Sm^{III} analogues of the iPrOH version can be confirmed from the IR spectra and by the matching solid state UVVis absorption spectra that are shown in figure 205. All compounds show four bands in the UV region at 206, 245, 252 and 268 nm as well as a broad band at 362 nm and a less intense band at 511 nm that in some compounds only manifests as a shoulder to the very broad lowest energy band in the spectrum centred at 652 nm.

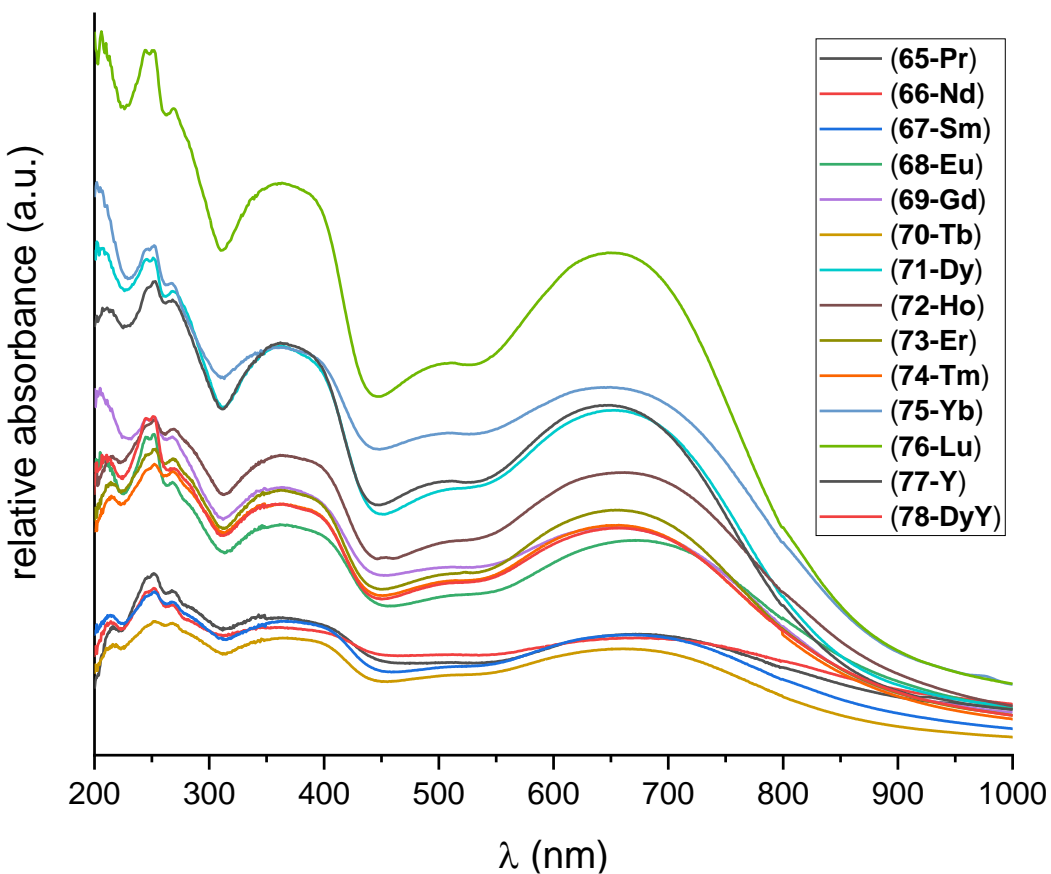


Figure 205. Solid state UVVis absorption spectra of (65-Pr)-(78-DyY).

In order to calculate the anisotropy axes using MAGELLAN, which is only programmed to deal with Dy^{III} ions with a $J = 15/2$ ground state, the crystal structure of (74-Tm) was used but Tm^{III} ions relabelled to Dy^{III}. This is only possible because the (74-Tm) and (71-Dy) are isostructural as evidenced by PXRD and differences between the molecular structures concerning bond lengths and angles are minimal. Nevertheless, this should be kept in mind when evaluating the results of the calculation. Since the resulting axes are essentially orthogonal to the Tm-Tm vector (89.9°) which is consistent with the results obtained for the MeOH and EtOH versions above, this appears to be the correct orientation for the anisotropy axes (see figure 206). As mentioned above this means that the dipolar coupling between the two Dy^{III} ions in (71-Dy) is antiferromagnetic.

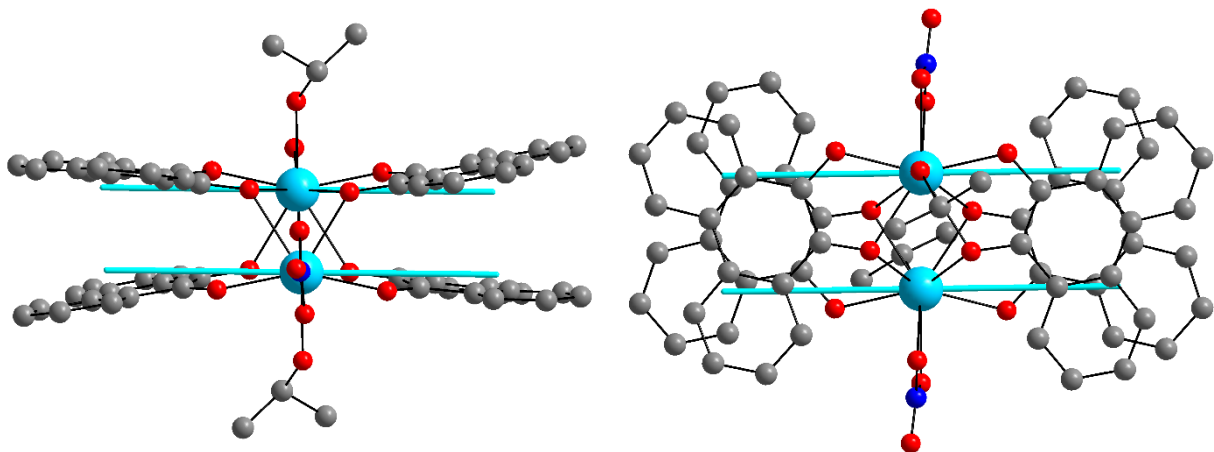


Figure 206. Anisotropy axes calculated using MAGELLAN on the crystal structure of (74-Tm) pretending the Tm^{III} ions are Dy^{III} ions based on the fact that (74-Tm) and (71-Dy) are isostructural.^[297]

Susceptibility measurements at temperatures between 1.8 and 300 K were performed on (71-Dy) with an applied dc field of 0.1 T. The RT value of 26.95 cm³Kmol⁻¹ in the $\chi_M T$ vs T plot (figure 207, left) is slightly lower than but in reasonable agreement with the expected value of 28.34 cm³Kmol⁻¹ for two uncoupled Dy^{III} ions. The $\chi_M T$ values decrease slowly with decreasing temperature which can be attributed to the depopulation of excited Stark levels. The decrease becomes steeper below 50 K indicating the possible involvement of antiferromagnetic coupling in addition to the depopulation of excited states and leading to a minimum $\chi_M T$ value of 6.99 cm³Kmol⁻¹ at 1.8 K. From the Curie-Weiss fit to the χ_M^{-1} vs T plot (figure 207, right) at temperatures between 10 and 300 K, an antiferromagnetic interaction can be confirmed with the Weiss constant θ of -10.6 K and the Curie constant $C = 27.62$ cm³Kmol⁻¹.

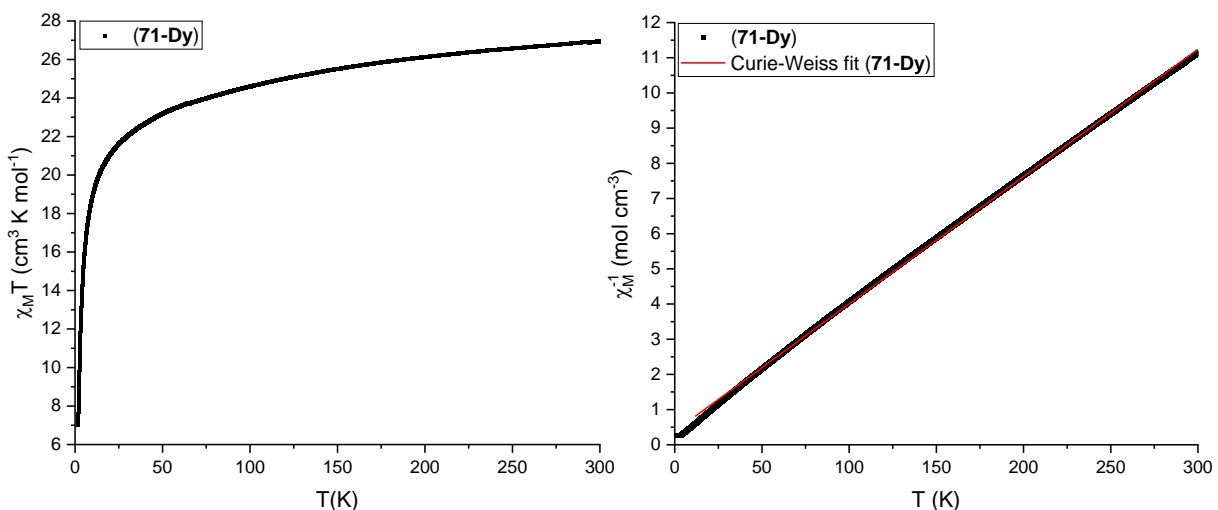


Figure 207. $\chi_M T$ vs T plot (left) and χ_M^{-1} vs T plot (right) obtained from susceptibility measurements performed on an immobilised powder sample of (71-Dy) at temperatures between 1.8 and 300 K with an applied dc field of 0.1 T.

Magnetisation measurements on **(71-Dy)** at 1.8, 3 and 5 K and fields between 0 and 7 T look very similar to the ones obtained for **(60-Dy)**. In the magnetisation vs applied magnetic field graph (figure 208, left) the three curves superpose at low fields and in the case of the 1.8 and 3 K curves up to circa 0.35 T. This field value at which the curves no longer superpose corresponded to the switching field of the level crossing in **(60-Dy)**. Therefore, by comparison of the values (0.27 T in **(60-Dy)** and 0.35 T in **(71-Dy)**), it can be expected that a level crossing would occur at higher fields for the iso-propanol version of the Ln_2Rad_4 complexes. From the reduced magnetisation plots (figure 208, right), the involvement of excited states and significant anisotropy is suggested as the curves do not superpose at all.

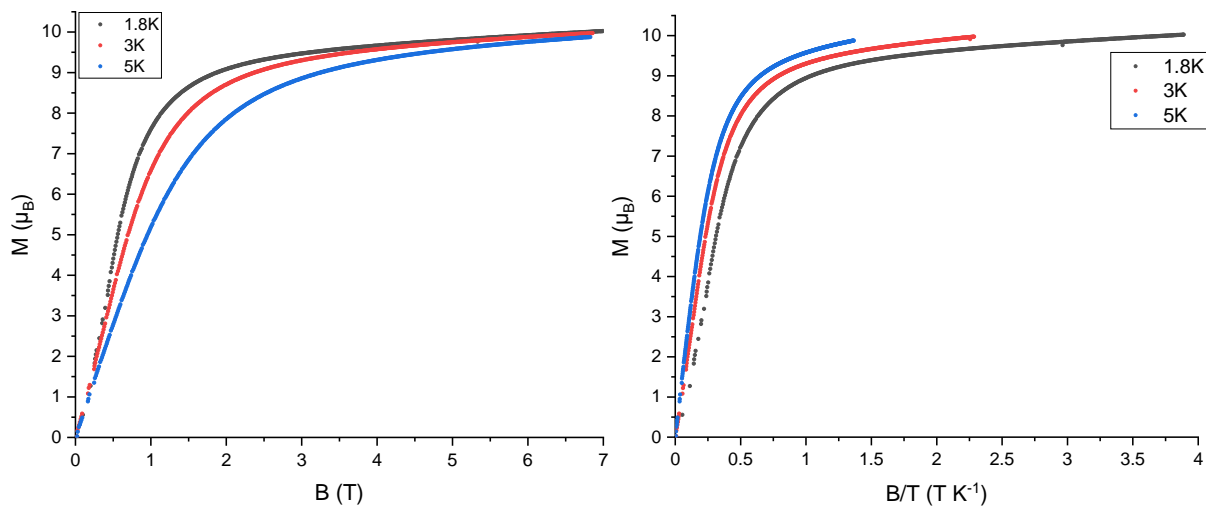


Figure 208. Magnetisation (left) and reduced magnetisation plots of **(71-Dy)** (right) at 1.8, 3 and 5 K and fields between 0 and 7 T.

The magnetic behaviour of **(71-Dy)** was also investigated under an applied ac field at frequencies between 1 and 1000 Hz and temperatures between 1.8 and 20 K. Clear maxima can be observed in the out-of-phase susceptibility (figure 209, right) indicating slow relaxation of magnetisation. The curves were fitted using the generalised Debye model in order to extract the τ values to gain information on the relaxation dynamics present here.

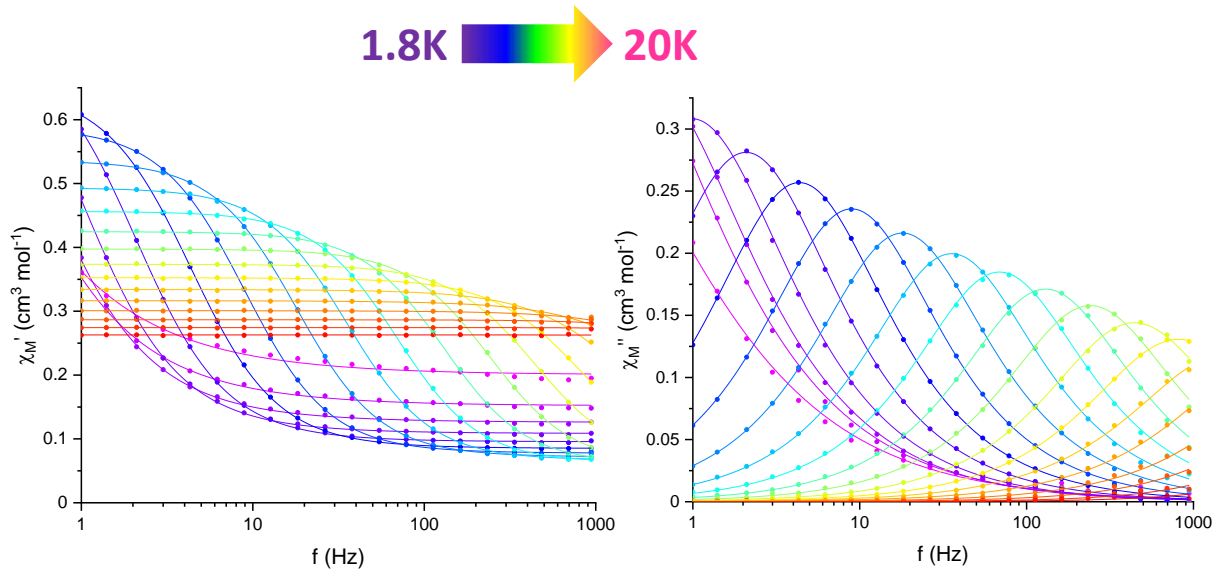


Figure 209. In- and out-of phase susceptibility vs frequency plots (left and right, respectively) obtained from ac susceptibility measurements on (71-Dy).

In order to fit the $\ln(\tau)$ vs $1/T$ plot and investigate the relaxation processes an additional Arrhenius term taking the Orbach relaxation process into account was added to the equation proposed by Lunghi *et al.* (equation 13). The data points (black dots in figure 210) that were obtained from the Debye fit do not plateau in the low temperature region, never reaching the quantum regime in the low temperature region in which tunnelling processes provide a fast-track to magnetisation reversal. Both this and the fitting parameters (see table 22) indicate effective quenching of such tunnelling processes at low temperatures in (71-Dy) which is in line with the behaviour observed for the parent compound. On the other hand, in (60-Dy) tunnelling was far more effective as seen from the fit shown in figure 199 above. From the linear fit U_{Orbach} was obtained as 179.0 K and T_{B100} as 7.1 K. The parameters obtained from fitting with equation 13 are comparable to the ones obtained for the parent compound with slightly less contribution from direct relaxation and slightly more contribution from Raman relaxation possibly due to the floppier nature of the neutral co-ligand. The energy barrier however is significantly higher for (71-Dy) and more comparable to the one obtained for the EtOH version (60-Dy).

Table 22. Fitting parameters used to fit the relaxation processes present in (71-Dy) using equation 13.

A ($\text{s}^{-1} \text{K}^{-1}$)	B (s^{-1})	V (s^{-1})	w (K)	τ_0 (s)	U (K)
0.71	0	28614	46.2	3.92E-10	188.8

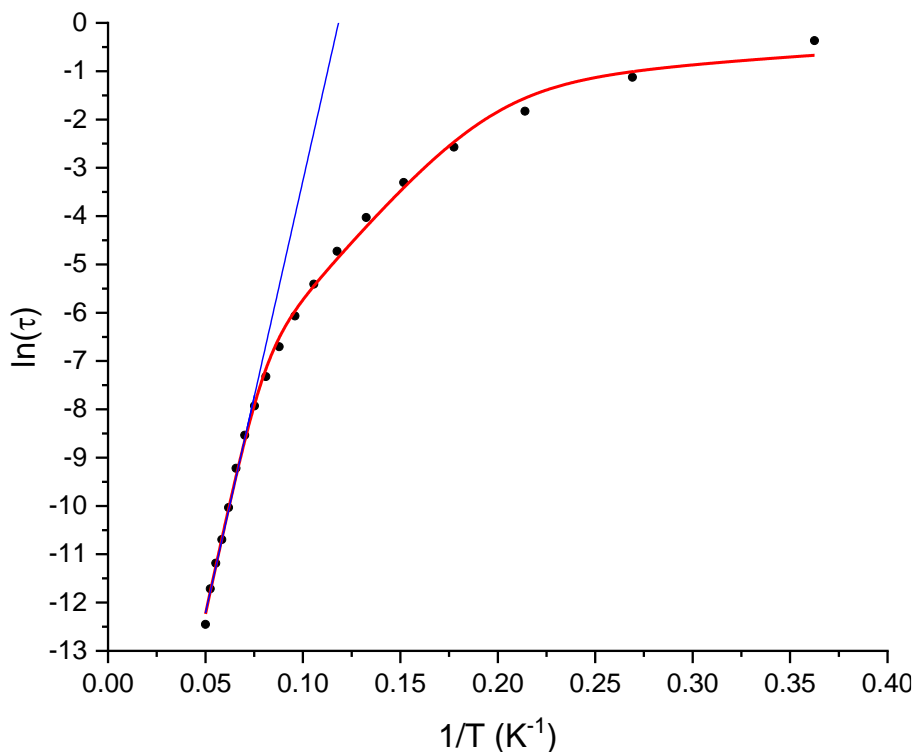


Figure 210. Relaxation processes fitted using equation 13 (red line) as well as using a linear fit to the high temperature region (blue).

The low temperature magnetic behaviour was investigated in MicroSQUID measurements on single crystals of **(71-Dy)** in collaboration with Dr. Sagar Paul in the group of Prof. Dr. Wolfgang Wernsdorfer (KIT, PHI). The temperature dependence between 0.03 and 5 K as well as the sweep rate dependence between 1 and 128 mT/s (figure 211, top left and right, respectively) confirm the similarity between the *isopropanol* version and the parent MeOH version of the Ln_2Rad_4 clusters. This becomes obvious looking at the region around zero field in which in **(71-Dy)** as well as the parent dimer exhibit an essentially non-magnetic ground state. In the case of **(71-Dy)** this persists up to 0.41 T, which is significantly higher than the value of 0.3 T obtained for the original MeOH dimer indicating that the quenching of ZFQTM responsible for the stabilisation of the essentially non-magnetic ground state is more effective in **(71-Dy)**.

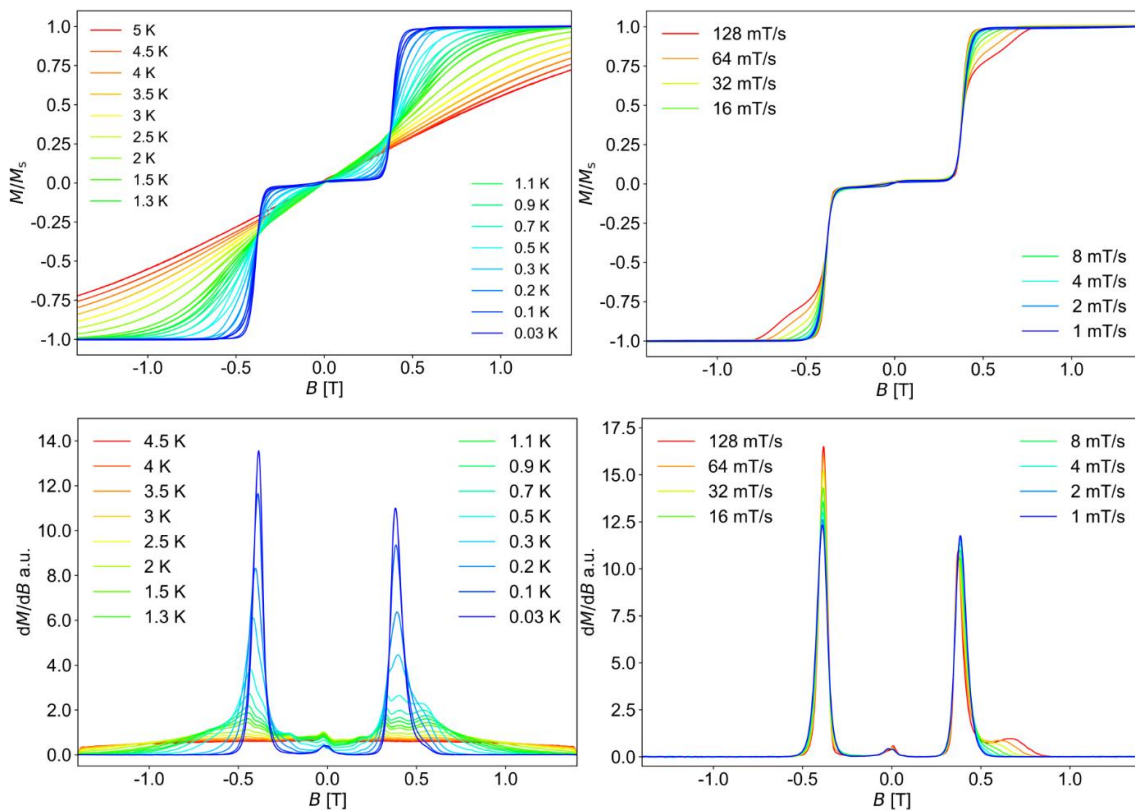


Figure 211. MicroSQUID measurements performed on single crystals of (71-Dy). Temperature dependence between 0.03 and 5 K (left) and sweep rate dependence between 1 and 128 mT/s (right). Derivative plots for both dependencies highlighting the switching field of the level crossing from the essentially non-magnetic ground state at 0.41 T (bottom).

6.4 Varying the Anionic Co-Ligand

Exchanging the anionic co-ligand was shown to be possible through the accidental isolation of the Er^{III} and Cl^- containing dimer during the doctoral work of Dr. Thomas Kriese.^[33] This was attributed to the size of the Ln^{III} ion as the larger Ln^{III} ions led to Ln_2Rad_6 complexes and the same recipe using Er^{III} resulted in $[\text{Er}_2(\text{phsq})_4(\text{Cl})_2(\text{MeOH})_2]$. Later the reproduction of $\text{Er}_2(\text{phsq})_4(\text{Cl})_2(\text{MeOH})_2$ proved difficult. However, the first successful synthesis of the pure Dy compound with chloride co-ligands instead of nitrate is presented in my Master thesis. This complex was obtained by changing multiple reaction parameters, in particular the crystallisation time and temperature (-20°C for two weeks).^[31]

6.4.1 $[\text{Ln}_2(\text{phsq})_4(\text{Cl})_2(\text{MeOH})_2]$

Attempts to repeat the synthesis of this Cl-containing dimer during the work on this doctoral thesis proved a challenge since it became obvious that the crystallisation time and temperature were not actually the determining factor for the formation of the desired compounds. Rather, the reaction time and the basicity of the reaction mixture turn out to be the key to reproducible syntheses of $[\text{Ln}_2(\text{phsq})_4(\text{Cl})_2(\text{MeOH})_2]$. Thus, using one equivalent of NaN_3 in the mixture, which acts as a weak base, it was possible to obtain $[\text{Ln}_2(\text{phsq})_4(\text{Cl})_2(\text{MeOH})_2]$ for $\text{Ln} = \text{Nd}^{\text{III}}\text{-Tm}^{\text{III}}$ (**79-Nd**), (**80-Sm**), (**81-Eu**), (**82-Gd**), (**83-Tb**), (**84-Dy**), (**85-Ho**), (**86-Er**), (**87-Tm**) and (**88-Y**) as well as the Dy-Y-doped version (**89-DyY**). The fact that also larger Ln^{III} ions to the left of gadolinium are shown to form the Cl-dimers here strengthens the suggestion that basicity and reaction time are the more important factors in the synthesis of these compounds. However, a size dependency was also observed as the smaller Ln^{III} ions form the Cl-dimers much more readily and in higher yields, while the crystals of the larger Ln^{III} ions are occasionally accompanied by an unidentified air sensitive green precipitate that turns pale yellow upon opening the autoclaves and ultimately becomes a white powder. Furthermore, the reaction was tested using different bases. Pure samples of crystals of (**84-Dy**) were obtained using NaN_3 , Et_3N , mdeAH_2 , teAH_3 and LiOH . Other bases such as KHCO_3 and K_2CO_3 yielded dark crystals that were confirmed to be (**84-Dy**) but also the air sensitive side product that was usually only observed in reactions with larger Ln^{III} ions when using NaN_3 . The best results in terms of yield were obtained using NaN_3 therefore further reactions were performed with NaN_3 as the base. The crystallinity of the Cl-dimers is maintained for a significantly shorter time than the series containing nitrate as the Cl-dimers turn to green amorphous powder within 2-4 weeks in air.

The molecular structure of (**84-Dy**) is shown in figure 212 and shows usual biplane structure with chlorides replacing the nitrates. The C-O bond lengths of the ligands of $\text{C}(1)\text{-O}(1) = 1.301(4) \text{ \AA}$, $\text{C}(2)\text{-O}(2) = 1.267(4) \text{ \AA}$, $\text{C}(15)\text{-O}(3) = 1.297 \text{ \AA}$ and $\text{C}(16)\text{-O}(4) = 1.275$ confirm the radical nature of the ligand. The pancake bond is intact in these compounds as well, as evidenced by the shortest inter-ligand C-C and O-O distances of $2.712(5) \text{ \AA}$ and $2.581(4) \text{ \AA}$, respectively. This leads to Dy-Dy distances of $3.3562(3) \text{ \AA}$ which is comparable to the distance in the original $[\text{Dy}_2(\text{phsq})_4(\text{NO}_3)_2(\text{MeOH})_2]$ compound.

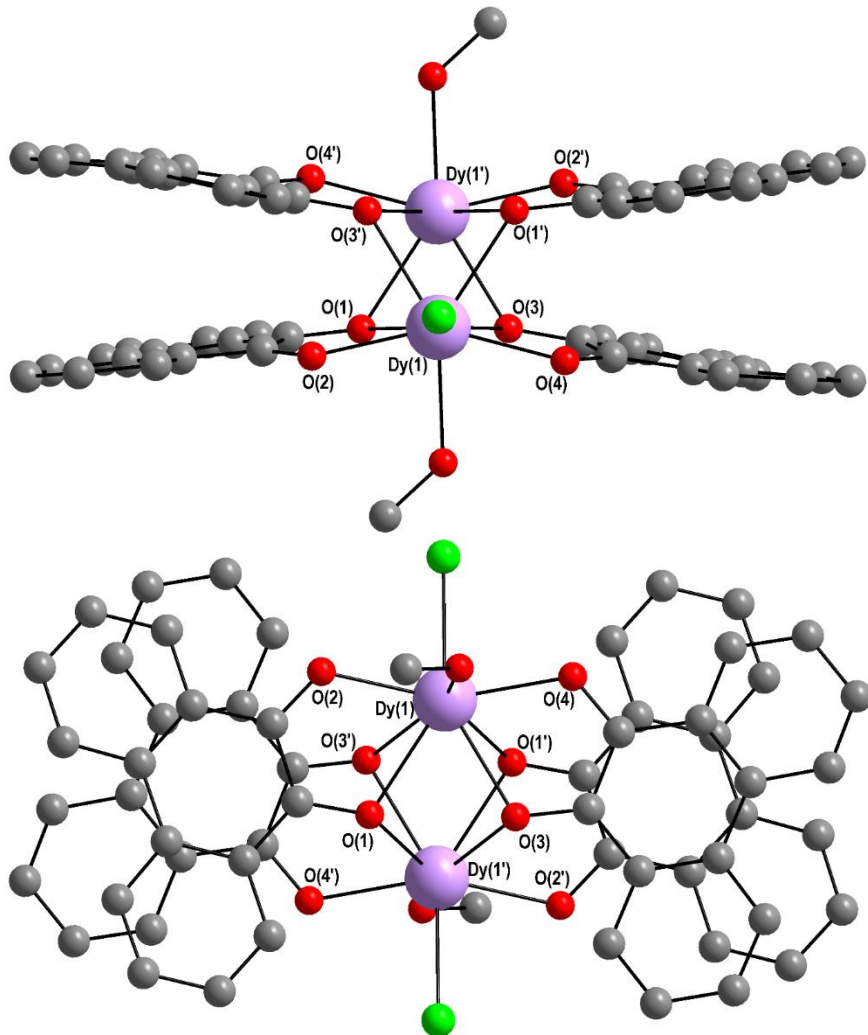


Figure 212. Top and side view on the molecular structure of (84-Dy) as a representative for the $[\text{Ln}_2(\text{phsq})_4(\text{Cl})_2(\text{MeOH})_2]$ series.

(84-Dy) crystallises in the monoclinic space group $\text{P}2_1/\text{c}$ with $Z = 2$ and no additional lattice solvent. The packing is shown in figure 213 and reveals π - π stacked zig-zag chains along the b axis in the a - b plane that are held together by non-classical HBs between the proton of a MeOH ligand and a chloride on the neighbouring molecule. The $\text{O}(5)\text{-H}(5)\dots\text{Cl}(1)$ distance is $3.044(3)$ Å and the angle is $162(5)^\circ$.

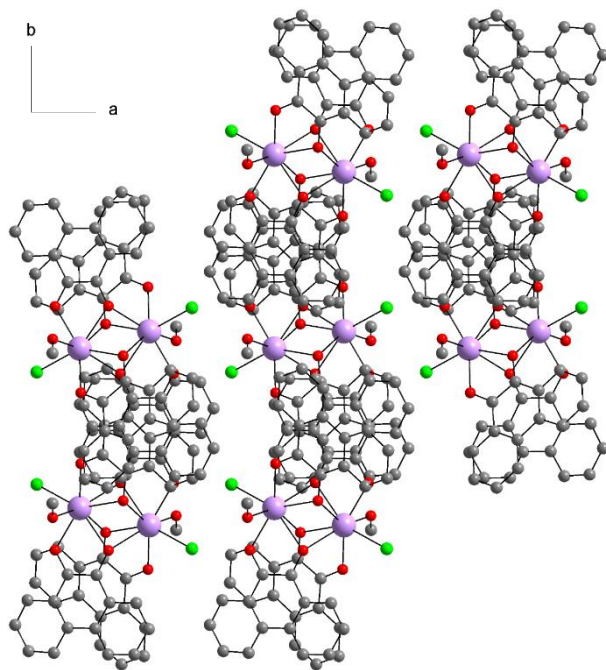


Figure 213. View along the crystallographic c axis on the packing of **(84-Dy)** showing the zig-zag chains formed by intermolecular π - π interactions which are held together by non-classical HBs.

The Cl-dimers presented here are all isostructural as evidenced by SC-XRD, PXRD and/or IR and UVVis spectroscopy. The PXRDs are compared to the simulated powder pattern obtained using the SC-XRD data of **(84-Dy)** in figure 214.

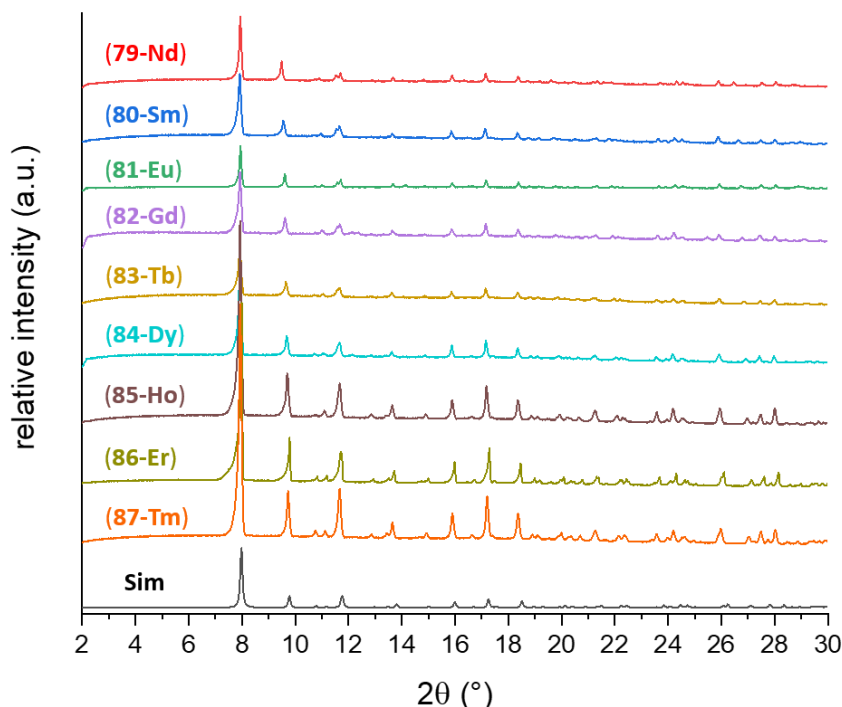


Figure 214. Comparison of the PXRDs of the isostructural series of $[\text{Ln}_2(\text{phsq})_4(\text{Cl})_2(\text{MeOH})_2]$ compounds to the simulated powder pattern of **(84-Dy)**.

Further members of this series such as (**88-Y**) and (**89-DyY**) were shown to be present by determining the unit cell using SC-XRD and IR, respectively.

Due to the less robust nature of this series of compounds even in solid state, UVVis absorption spectra have been recorded for (**83-Tb**) and (**84-Dy**) acting as representatives for the series (figure 215). Both samples show the same spectra with three distinct bands visible in the UV region at 206, 251 and 267 nm, a broad band centred at 371 nm and the already known very broad band assigned to the ILCT transition which occurs at 660 nm for the Cl-versions of the dimers with a shoulder at 507 nm.

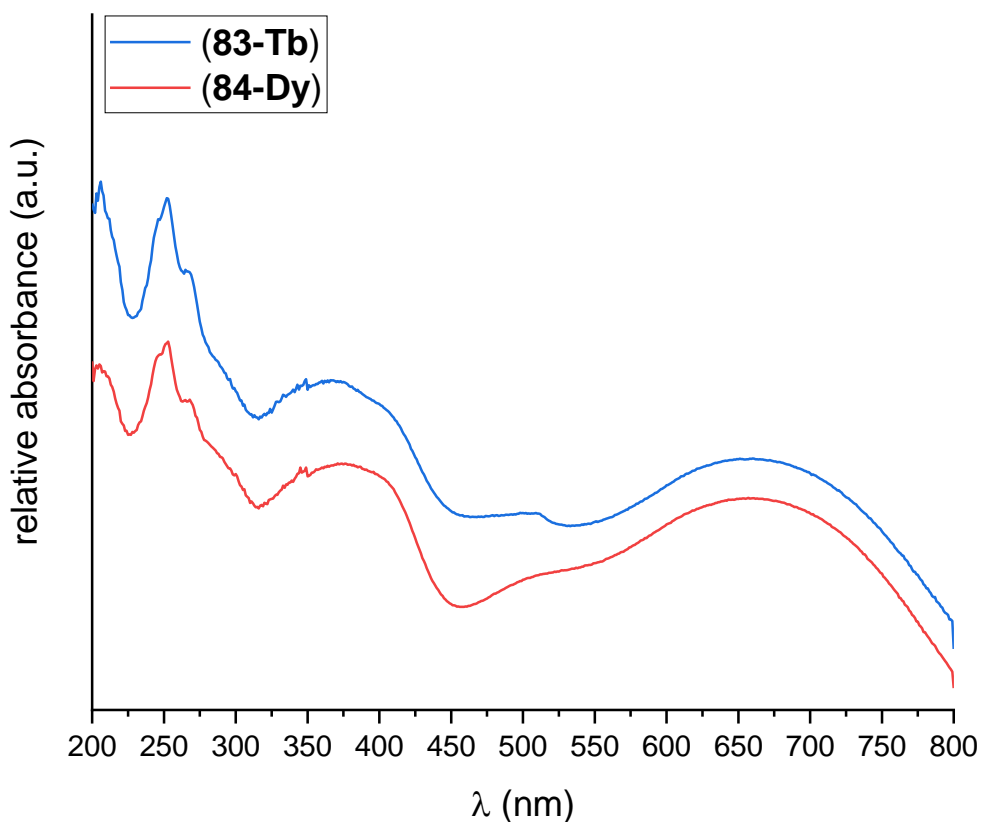


Figure 215. Solid state UVVis absorption spectra of (**83-Tb**) and (**84-Dy**) as representatives for the $[\text{Ln}_2(\text{phsq})_4(\text{Cl})_2(\text{MeOH})_2]$ series between 200 and 800 nm.

The optical properties of (**84-Dy**) were also investigated in solution. For that 10 μM MeCN solutions were prepared the same way as described for (**48-Dy**) and (**60-Dy**) above. The solution and solid state spectra of (**84-Dy**) match each other well (see figure 216). The solution spectrum also compares well to the ones of (**48-Dy**) and (**60-Dy**) showing the same general structure with two bands in the UV region, a band with red-shifted shoulder at around 350 nm and the broad ILCT band at 625 nm. It is noteworthy that the intensity of the absorptions in the UV region is higher than for the

other compounds while the intensities in the visible range are lower than for **(48-Dy)** and comparable to the ones for **(60-Dy)**. This might indicate faster degradation in solution of the Cl dimers compared to their nitrate analogues which would also be in line with the faster degradation observed in the solid state.

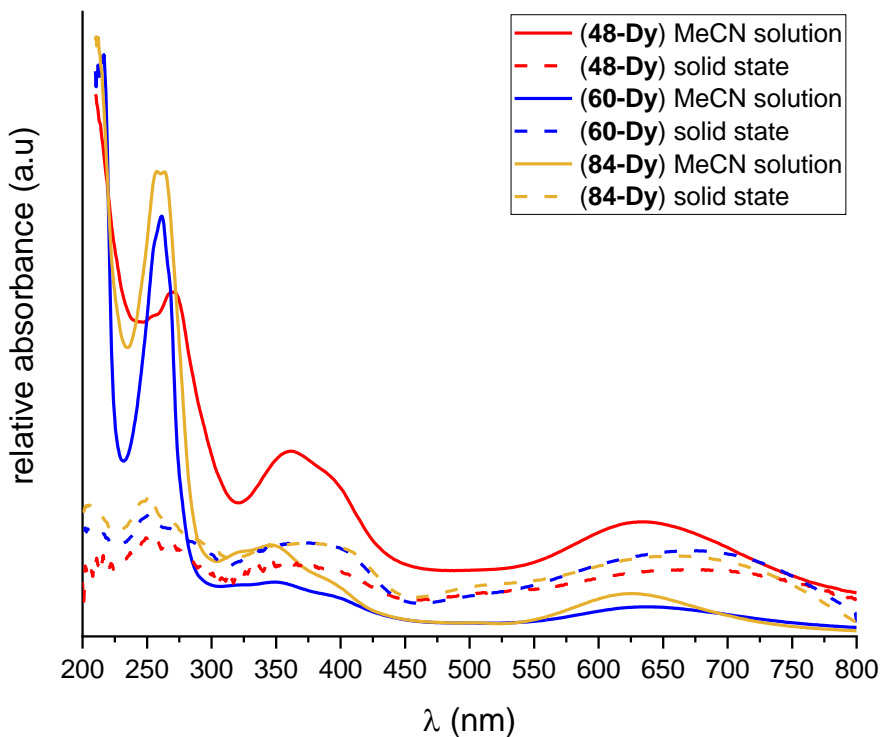


Figure 216. Comparison of the UVVis absorption spectrum of **(84-Dy)** in 10 μ M MeCN solution to the solid state spectrum as well as the solution and solid state spectra of **(48-Dy)** and **(60-Dy)**.

The orientation of the anisotropy axes in **(84-Dy)** was calculated using MAGELLAN^[297] which resulted in the same orientations as for the above-mentioned variations on the Ln₂Rad₄ complexes (see figure 217). The axes are at an angle of 89.7° to the Dy-Dy vector leading to antiferromagnetic dipolar coupling between the two Dy^{III} ions.

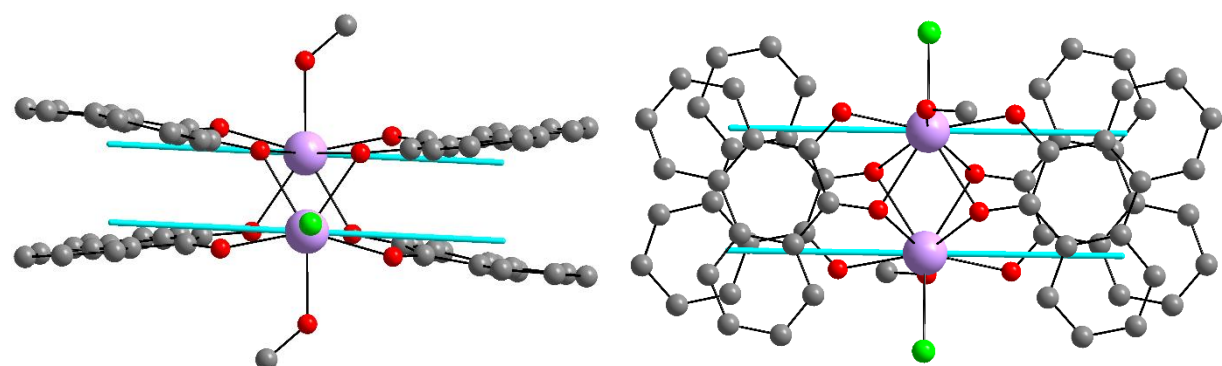


Figure 217. Side and top view on the molecular structure of **(84-Dy)** with the anisotropy axes calculated using MAGELLAN shown in cyan.^[297]

Susceptibility measurements were performed on **(84-Dy)** at temperatures between 1.8 and 300 K with an applied dc field of 0.1 T. In figure 218, left the $\chi_M T$ vs T plot is shown. At 300 K the $\chi_M T$ value of **(84-Dy)** reaches $28.35 \text{ cm}^3 \text{Kmol}^{-1}$ almost perfectly fitting the value of $28.34 \text{ cm}^3 \text{Kmol}^{-1}$ for two uncoupled Dy^{III} ions. The slow decrease in $\chi_M T$ can be attributed to thermal depopulation of excited Stark levels. Below 50 K the decrease becomes steeper due to a possible combination with an additional antiferromagnetic interaction and reaches a minimum value of $14.55 \text{ cm}^3 \text{Kmol}^{-1}$ at 1.8 K. The χ_M^{-1} vs T plot follows the Curie-Weiss law between 3 and 300 K and a Weiss constant θ of -2.9 K confirming an antiferromagnetic interaction to be present and a Curie constant C of $28.65 \text{ cm}^3 \text{Kmol}^{-1}$ can be extracted from the linear fit shown in red in figure 218, right.

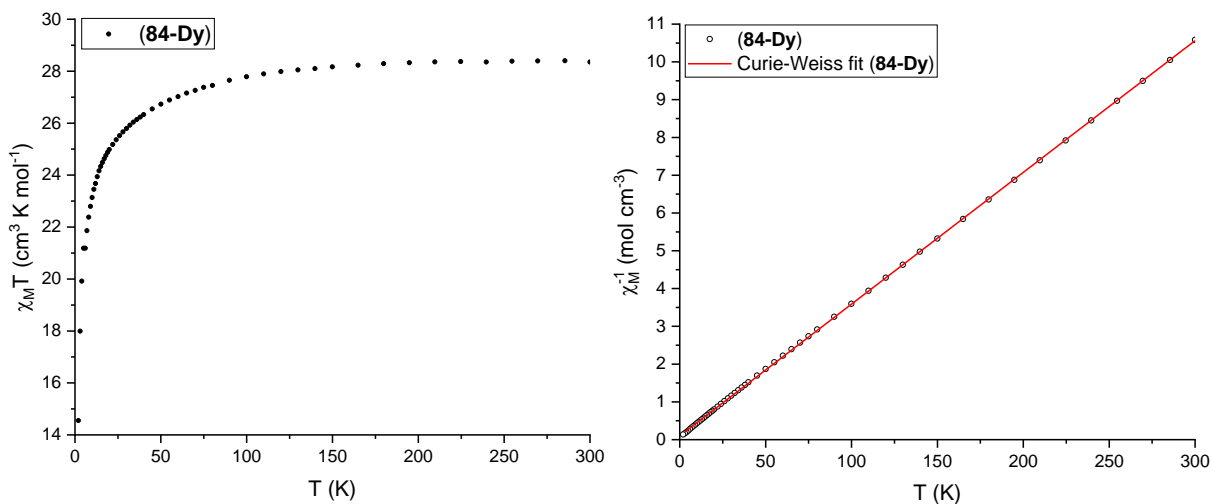


Figure 218. $\chi_M T$ vs T plot (left) and χ_M^{-1} vs T plot with Curie-Weiss fit (right) of **(84-Dy)** at temperatures between 1.8 and 300 K with an applied dc field of 0.1 T.

Additionally, the expected slow relaxation of magnetisation was indeed observed using an ac field and measuring the in- and out-of-phase susceptibility at frequencies between 0.1 and 1500 Hz and temperatures between 10 and 35 K (figure 219 left and right, respectively). Comparing the signal of the out-of-phase magnetic susceptibility of **(84-Dy)** which still clearly shows maxima around 30 K within the measuring window (up to 1500 Hz) to those of the dimers already presented, indicates that the relaxation in **(84-Dy)** is slower than in the other ones described above. While the changes to the neutral co-ligand did have an influence on the magnetic properties of the Ln_2Rad_4 compounds (especially EtOH compared to MeOH and iPrOH), the slow relaxation is now clearly shifted to significantly higher temperatures within the observable frequency window by changing the nitrate co-ligand to a chloride.

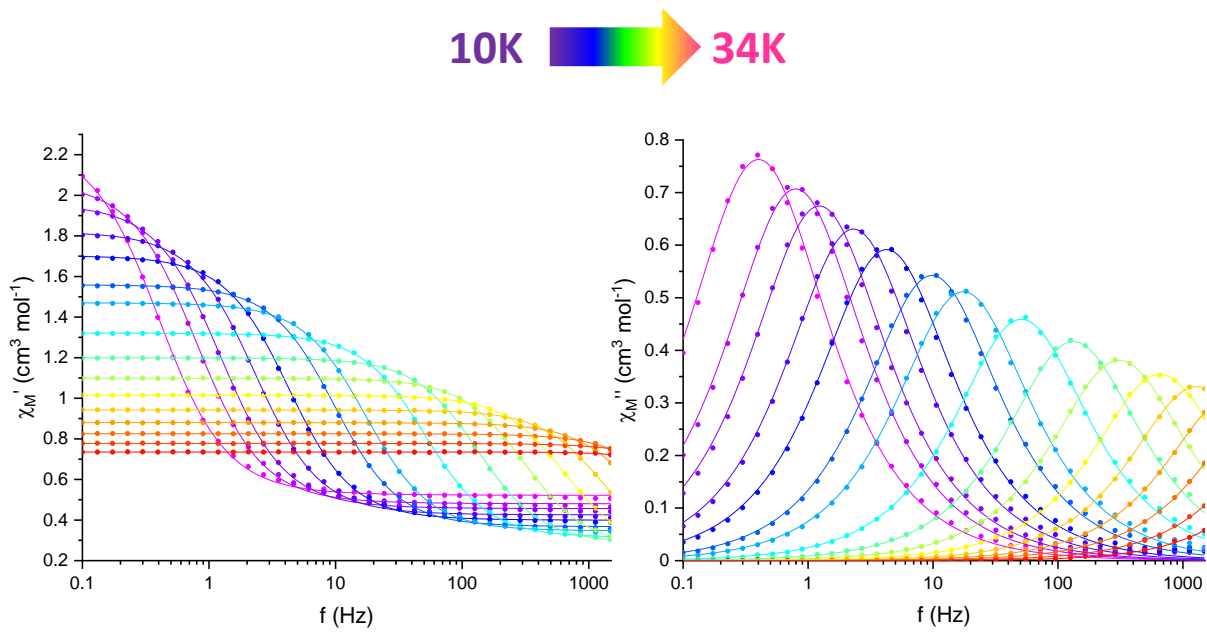


Figure 219. In- and out-of-phase susceptibility of (84-Dy) (left and right, respectively) plotted vs the frequency of the applied ac field revealing slow relaxation of magnetisation up to around 30 K within the measured frequency range.

The relaxation mechanisms in (84-Dy) were investigated by fitting the τ values obtained from the Debye fit to equation 13 (see figure 220) and the results are listed in table 23. No ZFQTM was observed for (84-Dy) either, additionally, the direct processes are much slower than for the previously described dimers. Both Raman and Orbach terms show much faster rates as well as much higher energy barriers, suggesting that although these pathways are faster than in the other dimers, they only start to become relevant at much higher temperatures. This is in line with the maxima in the out-of-phase susceptibility measurements which can clearly be seen up to *circa* 30 K and therefore up to between 50 and 100% higher temperatures than the other dimers.

Table 23. Fitting parameters used to fit the relaxation data of (84-Dy) to equation 13.

A ($\text{s}^{-1} \text{K}^{-1}$)	B (s^{-1})	V (s^{-1})	w (K)	τ_0 (s)	U (K)
0.29	0	5388707	175.5	6.64E-12	475.8

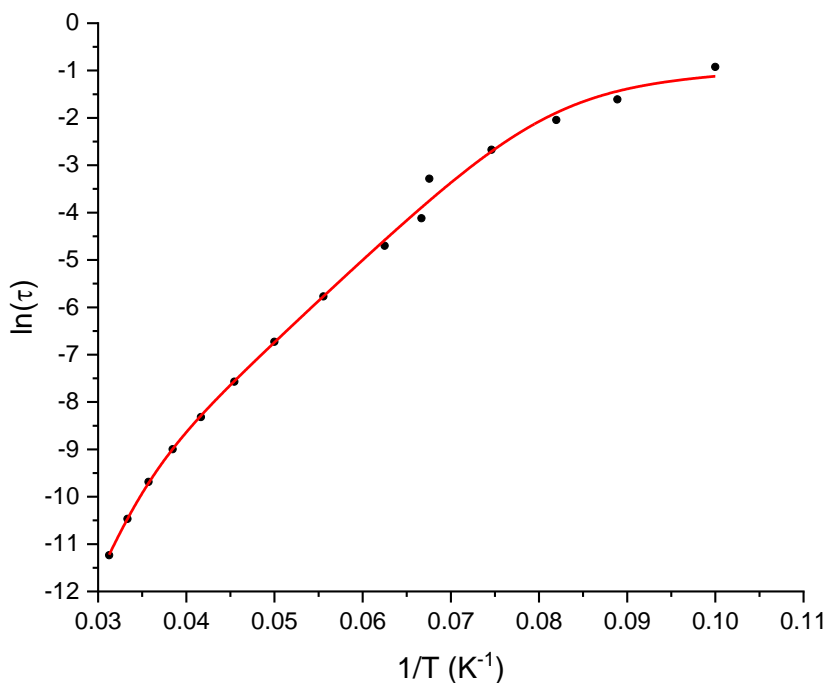


Figure 220. Relaxation processes in (84-Dy) fitted using equation 13.

For further investigations of the magnetic properties, (89-DyY) will be explored using SQUID magnetometry. Additionally, microSQUID measurements are planned on single crystals of (84-Dy) as well as (89-DyY) to reveal the low temperature behaviour of these modified Ln_2Rad_4 which (in the case of (84-Dy)) show improved SMM behaviour.

6.4.2 Further Attempts to Vary the Anionic Co-Ligand

Since changing the nitrate co-ligand to chloride had a significant impact on the magnetic properties of this extended family of Ln_2Rad_4 dimers by improving the temperature at which blocking of magnetisation reversal is observed, reactions using further anions were performed. Attempts in producing the acetate analogue of the known dimeric structure using Dy(OAc)_3 did not yield any crystals. But using Dy(OTf)_3 with additional Na(OAc) in the reaction mixture resulted in dark crystals. This dark compound was only obtained in very low quantities and the crystals were not suitable for structure determination using SC-XRD. Nevertheless, this appears to be a recipe that with some optimisation of the reaction conditions could lead to the desired acetate dimers. This would further extend this family of compounds and provide more insight into the relaxation dynamics of this system.

An approach that often yields compounds with essentially identical molecular structures is exchanging chloride for bromide ligands as exemplified by the syntheses of (**8**- and **9-Ce**) as well as (**10**- and **11-Cu**) described above in chapter 4.3. In the case of the Ln_2Rad_4 complexes this has not yet been successful.

Furthermore, the reproduction of the dimeric complexes employing six of the phenanthrenesemiquinonate radical ligands that were described in the doctoral thesis of Dr. Thomas Kriese was attempted.^[33] Using the same procedure that was described therein was unsuccessful. The use of Ce^{III} salts in the synthetic procedures described here for the different variations of dimers also proved unfruitful. Changing the usual method and heating the reaction mixture of $\text{CeCl}_3 \cdot 6\text{H}_2\text{O}$ in methanolic solution with added Na_2CO_3 to reflux in a Schlenk vial under inert atmosphere, instead of doing the reaction in an autoclave, the reproduction of $[\text{Ce}_2(\text{phsq})_6(\text{MeOH})_2] \cdot 10\text{MeOH}$ (**90-Ce**) was successful. The molecular structure (see figure 221) is the same as for the other dimers only with two additional phsq radical ligands instead of the negatively charged co-ligands.

The C-O bond lengths of all six phenanthrene-based ligands (see table 24) confirm all of them to be in the radical state.

Table 24. C-O bond lengths of the ligand confirming the radical oxidation state of the ligand. The other three ligands are the same per inversion symmetry.

ligand 1	$d(\text{O}(1)-\text{C}(1)) = 1.259(2) \text{ \AA}$	$d(\text{O}(2)-\text{C}(2)) = 1.308(2) \text{ \AA}$
ligand 2	$d(\text{O}(3)-\text{C}(15)) = 1.252(2) \text{ \AA}$	$d(\text{O}(4)-\text{C}(16)) = 1.269(2) \text{ \AA}$
ligand 3	$d(\text{O}(5)-\text{C}(29)) = 1.319(2) \text{ \AA}$	$d(\text{O}(6)-\text{C}(30)) = 1.280(2) \text{ \AA}$

The shortest inter-ligand C-C and O-O distances of $2.737(19) \text{ \AA}$ and $2.654(11) \text{ \AA}$ are in line with the distances observed the other dimers above. Therefore, it can be concluded that the presence of additional radical ligands in the system does not affect the pancake bonding between the four radical ligands observed in all the variations. The Ce-Ce distance of $3.637(2) \text{ \AA}$ is longer than the ones observed for Dy^{III} -containing dimers as expected from the significantly larger ionic radius of Ce^{III} leading to longer however still short M-M distances. The same trend was observed in the series of $[\text{Ln}_2(\text{phsq})_4(\text{NO}_3)_2(\text{MeOH})_2]$ complexes in which the M-M distance with the largest lanthanide ion for which the complex could be obtained (Pr^{III}) was 3.539 \AA .^[31-32] The oxidation state of the cerium ions were confirmed to be Ce^{III} by looking at the overall

charge balance as well as doing a BVS analysis, the results of which are shown in table 25.

Table 25. BVS analysis for the cerium ion in **(90-Ce)** using the parameters $B = 0.37$ and $R_0 = 2.121 \text{ \AA}$ for the 3+ oxidation state and 2.068 \AA for the 4+ oxidation state.^[254] As **(90-Ce)** is a dimer and therefore centrosymmetric with $Z' = 0.5$ the two cerium ions are identical, therefore only one calculation had to be performed per oxidation state. The Ce-O bond lengths are listed below as well as the results of the two calculations highlighting the best result in red.

Ce-O bond lengths [Å]	
Ce(1)-O(1)	2.582(8)
Ce(1)-O(1')	2.632(10)
Ce(1)-O(2)	2.446(10)
Ce(1)-O(3)	2.606(9)
Ce(1)-O(3')	2.691(9)
Ce(1)-O(4)	2.452(9)
Ce(1)-O(5)	2.516(9)
Ce(1)-O(6)	2.458(9)
Ce(1)-O(7)	2.501(9)
Results BVS	
Ce ^{III}	Ce ^{IV}
2.95	2.56

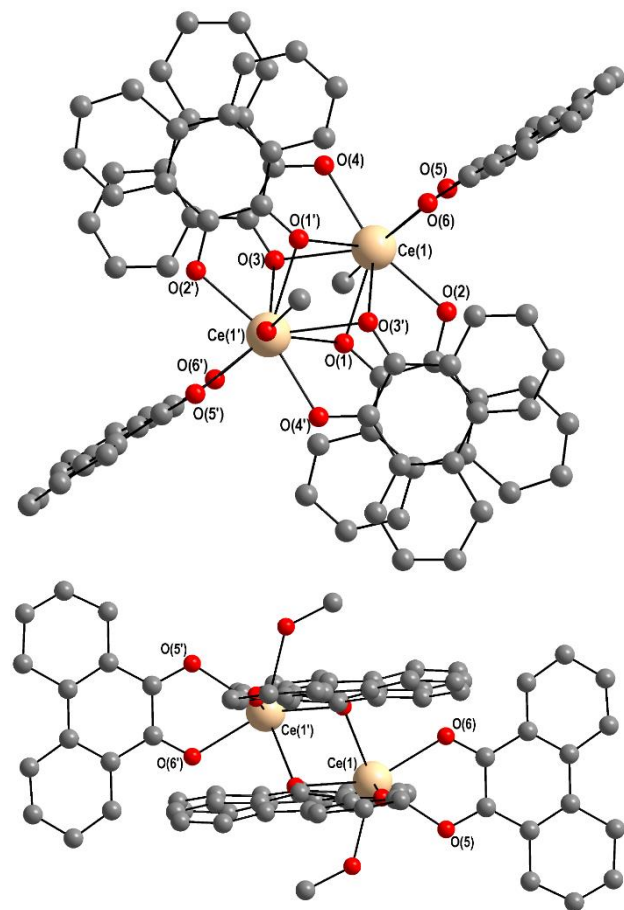


Figure 221. Two views on the molecular structure of **(90-Ce)**. A top view (top) highlighting the similarities to the previously described dimers and a side view showing the new 5th and 6th phenanthrenesemiquinonate radical ligand.

(90-Ce) crystallises in the monoclinic space group $P2_1/n$ with $Z = 2$. The complexes pack in alternating angled stacks as shown in figure 222 with no obvious intermolecular interactions. The shortest intermolecular Ce-Ce distance is $11.317(1)$ Å which is comparable to the intermolecular distances observed for the other variations of these dimers.

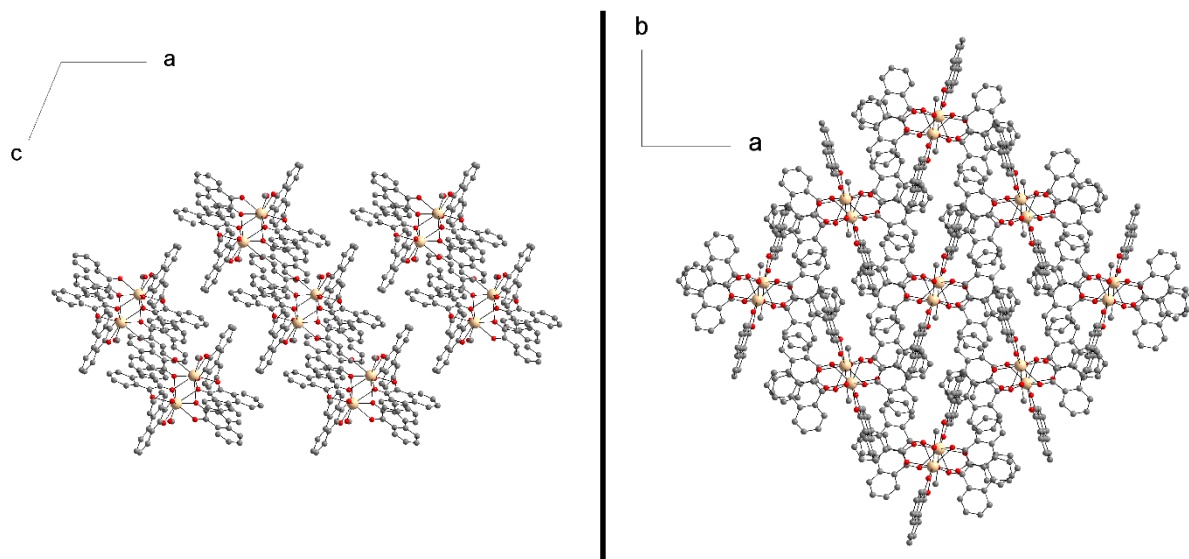


Figure 222. Views on the packing of **(90-Ce)** along the crystallographic b and c axes showing the alternating angled stacks of complexes.

(90-Ce) becomes amorphous in air within minutes likely due to the loss of lattice solvent and forms a fluffy dark solid instead of well-defined crystals. This fluffy solid, changes its colour to dark green over the course of 1 d in air indicating air sensitivity as well. Nevertheless, the successful isolation of this compound via a new synthetic route that worked reproducibly for Ce^{III} may open the door for the synthesis of analogous compounds featuring magnetically more interesting Ln^{III} ions.

6.5 Changing the Radical Ligand

6.5.1 Pyrene-4,5-dione

The radical ligand, as the fourth component of this family of compounds, was also varied. As a first alternative to 9,10-phenanthrenequinone, pyrene-4,5-dione was chosen in order to increase the π - π interactions between the radicals on either side of the two metal ions. This in turn might shorten the already extremely short M-M distance that is thought to be responsible for the effective quenching of ZFQTM. The synthetic

work presented in this section was supported by the efforts of Prashant Anand who performed an internship using an Aspirant Grant by the DAAD under my supervision. Pyrene-4,5-dione (pydi) was synthesised using a slightly modified literature procedure^[350] and purified via column chromatography. The ¹H-NMR and UVVis absorption spectrum in 10 μM MeCN solution are shown in figure 223.

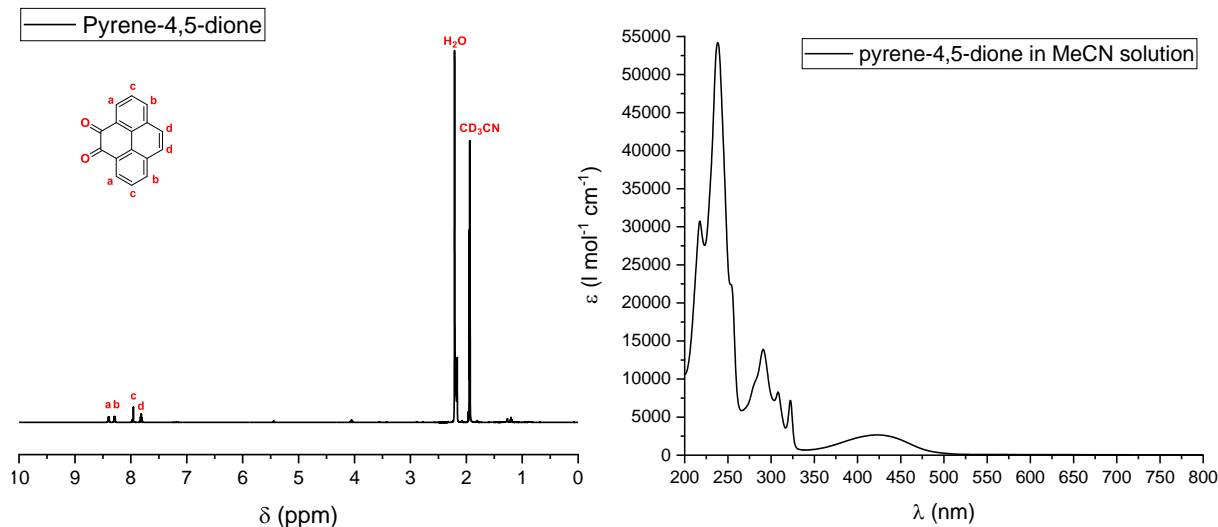


Figure 223. ¹H-NMR and UVVis absorption spectrum of the modified precursor for a radical ligand pyrene-4,5-dione in 10 μM MeCN solution.

Pydi (see figure 224, left) was used as starting material following the same procedure that was used to obtain the EtOH and ⁱPrOH versions of the compound. The pyrenesemiquinonate radical anion (figure 224, right) will be abbreviated as pysq in the following. The synthesis of $[\text{Ln}_2(\text{pysq})_4(\text{NO}_3)_2(\text{MeOH})_2]$ was successful for $\text{Ln} = \text{Tb}^{\text{III}}\text{-Er}^{\text{III}}$ plus Y^{III} (**91-Tb**), (**92-Dy**), (**93-Ho**), (**94-Er**) and (**95-Y**). Initially, a red precipitate that was identified as the ligand starting material was obtained along with dark crystals of the desired compounds. By changing the metal salt to ligand ratio from 2:1 to 4:1 this co-precipitation was successfully suppressed.

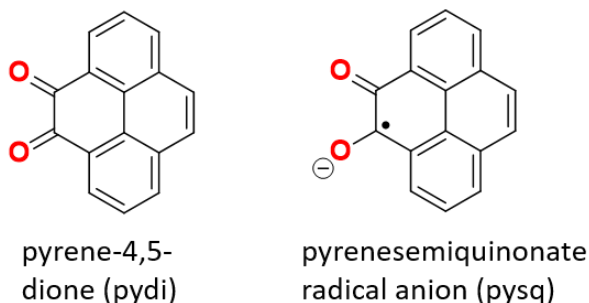


Figure 224. The pyrene-4,5-dione (pydi) starting material as well as the *in-situ* generated radical ligand.

The molecular structure of (**94-Er**) forming the known biplane type cluster is shown in figure 225. The C-O distances of $d(C(1)-O(1)) = 1.285(6)$ Å, $d(C(2)-O(2)) = 1.271(5)$ Å, $d(C(17)-O(3)) = 1.297(6)$ Å and $d(C(18)-O(4)) = 1.264(6)$ Å in the ligands confirm the four pyrene-based ligands to be in the semiquinonate radical state. The inter-ligand radical-radical interaction leading to the formation of a pancake bond is observed in (**94-Er**) as well as evidenced by the shortest C-C distance of 2.697(6) Å and the shortest O-O distance of 2.553(5) Å. These values are marginally shorter than the ones observed for other dimers in this chapter. Nevertheless, it can be concluded that the addition of a fourth phenyl ring to the ligand going from a phenanthrene-based to a pyrene-based system did not significantly improve the intramolecular π - π interactions. This also becomes clear when looking at the C-C distances between the added phenyl rings which are between 3.399(6) Å and 4.236(6) Å and therefore the same as double the VdW radius (= 3.4 Å)^[164] of carbon or more and therefore do not take part in the pancake bonds restraining this system. The Er-Er distance in (**94-Er**) of 3.3347(5) Å is in line with the ones observed for other dimers above, strengthening the hypothesis that the intramolecular interactions are not significantly altered by the size of the π -system of the radical ligand.

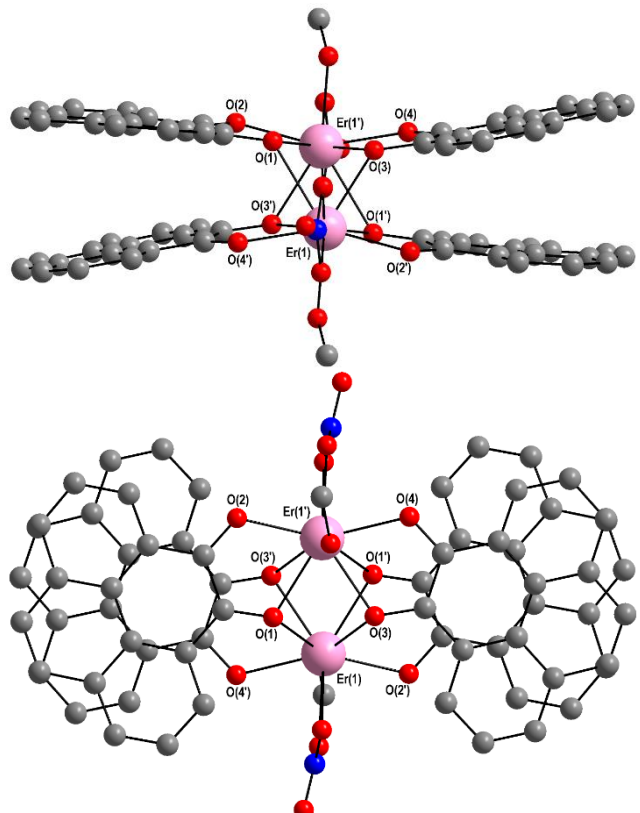


Figure 225. Top and side view on the molecular structure of (**94-Er**) as a representative of the series of $[\text{Ln}_2(\text{pysq})_4(\text{NO}_3)_2(\text{MeOH})_2]$ complexes (**91-Tb**)-(95-Y).

The complexes co-crystallise with two additional organic pyrene-dione molecules per cluster (figures 226 and 227). These were confirmed to be in the dione-form from looking at the overall charge balance as well as the C-O bond lengths of 1.186(7) Å between C(35)-O(10) and 1.235(8) Å between C(34)-O(9). The lattice pydi molecules link the Ln_2Rad_4 clusters together via π - π interactions to form stacks throughout the crystal along the crystallographic c axis with the shortest C-C distance between pysq and pydi ligand of 3.518(8) Å, therefore significantly increasing the possibility for intermolecular interactions and potentially having an impact on the magnetic properties.^[351-352]

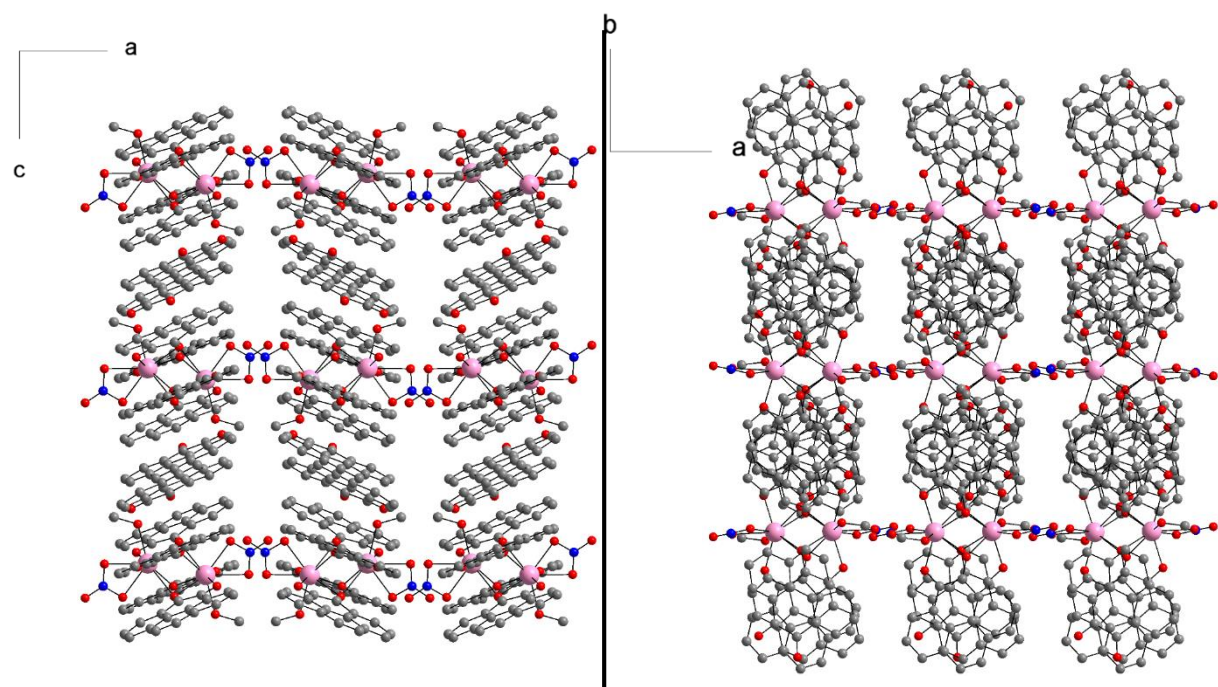


Figure 226. Two views on the packing of (94-Er) showing the stacks of clusters formed by π - π stacking between the pysq radicals coordinating to the Er^{3+} ions and the co-crystallising pydi ligands.

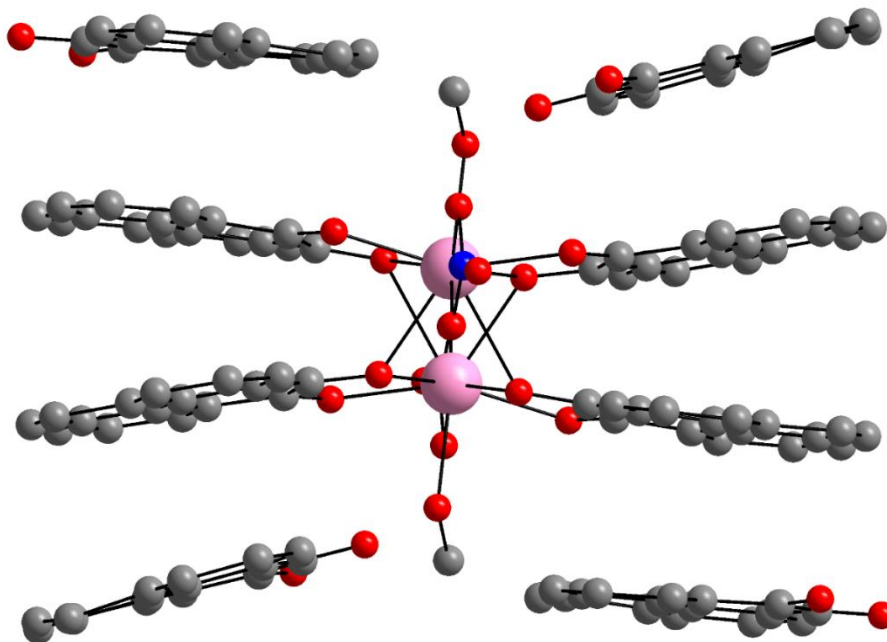


Figure 227. Close-up on the intermolecular π - π interactions around an individual $[\text{Er}_2(\text{pysq})_4(\text{NO}_3)_2(\text{MeOH})_2]$ cluster determining the packing in **(94-Er)**.

The PXRD of **(93-Ho)** was measured and compared to the simulated powder pattern using the crystal structure of **(94-Er)** (see figure 228). This confirmed the compounds to be isostructural and **(93-Ho)** to be phase pure. The syntheses of other members of this series of complexes was confirmed by unit cell determination, IR spectroscopy and elemental analysis.

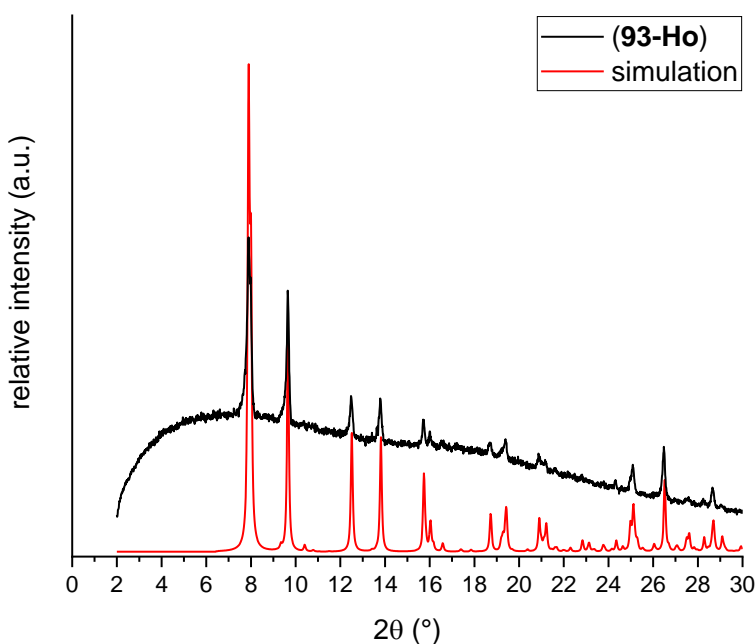


Figure 228. PXRD of **(93-Ho)** compared to the simulated pattern using the crystal structure of **(94-Er)** confirming isostructural complexes.

Solid state UVVis absorption spectra of (**93-Ho**) and (**95-Y**) were recorded and are shown in figure 229. In the UV region a band can be observed at 246 nm with a shoulder at 219 nm that correspond well to the absorption spectrum of pydi that was shown above in figure 223. This is consistent with the observations on the optical properties of the other dimers which also exhibited bands in the UV region that also occur in the phenanthrenedione starting material at the same energies. Additionally, bands in the spectra of (**93-Ho**) and (**95-Y**) occur at 302, 357, 451 with a shoulder at 542 nm. The ILCT transition in (**93-Ho**) is centred around 729 nm while it is red-shifted to be centred around 768 nm in (**95-Y**).

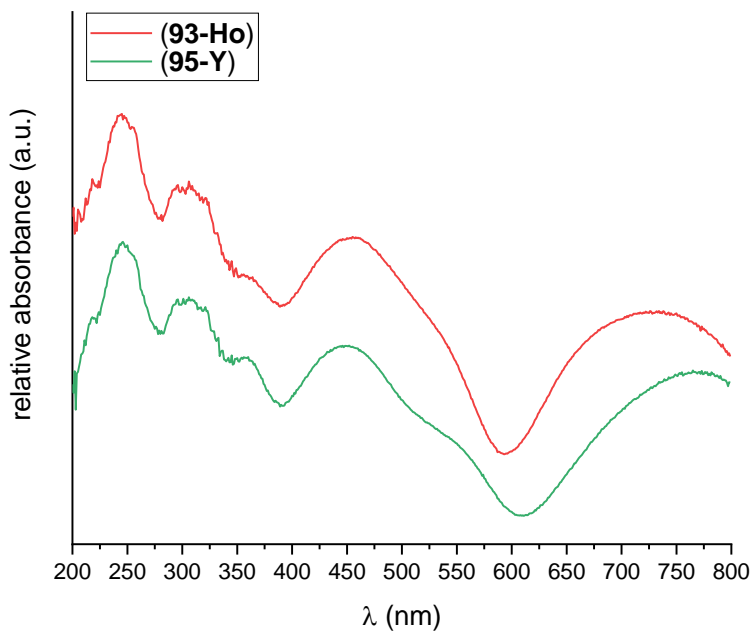


Figure 229. Solid state absorption spectroscopy of (**93-Ho**) and (**95-Y**) as representatives for the series of $[\text{Ln}_2(\text{pysq})_4(\text{NO}_3)_2(\text{MeOH})_2]$.

The anisotropy axes were calculated using MAGELLAN^[297] and the results are shown in figure 230. The angle between the anisotropy axes and the Dy-Dy vector is 88.6° leading to antiferromagnetic dipolar coupling which is in line with the axes obtained for the other dimer that are presented in this chapter. It is noteworthy that in the crystal structure measured of (**92-Dy**), which has the same unit cell as (**94-Er**), the MeOH co-ligands are exchanged for water. This was previously observed for the original MeOH and nitrate dimers in the doctoral thesis of Dr. Thomas Kriese which tend to exchange their MeOH co-ligands for water after some time as well.

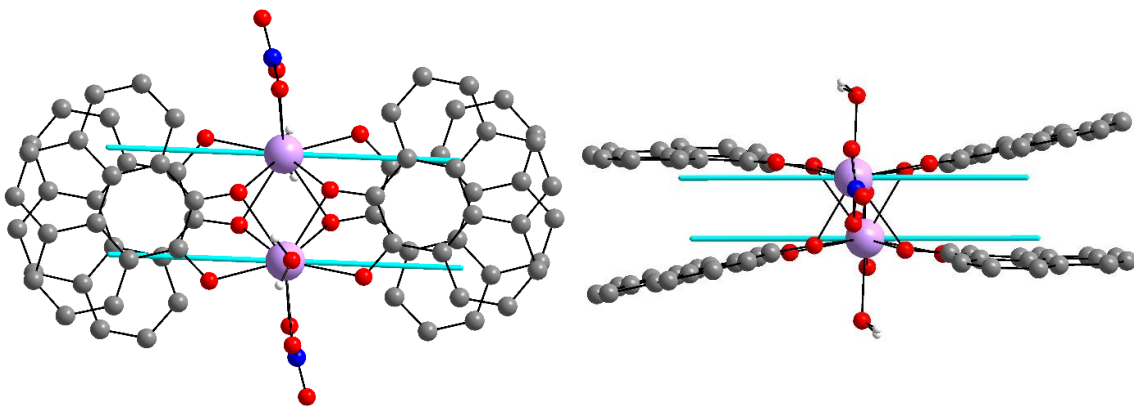


Figure 230. Anisotropy axes of (92-Dy) calculated using MAGELLAN.^[297]

Susceptibility measurements were performed on an immobilised powder sample of (92-Dy) between 2 and 300 K with an applied magnetic dc field of 0.1 T. The $\chi_M T$ vs T as well as the χ_M^{-1} vs T plots are shown in figure 231. During the sample preparation for this experiment the capsule was dropped accidentally leading to a loss of sample. Therefore, the actual mass of (92-Dy) that went into the SQUID magnetometer is unknown. The qualitative course of the curve is not affected by this, the curve(s) are simply shifted vertically. In order to get an idea of how the magnetic behaviour of (92-Dy) compares to the other dimers, the mass of the sample during data processing was therefore altered to make the RT $\chi_M T$ value match the expected value of $28.34 \text{ cm}^3 \text{Kmol}^{-1}$ of two uncoupled Dy^{III} ions. The trend of the $\chi_M T$ curve is the same as observed for the other Dy^{III} dimers with a slow decrease upon decreasing temperature which becomes steeper at temperatures below 50 K attributed to thermal depopulation of excited states as well as a possible antiferromagnetic interaction. This antiferromagnetic interaction is confirmed by the Curie-Weiss fit to the χ_M^{-1} vs T plot leading to a negative Weiss constant θ of -3.9 K.

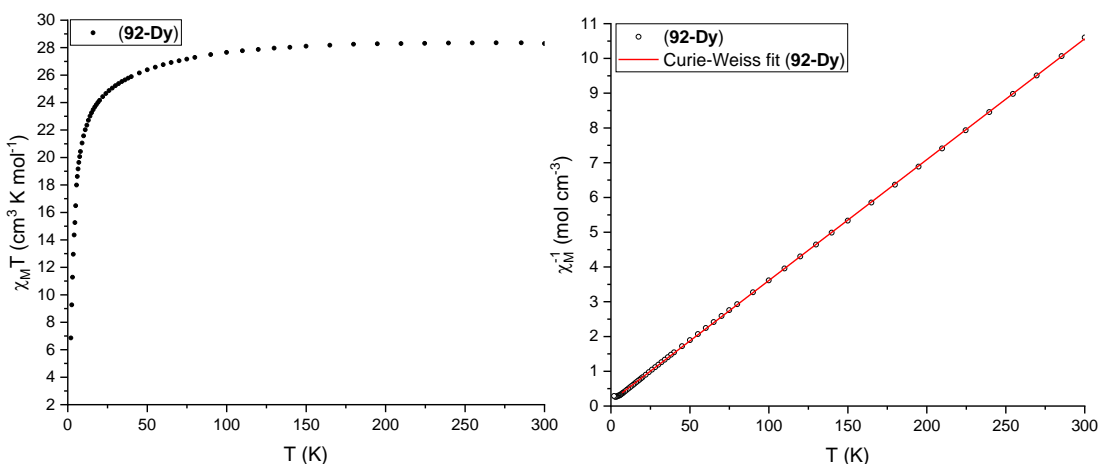


Figure 231. $\chi_M T$ vs T (left) and χ_M^{-1} vs T plot (right) of (92-Dy) fitted to the Curie-Weiss law.

In susceptibility measurements using an ac magnetic field with frequencies between 0.1 and 1500 Hz at temperatures between 2 and 16 K slow relaxation was observed in the in- and out-of-phase data (see figure 232, left and right, respectively). The measurement was interrupted and restarted twice due to critical failures of the software leading to the steps in the graphs below. The experimental data was fitted using the generalised Debye model and τ values were extracted in order to gain information on the relaxation processes present here. By the temperature range in which maxima occurred in the measuring window up to 1500 Hz in the out-of-phase data, it can be concluded that the SMM behaviour of **(92-Dy)** is worse when compared to the other dimers presented in this chapter. This may be the result of the π - π stacks facilitated by the pydi molecules in the lattice leading to intermolecular effects.

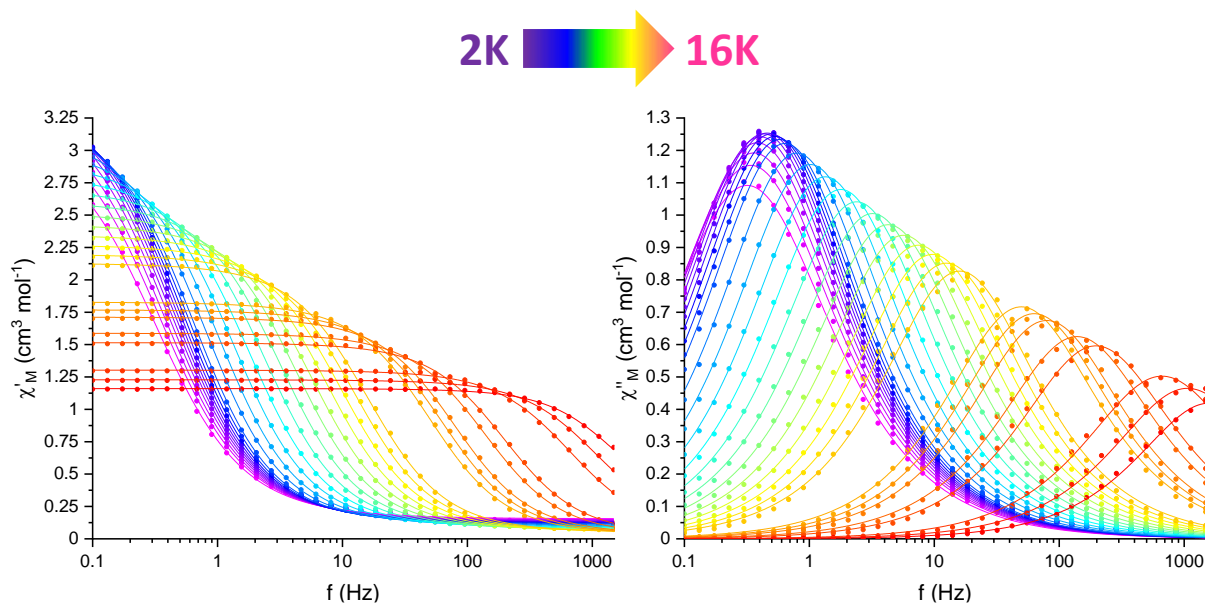


Figure 232. In- and out-of-phase susceptibility vs frequency plots of **(92-Dy)** obtained from ac measurements.

The extracted τ values were used to generate an Arrhenius plot that is shown by the black dots in figure 233 and which was fitted using equation 13 proposed by Lunghi *et al.* leading to the conclusion that little ZFQTM is observed in **(92-Dy)** at low temperatures. This is concluded from the fact that the parameter B is needed here to satisfactorily include the last data point in the fit. Therefore, the enhanced intermolecular interactions seem to have moved the observable slow relaxation to lower temperatures in **(92-Dy)** by allowing for small amounts of ZFQTM. The fitting parameters are listed in table 26.

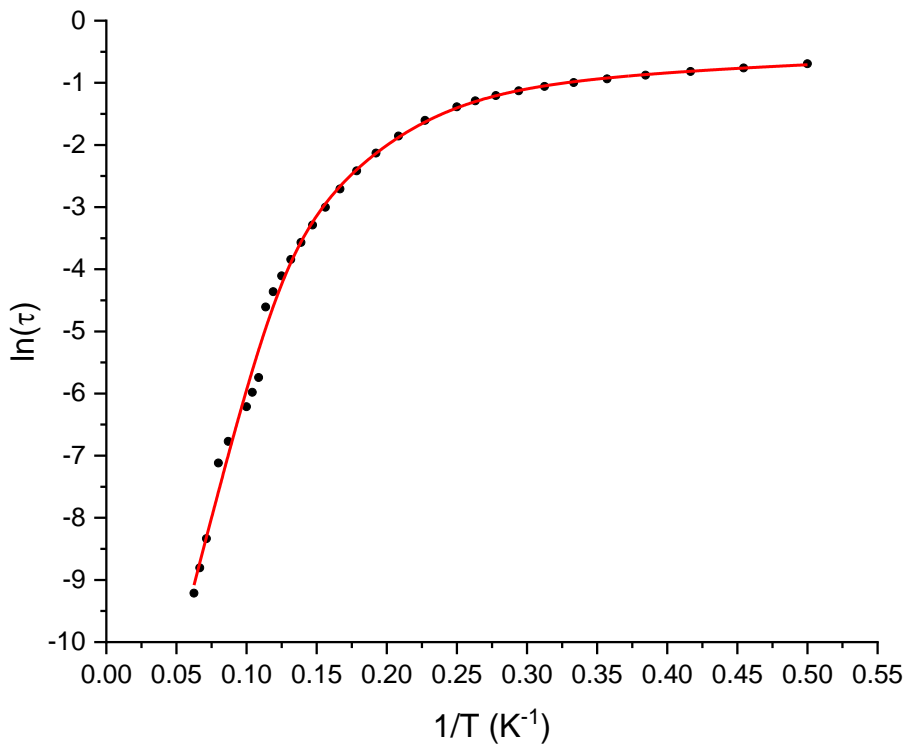


Figure 233. Arrhenius plot (92-Dy) using the τ values extracted from the Debye fit to the ac data (black dots) fitted using equation 13 (red line).

Table 26. Fitting parameters to fit the relaxation data of (92-Dy) to equation 13.

A (s ⁻¹ K ⁻¹)	B (s ⁻¹)	V (s ⁻¹)	w (K)	τ_0 (s)	U (K)
0.54	0.95	825.5	27.0	4.67E-7	88.4

Due to the presence of some ZFQTM, the rates of the other relaxation processes are rather low, however the energy barriers for Raman and Orbach relaxation are also rather low. This is supported by the fact that maxima are only observed in the out-of-phase susceptibility measurements up to *circa* 15 K.

MicroSQUID measurements on single crystals of (92-Dy) were performed in collaboration with Dr. Sagar Paul in the group of Prof. Dr. Wolfgang Wernsdorfer (KIT, PHI). The results of the temperature and sweep rate dependencies as well as the respective dM/dB derivatives are shown in figure 234. In the region around zero field the magnetisation does not stay constant as observed for the original MeOH dimer as well as the ⁱPrOH variant, which may indicate a small amount of quantum tunnelling in this system. This is in line with the fitting of the relaxation data to equation 13. The magnetisation increases gradually before the pronounced level crossing at 0.8 T. This is a much higher switching field value than observed for the other dimers, with the maximum value previously being observed for the ⁱPrOH version at a value of 0.41 T.

This indicates a larger stabilisation of the mainly dark magnetic state as a result of the enhanced intermolecular interactions present in (92-Dy).

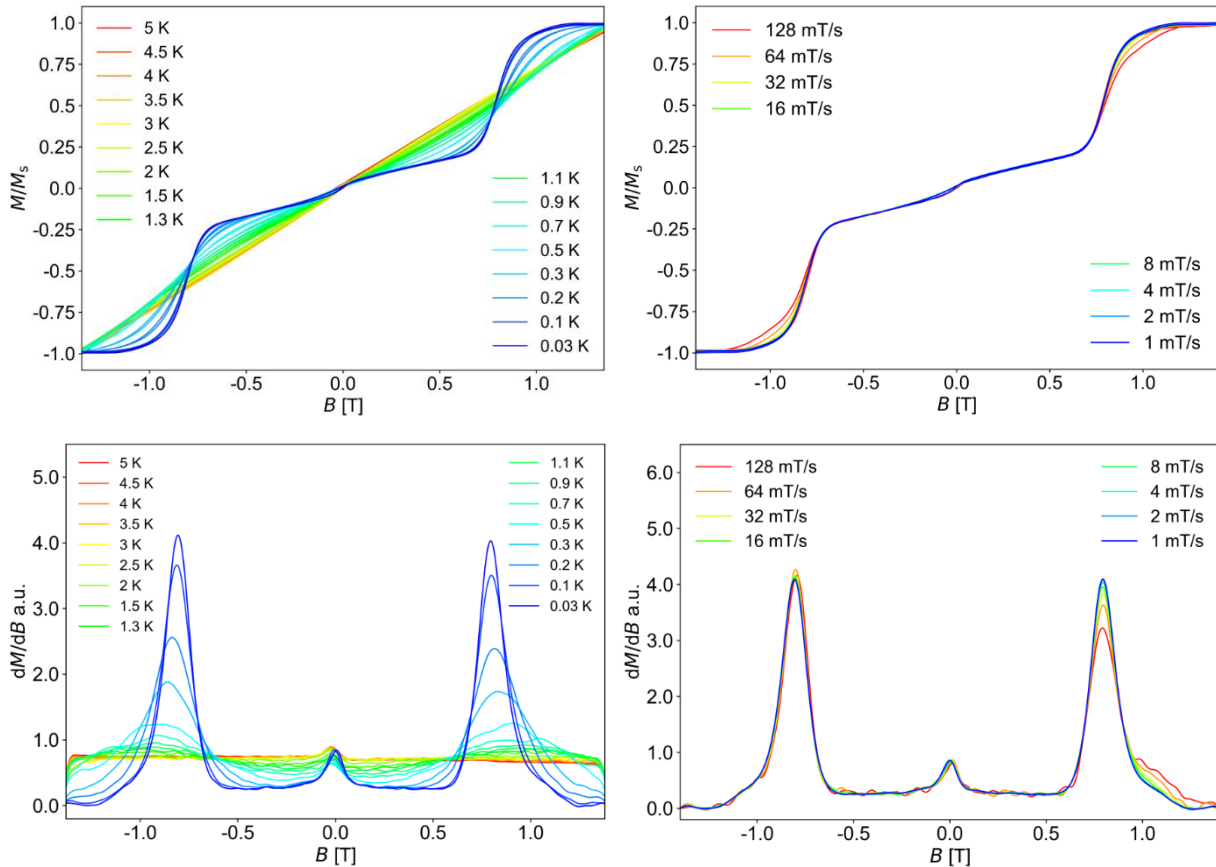


Figure 234. MicroSQUID measurements performed on single crystals of (92-Dy). The temperature dependence between 0.03 and 5 K is shown on the left and the sweep rate dependence between 1 and 128 mT/s shown on the right. The derivatives of either measurement are shown in the bottom.

6.5.2 Further Attempts to Vary the Radical Ligand

After the successful modification of the radical ligand increasing the π system, the opposite was attempted using commercially available 3,5-di-^tBu-benzoquinone as well as 1,2-naphthoquinone (see figure 235, left and middle) using the reaction conditions that led to the $[\text{Ln}_2(\text{phsq})_4(\text{NO}_3)_2(\text{MeOH})_2]$ series. This did not yield the desired product yet which may indicate that the π - π interactions, since the π -systems are now smaller, become too weak to provide the thermodynamic stability of the dimeric species through pancake bonding. Similarly, the use of commercial 3,6-di-bromo-9,10-phenanthrenequinone (see figure 235, right) in order to possibly introduce additional

intermolecular interactions via halogen interactions did not yield crystals suitable for SC-XRD nor dark product in sufficient quantities to characterise the material another way. Nevertheless, the fact that small amounts of dark product appear to be formed indicate that with further optimisation of the reaction parameters further compounds of this extended family of dimers may be obtained.

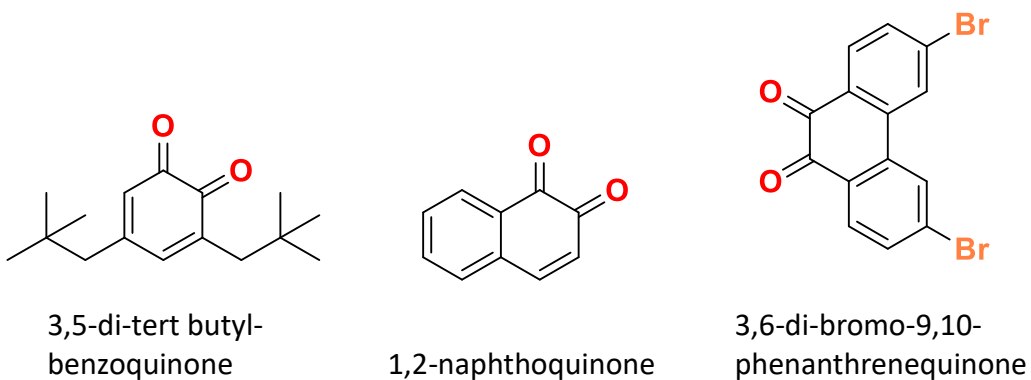


Figure 235. Other diones used as starting material in attempts to produce complexes employing their *in-situ* generated semiquinone radical anions as ligand to form Ln_2Rad_4 clusters.

6.6 Comparison of Optical and Magnetic Properties

Optical Spectroscopy

One representative solid state UVVis absorption spectrum for all the different varieties of Ln_2Rad_4 (**48-Dy**) – the archetype complex, (**60-Dy**) – the EtOH version, (**71-Dy**) – the *iso*-propanol version, (**84-Dy**) – the chloride version and (**93-Ho**) – the version using the new pyrene-based radical ligand) are shown in figure 236. It is immediately clear that the spectrum of (**93-Ho**), the compound with the pysq ligand differs the most from all the others. This is unsurprising as all the other are made with the phsq ligand. This is particularly noticeable from the energies of the ILCT bands of the five compounds. The ILCT band of (**93-Ho**) is barely recorded within the measuring window with a maximum at 765 nm, while the ILCT bands of the phsq-containing clusters are centred at higher energies between 650 nm for (**71-Dy**) and 675 nm for (**60-EtOH**). Interestingly, while the ILCT bands of (**48-Dy**) and (**60-Dy**) occur at essentially the same wavelength, the same band is blue-shifted in the *iso*-propanol version by about 25 nm. Also, comparing (**48-Dy**) to (**84-Dy**), so the compounds with the same molecular structure apart from the swapping of the nitrate for chloride, the ILCT band

is blue-shifted by 18 nm to 657 nm. The other bands in the spectra of phsq-containing compounds compare well to each other, while the spectrum of **(93-Ho)**, again unsurprisingly due to the different ligand, is entirely different.

The spectra of **(48-Dy)**, **(60-Dy)** and **(84-Dy)** in MeCN solution are already compared in figure 216 above and show the same trend with the ILCT band of the chloride-containing **(84-Dy)** being slightly blue-shifted.

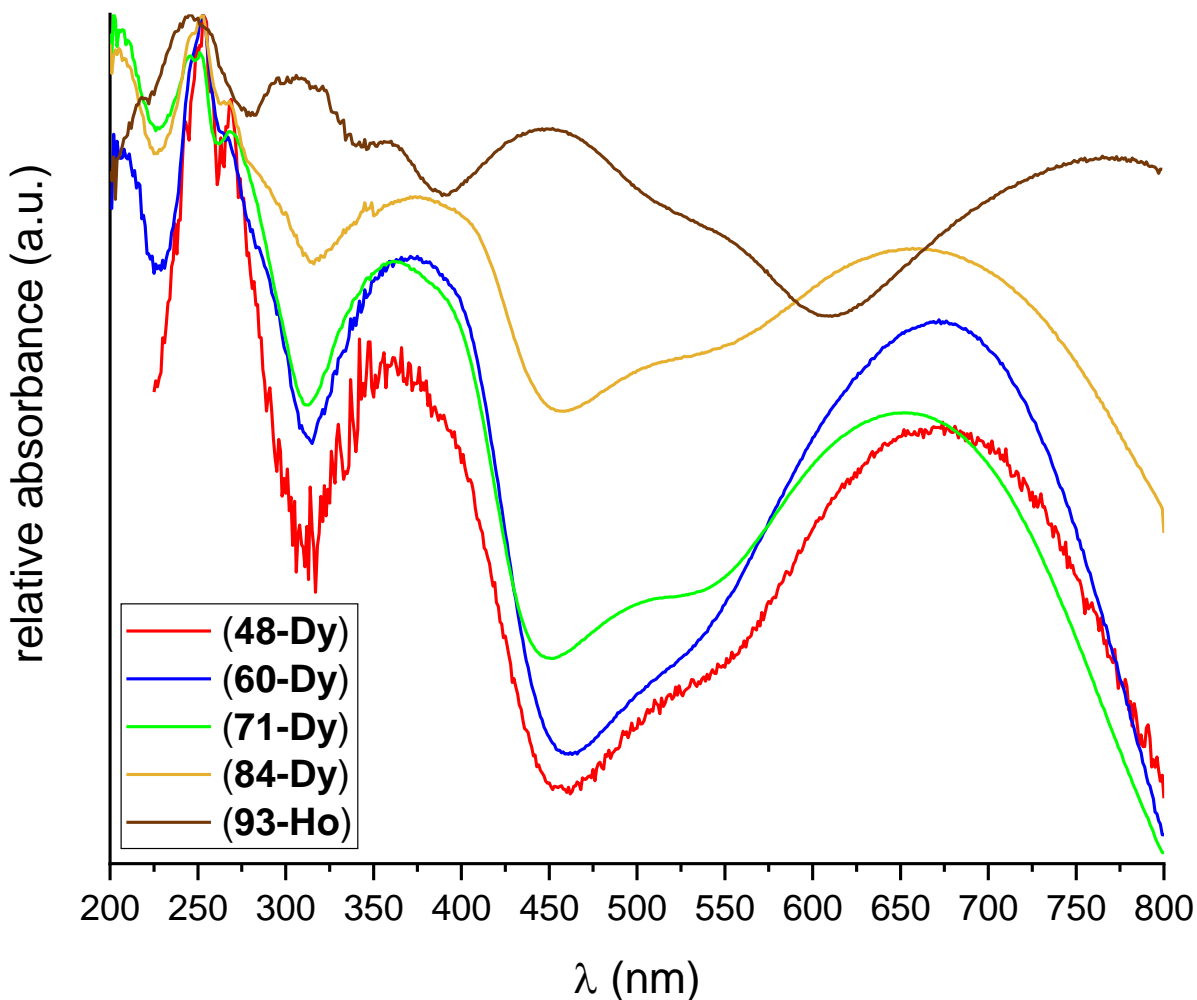


Figure 236. Solid state UVVis absorption spectra of **(48-Dy)**, **(60-Dy)**, **(71-Dy)**, **(84-Dy)** and **(93-Ho)** in the spectral range between 200 and 800 nm.

Magnetic Properties

The ac susceptibility data of **(60-Dy)**, **(71-Dy)**, **(84-Dy)** and **(92-Dy)** were fitted using the generalised Debye model and the extracted τ values were used to obtain Arrhenius plots. The parameters used to fit these Arrhenius plots to equation 13 and therefore the rates of the respective relaxation mechanisms and energy barriers are summarised

in table 27. The same was done for the parameters that were previously obtained for the parent compound (**48-Dy**).^[339]

The parameter B is only necessary in order to satisfactorily fit the data of (**92-Dy**) whereas there is no ZFQTM contribution needed for all the other variants. Since (**92-Dy**) employs a different radical ligand from the others which engages in intermolecular interactions, this is probably the reason why a ZFQTM contribution needs to be taken into account. The accessibility of this relaxation process at low temperatures also explains why (**92-Dy**) only shows maxima in the out-of-phase susceptibility up to 15 K.

The other compound that shows drastically different magnetic behaviour is (**84-Dy**). It shows maxima up to the highest temperature for the series of 30 K, which is in line with the high energy barriers to Raman and Orbach relaxation of 175.5 K and 475.8 K, respectively. Furthermore, the degree of relaxation *via* the direct process is the lowest for this family of dimers, which is why it shows the best SMM properties. Therefore, it can be concluded that the nitrate anion has an adverse effect on SMM properties, which is especially reflected in lower energy barriers. On the other hand, the dimers involving the nitrate co-ligand are more stable against oxidation in air. This is shown by the fact that the Cl-dimers turn to amorphous green powder in a timeframe of 2-4 weeks, whereas the nitrate dimers are still stable after more than 6 months of storage in air.

The variation of the neutral co-ligand from MeOH in the original dimer to EtOH and ⁱPrOH shows that EtOH behaves differently from the other two. This becomes especially obvious when looking at the direct relaxation parameter A and the preexponential factor for the Raman relaxation (V) which are both higher than the ones of the MeOH and ⁱPrOH versions. The MeOH and ⁱPrOH variants behave similarly to each other with subtle differences in the direct and Raman relaxation rates.

These changes made to neutral, anionic and radical (co-)ligand can be regarded as tuning handles that allow for the systematic improvement of SMM properties.

Table 27. Comparison of the parameters used to fit the relaxation data of the different variations of dimers to equation 13. The specific tuning handle of the respective compounds are given in the second column.

Compound	Tuning handle	A (s ⁻¹ K ⁻¹)	B (s ⁻¹)	V (s ⁻¹)	w (K)	τ ₀ (s)	U (K)
(48-Dy) ^[32, 339]	MeOH	0.85	0	25547	56.8	3.20E-8	160.5
(60-Dy)	EtOH	1.41	0	72000	62.2	2.27E-9	185.3
(71-Dy)	iPrOH	0.71	0	28614	46.2	3.92E-10	188.8
(84-Dy)	Cl	0.29	0	5388707	175.5	6.64E-12	475.8
(92-Dy)	Pysq	0.54	0.95	825.5	27.0	4.67E-7	88.4

MicroSQUID measurements on (60-Dy), (71-Dy) and (92-Dy) were performed and the characteristic switching fields of the pronounced level crossings are compared to the one previously obtained for (48-Dy) in table 28. The corresponding derivative plots for the temperature dependences of the four compounds are shown and compared in figure 237.

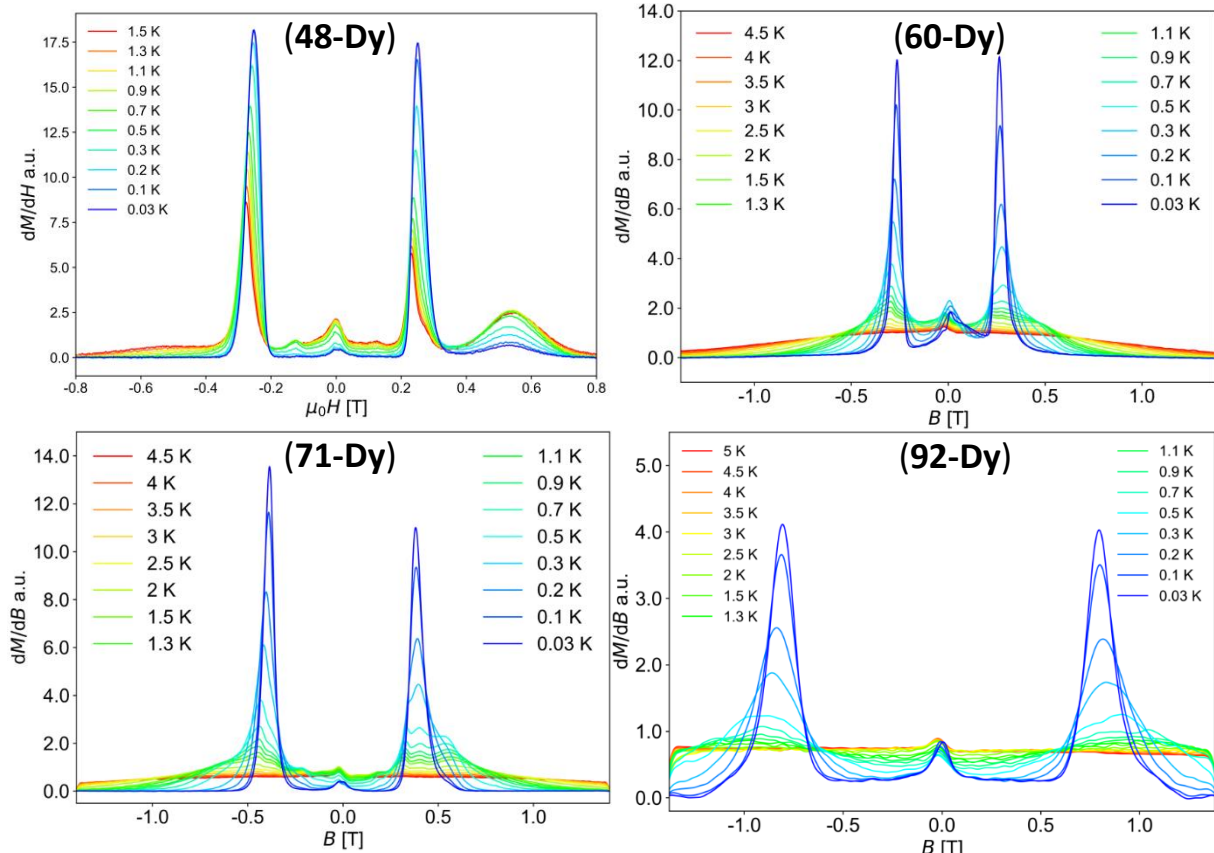


Figure 237. Derivative plots of the temperature dependence in microSQUID measurements on (60-Dy), (71-Dy) and (92-Dy) as well as the previously obtained (48-Dy) that was mentioned in the preliminary results section.^[339]

Table 28. Switching fields corresponding to the predominant level crossing in the different variations of the Ln_2Rad_4 dimers.

(48-Dy)	(60-Dy)	(71-Dy)	(92-Dy)
0.30 T	0.27 T	0.41 T	0.80 T

While the switching field of the EtOH variant (**60-Dy**) is slightly lower than the original dimer, the field at which (**71-Dy**) undergoes the pronounced level crossing is elevated. This is in line with the parameter A describing direct relaxation which show rates in the following order (**60-Dy**) > (**48-Dy**) > (**71-Dy**). Other relaxation processes are not relevant yet at temperatures of 30 mK. This can also explain the largest switching field obtained for (**92-Dy**) of 0.8 T. The ZFQTM in this compound as indicated by a non-zero parameter B is responsible for the jump at 0 T. This jump is most pronounced in (**92-Dy**) comparing the relative peak heights in the derivative plots shown above to the ones of the other dimers (circa 25% in (**92-Dy**))). Nevertheless, the low rate observed for direct processes results in the high switching field, however as mentioned with the lowest relative intensity. From the fitting of the relaxation processes one would expect an even higher switching field and even more pronounced level crossing for (**84-Dy**). Measuring microSQUID of the chloride dimer is the top priority continuing this project.

6.7 Summary and Conclusions on Semiquinonate Radical Complexes

The reproduction of the lanthanide series of the archetypal $[\text{Ln}_2(\text{phsq})_4(\text{NO}_3)_2(\text{MeOH})_2]$ (with $\text{Ln}^{\text{III}} = \text{Nd}^{\text{III}}\text{-Lu}^{\text{III}}$) was successful and additional magnetic studies on the Eu^{III} (**45-Eu**) and Tb^{III} (**47-Tb**) analogues were performed. While (**45-Eu**) shows significant population of its excited $^7\text{F}_1$ state, (**47-Tb**) was shown to be a field-induced SMM. From the fact that an applied magnetic dc field is necessary to observe maxima in ac out-of-phase susceptibility measurements, it can be concluded that the quenching of ZFQTM that was observed for the Dy^{III} parent compound is not present in the Tb^{III} version. The reason for this may be the non-degenerate ground state of these non-Kramers ions.

Furthermore, solution state UVVis absorption spectroscopy was performed under inert atmosphere to prevent the oxidation of the ligand which was described in section 6.1. In order to compare the UVVis spectra of the complexes to a reference of the “free” radical, the cobaltocenium salt of the phenanthrene radical anion was prepared. First the absorption spectrum was measured in MeCN solution under the exclusion of oxygen and subsequently it was shown that this sample oxidises once opened to air reproducing the absorption spectrum of the 9,10-phenanthrenequinone starting material. This is in line with the observations by Rennert *et al.*.^[338]

The UVVis spectra of the lanthanide complexes show the ILCT band, which was also observed in the measurements of Rennert *et al.* and indicates the stabilisation of the radical ligand on coordination to a metal ion.^[338] The reproduction of the UVVis spectrum of the starting material through oxidation of the complex solutions in air was also shown from successive absorption spectra recorded after opening the cuvette to air. Moreover, it was shown that the complexes decompose over time when in solution from the Eu^{III} luminescence, which could not be observed in freshly prepared solutions but was observed in samples stored for a couple of days under inert atmosphere. This was attributed to ligand rearrangement in solution.

There are four variables in this system. The variation of the Ln^{III} ion was previously performed. The next step was the variation of the neutral co-ligand. This was done by changing the solvent in which the reaction is performed from MeOH to EtOH. The first crystal structure of the desired compound using EtOH co-ligands was already reported

in my Master thesis,^[31] however significant reaction optimisation was necessary to reproducibly obtain these complexes. The analogues with $\text{Ln}^{\text{III}} = \text{Eu}^{\text{III}}\text{-Tm}^{\text{III}}$ as well as the Dy-Y-doped samples of $[\text{Ln}_2(\text{phsq})_4(\text{NO}_3)_2(\text{EtOH})_2]$ were synthesised and shown to exhibit the same molecular structures from spectroscopic methods. PXRD measurements showed however that there are several structure types possible, which is also indicated by the different unit cells of the Ho^{III} containing compound obtained during the work for my Master thesis and the Dy^{III} compound obtained here. The reason for this appears to be the (partial) evaporation of lattice EtOH and (partial) replacement with water as suggested by elemental analysis. Magnetic measurements performed on **(60-Dy)** showed slow relaxation of magnetisation and fitting of the relaxation dynamics revealed that, while ZFQTM is also quenched in **(60-Dy)**, the EtOH version shows faster relaxation *via* direct and Raman processes in comparison to the parent compound. Furthermore, microSQUID measurements revealed that the switching field of the pronounced level crossing in **(60-Dy)** is 0.27 T and therefore lower than the one observed for the parent compound (0.3 T). Additionally, it was possible to observe magnetic hysteresis at fields below the switching field whereas a non-magnetic ground state is observed in the MeOH version.

The solvent of the reaction was further changed to *iso*-propanol resulting in the synthesis of $[\text{Ln}_2(\text{phsq})_4(\text{NO}_3)_2(\text{iPrOH})_2]$ complexes with $\text{Ln}^{\text{III}} = \text{Pr}^{\text{III}}\text{-Lu}^{\text{III}}$ as well as the Y^{III} and the Dy-Y-doped analogues that were shown to be isostructural from PXRD. This demonstrated that the formation and crystallisation of the *iso*-propanol series happen much more readily than for the EtOH dimers described above. This further strengthens the suggestion that the EtOH lattice solvent appears to be unfavourable for the formation of these radical compounds. Out-of-phase maxima in ac measurements on **(71-Dy)** were observed up to the same temperature as in the MeOH and EtOH versions, indicating that the neutral co-ligand has a negligible effect on the SMM properties. Fitting the relaxation dynamics using equation 13, it was confirmed that no ZFQTM is present in the *iso*-propanol version. Furthermore, it was shown that while the parameters describing the other relaxation processes are similar to the ones obtained for the parent compound, the parameter A describing direct processes is lower while the parameters describing Raman relaxation are slightly higher. In microSQUID measurements it was shown that the switching field is increased to 0.41 T in **(71-Dy)** compared to the MeOH version. This indicates that the concomitant

reduction of the contribution of direct relaxation processes significantly improves the stability of the essentially non-magnetic ground state.

As can be seen, changing the neutral co-ligand induces subtle differences to the relaxation dynamics shown by the comparison of **(71-Dy)** with the parent MeOH version. It can also be concluded that further work is needed to elucidate the crystallisation issues of the EtOH version before being able to deliver a proper comparison of the magnetic properties of **(60-Dy)** to the other variations presented here.

The next component of the system that was varied is the anionic co-ligand. It was already shown by Dr. Thomas Kriese that the exchange of nitrate with chloride is possible. The Er^{III} containing compound he obtained exhibited impressive SMM properties for Er^{III} compounds. During the work on my Master thesis the Dy^{III} version was obtained. However, in the context of this doctoral thesis, careful variation of the reaction conditions was necessary to successfully and reproducibly obtain the $[\text{Ln}_2(\text{phsq})_4(\text{Cl})_2(\text{MeOH})_2]$ complexes. The key to obtaining the isostructural series of complexes with $\text{Ln}^{\text{III}} = \text{Nd}^{\text{III}}\text{-Tm}^{\text{III}}$ as well as the Y^{III} and the Dy-Y-doped version, is the basicity of the solution. Multiple bases were tested with the best results obtained using NaN_3 .

In **(84-Dy)** out-of-phase signals in ac measurements were obtained up to *circa* 30 K and therefore significantly higher temperatures than for the previously presented compounds. Investigation of the relaxation dynamics resulted in a significant reduction of the parameter A describing the direct relaxation processes. While the rate for Raman relaxation is magnitudes higher than for the parent compound, the corresponding energy barrier is also much higher, explaining why the Raman relaxation requires higher temperatures to influence the magnetic behaviour. The energy barrier obtained for the Orbach process of 475.8 K is also the highest amongst the compounds presented here. Although no single crystal microSQUID measurements were performed so far, it can be expected that the pronounced level crossing from the non-magnetic ground state would occur at fields higher than the ones observed for the other dimers presented here. This would mean that the stability of the non-magnetic ground state could be compared to the stability of toroidal states.^[118-119, 353-354]

With $[\text{Ce}_2(\text{phsq})_6(\text{MeOH})_2]$ a compound with two additional phsq⁻ radical ligands could be obtained. This compound was previously described by Dr. Thomas Kriese but could

not reproduced until a suitable synthetic method using common Schlenk techniques instead of solvothermal synthesis in autoclaves was found. This opens the door for the synthesis of further analogues of the $[\text{Ln}_2(\text{phsq})_6(\text{MeOH})_2]$ complex in future work.

The last tuning handle that can be used in this system is changing the radical ligand itself. Since the key to the quenching of quantum tunnelling appears to be the short Dy-Dy distances in all the variants presented above and this short distance stems from strong radical-radical interactions between the π systems on either side of the Dy^{III} ions, it was decided to synthesise the pyrene analogue of the ligand precursor in order to obtain complexes that might show even stronger interactions between the π systems. The successful synthesis of pyrene-4,5-dione following a modified literature procedure was confirmed by NMR spectroscopy. After optimisation of the reaction conditions, increasing the metal salt to ligand ratio to 4:1, $[\text{Ln}_2(\text{pysq})_4(\text{NO}_3)_2(\text{MeOH})_2]$ complexes with $\text{Ln}^{\text{III}} = \text{Tb}^{\text{III}}\text{-Er}^{\text{III}}$ and the Y^{III} version were obtained. Analysis of the crystal structure showed that the intramolecular $\pi\text{-}\pi/\text{radical-radical}$ interactions were not enhanced by the ligand modification, since the distances between the ligands are comparable to that obtained for phsq[·] ligand containing compounds. Instead, two pyrenedione molecules co-crystallise with the complexes and these form new intermolecular $\pi\text{-}\pi$ interactions. These enhanced intermolecular interactions result in maxima in out-of-phase susceptibility measurements only observable up to 15 K in (92-Dy). The analysis of the relaxation mechanisms shows that ZFQTM cannot be disregarded. This is also seen in microSQUID measurements which show that about 25% of the magnetisation tunnels around zero field. However, the pronounced switching field is greatly enhanced up to 0.8 T. It appears that the strong intermolecular interactions have a detrimental effect on the SMM behaviour at zero field, allowing for QTM, but quenching direct processes quite effectively. This results in the higher field necessary for complete magnetisation reversal.

7. General Conclusion and Outlook

Overall 82 new compounds were synthesised that are presented above. This includes organic molecules such as luminescent dyes (biquinoxen adducts) and modified ligands (H₂opch family), a cobaltocenium salt of the phenanthrene semiquinonate radical anion as well as transition metal and lanthanide complexes employing radical ligands and/or employing supramolecular interactions. Furthermore, related compounds, which were previously reported in theses from the Powell group, were reproduced and their properties analysed further.

In order to gain insights into the structural changes induced by the design of ligands capable of promoting supramolecular interactions as well as the possible influences on optical and magnetic properties, collaborations were initiated with groups within KIT (Prof. Dr. Andreas-Neil Unterreiner, Prof. Dr. Karin Fink, Prof. Dr. Claus Feldmann, Prof. Dr. Mario Ruben and Prof. Dr. Wolfgang Wernsdorfer), across Germany (Prof. Dr. Alexander Schnegg and Prof. Dr. Rüdiger Klingeler) and all over the world (Dr. Joy Farnaby, Dr. Stephen Sproules, Dr. George Kostakis and Prof. Dr. Jinkui Tang).

The overall goal was to systematically study the influence of intra- and intermolecular interactions on the magnetic and optical properties of transition metal and lanthanide complexes. This was achieved in a variety of novel systems. It was shown that harnessing supramolecular interactions such as halogen bonds in the synthesis of metal complexes can lead to the possibility for the design of crystals which steer these properties. In the following, the results of the different sub-projects are summarised and an outlook is given on how research in these projects could be continued.

Fluorescent biquinoxen adducts

In chapter 4, seven new fluorescent adducts (**1**)-(7) were synthesised using the methylbiquinoxen dipseudobase. These adducts were produced using nucleophiles based on three different elements: O (**1**), (**2**), (**5**) and (**6**), S: (**3**) and (**4**) as well as C: (**7**). It was shown that by changing the residue on the adduct it was possible to tune the emission wavelength by 63 nm between yellow/green and red light. Furthermore, the O-based adducts were shown to exhibit excellent quantum yields of up to 97%. However, they were also shown to decompose in solution over the timespan of several

days. This likely happens *via* a pH-sensitive equilibrium in solution favouring the non-luminescent starting material.^[29, 189] Therefore, future work will include a study on how and if the basicity of the solutions impacts the decomposition. The S-based adducts have significantly lower quantum yields of sub-10% and were shown to decompose much more quickly in solution (over the course of hours). Following this decomposition using NMR spectroscopy should yield further insights into the mechanism. Further steps in continuing this project will be the reproduction of the C-based acetone adduct to obtain quantities sufficient to perform optical studies. Furthermore, the biquinoxen system provides additional modification possibilities (see figure 238), which should enable an expansion of the range of emission wavelengths for this system. These can further be used in order to enhance the quantum yield of non-O-based adducts. Preliminary results for this include an *n*-butylthiol adduct with R¹ = benzyl which shows more intense luminescence at a higher energetic wavelength as shown in figure 238, middle (yellow/orange rather than red like its R¹ = methyl counterpart compound (4)) as well as an N-based adduct showing bright orange luminescence (see figure 238, right). Both compounds could not be characterised satisfactorily within the scope of this thesis, but further work on these as well as additional variations will be conducted.



Figure 238. The biquinoxen system with two easily modifiable positions (left) and two adducts that could not be satisfactorily characterised yet with R¹ = benzyl and R² = ⁿSBu (middle) and an N-based compound with R¹ = methyl and R² likely = piperidine.

Biquinoxen transition metal complexes

Three new mononuclear complexes, using the *in-situ* generated radical MbqnO ligand, with the same molecular structures as the Co^{II} complexes presented in my Bachelor thesis,^[28] were obtained with Cu^{II} and Zn^{II} ions. Additionally, the previously known Co^{II} complexes were reproduced. A detailed investigation of the crystal packing revealed

supramolecular chain formation via π - π interactions that are assisted by radical-radical interactions on neighbouring ligands in addition to non-classical hydrogen bonding. It was furthermore shown that the Zn^{II} complex crystallises in two polymorphs (**12-Zn A** and **B**), one forming the intermolecular chains mentioned above, but the other forming supramolecular dimers.

The radical nature of the ligand was previously deduced from an antiferromagnetic interaction in the Co^{II} containing samples, which could not result from intermolecular Co^{II}-Co^{II} interactions since the ions are too far apart and therefore suggests a paramagnetic contribution of the ligand. This radical nature of the ligand was further proved here using SQUID magnetometry on (**12-Zn**) resulting in a paramagnetic signal. The observed antiferromagnetic interaction appears to be exceptionally strong as seen from the $\chi_M T$ vs T plot. Magnetic measurements on the Cu^{II} complexes will be conducted in the future and may provide further insights into the properties of this system. Cu^{II} ions due to their single unpaired electron can be viewed as an inorganic equivalent to an organic radical, therefore strong magnetic coupling is also expected for these analogues. The theoretical modelling of the magnetic interactions in these compounds is performed in collaboration with Prof. Dr. Karin Fink. Additionally, further characterisation using high-frequency EPR spectroscopy is ongoing in collaboration with the group Prof. Dr. Alexander Schnegg.

Furthermore, a proof of concept using the aforementioned adducts as ligands is provided by the successful synthesis of (**13-Zn**) which has a strongly connected 3D network of supramolecular interactions. Future challenges here include the reaction optimisation to improve the yield of the synthesis, variation of the metal ion and engineering crystal structures by choosing adducts that facilitate the desired supramolecular interactions. Additionally, since the viologen-like biquinoxen system has been shown to be able to capable of stabilising multiple different radical species,^[28, 30] electrochemical and/or chemical reduction and oxidation of these adduct-complexes will be performed in the future.

Lanthanide complexes using H₂opch

In chapter 5, eleven lanthanide (including Y^{III} as a diamagnetic lanthanide substitute with similar ionic radius) using the same reaction procedure complexes were obtained.

These crystallised in six different crystal structures. This was found to be linked to the different sizes of the respective lanthanide ions. This also exemplifies the versatility of the ligand in accommodating ions with a size difference of almost 0.3 Å between La^{III} and Er^{III}^[248] in complexes having nuclearities between four and eight.

One of the obtained complexes, the tetranuclear (**15-Ce**), was shown to be mixed valent through SC-XRD, BVS analysis and solid state UVVis absorption spectroscopy. The magnetic measurements on this complex showed significant intramolecular magnetic interactions at higher temperatures, which can be ascribed to the delocalisation of the electrons of the two Ce^{III} ions over the four possible sites. This interaction vanishes at low temperatures indicating localisation of the electrons on opposite corners of the essentially square complex. Future studies on this compound using femtosecond spectroscopy are planned as well as SQUID measurements under simultaneous irradiation with light, in collaboration with Prof. Dr. Andreas-Neil Unterreiner and Prof. Dr. Rüdiger Klingeler, respectively. The irradiation with visible light at low temperatures might re-enable the electron delocalisation, as suggested from the IVCT band in the UVVis absorption spectra, switching the antiferromagnetic coupling back on.

Furthermore, magnetic studies were performed on different analogues of Ln₈ clusters. The Tb^{III} and Dy^{III} analogues (**20-Tb**) and (**21-Dy**) were shown to be field-induced SMMs. This is interesting, since Prof. Dr. Jinkui Tang with whom we are collaborating on this project, published a Dy₈ cluster with the same molecular structure which exhibits zero-field SMM behaviour. The difference between the two samples lies in the crystal packing which is determined by the amount and distribution of the lattice solvent molecules giving an example of how small changes can lead to significant impact on the relaxation dynamics of magnetisation reversal. The Gd^{III} analogue (**19-Gd**) was shown to exhibit a strong MCE as shown by the entropy change of 30.22 J kg⁻¹ K⁻¹ which is 86.5% of the maximum entropy change this compound is capable of, placing it amongst the best Gd₈ clusters for MCE in the literature.^[285]

Lanthanide complexes using modified H₂opch ligands

Five modifications of the H₂opch ligand were synthesised in order to tune the intra- and especially intermolecular interactions of lanthanide complexes. In total 18 new

complexes were synthesised using these modified ligands, which can be categorised into three types of structures. Carbonate bridged clusters, hydroxo bridged clusters and dimers.

A mechanism could be proposed for the formation of the carbonate bridged clusters (**25-Tb**, **26-Dy**, **27-Ho**, **28-Er**, **29-Er** and **30-Er**) *via* fixation of CO₂ from air in section 5.3.3.3. The two trigonal prismatic Er₆ clusters (**28-Er**) and (**29-Er**) have the same molecular structure, but differ in their packing. One crystallises in P $\bar{1}$ and is held together by conventional HBs, the other crystallises in the tetragonal space group $P\bar{4}2_1c$. The increase in symmetry is explained by the formation of intermolecular halogen-halogen bonds, enabled by the introduction of a bromine atom to the back of the modified ligand used to obtain (**29-Er**). In the crystal structure four halogen bonded Er₆ clusters form the vertices of giant tetrahedra and are further connected to form a network that was investigated using topological analysis in collaboration with Dr. George Kostakis. Attempts to synthesise further carbonate bridged clusters will be performed by bubbling CO₂ through the reaction solutions and adding carbonate sources such as carbonate and bicarbonate salts in future work.

Variations of the previously mentioned hydroxo bridged mixed-valent Ce₄ complex (**15-Ce**) were obtained with three of the five ligand modifications. However, the dark colour of the reaction mixtures of the other modifications indicates that the Ce₄ compound is also present for these in solution but so far could not be crystallised. This is a future challenge as well as performing the same experiments that were described for (**15-Ce**) above in order to gauge whether the ligand modification has an effect on the optical and magnetic properties of these mixed-valent Ce₄ clusters.

Furthermore, hydroxo bridged Ln₇ clusters were obtained. For the Gd^{III} complex, using the ligand with an iodine atom on the back, two polymorphs were obtained (**35-Gd A** and **B**). Compound (**35-Gd A**) shows supramolecular dimer formation promoted by halogen-halogen bonds between the iodine atoms on neighbouring molecules, whereas (**35-Gd B**) forms supramolecular type I halogen-halogen interactions between the iodine atoms on neighbouring molecules. The next step would be to reproduce and optimise the reaction conditions to obtain these Ln₇ clusters. Since similar Gd₇ complexes in the literature^[269-270] have shown MCE, it will be interesting to see whether the intermolecular halogen interactions have an influence on this behaviour.

Six dimeric lanthanide complexes are presented in section 5.3.5, one using the unmodified H₂opch ligand and five using the modified ligands. It was shown that the coordination mode of the ligand has a significant effect on the observed magnetic behaviour in these Dy^{III} dimers, through the influence on the sign of the dipolar coupling. Dimers whose Dy^{III} ions are bridged by the enolate oxygen of the ligand exhibit ferromagnetic dipolar coupling, while the dimer in which the Dy^{III} ions are bridged by the harder phenolate oxygen show antiferromagnetic dipolar coupling.

In two closely related dimers (**41**- and **42-Dy**), employing modified ligands with a bromine or an iodine atom on the ligand, respectively, it could be shown that the polarisability of the halogen atom has a strong impact on the strength of halogen interactions. These results are currently being investigated using theoretical calculations in collaboration with the group of Prof. Dr. Karin Fink. Preliminary results include the visualisation of the σ -hole on the iodine atom in (**42-Dy**) (see figure 284) suggesting that halogen bonds are, indeed, present in this complex. Thus, a reproduction of this compound followed by magnetic measurements is the next step here in order to elucidate how halogen bonds can alter magnetic behaviour.

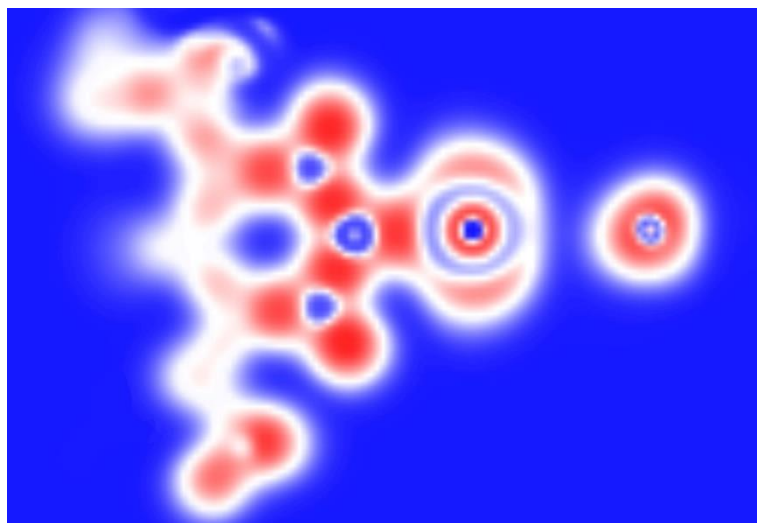


Figure 239. Visualisation of the σ -hole on the iodine atom of the ligand used for the synthesis of (**42-Dy**) as one of the preliminary results of the theoretical description of the halogen bonds in (**42-Dy**) in collaboration with Christian Pachl from the groups of Prof. Dr. Karin Fink and Prof. Dr. Annie Powell. Areas of low electron localisation are coloured in blue while areas of high electron localisation are shown in red.

The versatility of the Schiff base ligand synthesis can be used to produce further modified ligands that, for example, could employ a chromophore-unit, such as anthracene, in order to tune the optical properties and thereby investigate the interplay between the optical and magnetic properties. Furthermore, the H₂opch-Cl ligand will

be synthesised in order to tune the strength of the intermolecular halogen interactions. A general challenge using the H₂opch ligand system is to steer the equilibria clearly present in solution in order to target a specific product.

Lanthanide-semiquinonate radical dimers

In chapter 6, the systematic variation of a system containing semiquinonate radical ligands was shown. Firstly, the archetypal complexes $[\text{Ln}_2(\text{phsq})_4(\text{NO}_3)_2(\text{MeOH})_2]$ were reproduced and analysed further. The magnetic properties of the Eu^{III} and Tb^{III} analogues (**45-Eu**) and (**47-Tb**) were measured and showed a partial occupation of the ⁷F₁ excited state, leading to an observable paramagnetic signal in the former, and field-induced SMM behaviour in the latter. Magnetic measurements of further analogues of this series of complexes are planned. Moreover, the optical properties of these complexes were tested in MeCN solution. For this it was necessary to work under the meticulous exclusion of air and the experiments were performed during a two week visit to the labs of Dr. Joy Farnaby at the University of Glasgow, which was made possible by the Networking Grant of the Karlsruhe House of Young Scientists (KHYS). In order to obtain a reference spectrum of the “free” radical the cobaltocenium salt of the phenanthrene semiquinonate radical was synthesised using CoCp₂ as a reducing agent on the 9,10-phenanthrenequinone starting material. The optical behaviour of the radical-lanthanide complexes in solution is in agreement with results obtained from experiments stabilising the phenanthrene semiquinonate radical anion by interaction with diamagnetic metal cations.^[338] In addition to the air sensitivity, the complexes were shown to decompose after storage under inert atmosphere after several days through the observation of the characteristic Eu^{III} luminescence, which was absent in freshly prepared solutions.

There are four tuning handles that can be used to systematically vary the magnetic behaviour of these radical complexes: The lanthanide ion, the neutral co-ligand, the anionic co-ligand and the radical ligand itself. While the effects of the variations on the magnetic properties are summarised in the following, it should be noted that the variations did not significantly alter the core structure of the complexes, especially in regard to the short inter-ligand and inter-metal distances.

The neutral MeOH co-ligand was changed to EtOH and $^i\text{PrOH}$ resulting in the observation that while the $^i\text{PrOH}$ complexes crystallise readily and are isostructural across the majority of the lanthanide series, the EtOH version crystallises in multiple structure types. The magnetic properties of the respective Dy^{III} analogues were investigated and it was found that the EtOH variant, especially in microSQUID measurements, shows behaviour significantly different from the original dimer. Further experiments will be conducted in order to investigate this in greater detail. The $^i\text{PrOH}$ variant shows very similar, but slightly improved magnetic behaviour compared to the parent compound. This is judged from finding the limits of the non-magnetic ground states in both compounds and which is stabilised more in the $^i\text{PrOH}$ version. This is seen from the pronounced level crossing which occurs at 0.41 T in the $^i\text{PrOH}$ variant and was observed at 0.3 T in the original compound. This is attributed to the more effective quenching of direct relaxation processes as judged from the parameters used in the fitting of the relaxation behaviour. The ZFQTM was shown to remain quenched in both the EtOH and $^i\text{PrOH}$ variants, which is in line with the behaviour observed in the parent dimer.

The second tuning handle, varying the anionic co-ligand, resulted in an isostructural series of compounds with coordinating chlorides instead of nitrates. This led to a significant improvement of the SMM behaviour with maxima in the ac out-of-phase susceptibility up to 30 K (more than 10 K higher compared to the archetype complex). Fitting the relaxation dynamics, it could be concluded that ZFQTM is still quenched, but in contrast to the other dimers that are presented here, the parameter describing direct relaxation is very low. Additionally, although the rates for both Raman and Orbach relaxation are higher than for the other compounds, the energy barriers related to both mechanisms of 175.5 K and 475.8 K, respectively, result in SMM behaviour observable to higher temperatures. The next step here is the measurement of single crystals of the Dy^{III} analogue in the microSQUID. From the fitting parameters of the relaxation dynamics it can be expected that the Cl-version should show significantly stronger stabilisation of the non-magnetic ground state, since direct processes and ZFQTM are effectively quenched and Raman as well as Orbach relaxation require higher temperatures to become relevant.

The last tuning handle of changing the radical ligand was successfully used as seen from the synthesis of five analogues of the radical complex using pyrene

semiquinonate radical ligands replacing the phenanthrene semiquinonate ones. The crystal structures obtained from complexes of this series show the co-crystallisation of two pyrene-4,5-dione molecules per cluster, which engage in π - π interactions to form stacks of lanthanide radical complexes throughout the whole crystal. This is shown to have a significant effect on the magnetic properties from measurements conducted on the Dy^{III} analogue. It can be observed that ZFQTM is not completely quenched resulting in a tunnelling of *circa* 25% of the magnetisation. However, it is also shown that the intermolecular interactions suppress direct processes leading to a switching field of 0.8 T for the dominant level crossing seen in microSQUID measurements.

The discovery of an alternative synthesis route for a complex employing six phenanthrene semiquinonate radical ligands, using Schlenk techniques instead of autoclaves, may improve the reproducibility of the synthesis of such complexes.

The next steps in the systematic investigation of this extended family of lanthanide radical complexes will be the magnetic measurements of further lanthanide analogues as well as further samples of the modified complexes doped with diamagnetic Y^{III} ions in both SQUID and microSQUID experiments. Furthermore, additional neutral, anionic and radical ligands will be used in the synthesis of these lanthanide complexes in order to investigate how these variations impact the magnetic behaviour. This should help to further illuminate the connection between intra- (Cl-version) and intermolecular interactions (pyrene seqquinonate version) and the quenching of direct relaxation processes which appears to be the key to stabilise the essentially non-magnetic ground states observed in these complexes.

8. Experimental

General Procedure

Unless otherwise stated, chemicals were obtained from commercial sources and used without further purification. Lanthanide salts were synthesised using the respective oxide and acid. All syntheses, if not indicated otherwise, were performed under aerobic conditions. When working with azides caution is advised due to their potential explosiveness.

Instruments

General comment: Due to the Covid-19 pandemic and the renovation of the Institute of Inorganic Chemistry (AOC, KIT) it was necessary to perform magnetic measurements on multiple different machines due to the unavailability of our own in-house SQUID for the majority of time working on this thesis.

ATR-IR spectroscopy was performed on a Bruker Platinum Alpha ATR IR located at the Institute of Inorganic Chemistry (AOC, KIT) and on a Nicolet iS 50 with ATR attachment located at the Institute for Nanotechnology (INT, KIT).

UVVis absorption spectroscopy was performed on an Agilent Cary 5000 UVVis spectrometer located at the Institute for Nanotechnology (INT, KIT) and on a Duetta by Horiba Scientific located at the School of Chemistry at the University of Glasgow.

Emission spectroscopy was performed on an Agilent Cary Varian Eclipse located at the Institute for Nanotechnology (INT, KIT), on a Fluolog-3 by Horiba Jobin equipped with integration sphere located at the Institute of Inorganic Chemistry (AOC, KIT) in collaboration with Dr. Mikhail Khorenko from the group of Prof. Dr. Claus Feldmann and on a Cary 500, Varian Analytical Instruments located at the Institut of Organic Chemistry (IOC, KIT) in collaboration with Dr. Julia Leier from the working group of Prof. Dr. Andreas-Neil Unterreiner.

Femtosecond spectroscopy was performed by Dr. Julia Leier from the working group of Prof. Dr. Andreas-Neil Unterreiner.

Powder X-ray diffraction (PXRD) was performed on a STOE STADI-P equipped with a Cu-K α source with a characteristic wave length of 1.5405 Å.

Single crystal X-ray diffraction (SC-XRD) was performed on a STADIVARI by STOE using Mo-K α radiation with a characteristic wavelength of 0.71073 Å, on a STADIVARI by STOE with Ga-Jet X-ray source by Excilium using Ga-K α radiation with a wavelength of 1.3143 Å and on an IPDS II by STOE with Mo-K α radiation all located at the Institute for Nanotechnology (INT, KIT). Additionally, measurements were performed on an Agilent SuperNova diffractometer using Cu-K α radiation.

Elemental analysis was performed on an Elementar Vario MicroCube located at the Institute for Nanotechnology (INT, KIT).

NMR spectroscopy was performed on a Bruker Avance III 500 MHz located at Institute for Nanotechnology (INT, KIT) and on a Bruker Avance III 300MHz located at the Institute of Inorganic Chemistry (AOC, KIT).

Magnetic SQUID measurements were performed on a Quantum Design MPMS-XL-7 located at the Institute of Inorganic Chemistry (AOC), on a Quantum Design MPMS-XL-1 located at the Institute of Nanotechnology in collaboration with Sören Schlittenhardt from the group of Prof. Dr. Mario Ruben, on a Quantum Design MPMS-XL-7 located at the Changchun Institute of Applied Chemistry in collaboration with Prof. Dr. Jinkui Tang and on a Quantum Design MPMS-3 located at the Kirchhoff Institute For Physics at the University of Heidelberg in collaboration with Jan Arneth from the working group of Prof. Dr. Rüdiger Klingeler.

MicroSQUID measurements were performed by Dr. Michael Schulze and Dr. Sagar Paul from the group of Prof. Dr. Wolfgang Wernsdorfer on an in-house designed machine developed by Prof. Dr. Wolfgang Wernsdorfer that is located at the Institute for Physics (PHI, KIT).

An EPR measurement was performed by Dr. Stephen Sproules on a Bruker ELEXSYS E500 located at the School of Chemistry at the University of Glasgow and simulations were performed using Bruker's Xsophe software package.^[355]

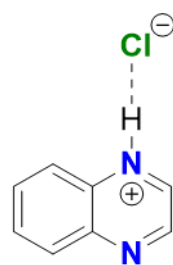
Data Handling

Spectroscopic and magnetic data was analysed and all graphs were plotted and fits performed using Origin 2019. Crystal structures were solved and refined using Olex

with ShelXL and ShelXT.^[356-358] Pictures of crystal structures were produced using Diamond 4.0. Powder patterns were simulated using Mercury 2020.3.0.^[186]

8.1 Biquinoxen

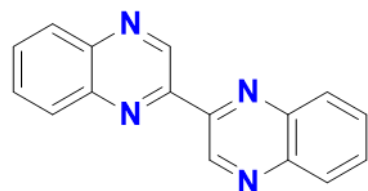
Quinoxaline hydrochloride^[30]



Quinoxaline (15.96 g, 122.6 mmol) was dissolved in 200 ml THF at 0°C. 10 ml hydrochloric acid (32%) was added dropwise to the stirred solution leading to a light-red precipitate which was collected by filtration, washed with cold THF and dried under reduced pressure. The product was obtained as light-red powder in a yield of 18.4 g (90%).

¹H-NMR (300 MHz, DMSO-d₆): δ/ ppm = 9.17 (s, 2H, NH), 8.96 (s, 2H, CH_{Ar}), 8.15-8.07 (m, 2H, CH_{Ar}), 7.92-7.83 (m, 2H, CH_{Ar}). **IR (4000-400 cm⁻¹):** 3059(w); 3023(w); 2288(b, w); 2234(m); 2189(w); 2076(b, w); 1990(b, m); 1908(m); 1822(m); 1614(m); 1569(w); 1519(s); 1474(m); 1378(m); 1333(m); 1261(m); 1207(s); 1130(s); 1071(s); 1030(s); 975(m); 934(m); 857(s); 821(m); 753(s); 595(s); 572(m).

Biquinoxaline^[30]

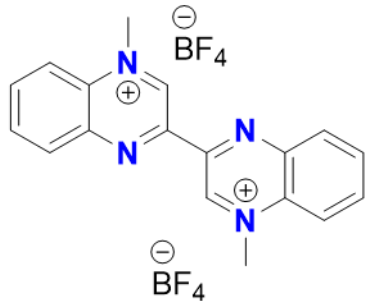


Quinoxaline hydrochloride (11.0 g, 66.0 mmol, 1.0 eq.) was dissolved in dry DMF (80 ml) under inert atmosphere and N,N'-dimethylaniline (7.6 ml, 66.0 mmol, 1.0 eq.) was added. The mixture was stirred at 140°C for 1h. After letting the mixture cool down to RT, 800 ml of 2M aqueous NH₃ was added to generate a sticky brown precipitate which was filtered, washed with MeOH and dried in air. This crude product was dissolved in 2 l of CHCl₃ and stirred with activated charcoal (2 g) for 15 min. The red solution was evaporated under reduced pressure to yield the product as red crystals in a yield of 4.96 g (58%).

¹H-NMR (300 MHz, CDCl₃): δ/ ppm = 10.13 (s, 2H, CH_{Ar}), 8.33-8.21 (m, 4H, CH_{Ar}), 7.92-7.83 (m, 4H, CH_{Ar}). **¹³C-NMR (300 MHz, CDCl₃) δ/ ppm** = 148.6 (s, 2C, C_{Ar}), 144.0 (s, 2C, C_{Ar}), 142.5 (s, 2C, C_{Ar}), 141.7 (s, 2C, C_{Ar}), 131.0 (s, 2C, C_{Ar}), 130.7 (s, 2C, C_{Ar}), 130.0 (s, 2C, C_{Ar}), 129.3 (s, 2C, C_{Ar}). **IR (4000-400 cm⁻¹):** 3182(b, m); 3086(w); 1603(m); 1553(w); 1499(s); 1449(m); 1422(m); 1363(w); 1372(w); 1277(m); 1167(m);

1149(m); 1058(m); 1022(m); 972(w); 940(s); 890(s); 827(s); 750(s); 714(w); 697(s); 559(m); 518(m); 473(m); 437(m).

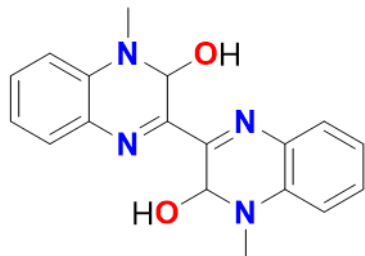
Methylbiquinoxen dication ((Mbqn)(BF₄)₂)^[30]



Trimethyloxonium tetrafluoroborate (14.32 g, 96.8 mmol, 5.0 eq.) was dissolved in MeCN (500 ml) and biquinoxaline (5.0 g, 19.3 mmol, 1.0 eq.) added portion-wise at 0°C. The resulting mixture was left stirring at RT for 5d. After that the formed precipitate was filtered, washed with Et₂O and dried in air. This crude product was dissolved in water (400 ml) heated to 100°C and filtered while hot. The yellow solution was stored at 4°C overnight before filtration of the product in the form of brown crystals that were dried under vacuum in a yield of 4.69 g (52%).

¹H-NMR (300 MHz, DMSO-d₆): δ/ppm = 10.73 (s, 2H, CH_{Ar}), 8.83-8.74 (m, 2H, CH_{Ar}), 8.71-8.64 (m, 2H, CH_{Ar}), 8.56-8.41 (m, 4H, CH_{Ar}), 4.97 (s, 6H, CH₃). **¹³C-NMR (300 MHz, CDCl₃)** δ/ppm = 149.3 (s, 2C, C_{Ar}), 144.1 (s, 2C, C_{Ar}), 141.7 (s, 2C, C_{Ar}), 138.0 (s, 2C, C_{Ar}), 135.5 (s, 2C, C_{Ar}), 132.1 (s, 2C, C_{Ar}), 131.5 (s, 2C, C_{Ar}), 120.6 (s, 2C, C_{Ar}), 46.6 (s, 6C, CH₃). **IR (4000-400 cm⁻¹):** 3082(w); 2116(w); 1604(w); 1545(w); 1513(m); 1454(w); 1418(w); 1373(m); 1323(w); 1286(w); 1232(m); 1178(w); 1033(b, s); 911(s); 874(w); 824(w); 783(s); 711(w); 634(w); 571(m); 517(m); 494(m); 421(m).

Methylbiquinoxen dipseudobase (Mbqn-(OH)₂)^[29]

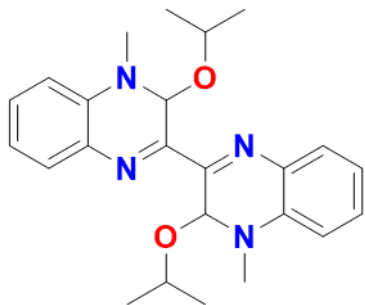


(Mbqn)(BF₄)₂ (1.5 g, 3.25 mmol, 1.0 eq.) and K₂CO₃ (2.0 g, 14.5 mmol, 4.5 eq.) were suspended in water (400 ml) and put into a sonicator for 2 h. The resultant powder was filtered and dried under vacuum to yield the product as orange powder in a yield of 1.0 g (95%).

¹H-NMR (300 MHz, DMSO-d₆): δ/ppm = 7.49-7.46 (m, 2H, OH), 7.35-7.30 (m, 2H, CH_{Ar}), 7.01-6.98 (m, 2H, CH_{Ar}), 6.92-6.90 (m, 2H, CH_{Ar}), 6.17-6.15 (d, 2H, CH_{Ar}), 6.09-6.06 (d, 2H, CH_{Ar}), 3.20 (s, 6H, CH₃). **¹³C-NMR (300 MHz, CDCl₃)** δ/ppm = 153.2 (s, 2C, C_{Ar}), 152.7 (s, 2C, C_{Ar}), 144.9 (s, 2C, C_{Ar}), 138.1 (s, 2C, C_{Ar}), 133.7 (s, 2C, C_{Ar}), 130.2 (s, 2C, C_{Ar}), 128.9 (s, 2C, C_{Ar}), 113.3 (s, 2C, C_{Ar}), 72.4 (s, 6C, CH₃). **IR (4000-400 cm⁻¹):** 3181(b, m); 3068(w); 2955(w); 2806(w); 1604(s); 1550(m); 1496(s);

1428(m); 1387(w); 1328(s); 1287(m); 1254(m); 1222(s); 1159(m); 1141(w); 1114(m); 1055(w); 1037(w); 969(s); 937(m); 878(s); 828(w); 755(s); 655(m); 560(m); 497(m).

Methylbiquinoxen *iso*-propyl-adduct (Mbqn-(OⁱPr)₂) (1)

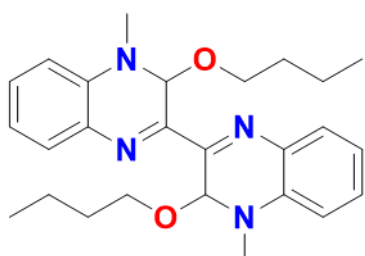


Mbqn-(OH)₂ (50.0 mg, 0.155 mmol, 1.0 eq.) was dissolved in hot 2-propanol (30 ml) over the course of 30 min. The hot mixture was filtered and put aside for slow evaporation. The product is obtained after 2 d as bright orange crystals in a yield of 52.2 mg (83%).

¹H-NMR (500 MHz, DMF-d7): δ/ppm = 7.55-7.53 (m, 2H, CH_{AR}); 7.38-7.35 (m, 2H, CH_{AR}); 7.11-7.09 (m, 2H, CH_{AR}); 7.02-6.98 (m, 2H, CH_{AR}); 6.27 (s, 2H, CH_{AR}); 4.12 (hept, J = 6.1 Hz, 2H, CH); 3.44 (s, 6H, CH₃); 1.08 (d, J = 6.1 Hz, 6H, CH₃); 0.95 (d, J = 6.1 Hz, 6H, CH₃). **IR (4000-400 cm⁻¹):** 3050 (b, w); 2970 (m); 2929 (w), 2865 (w), 1677 (b, w); 1603 (m); 1554 (m); 1492 (s); 1449 (m); 1428 (w); 1371 (m); 1330 (m); 1309 (s); 1275 (m); 1221 (s); 1162 (m); 1137 (m); 1116 (m); 1098 (m); 1051 (w); 1032 (w); 985 (s); 973 (s); 911 (s); 874 (m); 800 (m); 753 (s); 739 (s), 710 (m); 636 (w); 587 (w); 562 (m); 530 (w); 519 (w); 478 (m); 435 (w); 419 (w); 404 (w). **UV-VIS (DCM):** λ/nm = 225, 239, 264, 316, 439, 458 (shoulder). **UV-VIS (DMF):** λ/nm = 265, 313, 440, 459 (shoulder). **UV-VIS (Et₂O):** λ/nm = 212, 238, 265, 316, 432, 455 (shoulder).

Crystal Data for C₂₄H₃₀N₄O₂ (M = 406.52 g/mol): triclinic, space group P-1 (no. 2), a = 9.2870(3) Å, b = 10.6054(3) Å, c = 11.8298(3) Å, α = 98.896(2)°, β = 90.332(2)°, γ = 110.925(2)°, V = 1072.86(6) Å³, Z = 2, T = 180(2) K, $\mu(\text{GaK}\alpha)$ = 0.417 mm⁻¹, D_{calc} = 1.258 g/cm³, 15238 reflections measured (6.594° $\leq 2\Theta \leq$ 128.41°), 5211 unique (R_{int} = 0.0144, R_{sigma} = 0.0176) which were used in all calculations. The final R_1 was 0.0384 ($I > 2\sigma(I)$) and wR_2 was 0.1048 (all data).

Methylbiquinoxen *n*-butyl-adduct (Mbqn-(OⁿBu)₂) (2)

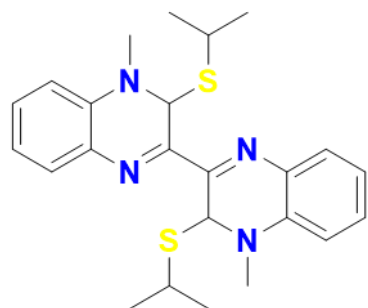


Mbqn-(OH)₂ (50.0, 0.155 mmol, 1.0 eq.) was dissolved in hot 1-butanol (30 ml) over the course of 30 min. The hot mixture was filtered and put aside for slow evaporation. The product was obtained after 2 d as bright orange crystals in a yield of 43.9 mg (65%).

IR (4000-400 cm⁻¹): 3056 (b, w), 2947 (w), 2927 (m), 2859 (m), 1605 (m), 1552 (m), 1490 (m), 1448 (m), 1430 (w), 1389 (w), 1377 (w), 1311 (m), 1274 (m), 1225 (m), 1162 (m), 1127 (m), 1104 (w), 1049 (s), 1030 (m), 1015 (w), 997 (m), 975 (w), 930 (s), 895 (w), 872 (m), 819 (m), 784 (w), 753 (m), 741 (s), 642 (m), 590 (m), 560 (m), 544 (w), 521 (m), 476 (m), 425 (m). **UV-VIS (DMF):** $\lambda/\text{nm} = 262, 312, 440, 463$ (shoulder).

Crystal Data for C₂₆H₃₄N₄O₂ ($M=434.57$ g/mol): monoclinic, space group P2₁/c (no. 14), $a = 9.1279(5)$ Å, $b = 11.5688(6)$ Å, $c = 22.0877(12)$ Å, $\beta = 93.047(4)^\circ$, $V = 2329.1(2)$ Å³, $Z = 4$, $T = 150$ K, $\mu(\text{Mo K}\alpha) = 0.404$ mm⁻¹, $D_{\text{calc}} = 1.239$ g/cm³, 16867 reflections measured ($6.974^\circ \leq 2\Theta \leq 114.988^\circ$), 16867 unique ($R_{\text{int}} = 0.0262$, $R_{\text{sigma}} = 0.0213$) which were used in all calculations. The final R_1 was 0.0413 ($\text{I} > 4\text{u(I)}$) and wR_2 was 0.1310 (all data).

Methylbiquinoxen iso-thiopropyl-adduct (Mbqn-(SⁱPr)₂) (3)

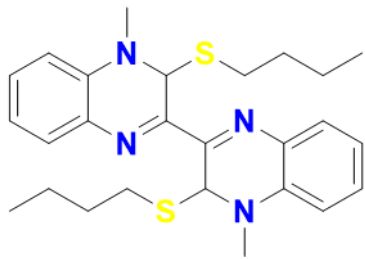


Mbqn-(OH)₂ (50.0 mg, 0.155 mmol, 1.0 eq.) was dissolved in hot THF (100 ml) and an excess of 2-propanthiol (6 ml, 63.8 mmol) was added using a syringe. The mixture was stirred for 30 min at 60°C before filtration and putting it aside to evaporate to dryness. The resulting solid was taken up in acetone and Et₂O, filtered and dried in air. The product was obtained as red crystals in a yield of 39.3 mg (58%).

IR (4000-400 cm⁻¹): 3060 (w), 3040 (w), 2955 (m), 2922 (m), 2861 (m), 1603 (m), 1554 (m), 1486 (m), 1449 (m), 1426 (w), 1375 (m), 1324 (m), 1303 (m), 1271 (m), 1242 (w), 1223 (m), 1197 (m), 1160 (m), 1123 (w), 1114 (w), 1096 (m), 1053 (w), 1034 (m), 965 (m), 930 (m), 872 (w), 817 (w), 754 (m), 741 (s), 712 (s), 683 (s), 632 (m), 587 (m), 550 (s), 524 (m), 480 (m), 472 (m), 445 (m), 423 (m). **UV-VIS (DMF):** $\lambda/\text{nm} = 262, 327, 464$.

Crystal Data for C₂₄H₃₀N₄S₂ ($M=438.64$ g/mol): monoclinic, space group P2₁/c (no. 14), $a = 10.6835(11)$ Å, $b = 11.7694(12)$ Å, $c = 9.3090(9)$ Å, $\beta = 94.629(8)^\circ$, $V = 1166.7(2)$ Å³, $Z = 2$, $T = 180$ K, $\mu(\text{Mo K}\alpha) = 0.246$ mm⁻¹, $D_{\text{calc}} = 1.249$ g/cm³, 9964 reflections measured ($3.824^\circ \leq 2\Theta \leq 69.114^\circ$), 10229 unique ($R_{\text{int}} = 0.1207$, $R_{\text{sigma}} = 0.1235$) which were used in all calculations. The final R_1 was 0.1377 ($\text{I} > 4\text{u(I)}$) and wR_2 was 0.3828 (all data).

Methylbiquinoxen *n*-thiobutyl-adduct (Mbqn-(SⁿBu)₂) (4)

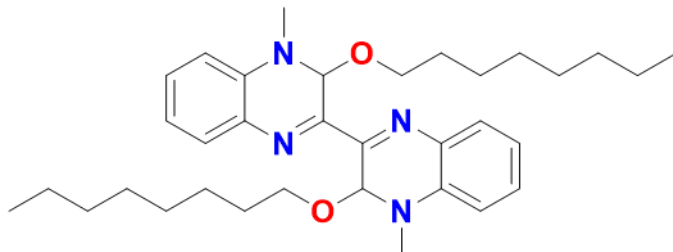


Mbqn-(OH)₂ (50.0 mg, 0.155 mmol, 1.0 eq.) was dissolved in hot THF (100 ml) and an excess of 1-butanethiol (6 ml, 55.9 mmol) was added using a syringe. The mixture was stirred for 30 min at 60°C before filtration and putting it aside to evaporate to dryness. The resulting solid was

taken up in acetone and Et₂O, filtered and dried in air. The product was obtained as red crystals in a yield of 24.1 mg (33%).

IR (4000-400 cm⁻¹): 3064 (w), 3045 (w), 2947 (m), 2921 (m), 2860 (m), 1603 (m), 1557 (m), 1484 (m), 1447 (m), 1422 (m), 1375 (m), 1326 (m), 1303 (m), 1268 (m), 1231 (m), 1219 (m), 1196 (m), 1160 (m), 1127 (w), 1116 (w), 1100 (m), 1069 (w), 1041 (m), 1008 (w), 963 (m), 932 (m), 911 (w), 893 (w), 870 (m), 850 (w), 815 (w), 777 (w), 741 (s), 711 (s), 673 (s), 575 (m), 550 (s), 523 (m), 480 (m), 470 (s), 441 (s). **UV-VIS (DMF):** λ/nm = 262, 328, 470.

Methylbiquinoxen *n*-octanyl-adduct (Mbqn-(OⁿOct)₂) (5)

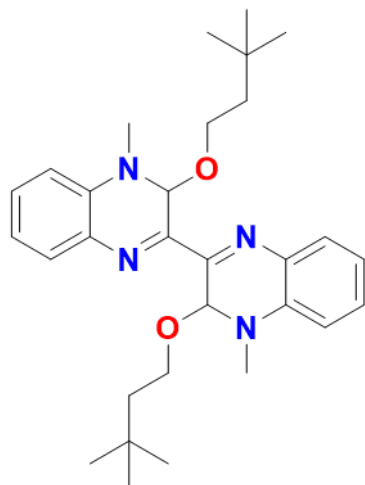


Mbqn-(OH)₂ (50.0 mg, 0.155 mmol, 1.0 eq.) was dissolved in hot 1-octanol (30 ml) over the course of 30 min. The hot mixture was filtered and put aside for slow evaporation.

The product was obtained after 2 d as bright orange solid in a yield of 58.7 mg (69%).

IR (4000-400 cm⁻¹): 3058 (m), 3037 (w), 2951 (m), 2919 (s), 2854 (s), 2772 (w), 1607 (m), 1553 (m), 1494 (s), 1480 (w), 1467 (m), 1453 (m), 1433 (m), 1391 (m), 1378 (w), 1316 (s), 1278 (m), 1229 (m), 1165 (m), 1130 (m), 1110 (w), 1052 (s), 1034 (s), 1009 (m), 925 (s), 871 (m), 823 (m), 755 (m), 744 (s), 724 (w), 648 (w), 594 (w), 565 (m), 534 (w), 482 (m), 460 (w), 444 (w), 425 (w), 406 (w). **UV-VIS (DMF):** λ/nm = 269, 312, 441, 463 (shoulder).

Methylbiquinoxen dimethylbutyl-adduct (Mbqn-(O-Bu(Me)2)2) (6)

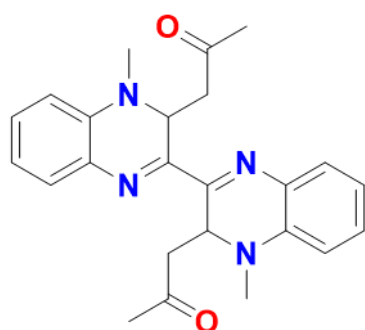


Mbqn-(OH)₂ (50.0 mg, 0.155 mmol, 1.0 eq.) was dissolved in hot 3,3-dimethyl-1-butanol (30 ml) over the course of 30 min. The hot mixture was filtered and put aside for slow evaporation. The product was obtained after 2 d as bright orange crystals in a yield of 63.0 mg (83%).

IR (4000-400 cm⁻¹): 2954 (m), 2900 (w), 2863 (w), 1602 (m), 1552 (m), 1490 (m), 1474 (w), 1447 (w), 1430 (w), 1389 (w), 1361 (m), 1325 (m), 1311 (m), 1275 (m), 1223 (m), 1162 (m), 1127 (w), 1102 (w), 1082 (w), 1045 (s), 1010 (w), 1000 (m), 950 (s), 929 (m), 909 (m), 872 (m), 815 (m), 754 (s), 745 (s), 714 (w), 661 (w), 644 (w), 624 (w), 610 (w), 597 (w), 562 (m), 544 (m), 476 (m), 433 (m), 425 (m). **UV-VIS (DMF):** $\lambda/\text{nm} = 269, 312, 440, 463$ (shoulder).

Crystal Data for C₃₀H₄₂N₄O₂ ($M=490.67$ g/mol): monoclinic, space group P2₁/n (no. 14), $a = 9.6925(7)$ Å, $b = 11.6760(6)$ Å, $c = 24.890(2)$ Å, $\beta = 94.535(6)^\circ$, $V = 2808.0(3)$ Å³, $Z = 4$, $T = 180.0$ K, $\mu(\text{GaK}\alpha) = 0.369$ mm⁻¹, $D_{\text{calc}} = 1.161$ g/cm³, 15186 reflections measured ($6.198^\circ \leq 2\Theta \leq 99.976^\circ$), 4331 unique ($R_{\text{int}} = 0.0637$, $R_{\text{sigma}} = 0.0715$) which were used in all calculations. The final R_1 was 0.1996 ($I > 2\sigma(I)$) and wR_2 was 0.5832 (all data).

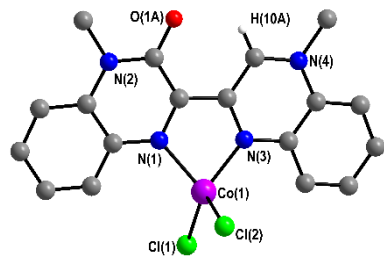
Methylbiquinoxen acetone-adduct (Mbqn-(acetone)₂) (7)



Mbqn-(OH)₂ (50.0 mg, 0.155 mmol, 1.0 eq.) was dissolved in hot freshly distilled acetone (30 ml). The hot mixture was filtered and put aside for slow evaporation. The product is obtained after 2 d as bright yellow crystals in a very low yield (few crystals).

Crystal Data for C₂₄H₂₆N₄O₂ ($M=402.49$ g/mol): monoclinic, space group P2₁/n (no. 14), $a = 8.0271(4)$ Å, $b = 8.8950(4)$ Å, $c = 14.4670(8)$ Å, $\beta = 93.209(4)^\circ$, $V = 1031.34(9)$ Å³, $Z = 2$, $T = 180.0$ K, $\mu(\text{Ga K}/a) = 0.433$ mm⁻¹, $D_{\text{calc}} = 1.296$ g/cm³, 7115 reflections measured ($10.16^\circ \leq 2\Theta \leq 123.964^\circ$), 2401 unique ($R_{\text{int}} = 0.0106$, $R_{\text{sigma}} = 0.0075$) which were used in all calculations. The final R_1 was 0.0428 ($I > 2\sigma(I)$) and wR_2 was 0.1189 (all data).

[Co^{II}Cl₂(MbqnO)] (8-Co)^[28]



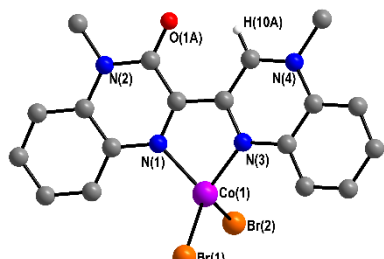
Mbqn-(OH)₂ (50.0 mg, 0.155 mmol, 2.00 eq.) was dissolved in 5 ml DMF leading to a dark red solution, to which CoCl₂·6H₂O (18.4 mg, 0.078 mmol, 1.0 eq.) was added. The colour changed immediately to dark purple. The mixture was stirred for 30 min at RT before filtration and layering with 45 ml MeCN. The mixture was left to diffuse undisturbed for 4d after which the product was obtained as dark purple crystals in a yield of 14.9 mg (44%).

IR (4000-400 cm⁻¹): 3084, 2105, 1808, 1662, 1642, 1601, 1574, 1517, 1492, 1478, 1445, 1426, 1365, 1340, 1328, 1314, 1293, 1215, 1158, 1135, 1112, 1073, 1040, 1028, 987, 952, 929, 917, 878, 747, 735, 659, 636, 624, 579, 562, 542, 515, 482, 460, 416.

C/H/N (calculated): C: 49.91%, H: 3.48%, N: 12.93%. **C/H/N (found):** C: 51.40%, H: 3.43%, N: 14.03%.

Crystal Data for C₁₈H₁₅Cl₂CoN₄O ($M = 433.17$ g/mol): monoclinic, space group P2₁/c (no. 14), $a = 13.2510(2)$ Å, $b = 8.2064(1)$ Å, $c = 16.2872(3)$ Å, $\beta = 100.477(2)^\circ$, $V = 1741.59(5)$ Å³, $Z = 4$, $T = 293(2)$ K, $\mu(\text{CuK}\alpha) = 10.681$ mm⁻¹, $D_{\text{calc}} = 1.652$ g/cm³, 13150 reflections measured ($6.784^\circ \leq 2\Theta \leq 142.076^\circ$), 3314 unique ($R_{\text{int}} = 0.0248$, $R_{\text{sigma}} = 0.0253$) which were used in all calculations. The final R_1 was 0.0316 ($I > 2\sigma(I)$) and wR_2 was 0.0783 (all data).

[Co^{II}Br₂(MbqnO)] (9-Co)^[28]

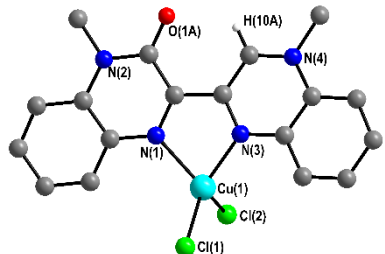


Mbqn-(OH)₂ (50.0 mg, 0.155 mmol, 2.0 eq.) was dissolved in 5 ml DMF leading to a dark red solution, to which CoBr₂·6H₂O (25.5 mg, 0.078 mmol, 1.0 eq.) was added. The colour changed immediately to dark purple. The mixture was stirred for 30 min at RT before filtration and layering with 45 ml MeCN. The mixture was left to diffuse undisturbed for 4d after which the product was obtained as dark purple crystals in a yield of 19.9 mg (49%).

IR (4000-400 cm⁻¹): 3077, 1646, 1600, 1574, 1517, 1493, 1443, 1423, 1408, 1369, 1342, 1330, 1314, 1297, 1214, 1156, 1133, 1115, 1073, 1038, 991, 953, 935, 918, 883, 758, 741, 663, 636, 622, 576, 563, 544, 514, 463, 415. **C/H/N (calculated):** C: 41.41%, H: 2.90%, N: 10.73%. **C/H/N (found):** C: 42.15%, H: 2.74%, N: 11.07%.

Crystal Data for $C_{18}H_{15}Br_2CoN_4O$ ($M=522.09$ g/mol): monoclinic, space group $P2_1/c$ (no. 14), $a = 13.9510(19)$ Å, $b = 8.1083(6)$ Å, $c = 16.014(2)$ Å, $\beta = 100.178(11)^\circ$, $V = 1783.0(4)$ Å³, $Z = 4$, $T = 180(2)$ K, $\mu(\text{MoK}\alpha) = 5.460$ mm⁻¹, $D_{\text{calc}} = 1.945$ g/cm³, 9552 reflections measured ($2.966^\circ \leq 2\Theta \leq 51.358^\circ$), 3362 unique ($R_{\text{int}} = 0.0595$, $R_{\text{sigma}} = 0.0481$) which were used in all calculations. The final R_1 was 0.0353 ($I > 2\sigma(I)$) and wR_2 was 0.0898 (all data).

[Cu^{II}Cl₂(MbqnO)] (10-Cu)

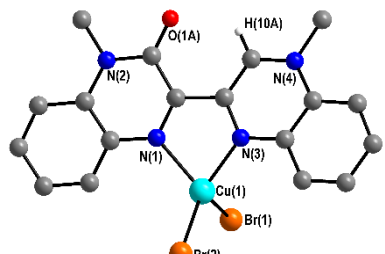


Mbqn(OH)_2 (50.0 mg, 0.155 mmol, 2.0 eq.) was dissolved in 5 ml DMF leading to a dark red solution, to which $\text{CuCl}_2 \cdot 2\text{H}_2\text{O}$ (13.3 mg, 0.078 mmol, 1.0 eq.) was added. The colour changed immediately to dark purple. The mixture was stirred for 30 min at RT before filtration and layering with 45 ml MeCN. The mixture was left to diffuse undisturbed for 4d after which the product was obtained as dark purple crystals in a yield of 14.0 mg (41%).

IR (4000-400 cm⁻¹): 3052, 2350, 2101, 1835, 1644, 1597, 1570, 1523, 1494, 1465, 1421, 1357, 1330, 1309, 1293, 1256, 1242, 1209, 1153, 1133, 1108, 1077, 1032, 991, 975, 924, 901, 874, 790, 770, 659, 649, 616, 559, 540, 509, 484, 464, 456, 412. **C/H/N (calculated):** C: 49.38%, H: 3.45%, N: 12.80%. **C/H/N (found):** C: 50.23%, H: 3.39%, N: 13.43%.

Crystal Data for $C_{18}H_{15}Cl_2CuN_4O$ ($M=437.78$ g/mol): monoclinic, space group $P2_1/c$ (no. 14), $a = 13.4398(4)$ Å, $b = 7.8086(3)$ Å, $c = 16.2480(4)$ Å, $\beta = 101.519(2)^\circ$, $V = 1670.82(9)$ Å³, $Z = 4$, $T = 180.00$ K, $\mu(\text{MoK}\alpha) = 1.643$ mm⁻¹, $D_{\text{calc}} = 1.740$ g/cm³, 29842 reflections measured ($5.118^\circ \leq 2\Theta \leq 66.276^\circ$), 6356 unique ($R_{\text{int}} = 0.0309$, $R_{\text{sigma}} = 0.0319$) which were used in all calculations. The final R_1 was 0.0383 ($I > 2\sigma(I)$) and wR_2 was 0.1000 (all data).

[Cu^{II}Br₂(MbqnO)] (11-Cu)



Mbqn(OH)_2 (50.0 mg, 0.155 mmol, 2.0 eq.) was dissolved in 5 ml DMF leading to a dark red solution, to which CuBr_2 (17.4 mg, 0.078 mmol, 1.0 eq.) was added. The colour changed immediately to dark purple. The mixture is stirred for 30 min at RT before filtration and

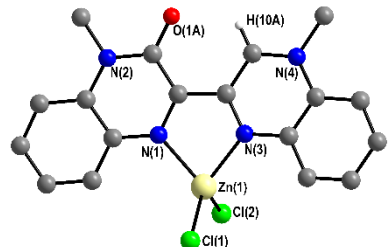
layering with 45 ml MeCN. The mixture was left to diffuse undisturbed for 4d after which the product was obtained as dark purple crystals in a yield of 16.9 mg (41%).

IR (4000-400 cm⁻¹): 3055, 2338, 2099, 1822, 1644, 1593, 1568, 1492, 1459, 1431, 1357, 1330, 1307, 1291, 1254, 1236, 1209, 1153, 1133, 1108, 1075, 1032, 989, 978, 922, 897, 870, 790, 770, 657, 649, 610, 560, 540, 521, 507, 484, 464, 452, 431, 413.

C/H/N (calculated): C: 41.05%, H: 2.87%, N: 10.64%. **C/H/N (found):** C: 41.96%, H: 2.85%, N: 11.08%.

Crystal Data for C₁₈H₁₅Br₂CuN₄O ($M=526.70$ g/mol): monoclinic, space group P2₁/c (no. 14), $a = 14.0992(6)$ Å, $b = 7.8107(5)$ Å, $c = 16.1742(8)$ Å, $\beta = 101.516(4)^\circ$, $V = 1745.32(16)$ Å³, $Z = 4$, $T = 180$ K, $\mu(\text{Mo K}\alpha) = 5.846$ mm⁻¹, $D_{\text{calc}} = 2.004$ g/cm³, 11528 reflections measured ($5.14^\circ \leq 2\Theta \leq 56.562^\circ$), 4311 unique ($R_{\text{int}} = 0.0279$, $R_{\text{sigma}} = 0.0414$) which were used in all calculations. The final R_1 was 0.0384 ($I > 2\sigma(I)$) and wR_2 was 0.0932 (all data).

[Zn^{II}Cl₂(MbqnO)] (12-Zn A) and (12-Zn B)



Mbqn-(OH)₂ (50.0 mg, 0.155 mg, 2.0 eq.) was dissolved in 5 ml DMF leading to a dark red solution, to which ZnCl₂·4H₂O (16.3 mg, 0.078 mmol, 1.0 eq.) was added. The colour changed immediately to dark purple. The mixture was stirred for 30 min at RT before filtration and

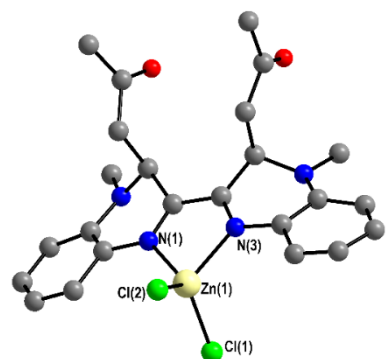
layering with 45 ml MeCN. The mixture was left to diffuse undisturbed for 4d after which the product was obtained as dark purple crystals in a yield of 13.0 mg (38%).

IR (4000-400 cm⁻¹): 3079, 2109, 1828, 1644, 1597, 1570, 1541, 1521, 1482, 1445, 1432, 1416, 1361, 1326, 1308, 1233, 1209, 1160, 1133, 1102, 1075, 1026, 989, 950, 932, 884, 862, 815, 749, 659, 623, 599, 573, 554, 542, 530, 513, 484, 466, 460, 431, 406. **C/H/N (calculated):** C: 49.18%, H: 3.44%, N: 12.74. **C/H/N (found):** C: 50.11%, H: 3.41%, N: 13.05%.

Crystal Data (12-Zn A) for C₁₈H₁₅Cl₂N₄OZn ($M=439.61$ g/mol): monoclinic, space group P2₁/c (no. 14), $a = 13.4372(8)$ Å, $b = 8.0886(3)$ Å, $c = 16.1358(11)$ Å, $\beta = 100.631(5)^\circ$, $V = 1723.67(17)$ Å³, $Z = 4$, $T = 170$ K, $\mu(\text{Ga K}\alpha) = 3.291$ mm⁻¹, $D_{\text{calc}} = 1.694$ g/cm³, 10103 reflections measured ($9.704^\circ \leq 2\Theta \leq 124.968^\circ$), 4038 unique ($R_{\text{int}} = 0.0142$, $R_{\text{sigma}} = 0.0123$) which were used in all calculations. The final R_1 was 0.0271 ($I > 2\sigma(I)$) and wR_2 was 0.0870 (all data).

Crystal Data (12-Zn B) for $C_{18}H_{15}Cl_2N_4OZn$ ($M = 439.61$ g/mol): monoclinic, space group $P2_1/n$ (no. 14), $a = 9.2305(4)$ Å, $b = 14.3251(6)$ Å, $c = 13.6905(7)$ Å, $\beta = 106.283(5)^\circ$, $V = 1737.65(14)$ Å 3 , $Z = 4$, $T = 293(2)$ K, $\mu(\text{CuK}\alpha) = 4.925$ mm $^{-1}$, $D_{\text{calc}} = 1.680$ g/cm 3 , 9780 reflections measured ($9.132^\circ \leq 2\Theta \leq 141.884^\circ$), 3304 unique ($R_{\text{int}} = 0.0272$, $R_{\text{sigma}} = 0.0300$) which were used in all calculations. The final R_1 was 0.0366 ($I > 2\sigma(I)$) and wR_2 was 0.0999 (all data).

[Zn^{II}Cl₂(Mbqn-acetone)₂] (13-Zn)

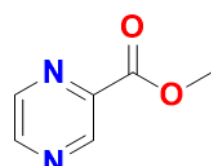


Mbqn-(OH) $_2$ (50.0 mg, 0.155 mg, 2.0 eq.) was dissolved in 30 ml of hot acetone (ca. 50°C) over the course of 30 min, any undissolved starting material was filtered off through cotton wool. To the clear fluorescent solution $ZnCl_2$ (16.3 mg, 0.078 mmol, 1.0 eq.) was added and the mixture heated to reflux for 1 h before hot filtration. The vial was put aside for slow evaporation. After 1 week the product is obtained as black crystals in a very low yield (few crystals).

Crystal Data for $C_{24}H_{26}Cl_2N_4O_2Zn$ ($M = 538.76$ g/mol): monoclinic, space group $P2_1/n$ (no. 14), $a = 14.6281(8)$ Å, $b = 8.3601(3)$ Å, $c = 24.0629(15)$ Å, $\beta = 104.345(5)^\circ$, $V = 2851.0(3)$ Å 3 , $Z = 4$, $T = 150.00$ K, $\mu(\text{GaK}\alpha) = 1.993$ mm $^{-1}$, $D_{\text{calc}} = 1.255$ g/cm 3 , 15752 reflections measured ($6.598^\circ \leq 2\Theta \leq 128.094^\circ$), 6807 unique ($R_{\text{int}} = 0.0774$, $R_{\text{sigma}} = 0.0565$) which were used in all calculations. The final R_1 was 0.2507 ($I > 2\sigma(I)$) and wR_2 was 0.6273 (all data).

8.2 The H₂opch Family

Methyl pyrazine-2-carboxylate^[359-360]

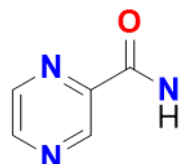


Pyrazine-2-carboxylic acid (15 g, 0.12 mol, 1.0 eq.) was suspended in MeOH (350 ml) and cooled to 0°C in an ice bath. Under constant and vigorous stirring $SOCl_2$ (34.8 ml, 0.48 mmol, 4.0 eq.) was added dropwise over the course of 15 min. After the completed addition the mixture was allowed to warm up to RT before removing excess $SOCl_2$ under reduced pressure. The crude product was neutralised with 200 ml of saturated $NaHCO_3$ solution

and extracted three times with DCM (ca. 100 ml each). The combined organic phases were dried over Na_2SO_4 after which the solvent was removed. The product was obtained as a colourless solid in a yield of 3.20 g (19%).

$^1\text{H-NMR}$ (500 MHz, CDCl_3): δ/ppm = 9.31 (d, J = 1.2 Hz, 1H, CH_{AR}), 8.77 (d, J = 2.4 Hz, 1H, CH_{AR}), 8.73-8.71 (m, 1H, CH_{AR}), 4.04 (s, 3H, CH_3). **IR (4000-400 cm⁻¹)**: 3097 (w); 3066 (m); 3032 (w); 2969 (w), 2925 (w); 2802 (b, w); 2648 (w); 2447 (b, m); 1883 (b, m); 1716 (b, s); 1529 (m); 1485 (w); 1442 (m); 1394 (s); 1311 (s); 1274 (s); 1173 (m); 1154 (s); 1053 (s); 1020 (s); 959 (m); 887 (m); 844 (w); 823 (m); 780 (m); 724 (m); 712 (m); 702 (m); 647 (m); 499 (m); 434 (m); 404 (m).

Pyrazine-2-carbohydrazide^[360-361]

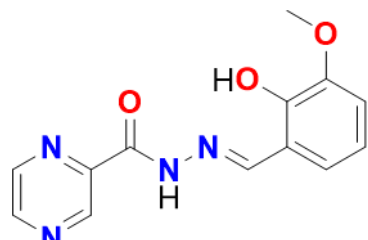


Methyl pyrazine-2-carboxylate (3.2 g, 23.2 mmol, 1.0 eq.) was dissolved in EtOH (80 ml) and hydrazine hydrate (80%, 8.7 ml, 278.1 mmol, 12.0 eq.) added dropwise. The mixture was heated to reflux for 12 h before cooling it down in an ice bath. The product crystallises in colourless needles that are filtered washed with Et_2O and dried under reduced pressure. The product was obtained in a yield of 2.33 g (73%).

$^1\text{H-NMR}$ (500 MHz, DMSO-d_6): δ/ppm = 10.14 (s, 1H, NH), 9.13 (d, J = 1.4 Hz, 1H, CH_{AR}), 8.83 (d, J = 2.5 Hz, 1H, CH_{AR}), 8.69 (dd, J = 2.5, 1.4 Hz, 1H, CH_{AR}), 4.65 (s, 2H, NH_2). **IR (4000-400 cm⁻¹)**: 3303 (s); 3225 (b, s); 3017 (b, w); 1675 (m); 1642 (s); 1578 (m); 1515 (m); 1459 (m); 1393 (m); 1306 (m); 1207 (m); 1160 (m); 1106 (m); 1054 (m); 1017 (m); 958 (m); 891 (w); 858 (m); 751 (m); 660 (b, s); 489 (m); 443 (m).

(E)-N'-(2-hydroxy-3-methoxybenzylidene)pyrazine-2-carbohydrazide

(H₂opch)^[360-361]

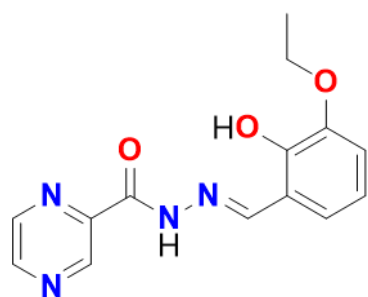


Pyrazine-2-carbohydrazide (1.00 g, 7.24 mmol, 1.0 eq.) was dissolved in H_2O (15 ml) and a solution of 2-hydroxy-3-methoxybenzaldehyde (1.32 g, 8.69 mmol, 1.2 eq.) in EtOH (25 ml) was added dropwise. The yellow suspension was stirred for 24 h at RT before filtration and washing with cold Et_2O . The product was obtained as a colourless powder in a yield of 1.90 g (96%).

$^1\text{H-NMR}$ (500 MHz, DMSO-d_6): δ/ppm = 12.63 (s, 1H, OH); 10.99 (s, 1H, NH); 9.28 (d, J = 1.4 Hz, 1H, N=CH); 8.94 (d, J = 2.5 Hz, 1H, CH_{AR}); 8.84 (s, 1H, CH_{AR}); 8.80

(dd, $J = 2.4, 1.5$ Hz, 1H, CH_{AR}); 7.12 (dd, $J = 7.9, 1.3$ Hz, 1H, CH_{AR}); 7.05 (dd, $J = 8.0, 1.3$ Hz, 1H, CH_{AR}); 6.87 (t, $J = 7.9$ Hz, 1H, CH_{AR}); 3.82 (s, 3H, CH_3). **IR (4000-400 cm⁻¹)**: 3454 (b, m), 3413 (b, m), 3256 (b, m), 3014 (m), 2948 (w), 2845 (w), 1673 (s), 1648 (w), 1610 (m), 1578 (m), 1528 (m), 1463 (m), 1443 (w), 1406 (m), 1362 (m), 1248 (m), 1154 (m), 1082 (m), 1051 (w), 1019 (m), 985 (w), 972 (w), 962 (w), 945 (w), 904 (m), 873 (w), 841 (w), 782 (w), 769 (w), 737 (m), 595 (b, m), 561 (w), 543 (w), 489 (b, w), 460 (w), 444 (w).

(E)-N'-(2-hydroxy-3-ethoxybenzylidene)pyrazine-2-carbohydrazide (H₂oepch)^[360-361]

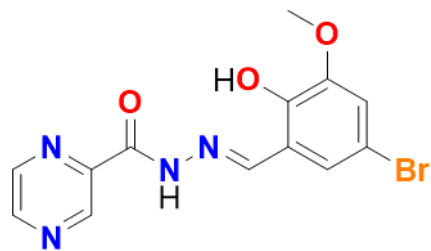


Pyrazine-2-carbohydrazide (1.00 g, 7.24 mmol, 1.0 eq.) was dissolved in H_2O (15 ml) and a solution of 2-hydroxy-3-ethoxybenzaldehyde (1.44 g, 8.69 mmol, 1.2 eq.) in EtOH (25 ml) was added dropwise. The yellow suspension was stirred for 24 h at RT before filtration and washing with cold Et_2O . The product was obtained as a colourless powder in a yield of 1.87 g (90%).

¹H-NMR (500 MHz, DMSO-d₆): $\delta/\text{ppm} = 12.62$ (s, 1H, OH); 11.00 (s, 1H, NH); 9.28 (d, $J = 1.4$ Hz, 1H, CH_{AR}); 8.94 (d, $J = 2.5$ Hz, 1H, CH_{AR}); 8.84 (s, 1H, N=CH); 8.80 (dd, $J = 2.4, 1.5$ Hz, 1H, CH_{AR}); 7.10 (dd, $J = 7.9, 1.3$ Hz, 1H, CH_{AR}); 7.04 (dd, $J = 8.0, 1.3$ Hz, 1H, CH_{AR}); 6.85 (t, $J = 7.9$ Hz, 1H, CH_{AR}); 4.07 (q, $J = 7.0$ Hz, 2H, CH_2); 1.35 (t, $J = 7.0$ Hz, 3H, CH_3). **IR (4000-400 cm⁻¹)**: 3297 (m), 2981 (m), 2924 (b, w), 2886 (b, w), 1695 (s), 1610 (m), 1575 (w), 1527 (s), 1473 (m), 1403 (m), 1373 (m), 1272 (m), 1251 (s), 1163 (m), 1150 (m), 1117 (m), 1084 (m), 1069 (m), 1047 (w), 1022 (m), 971 (w), 883 (m), 869 (w), 832 (w), 781 (m), 755 (w), 734 (m), 695 (b, w), 644 (w), 601 (m), 573 (w), 545 (w), 489 (w), 461 (w), 441 (m). **UV-VIS (MeCN)**: $\lambda/\text{nm} = 202, 222, 265, 306, 348$ (shoulder). **UV-VIS (DMF)**: $\lambda/\text{nm} = 264, 310, 348$ (shoulder). **UV-VIS (solid state)**: $\lambda/\text{nm} = 227, 272, 328$.

(E)-N'-(5-bromo-2-hydroxy-3-methoxybenzylidene)pyrazine-2-carbohydrazide

(H₂opch-Br)

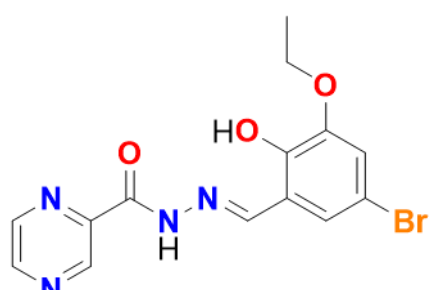


Pyrazine-2-carbohydrazide (1.50 g, 10.86 mmol, 1.0 eq.) was dissolved in H₂O (25 ml) and a solution of 5-bromo-2-hydroxy-3-methoxybenzaldehyde (3.01 g, 13.03 mmol, 1.2 eq.) in EtOH (50 ml) was added dropwise. The yellow suspension was stirred for 24 h at RT before filtration and washing with cold Et₂O. The product was obtained as a pale yellow, fluffy powder in a yield of 3.53 g (93%).

¹H-NMR (500 MHz, DMSO-d₆): δ /ppm = 12.67 (s, 1H, OH); 10.82 (s, 1H, NH); 9.27 (s, 1H, CH), 8.93 (s, 1H, CH_{AR}), 8.82 (s, 1H, CH_{AR}), 8.80 (s, 1H, CH_{AR}), 7.38 (d, J = 2.2 Hz, 1H, CH_{AR}), 7.18 (d, J = 2.2 Hz, 1H, CH_{AR}), 3.85 (s, 3H, CH₃). **IR (4000-400 cm⁻¹):** 3603 (s), 3410 (b, m), 3143 (b, w), 3015 (m), 2975 (w), 2939 (m), 2838 (m), 1676 (s), 1634 (m), 1603 (m), 1550 (s), 1477 (s), 1406 (m), 1367 (m), 1292 (m), 1266 (m), 1246 (s), 1219 (m), 1167 (m), 1110 (w), 1097 (m), 1077 (m), 1048 (w), 1021 (s), 979 (m), 962 (m), 905 (m), 863 (m), 833 (m), 759 (m), 740 (m), 705 (m), 694 (m), 578 (w), 503 (w), 468 (w), 444 (m). **UV-VIS (MeCN):** λ /nm = 206, 228, 265 (shoulder), 303, 351 (shoulder). **UV-VIS (solid state):** λ /nm = 231, 272, 315, 375 (shoulder).

(E)-N'-(5-bromo-2-hydroxy-3-ethoxybenzylidene)pyrazine-2-carbohydrazide

(H₂oepch-Br)

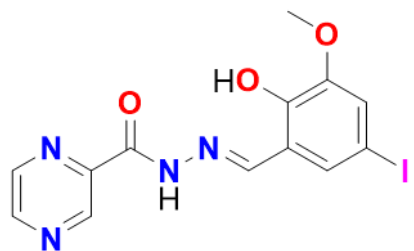


Pyrazine-2-carbohydrazide (56.4 mg, 0.408 mmol, 1.0 eq.) was dissolved in H₂O (6 ml) and a solution of 5-bromo-2-hydroxy-3-ethoxybenzaldehyde (100.0 mg, 0.408 mmol, 1.0 eq.) in EtOH (12 ml) was added dropwise. The yellow suspension was stirred for 24 h at RT before filtration and washing with cold Et₂O. The product is obtained as a colourless powder in a yield of 120.0 mg (81%).

¹H-NMR (500 MHz, DMSO-d₆): δ /ppm = 12.68 (s, 1H, OH), 10.81 (s, 1H, NH), 9.27 (d, J = 1.4 Hz, 1H, CH), 8.93 (d, J = 2.5 Hz, 1H, CH_{AR}), 8.82 (s, 1H, CH_{AR}), 8.80 (dd, J = 2.4 Hz, 1.5 Hz, 1H, CH_{AR}), 7.36 (d, J = 2.3 Hz, 1H, CH_{AR}), 7.16 (d, J = 2.3 Hz, 1H, CH_{AR}), 4.09 (q, J = 6.9 Hz, 2H, CH₂), 1.35 (t, J = 7.0 Hz, 3H, CH₃). **IR (4000-400 cm⁻¹):** 3456 (b, m), 3280 (w), 3142 (b, w), 3043 (b, w), 2986 (m), 2976 (m), 2934 (w), 2901

(w), 1695 (m), 1660 (s), 1606 (m), 1566 (m), 1545 (m), 1520 (m), 1478 (m), 1465 (m), 1444 (w), 1396 (m), 1372 (m), 1319 (m), 1298 (m), 1252 (s), 1217 (w), 1174 (m), 1155 (m), 1114 (w), 1097 (w), 1073 (m), 1020 (m), 957 (w), 926 (m), 888 (m), 868 (w), 854 (w), 846 (w), 828 (w), 765 (m), 741 (m), 714 (w), 696 (w), 615 (w), 594 (w), 580 (w), 502 (b, w), 445 (w).

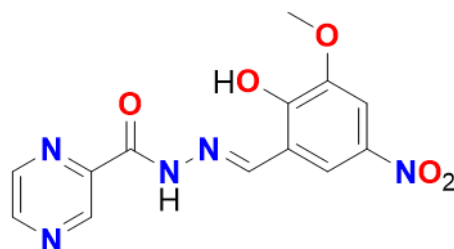
(E)-N'-(5-iodo-2-hydroxy-3-methoxybenzylidene)pyrazine-2-carbohydrazide (H₂opch-I)



Pyrazine-2-carbohydrazide (280.3 mg, 2.03 mmol, 1.0 eq.) was dissolved in H₂O (15 ml) and a solution of 5-iodo-2-hydroxy-3-methoxybenzaldehyde (400.0 mg, 2.03 mmol, 1.0 eq.) in EtOH (30 ml) was added dropwise. The yellow suspension is stirred for 24 h at RT before filtration and washing with cold Et₂O. The product was obtained as a colourless powder in a yield of 554.0 mg (67%).

¹H-NMR (500 MHz, DMSO-d₆): δ /ppm = 12.65 (s, 1H, OH), 10.80 (s, 1H, NH), 9.27 (d, J = 1.4 Hz, 1H, CH), 8.93 (d, J = 2.5 Hz, 1H, CH_{AR}), 8.80 (dd, J = 2.4 Hz, 1.5 Hz, 2H, CH_{AR}), 8.79 (s, 1H, CH_{AR}), 3.83 (s, 3H, CH₃). **IR (4000-400 cm⁻¹):** 3605 (s), 3410 (b, m), 3140 (b, w), 3013 (m), 2975 (w), 2939 (m), 2838 (m), 1676 (s), 1634 (m), 1603 (m), 1550 (s), 1477 (s), 1405 (m), 1367 (m), 1292 (m), 1266 (m), 1246 (s), 1219 (m), 1167 (m), 1110 (w), 1097 (m), 1075 (m), 1048 (w), 1018 (s), 979 (m), 962 (m), 905 (m), 863 (m), 834 (m), 759 (m), 740 (m), 705 (m), 696 (m), 578 (w), 502 (w), 468 (w), 444 (m).

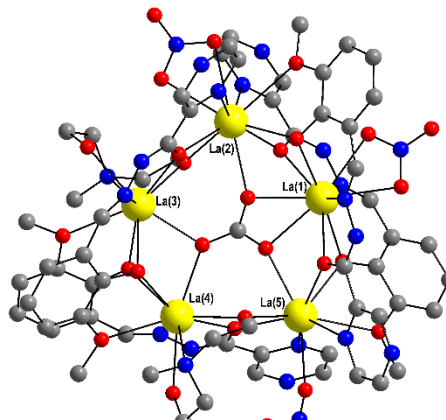
(E)-N'-(2-hydroxy-3-methoxy-5-nitrobenzylidene)pyrazine-2-carbohydrazide (H₂opch-NO₂)



Pyrazine-2-carbohydrazide (210.2 mg, 1.52 mmol, 1.0 eq.) was dissolved in H₂O (10 ml) and a solution of 2-hydroxy-3-methoxy-5-nitrobenzaldehyde (300.0 mg, 1.52 mmol, 1.0 eq.) in EtOH (20 ml) was added dropwise. The yellow suspension is stirred for 24 h at RT before filtration and washing with cold Et₂O. The product was obtained as a colourless powder in a yield of 400.3 mg (83%).

¹H-NMR (500 MHz, DMSO-d₆): δ/ppm = 12.78 (s, 1H, OH), 11.91 (s, 1H, NH), 9.28 (d, J = 1.3 Hz, 1H, CH), 8.96-8.94 (m, 1H, CH_{AR}), 8.81 (dd, J = 2.4, 1.5 Hz, 1H, CH_{AR}), 8.24 (d, J = 2.6 Hz, 1H, CH_{AR}), 7.80 (d, J = 2.6 Hz, 1H, CH_{AR}), 3.96 (s, 3H, CH₃). **IR (4000-400 cm⁻¹):** 3634 (b, w), 3447 (b, w), 3251 (b, w), 3197 (m), 2954 (w), 2855 (w), 1686 (s), 1876 (s), 1626 (w), 1606 (m), 1581 (m), 1521 (s), 1485 (s), 1468 (w), 1437 (m), 1412 (w), 1382 (w), 1339 (b, s), 1261 (b, s), 1207 (w), 1192 (w), 1162 (b, m), 1098 (m), 1085 (w), 1064 (m), 1019 (m), 983 (m), 957 (m), 935 (w), 900 (m), 894 (m), 872 (w), 864 (m), 792 (m), 768 (w), 740 (m), 639 (b, w), 623 (b, w), 545 (w), 513 (w), 487 (w), 444 (m), 403 (m).

[La^{III}₅(CO₃)(mdeaH)₂(NO₃)₃(opch)₄]_·4.5MeCN (14-La)

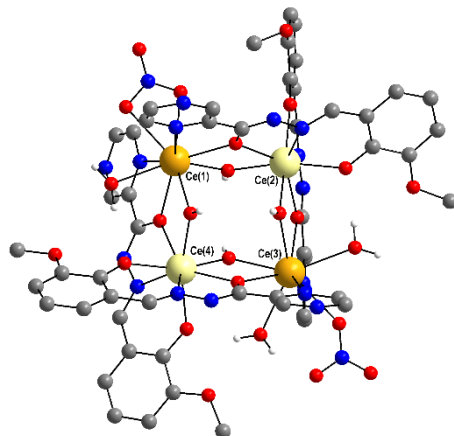


H₂opch (27.2 mg, 0.10 mmol, 1.0 eq.) was dissolved in 5 ml of MeCN before adding mdeaH₂ (34.4 μl, 0.30 mmol, 3.0 eq.). La(NO₃)₃·6H₂O (43.3 mg, 0.10 mmol, 1.0 eq.) was dissolved separately in 5 ml MeCN and then added dropwise to the ligand and base solution. The yellow solution was stirred overnight at RT, filtered and then left to slowly evaporate. After three weeks the product was obtained as yellow crystals in a yield of 32.2 mg (70% based on La^{III}).

IR (4000-400 cm⁻¹): 3058 (m), 2934 (m), 2896 (m), 2841 (m), 1602 (s), 1557 (s), 1540 (s), 1521 (m), 1434 (s), 1340 (s), 1293 (s), 1213 (s), 1183 (m), 1155 (s), 1075 (s), 1025 (s), 965 (m), 916 (m), 893 (w), 850 (m), 819 (w), 771 (w), 731 (s), 640 (w), 512 (w), 482 (w), 423 (w). **UV-VIS (DMF):** λ/nm = 336, 410. **UV-VIS (solid state):** λ/nm = 238, 339, 409. **C/H/N (calculated) corresponds to exchange of all lattice MeCN by 6H₂O:** C: 31.98%, H: 3.24%, N: 12.43%. **C/H/N (found):** C: 32.14%, H: 2.90%, N: 12.57%.

Crystal Data for C₇₂H_{77.5}La₅N_{25.5}O₂₈ ($M=2442.64$ g/mol): triclinic, space group P-1 (no. 2), $a = 14.7042(7)$ Å, $b = 16.2377(5)$ Å, $c = 19.1380(11)$ Å, $\alpha = 100.118(4)$ °, $\beta = 91.686(4)$ °, $\gamma = 95.207(3)$ °, $V = 4475.0(4)$ Å³, $Z = 2$, $T = 180.15$ K, $\mu(\text{GaK}\alpha) = 12.925$ mm⁻¹, $D_{\text{calc}} = 1.813$ g/cm³, 51941 reflections measured ($4.084^\circ \leq 2\Theta \leq 125.21^\circ$), 20787 unique ($R_{\text{int}} = 0.0337$, $R_{\text{sigma}} = 0.0460$) which were used in all calculations. The final R_1 was 0.0398 ($I > 2\sigma(I)$) and wR_2 was 0.1041 (all data).

[Ce^{III}₂Ce^{IV}₂(H₂O)₃(NO₃)₂(μ₂-OH)₄(opch)₄]_·4MeCN·H₂O (15-Ce)

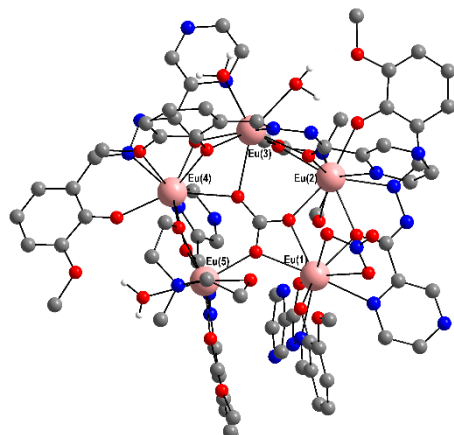


H₂opch (27.2 mg, 0.10 mmol, 1.0 eq.) was dissolved in 5 ml of MeCN before adding mdeaH₂ (34.4 μ l, 0.30 mmol, 3.0 eq.). Ce(NO₃)₃·6H₂O (43.4 mg, 0.10 mmol, 1.0 eq.) was dissolved separately in 5 ml MeCN and then added dropwise to the ligand and base solution leading to a rapid colour change towards dark brown. The dark mixture was stirred overnight at RT, filtered and then left to slowly evaporate. After two weeks the product was obtained as brown crystals in a yield of 40.1 mg (76% based on Ce^{III/IV}).

IR (4000-400 cm⁻¹): 3347 (b, s), 2939 (m), 2834 (m), 1599 (s), 1563 (s), 1520 (m), 1473 (s), 1436 (s), 1414 (s), 1333 (s), 1283 (s), 1244 (s), 1220 (s), 1178 (m), 1153 (s), 1105 (m), 1082 (s), 1059 (m), 1028 (s), 973 (m), 922 (m), 856 (s), 768 (m), 733 (s), 700 (m), 634 (m), 524 (m), 446 (m). **UV-VIS (solid state):** $\lambda/\text{nm} = 238, 267$ (shoulder), 370.

Crystal Data for C₆₀H₆₅Ce₄N₂₂O₂₆ ($M=2070.82$ g/mol): monoclinic, space group P2₁/n (no. 14), $a = 16.6925(6)$ Å, $b = 26.1270(10)$ Å, $c = 19.1392(11)$ Å, $\beta = 114.860(3)^\circ$, $V = 7573.6(6)$ Å³, $Z = 4$, $T = 180$ K, $\mu(1.3401270, 1.34 \text{ K}) = 12.509 \text{ mm}^{-1}$, $D_{\text{calc}} = 1.816 \text{ g/cm}^3$, 43483 reflections measured ($5.316^\circ \leq 2\Theta \leq 125.072^\circ$), 17695 unique ($R_{\text{int}} = 0.0313$, $R_{\text{sigma}} = 0.0276$) which were used in all calculations. The final R_1 was 0.0425 ($I > 2\sigma(I)$) and wR_2 was 0.1244 (all data).

[Eu₅(CO₃)(H₂O)₃(mdeaH)₂(NO₃)₅]_·17.33MeCN·H₂O (16-Eu)

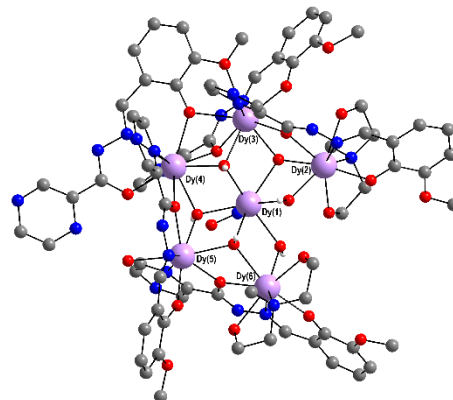


H₂opch (27.2 mg, 0.10 mmol, 1.0 eq.) was dissolved in 5 ml of MeCN before adding mdeaH₂ (34.4 μ l, 0.30 mmol, 3.0 eq.). Eu(NO₃)₃·5H₂O (42.8 mg, 0.10 mmol, 1.0 eq.) was dissolved separately in 5 ml MeCN and then added dropwise to the ligand and base solution. The yellow solution was stirred overnight at RT, filtered and then left to slowly evaporate. After two weeks the product was obtained as orange crystals in a yield of 27.9 mg (45% based on Eu^{III}).

IR (4000-400 cm⁻¹): 3069 (b, m), 3055 (m), 2936 (m), 2900 (m), 2834 (m), 1603 (s), 1555 (s), 1521 (m), 1535 (s), 1442 (s), 1412 (s), 1372 (m), 1342 (s), 1310 (s), 1235 (s), 1212 (s), 1182 (m), 1155 (s), 1080 (s), 1059 (m), 1027 (s), 970 (m), 919 (m), 893 (w), 857 (m), 769 (w), 734 (s), 641 (w), 523 (w), 483 (w), 425 (w). **UV-VIS (solid state):** $\lambda/\text{nm} = 207, 240, 347, 428$.

Crystal Data for $\text{C}_{110.67}\text{H}_{130}\text{Eu}_5\text{N}_{40.33}\text{O}_{29}$ ($M=3249.01$ g/mol): trigonal, space group P-3 (no. 147), $a = 32.0835(4)$ Å, $c = 25.7765(3)$ Å, $V = 22978.3(6)$ Å³, $Z = 6$, $T = 180$ K, $\mu(\text{Mo K}\alpha) = 2.091$ mm⁻¹, $D_{\text{calc}} = 1.409$ g/cm³, 130164 reflections measured ($3.878^\circ \leq 2\Theta \leq 51.362^\circ$), 29076 unique ($R_{\text{int}} = 0.0678$, $R_{\text{sigma}} = 0.0639$) which were used in all calculations. The final R_1 was 0.0437 ($I > 2\sigma(I)$) and wR_2 was 0.1191 (all data).

[Dy^{III}₆(H₂O)(mdeaH₂)₂(NO₃)₄(μ₃-OH)₄(μ₂-OH)₂(opch)₅](NO₃)·8MeCN (17-Dy)



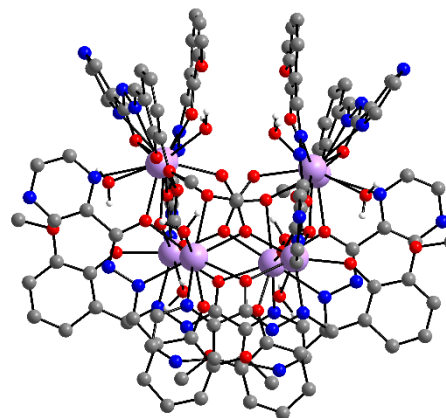
H_2opch (27.2 mg, 0.10 mmol, 1.0 eq.) was dissolved in 5 ml of MeCN before adding mdeaH_2 (34.4 μl , 0.30 mmol, 3.0 eq.). $\text{Ln}(\text{NO}_3)_3 \cdot x\text{H}_2\text{O}$ (0.10 mmol, 1.0 eq.) was dissolved separately in 5 ml MeCN and then added dropwise to the ligand and base solution. The yellow solution was stirred overnight at RT, filtered and then left to slowly evaporate. After two weeks the product was obtained as bright yellow

crystals in combination with red crystals of (21-Dy).

IR (4000-400 cm⁻¹): 3390 (b, s), 2928 (b, w), 2831 (w), 1605 (s), 1562 (m), 1545 (w), 1521 (m), 1444 (s), 1421 (m), 1378 (w), 1343 (s), 1298 (m), 1238 (m), 1216 (s), 1184 (m), 1158 (m), 1104 (w), 1078 (m), 1064 (w), 1029 (m), 972 (m), 923 (m), 858 (m), 769 (w), 739 (m), 702 (w), 646 (w), 630 (w), 586 (w), 531 (w), 482 (w), 426 (w).

Crystal Data for $\text{C}_{91}\text{H}_{108}\text{Dy}_6\text{N}_{32}\text{O}_{32}$ ($M=3137.09$ g/mol): triclinic, space group P-1 (no. 2), $a = 18.4408(8)$ Å, $b = 18.7612(7)$ Å, $c = 19.2293(9)$ Å, $\alpha = 76.764(3)^\circ$, $\beta = 76.403(4)^\circ$, $\gamma = 60.463(3)^\circ$, $V = 5575.4(5)$ Å³, $Z = 2$, $T = 180.15$ K, $\mu(\text{MoK}\alpha) = 4.060$ mm⁻¹, $D_{\text{calc}} = 1.869$ g/cm³, 38433 reflections measured ($4.35^\circ \leq 2\Theta \leq 50.7^\circ$), 20094 unique ($R_{\text{int}} = 0.0935$, $R_{\text{sigma}} = 0.1062$) which were used in all calculations. The final R_1 was 0.0937 ($I > 2\sigma(I)$) and wR_2 was 0.2703 (all data).

[Ln₈(CO₃)₄(H₂O)₈(opch)₈] (Ln = Y^{III}, Sm^{III}, Gd^{III}, Tb^{III}, Dy^{III}, Ho^{III}, Er^{III})



crystals.

H₂opch (27.2 mg, 0.10 mmol, 1.0 eq.) was dissolved in 5 ml of MeCN before adding mdeah₂ (34.4 μ l, 0.30 mmol, 3.0 eq.). Ln(NO₃)₃ \cdot xH₂O (0.10 mmol, 1.0 eq.) was dissolved separately in 5 ml MeCN and then added dropwise to the ligand and base solution. The yellow solution was stirred overnight at RT, filtered and then left to slowly evaporate. After two weeks the product was obtained as bright red

[Sm₈(CO₃)₄(H₂O)₈(opch)₈] \cdot 12MeCN \cdot 4H₂O (18-Sm)

Amount of Sm(NO₃)₃ \cdot 6H₂O used = 44.4 mg. **Yield (based on Sm^{III})** = 10.8 mg (23%).

IR (4000-400 cm⁻¹): 3400 (b, s), 2834 (w), 1642 (w), 1604 (s), 1592 (s), 1551 (s), 1523 (s), 1473 (s), 1460 (s), 1442 (s), 1413 (s), 1378 (s), 1340 (s), 1317 (m), 1234 (s), 1209 (s), 1180 (m), 1157 (s), 1193 (w), 1079 (m), 1060 (w), 1029 (m), 970 (s), 920 (m), 855 (m), 841 (m), 785 (w), 769 (w), 734 (m), 635 (b, w), 595 (w), 581 (w), 547 (w), 512 (m), 477 (w), 428 (m). **UV-VIS (solid state)**: λ/nm = 207, 239, 348, 429.

Crystal Data for C₁₃₂H₁₄₀N₄₄O₄₈Sm₈ ($M=4313.67$ g/mol): triclinic, space group P-1 (no. 2), $a = 18.1493(2)$ Å, $b = 18.5612(2)$ Å, $c = 28.3525(3)$ Å, $\alpha = 72.8270(10)^\circ$, $\beta = 77.4670(10)^\circ$, $\gamma = 61.3850(10)^\circ$, $V = 7978.17(17)$ Å³, $Z = 2$, $T = 180$ K, $\mu(\text{Mo Ka}) = 2.989$ mm⁻¹, $D_{\text{calc}} = 1.796$ g/cm³, 71829 reflections measured ($4.136^\circ \leq 2\Theta \leq 59.144^\circ$), 40957 unique ($R_{\text{int}} = 0.0311$, $R_{\text{sigma}} = 0.0329$) which were used in all calculations. The final R_1 was 0.0505 ($I > 2\sigma(I)$) and wR_2 was 0.1367 (all data).

[Gd₈(CO₃)₄(H₂O)₈(opch)₈] \cdot 10MeCN \cdot 4H₂O (19-Gd)

Amount of Gd(NO₃)₃ \cdot 6H₂O used = 45.1 mg. **Yield (based on Gd^{III})** = 17.9 mg (38%).

IR (4000-400 cm⁻¹): 3388 (b, s), 3054 (m), 2996 (m), 2924 (m), 2831 (m), 1603 (s), 1591 (s), 1549 (s), 1530 (s), 1520 (s), 1474 (s), 1414 (s), 1389 (s), 1337 (s), 1237 (s), 1209 (s), 1180 (m), 1154 (s), 1104 (m), 1078 (m), 1059 (w), 1027 (m), 968 (w), 919 (m), 857 (m), 844 (m), 784 (w), 769 (w), 730 (m), 641 (w), 523 (w), 481 (w), 429 (w).

Crystal Data for C₁₂₈H₁₃₅Gd₈N₄₂O₄₈ ($M=4287.77$ g/mol): triclinic, space group P-1 (no. 2), $a = 18.0662(6)$ Å, $b = 18.3969(6)$ Å, $c = 28.2356(10)$ Å, $\alpha = 72.485(3)^\circ$, $\beta =$

$77.273(3)^\circ$, $\gamma = 61.037(2)^\circ$, $V = 7798.8(5) \text{ \AA}^3$, $Z = 2$, $T = 180 \text{ K}$, $\mu(\text{Mo K}\alpha) = 3.445 \text{ mm}^{-1}$, $D_{\text{calc}} = 1.826 \text{ g/cm}^3$, 54635 reflections measured ($3.81^\circ \leq 2\Theta \leq 52.044^\circ$), 29573 unique ($R_{\text{int}} = 0.0428$, $R_{\text{sigma}} = 0.0888$) which were used in all calculations. The final R_1 was 0.0438 ($I > 2\sigma(I)$) and wR_2 was 0.0973 (all data).

[Tb₈(CO₃)₄(H₂O)₈(opch)₈]₁ (20-Tb)

Amount of Tb(NO₃)₃·6H₂O used = 45.3 mg. **Yield (based on Tb^{III})** = 15.6 mg (33%).
IR (4000-400 cm⁻¹): 3388 (b, s), 3052 (m), 3000 (m), 2926 (m), 2831 (m), 1603 (s), 1550 (s), 1534 (s), 1521 (s), 1474 (s), 1462 (s), 1445 (s), 1416 (s), 1394 (s), 1339 (s), 1319 (s), 1237 (s), 1211 (s), 1181 (s), 1155 (s), 1105 (m), 1080 (m), 1060 (s), 1027 (s), 971 (m), 920 (m), 858 (m), 844 (m), 785 (w), 769 (w), 731(s), 642 (w), 526 (w), 478 (w), 426 (w).

Crystal Data for C₁₂₂H₁₀₁N₃₉O₄₄Tb₈ ($M = 4088.77 \text{ g/mol}$): monoclinic, space group C2/c (no. 15), $a = 30.6281(17) \text{ \AA}$, $b = 18.2659(4) \text{ \AA}$, $c = 28.4471(12) \text{ \AA}$, $\beta = 116.953(3)^\circ$, $V = 14186.0(11) \text{ \AA}^3$, $Z = 4$, $T = 150 \text{ K}$, $\mu(\text{1.3401270, 1.34 K}\alpha) = 21.363 \text{ mm}^{-1}$, $D_{\text{calc}} = 1.914 \text{ g/cm}^3$, 33714 reflections measured ($5.206^\circ \leq 2\Theta \leq 96.36^\circ$), 9983 unique ($R_{\text{int}} = 0.0571$, $R_{\text{sigma}} = 0.0635$) which were used in all calculations. The final R_1 was 0.0858 ($I > 2\sigma(I)$) and wR_2 was 0.2712 (all data).

[Dy₈(CO₃)₄(H₂O)₈(opch)₈]₁·11MeCN·3H₂O (21-Dy)

Amount of Dy(NO₃)₃·6H₂O used = 45.7 mg. **Yield (based on Dy^{III})** = 16.5 mg (34%).
IR (4000-400 cm⁻¹): 3386 (b, s), 3054 (m), 2998 (m), 2925 (m), 2831 (m), 1602 (s), 1570 (s), 1551 (s), 1535 (s), 1521 (s), 1474 (s), 1446 (s), 1416 (s), 1394 (s), 1338 (s), 1316 (s), 1237 (s), 1211 (s), 1182 (s), 1154 (s), 1106 (m), 1078 (m), 1059 (m), 1027 (m), 972 (m), 920 (m), 858 (m), 844 (m), 785 (w), 770 (w), 731 (m), 641 (w), 527 (w), 481 (w), 426 (w).

Crystal Data for C₁₃₀H₁₃₁Dy₈N₄₄O₄₇ ($M = 4361.78 \text{ g/mol}$): triclinic, space group P-1 (no. 2), $a = 18.0547(5) \text{ \AA}$, $b = 18.4130(5) \text{ \AA}$, $c = 28.1573(11) \text{ \AA}$, $\alpha = 72.716(3)^\circ$, $\beta = 77.295(3)^\circ$, $\gamma = 60.889(2)^\circ$, $V = 7777.0(5) \text{ \AA}^3$, $Z = 2$, $T = 180 \text{ K}$, $\mu(\text{Ga-K}\alpha) = 20.145 \text{ mm}^{-1}$, $D_{\text{calc}} = 1.863 \text{ g/cm}^3$, 86126 reflections measured ($4.894^\circ \leq 2\Theta \leq 125.132^\circ$), 36056 unique ($R_{\text{int}} = 0.0366$, $R_{\text{sigma}} = 0.0404$) which were used in all calculations. The final R_1 was 0.0532 ($I > 2\sigma(I)$) and wR_2 was 0.1484 (all data).

[Ho₈(CO₃)₄(H₂O)₈(opch)₈] (22-Ho)

Amount of Ho(NO₃)₃·5H₂O used = 44.1 mg. **Yield (based on Ho^{III})** = 26.2 mg (54%).

IR (4000-400 cm⁻¹): 3379 (b, m), 3054 (m), 2999 (m), 2962 (m), 2831 (m), 1602 (m), 1570 (m), 1551 (m), 1536 (m), 1521 (m), 1475 (m), 1446 (m), 1427 (m), 1417 (m), 1399 (m), 1339 (m), 1238 (m), 1211 (m), 1181 (m), 1151 (m), 1106 (w), 1078 (w), 1060 (w), 1028 (m), 971 (w), 921 (w), 858 (w), 844 (w), 784 (w), 770 (w), 731 (m), 642 (w), 529 (w), 483 (w), 426 (w). **UV-VIS (solid state)**: λ/nm = 209, 240, 350, 442. **UV-VIS (DMF)**: λ/nm = 341, 427. **C/H/N (calculated) corresponds to addition of 7H₂O**: C: 32.62%, H: 2.89%, N: 11.27%. **C/H/N (found)**: C: 32.26%, H: 2.44%, N: 11.44%.

Crystal Data for C₁₂₂H₁₀₁Ho₈N₃₉O₄₄ ($M=4136.85$ g/mol): monoclinic, space group C2/c (no. 15), $a = 31.4540(8)$ Å, $b = 18.2274(3)$ Å, $c = 28.5809(7)$ Å, $\beta = 117.543(2)$ °, $V = 14529.0(6)$ Å³, $Z = 4$, $T = 273.15$ K, $\mu(\text{MoK}\alpha) = 4.396$ mm⁻¹, $D_{\text{calc}} = 1.891$ g/cm³, 40225 reflections measured (2.67° $\leq 2\Theta \leq 50.706$ °), 13058 unique ($R_{\text{int}} = 0.0413$, $R_{\text{sigma}} = 0.0471$) which were used in all calculations. The final R_1 was 0.0627 ($I > 2\sigma(I)$) and wR_2 was 0.1582 (all data).

[Er₈(CO₃)₄(H₂O)₈(opch)₈]_·3MeCN·H₂O (23-Er)

Amount of Er(NO₃)₃·5H₂O used = 44.3 mg. **Yield (based on Er^{III})** = 6.0 mg (12%).

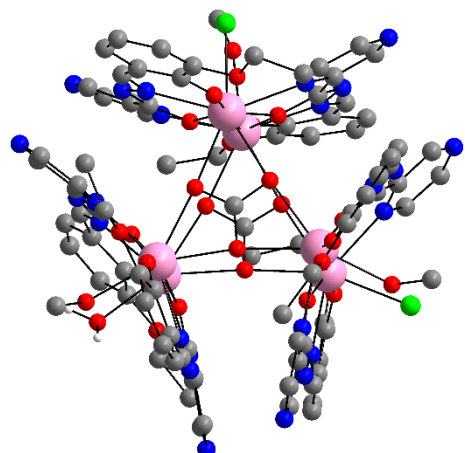
Crystal Data for C₁₂₂H₁₀₁Er₈N₃₉O₄₄ ($M=4155.49$ g/mol): monoclinic, space group C2/c (no. 15), $a = 31.2914(5)$ Å, $b = 18.2141(3)$ Å, $c = 28.4812(6)$ Å, $\beta = 117.6360(10)$ °, $V = 14380.8(5)$ Å³, $Z = 4$, $T = 273.15$ K, $\mu(\text{MoK}\alpha) = 4.708$ mm⁻¹, $D_{\text{calc}} = 1.919$ g/cm³, 44203 reflections measured (2.75° $\leq 2\Theta \leq 54.966$ °), 16123 unique ($R_{\text{int}} = 0.0479$, $R_{\text{sigma}} = 0.0497$) which were used in all calculations. The final R_1 was 0.0714 ($I > 2\sigma(I)$) and wR_2 was 0.2156 (all data).

[Y₈(CO₃)₄(H₂O)₈(opch)₈] (24-Y)

Amount of Y(NO₃)₃·6H₂O used = 38.3 mg. **Yield (based on Y^{III})** = 7.2 mg (18%). **IR (4000-400 cm⁻¹)**: 3381(b, s), 3054 (m), 2999 (m), 2927 (m), 2832 (m), 1602 (s), 1572 (s), 1552 (s), 1537 (s), 1521 (s), 1476 (s), 1463 (s), 1447 (s), 1430 (s), 1418 (s), 1402 (m), 1339 (s), 1319 (s), 1238 (s), 1212 (s), 1182 (s), 1155 (s), 1107 (m), 1079 (m), 1061 (m), 1028 (s), 971 (m), 922 (m), 858 (m), 845 (m), 784 (w), 770 (w), 732 (s), 642 (w), 527 (w), 484 (w), 426 (w).

Crystal Data for $C_{80}H_{80}N_{20}O_{20}Y_4$ ($M=1997.28$ g/mol): monoclinic, space group C2/c (no. 15), $a = 31.6698(16)$ Å, $b = 18.2460(4)$ Å, $c = 31.2023(15)$ Å, $\beta = 126.314(3)^\circ$, $V = 14528.4(12)$ Å³, $Z = 8$, $T = 180$ K, $\mu(\text{Mo K}\alpha) = 3.260$ mm⁻¹, $D_{\text{calc}} = 1.826$ g/cm³, 35474 reflections measured ($4.464^\circ \leq 2\Theta \leq 63.062^\circ$), 19530 unique ($R_{\text{int}} = 0.1179$, $R_{\text{sigma}} = 0.2485$) which were used in all calculations. The final R_1 was 0.1877 ($I > 2\sigma(I)$) and wR_2 was 0.5067 (all data).

[Ln₆(Cl)₂(CO₃)₂(H₂O)(MeOH)₃(oepch)₆]



$H_2\text{oepch}$ (42.9 mg, 0.15 mmol, 1.0 eq.) was dissolved in a mixture of 2.5 ml MeOH and 5 ml DCM before adding Et₃N (55.5 μ l, 0.40 mmol, 2.7 eq.). $\text{LnCl}_3 \cdot 6\text{H}_2\text{O}$ (0.15 mmol, 1.0 eq.) was dissolved separately in a mixture of 2.5 ml MeOH and 5 ml DCM and then added dropwise to the ligand and base solution leading to a rapid colour change towards dark orange. The mixture was stirred overnight at RT, filtered and then left to slowly

evaporate. After three weeks the product was obtained as orange crystals on the side of the vial.

[Tb₆(Cl)₂(CO₃)₂(H₂O)(MeOH)₃(oepch)₆] (25-Tb)

Amount of $\text{TbCl}_3 \cdot 6\text{H}_2\text{O}$ used = 56.0 mg. **Yield (based on Tb^{III})** = very low yield (few crystals).

Confirmed by unit cell determination.

[Dy₆(Cl)₂(CO₃)₂(H₂O)(MeOH)₃(oepch)₆]·2H₂O·10MeOH (26-Dy)

Amount of $\text{DyCl}_3 \cdot 6\text{H}_2\text{O}$ used = 56.5 mg. **Yield (based on Dy^{III})** = very low yield (few crystals).

Crystal Data for $C_{99}H_{130}Cl_2Dy_6N_{24}O_{40}$ ($M=3342.16$ g/mol): triclinic, space group P-1 (no. 2), $a = 14.8753(5)$ Å, $b = 18.6119(6)$ Å, $c = 23.2645(10)$ Å, $\alpha = 103.985(3)^\circ$, $\beta = 92.525(3)^\circ$, $\gamma = 104.587(2)^\circ$, $V = 6010.7(4)$ Å³, $Z = 2$, $T = 180$ K, $\mu(\text{Mo K}\alpha) = 3.818$ mm⁻¹, $D_{\text{calc}} = 1.847$ g/cm³, 53226 reflections measured ($4.148^\circ \leq 2\Theta \leq 56.564^\circ$), 28336

unique ($R_{\text{int}} = 0.0759$, $R_{\text{sigma}} = 0.1022$) which were used in all calculations. The final R_1 was 0.0828 ($\text{I} > 4\text{u}(\text{I})$) and wR_2 was 0.2324 (all data).

[Ho₆(Cl)₂(CO₃)₂(H₂O)(MeOH)₃(oepch)₆]2H₂O_·10MeOH (27-Ho)

Amount of HoCl₃_·6H₂O used = 56.9 mg. **Yield (based on Ho^{III})** = 16.8 mg (20%). **IR (4000-400 cm⁻¹)**: 3321 (b, m), 2980 (m), 1601 (s), 1556 (m), 1502 (m), 1471 (s), 1444 (s), 1418 (m), 1392 (w), 1331 (s), 1237 (m), 1211 (s), 1175 (m), 1153 (m), 1114 (w), 1090 (w) 1082 (w), 1055 (w), 1037 (m), 1021 (m), 991 (m), 930 (w), 899 (m), 881 (m), 855 (m), 835 (w), 787 (w), 739 (m), 704 (w), 638 (w), 588 (w), 542 (m), 490 (w), 474 (w), 426 (w), 408 (w). **UV-VIS (DMF)**: $\lambda/\text{nm} = 337, 419$. **C/H/N (calculated corresponds to 8H₂O lattice solvent**: C: 34.00%, H: 3.27%, N: 10.69%. **C/H/N (found)**: C: 33.03%, H: 2.67%, N: 10.76%.

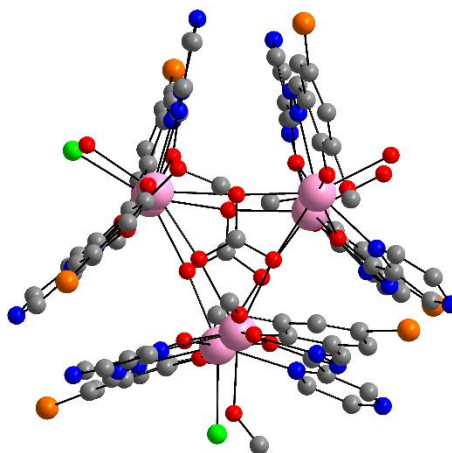
[Er₆(Cl)₂(CO₃)₂(H₂O)(MeOH)₃(oepch)₆]2H₂O_·9MeOH (28-Er)

Amount of ErCl₃_·6H₂O used = 57.3 mg. **Yield (based on Er^{III})** = 21.0 mg (25%).

IR (4000-400 cm⁻¹): 3320 (b, m), 2982 (m), 1602 (s), 1556 (m), 1503 (m), 1470 (s), 1446 (s), 1418 (m), 1392 (w), 1330 (s), 1237 (m), 1212 (s), 1175 (m), 1153 (m), 1114 (w), 1093 (w) 1082 (w), 1055 (w), 1037 (m), 1022 (m), 991 (m), 930 (w), 898 (m), 881 (m), 855 (m), 840 (w), 787 (w), 739 (m), 701 (w), 638 (w), 588 (w), 542 (m), 490 (w), 474 (w), 426 (w), 404 (w).

Crystal Data for C₉₈H₁₂₆Cl₂Er₆N₂₄O₃₉ ($M = 3338.68$ g/mol): triclinic, space group P-1 (no. 2), $a = 14.7811(5)$ Å, $b = 18.5462(5)$ Å, $c = 23.0864(8)$ Å, $\alpha = 104.257(2)^\circ$, $\beta = 92.410(3)^\circ$, $\gamma = 105.124(2)^\circ$, $V = 5883.0(3)$ Å³, $Z = 2$, $T = 180$ K, $\mu(1.3401270, 1.34\text{ K}) = 14.566$ mm⁻¹, $D_{\text{calc}} = 1.885$ g/cm³, 62900 reflections measured ($5.424^\circ \leq 2\Theta \leq 109.758^\circ$), 21808 unique ($R_{\text{int}} = 0.0818$, $R_{\text{sigma}} = 0.1324$) which were used in all calculations. The final R_1 was 0.0426 ($\text{I} > 2\text{s}(\text{I})$) and wR_2 was 0.1008 (all data).

[Er₆(Cl)₂(CO₃)₂(H₂O)₃(MeOH)(opch-Br)₆]·2MeOH (29-Er)



H₂opch-Br (52.5 mg, 0.15 mmol, 1.0 eq.) was dissolved in a mixture of 2.5 ml MeOH and 5 ml DCM before adding Et₃N (55.5 µl, 0.40 mmol, 2.7 eq.). ErCl₃·6H₂O (53.8 mg, 0.15 mmol, 1.0 eq.) was dissolved separately in a mixture of 2.5 ml MeOH and 5 ml DCM and then added dropwise to the ligand and base solution leading to a rapid colour change towards dark orange. The mixture was stirred overnight at RT, filtered and then left to slowly

evaporate. After two weeks the product was obtained as bright orange crystals in a yield of 33.2 mg (39%).

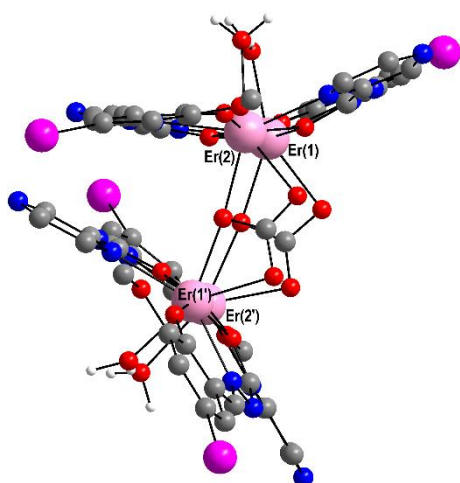
IR (4000-400 cm⁻¹): 3279 (b, m), 2831 (m), 1604 (s), 1554 (m), 1510 (b, w), 1472 (s), 1452 (s), 1443 (s), 1333 (m), 1311 (m), 1232 (s), 1207 (m), 1177 (m), 1154 (m), 1118 (w), 1057 (w), 1035 (s), 1002 (b, w), 977 (s), 923 (m), 860 (w), 839 (w), 792 (m), 767 (m), 742 (m), 694 (m), 640 (w), 617 (w), 579 (w), 548 (m), 486 (w), 463 (w), 429 (m).

UV-VIS (DMF): $\lambda/\text{nm} = 332, 421$. **UV-VIS (solid state):** $\lambda/\text{nm} = 208, 241, 333, 430$.

C/H/N (calculated) corresponds to 12H₂O lattice solvent: C:27.19%, H: 2.11%, N: 9.39%. **C/H/N (found):** C: 27.43%, H: 2.18%, N: 9.07%.

Crystal Data for C₈₃H₆₈Br₆Cl₂Er₆N₂₄O₃₀ ($M=3435.53$ g/mol): tetragonal, space group P-42₁c (no. 114), $a = 30.4283(4)$ Å, $c = 27.2210(4)$ Å, $V = 25203.4(8)$ Å³, $Z = 8$, $T = 293(2)$ K, $\mu(\text{MoK}\alpha) = 5.967$ mm⁻¹, $D_{\text{calc}} = 1.811$ g/cm³, 46293 reflections measured ($5.184^\circ \leq 2\Theta \leq 52.044^\circ$), 23896 unique ($R_{\text{int}} = 0.0351$, $R_{\text{sigma}} = 0.0575$) which were used in all calculations. The final R_1 was 0.0442 ($I > 2\sigma(I)$) and wR_2 was 0.1096 (all data).

[Er₄(CO₃)₂(H₂O)₄(opch-I)₄]₁₀acetone (30-Er)



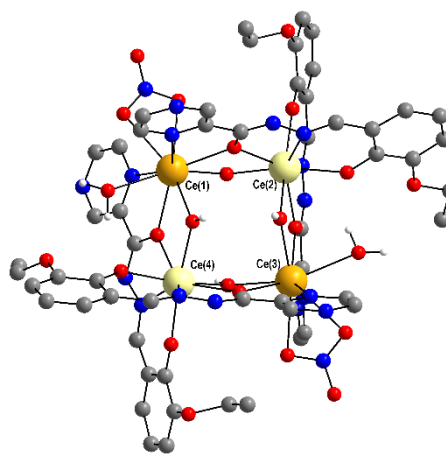
H₂opch-I (39.8 mg, 0.10 mmol, 1.0 eq.) was dissolved in 5 ml of freshly distilled acetone before addition of Et₃N (41.5 μ l, 0.30 mmol, 3.0 eq.). ErCl₃·6H₂O (38.2 mg, 0.10 mmol, 1.0 eq.) was dissolved separately in 5 ml of freshly distilled acetone and added dropwise to the ligand and base solution leading to a rapid colour change to dark orange. The mixture was stirred overnight at RT before filtration and leaving the filtrate undisturbed

for slow evaporation. The product was obtained as orange crystals in a yield of 15.2 mg (20% based on Er^{III}).

IR (4000-400 cm⁻¹): 3368 (b, m), 3050 (w), 2976 (m), 2930 (w), 2827 (w), 1697 (m), 1603 (s), 1549 (s), 1521 (m), 1473 (s), 1453 (s), 1417 (w), 1384 (w), 1336 (s), 1297 (m), 1232 (m), 1215 (s), 1176 (m), 1153 (m), 1119 (w), 1099 (w), 1056 (w), 1034 (m), 1010 (m), 973 (m), 922 (m), 863 (w), 841 (m), 770 (m), 749 (m), 708 (w), 684 (m), 637 (w), 612 (w), 578 (w), 543 (m), 487 (w), 461 (w), 429 (m).

Crystal Data for C₈₄H₁₀₄Er₄I₄N₁₆O₃₂ ($M = 3026.47$ g/mol): orthorhombic, space group Fdd2 (no. 43), $a = 49.8935(11)$ Å, $b = 20.3426(4)$ Å, $c = 20.7397(6)$ Å, $V = 21050.0(9)$ Å³, $Z = 8$, $T = 180$ K, $\mu(1.3401270, 1.34 \text{ K}\alpha) = 17.077 \text{ mm}^{-1}$, $D_{\text{calc}} = 1.910 \text{ g/cm}^3$, 63357 reflections measured ($5.514^\circ \leq 2\Theta \leq 109.76^\circ$), 9853 unique ($R_{\text{int}} = 0.1302$, $R_{\text{sigma}} = 0.1161$) which were used in all calculations. The final R_1 was 0.0438 ($I > 2\sigma(I)$) and wR_2 was 0.0967 (all data).

[Ce^{III}₂Ce^{IV}₂(H₂O)₂(NO₃)₂(oepch)₄(μ_2 -OH)₄]₂MeCN (31-Ce)



H₂oepch (28.6 mg, 0.10 mmol, 1.0 eq.) was dissolved in 5 ml of MeCN before adding mdeaH₂ (34.4 μ l, 0.30 mmol, 3.0 eq.). Ce(NO₃)₃·6H₂O (43.4 mg, 0.10 mmol, 1.0 eq.) was dissolved separately in 5 ml MeCN and then added dropwise to the ligand and base solution leading to a rapid colour change towards dark brown. The dark mixture was stirred overnight at RT, filtered and then left to

slowly evaporate. After two weeks the product was obtained as brown crystals in a yield of 37.3 mg (74% based on Ce^{III/IV}).

IR (4000-400 cm⁻¹): 3326 (b, s), 2985 (m), 1601 (s), 1563 (s), 1522 (w), 1475 (m), 1441 (s), 1416 (s), 1394 (m), 1334 (s), 1285 (s), 1246 (s), 1218 (s), 1180 (m), 1154 (s), 1115 (m), 1081 (m), 1062 (w), 1030 (s), 998 (w), 978 (w), 935 (w), 896 (m), 852 (m), 824 (w), 764 (w), 731 (m), 701 (w), 643 (b, w), 578 (w), 526 (w), 485 (w), 455 (w), 417 (w).

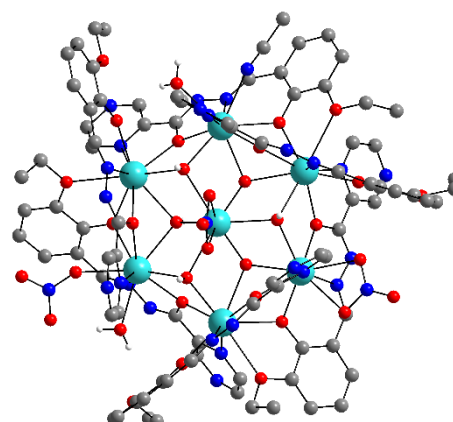
[Ce^{III}₂Ce^{IV}₂(H₂O)₂(NO₃)₂(opch-Br)₄(μ₂-OH)₄] (32-Ce)

H₂opch-Br (35.0 mg, 0.10 mmol, 1.0 eq.) was dissolved in 5 ml of MeCN before adding mdeaH₂ (34.4 µl, 0.30 mmol, 3.0 eq.). Ce(NO₃)₃·6H₂O (43.4 mg, 0.10 mmol, 1.0 eq.) was dissolved separately in 5 ml MeCN and then added dropwise to the ligand and base solution leading to a rapid colour change towards dark brown. The dark mixture was stirred overnight at RT, filtered and then left to slowly evaporate. After two weeks the product was obtained as brown crystals in a yield of 7.1 mg (13% based on Ce^{III/IV}).

[Ce^{III}₂Ce^{IV}₂(H₂O)₂(NO₃)₂(opch-Br)₄(μ₂-OH)₄] (33-Ce)

H₂opch-I (39.8 mg, 0.10 mmol, 1.0 eq.) was dissolved in 5 ml of MeCN before adding mdeaH₂ (34.4 µl, 0.30 mmol, 3.0 eq.). Ce(NO₃)₃·6H₂O (43.4 mg, 0.10 mmol, 1.0 eq.) was dissolved separately in 5 ml MeCN and then added dropwise to the ligand and base solution leading to a rapid colour change towards dark brown. The dark mixture was stirred overnight at RT, filtered and then left to slowly evaporate. After two weeks the product was obtained as brown crystals in a yield of 5.3 mg (8.9% based on Ce^{III/IV}).

[Nd₇(H₂O)₂(MeCN)(NO₃)₃(oepch)₆(μ₃-OH)₆]·6MeCN (34-Nd)



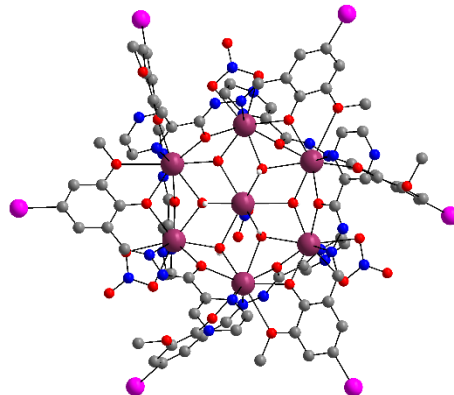
H₂oepch (28.6 mg, 0.10 mmol, 1.0 eq.) was dissolved in 5 ml of MeCN before adding Et₃N (30.6 µl, 0.27 mmol, 2.7 eq.). Nd(NO₃)₃·6H₂O (43.8 mg, 0.10 mmol, 1.0 eq.) was dissolved separately in 5 ml MeCN and then added dropwise to the ligand and base solution leading to a rapid colour change towards dark orange. The mixture was stirred overnight at RT, filtered and then left to

slowly evaporate. After four weeks the product was obtained as orange crystals in a yield of 33.9 mg (77% based on Nd^{III}).

IR (4000-400 cm⁻¹): 3611 (w), 3377 (b, s), 2979 (m), 2933 (w), 1604 (s), 1557 (m), 1537 (m), 1519 (m), 1474 (m), 1448 (s), 1412 (m), 1336 (s), 1287 (m), 1237 (w), 1214 (s), 1178 (m), 1154 (m), 1090 (m), 1069 (m), 1027 (m), 991 (w), 926 (w), 882 (m), 851 (w), 789 (w), 769 (w), 733 (m), 644 (w), 515 (w), 484 (w), 463 (w), 422 (b, w). **UV-VIS (solid state):** λ/nm = 363 (very broad), 581, 628, 679, 741, 800, 870.

Crystal Data for $\text{C}_{98}\text{H}_{103}\text{N}_{34}\text{Nd}_7\text{O}_{35}$ ($M=3326.82$ g/mol): monoclinic, space group $\text{P}2_1/\text{n}$ (no. 14), $a = 18.3632(3)$ Å, $b = 22.6238(4)$ Å, $c = 29.8565(5)$ Å, $\beta = 103.6820(10)^\circ$, $V = 12051.8(4)$ Å³, $Z = 4$, $T = 180$ K, $\mu(\text{Mo K}\alpha) = 3.050$ mm⁻¹, $D_{\text{calc}} = 1.834$ g/cm³, 69949 reflections measured ($7.312^\circ \leq 2\Theta \leq 61.996^\circ$), 37252 unique ($R_{\text{int}} = 0.0261$, $R_{\text{sigma}} = 0.0286$) which were used in all calculations. The final R_1 was 0.0409 ($I > 2\sigma(I)$) and wR_2 was 0.1065 (all data).

[Gd₇(acetone)(NO₃)₃(μ₃-OH)₆(opch-I)₆]



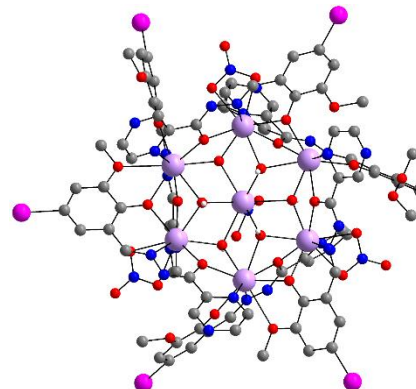
$\text{H}_2\text{opch-I}$ (39.8 mg, 0.10 mmol, 1.0 eq.) was dissolved in 5 ml acetone before adding Et_3N (41.5 μl , 0.30 mmol, 3.0 eq.). $\text{Gd}(\text{NO}_3)_3 \cdot 6\text{H}_2\text{O}$ (45.1 mg, 0.10 mmol, 1.0 eq.) was suspended separately in of 5 ml. The ligand and base solution was then added dropwise to the metal salt suspension. The mixture was stirred for 4 h at RT, filtered and then left to slowly evaporate. After 10 d

the product was obtained as orange crystals in a very low yield (few crystals) in both cases.

Crystal Data for $\text{C}_{99}\text{H}_{103}\text{Gd}_7\text{I}_6\text{N}_{28}\text{O}_{43}$ ($M=4235.24$ g/mol) (**35-Gd A**): triclinic, space group $\text{P}-1$ (no. 2), $a = 15.7505(5)$ Å, $b = 18.7129(7)$ Å, $c = 24.9310(7)$ Å, $\alpha = 108.546(3)^\circ$, $\beta = 98.831(2)^\circ$, $\gamma = 92.782(3)^\circ$, $V = 6846.6(4)$ Å³, $Z = 2$, $T = 150$ K, $\mu(1.3401270, 1.34 \text{ K}\alpha) = 25.231$ mm⁻¹, $D_{\text{calc}} = 2.054$ g/cm³, 63552 reflections measured ($6.44^\circ \leq 2\Theta \leq 100.876^\circ$), 21300 unique ($R_{\text{int}} = 0.0857$, $R_{\text{sigma}} = 0.0801$) which were used in all calculations. The final R_1 was 0.0682 ($I > 2\sigma(I)$) and wR_2 was 0.2013 (all data).

Crystal Data for $C_{114}H_{133}Gd_7I_6N_{28}O_{48}$ ($M=4525.63$ g/mol) (**35-Gd B**): triclinic, space group P-1 (no. 2), $a = 15.7498(4)$ Å, $b = 20.1100(5)$ Å, $c = 24.5300(7)$ Å, $\alpha = 92.311(2)^\circ$, $\beta = 98.748(2)^\circ$, $\gamma = 92.601(2)^\circ$, $V = 7662.3(4)$ Å³, $Z = 2$, $T = 180$ K, $\mu(1.3401270, 1.34$ K $\alpha) = 22.593$ mm $^{-1}$, $D_{\text{calc}} = 1.962$ g/cm 3 , 100697 reflections measured ($5.45^\circ \leq 2\Theta \leq 107.82^\circ$), 27608 unique ($R_{\text{int}} = 0.1186$, $R_{\text{sigma}} = 0.1359$) which were used in all calculations. The final R_1 was 0.0638 ($I > 2\sigma(I)$) and wR_2 was 0.1558 (all data).

[Dy₇(acetone)(NO₃)₃(μ₃-OH)₆(opch-I)₆]·3acetone (36-Dy)

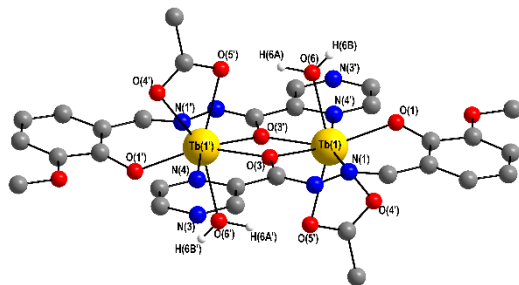


$H_2opch-I$ (39.8 mg, 0.10 mmol, 1.0 eq.) was dissolved in 5 ml acetone before adding Et_3N (41.5 μ l, 0.30 mmol, 3.0 eq.). $Gd(NO_3)_3 \cdot 6H_2O$ (45.1 mg, 0.10 mmol, 1.0 eq.) was suspended separately in of 5 ml. The ligand and base solution was then added dropwise to the metal salt suspension. The mixture was stirred for 3 h at RT, filtered and then left to slowly evaporate. After 2 weeks the product was obtained as orange crystals in a yield of 30.4 mg (31% based on Dy^{III}).

IR (4000-400 cm $^{-1}$): 3398 (b, m), 3042 (m), 2985 (m), 2939 (w), 2829 (w), 2704 (w), 1601 (s), 1556 (m), 1519 (w), 1455 (s), 1421 (w), 1343 (s), 1291 (s), 1281 (s), 1232 (m), 1211 (s), 1175 (m), 1155 (m), 1118 (w), 1094 (w), 1059 (w), 1029 (m), 976 (w), 926 (m), 845 (w), 815 (w), 770 (m), 750 (m), 705 (w), 687 (m), 620 (w), 580 (w), 537 (m), 488 (w), 430 (m).

Crystal Data for $C_{114}H_{133}Dy_7I_6N_{28}O_{48}$ ($M=4562.38$ g/mol): triclinic, space group P-1 (no. 2), $a = 15.6369(11)$ Å, $b = 20.0265(14)$ Å, $c = 24.3457(16)$ Å, $\alpha = 92.517(6)^\circ$, $\beta = 98.153(5)^\circ$, $\gamma = 92.766(6)^\circ$, $V = 7528.1(9)$ Å³, $Z = 2$, $T = 180.00$ K, $\mu(MoK\alpha) = 4.747$ mm $^{-1}$, $D_{\text{calc}} = 2.013$ g/cm 3 , 51253 reflections measured ($2.92^\circ \leq 2\Theta \leq 53.466^\circ$), 29808 unique ($R_{\text{int}} = 0.0642$, $R_{\text{sigma}} = 0.0779$) which were used in all calculations. The final R_1 was 0.0506 ($I > 2\sigma(I)$) and wR_2 was 0.1328 (all data).

[Tb₂(H₂O)₂(OAc)₂(opch)₂] (37-Tb)

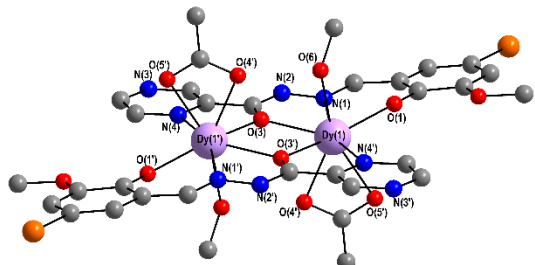


H₂opch (27.2 mg, 0.10 mmol, 1.0 eq.) was dissolved in 5 ml of MeCN before adding mdeaH₂ (34.4 μ l, 0.30 mmol, 3.0 eq). Tb(OAc)₃ (33.6 mg, 0.10 mmol, 1.0 eq.) was dissolved separately in 5 ml of MeCN and then

added dropwise to the ligand and base solution. The yellow solution was stirred overnight at RT, filtered and then left to slowly evaporate. After 2 weeks orange crystals were obtained in a very low yield (few crystals).

Crystal Data for C₃₀H₃₄N₈O₁₄Tb₂ ($M=1048.49$ g/mol): monoclinic, space group P2₁/n (no. 14), $a = 8.8236(3)$ \AA , $b = 15.2808(4)$ \AA , $c = 13.4820(6)$ \AA , $\beta = 104.464(2)^\circ$, $V = 1760.18(11)$ \AA^3 , $Z = 2$, $T = 180$ K, $\mu(\text{MoK}\alpha) = 4.065$ mm⁻¹, $D_{\text{calc}} = 1.978$ g/cm³, 9613 reflections measured ($5.332^\circ \leq 2\Theta \leq 59.148^\circ$), 4597 unique ($R_{\text{int}} = 0.0657$, $R_{\text{sigma}} = 0.0579$) which were used in all calculations. The final R_1 was 0.0572 ($I > 2\sigma(I)$) and wR_2 was 0.1457 (all data).

[Dy₂(MeOH)₂(OAc)₂(opch-Br)₂] (38-Dy)

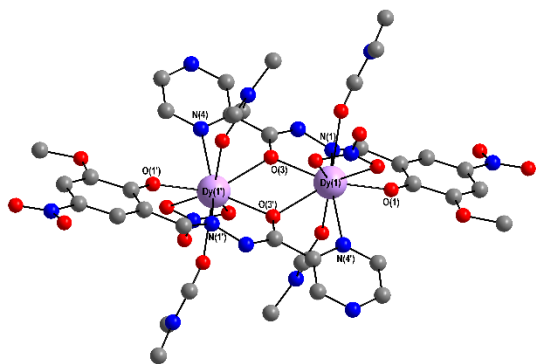


H₂opch-Br (52.5 mg, 0.15 mmol, 1.5 eq.) was dissolved in a mixture of 2.5 ml MeOH and 5 ml DCM before adding Et₃N (41.6 μ l, 0.30 mmol, 3.0 eq.). Dy(OAc)₃·6H₂O (45.1 mg, 0.10 mmol, 1.0 eq.) was dissolved separately in a mixture

of 2.5 ml MeOH and 5 ml DCM and then added dropwise to the ligand and base solution. The mixture was stirred overnight at RT, filtered and then left to slowly evaporate. After 6 d the product was obtained as bright yellow needles on the side of the glass vial in a yield of 33.2 mg (39% based on Dy^{III}).

Crystal Data for C₃₂H₃₂Br₂Dy₂N₈O₁₂ ($M=1205.47$ g/mol): monoclinic, space group P2₁/n (no. 14), $a = 13.7340(9)$ \AA , $b = 8.6025(3)$ \AA , $c = 17.1665(10)$ \AA , $\beta = 100.961(5)^\circ$, $V = 1991.17(19)$ \AA^3 , $Z = 2$, $T = 180$ K, $\mu(\text{Mo K}\alpha) = 5.799$ mm⁻¹, $D_{\text{calc}} = 2.011$ g/cm³, 10603 reflections measured ($4.834^\circ \leq 2\Theta \leq 59.15^\circ$), 5488 unique ($R_{\text{int}} = 0.0382$, $R_{\text{sigma}} = 0.0648$) which were used in all calculations. The final R_1 was 0.0378 ($I > 2\sigma(I)$) and wR_2 was 0.0822 (all data).

[Dy₂(DMF)₄(NO₃)₂(opch-NO₂)₂] (39-Dy)



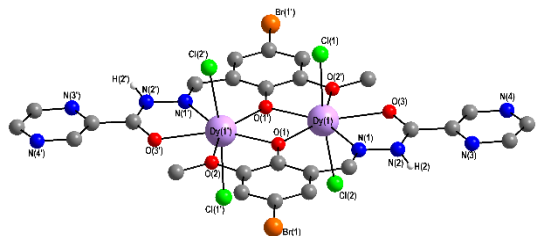
H₂opch-NO₂ (35.0 mg, 0.110 mmol, 1.00 eq.) was dissolved in 8 ml MeCN and mdeaH₂ (33.7 μ l, 0.294 mmol, 2.67 eq.) added. Dy(NO₃)₃·6H₂O (50.2 mg, 0.110 mmol, 1.00 eq.) was dissolved separately in 5 ml DMF and subsequently added dropwise to the ligand and base solution. The mixture was

stirred at RT overnight before filtration and putting the vial aside for slow evaporation. After 4 weeks the product was obtained as bright yellow crystals in a yield of 41.9 mg (55% based on Dy^{III}).

IR (4000-400 cm⁻¹): 3080 (w), 2949 (w), 2904 (w), 2831 (w), 1718 (w), 1657 (s), 1609 (s), 1600 (s), 1570 (w), 1550 (w), 1495 (s), 1474 (s), 1455 (s), 1380 (m), 1314 (s), 1280 (s), 1252 (s), 1216 (m), 1168 (m), 1151 (m), 1106 (m), 1053 (w), 1034 (m), 1008 (w), 938 (m), 918 (m), 899 (w), 862 (w), 842 (w), 816 (w), 780 (m), 745 (m), 709 (m), 688 (m), 639 (w), 552 (m), 489 (w), 479 (w), 432 (m), 415 (m).

Crystal Data for C₃₈H₄₆Dy₂N₁₆O₂₀ ($M=1371.91$ g/mol): triclinic, space group P-1 (no. 2), $a = 9.7649(3)$ Å, $b = 10.7782(4)$ Å, $c = 12.7771(4)$ Å, $\alpha = 106.587(3)^\circ$, $\beta = 100.331(3)^\circ$, $\gamma = 99.037(3)^\circ$, $V = 1236.59(8)$ Å³, $Z = 1$, $T = 180.0$ K, $\mu(\text{GaK}\alpha) = 16.264$ mm⁻¹, $D_{\text{calc}} = 1.842$ g/cm³, 14034 reflections measured ($6.464^\circ \leq 2\Theta \leq 127.892^\circ$), 5930 unique ($R_{\text{int}} = 0.0229$, $R_{\text{sigma}} = 0.0173$) which were used in all calculations. The final R_1 was 0.0284 ($I > 2\sigma(I)$) and wR_2 was 0.0746 (all data).

[Dy₂(Cl)₄(Hopch-Br)₂]_{0.5}CCl₄ (40-Dy)

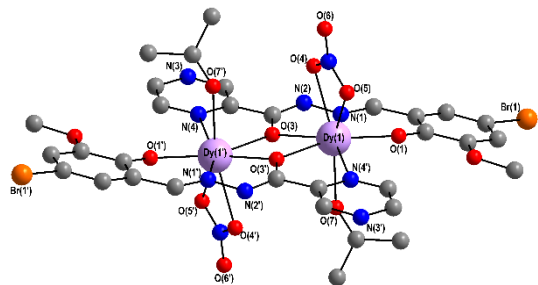


A glass autoclave was loaded with H₂opch-Br (52.5 mg, 0.15 mmol, 1.0 eq.) and DyCl₃·6H₂O (56.5 mg, 0.15 mmol, 1.0 eq.) before the addition of 7 ml CCl₄, 3 ml and MeOH as well as Et₃N (104 μ l, 0.750 mmol, 5.00 eq.). The

autoclave was placed in an oven at 90°C for 1 d (8 ml of solvent evaporated during that time as the autoclave did not seal tightly), subsequently the autoclave was taken out of the oven and left to cool down to RT. The product was obtained as orange cubes in a yield of 15.1 mg (15% based on Dy^{III}).

Crystal Data for $C_{27}H_{20}Br_2Cl_8Dy_2N_8O_6$ ($M=1320.93$ g/mol): tetragonal, space group $P4/n$ (no. 85), $a = 20.9056(4)$ Å, $c = 9.1595(2)$ Å, $V = 4003.11(18)$ Å 3 , $Z = 4$, $T = 180$ K, $\mu(1.3401270, 1.34$ K $\alpha) = 24.286$ mm $^{-1}$, $D_{\text{calc}} = 2.192$ g/cm 3 , 12934 reflections measured ($8.398^\circ \leq 2\Theta \leq 128.31^\circ$), 4746 unique ($R_{\text{int}} = 0.0340$, $R_{\text{sigma}} = 0.0311$) which were used in all calculations. The final R_1 was 0.0490 ($I > 2\sigma(I)$) and wR_2 was 0.1485 (all data).

[Dy₂(acetone)₂(NO₃)₂(opch-Br)₂] (41-Dy)



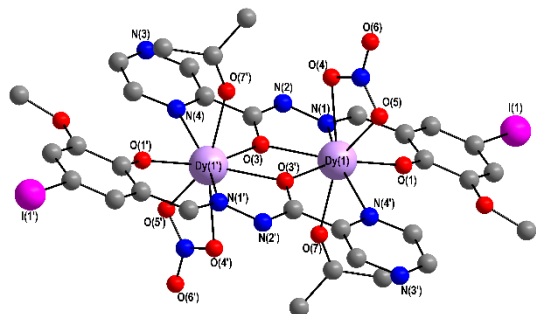
$H_2\text{opch-Br}$ (50.0 mg, 0.143 mmol, 1.0 eq.) was dissolved in 5 ml acetone before adding Et_3N (59.5 μ l, 0.492 mmol, 3.0 eq.). $\text{Dy}(\text{NO}_3)_3 \cdot 6\text{H}_2\text{O}$ (53.9 mg, 0.143 mmol, 1.0 eq.) was suspended separately in 5 ml. The ligand and base solution was then added dropwise to

the metal salt suspension. The mixture was stirred overnight at RT, filtered and then left to slowly evaporate. After 2 weeks the product was obtained as yellow crystals in a yield of 67.8 mg (72% based on Dy^{III}).

IR (4000-400 cm $^{-1}$): 3620 (w), 3015 (m), 2964 (m), 2930 (m), 2833 (w), 2575 (w), 2523 (w), 1673 (s), 1605 (s), 1561 (m), 1535 (w), 1495 (m), 1478 (s), 1452 (s), 1420 (s), 1374 (m), 1355 (m), 1335 (s), 1317 (m), 1275 (s), 1235 (s), 1212 (s), 1187 (w), 1172 (m), 1153 (s), 1116 (m), 1097 (m), 1056 (m), 1038 (s), 1027 (s), 1009 (m), 991 (w), 977 (m), 923 (m), 865 (m), 840 (m), 816 (w), 795 (m), 771 (m), 744 (m), 709 (w), 696 (m), 638 (w), 615 (w), 582 (m), 538 (m), 482 (m), 463 (w), 431 (m), 417 (w).

Crystal Data for $C_{32}H_{30}Br_2Dy_2N_{10}O_{14}$ ($M=1263.48$ g/mol): monoclinic, space group $P2_1/c$ (no. 14), $a = 8.4229(5)$ Å, $b = 9.1407(4)$ Å, $c = 26.4480(14)$ Å, $\beta = 92.073(5)^\circ$, $V = 2034.93(18)$ Å 3 , $Z = 2$, $T = 180.00$ K, $\mu(\text{MoK}\alpha) = 5.684$ mm $^{-1}$, $D_{\text{calc}} = 2.062$ g/cm 3 , 11484 reflections measured ($4.716^\circ \leq 2\Theta \leq 66.69^\circ$), 6754 unique ($R_{\text{int}} = 0.0925$, $R_{\text{sigma}} = 0.0815$) which were used in all calculations. The final R_1 was 0.1356 ($I > 2\sigma(I)$) and wR_2 was 0.3633 (all data).

[Dy₂(acetone)₂(NO₃)₂(opch-I)₂] (42-Dy)

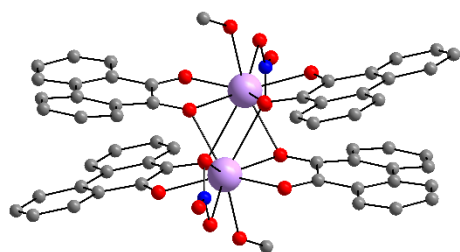


H₂opch-I (39.8 mg, 0.10 mmol, 1.0 eq.) was dissolved in 5 ml acetone before adding Et₃N (41.5 µl, 0.30 mmol, 3.0 eq.). Dy(NO₃)₃·6H₂O (45.7 mg, 0.10 mmol, 1.0 eq.) was suspended separately in 5 ml. The ligand and base solution was then added dropwise to the metal salt suspension. The mixture was stirred overnight at RT, filtered and then left to slowly evaporate. After 2 weeks the product was obtained as yellow crystals in a very low yield (few crystals).

Crystal Data for C₃₂H₃₀Dy₂I₂N₁₀O₁₄ ($M=1357.46$ g/mol): monoclinic, space group P2₁/c (no. 14), $a = 8.2803(4)$ Å, $b = 28.0217(10)$ Å, $c = 9.1873(4)$ Å, $\beta = 95.062(4)$ °, $V = 2123.40(16)$ Å³, $Z = 2$, $T = 150$ K, $\mu(1.3401270, 1.34 \text{ K}\alpha) = 26.339$ mm⁻¹, $D_{\text{calc}} = 2.123$ g/cm³, 13465 reflections measured ($8.844^\circ \leq 2\Theta \leq 128.198^\circ$), 5105 unique ($R_{\text{int}} = 0.0308$, $R_{\text{sigma}} = 0.0295$) which were used in all calculations. The final R_1 was 0.0408 ($I > 2\sigma(I)$) and wR_2 was 0.1202 (all data).

8.3 Lanthanide-Radical Dimers

[Ln₂(phsq)₄(NO₃)₂(MeOH)₂]·2MeOH (Ln = Y^{III}, Nd^{III}, Sm^{III}, Eu^{III}, Gd^{III}, Tb^{III}, Dy^{III}, Ho^{III}, Er^{III}, Tm^{III}, Yb^{III}, Lu^{III})^[31-33]



These compounds have been described in the doctoral theses of two former members of the Powell group as well as in my own Master thesis in which I optimised the reaction to give the procedure below.

All compounds have been reproduced during the work on this thesis for further study of the complexes in solution (see section 6.2.2) as well as for a collaboration on solid and solution state EPR with Dr. Violeta Voronkova in Kazan which was suspended due to the political situation concerning Russia and Ukraine.

A Teflon insert was loaded with 9,10-phenanthrenequinone (100.0 mg, 0.48 mmol, 1.0 eq.), Ln(NO₃)₃·xH₂O (0.50 mmol, 1.04 eq.) and 10 ml MeOH. The vessel was

closed with a lid and put into a steel autoclave that was sealed tightly and put into an oven at 90°C for 5 d. Subsequently, the autoclave was removed from the oven and allowed to cool down to RT on the bench before opening it. The contents of the Teflon vessel were filtered and washed with cold MeOH. The resulting dark crystals were dried in air.

[Nd₂(MeOH)₂(NO₃)₂(phsq)₄]_·2MeOH (43-Nd)

Amount of Nd(NO₃)₃_·6H₂O used = 219.2 mg. **Yield** = 108.2 mg (66% based on Nd^{III}).

IR (4000-400 cm⁻¹): 3462 (b, w), 3173 (b, w), 3062 (w), 2970 (w), 2943 (w), 2836 (w), 2108 (b, w), 1600 (w), 1580 (w), 1562 (m), 1517 (m), 1476 (m), 1453 (s), 1463 (w), 1348 (s), 1302 (s), 1272 (s), 1221 (m), 1162 (w), 1121(m), 1102 (m), 1075 (m), 1037 (m), 1002 (m), 932 (m), 869 (w), 813 (w), 788 (m), 757 (s), 737 (m), 718 (s), 682 (m), 665 (m), 630 (m), 575 (m), 550 (w), 495 (s), 470 (w), 433 (w).

[Sm₂(MeOH)₂(NO₃)₂(phsq)₄]_·2MeOH (44-Sm)

Amount of Sm(NO₃)₃_·6H₂O used = 222.2 mg. **Yield** = 78.7 mg (47%). **IR (4000-400 cm⁻¹)**: 3655 (w), 3490 (b, w), 3176 (b, w), 1066 (w), 2955 (w), 2823 (w), 2106 (b, w), 1601 (w), 1562 (m), 1519 (m), 1474 (s), 1456 (s), 1350 (s), 1307 (s), 1271 (s), 1218 (s), 1162 (w), 1123 (m), 1104 (m), 1077 (m), 1032 (m), 1004 (s), 954 (w), 932 (m), 867 (w), 812 (w), 786 (m), 757 (s), 718 (s), 683 (s), 667 (m), 630 (m), 578 (s), 552 (w), 500 (s), 440 (m).

[Eu₂(MeOH)₂(NO₃)₂(phsq)₄]_·2MeOH (45-Eu)

Amount of Eu(NO₃)₃_·6H₂O used = 223.0 mg. **Yield** = 51.9 mg (31%). **IR (4000-400 cm⁻¹)**: 3493 (b, w), 3163 (b, w), 3062 (w), 2969 (w), 2834 (w), 2103 (b, w), 1600 (w), 1580 (w), 1562 (m), 1517 (m), 1476 (s), 1455 (s), 1437 (w), 1350 (s), 1305 (s), 1271 (s), 1221 (s), 1162 (w), 1121 (m), 1099 (m), 1073 (m), 1036 (w), 1006 (m), 932 (m), 868 (w), 809 (w), 786 (w), 757 (s), 741 (w), 718 (s), 681 (m), 667 (m), 630 (m), 575 (s), 552 (w), 499 (s), 472 (w), 437 (w).

[Gd₂(MeOH)₂(NO₃)₂(phsq)₄]_·2MeOH (46-Gd)

Amount of Gd(NO₃)₃_·6H₂O used = 225.7 mg. **Yield** = 63.0 mg (38%). **IR (4000-400 cm⁻¹)**: 3491 (b, w), 3167 (b, w), 3060 (w), 2950 (w), 2831 (w), 2110 (b, w), 1601 (w), 1580 (w), 1562 (m), 1515 (m), 1476 (s), 1453 (s), 1436 (w), 1428 (w), 1348 (s), 1303

(s), 1270 (s), 1221 (s), 1163 (w), 1122 (m), 1102 (m), 1075 (m), 1038 (w), 1026 (w), 1006 (m), 934 (m), 870 (w), 809 (w), 788 (m), 753 (s), 717 (s), 694 (w), 683 (m), 667 (m), 630 (m), 579 (s), 554 (w), 499 (s), 475 (w), 438 (m).

[Tb₂(MeOH)₂(NO₃)₂(phsq)₄]₂MeOH (47-Tb)

Amount of Tb(NO₃)₃·6H₂O used = 226.5 mg. **Yield** = 67.1 mg (40%). **IR (4000-400 cm⁻¹)**: 3647 (b, w), 3491 (b, w), 3162 (b, w), 3060 (w), 2961 (w), 2836 (w), 2118 (b, w), 1600 (w), 1564 (m), 1519 (m), 1475 (s), 1221 (s), 1164 (w), 1121 (m), 1101 (m), 1073 (m), 1036 (w), 1026 (w), 1006 (m), 956 (m), 934 (m), 868 (w), 811 (w), 788 (m), 753 (s), 716 (s), 686 (m), 669 (m), 632 (m), 579 (s), 552 (w), 499 (s), 476 (w), 439 (m).

[Dy₂(MeOH)₂(NO₃)₂(phsq)₄]₂MeOH (48-Dy)

Amount of Dy(NO₃)₃·6H₂O used = 228.3 mg. **Yield** = 99.1 mg (59%). **IR (4000-400 cm⁻¹)**: 3653 (w), 3491 (b, w), 3173 (b, w), 1066 (w), 2955 (w), 2823 (w), 2106 (b, w), 1600 (w), 1562 (m), 1519 (m), 1474 (s), 1456 (s), 1350 (s), 1307 (s), 1270 (s), 1218 (s), 1162 (w), 1123 (m), 1102 (m), 1077 (m), 1032 (m), 1007 (s), 954 (w), 932 (m), 867 (w), 811 (w), 786 (m), 757 (s), 718 (s), 683 (s), 667 (m), 630 (m), 578 (s), 552 (w), 501 (s), 439 (m).

[Ho₂(MeOH)₂(NO₃)₂(phsq)₄]₂MeOH (49-Ho)

Amount of Ho(NO₃)₃·5H₂O used = 220.5 mg. **Yield** = 146.8 mg (87%). **IR (4000-400 cm⁻¹)**: 3650 (w), 3486 (b, w), 3171 (b, w), 3076 (w), 2957 (w), 2836 (w), 2106 (b, w), 1602 (w), 1564 (m), 1517 (m), 1476 (s), 1453 (s), 1416 (w), 1348 (s), 1307 (s), 1272 (s), 1221 (m), 1162 (w), 1121 (m), 1104 (m), 1073 (m), 1036 (m), 1010 (m), 956 (w), 934 (m), 870 (w), 811 (w), 786 (w), 769 (w), 755 (s), 717 (s), 683 (m), 669 (m), 631 (w), 579 (m), 551 (m), 503 (s), 443 (m).

[Er₂(MeOH)₂(NO₃)₂(phsq)₄]₂MeOH (50-Er)

Amount of Er(NO₃)₃·5H₂O used = 221.7 mg. **Yield** = 46.5 mg (27%). **IR (4000-400 cm⁻¹)**: 3624 (w), 3466 (b, w), 3068 (w), 2113 (b, w), 1602 (w), 1564 (m), 1519 (m), 1478 (s), 1453 (s), 1349 (s), 1303 (s), 1272 (s), 1219 (s), 1159 (w), 1121 (m), 1104 (m), 1073 (m), 1034 (m), 958 (w), 934 (m), 869 (w), 808 (w), 787 (w), 756 (s), 718 (s), 683 (m), 669 (m), 632 (w), 578 (m), 549 (w), 499 (s), 441 (m).

[Tm₂(MeOH)₂(NO₃)₂(phsq)₄]₂MeOH (51-Tm)

Amount of Tm(NO₃)₃·6H₂O used = 231.5 mg. **Yield** = 101.1 mg (59%). **IR (4000-400 cm⁻¹)**: 3632 (w), 3473 (b, w), 3171 (b, w), 1068 (w), 2962 (w), 2108 (b, w), 1676 (w), 1597 (w), 1562 (m), 1520 (m), 1476 (s), 1453 (s), 1353 (s), 1307 (s), 1274 (s), 1220 (m), 1160 (w), 1122 (m), 1104 (m), 1075 (m), 1036 (m), 1009 (m), 956 (w), 936 (m), 669 (m), 632 (w), 581 (m), 552 (w), 534 (w), 502 (s), 460 (w), 442 (m).

[Yb₂(MeOH)₂(NO₃)₂(phsq)₄]₂MeOH (52-Yb)

Amount of Yb(NO₃)₃·6H₂O used = 233.6 mg. **Yield** = 56.4 mg (33%). **IR (4000-400 cm⁻¹)**: 3649 (w), 3466 (b, w), 3074 (w), 2955 (w), 2834 (w), 2106 (b, w), 1601 (w), 1560 (m), 1521 (m), 1478 (s), 1452 (s), 1349 (s), 1316 (s), 1272 (s), 1221 (s), 1163 (w), 1121 (m), 1102 (m), 1075 (m), 1038 (m), 1008 (s), 956 (w), 934 (m), 870 (w), 809 (w), 786 (w), 768 (w), 754 (s), 719 (s), 683 (m), 671 (w), 632 (w), 579 (m), 552 (w), 505 (s), 441 (m).

[Lu₂(MeOH)₂(NO₃)₂(phsq)₄]₂MeOH (53-Lu)

Amount of Lu(NO₃)₃·6H₂O used = 234.5 mg. **Yield** = 73.8 mg (43%). **IR (4000-400 cm⁻¹)**: 3649 (w), 3464 (b, w), 3074 (w), 2957 (w), 2836 (w), 2112 (b, w), 1603 (w), 1563 (m), 1523 (m), 1478 (s), 1455 (s), 1349 (s), 1329 (s), 1272 (s), 1219 (s), 1164 (w), 1122 (m), 1102 (m), 1075 (m), 1038 (m), 1010 (s), 952 (w), 934 (m), 871 (w), 811 (w), 788 (m), 753 (s), 718 (s), 683 (m), 667 (m), 632 (m), 579 (s), 554 (w), 503 (s), 462 (w), 443 (m), 401 (m).

[Y₂(MeOH)₂(NO₃)₂(phsq)₄]₂MeOH (54-Y)

Amount of Y(NO₃)₃·6H₂O used = 191.5 mg. **Yield** = 57.3 mg (38%). **IR (4000-400 cm⁻¹)**: 3650 (w), 3487 (b, w), 3166 (b, w), 3069 (w), 2953 (w), 2838 (w), 2107 (b, w), 1602 (w), 1564 (m), 1519 (m), 1476 (s), 1453 (s), 1350 (s), 1309 (s), 1274 (s), 1220 (s), 1164 (w), 1122 (m), 1102 (m), 1075 (m), 1033 (m), 1007 (s), 957 (w), 934 (m), 896 (w), 811 (w), 787 (m), 753 (s), 718 (m), 682 (m), 669 (m), 630 (w), 579 (m), 552 (w), 503 (s), 439 (m).

[DyLu(MeOH)₂(NO₃)₂(phsq)₄]₂MeOH (doped compound 10:90) (55-DyLu)

To produce the doped compound Lu(NO₃)₃·6H₂O (405.3 mg, 0.864 mmol, 1.8 eq.) and Dy(NO₃)₃·6H₂O (43.8 mg, 0.096 mmol, 0.2 eq.) were loaded into a Teflon vessel

together with 9,10-phenanthrenequinone (100.0 mg, 0.480 mmol, 1.0 eq.) and 10 ml MeOH. The vessel was closed and put into a steel autoclave that was sealed tightly and put into a 90°C oven for 2 weeks. The autoclave was cooled down to RT slowly by turning off the oven but leaving the oven door shut. After 24 h the autoclave was removed from the oven, opened and the contents were filtered. The product was obtained as dark crystals in a yield of 48.3 mg.

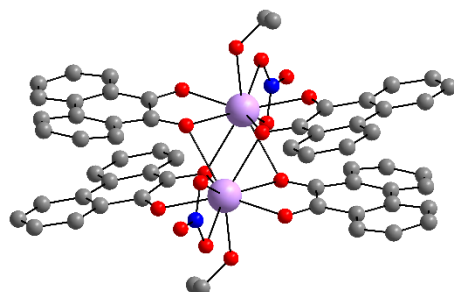
IR (4000-400 cm⁻¹): 3624 (w), 3466 (b, w), 3068 (w), 2113 (b, w), 1602 (w), 1564 (m), 1519 (m), 1478 (s), 1453 (s), 1349 (s), 1303 (s), 1272 (s), 1219 (s), 1159 (w), 1121 (m), 1104 (m), 1073 (m), 1034 (m), 958 (w), 934 (m), 869 (w), 808 (w), 788 (m), 753 (s), 716 (s), 686 (m), 669 (m), 632 (m), 579 (s), 552 (w), 499 (s), 476 (w), 440 (m).

[GdDy(MeOH)₂(NO₃)₂(phsq)₄]·2MeOH (doped compound 90:10) (56-GdDy)

To produce the doped compound Gd(NO₃)₃·6H₂O (389.98 mg, 0.864 mmol, 1.8 eq.) and Dy(NO₃)₃·6H₂O (43.8 mg, 0.096 mmol, 0.2 eq.) were loaded into a Teflon vessel together with 9,10-phenanthrenequinone (100.0 mg, 0.480 mmol, 1.0 eq.) and 10 ml MeOH. The vessel was closed and put into a steel autoclave that was sealed tightly and put into a 90°C oven for 2 weeks. The autoclave was cooled down to RT slowly by turning off the oven but leaving the oven door shut. After 24 h the autoclave was removed from the oven, opened and the contents were filtered. The product was obtained as dark crystals in a yield of 24.9 mg.

IR (4000-400 cm⁻¹): 3650 (w), 3487 (b, w), 3166 (b, w), 3069 (w), 2953 (w), 2838 (w), 2107 (b, w), 1602 (w), 1564 (m), 1519 (m), 1476 (s), 1453 (s), 1350 (s), 1309 (s), 1274 (s), 1220 (s), 1164 (w), 1122 (m), 1102 (m), 1073 (m), 1036 (m), 1010 (m), 956 (w), 934 (m), 870 (w), 811 (w), 786 (w), 769 (w), 755 (s), 717 (s), 683 (m), 669 (m), 631 (w), 579 (m), 551 (m), 505 (s), 441 (m).

[Ln₂(EtOH)₂(NO₃)₂(phsq)₄]·4EtOH (Ln = Eu^{III}, Gd^{III}, Tb^{III}, Dy^{III}, Ho^{III}, Er^{III}, Tm^{III})



The Dy^{III} and Ho^{III} version of this compound were synthesised by me during my Master thesis and are also described in the doctoral thesis of my then supervisor in the lab Dr. Anthony Blue Carter.^[31-32] During the work on this thesis these two compounds were reproduced to be analysed further and more

lanthanide variations were synthesised using the following optimised procedure.

A Teflon insert was loaded with 9,10-phenanthrenequinone (100.0 mg, 0.48 mmol, 1.0 eq.), Ln(NO₃)₃·xH₂O (0.96 mmol, 2.0 eq.) and 10 ml EtOH. The vessel was closed with a lid and put into a steel autoclave that was sealed tightly and put in an oven at 90°C for 2 weeks. The autoclave was cooled down to RT slowly by turning off the oven but leaving the oven door shut. After 24 h the autoclave was removed from the oven, opened and the contents were filtered. The product was obtained as dark crystals that were dried in air.

[Eu₂(EtOH)₂(NO₃)₂(phsq)₄]·4EtOH (57-Eu)

Amount of Eu(NO₃)₃·6H₂O used = 428.2 mg. Yield = 6.2 mg (3.3%). IR (4000-400 cm⁻¹): 3642 (w), 3493 (b, s), 3076 (w), 2976 (w), 1634 (w), 1600 (m), 1581 (w), 1563 (m), 1517 (s), 1477 (s), 1456 (s), 1348 (s), 1305 (s), 1272 (s), 1221 (s), 1163 (w), 1123 (m), 1102 (m), 1076 (m), 1027 (s), 958 (w), 934 (m), 871 (m), 812 (m), 788 (w), 755 (s), 717 (s), 693 (w), 684 (m), 666 (w), 631 (m), 578 (m), 554 (w), 497 (s), 475 (m), 439 (m), 421 (w).

[Gd₂(EtOH)₂(NO₃)₂(phsq)₄]·4EtOH (58-Gd)

Amount of Gd(NO₃)₃·6H₂O used = 433.3 mg. Yield = 15.0 mg (8.1%). IR (4000-400 cm⁻¹): 3497 (b, m), 3069 (w), 1671 (m), 1648 (w), 1614 (w), 1593 (m), 1562 (m), 1517 (m), 1478 (s), 1454(s), 1433 (m), 1349 (s), 1303 (s), 1271 (s), 1220 (s), 1160 (m), 1121 (m), 1102 (m), 1075 (m), 1033 (s), 959 (w), 937 (m), 874 (m), 814 (m), 788 (m), 774 (m), 757 (m), 721 (s), 696 (w), 683 (m), 670 (w), 630 (w), 580 (m), 554 (w), 504 (m), 484 (w), 441 (m).

[Tb₂(EtOH)₂(NO₃)₂(phsq)₄]·4EtOH (59-Tb)

Amount of Tb(NO₃)₃·6H₂O used = 434.9 mg. **Yield** = 15.0 mg (8.1%). **IR (4000-400 cm⁻¹)**: 3516 (m), 3084 (w), 2975 (m), 2899 (w), 1601 (m), 1583 (w), 1565 (m), 1523 (s), 1479 (s), 1456 (s), 1422 (w), 1348 (s), 1305 (s), 1275 (s), 1219 (s), 1173 (w), 1165 (w), 1125 (m), 1103 (m), 1074 (m), 1032 (s), 958 (w), 936 (m), 874 (m), 812 (m), 790 (m), 775 (m), 755 (s), 719 (s), 694 (w), 686 (m), 669 (w), 631 (m), 579 (m), 555 (w), 501 (s), 480 (w), 443 (m). **UV-VIS (solid state)**: λ/nm = 207, 252, 267 (shoulder), 291, 353, 509, 654.

[Dy₂(EtOH)₂(NO₃)₂(phsq)₄]·4EtOH (60-Dy)

Amount of Dy(NO₃)₃·6H₂O used = 438.3 mg. **Yield** = 42.2 mg (23%). **IR (4000-400 cm⁻¹)**: 3497 (b, m), 3069 (w), 1671 (m), 1647 (w), 1614 (w), 1593 (m), 1562 (m), 1517 (m), 1478 (s), 1454(s), 1433 (m), 1349 (s), 1303 (s), 1271 (s), 1220 (s), 1160 (m), 1121 (m), 1102 (m), 1075 (m), 1039 (m), 1022 (m), 960 (w), 936 (m), 925 (m), 872 (w), 812 (w), 786 (w), 756 (m), 717 (m), 685 (m), 666 (w), 634 (w), 578 (m), 532 (w), 500 (m), 434 (w).

Crystal Data for C₆₈H₆₈Dy₂N₂O₂₀ ($M=1558.24$ g/mol): monoclinic, space group P2₁/n (no. 14), $a = 11.6579(5)$ Å, $b = 18.4992(5)$ Å, $c = 14.5998(6)$ Å, $\beta = 94.545(3)^\circ$, $V = 3138.7(2)$ Å³, $Z = 2$, $T = 180(2)$ K, $\mu(\text{MoK}\alpha) = 2.441$ mm⁻¹, $D_{\text{calc}} = 1.649$ g/cm³, 15826 reflections measured ($4.14^\circ \leq 2\Theta \leq 56.56^\circ$), 7688 unique ($R_{\text{int}} = 0.0777$, $R_{\text{sigma}} = 0.0910$) which were used in all calculations. The final R_1 was 0.0543 ($I > 2\sigma(I)$) and wR_2 was 0.1421 (all data).

[Ho₂(EtOH)₂(NO₃)₂(phsq)₄]·4EtOH (61-Ho)

Amount of Ho(NO₃)₃·5H₂O used = 423.4 mg. **Yield** = 29.8 mg (16%). **IR (4000-400 cm⁻¹)**: 3509 (b, s), 3087 (b, w), 2981 (b, m), 2899 (b, w), 1601 (w), 1585 (w), 1567 (m), 1524 (s), 1493 (m), 1477 (s), 1456 (s), 1425 (s), 1368 (s), 1349 (s), 1309 (b, s), 1275 (s), 1215 (s), 1176 (w), 1166 (w), 1123 (m), 1101 (m), 1075 (m), 1034 (s), 958 (w), 938 (m), 871 (m), 811 (m), 790 (w), 777 (m), 755 (s), 719 (s), 694 (w), 686 (m), 669 (w), 631 (m), 579 (m), 555 (w), 501 (s), 480 (w), 443 (m).

[Er₂(EtOH)₂(NO₃)₂(phsq)₄]₁·4EtOH (62-Er)

Amount of Er(NO₃)₃·5H₂O used = 425.6 mg. **Yield** = 25.0 mg (13%). **IR (4000-400 cm⁻¹)**: 3511 (m), 3076 (b, w), 2976 (b, w), 2899 (w), 1603 (m), 1583 (w), 1564 (m), 1522 (s), 1480 (s), 1456 (s), 1424 (w), 1348 (s), 1308 (s), 1374 (s), 1217 (s), 1165 (w), 1124 (m), 1101 (m), 1076 (m), 1031 (s), 959 (w), 937 (m), 874 (m), 813 (m), 788 (m), 774 (m), 757 (m), 721 (s), 696 (w), 683 (m), 670 (w), 630 (w), 580 (m), 555 (w), 504 (m), 484 (w), 442 (m).

[Tm₂(EtOH)₂(NO₃)₂(phsq)₄]₁·4EtOH (63-Tm)

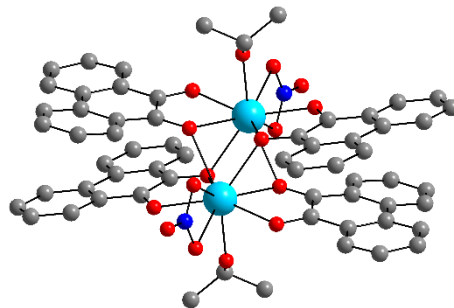
Amount of Tm(NO₃)₃·6H₂O used = 444.5 mg. **Yield** = 22.1 mg (12%). **IR (4000-400 cm⁻¹)**: 3509 (b, s), 3087 (b, w), 2981 (b, m), 2899 (b, w), 1601 (w), 1585 (w), 1567 (m), 1524 (s), 1493 (m), 1477 (s), 1456 (s), 1425 (s), 1368 (s), 1349 (s), 1309 (b, s), 1275 (s), 1215 (s), 1176 (w), 1166 (w), 1123 (m), 1101 (m), 1075 (m), 1034 (s), 958 (w), 938 (m), 871 (m), 811 (m), 790 (w), 777 (m), 755 (s), 721 (s), 695 (m), 684 (m), 668 (m), 632 (w), 580 (m), 554 (w), 505 (m), 460 (w), 444 (m), 428 (w), 403 (w). **UV-VIS (solid state)**: λ/nm = 205, 246, 252, 268, 363, 507 (shoulder), 652. **C/H/N (calculated corresponds to 2 H₂O lattice solvent)**: C:51.30%, H: 3.30%, N: 1.99%. **C/H/N (found)**: C: 51.05%, H: 3.63%, N: 1.96%.

[YDy(EtOH)₂(NO₃)₂(phsq)₄]₁·4EtOH (doped compound Y:Dy = 90:10) (64-DyY)

To produce the doped compound Y(NO₃)₃·6H₂O (330.9 mg, 0.864 mmol, 1.8 eq.) and Dy(NO₃)₃·6H₂O (43.8 mg, 0.096 mmol, 0.2 eq.) were loaded into a Teflon vessel together with 9,10-phenanthrenequinone (100.0 mg, 0.480 mmol, 1.0 eq.) and 10 ml EtOH. The vessel was closed and put into a steel autoclave that was sealed tightly and put into a 90°C oven for 2 weeks. The autoclave was cooled down to RT slowly by turning off the oven but leaving the oven door shut. After 24 h the autoclave was removed from the oven, opened and the contents were filtered. The product was obtained as dark crystals

IR (4000-400 cm⁻¹): 3511 (b, s), 3087 (b, w), 2981 (b, m), 2898 (b, w), 1601 (w), 1585 (w), 1567 (m), 1524 (s), 1493 (m), 1477 (s), 1456 (s), 1425 (s), 1368 (s), 1349 (s), 1309 (b, s), 1273 (s), 1215 (s), 1176 (w), 1166 (w), 1123 (m), 1101 (m), 1075 (m), 1034 (s), 958 (w), 939 (m), 871 (m), 811 (m), 790 (w), 777 (m), 755 (s), 721 (s), 695 (m), 684 (m), 668 (m), 632 (w), 580 (m), 554 (w), 507 (m), 460 (w), 444 (m), 429 (w), 400 (w).

[Ln₂(ⁱPrOH)₂(NO₃)₂(phsq)₄]₁·2ⁱPrOH (Ln = Y^{III}, Pr^{III}, Nd^{III}, Sm^{III}, Eu^{III}, Gd^{III}, Tb^{III}, Dy^{III}, Ho^{III}, Er^{III}, Tm^{III}, Yb^{III}, Lu^{III})



A Teflon insert was loaded with 9,10-phenanthrenequinone (100.0 mg, 0.48 mmol, 1.0 eq.), Ln(NO₃)₃·xH₂O (0.96 mmol, 2.0 eq.) and 10 ml isopropanol. The vessel was closed with a lid and put into a steel autoclave that was sealed tightly and put in an oven at 90°C for 2 weeks. The autoclave was cooled down to RT slowly by turning off the oven but leaving the oven door shut. After 24 h the autoclave was removed from the oven, opened and the contents were filtered. The product was obtained as dark crystals that were dried in air.

[Pr₂(ⁱPrOH)₂(NO₃)₂(phsq)₄]₁·2ⁱPrOH (65-Pr)

Amount of Pr(NO₃)₃·6H₂O used = 417.6 mg. **Yield** = 17.3 mg (10 %). **IR (4000-400 cm⁻¹)**: 3414 (b, w), 2970 (m), 2921 (w), 1672 (s), 1604 (w), 1565 (m), 1522 (s), 1477 (s), 1457 (s), 1439 (w), 1425 (w), 1351 (s), 1321 (s), 1302 (s), 1289 (s), 1274 (s), 1248 (m), 1226 (s), 1158 (m), 1123 (m), 1106 (s), 1075 (s), 1040 (m), 1028 (m), 935 (s), 870 (w), 812 (m), 786 (m), 774 (w), 760 (s), 722 (s), 685 (m), 672 (w), 634 (w), 580 (m), 553 (w), 499 (s), 458 (w), 443 (m), 422 (w).

[Nd₂(ⁱPrOH)₂(NO₃)₂(phsq)₄]₁·2ⁱPrOH (66-Nd)

Amount of Nd(NO₃)₃·6H₂O used = 420.8 mg. **Yield** = 27.1 mg (15%). **IR (4000-400 cm⁻¹)**: 3469 (b, w), 2970 (m), 2921 (w), 1672 (s), 1604 (w), 1565 (m), 1522 (s), 1477 (s), 1457 (s), 1439 (w), 1425 (w), 1351 (s), 1321 (s), 1302 (s), 1289 (s), 1274 (s), 1248 (m), 1224 (s), 1158 (m), 1121 (m), 1106 (s), 1075 (s), 1040 (m), 1029 (m), 935 (s), 871 (w), 812 (m), 786 (m), 776 (w), 760 (s), 722 (s), 685 (m), 672 (w), 634 (w), 581 (m), 553 (w), 499 (s), 458 (w), 444 (m), 420 (w).

[Sm₂(ⁱPrOH)₂(NO₃)₂(phsq)₄]₁·2ⁱPrOH (67-Sm)

Amount of Sm(NO₃)₃·6H₂O used = 426.7 mg. **Yield** = 26.2 mg (15%). **IR (4000-400 cm⁻¹)**: 3532 (b, m), 3206 (b, m), 3084 (m), 2966 (s), 2925 (w), 2898 (w), 1604 (w), 1565 (m), 1520 (s), 1477 (s), 1457 (s), 1440 (w), 1425 (w), 1351 (s), 1321 (s), 1302 (s), 1289 (s), 1275 (s), 1248 (m), 1226 (s), 1158 (m), 1122 (m), 1106 (s), 1074 (s), 1040 (m),

1028 (m), 935 (s), 870 (w), 812 (m), 786 (m), 774 (w), 760 (s), 722 (s), 685 (m), 672 (w), 634 (w), 581 (m), 553 (w), 499 (s), 460 (w), 443 (m), 420 (w).

[Eu₂(iPrOH)₂(NO₃)₂(phsq)₄]·2iPrOH (68-Eu)

Amount of Eu(NO₃)₃·6H₂O used = 428.2 mg. **Yield** = 58.8 mg (33%). **IR (4000-400 cm⁻¹)**: 3499 (b, w), 2970 (m), 2921 (w), 1672 (s), 1604 (w), 1565 (m), 1522 (s), 1477 (s), 1457 (s), 1439 (w), 1428 (w), 1351 (s), 1321 (s), 1302 (s), 1289 (s), 1274 (s), 1248 (m), 1224 (s), 1159 (m), 1121 (m), 1108 (s), 1075 (s), 1042 (m), 1029 (m), 935 (s), 871 (w), 812 (m), 786 (m), 776 (w), 760 (s), 722 (s), 685 (m), 672 (w), 634 (w), 580 (m), 553 (w), 499 (s), 459 (w), 444 (m), 422 (w).

[Gd₂(iPrOH)₂(NO₃)₂(phsq)₄]·2iPrOH (69-Gd)

Amount of Gd(NO₃)₃·6H₂O used = 433.3 mg. **Yield** = 25.3 mg (14%). **IR (4000-400 cm⁻¹)**: 3560 (b, m), 3197 (b, m), 3080 (m), 2966 (s), 2920 (w), 1600 (m), 1582 (w), 1563 (m), 1520 (s), 1476 (s), 1455 (s), 1440 (w), 1419 (w), 1367 (w), 1349 (s), 1319 (s), 1304 (s), 1276 (s), 1250 (w), 1225 (s), 1159 (m), 1123 (m), 1104 (s), 1075 (s), 1040 (m), 1026 (m), 960 (w), 933 (w), 871 (w), 814 (m), 787 (m), 775 (w), 759 (s), 744 (m), 722 (m), 693 (w), 685 (m), 666 (w), 633 (w), 578 (m), 552 (w), 496 (m), 445 (m), 421 (w). **UV-VIS (solid state)**: λ/nm = 206, 245, 252, 268, 362, 511, 652. **C/H/N (calculated) corresponds to loss of all lattice solvent**: C:53.51%, H: 3.48%, N: 2.01%. **C/H/N (found)**: C: 53.22%, H: 3.88%, N: 1.88%.

[Tb₂(iPrOH)₂(NO₃)₂(phsq)₄]·2iPrOH (70-Tb)

Amount of Tb(NO₃)₃·6H₂O used = 434.9 mg. **Yield** = 48.0 mg (26%). **IR (4000-400 cm⁻¹)**: 3565 (b, m), 3202 (b, m), 3084 (m), 2971 (s), 2926 (w), 2899 (w), 1602 (w), 1582 (w), 1564 (m), 1520 (m), 1477 (s), 1455 (s), 1440 (w), 1423 (w), 1350 (s), 1321 (s), 1305 (s), 1275 (s), 1248 (w), 1226 (s), 1158 (m), 1125 (m), 1106 (s), 1075 (s), 1040 (m), 1027 (m), 961 (w), 935 (s), 871 (w), 813 (m), 787 (m), 772 (w), 759 (s), 744 (m), 722 (m), 695 (w), 685 (w), 669 (m), 631 (w), 580 (m), 553 (w), 499 (s), 442 (m), 422 (w). **C/H/N (calculated) corresponds to exchange of one lattice isopropanol to H₂O**: C: 53.00%, H: 3.97%, N: 1.90%. **C/H/N (found)**: C: 53.33%, H: 4.02%, N: 1.86%.

[Dy₂(ⁱPrOH)₂(NO₃)₂(phsq)₄]₂ⁱPrOH (71-Dy)

Amount of Dy(NO₃)₃·6H₂O used = 438.3 mg. **Yield** = 110.5 mg (61%). **IR (4000-400 cm⁻¹)**: 3563 (m), 3528 (b, m), 3213 (b, m), 3085 (m), 2972 (s), 2924 (w), 2899 (w), 1595 (w), 1582 (w), 1563 (m), 1520 (s), 1476 (s), 1457 (s), 1436 (b, m), 1351 (s), 1319 (s), 1303 (s), 1275 (s), 1250 (m), 1226 (s), 1159 (m), 1123 (m), 1106 (s), 1077 (s), 1041 (m), 1029 (m), 961 (w), 937 (s), 872 (w), 814 (m), 786 (m), 758 (s), 745 (m), 723 (s), 683 (m), 669 (w), 624 (w), 580 (m), 554 (w), 533 (w), 500 (s), 456 (w), 442 (m), 421 (w). **UV-VIS (solid state)**: λ/nm = 202, 245, 251, 268, 362, 506 (shoulder), 651. **C/H/N (calculated) corresponds to one lattice H₂O**: C: 52.44%, H: 3.55%, N: 1.97%. **C/H/N (found)**: C: 52.62%, H: 4.00%, N: 1.91%.

[Ho₂(ⁱPrOH)₂(NO₃)₂(phsq)₄]₂ⁱPrOH (72-Ho)

Amount of Ho(NO₃)₃·5H₂O used = 423.4 mg. **Yield** = 60.8 mg (33%). **IR (4000-400 cm⁻¹)**: 3562 (b, m), 3206 (b, m), 3084 (m), 2966 (s), 2925 (w), 2898 (w), 1604 (w), 1565 (m), 1522 (s), 1477 (s), 1457 (s), 1439 (w), 1425 (w), 1351 (s), 1321 (s), 1302 (s), 1289 (s), 1274 (s), 1248 (m), 1226 (s), 1158 (m), 1123 (m), 1106 (s), 1075 (s), 1040 (m), 1028 (m), 935 (s), 870 (w), 812 (m), 786 (m), 774 (w), 760 (s), 722 (s), 685 (m), 672 (w), 634 (w), 580 (m), 553 (w), 499 (s), 458 (w), 443 (m), 422 (w). **C/H/N (calculated) corresponds to loss of one lattice isopropanol**: C: 53.22%, H: 3.85%, N: 1.91%. **C/H/N (found)**: C: 53.04%, H: 4.05%, N: 1.93%.

[Er₂(ⁱPrOH)₂(NO₃)₂(phsq)₄]₂ⁱPrOH (73-Er)

Amount of Er(NO₃)₃·5H₂O used = 425.6 mg. **Yield** = 70.0 mg (38%). **IR (4000-400 cm⁻¹)**: 3563 (m), 3529 (b, w), 3207 (b, m), 3085 (m), 2972 (s), 2924 (w), 2897 (w), 1602 (w), 1565 (m), 1520 (s), 1475 (s), 1456 (s), 1431 (b, m), 1351 (s), 1321 (s), 1303 (s), 1289 (s), 1273 (s), 1251 (m), 1225 (s), 1159 (m), 1121 (m), 1105 (s), 1077 (s), 1040 (m), 1030 (m), 937 (s), 870 (w), 814 (m), 786 (m), 774 (w), 757 (s), 721 (s), 685 (m), 669 (w), 633 (w), 579 (m), 553 (w), 500 (s), 460 (w), 443 (m), 424 (w). **UV-VIS (solid state)**: λ/nm = 215, 251, 268, 361, 506, 654. **C/H/N (calculated) corresponds to one lattice H₂O**: C: 52.16%, H: 3.39%, N: 1.96%. **C/H/N (found)**: C: 52.84%, H: 3.78%, N: 1.88%.

[Tm₂(iPrOH)₂(NO₃)₂(phsq)₄]₂iPrOH (74-Tm)

Amount of Tm(NO₃)₃·6H₂O used = 444.5 mg. **Yield** = 30.3 mg (16%). **IR (4000-400 cm⁻¹)**: 3562 (m), 3528 (b, w), 3210 (b, m), 3080 (m), 2970 (s), 2921 (w), 2893 (w), 1603 (w), 1581 (w), 1564 (m), 1522 (m), 1475 (s), 1457 (s), 1432 (b, m), 1352 (s), 1321 (s), 1303 (s), 1290 (s), 1274 (s), 1248 (m), 1226 (s), 1158 (m), 1122 (m), 1107 (s), 1078 (s), 1041 (m), 1031 (m), 961 (w), 937 (s), 872 (w), 815 (m), 786 (m), 774 (w), 759 (s), 722 (s), 685 (m), 672 (w), 634 (w), 614 (w), 580 (m), 553 (w), 501 (s), 460 (w), 444 (m), 424 (w). **UV-VIS (solid state)**: λ/nm = 203, 245, 252, 268, 360, 406 (shoulder), 509 (shoulder), 645. **C/H/N (calculated)**: C: 52.36%, H: 3.42%, N: 1.98%. **C/H/N (found)**: C: 52.40%, H: 3.76%, N: 1.86%.

Crystal Data for C₆₈H₆₄N₂O₁₈Tm₂ ($M=1535.07$ g/mol): monoclinic, space group P2₁/n (no. 14), $a = 12.8549(4)$ Å, $b = 17.7648(4)$ Å, $c = 13.3236(4)$ Å, $\beta = 93.486(2)^\circ$, $V = 3037.01(15)$ Å³, $Z = 2$, $T = 180.0$ K, $\mu(\text{GaK}\alpha) = 9.944$ mm⁻¹, $D_{\text{calc}} = 1.679$ g/cm³, 19632 reflections measured ($7.224^\circ \leq 2\Theta \leq 124.98^\circ$), 7151 unique ($R_{\text{int}} = 0.0219$, $R_{\text{sigma}} = 0.0301$) which were used in all calculations. The final R_1 was 0.0261 ($I > 2\sigma(I)$) and wR_2 was 0.0658 (all data).

[Yb₂(iPrOH)₂(NO₃)₂(phsq)₄]₂iPrOH (75-Yb)

Amount of Yb(NO₃)₃·6H₂O used = 448.5 mg. **Yield** = 175.8 mg (95%). **IR (4000-400 cm⁻¹)**: 3565 (m), 3530 (b, w), 3212 (b, m), 3083 (m), 2972 (s), 2962 (w), 2890 (w), 1603 (w), 1564 (m), 1522 (s), 1476 (s), 1458 (s), 1437 (b, m), 1352 (s), 1321 (s), 1304 (s), 1291 (s), 1272 (s), 1250 (m), 1227 (s), 1159 (m), 1123 (m), 1105 (s), 1078 (s), 1040 (m), 1031 (m), 961 (w), 939 (s), 871 (w), 814 (m), 787 (m), 775 (w), 757 (s), 722 (s), 695 (w), 686 (m), 672 (m), 635 (m), 615 (w), 579 (m), 553 (w), 501 (s), 463 (w), 444 (m), 424 (w). **UV-VIS (solid state)**: λ/nm = 202, 245, 252, 267, 361, 508, 646. **C/H/N (calculated) corresponds to loss of one lattice isopropanol**: C: 52.64%, H: 3.81%, N: 1.89%. **C/H/N (found)**: C: 52.94%, H: 3.77%, N: 1.93%.

[Lu₂(iPrOH)₂(NO₃)₂(phsq)₄]₂iPrOH (76-Lu)

Amount of Lu(NO₃)₃·6H₂O used = 450.3 mg. **Yield** = 65.5 mg (35%). **IR (4000-400 cm⁻¹)**: 3560 (m), 3524 (b, w), 3197 (b, m), 3085 (m), 2974 (s), 2924 (w), 2905 (w), 1605 (w), 1565 (m), 1522 (s), 1477 (s), 1457 (s), 1430 (b, m), 1351 (s), 1320 (s), 1303 (s), 1291 (s), 1273 (s), 1249 (m), 1223 (s), 1161 (m), 1124 (m), 1106 (s), 1077 (s), 1039

(m), 1032 (m), 937 (s), 872 (w), 813 (m), 787 (m), 773 (w), 755 (s), 723 (m), 686 (m), 671 (m), 633 (m), 616 (w), 581 (m), 553 (w), 499 (m), 464 (w), 444 (m), 424 (w). **UV-VIS (solid state):** $\lambda/\text{nm} = 205, 244, 252, 268, 362, 510, 651$.

$[\text{Y}_2(\text{iPrOH})_2(\text{NO}_3)_2(\text{phsq})_4]\cdot 2\text{iPrOH}$ (77-Y)

Amount of $\text{Y}(\text{NO}_3)_3\cdot 6\text{H}_2\text{O}$ used = 367.7 mg. **Yield** = 47.1 mg (29%). **IR (4000-400 cm^{-1})**: 3561 (b, m), 3207 (b, m), 3085 (m), 2972 (m), 2922 (w), 2897 (w), 1602 (m), 1583 (w), 1564 (m), 1522 (m), 1475 (s), 1456 (s), 1435 (b, m), 1370 (m), 1350 (s), 1318 (s), 1302 (s), 1289 (s), 1273 (s), 1249 (m), 1226 (s), 1158 (m), 1123 (m), 1105 (s), 1078 (s), 1042 (m), 1029 (m), 934 (m), 869 (w), 813 (m), 788 (m), 775 (w), 759 (m), 749 (m), 723 (m), 685 (m), 668 (m), 633 (w), 579 (m), 554 (w), 500 (m), 445 (m), 424 (w). **UV-VIS (solid state):** $\lambda/\text{nm} = 209, 246$ (shoulder), 252, 268, 362, 509, 647. **C/H/N (calculated) corresponds to 1 iPrOH lattice solvent:** C: 59.37%, H: 4.29%, N: 2.13%. **C/H/N (found):** C: 59.34%, H: 4.49%, N: 2.02%.

$[\text{YDy}(\text{iPrOH})_2(\text{NO}_3)_2(\text{phsq})_4]\cdot 2\text{iPrOH}$ (doped compound Y: Dy = 90:10) (78-DyY)

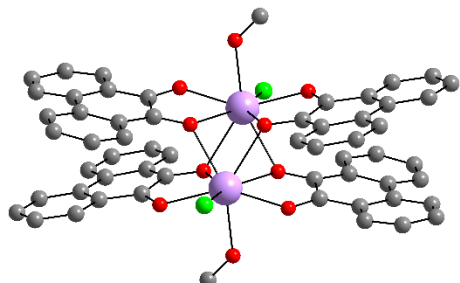
To produce the doped compound $\text{Y}(\text{NO}_3)_3\cdot 6\text{H}_2\text{O}$ (330.9 mg, 0.864 mmol, 1.8 eq.) and $\text{Dy}(\text{NO}_3)_3\cdot 6\text{H}_2\text{O}$ (43.8 mg, 0.096 mmol, 0.2 eq.) were loaded into a Teflon vessel together with 9,10-phenanthrenequinone (100.0 mg, 0.480 mmol, 1.0 eq.) and 10 ml isopropanol. The vessel was closed and put into a steel autoclave that was sealed tightly and put into a 90°C oven for 2 weeks. The autoclave was cooled down to RT slowly by turning off the oven but leaving the oven door shut. After 24 h the autoclave was removed from the oven, opened and the contents were filtered. The product was obtained as dark crystals.

IR (4000-400 cm^{-1}): 3565 (b, m), 3206 (b, m), 3084 (m), 2972 (s), 2923 (w), 2900 (w), 1602 (w), 1581 (w), 1565 (m), 1523 (s), 1478 (s), 1457 (s), 1433 (b, m), 1371 (m), 1350 (s), 1320 (s), 1302 (s), 1291 (s), 1275 (s), 1250 (m), 1226 (s), 1159 (m), 1122 (m), 1106 (s), 1076 (s), 1039 (m), 1029 (m), 936 (s), 871 (w), 814 (m), 788 (m), 774 (w), 758 (s), 749 (m), 721 (s), 695 (w), 685 (m), 671 (w), 632 (m), 614 (w), 580 (m), 553 (w), 500 (s), 445 (m), 425 (w).

Crystal Data for $\text{C}_{68}\text{H}_{64}\text{Dy}_{0.58}\text{N}_2\text{O}_{18}\text{Y}_{1.42}$ ($M=1417.71$ g/mol): monoclinic, space group $\text{P}2_1/n$ (no. 14), $a = 12.8440(3)$ Å, $b = 17.7484(4)$ Å, $c = 13.3983(4)$ Å, $\beta = 93.324(2)^\circ$, $V = 3049.14(13)$ Å³, $Z = 2$, $T = 180$ K, $\mu(1.3401270, 1.34 \text{ K}\alpha) = 5.273 \text{ mm}^{-1}$, $D_{\text{calc}} =$

1.544 g/cm³, 32027 reflections measured ($7.2^\circ \leq 2\Theta \leq 125.06^\circ$), 7311 unique ($R_{\text{int}} = 0.0152$, $R_{\text{sigma}} = 0.0103$) which were used in all calculations. The final R_1 was 0.0222 ($I > 2\sigma(I)$) and wR_2 was 0.0570 (all data).

[Ln₂(Cl)₂(MeOH)₂(phsq)₄] (Ln = Y^{III}, Nd^{III}, Sm^{III}, Eu^{III}, Gd^{III}, Tb^{III}, Dy^{III}, Ho^{III}, Er^{III}, Tm^{III})



The Er^{III} version of this was reported in the doctoral thesis of a former group member^[33] but it was never possible to reproduce this compound until poorly grown crystals were obtained during the work on my Master thesis, where it crystallised with an additional impurity of starting material.^[31] During the work on this thesis the optimisation of the reaction procedure in order to obtain the compounds reproducibly in a pure phase was successful. Therefore, it was possible to synthesise and study further lanthanide analogues.

A Teflon insert was loaded with 9,10-phenanthrenequinone (100.0 mg, 0.48 mmol, 1.0 eq.), LnCl₃·6H₂O (0.96 mmol, 2.0 eq.), NaN₃ (31.2 mg, 0.48 mmol, 1.0 eq.) and 10 ml MeOH. The vessel was closed with a lid and put into a steel autoclave that was sealed tightly and put in an oven at 90°C for 2 weeks. The autoclave was cooled down to RT slowly by turning off the oven but leaving the oven door shut. After 24 h the autoclave was removed from the oven, opened and the contents were filtered. The product was obtained as dark crystals that were dried in air.

[Nd₂(Cl)₂(MeOH)₂(phsq)₄] (79-Nd)

Amount of NdCl₃·6H₂O used = 344.3 mg. **Yield** = 27.7 mg (18%). **IR (4000-400 cm⁻¹)**: 3568 (s), 3545 (s), 3345 (b, m), 3222 (b, m), 3065 (m), 2950 (w), 2850 (w), 1674 (m), 1651 (w), 1594 (m), 1580 (m), 1563 (m), 1518 (s), 1489 (s), 1474 (s), 1456 (s), 1437 (w), 1420 (w), 1348 (s), 1301 (s), 1288 (m), 1271 (s), 1224 (s), 1162 (m), 1122 (m), 1101 (m), 1075 (m), 1040 (m), 1011 (m), 932 (m), 925 (m), 859 (w), 790 (m), 768 (m), 752 (s), 716 (s), 684 (m), 665 (w), 614 (b, m), 573 (m), 552 (w), 495 (s), 470 (w), 437 (m), 417 (w).

[Sm₂(Cl)₂(MeOH)₂(phsq)₄] (80-Sm)

Amount of SmCl₃·6H₂O used = 350.2 mg. **Yield** = 23.6 mg (16%). **IR (4000-400 cm⁻¹)**: 3564 (s), 3542 (s), 3346 (b, m), 3212 (b, m), 3069 (m), 2952 (w), 2848 (w), 1673

(m), 1597 (m), 1580 (m), 1563 (s), 1518 (s), 1489 (s), 1474 (s), 1456 (s), 1438 (m), 1423 (w), 1347 (s), 1301 (s), 1272 (s), 1224 (s), 1163 (m), 1122 (m), 1101 (s), 1076 (m), 1041 (m), 1014 (m), 959 (w), 934 (m), 858 (w), 788 (m), 770 (m), 754 (s), 716 (s), 686 (m), 665 (m), 630 (w), 615 (w), 574 (s), 552 (w), 493 (s), 474 (w), 440 (m), 420 (w).

[Eu₂(Cl)₂(MeOH)₂(phsq)₄] (81-Eu)

Amount of EuCl₃·6H₂O used = 351.8 mg. **Yield** = 30.8 mg (20%). **IR (4000-400 cm⁻¹)**: 3569 (s), 3545 (s), 3345 (b, m), 3223 (b, m), 3065 (m), 2950 (w), 2850 (w), 1674 (m), 1651 (w), 1594 (m), 1580 (m), 1563 (m), 1518 (s), 1489 (s), 1474 (s), 1456 (s), 1437 (w), 1420 (w), 1346 (s), 1301 (s), 1288 (m), 1271 (s), 1224 (s), 1162 (m), 1122 (m), 1101 (m), 1075 (m), 1041 (m), 1011 (m), 932 (m), 925 (m), 859 (w), 790 (m), 768 (m), 752 (s), 716 (s), 684 (m), 665 (w), 614 (b, m), 573 (m), 552 (w), 495 (s), 470 (w), 437 (m), 420 (w).

[Gd₂(Cl)₂(MeOH)₂(phsq)₄] (82-Gd)

Amount of GdCl₃·6H₂O used = 356.8 mg. **Yield** = 55.1 mg (36%). **IR (4000-400 cm⁻¹)**: 3564 (w), 3540 (w), 3202 (b, m), 3070 (b, m), 2955 (w), 2851 (w), 1674 (m), 1597 (m), 1580 (m), 1564 (s), 1519 (s), 1492 (s), 1476 (s), 1456 (s), 1439 (w), 1421 (w), 1348 (s), 1302 (s), 1270 (s), 1224 (s), 1164 (m), 1122 (m), 1101 (s), 1075 (m), 1040 (m), 1013 (s), 958 (w), 933 (m), 856 (m), 788 (m), 769 (m), 754 (s), 717 (s), 684 (m), 663 (m), 629 (w), 614 (w), 575 (m), 551 (w), 495 (s), 474 (w), 437 (w).

Crystal Data for C₅₈H₄₀Cl₂Gd₂O₁₀ ($M=1282.30$ g/mol): monoclinic, space group P2₁/c (no. 14), $a = 9.2625(3)$ Å, $b = 16.4397(6)$ Å, $c = 15.2753(5)$ Å, $\beta = 100.939(2)^\circ$, $V = 2283.75(14)$ Å³, $Z = 2$, $T = 180$ K, $\mu(\text{Ga-K}\alpha) = 16.106$ mm⁻¹, $D_{\text{calc}} = 1.865$ g/cm³, 14909 reflections measured ($8.46^\circ \leq 2\Theta \leq 128.39^\circ$), 5469 unique ($R_{\text{int}} = 0.0276$, $R_{\text{sigma}} = 0.0292$) which were used in all calculations. The final R_1 was 0.0356 ($I > 2\sigma(I)$) and wR_2 was 0.0926 (all data).

[Tb₂(Cl)₂(MeOH)₂(phsq)₄] (83-Tb)

Amount of TbCl₃·6H₂O used = 358.4 mg. **Yield** = 50.0 mg (32%). **IR (4000-400 cm⁻¹)**: 3516 (b, s), 3070 (m), 2952 (w), 2843 (w), 1674 (w), 1597 (m), 1582 (m), 1563 (s), 1521 (s), 1494 (s), 1474 (s), 1458 (s), 1442 (w), 1424 (w), 1349 (s), 1303 (s), 1270 (s), 1225 (s), 1166 (m), 1121 (m), 1105 (s), 1078 (m), 1042 (m), 1013 (s), 959 (w), 937

(m), 859 (m), 790 (m), 769 (m), 753 (s), 718 (s), 686 (m), 668 (w), 634 (w), 614 (w), 577 (m), 553 (w), 499 (s), 462 (w), 442 (m). **UV-VIS (solid state):** $\lambda/\text{nm} = 205, 246$ (shoulder), 252, 265, 366, 509, 660.

[Dy₂(Cl)₂(MeOH)₂(phsq)₄] (84-Dy)

Amount of DyCl₃·6H₂O used = 361.9 mg. **Yield** = 41.9 mg (27%). **IR (4000-400 cm⁻¹)**: 3198 (b, s), 3072 (m), 2952 (w), 2848 (w), 1600 (m), 1581 (m), 1564 (s), 1520 (s), 1493 (s), 1474 (s), 1456 (s), 1441 (w), 1425 (w), 1349 (s), 1303 (s), 1272 (s), 1226 (s), 1166 (m), 1121 (w), 1102 (s), 1076 (m), 1041 (m), 1014 (s), 958 (w), 936 (m), 857 (m), 788 (m), 770 (m), 753 (s), 716 (s), 686 (s), 665 (m), 630 (w), 614 (w), 576 (s), 553 (w), 498 (s), 455 (w), 440 (m). **UV-VIS (solid state):** $\lambda/\text{nm} = 205, 245$ (shoulder), 252, 268 (shoulder), 374, 510 (shoulder), 660.

Crystal Data for C₅₈H₄₀Cl₂Dy₂O₁₀ ($M = 1292.80$ g/mol): monoclinic, space group P2₁/c (no. 14), $a = 9.2078(2)$ Å, $b = 16.3944(3)$ Å, $c = 15.3029(4)$ Å, $\beta = 100.981(2)^\circ$, $V = 2267.77(9)$ Å³, $Z = 2$, $T = 180$ K, $\mu(\text{Ga-K}\alpha) = 18.233$ mm⁻¹, $D_{\text{calc}} = 1.893$ g/cm³, 13809 reflections measured ($8.51^\circ \leq 2\Theta \leq 124.932^\circ$), 5280 unique ($R_{\text{int}} = 0.0249$, $R_{\text{sigma}} = 0.0289$) which were used in all calculations. The final R_1 was 0.0322 (I>2s(I)) and wR_2 was 0.0841 (all data).

[Ho₂(Cl)₂(MeOH)₂(phsq)₄] (85-Ho)

Amount of HoCl₃·6H₂O used = 364.2 mg. **Yield** = 73.4 mg (47%). **IR (4000-400 cm⁻¹)**: 3209 (b, s), 3076 (m), 3065 (m), 2954 (m), 2850 (w), 1600 (m), 1581 (w), 1564 (s), 1519 (s), 1493 (s), 1475 (s), 1456 (s), 1441 (m), 1424 (w), 1349 (s), 1303 (s), 1270 (s), 1224 (s), 1165 (m), 1122 (m), 1101 (s), 1074 (m), 1041 (m), 1012 (s), 959 (w), 936 (m), 858 (m), 789 (m), 769 (m), 752 (s), 717 (s), 683 (s), 665 (m), 634 (w), 615 (w), 576 (s), 552 (w), 499 (s), 442 (m).

[Er₂(Cl)₂(MeOH)₂(phsq)₄] (86-Er)

Amount of ErCl₃·6H₂O used = 366.4 mg. **Yield** = 21.7 mg (13%). **IR (4000-400 cm⁻¹)**: 3198 (b, s), 3072 (m), 2952 (w), 2848 (w), 1600 (m), 1581 (m), 1564 (s), 1520 (s), 1493 (s), 1474 (s), 1456 (s), 1441 (w), 1425 (w), 1349 (s), 1303 (s), 1272 (s), 1226 (s), 1166 (m), 1121 (w), 1102 (s), 1076 (m), 1041 (m), 1014 (s), 958 (w), 936 (m), 857 (m), 788 (m), 770 (m), 753 (s), 717 (s), 686 (s), 665 (m), 630 (w), 612 (w), 576 (s), 553 (w), 498 (s), 454 (w), 442 (m).

Crystal Data for $C_{58}H_{40}Cl_2Er_2O_{10}$ ($M=1302.32$ g/mol): monoclinic, space group $P2_1/c$ (no. 14), $a = 9.1772(6)$ Å, $b = 16.3704(6)$ Å, $c = 15.3322(10)$ Å, $\beta = 101.206(5)^\circ$, $V = 2259.5(2)$ Å³, $Z = 2$, $T = 180$ K, $\mu(\text{Mo K}\alpha) = 3.875$ mm⁻¹, $D_{\text{calc}} = 1.914$ g/cm³, 11174 reflections measured ($4.524^\circ \leq 2\Theta \leq 56.562^\circ$), 5528 unique ($R_{\text{int}} = 0.0874$, $R_{\text{sigma}} = 0.1024$) which were used in all calculations. The final R_1 was 0.0757 ($I > 2\sigma(I)$) and wR_2 was 0.2176 (all data).

[Tm₂(Cl)₂(MeOH)₂(phsq)₄] (87-Tm)

Amount of TmCl₃·6H₂O used = 368.0 mg. **Yield** = 32.1 mg (21%). **IR (4000-400 cm⁻¹)**: 3207 (b, s), 3071 (m), 2953 (w), 2849 (w), 1673 (w), 1598 (w), 1581 (m), 1565 (s), 1523 (s), 1494 (s), 1476 (s), 1458 (s), 1442 (w), 1349 (s), 1304 (s), 1273 (s), 1227 (s), 1165 (m), 1123 (m), 1105 (s), 1077 (m), 1042 (m), 1016 (m), 960 (w), 938 (m), 859 (w), 788 (m), 769 (w), 754 (s), 716 (s), 685 (m), 666 (w), 632 (w), 613 (w), 577 (m), 554 (w), 498 (s), 442 (m).

[Y₂(Cl)₂(MeOH)₂(phsq)₄] (88-Y)

Amount of YCl₃·6H₂O used = 291.2 mg. **Yield** = very low (couple of crystals). **IR (4000-400 cm⁻¹)**: 3194 (b, s), 3071 (m), 2953 (w), 2849 (w), 1673 (w), 1598 (m), 1583 (m), 1564 (s), 1522 (s), 1494 (s), 1476 (s), 1456 (s), 1441 (m), 1425 (w), 1349 (s), 1303 (s), 1272 (s), 1225 (s), 1166 (m), 1125 (w), 1103 (s), 1076 (m), 1040 (m), 1014 (s), 959 (w), 937 (s), 859 (m), 790 (m), 770 (m), 754 (s), 717 (s), 685 (m), 665 (m), 624 (b, m), 578 (s), 553 (w), 500 (s), 441 (m).

Crystal Data for $C_{58}H_{40}Cl_2O_{10}Y_2$ ($M=1145.62$ g/mol): monoclinic, space group $P2_1/c$ (no. 14), $a = 9.1968(4)$ Å, $b = 16.3971(9)$ Å, $c = 15.3154(7)$ Å, $\beta = 100.933(4)^\circ$, $V = 2267.66(19)$ Å³, $Z = 2$, $T = 180$ K, $\mu(\text{Mo K}\alpha) = 2.732$ mm⁻¹, $D_{\text{calc}} = 1.678$ g/cm³, 10833 reflections measured ($4.968^\circ \leq 2\Theta \leq 63.026^\circ$), 6212 unique ($R_{\text{int}} = 0.0266$, $R_{\text{sigma}} = 0.0360$) which were used in all calculations. The final R_1 was 0.0379 ($I > 2\sigma(I)$) and wR_2 was 0.0910 (all data).

[YDy(Cl)₂(MeOH)₂(phsq)₄] (doped compound 90:10) (89-DyY)

To produce the doped compound YCl₃·6H₂O (262.1 mg, 0.864 mmol, 1.8 eq.) and DyCl₃·6H₂O (30.2 mg, 0.096 mmol, 0.2 eq.) were loaded into a Teflon vessel together with 9,10-phenanthrenequinone (100.0 mg, 0.480 mmol, 1.0 eq.) and 10 ml MeOH. The vessel was closed and put into a steel autoclave that was sealed tightly and put

into a 90°C oven for 2 weeks. The autoclave was cooled down to RT slowly by turning off the oven but leaving the oven door shut. After 24 h the autoclave was removed from the oven, opened and the contents were filtered. The product was obtained as dark crystals.

IR (4000-400 cm⁻¹): 3193 (b, s), 3071 (m), 2953 (w), 2849 (w), 1673 (w), 1598 (m), 1583 (m), 1564 (s), 1522 (s), 1494 (s), 1476 (s), 1456 (s), 1441 (m), 1425 (w), 1349 (s), 1303 (s), 1272 (s), 1225 (s), 1166 (m), 1124 (w), 1102 (s), 1076 (m), 1040 (m), 1014 (s), 959 (w), 937 (s), 859 (m), 790 (m), 770 (m), 754 (s), 717 (s), 685 (m), 665 (m), 624 (b, m), 578 (s), 553 (w), 499 (s), 439 (m).

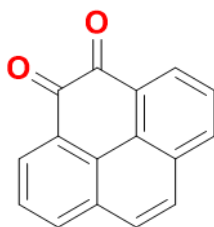
[Ce₆(MeOH)₂(phsq)₆] (90-Ce)

CeCl₃ (295.8 mg, 1.20 mmol, 1.0 eq.), 9,10-phenanthrenequinone (250.0 mg, 1.20 mmol, 1.0 eq.) and Na₂CO₃ (190.8 mg, 1.80 mmol, 1.5 eq.) were suspended in deoxygenated MeOH under N₂ atmosphere. The mixture was heated to reflux for 4 h changing the colour from yellow to dark green. Subsequently, the mixture was allowed to cool to RT before filtration. The dark green solution was left undisturbed for 3 d. The product was obtained as dark crystals in a yield of 35.6 mg (11%).

IR (4000-400 cm⁻¹): 3347 (b, s), 3071 (w), 2944 (w), 2835 (w), 1674 (m), 1647 (w), 1596 (m), 1563 (s), 1519 (s), 1492 (w), 1460 (s), 1427 (s), 1372 (s), 1350 (s), 1309 (s), 1272 (s), 1228 (s), 1161 (m), 1122 (m), 1103 (m), 1078 (m), 1040 (m), 1015 (m), 958 (w), 933 (m), 871 (w), 788 (w), 758 (s), 717 (m), 682 (m), 665 (m), 630 (m), 617 (m), 575 (m), 545 (m), 487 (m), 431 (m).

Crystal Data for C₉₅H₉₄Ce₂O₂₄ ($M=1899.94$ g/mol): monoclinic, space group P2₁/n (no. 14), $a = 17.3653(17)$ Å, $b = 15.2064(9)$ Å, $c = 17.1838(15)$ Å, $\beta = 112.508(7)^\circ$, $V = 4192.0(6)$ Å³, $Z = 2$, $T = 180$ K, $\mu(1.3401270, 1.34 \text{ K}\alpha) = 6.132 \text{ mm}^{-1}$, $D_{\text{calc}} = 1.505 \text{ g/cm}^3$, 17130 reflections measured ($5.354^\circ \leq 2\Theta \leq 92.292^\circ$), 5298 unique ($R_{\text{int}} = 0.0899$, $R_{\text{sigma}} = 0.0693$) which were used in all calculations. The final R_1 was 0.1101 ($I > 2\sigma(I)$) and wR_2 was 0.3023 (all data).

Pyrene-4,5-dione (prepared using modified literature procedure)^[350]

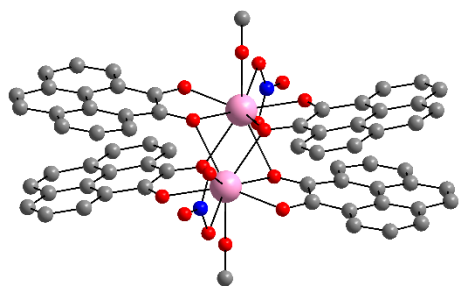


In a round bottom flask pyrene (10.0 g, 49.4 mmol, 1.00 equiv) and RuCl₃·3H₂O (987 mg, 4.74 mmol, 0.096 equiv) were dissolved in 150 mL MeCN. NaIO₄ (42.3 g, 198 mmol, 4.00 equiv) was dissolved in 200 ml hot H₂O and carefully added to the pyrene solution. Another 100 ml of DCM were added and the reaction mixture was vigorously stirred for 24 h at RT. After filtration of the suspension through Celite, the filtrate was extracted with DCM (3x 50 mL) and the combined organic phases were washed with saturated aqueous Na₂S₂O₃ and H₂O and then dried over Na₂SO₄. After removing the solvent under reduced pressure, the product was obtained as a dark orange solid in a yield of 6.7 g (58%).

¹H-NMR (500 MHz, CD₃CN): δ/ppm = 8.40 (d, J = 5.9 Hz, 2H, CH_{AR}), 8.29 (d, J = 6.4 Hz, 2H, CH_{AR}), 7.97 (d, 9.7 Hz, 2H, CH_{AR}), 7.81 (t, J = 6.1 Hz, 2H, CH_{AR}).

UV-VIS (MeCN): λ/nm = 218, 238, 254, 280 (shoulder), 291, 308, 322, 423.

[Ln₂(MeOH)₂(NO₃)₂(pysq)₄]-2pyrene-4,5-dione (Ln = Y^{III}, Tb^{III}, Dy^{III}, Ho^{III}, Er^{III})



A Teflon insert was loaded with pyrene-4,5-dione (100.0 mg, 0.431 mmol, 1.0 eq.), Ln(NO₃)₃·xH₂O (0.431 mmol, 1.0 eq.) and 10 ml MeOH. The vessel was closed with a lid and put into a steel autoclave that was sealed tightly and put in an oven at 90°C for 2 weeks. The autoclave was cooled down to RT slowly by turning off the oven but leaving the oven door shut. After 24 h the autoclave was removed from the oven, opened and the contents were filtered. The product was obtained as dark crystals that were dried in air.

[Tb₂(MeOH)₂(NO₃)₂(pysq)₄]-2pyrene-4,5-dione (91-Tb)

Amount of Tb(NO₃)₃·6H₂O used = 195.3 mg. Yield = 31.0 mg (22%). IR (4000-400 cm⁻¹): 3489 (b, m), 3303 (b, m), 3046 (m), 2950 (w), 2927 (m), 2847 (m), 1658 (m), 1617 (m), 1585 (m), 1524 (s), 1491 (m), 1467 (s), 1426 (m), 1414 (m), 1346 (s), 1294 (s), 1279 (s), 1266 (s), 1232 (m), 1214 (m), 1174 (m), 1105 (m), 1070 (w), 1059 (m), 1023 (m), 1010 (b, m), 906 (m), 894 (m), 828 (s), 814 (m), 791 (m), 763 (m), 745 (w), 735 (m), 708 (s), 671 (w), 623 (m), 600 (w), 581 (w), 560 (m), 508 (s), 485 (w), 476

(w), 451 (w), 441 (w), 432 (m), 413 (w). **UV-VIS (solid state):** λ/nm = 237, 297, 358 (shoulder), 452, 542 (shoulder), 741.

[Dy₂(MeOH)₂(NO₃)₂(pysq)₄]-2pyrene-4,5-dione (92-Dy)

Amount of Dy(NO₃)₃·6H₂O used = 196.8 mg. **Yield** = 29.8 mg (22%). **IR (4000-400 cm⁻¹)**: 3544 (w), 3259 (b, w), 3044 (w), 2931 (b, w), 2105 (b, m), 1991 (w), 1855 (b, m), 1659 (m), 1611 (m), 1582 (m), 1519 (m), 1492 (m), 1467 (s), 1424 (m), 1413 (m), 1346 (s), 1293 (s), 1266 (s), 1229 (w), 1211 (w), 1172 (m), 1104 (m), 1059 (m), 1020 (b, m), 905 (w), 889 (m), 827 (s), 811 (w), 788 (m), 765 (m), 735 (m), 704 (s), 671 (w), 622 (m), 599 (w), 579 (w), 557 (m), 505 (s), 474 (m), 449 (m), 439 (w), 429 (m). **C/H/N (calculated) corresponds to 1 co-crystallising pyrene-4,5-dione**: C:58.82%, H: 2.89%, N: 1.67%. **C/H/N (found)**: C: 58.86%, H: 2.89%, N: 1.58%.

Crystal Data for C_{96.5}H₅₅Dy₂N₂O₂₁ ($M=1903.42$ g/mol): orthorhombic, space group Pbca (no. 61), $a = 18.3532(2)$ Å, $b = 18.4489(2)$ Å, $c = 22.1516(5)$ Å, $V = 7500.5(2)$ Å³, $Z = 4$, $T = 293(2)$ K, $\mu(\text{Cu K}\alpha) = 11.244$ mm⁻¹, $D_{\text{calc}} = 1.686$ g/cm³, 21108 reflections measured ($7.88^\circ \leq 2\Theta \leq 141.984^\circ$), 7080 unique ($R_{\text{int}} = 0.0256$, $R_{\text{sigma}} = 0.0287$) which were used in all calculations. The final R_1 was 0.0402 ($I > 2\sigma(I)$) and wR_2 was 0.1295 (all data).

[Ho₂(MeOH)₂(NO₃)₂(pysq)₄]-2pyrene-4,5-dione (93-Ho)

Amount of Ho(NO₃)₃·5H₂O used = 190.1 mg. **Yield** = 29.8 mg (22%). **IR (4000-400 cm⁻¹)**: 2549 (b, w), 3298 (b, m), 3046 (b, w), 2922 (m), 2849 (w), 1659 (m), 1616 (m), 1586 (m), 1523 (s), 1493 (s), 1469 (s), 1426 (m), 1415 (m), 1347 (s), 1295 (s), 1283 (w), 1267 (s), 1230 (m), 1213 (m), 1173 (m), 1143 (w), 1106 (m), 1070 (w), 1025 (m), 904 (m), 890 (m), 830 (s), 813 (m), 791 (m), 766 (m), 747 (w), 737 (m), 717 (m), 707 (s), 670 (w), 624 (m), 602 (w), 582 (w), 561 (m), 509 (s), 486 (w), 477 (w), 455 (m), 444 (w), 433 (m), 414 (w). **UV-VIS (solid state):** λ/nm = 217 (shoulder), 245, 304, 359 (shoulder), 455, 539 (shoulder), 731.

[Er₂(MeOH)₂(NO₃)₂(pysq)₄]-2pyrene-4,5-dione (94-Er)

Amount of Er(NO₃)₃·5H₂O used = 191.1 mg. **Yield** = 33.2 mg (24%). **IR (4000-400 cm⁻¹)**: 3546 (b, w), 3320 (b, m), 3057 (b, w), 2939 (w), 1658 (s), 1614 (s), 1586 (m), 1529 (s), 1494 (s), 1470 (s), 1424 (m), 1415 (m), 1348 (s), 1298 (s), 1267 (s), 1233 (m), 1211 (m), 1172 (m), 1147 (w), 1106 (m), 1058 (m), 1026 (m), 1003 (w), 926 (w),

905 (w), 887 (m), 830 (s), 813 (w), 790 (m), 766 (m), 749 (m), 735 (m), 717 (w), 706 (s), 625 (m), 602 (w), 558 (m), 509 (m), 478 (m), 455 (m), 442 (m), 431 (w), 416 (w).

Crystal Data for $C_{97}H_{56}Er_2N_2O_{21}$ ($M=1919.95$ g/mol): orthorhombic, space group Pbca (no. 61), $a = 18.3067(7)$ Å, $b = 18.4019(5)$ Å, $c = 22.0921(7)$ Å, $V = 7442.3(4)$ Å³, $Z = 4$, $T = 180$ K, $\mu(1.3401270, 1.34 \text{ K}\alpha) = 7.777$ mm⁻¹, $D_{\text{calc}} = 1.714$ g/cm³, 24987 reflections measured ($6.872^\circ \leq 2\Theta \leq 118.606^\circ$), 7806 unique ($R_{\text{int}} = 0.0355$, $R_{\text{sigma}} = 0.0409$) which were used in all calculations. The final R_1 was 0.0479 ($I > 2\sigma(I)$) and wR_2 was 0.1640 (all data).

[Y₂(MeOH)₂(NO₃)₂(pysq)₄]₂pyrene-4,5-dione (95-Y)

Amount of Y(NO₃)₃·6H₂O used = 165.1 mg. **Yield** = 31.0 mg (25%). **IR (4000-400 cm⁻¹)**: 3420 (b, m), 3048 (m), 2938 (b, m), 2852 (w), 1659 (m), 1618 (m), 1585 (m), 1530 (s), 1503 (w), 1492 (w), 1485 (w), 1470 (s), 1450 (m), 1425 (s), 1413 (s), 1347 (s), 1292 (s), 1261 (s), 1228 (w), 1211 (m), 1172 (m), 1104 (m), 1070 (m), 1056 (m), 1031 (m), 1019 (m), 994 (m), 907 (m), 893 (m), 825 (s), 814 (w), 791 (m), 761 (m), 747 (m), 731 (m), 706 (s), 671 (w), 624 (m), 598 (m), 582 (m), 561 (m), 512 (s), 483 (m), 456 (m), 440 (m), 431 (m), 414 (m). **UV-VIS (solid state):** $\lambda/\text{nm} = 218$ (shoulder), 245, 306, 358, 448, 547 (shoulder), 767.

9. References

- [1] R. Sessoli, D. Gatteschi, A. Caneschi, M. A. Novak, *Nature* **1993**, 365, 141-143.
- [2] D. Gatteschi, R. Sessoli, J. Villain, *Molecular Nanomagnets*, Vol. 1, Oxford University Press, Oxford, **2006**.
- [3] I. G. Rau, S. Baumann, S. Rusponi, F. Donati, S. Stepanow, L. Gragnaniello, J. Dreiser, C. Piamonteze, F. Nolting, S. Gangopadhyay, O. R. Albertini, R. M. Macfarlane, C. P. Lutz, B. A. Jones, P. Gambardella, A. J. Heinrich, H. Brune, *Science* **2014**, 344, 988-992.
- [4] J.-P. Launay, M. Verdaguer, *Electrons in Molecules*, Vol. 1, Oxford University Press, Oxford, **2014**.
- [5] L. Bogani, W. Wernsdorfer, *Nat. Mater.* **2008**, 7, 179-186.
- [6] A. Fert, *Rev. Mod. Phys.* **2008**, 80, 1517-1530.
- [7] P. A. Grünberg, *Rev. Mod. Phys.* **2008**, 80, 1531-1540.
- [8] A. R. Rocha, V. M. Garcia-Suarez, S. W. Bailey, C. J. Lambert, J. Ferrer, S. Sanvito, *Nat. Mater.* **2005**, 4, 335-339.
- [9] S. Sanvito, A. R. Rocha, *J. Comput. Theor. Nanosci.* **2006**, 3, 624-642.
- [10] H. B. Heersche, Z. de Groot, J. A. Folk, H. S. van der Zant, C. Romeike, M. R. Wegewijs, L. Zobbi, D. Barreca, E. Tondello, A. Cornia, *Phys. Rev. Lett.* **2006**, 96, 206801.
- [11] W. Liang, M. P. Shores, M. Bockrath, J. R. Long, H. Park, *Nature* **2002**, 417, 725-729.
- [12] L. E. Hueso, J. M. Pruneda, V. Ferrari, G. Burnell, J. P. Valdes-Herrera, B. D. Simons, P. B. Littlewood, E. Artacho, A. Fert, N. D. Mathur, *Nature* **2007**, 445, 410-413.
- [13] M. Urdampilleta, S. Klyatskaya, J. P. Cleuziou, M. Ruben, W. Wernsdorfer, *Nat. Mater.* **2011**, 10, 502-506.
- [14] M. Affronte, F. Troiani, A. Ghirri, A. Candini, M. Evangelisti, V. Corradini, S. Carretta, P. Santini, G. Amoretti, F. Tuna, G. Timco, R. E. P. Winpenny, *J. Phys. D: Appl. Phys.* **2007**, 40, 2999-3004.
- [15] G. Aromi, D. Aguilà, P. Gamez, F. Luis, O. Roubeau, *Chem. Soc. Rev.* **2012**, 41, 537-546.

[16] S. Bertaina, S. Gambarelli, T. Mitra, B. Tsukerblat, A. Müller, B. Barbara, *Nature* **2008**, 453, 203-206.

[17] M. N. Leuenberger, D. Loss, *Nature* **2001**, 410, 789-793.

[18] R. Sessoli, *ACS Cent. Sci.* **2015**, 1, 473-474.

[19] M. Shiddiq, D. Komijani, Y. Duan, A. Gaita-Arino, E. Coronado, S. Hill, *Nature* **2016**, 531, 348-351.

[20] J. M. Zadrozny, J. Niklas, O. G. Poluektov, D. E. Freedman, *ACS Cent. Sci.* **2015**, 1, 488-492.

[21] S. T. Liddle, J. van Slageren, *Chem Soc Rev* **2015**, 44, 6655-6669.

[22] S. Mondal, A. Lunghi, *J. Am. Chem. Soc.* **2022**, 144, 22965-22975.

[23] R. Sessoli, A. K. Powell, *Coord. Chem. Rev.* **2009**, 253, 2328-2341.

[24] A. Swain, T. Sharma, G. Rajaraman, *Chem. Commun.* **2023**, 59, 3206-3228.

[25] L. Ungur, L. F. Chibotaru, *Inorg. Chem.* **2016**, 55, 10043-10056.

[26] C. A. Gould, R. K. McClain, D. Reta, J. G. C. Kragskow, D. A. Marchiori, E. Lachman, E.-S. Choi, J. G. Analytis, R. D. Britt, N. F. Chilton, B. G. Harvey, J. R. Long, *Science* **2022**, 375, 198-202.

[27] F.-S. Guo, B. M. Day, Y.-C. Chen, M.-L. Tong, A. Mansikkämäki, R. A. Layfield, *Science* **2018**, 362, 1400-1403.

[28] J. Braun, *Exploring the coordination chemistry of biquinoxen ligands*, Karlsruhe Institute of Technology (KIT), Bachelor thesis (KIT), **2017**.

[29] N. Leblanc, D. Genovese, L. De Cola, A. K. Powell, *Phys. Chem. Chem. Phys.* **2017**, 19, 6981-6988.

[30] N. Leblanc, S. Sproules, K. Fink, L. Sanguinet, O. Aleveque, E. Levillain, P. Rosa, A. K. Powell, *Chem. Sci.* **2016**, 7, 3820-3828.

[31] J. Braun, *Metal Complexes of 9,10-Phenanthrenequinone*, Karlsruhe Institute of Technology (KIT), Master thesis (KIT), **2019**.

[32] A. B. Carter, *The Role of Supramolecular Interactions in Magnetic Systems: 1,8-Naphthalimides and Other π -Containing Species*, University of Southampton, PhD thesis (Southampton), **2020**.

[33] T. Kriese, *Untersuchungen an Eisen- und Lanthanoidhaltigen Koordinationsclustern mit Triazolat- sowie Semiquinonato-Liganden*, Karlsruhe Institute of Technology (KIT), PhD thesis, (KIT), **2016**.

[34] E. Hecht, *Optik*, Vol. 7, Walter de Gruyter GmbH, Berlin/Boston, **2018**.

[35] T. G. Mayerhofer, S. Pahlow, J. Popp, *Chem. Phys. Chem.* **2020**, *21*, 2029-2046.

[36] A. Jablonski, *Z. Phys.* **1935**, *94*, 38-46.

[37] J. R. Lakowicz, *Principles of Fluorescence Spectroscopy*, Vol. 3, Springer, Singapore, **2006**.

[38] C. Janiak, H.-J. Meyer, D. Gudat, P. Kurz, *Moderne Anorganische Chemie*, Vol. 5, Walter de Gruyter GmbH, Berlin/Boston, **2018**.

[39] B. Weber, *Coordination Chemistry*, Vol. 1, Springer, Berlin, **2023**.

[40] P. Müller, K. Brettel, *Photochem. Photobiol. Sci.* **2012**, *11*, 632-636.

[41] K. Suzuki, A. Kobayashi, S. Kaneko, K. Takehira, T. Yoshihara, H. Ishida, Y. Shiina, S. Oishi, S. Tobita, *Phys. Chem. Chem. Phys.* **2009**, *11*, 9850-9860.

[42] J.-C. G. Bünzli, *Chem. Rev.* **2010**, *110*, 2729-2755.

[43] J.-C. G. Bünzli, *Coord. Chem. Rev.* **2015**, *293-294*, 19-47.

[44] D. Möncke, D. Ehrt, *Opt. Mater. X* **2021**, *12*, 100092.

[45] F. Ferrari, J. Braun, C. E. Anson, B. D. Wilts, D. Moatsou, C. Bizzarri, *Molecules* **2021**, *26*, 2567.

[46] O. Mrozek, M. Gernert, A. Belyaev, M. Mitra, L. Janiak, C. M. Marian, A. Steffen, *Chem. Eur. J.* **2022**, *28*, e202201114.

[47] F. Reichenauer, C. Wang, C. Forster, P. Boden, N. Ugur, R. Baez-Cruz, J. Kalmbach, L. M. Carrella, E. Rentschler, C. Ramanan, G. Niedner-Schatteburg, M. Gerhards, M. Seitz, U. Resch-Genger, K. Heinze, *J. Am. Chem. Soc.* **2021**, *143*, 11843-11855.

[48] C. Wegeberg, O. S. Wenger, *J. Am. Chem. Soc. Au* **2021**, *1*, 1860-1876.

[49] C. Wei, L. Ma, H. B. Wei, Z. W. Liu, Z. Q. Bian, C. H. Huang, *Sci. China Technol. Sci.* **2018**, *61*, 1265-1285.

[50] W. S. Perry, S. J. Pope, C. Allain, B. J. Coe, A. M. Kenwright, S. Faulkner, *Dalton Trans.* **2010**, *39*, 10974-10983.

[51] O. Kahn, *Magnetochemistry*, Vol. 1, VCH, New York, **1993**.

[52] H. Luecken, *Magnetochemie*, Vol. 1, Teubner, Stuttgart - Leipzig, **1999**.

[53] W. H. Bragg, *Nature* **1915**, *95*, 561.

[54] E. J. W. Verwey, J. H. De Boer, *Recl. Trav. Chim. Pays-Bas* **1936**, 531-540.

[55] P. W. Anderson, *Phys. Rev.* **1950**, *79*, 350-356.

[56] J. B. Goodenough, *Phys. Rev.* **1955**, *100*, 564-573.

[57] J. Kanamori, *J. Phys. Chem. Solids* **1959**, *10*, 87-98.

[58] C. Zener, *Phys. Rev.* **1951**, *82*, 403-405.

[59] B. Bechlars, D. M. D'Alessandro, D. M. Jenkins, A. T. Iavarone, S. D. Glover, C. P. Kubiak, J. R. Long, *Nat. Chem.* **2010**, *2*, 362-368.

[60] A. K. Powell, *Nat. Chem.* **2010**, *2*, 351-352.

[61] A. Abragam, B. Bleaney, *Electron Paramagnetic Resonance of Transition Ions*, Vol. 1, Clarendon Press, Oxford, **1970**.

[62] P. Kalita, J. Goura, J. Manuel Herrera Martínez, E. Colacio, V. Chandrasekhar, *Eur. J. Inorg. Chem.* **2019**, 212-220.

[63] G. Czycholl, *Theoretische Festkörperphysik Band 2*, Vol. 4, Springer Spektrum, Berlin, **2017**.

[64] F. Biedermann, H. J. Schneider, *Chem. Rev.* **2016**, *116*, 5216-5300.

[65] J. D. Watson, F. H. C. Crick, *Nature* **1953**, *171*, 737-738.

[66] J. Emsley, *Chem. Soc. Rev.* **1980**, *9*, 91-124.

[67] J. W. Larson, T. B. McMahon, *Inorg. Chem.* **1984**, *23*, 2029-2033.

[68] F. B. van Duijneveldt, J. N. Murrell, *J. Chem. Phys.* **1967**, *46*, 1759-1767.

[69] V. Bertolasi, P. Gilli, V. Ferretti, G. Gilli, *J. Am. Chem. Soc.* **1991**, *113*, 4917-4925.

[70] G. Gilli, F. Belluci, V. Ferretti, V. Bertolasi, *J. Am. Chem. Soc.* **1989**, *111*, 1023-1028.

[71] J. F. Beck, Y. Mo, *J. Comput. Chem.* **2007**, *28*, 455-466.

[72] S. Grimme, *Angew. Chem. Int. Ed.* **2008**, *47*, 3430-3434.

[73] C. R. Martinez, B. L. Iverson, *Chem. Sci.* **2012**, *3*, 2191-2201.

[74] Y. Zhao, D. G. Truhlar, *J. Phys. Chem. A Lett.* **2005**, *109*, 4209-4212.

[75] C. A. Hunter, J. K. M. Sanders, *J. Am. Chem. Soc.* **1990**, *112*, 5525-5534.

[76] J. Björk, F. Hanke, C.-A. Palma, P. Samori, M. Cecchini, M. Persson, *J. Phys. Chem. Lett.* **2010**, *1*, 3407-3412.

[77] P. Kalita, P. Nayak, N. Ahmed, J. M. Herrera, K. Venkatasubbaiah, E. Colacio, V. Chandrasekhar, *Dalton Trans.* **2020**, *49*, 15404-15416.

[78] G. Cavallo, P. Metrangolo, R. Milani, T. Pilati, A. Priimagi, G. Resnati, G. Terraneo, *Chem. Rev.* **2016**, *116*, 2478-2601.

[79] P. Metrangolo, F. Meyer, T. Pilati, G. Resnati, G. Terraneo, *Angew. Chem. Int. Ed.* **2008**, *47*, 6114-6127.

[80] X. Yu, C. Houtman, R. H. Atalla, *Carbohydr. Res.* **1996**, *292*, 129-141.

[81] J. Rezac, A. de la Lande, *Phys. Chem. Chem. Phys.* **2016**, *19*, 791-803.

[82] L. P. Wolters, P. Schyman, M. J. Pavan, W. L. Jorgensen, F. M. Bickelhaupt, S. Kozuch, *Comput. Mol. Sci.* **2014**, *4*, 523-540.

[83] K. E. Riley, P. Hobza, *J. Chem. Theory Comput.* **2008**, *4*, 232-242.

[84] T. Clark, M. Hennemann, J. S. Murray, P. Politzer, *J. Mol. Model.* **2007**, *13*, 291-296.

[85] K. E. Riley, P. Hobza, *Phys. Chem. Chem. Phys.* **2013**, *15*, 17742-17751.

[86] P. Metrangolo, H. Neukirch, T. Pilati, G. Resnati, *Acc. Chem. Res.* **2005**, *38*, 386-395.

[87] F. Guthrie, *J. Chem. Soc.* **1863**, *16*, 239-244.

[88] O. Hassel, J. Hvoslef, *Acta Chem. Scand.* **1954**, *8*, 873.

[89] O. Hassel, K. O. Stromme, *Acta Chem. Scand.* **1958**, *12*, 1146.

[90] G. R. Desiraju, R. Parthasarathy, *J. Am. Chem. Soc.* **1989**, *111*, 8725-8726.

[91] S. Scheiner, *Cryst. Growth Des.* **2022**, *22*, 2692-2702.

[92] A. Mukherjee, S. Tothadi, G. R. Desiraju, *Acc. Chem. Res.* **2014**, *47*, 2514-2524.

[93] T. Lis, *Acta Cryst B* **1980**, *36*, 2042-2046.

[94] A. M. Ako, I. J. Hewitt, V. Mereacre, R. Clerac, W. Wernsdorfer, C. E. Anson, A. K. Powell, *Angew. Chem. Int. Ed.* **2006**, *45*, 4926-4929.

[95] O. Waldmann, *Inorg. Chem.* **2007**, *46*, 10035-10037.

[96] C.-I. Yang, W. Wernsdorfer, G.-H. Lee, H.-L. Tsai, *J. Am. Chem. Soc.* **2007**, *129*, 456-457.

[97] J. M. Zadrozny, D. J. Xiao, M. Atanasov, G. J. Long, F. Grandjean, F. Neese, J. R. Long, *Nat. Chem.* **2013**, *5*, 577-581.

[98] P. C. Bunting, M. Atanasov, E. Damgaard-Moller, M. Perfetti, I. Crassee, M. Orlita, J. Overgaard, J. van Slageren, F. Neese, J. R. Long, *Science* **2018**, *362*, eaat7319.

[99] N. Ishikawa, M. Sugita, T. Ishikawa, S.-Y. Koshihara, Y. Kaizu, *J. Am. Chem. Soc.* **2003**, *125*, 8694-8695.

[100] N. Ishikawa, M. Sugita, T. Ishikawa, S.-Y. Koshihara, Y. Kaizu, *J. Chem. Phys. B* **2004**, *108*, 11265-11271.

[101] L. Ungur, L. F. Chibotaru, *Phys. Chem. Chem. Phys.* **2011**, *13*, 20086-20090.

[102] K. Karachousos-Spiliotakopoulos, V. Tangoulis, N. Panagiotou, A. Tasiopoulos, E. Moreno-Pineda, W. Wernsdorfer, M. Schulze, A. M. P. Botas, L. D. Carlos, *Dalton. Trans.* **2022**, *51*, 8208-8216.

[103] S. Xue, L. Ungur, Y. N. Guo, J. Tang, L. F. Chibotaru, *Inorg. Chem.* **2014**, 53, 12658-12663.

[104] E. Colacio, J. Ruiz, E. Ruiz, E. Cremades, J. Krzystek, S. Carretta, J. Cano, T. Guidi, W. Wernsdorfer, E. K. Brechin, *Angew. Chem. Int. Ed.* **2013**, 52, 9130-9134.

[105] D. Gatteschi, R. Sessoli, *Angew. Chem. Int. Ed.* **2003**, 42, 268-297.

[106] H. A. Kramers, *Proc. R. Acad. Sci.* **1930**, 33, 959-972.

[107] J. D. Rinehart, J. R. Long, *Chem. Sci.* **2011**, 2, 2078-2085.

[108] S. Osa, T. Kido, N. Matsumoto, N. Re, A. Pochaba, J. Mrozinski, *J. Am. Chem. Soc.* **2004**, 126, 420-421.

[109] A. Dey, J. Acharya, V. Chandrasekhar, *Chem. Asian J.* **2019**, 14, 4433-4453.

[110] L. R. Piquer, E. C. Sanudo, *Dalton Trans.* **2015**, 44, 8771-8780.

[111] Y. Peng, A. K. Powell, *Coord. Chem. Rev.* **2021**, 426, 213490.

[112] T. Gupta, M. F. Beg, G. Rajaraman, *Inorg. Chem.* **2016**, 55, 11201-11215.

[113] G. Rajaraman, F. Totti, A. Bencini, A. Caneschi, R. Sessoli, D. Gatteschi, *Dalton Trans.* **2009**, 3153-3161.

[114] K. R. Vignesh, S. K. Langley, K. S. Murray, G. Rajaraman, *Chem. Eur. J.* **2017**, 23, 1654-1666.

[115] A. M. Ako, V. Mereacre, R. Clerac, W. Wernsdorfer, I. J. Hewitt, C. E. Anson, A. K. Powell, *Chem. Commun.* **2009**, 544-546.

[116] A. Baniodeh, Y. Liang, C. E. Anson, N. Magnani, A. K. Powell, A.-N. Unterreiner, S. Seyfferle, M. Slota, M. Dressel, L. Bogani, K. Goß, *Adv. Funct. Mater.* **2014**, 24, 6280-6290.

[117] A. Baniodeh, N. Magnani, Y. Lan, G. Buth, C. E. Anson, J. Richter, M. Affronte, J. Schnack, A. K. Powell, *npj Quant. Mater.* **2018**, 3, 10.

[118] K. R. Vignesh, A. Soncini, S. K. Langley, W. Wernsdorfer, K. S. Murray, G. Rajaraman, *Nat. Commun.* **2017**, 8, 1023.

[119] H. Kaemmerer, A. Baniodeh, Y. Peng, E. Moreno-Pineda, M. Schulze, C. E. Anson, W. Wernsdorfer, J. Schnack, A. K. Powell, *J. Am. Chem. Soc.* **2020**, 142, 14838-14842.

[120] S. Demir, M. I. Gonzalez, L. E. Darago, W. J. Evans, J. R. Long, *Nat. Commun.* **2017**, 8, 2144-.

[121] J. D. Rinehart, M. Fang, W. J. Evans, J. R. Long, *Nat. Chem.* **2011**, 3, 538-542.

[122] S. Demir, I.-R. Jeon, J. R. Long, T. D. Harris, *Coord. Chem. Rev.* **2015**, 289-290, 149-176.

[123] S. Demir, M. Nippe, M. I. Gonzalez, J. R. Long, *Chem. Sci.* **2014**, 5, 4701-4711.

[124] S. Demir, J. M. Zadrozny, M. Nippe, J. R. Long, *J. Am. Chem. Soc.* **2012**, 134, 18546-18549.

[125] E. M. Fatila, M. Rouzieres, M. C. Jennings, A. J. Lough, R. Clerac, K. E. Preuss, *J. Am. Chem. Soc.* **2013**, 135, 9596-9599.

[126] C. A. Gould, L. E. Darago, M. I. Gonzalez, S. Demir, J. R. Long, *Angew. Chem. Int. Ed.* **2017**, 56, 10103-10107.

[127] F. S. Guo, R. A. Layfield, *Chem. Commun.* **2017**, 53, 3130-3133.

[128] B. S. Dolinar, S. Gomez-Coca, D. I. Alexandropoulos, K. R. Dunbar, *Chem. Commun.* **2017**, 53, 2283-2286.

[129] F. Liu, G. Velkos, D. S. Krylov, L. Spree, M. Zalibera, R. Ray, N. A. Samoylova, C. H. Chen, M. Rosenkranz, S. Schiemenz, F. Ziegs, K. Nenkov, A. Kostanyan, T. Greber, A. U. B. Wolter, M. Richter, B. Buchner, S. M. Avdoshenko, A. A. Popov, *Nat. Commun.* **2019**, 10, 571.

[130] J. J. Baldovi, S. Cardona-Serra, J. M. Clemente-Juan, E. Coronado, A. Gaita-Arino, A. Palii, *Inorg. Chem.* **2012**, 51, 12565-12574.

[131] S. K. Singh, T. Gupta, G. Rajaraman, *Inorg. Chem.* **2014**, 53, 10835-10845.

[132] J. D. Hilgar, M. G. Bernbeck, B. S. Flores, J. D. Rinehart, *Chem. Sci.* **2018**, 9, 7204-7209.

[133] S. D. Jiang, B. W. Wang, H. L. Sun, Z. M. Wang, S. Gao, *J. Am. Chem. Soc.* **2011**, 133, 4730-4733.

[134] J. J. Le Roy, L. Ungur, I. Korobkov, L. F. Chibotaru, M. Murugesu, *J. Am. Chem. Soc.* **2014**, 136, 8003-8010.

[135] K. R. Meihaus, J. R. Long, *J. Am. Chem. Soc.* **2013**, 135, 17952-17957.

[136] C. A. P. Goodwin, F. Ortu, D. Reta, N. F. Chilton, D. P. Mills, *Nature* **2017**, 548, 439-442.

[137] R. K. McClain, C. A. Gould, K. Chakarawet, S. J. Teat, T. J. Groshens, J. R. Long, B. G. Harvey, *Chem. Sci.* **2018**, 9, 8492-8503.

[138] T. Shang, F. Lu, J. Tao, Y. Q. Zhang, *J. Phys. Chem. A* **2023**, 127, 3088-3095.

[139] M. Briganti, F. Santanni, L. Tesi, F. Totti, R. Sessoli, A. Lunghi, *J. Am. Chem. Soc.* **2021**, 143, 13633-13645.

[140] L. Gu, R. Wu, *Phys. Rev. Lett.* **2020**, *125*, 117203.

[141] L. Gu, R. Wu, *Phys. Rev. B* **2021**, *103*, 014401.

[142] A. Lunghi, F. Totti, R. Sessoli, S. Sanvito, *Nat. Commun.* **2017**, *8*, 14620.

[143] R. F. Pfleger, S. Schlittenhardt, M. P. Merkel, M. Ruben, K. Fink, C. E. Anson, J. Bendix, A. K. Powell, *Chem. Eur. J.* **2021**, *27*, 15085-15094.

[144] Y.-Q. Zhai, Y.-Z. Zheng, *J. Mater. Chem. C* **2021**, *9*, 8096-8098.

[145] A. R. Forrester, R. H. Thomson, *Nature* **1964**, *203*, 74-75.

[146] G. Poneti, K. Bernot, L. Bogani, A. Caneschi, R. Sessoli, W. Wernsdorfer, D. Gatteschi, *Chem. Commun.* **2007**, 1807-1809.

[147] X. L. Wang, L. C. Li, D. Z. Liao, *Inorg. Chem.* **2010**, *49*, 4735-4737.

[148] D. Luneau, *Eur. J. Inorg. Chem.* **2020**, 597-604.

[149] R. Tanimoto, T. Wada, K. Okada, D. Shiomi, K. Sato, T. Takui, S. Suzuki, T. Naota, M. Kozaki, *Inorg. Chem.* **2022**, *61*, 3018-3023.

[150] G. Novitchi, S. Shova, C. Train, *Inorg. Chem.* **2022**, *61*, 17037-17048.

[151] M. B. Mills, H. K. S. Young, G. Wehrle, W. R. Verduyn, X. Feng, P. D. Boyle, P. Dechambenoit, E. R. Johnson, K. E. Preuss, *Cryst. Growth Des.* **2021**, *21*, 5669-5677.

[152] M. Witwicki, A. Lewinska, A. Ozarowski, *Phys. Chem. Chem. Phys.* **2021**, *23*, 17408-17419.

[153] R. G. Hicks, *Stable Radicals: Fundamentals and Applied Aspects of Odd-Electron Compounds*, John Wiley & Sons, Chichester, **2010**.

[154] K. Zhang, M. J. Monteiro, Z. Jia, *Polym. Chem.* **2016**, *7*, 5589-5614.

[155] Y. Hattori, R. Kitajima, W. Ota, R. Matsuoka, T. Kusamoto, T. Sato, K. Uchida, *Chem. Sci.* **2022**, *13*, 13418-13425.

[156] H.-D. Li, S.-G. Wu, M.-L. Tong, *Chem. Commun.* **2023**, *59*, 6159-6170.

[157] X. Ma, E. A. Suturina, M. Rouzieres, M. Platunov, F. Wilhelm, A. Rogalev, R. Clerac, P. Dechambenoit, *J. Am. Chem. Soc.* **2019**, *141*, 7721-7725.

[158] M. Takahashi, P. Turek, Y. Nakazawa, M. Tamura, K. Nozawa, D. Shiomi, M. Ishikawa, M. Kinoshita, *Phys. Rev. Lett.* **1991**, *67*, 746-748.

[159] M. B. Mills, T. Wohlhauser, B. Stein, W. R. Verduyn, E. Song, P. Dechambenoit, M. Rouzieres, R. Clerac, K. E. Preuss, *J. Am. Chem. Soc.* **2018**, *140*, 16904-16908.

[160] J. Mahmood, J.-B. Baek, *Chem* **2019**, *5*, 1012-1014.

[161] R. S. P. Mulliken, W. B. Person, *Molecular Complexes: A Lecture and Reprint Volume* John Wiley & Sons, New York, **1969**.

[162] K. E. Preuss, *Polyhedron* **2014**, 79, 1-15.

[163] C. A. Michalowicz, M. B. Mills, E. Song, D. V. Soldatov, P. D. Boyle, M. Rouzieres, R. Clerac, K. E. Preuss, *Dalton Trans.* **2019**, 48, 4514-4519.

[164] A. Bondi, *J. Phys. Chem.* **1964**, 68, 441-451.

[165] E. M. Fatila, R. A. Mayo, M. Rouzières, M. C. Jennings, P. Dechambenoit, D. V. Soldatov, C. Mathonière, R. Clérac, C. Coulon, K. E. Preuss, *Chem. Mater.* **2015**, 27, 4023-4032.

[166] S. Kanegawa, S. Karasawa, M. Maeyama, M. Nakano, N. Koga, *J. Am. Chem. Soc.* **2008**, 130, 3079-3094.

[167] G. K. Gransbury, M. E. Boulon, R. A. Mole, R. W. Gable, B. Moubaraki, K. S. Murray, L. Sorace, A. Soncini, C. Boskovic, *Chem. Sci.* **2019**, 10, 8855-8871.

[168] L. Michaelis, E. S. Hill, *J. Gen. Physiol.* **1933**, 16, 859-873.

[169] C. L. Bird, A. T. Kuhn, *Chem. Soc. Rev.* **1981**, 10, 49-82.

[170] W. Kaim, B. Schwederski, *Coord. Chem. Rev.* **2010**, 254, 1580-1588.

[171] R. J. Mortimer, D. R. Rosseinsky, P. M. S. Monk, *Electrochromic Materials and Devices*, Wiley-VCH, Weinheim, **2015**.

[172] F. Laghrib, M. Bakasse, S. Lahrich, M. A. El Mhammedi, *Mater. Sci. Eng. C* **2020**, 107, 110349.

[173] A. S. Abouelwafa, C. E. Anson, A. Hauser, H. H. Patterson, F. Baril-Robert, X. Li, A. K. Powell, *Inorg. Chem.* **2012**, 51, 1294-1301.

[174] M. Freitag, L. Gundlach, P. Piotrowiak, E. Galoppini, *J. Am. Chem. Soc.* **2012**, 134, 3358-3366.

[175] R. J. Mortimer, *Electrochim. Acta* **1999**, 44, 2971-2981.

[176] S. Durben, T. Baumgartner, *Angew. Chem. Int. Ed.* **2011**, 50, 7948-7952.

[177] A. Beneduci, S. Cospito, M. La Deda, L. Veltri, G. Chidichimo, *Nat. Commun.* **2014**, 5, 3105.

[178] L. Striepe, T. Baumgartner, *Chem. Eur. J.* **2017**, 23, 16924-16940.

[179] J. Ding, C. Zheng, L. Wang, C. Lu, B. Zhang, Y. Chen, M. Li, G. Zhai, X. Zhuang, *J. Mater. Chem. A* **2019**, 7, 23337-23360.

[180] S. Cantekin, A. J. Markvoort, J. A. Elemans, A. E. Rowan, R. J. Nolte, *J. Am. Chem. Soc.* **2015**, 137, 3915-3923.

[181] A. C. Fahrenbach, C. J. Bruns, H. Li, A. Trabolsi, A. Coskun, J. F. Stoddart, *Acc. Chem. Res.* **2014**, *47*, 482-493.

[182] A. Trabolsi, N. Khashab, A. C. Fahrenbach, D. C. Friedman, M. T. Colvin, K. K. Coti, D. Benitez, E. Tkatchouk, J. C. Olsen, M. E. Belowich, R. Carmielli, H. A. Khatib, W. A. Goddard, 3rd, M. R. Wasielewski, J. F. Stoddart, *Nat. Chem.* **2010**, *2*, 42-49.

[183] W. Matheis, J. Poppe, W. Kaim, S. Zalis, *J. Chem. Soc. Perkin Trans. 2* **1994**, 1923-1928.

[184] N. Leblanc, S. Sproules, A. K. Powell, *New J. Chem.* **2017**, *41*, 2949-2954.

[185] C. G. Claessens, J. F. Stoddart, *J. Phys. Org. Chem.* **1997**, *10*, 254-272.

[186] C. F. Macrae, I. Sovago, S. J. Cottrell, P. T. A. Galek, P. McCabe, E. Pidcock, M. Platings, G. P. Shields, J. S. Stevens, M. Towler, P. A. Wood, *J. Appl. Crystallogr.* **2020**, *53*, 226-235.

[187] G. Socrates, *Infrared and Raman Characteristic Group Frequencies: Tables and Charts*, Vol. 3, John Wiley & Sons, **2004**.

[188] K. L. Fu, M. Y. Yao, D. B. Wang, H. C. Zhao, G. W. Cheng, S. Yang, *IOP Conf. Series: Earth and Environmental Science* **2019**, 354.

[189] J. Leier, *Transiente Untersuchungen zu Ladungs-transferprozessen photoangeregter Moleküle in Lösung im UV-Vis-NIR-Bereich*, Karlsruhe Institute of Technology (KIT), PhD thesis, (KIT), **2021**.

[190] Y. F. Schneider, *Extending the Biquinoxen Ligand Platform*, Karsruhe Institute of Technology (KIT), Bachelor thesis (KIT), **2020**.

[191] N. E. Brese, M. O'Keeffe, *Acta Cryst. B* **1991**, *47*, 192-197.

[192] I. D. Brown, D. Altermatt, *Acta Cryst. B* **1985**, *41*, 244-247.

[193] W. Liu, H. H. Thorp, *Inorg. Chem.* **1993**, *32*, 4102-4105.

[194] G. P. Shields, P. R. Raithby, F. H. Allen, W. D. S. Motherwell, *Acta Cryst. B* **2000**, *56*, 455-465.

[195] M. Kertesz, *Chem. Eur. J.* **2019**, *25*, 400-416.

[196] Y. Hosokoshi, K. Katoh, Y. Nakazawa, H. Nakano, K. Inoue, *J. Am. Chem. Soc.* **2001**, *123*, 7921-7922.

[197] T. Li, G. Tan, D. Shao, J. Li, Z. Zhang, Y. Song, Y. Sui, S. Chen, Y. Fang, X. Wang, *J. Am. Chem. Soc.* **2016**, *138*, 10092-10095.

[198] H. Tian, L. Ungur, L. Zhao, S. Ding, J. Tang, L. F. Chibotaru, *Chem. Eur. J.* **2018**, *24*, 9928-9939.

[199] H. Tian, M. Wang, L. Zhao, Y. N. Guo, Y. Guo, J. Tang, Z. Liu, *Chem. Eur. J.* **2012**, *18*, 442-445.

[200] H. Tian, L. Zhao, Y. N. Guo, Y. Guo, J. Tang, Z. Liu, *Chem. Commun.* **2012**, *48*, 708-710.

[201] H. Tian, L. Zhao, H. Lin, J. Tang, G. Li, *Chem. Eur. J.* **2013**, *19*, 13235-13241.

[202] A. S. Chesman, D. R. Turner, B. Moubaraki, K. S. Murray, G. B. Deacon, S. R. Batten, *Dalton Trans.* **2012**, *41*, 10903-10909.

[203] W. Huang, W. Chen, Q. Bai, Z. Zhang, M. Feng, Z. Zheng, *Angew. Chem. Int. Ed.* **2022**, *61*, e202205385.

[204] X. M. Luo, Z. B. Hu, Q. F. Lin, W. Cheng, J. P. Cao, C. H. Cui, H. Mei, Y. Song, Y. Xu, *J. Am. Chem. Soc.* **2018**, *140*, 11219-11222.

[205] X.-Y. Zheng, J.-B. Peng, X.-J. Kong, L.-S. Long, L.-S. Zheng, *Inorg. Chem. Front.* **2016**, *3*, 320-325.

[206] Y. Zhou, X. Y. Zheng, J. Cai, Z. F. Hong, Z. H. Yan, X. J. Kong, Y. P. Ren, L. S. Long, L. S. Zheng, *Inorg. Chem.* **2017**, *56*, 2037-2041.

[207] J. Goura, E. Colacio, J. M. Herrera, E. A. Suturina, I. Kuprov, Y. Lan, W. Wernsdorfer, V. Chandrasekhar, *Chem. Eur. J.* **2017**, *23*, 16621-16636.

[208] P. C. Andrews, T. Beck, C. M. Forsyth, B. H. Fraser, P. C. Junk, M. Massi, P. W. Roesky, *Dalton Trans.* **2007**, 5651-5654.

[209] P. Bag, S. Dutta, P. Biswas, S. K. Maji, U. Florke, K. Nag, *Dalton Trans.* **2012**, *41*, 3414-3423.

[210] I. A. Gass, B. Moubaraki, S. K. Langley, S. R. Batten, K. S. Murray, *Chem. Commun.* **2012**, *48*, 2089-2091.

[211] K. S. Jeong, Y. S. Kim, Y. J. Kim, E. Lee, J. H. Yoon, W. H. Park, Y. W. Park, S. J. Jeon, Z. H. Kim, J. Kim, N. Jeong, *Angew. Chem. Int. Ed.* **2006**, *45*, 8134-8138.

[212] H. Ke, L. Zhao, G. F. Xu, Y. N. Guo, J. Tang, X. Y. Zhang, H. J. Zhang, *Dalton Trans.* **2009**, 10609-10613.

[213] P. Kumar, A. Swain, J. Acharya, Y. Li, V. Kumar, G. Rajaraman, E. Colacio, V. Chandrasekhar, *Inorg. Chem.* **2022**, *61*, 11600-11621.

[214] S. K. Langley, B. Moubaraki, K. S. Murray, *Inorg. Chem.* **2012**, *51*, 3947-3949.

[215] Y. M. Li, W. W. Kuang, L. L. Zhu, Y. Xu, P. P. Yang, *Eur. J. Inorg. Chem.* **2016**, *2016*, 4996-5003.

[216] H. J. Lun, M. H. Du, D. H. Wang, X. J. Kong, L. S. Long, L. S. Zheng, *Inorg. Chem.* **2020**, *59*, 7900-7904.

[217] M. C. Majee, S. M. Towsif Abtab, D. Mondal, M. Maity, M. Weselski, M. Witwicki, A. Bienko, M. Antkowiak, G. Kamieniarz, M. Chaudhury, *Dalton Trans.* **2018**, *47*, 3425-3439.

[218] L. Natrajan, J. Pecaut, M. Mazzanti, *Dalton Trans.* **2006**, 1002-1005.

[219] E. M. Pineda, G. Lorusso, K. H. Zangana, E. Palacios, J. Schnack, M. Evangelisti, R. E. P. Winpenny, E. J. L. McInnes, *Chem. Sci.* **2016**, *7*, 4891-4895.

[220] A. Rasamsetty, B. Viswanathan, E. C. Sañudo, *ChemistrySelect* **2016**, *1*, 3323-3327.

[221] X.-L. Tang, W.-H. Wang, W. Dou, J. Jiang, W.-S. Liu, W.-W. Qin, G.-L. Zhang, H.-R. Zhang, K.-B. Yu, L.-M. Zheng, *Angew. Chem. Int. Ed.* **2009**, *48*, 3499-3502.

[222] H. Tian, L. Zhao, J. Tang, *Cryst. Growth Des.* **2018**, *18*, 1173-1181.

[223] S. Xue, L. Zhao, Y. N. Guo, P. Zhang, J. Tang, *Chem. Commun.* **2012**, *48*, 8946-8948.

[224] L. Zhao, S. Xue, J. Tang, *Inorg. Chem.* **2012**, *51*, 5994-5996.

[225] A. S. Chesman, D. R. Turner, S. K. Langley, B. Moubaraki, K. S. Murray, G. B. Deacon, S. R. Batten, *Inorg. Chem.* **2015**, *54*, 792-800.

[226] Y. N. Guo, X. H. Chen, S. Xue, J. Tang, *Inorg. Chem.* **2012**, *51*, 4035-4042.

[227] J. Wu, X. L. Li, L. Zhao, M. Guo, J. Tang, *Inorg. Chem.* **2017**, *56*, 4104-4111.

[228] B. F. Abrahams, M. G. Haywood, R. Robson, D. A. Slizys, *Angew. Chem. Int. Ed.* **2003**, *42*, 1112-1115.

[229] G. J. Cooper, G. N. Newton, P. Kogerler, D. L. Long, L. Engelhardt, M. Luban, L. Cronin, *Angew. Chem. Int. Ed.* **2007**, *46*, 1340-1344.

[230] G. B. Deacon, C. M. Forsyth, P. C. Junk, A. Urbatsch, *Eur. J. Inorg. Chem.* **2010**, 2787-2797.

[231] S. Sun, D. Gebauer, H. Cölfen, *Chem. Commun.* **2016**, *52*, 7036-7038.

[232] X.-J. Kong, Y.-R. Ren, L.-S. Long, Z. Zheng, R.-B. Huang, L.-S. Zheng, *J. Am. Chem. Soc.* **2007**, *129*, 7016-7017.

[233] K. Xiong, F. Jiang, Y. Gai, Y. Zhou, D. Yuan, K. Su, X. Wang, M. Hong, *Inorg. Chem.* **2012**, *51*, 3283-3288.

[234] C. B. Aakeröy, N. R. Champness, C. Janiak, *CrystEngComm* **2010**, *12*, 22-43.

[235] V. R. Thalladi, B. S. Goud, V. J. Hoy, F. H. Allen, J. A. K. Howard, G. R. Desiraju, *Chem. Commun.* **1996**, 401-402.

[236] Z. Han, G. Czap, C.-L. Chiang, C. Xu, P. J. Wagner, X. Wei, Y. Zhang, R. Wu, W. Ho, *Science* **2017**, 358, 206-210.

[237] L. Brammer, G. Mínguez Espallargas, S. Libri, *CrystEngComm* **2008**, 10, 1712-1727.

[238] R. W. Troff, T. Mäkelä, F. Topić, A. Valkonen, K. Raatikainen, K. Rissanen, *Eur. J. Org. Chem.* **2013**, 2013, 1617-1637.

[239] K. P. Carter, S. J. A. Pope, M. Kalaj, R. J. Holmberg, M. Murugesu, C. L. Cahill, *Z. Anorg. Allg. Chem.* **2017**, 643, 1948-1955.

[240] K. P. Carter, K. E. Thomas, S. J. Pope, R. J. Holmberg, R. J. Butcher, M. Murugesu, C. L. Cahill, *Inorg. Chem.* **2016**, 55, 6902-6915.

[241] K. P. Carter, C. H. F. Zulato, C. L. Cahill, *CrystEngComm* **2014**, 16, 10189-10202.

[242] M. Atzori, F. Artizzu, E. Sessini, L. Marchio, D. Loche, A. Serpe, P. Deplano, G. Concas, F. Pop, N. Aavarvari, M. L. Mercuri, *Dalton Trans.* **2014**, 43, 7006-7019.

[243] R. T. Butcher, J. J. Novoa, J. Ribas-Arino, A. W. Sandvik, M. M. Turnbull, C. P. Landee, B. M. Wells, F. F. Awwadi, *Chem. Commun.* **2009**, 1359-1361.

[244] J. A. Schlueter, H. Park, G. J. Halder, W. R. Armand, C. Dunmars, K. W. Chapman, J. L. Manson, J. Singleton, R. McDonald, A. Plonczak, J. Kang, C. Lee, M. H. Whangbo, T. Lancaster, A. J. Steele, I. Franke, J. D. Wright, S. J. Blundell, F. L. Pratt, J. deGeorge, M. M. Turnbull, C. P. Landee, *Inorg. Chem.* **2012**, 51, 2121-2129.

[245] X. Pang, X. R. Zhao, H. Wang, H.-L. Sun, W. J. Jin, *Cryst. Growth Des.* **2013**, 13, 3739-3745.

[246] D. Wang, Z. Wang, S. Wu, Arramel, X. Yin, C. S. Tang, Y. P. Feng, J. Wu, A. T. S. Wee, *ACS Nanosci. Au* **2022**, 2, 333-340.

[247] D. Seufert, *Quantifying 3d-4f Interactions in Dimetallic Coordination Systems*, Karlsruhe Institute of Technology (KIT), Master thesis, (KIT), **2021**.

[248] R. D. Shannon, *Acta Cryst. A* **1976**, 32, 751-767.

[249] G. Busca, V. Lorenzelli, *Mater. Chem.* **1982**, 7, 89-126.

[250] S. R. Tamang, A. Singh, D. Bedi, A. R. Bazkiae, A. A. Warner, K. Glogau, C. McDonald, D. K. Unruh, M. Findlater, *Nat. Catal.* **2020**, 3, 154-162.

[251] C. Guo, F. Zhang, C. Yu, Y. Luo, *Inorg. Chem.* **2021**, *60*, 13122-13135.

[252] S. Ge, A. Meetsma, B. Hessen, *Organometallics* **2008**, *27*, 5339-5346.

[253] S. Ge, A. Meetsma, B. Hessen, *Organometallics* **2009**, *28*, 719-726.

[254] P. L. Roulhac, G. L. Palenik, *Inorg. Chem.* **2003**, *42*, 118-121.

[255] A. Trzesowska, R. Kruszynski, T. J. Bartczak, *Acta Cryst. B* **2006**, *62*, 745-753.

[256] V. Nair, L. Balagopal, R. Rajan, J. Mathew, *Acc. Chem. Res.* **2004**, *37*, 21-30.

[257] D. J. Wasylenko, C. Ganesamoorthy, M. A. Henderson, C. P. Berlinguette, *Inorg. Chem.* **2011**, *50*, 3662-3672.

[258] L. Mathey, M. Paul, C. Coperet, H. Tsurugi, K. Mashima, *Chem. Eur. J.* **2015**, *21*, 13454-13461.

[259] L. A. Solola, P. J. Carroll, E. J. Schelter, *J. Organometal. Chem.* **2018**, *857*, 5-9.

[260] D. Werner, G. B. Deacon, P. C. Junk, R. Anwander, *Chem. Eur. J.* **2014**, *20*, 4426-4438.

[261] D. E. Morris, D. E. Hobart, *Lanthanide Actinide Res.* **1987**, *2*, 91-103.

[262] N. A. Piro, J. R. Robinson, P. J. Walsh, E. J. Schelter, *Coord. Chem. Rev.* **2014**, *260*, 21-36.

[263] M. K. Assefa, G. Wu, T. W. Hayton, *Chem. Sci.* **2017**, *8*, 7873-7878.

[264] P. L. Damon, G. Wu, N. Kaltsoyannis, T. W. Hayton, *J. Am. Chem. Soc.* **2016**, *138*, 12743-12746.

[265] Y. K. Gun'ko, S. D. Elliott, P. B. Hitchcock, M. F. Lappert, *Dalton Trans.* **2002**, 1852-1856.

[266] V. Mereacre, A. M. Ako, M. N. Akhtar, A. Lindemann, C. E. Anson, A. K. Powell, *Helv. Chim. Acta* **2009**, *92*, 2507-2524.

[267] A. J. Tasiopoulos, A. Mishra, G. Christou, *Polyhedron* **2007**, *26*, 2183-2188.

[268] S. Arumugam, B. Shankar, K. C. Mondal, *Eur. J. Inorg. Chem.* **2020**, *2020*, 4127-4136.

[269] J. W. Sharples, D. Collison, E. J. L. McInnes, J. Schnack, E. Palacios, M. Evangelisti, *Nat. Commun.* **2014**, *5*, 5321-5326.

[270] J. W. Sharples, Y. Z. Zheng, F. Tuna, E. J. McInnes, D. Collison, *Chem. Commun.* **2011**, *47*, 7650-7652.

[271] D. M. D'Alessandro, F. R. Keene, *Chem. Soc. Rev.* **2006**, *35*, 424-440.

[272] D. M. D'Alessandro, F. R. Keene, *Chem. Rev.* **2006**, *106*, 2270-2298.

[273] G. C. Allen, N. S. Hush, *Intervalence-Transfer Absorption. Part 1. Qualitative Evidence for Intervalence Transfer Absorption in Inorganic Systems in Solution and in the Solid State*, John Wiley & Sons, **1967**.

[274] M. B. Robin, P. Day, *Adv. Inorg. Chem. Radiochem.* **1968**, *10*, 247-422.

[275] N. S. Hush, *Electrochim Acta* **1968**, *13*, 1005-1023.

[276] R. A. Marcus, *J. Chem. Phys.* **1956**, *24*, 966-978.

[277] R. A. Marcus, *J. Chem. Phys.* **1957**, *26*, 867-871.

[278] B. S. Brunschwig, C. Creutz, N. Sutin, *Chem. Soc. Rev.* **2002**, *31*, 168-184.

[279] K. D. Demadis, C. M. Hartshorn, T. J. Meyer, *Chem. Rev.* **2001**, *101*, 2655-2685.

[280] C. Creutz, H. Taube, *J. Am. Chem. Soc.* **1972**, *95*, 1086-1094.

[281] B. S. Brunschwig, N. Sutin, *Coord. Chem. Rev.* **1999**, *187*, 233-254.

[282] C. Creutz, M. D. S. Newton, N., *J. Photochem. Photobiol. A: Chem.* **1994**, *82*, 47-59.

[283] J. Tang, P. Zhang, *Lanthanide Single Molecule Magnets*, Springer, Berlin, **2015**.

[284] P. Kalita, J. Goura, P. Nayak, E. Colacio, V. Chandrasekhar, *J. Chem. Sci.* **2021**, *133*, 82.

[285] J. N. Li, N. F. Li, J. L. Wang, X. M. Liu, Q. D. Ping, T. T. Zang, H. Mei, Y. Xu, *Dalton Trans* **2021**, *50*, 13925-13931.

[286] W. M. Wang, X. Y. Xin, N. Qiao, Z. L. Wu, L. Li, J. Y. Zou, *Dalton Trans* **2022**, *51*, 13957-13969.

[287] B. Zhang, X. Zheng, H. Su, Y. Zhu, C. Du, M. Song, *Dalton Trans.* **2013**, *42*, 8571-8574.

[288] E. C. Mazarakioti, K. M. Poole, L. Cunha-Silva, G. Christou, T. C. Stamatatos, *Dalton Trans.* **2014**, *43*, 11456-11460.

[289] L.-F. Li, W.-W. Kuang, Y.-M. Li, L.-L. Zhu, Y. Xu, P.-P. Yang, *New J. Chem.* **2019**, *43*, 1617-1625.

[290] D. A. Galico, A. A. Kitos, J. S. Ovens, F. A. Sigoli, M. Murugesu, *Angew. Chem. Int. Ed.* **2021**, *60*, 6130-6136.

[291] G. Lu, Y. Liu, W. Deng, G.-Z. Huang, Y.-C. Chen, J.-L. Liu, Z.-P. Ni, M. Giansiracusa, N. F. Chilton, M.-L. Tong, *Inorg. Chem. Front.* **2020**, *7*, 2941-2948.

[292] A. S. Chesman, D. R. Turner, B. Moubaraki, K. S. Murray, G. B. Deacon, S. R. Batten, *Chem. Eur. J.* **2009**, *15*, 5203-5207.

[293] L.-Y. Kong, Z.-H. Zhang, H.-F. Zhu, H. Kawaguchi, T.-a. Okamura, M. Doi, Q. Chu, W.-Y. Sun, N. Ueyama, *Angew. Chem.* **2005**, *117*, 4426-4429.

[294] V. A. Blatov, M. O'Keeffe, D. M. Proserpio, *CrystEngComm* **2010**, *12*, 44-48.

[295] V. A. Blatov, A. P. Shevchenko, D. M. Proserpio, *Cryst. Growth Des.* **2014**, *14*, 3576-3586.

[296] R. Busch, A. B. Carter, K. F. Konidaris, I. A. Kuhne, R. Gonzalez, C. E. Anson, A. Powell, *Chem. Eur. J.* **2020**, *26*, 11835-11840.

[297] N. F. Chilton, D. Collison, E. J. McInnes, R. E. Winpenny, A. Soncini, *Nat. Commun.* **2013**, *4*, 2551.

[298] H. Tian, B. L. Wang, J. Lu, H. T. Liu, J. Su, D. Li, J. Dou, *Chem. Commun.* **2018**, *54*, 12105-12108.

[299] S. Lindskog, *Pharmacol. Ther.* **1997**, *74*, 1-20.

[300] Z.-W. Mao, G. Liehr, R. van Eldik, *Dalton Trans.* **2001**, 1593-1600.

[301] A. Company, J.-E. Jee, X. Ribas, J. M. Lopez-Valbuena, L. Gomez, M. Corbella, A. Llobet, J. Mahia, J. Benet-Buchholz, M. Costas, R. van Eldik, *Inorg. Chem.* **2007**, *46*, 9098-9110.

[302] Y. L. Li, H. L. Wang, Z. H. Zhu, J. Li, H. H. Zou, F. P. Liang, *Inorg. Chem.* **2021**, *60*, 16794-16802.

[303] Y. L. Li, H. L. Wang, Z. H. Zhu, J. Li, H. H. Zou, J. M. Peng, F. P. Liang, *Dalton Trans.* **2021**, *51*, 197-202.

[304] F. S. Guo, Y. C. Chen, L. L. Mao, W. Q. Lin, J. D. Leng, R. Tarasenko, M. Orendac, J. Prokleska, V. Sechovsky, M. L. Tong, *Chem. Eur. J.* **2013**, *19*, 14876-14885.

[305] P. Richardson, T. J. Hsu, C. J. Kuo, R. J. Holmberg, B. Gabidullin, M. Rouzieres, R. Clerac, M. Murugesu, P. H. Lin, *Dalton Trans.* **2018**, *47*, 12847-12851.

[306] P. Atkins, J. de Paula, J. Keeler, *Atkin's Physical Chemistry*, Oxford University Press, Oxford, **2018**.

[307] W. T. Carnall, P. R. Fields, B. G. Wybourne, *J. Chem. Phys.* **1965**, *42*, 3797-3806.

[308] G. H. Dieke, *Spectra and Energy Levels of Rare Earth Ions in Crystals*, Interscience Publishers New York, **1968**.

[309] A. V. Malakhovskii, *arXiv preprint arXiv:1507.04210* **2015**.

[310] Y. N. Guo, X. H. Chen, S. Xue, J. Tang, *Inorg. Chem.* **2011**, *50*, 9705-9713.

[311] J. Cirera, E. Ruiz, S. Alvarez, F. Neese, J. Kortus, *Chem. Eur. J.* **2009**, *15*, 4078-4087.

[312] F. Neese, D. A. Pantazis, *Faraday Discuss.* **2011**, *148*, 229-238.

[313] Y. Jiang, R. J. Holmberg, F. Habib, L. Ungur, I. Korobkov, L. F. Chibotaru, M. Murugesu, *RSC Adv.* **2016**, *6*, 56668-56673.

[314] L. Zhang, J. Jung, P. Zhang, M. Guo, L. Zhao, J. Tang, B. Le Guennic, *Chem. Eur. J.* **2016**, *22*, 1392-1398.

[315] H. M. Dong, H. Y. Li, Y. Q. Zhang, E. C. Yang, X. J. Zhao, *Inorg. Chem.* **2017**, *56*, 5611-5622.

[316] K. Zhang, C. Yuan, F. S. Guo, Y. Q. Zhang, Y. Y. Wang, *Dalton Trans.* **2017**, *46*, 186-192.

[317] Q. Chen, F. Ma, Y. S. Meng, H. L. Sun, Y. Q. Zhang, S. Gao, *Inorg. Chem.* **2016**, *55*, 12904-12911.

[318] Y. N. Guo, G. F. Xu, W. Wernsdorfer, L. Ungur, Y. Guo, J. Tang, H. J. Zhang, L. F. Chibotaru, A. K. Powell, *J. Am. Chem. Soc.* **2011**, *133*, 11948-11951.

[319] S. Xue, Y. N. Guo, L. Ungur, J. Tang, L. F. Chibotaru, *Chem. Eur. J.* **2015**, *21*, 14099-14106.

[320] P. Panissod, M. Drillon, *Magnetism: Molecules to Materials IV*, Wiley-VCH, Weinheim, **2002**.

[321] L. Michaelis, *Trans. Electrochem. Soc.* **1937**, *71*, 107-125.

[322] B. Kalyanaraman, *Meth. Enzymol.* **1990**, *186*, 333-343.

[323] F. L. Crane, M. D. Henninger, *Vitam. Horm.* **1966**, *24*, 489-517.

[324] N. Cox, L. Jin, A. Jaszewski, P. J. Smith, E. Krausz, A. W. Rutherford, R. Pace, *Biophys. J.* **2009**, *97*, 2024-2033.

[325] H. Y. Fu, D. Picot, Y. Choquet, G. Longatte, A. Sayegh, J. Delacotte, M. Guille-Collignon, F. Lemaitre, F. Rappaport, F. A. Wollman, *Nat. Commun.* **2017**, *8*, 15274.

[326] A. Caneschi, D. Gatteschi, R. Sessoli, *Acc. Chem. Res.* **1989**, *22*, 392-398.

[327] C. W. Lange, B. J. Conklin, C. G. Pierpont, *Inorg. Chem.* **1994**, *33*, 1276-1283.

[328] C. G. Pierpont, C. W. Lange, *Prog. Inorg. Chem.* **1994**, *41*, 331.

[329] J. Rall, W. Kaim, *J. Chem. Soc. Faraday Trans.* **1994**, *90*, 2905-2908.

[330] C. G. Pierpont, *Coord. Chem. Rev.* **2001**, *219-221*, 415-433.

[331] K. E. Vostrikova, *Coord. Chem. Rev.* **2008**, 252, 1409-1419.

[332] M. K. Biswas, S. C. Patra, A. N. Maity, S. C. Ke, T. Weyhermuller, P. Ghosh, *Dalton Trans.* **2013**, 42, 6538-6552.

[333] P. Zhang, M. Perfetti, M. Kern, P. P. Hallmen, L. Ungur, S. Lenz, M. R. Ringenberg, W. Frey, H. Stoll, G. Rauhut, J. van Slageren, *Chem. Sci.* **2018**, 9, 1221-1230.

[334] W. R. Reed, M. A. Dunstan, R. W. Gable, W. Phonsri, K. S. Murray, R. A. Mole, C. Boskovic, *Dalton Trans.* **2019**, 48, 15635-15645.

[335] A. D. Rae, A. C. Willis, *Z. Kristallogr.* **2003**, 218, 221-230.

[336] F. Calderazzo, C. Forte, F. Marchetti, G. Pampaloni, L. Pieretti, *Helv. Chim. Acta* **2004**, 87, 781-789.

[337] D. R. Eaton, *Inorg. Chem.* **1964**, 3, 1268-1271.

[338] J. Rennert, M. Mayer, J. Levy, J. Kaplan, *Photochem. Photobiol.* **1969**, 10, 267-271.

[339] A. B. Carter, J. Braun, T. Bodenstein, R. F. Pfleger, M. Schulze, T. Kriese, S. F. M. Habermann, E. Moreno Pineda, C. E. Anson, W. Wernsdorfer, L. F. Chibotaru, K. Fink, A. K. Powell, **To be submitted**.

[340] R. Glaum, W. Grunwald, N. Kannengießer, A. Bronova, *Z. Anorg. Allg. Chem.* **2020**, 646, 184-192.

[341] L. Babetto, S. Carlotto, A. Carlotto, M. Rancan, G. Bottaro, L. Armelao, M. Casarin, *Inorg. Chem.* **2021**, 60, 315-324.

[342] J. Chen, S. H. Carpenter, T. V. Fetrow, J. Mengell, M. L. Kirk, A. M. Tondreau, *Inorg. Chem.* **2022**, 61, 18466-18475.

[343] K. Binnemans, *Coord. Chem. Rev.* **2015**, 295, 1-45.

[344] J. R. Hickson, S. J. Horsewill, J. McGuire, C. Wilson, S. Sproules, J. H. Farnaby, *Chem. Commun.* **2018**, 54, 11284-11287.

[345] G. Richer, C. Sandorfy, *J. Mol. Struct. Theochem.* **1985**, 123, 317-327.

[346] M. K. Biswas, S. C. Patra, A. N. Maity, S. C. Ke, N. D. Adhikary, P. Ghosh, *Inorg. Chem.* **2012**, 51, 6687-6699.

[347] K. Binnemans, D. Moors, *J. Mater. Chem.* **2002**, 12, 3374-3376.

[348] J.-C. G. Bünzli, *Lanthanide Probes in Life, Chemical and Earth Sciences* Elsevier, Amsterdam, **1989**.

[349] G.-P. Li, H.-Z. Tang, R.-C. Gao, Y.-Y. Wang, X. Sun, K. Zhang, *Cryst. Growth Des.* **2023**, 23, 1575-1580.

[350] J. Merz, M. Dietz, Y. Vonhausen, F. Wober, A. Friedrich, D. Sieh, I. Krummenacher, H. Braunschweig, M. Moos, M. Holzapfel, C. Lambert, T. B. Marder, *Chem. Eur. J.* **2020**, *26*, 438-453.

[351] Y. H. Chi, J. M. Shi, H. N. Li, W. Wei, E. Cottrill, N. Pan, H. Chen, Y. Liang, L. Yu, Y. Q. Zhang, C. Hou, *Dalton Trans.* **2013**, *42*, 15559-15569.

[352] M. González M, H. Osiry, M. Martínez, J. Rodríguez-Hernández, A. A. Lemus-Santana, E. Reguera, *J. Magn. Magn. Mater.* **2019**, *471*, 70-76.

[353] J. Tang, I. Hewitt, N. T. Madhu, G. Chastanet, W. Wernsdorfer, C. E. Anson, C. Benelli, R. Sessoli, A. K. Powell, *Angew. Chem.* **2006**, *118*, 1761-1765.

[354] J. Luzon, K. Bernot, I. J. Hewitt, C. E. Anson, A. K. Powell, R. Sessoli, *Phys. Rev. Lett.* **2008**, *100*, 247205.

[355] G. R. Hanson, K. E. Gates, C. J. Noble, M. Griffin, A. Mitchell, S. Benson, *J. Inorg. Biochem.* **2004**, *98*, 903-916.

[356] O. V. Dolomanov, A. J. Blake, N. R. Champness, M. Schröder, *J. Appl. Cryst.* **2003**, *36*, 1283-1284.

[357] G. M. Sheldrick, *Acta Cryst. A* **2015**, *71*, 3-8.

[358] G. M. Sheldrick, *Acta Cryst. C* **2015**, *71*, 3-8.

[359] M. d. L. F. Bispo, R. S. B. Gonçalves, C. H. d. S. Lima, L. N. d. F. Cardoso, M. C. S. Lourenço, M. V. N. de Souza, *J. Heterocyclic Chem.* **2012**, *49*, 1317-1322.

[360] R. Busch, *Darstellung heterometallischer 3d/5d- und 5d/4f-Verbindungen mit Hilfe anisotroper Re(IV)-Bausteine*, Karlsruhe Institute of Technology (KIT), PhD thesis (KIT), **2016**.

[361] F. M. Vergara, C. H. Lima, M. Henriques, A. L. Candeia, M. C. Lourenco, L. Ferreira Mde, C. R. Kaiser, M. V. de Souza, *Eur. J. Med. Chem.* **2009**, *44*, 4954-4959.

10. Curriculum Vitae

Personal Details

Name: Jonas Braun
Date of Birth: 27.10.1995
Place of Birth: Karlsruhe
Nationality: German

Education

09/2005 – 06/2013 Goethe-Gymnasium, Karlsruhe
Allgemeine Hochschulreife
10/2014 – 10/2017 Karlsruhe Institute of Technology
Bachelor Chemie, Mark: 1.4
10/2017 – 10/2019 Karlsruhe Institute of Technology
Master Chemie, Mark: 1.0 (with distinction)
since 01/2020 PhD student under the supervision of Prof. Annie K. Powell,
Karlsruhe Institute of Technology using a
Landesgraduiertenförderungsstipendium until 03/2023
Responsible for the organisation of weekly group seminars
Supervision of the Bachelor student Yannik Schneider
2020, the student Daniel Seufert during his Vertieferarbeit
and Master thesis 2020 and 2021
Two-week stay at the University of Glasgow hosted by Dr.
Joy Farnaby using the KHYS Networking Grant in 11/2021

Extracurricular Activities

2013 – 2018 Captain and assistant coach of a local Volleyball team

Conference Attendances

09/2019 European Conference of Molecular Magnetism (ECMM)
2019 in Florence, poster presentation
12/2019 Spin Begins at 60, Meeting dedicated to Prof. Dr. Annie K.
Powell on the occasion of her 60th Birthday, member of the
organising committee
01/2021 Global Young Scientists Summit (GYSS) 2021 in
Singapore (held online), attendant

06/2021 International Conference of Molecular Magnetism (ICMM) 2021 in Manchester (held online), poster presentation

07/2022 ECMM 2022 in Rennes, poster presentation

09/2022 Koordinationschemietreffen (KCT) 2022 in Jena, oral contribution

09/2022 Schau-Ins-Land Meeting 2022 in Wildberg, oral contribution

11. List of Publications

1. F. Ferrari, J. Braun, C. E. Anson, B. D. Wilts, D. Moatsou, C. Bizzarri, *Molecules*, "Cyan-Emitting Cu(I) Complexes and Their Luminescent Metallocopolymers", **2021**, 26, 2567.
2. L.-L. Gracia, E. Barani, J. Braun, A. B. Carter, O. Fuhr, A. K. Powell, K. Fink, C. Bizzarri, *ChemCatChem*, "Photocatalytic Reduction of CO₂ by Highly Efficient Homogeneous Fe^{II} Catalyst based on 2,6-Bis(1',2',3'-triazolyl-methyl)pyridine. Comparison with Analogues." **2022**, 14, e202201163
3. D. Schray, D. Westerbeck, J. Braun, Y. Lan, S. Gómez-Coca, W. Wernsdorfer, E. Ruiz, C. E. Anson, J. Schnack, A. K. Powell, *Inorg. Chem.*, "Fe–Gd Ferromagnetic Cyclic Coordination Cluster [Fe^{III}₄Gd^{III}₄(teaH)₈(N₃)₈(H₂O)] with Magnetic Anisotropy—Theory and Experiment", **2023**, 62, 6642-6648.
4. A. B. Carter, J. Braun, T. Bodenstein, R. F. Pfleger, M. Schulze, T. Kriese, S. F. M. Habermann, E. Moreno-Pineda, C. E. Anson, W. Wernsdorfer, L. F. Chibotaru, K. Fink, A. K. Powell, *J. Am. Chem. Soc.*, „Listening for the Sound of One-Hand Clapping – The Importance of Dipole-Dipole Interactions in Dinuclear Dy SMMs", **to be submitted**.
5. J. Braun, C. E. Anson, G. E. Kostakis, J. Tang, A. K. Powell, „Achieving High Symmetry through Halogen Bonds in an Er₆ Cluster", **in preparation**.
6. J. Braun, Y. Peng, T. Yadav, A. B. Carter, Y. F. Schneider, N. Leblanc, C. E. Anson, K. Fink, A. K. Powell, "How to stabilise a neutral radical ligand using complexation to 3d metal ions and supramolecular interactions", **in preparation**.
7. F. K. Al-Zeidaneen, G. Abbas, O. Fuhr, S. Schlittenhardt, N. Suryadevara, J. Braun, Y. F. Schneider, T. Ruppert, R. F. Pfleger, S. Malik, C. E. Anson, A. K. Powell, *Synthesis*, "Structure and Magnetic properties of Fe₄Ln₄ clusters with a unique spin structure", **in preparation**
8. X. Li, J. Braun, S. Paul, J. Arneth, C. E. Anson, R. Klingeler, W. Wernsdorfer, A. K. Powell, "A Tridecanuclear [V^{III}₅Dy^{III}₈] 3d-4f Single Molecule Magnet" **in preparation**

12. Acknowledgements

First and foremost, I want to thank my supervisor Prof. Dr. Annie Powell not only for the opportunity to conduct the research regarding my interesting PhD project, but also for the ample opportunity for conference visits as well as always having an open ear to any problems that arise. I particularly enjoyed the hours spent in our common room in which she would teach me what molecular magnetism and science in general are about.

Dr. Christopher Anson I want to thank for his help with the refinement of the crystallographic data as well as excellent advice whenever I needed it.

Dr. Olaf Fuhr and Prof. Dr. Dieter Fenske I want to thank for their help and patience when measuring crystal structures.

For proof-reading this thesis, I want to thank Yannik Schneider as well as my father Dr. Matthias Braun.

Dr. Sharali Malik I want to thank for the opportunity to share his lab when lab space got tight as well as his advice whenever I asked for it.

I want to thank the whole Powell Group for the welcoming atmosphere providing a great work environment and especially Yannik Schneider, who shares a lab and office with me and thus has to deal with me every day, Dr. Rouven Pfleger who taught me how to interpret magnetic data as well as Daniel Seufert, Dr. Masooma Ibrahim, Dr. Hagen Kämmerer, Dr. Thomas Ruppert, Dr. Anthony Blue Carter, Umaira Shuaib, Luis Basche, Christian Pachl, Dr. Yan Peng, Dr. Nicolas Leblanc, Dr. Sebastian Habermann, Dr. Krisana Peewasan and Dr. Marcel Merkel for the many hours which we have spent together.

A very special thanks goes to Gertraud Amschlinger, who always listens to our problems and offers her expert support on matters concerning paperwork of any kind (of which I produced a lot).

I want to thank the people, who as students conducted research on this PhD project under my supervision: Yannik Schneider during his Bachelor thesis, Prashant Anand during an internship using the Aspirant Grant of the DAAD and Daniel Seufert during his Vertieferarbeit as well as Master thesis.

Furthermore, I want to thank the collaborators who have contributed to this work by calculations, experiments and helpful discussions:

Prof. Dr. Karin Fink, Christian Pachl and Dr. Twinkle Yadav for quantum chemical calculations.

Prof. Dr. Rüdiger Klingeler and Jan Arneth for Magnetic SQUID measurements.

Prof. Dr. Mario Ruben and Sören Schlittenhardt for the assistance with SQUID measurements.

Dr. Claudia Bizzarri for helpful discussions on the redox behaviour of Biquinoxens as well as the opportunity to use her (spectro-)electrochemical set-up.

Prof. Dr. Andreas-Neil Unterreiner and Dr. Julia Leier for emission spectroscopy as well as femtosecond spectroscopy helping to understand the behaviour of the Biquinoxens.

Prof. Dr. Wolfgang Wernsdorfer, Dr. Michael Schulze as well as Dr. Sagar Paul for microSQUID measurements.

Dr. Joy Farnaby for hosting me in her labs at the University of Glasgow as well as the great two weeks I spent there. Dr. Stephen Sproules for his EPR measurement and the simulation of the spectrum of the $[\text{CoCp}_2](\text{phsq})$.

Dr. Haiquan Tian and Prof. Dr. Jinkui Tang for providing a sample of their version of a Dy_8 cluster as well as assistance with magnetic SQUID measurements.

Prof. Dr. Jürgen Schnack and Dennis Westerbeck for helpful discussions providing insights into magnetic interactions.

Dr. Anthony Blue Carter and Dr. Thomas Kriese for their preliminary work on the lanthanide-radical dimers.

I want to furthermore thank the people ordering chemicals and equipment, perform NMR measurements and help whenever technical difficulties arise: Nikolai Bartnick, Helga Berberich, Lena Friedrich and Dr. Markus Schroth.

Last but not least I want to express my biggest thanks to my family, my friends, especially Yannik Schneider who has kept me going, together with my beloved wife Lisa who supported me in any possible way and made finishing this thesis possible.

13. Appendices

13.1 Table of Figures

Figure	Figure caption	Page
1	Jablonski diagram showing some of the possible processes upon irradiation of molecules with light.	7
2	The difference between the d-d transitions in the HS and LS spin state for a $3d^5$ ion.	9
3	Characteristic emission wavelengths of Ln^{III} ions. Reprinted with permission from reference ^[42] [American Chemical Society] copyright [2010].	10
4	$\chi_M T$ vs T curves for a ferro- and an antiferromagnet (left and right, respectively) highlighting the Curie and Néel temperatures adapted from reference ^[38] . The dashed lines correspond to the $\chi_M T$ vs T curve of a Curie paramagnet.	13
5	Curie-Weiss plot for a ferro- and an antiferromagnet showing the positive and negative Weiss constants of the respective interaction. Adapted from reference ^[39] .	14
6	Depiction of a magnetic hysteresis showing the saturation magnetisation and field (M_S and H_S) as well as the remanence M_R and the coercive field H_C . Adapted from reference ^[38] .	14
7	180° and 90° superexchange respectively leading to antiferro- and ferromagnetic interactions.	15
8	Illustration of the situation before (top) and after (bottom) the double exchange in mixed-valent manganites showing the ferromagnetically coupled manganese ions.	16
9	Schematic visualisation of a hydrogen bond HB highlighting the hydrogen atom (black) which is covalently bound to the hydrogen bond donor HB_D in blue and interacts with a lone pair of the hydrogen bond acceptor HB_A in red.	17
10	Different possibilities for the stacking of benzene dimers, face-face (left), edge-face (middle) and offset face-face (right). Adapted with permission from reference ^[74] [American Chemical Society] copyright [2005].	18
11	Schematic visualisation of a halogen bond. The halogen atom acts as the XB_D and an atom on the neighbouring molecule with a lone electron pair, that can interact with the σ -hole on the halogen, acts as XB_A . R often is an organic carbon that is covalently bound to the halogen.	19
12	Electrostatic potential surfaces revealing the existence and comparing the relative size of the σ -hole upon variation of the XB_D (left), and upon variation of the electron-withdrawing groups (right). Adapted with permission from reference ^[84] [Springer] copyright [2007] and reference ^[85] , respectively.	20
13	The classification into two types of halogen-halogen interactions according to the $R-X \dots X$ angles.	21

14	Type I halogen-halogen interactions as intermediate between two energetically degenerate type II halogen-halogen bond geometries as proposed by Scheiner. ^[91]	22
15	Scatter plot of short iodine-iodine contacts in the literature showing that if an iodine-iodine contact is asymmetric and therefore not type I, it will arrange close to type II geometry forming a halogen-halogen bond. Adapted from reference ^[92] [American Chemical Society] copyright [2014].	23
16	Core structure of Mn ₁₂ ac. The Mn ^{IV} ions are shown in pink and the Mn ^{III} ions in purple.	24
17	Energy barrier to magnetisation reversal in Mn ₁₂ ac with the m _J states indicated in blue. Adapted from reference ^[21] .	25
18	State splitting in a Dy ^{III} ion due to electronic repulsion, SOC and crystal field (top). Adapted from reference ^[107] . Possible relaxation mechanisms (bottom) with the red dashed line representing ZFQTM, the orange dashed lines representing TAQTM, the blue arrows showing relaxation via direct spin-phonon coupling and the green arrows showing Raman processes. Adapted with permission from reference ^[25] [American Chemical Society] copyright [2016].	27
19	Hysteresis of Mn ₁₂ ac showing the vertical steps due to QTM. Adapted with permission from reference ^[105] [John Wiley & Sons] copyright [2003].	28
20	Visualisation of the single ion anisotropy ellipsoids of the series of Ln ^{III} ions highlighting Dy ^{III} . Adapted from reference. ^[107]	28
21	Proposed mechanism for the strong exchange interactions in 3d-4f compounds responsible for the quenching of QTM. Reprinted with permission from reference ^[112] [American Chemical Society] copyright [2016].	29
22	Molecular structure of the first example of a radical bridged SMM, the N ₂ ³⁻ -radical bridged [K(18-crown-6)][Dy ₂ (μ ₂ -N ₂)(N(SiMe ₃) ₂) ₄ (THF) ₂]. ^[121]	30
23	Structure of [Ln ₂ @C ₈₀ (CH ₂ Ph)] showing the singly occupied molecular orbital (left) and schematic representation on the right highlighting the unpaired electron. Reprinted from reference ^[129] .	31
24	Molecular structures of the high temperature dysprosocenium SMMs. Counteranions and hydrogens are omitted for clarity. ^[27, 136-137]	33
25	Molecular structure of [Ln ₂ (Cp ^{iPr₅}) ₂ I ₃] highlighting the central metal-metal bond using one unpaired electron. ^[26]	34
26	Examples for four types of stable radicals.	36
27	Pancake bonding used for crystal design on the example of the 4-(2'-benzimidazolyl)-1,2,3,5-dithiadiazolyl radical, crystals of which exhibit magnetic bistability. Reproduced from reference ^[159] with permission [American Chemical Society], copyright [2018].	37
28	The viologen dication (left) and the biquinoxen dication (right) showing the similarities between the two systems.	38
29	Equilibrium process between the methylbiquinoxen dication, the alcohol-based adducts as well as the methylbiquinoxen dipseudobase. Reprinted from reference. ^[29]	38
30	Reaction steps in the synthesis of the methylbiquinoxen dipseudobase (Mbqn-(OH) ₂).	39

31	Reaction resulting in fluorescent methylbiquinoxen-adducts using alcohol-based nucleophiles (top) and luminescence indicating the same reaction to be possible using polymers with OH end groups (bottom). Reprinted from reference. ^[29]	40
32	Visual appearance of Mbqn-(OH) ₂ (left) and [CoCl ₂ (MbqnO)] (right) in DMF solution as well as solid state highlighting the colour change characteristic for the complexation reaction in which the ligand reacts to a radical species. ^[28]	40
33	Molecular structure of the starting material Mbqn-(OH) ₂ . Hydrogens omitted for clarity.	41
34	Alcohol-based reactants that yielded fluorescent products when used in attempted syntheses of luminescent methylbiquinoxen-adducts.	42
35	¹ H-NMR of Mbqn-(O ⁱ Pr) ₂ and Mbqn-(O ⁿ Bu) ₂ measured in DMF-d ₇ .	43
36	Starting materials for further methylbiquinoxen adducts (left) and a photograph of the luminescent solution of starting material Mbqn-(OH) ₂ in CHCl ₃ courtesy of Yannik Schneider.	43
37	The methylbiquinoxen adducts studied to shine light on the tuning of luminescent properties.	44
38	Molecular structure of (1) and visual appearance of crystals of (1) under a microscope.	45
39	Two views on the packing of (1) along the crystallographic a- and c-axis (left and right, respectively). The offset π-π stacking is highlighted with red circles.	45
40	Molecular structures of (2), (3), (6) and (7). The different arrangements of the ⁿ butyl residues in (2) leading to an asymmetric molecule are highlighted with red circles.	46
41	Two views on the packing (3), along the crystallographic b and c axes (left and right, respectively) showing the π-π stacked arrangement.	47
42	Deviation from planarity shown for the example of Mbqn-(O ⁱ Pr) ₂ in two views (top) and scheme explaining the distances used in the following table to describe the deviation from planarity.	48
43	Experimental and simulated powder patterns of (1), comparing the different samples prepared throughout the work on this thesis.	50
44	Experimental and simulated PXRDs of (3) (left) and (4) (right).	50
45	Comparison of the IR spectra of (1) and (5) in the range 3200-2600 cm ⁻¹ , exemplifying the CH ₂ -based vibrations at 2916 cm ⁻¹ and 2853 cm ⁻¹ (left); Comparison of the IR spectra of (1), (3) and (4) in the range of 800-600 cm ⁻¹ showing the thioether vibrations at 685 cm ⁻¹ and 674 cm ⁻¹ , respectively.	51
46	Appearance of O-based adducts exemplified using (5) as crystalline solid under normal white light (left), under UV light (365 nm) (middle) and between two quartz plates for solid state absorption spectroscopy under UV light of the same wavelength (right). Crystals of (3) under a microscope showing the appearance of the S-based adducts (bottom left) and ground powder of (3) under UV irradiation (bottom right).	52
47	Solid state UVVis absorption spectra of (1-6) in the range of 200 to 800 nm.	53

48	Solid state excitation and emission spectrum of compound (1), by excitation at 365 nm. The excitation spectrum was recorded for the emission at 615 nm.	53
49	UVVis absorption spectra of (1) in MeCN, DMF, DCM as well as in solid state between 200 and 800 nm.	55
50	A: UVVis absorption spectrum of (1) at four different concentrations between 10 and 50 μ mol/l. B-D Linear fit for extraction of extinction coefficients for peaks 2-4, respectively.	56
51	UVVis absorption spectra of (1-6) in DMF solutions in the range of 260 to 800 nm.	57
52	Normalised emission spectra of (1-6). The O-based adducts were excited at 440 nm, the S-based adducts at 465 nm.	58
53	Excerpt of the 1 H-NMR spectrum of (1) showing the decomposition in solution after 12 h.	59
54	Molecular structure of (10-Cu) as representative for the biquinoxen-radical complexes. The disorder of the carbonyl O(1) and the neighbouring vicinal H(10) was removed in favour of the atoms with higher occupancy.	62
55	Proposed structure of the complexes in terms of the location of single and double bonds.	63
56	Supramolecular chain formation dominating the packing of (8/9-Co , 10/11-Cu and 12-Zn A). Chains are held together by a mixture of offset π stacking (top view) and non-classical HBs shown in green (side view). This is illustrated here using the crystal structure of (10-Cu) as a representative.	66
57	Packing interactions in (12-Zn B) showing the pancake bonded dimers that are interconnected via HBs.	66
58	Experimental and simulated powder patterns of (8- and 9-Co) (top) as well as (10- and 11-Cu) (bottom) confirming phase purity of all samples but (8-Co) in which small amounts of crystalline impurity can be observed.	67
59	PXRD of the bulk sample of (12-Zn) compared to the simulated powder patterns of both polymorphs (12-Zn A) and (12-Zn B) in the region between 2 and 20°, revealing both polymorphs to be present.	68
60	$\chi_M T$ vs T plot (left) and Curie-Weiss plot and fit of (12-Zn) (right) confirming not only the radical nature of the ligand but also a strong antiferromagnetic interaction to be present between neighbouring molecules.	69
61	Molecular structure of (13-Zn) providing a proof of principle for the extension of complexes in this ligand system using the adducts presented in section 4.2.	70
62	Two views on the packing of four molecules of (13-Zn) showing the formation of supramolecular chains along the crystallographic a axis.	70
63	Packing of (13-Zn) along the crystallographic a axis, showing the interconnection of the previously observed chain structures by zipper-like HBs (green dashed lines) forming a 3-dimensional network.	71
64	Molecular components to prepare the chosen ligand system.	76

65	The molecular structures of a Dy ^{III} dinuclear, hexanuclear and octanuclear complex employing the H ₂ opch ligand reported by Tang <i>et al.</i> highlighting the versatility of this Schiff base ligand. ^[198-200]	77
66	Flexible coordination modes of CO ₃ ²⁻ . Adapted from reference ^[207] with permission [John Wiley and Sons] copyright [2017].	77
67	Halogen bound supramolecular dimers of (PPh ₄) ₃ [Cr ^{III} (I ₂ An) ₃] (left) and X _M vs T plot showing the induced antiferromagnetic interaction below 4.1 K (right). Reprinted from reference. ^[242]	79
68	Using the same reaction conditions with the Schiff base ligand H ₂ opch, mdeah ₂ as base and potential co-ligand as well as the corresponding lanthanide nitrate salt, six unique structures could be obtained depending on the Ln ³⁺ ion used (Ln = La-Lu and Y).	80
69	Visual appearance of the reaction mixtures using all Ln ³⁺ ions in combination with H ₂ opch (picture courtesy of Daniel Seufert).	80
70	Molecular structure of (14-La) (left) and top and side view of the essentially planar core (right).	81
71	View along the a-axis highlighting the hydrogen bonds responsible for the stacking of the La ₅ discs in green.	82
72	Two views on the packing of (14-La), along the a-axis (left) and along the c-axis (right). Everything but the core was omitted for clarity.	83
73	PXRD confirming the phase purity of (14-La) (left) and excerpt of the IR spectrum of (14-La) between 1600 and 1000 cm ⁻¹ highlighting the asymmetric CO stretch vibration of the multidentate CO ₃ ²⁻ ligand at 1430 cm ⁻¹ (right). ^[249]	83
74	Molecular structure (left) and two views of the square planar tetranuclear core of (15-Ce) (right).	85
75	View of the packing of (15-Ce) along the a-axis (left) and along the c-axis (right).	88
76	Experimental and simulated PXRD (left) and ATR-IR spectrum between 4000 and 400 cm ⁻¹ (right) of (15-Ce).	88
77	Hexagonal prismatic crystal of (16-Eu) in perfluoroether oil (left) and on the goniometer head (right).	89
78	Molecular structure (left) and two views of the core of (16-Eu) (right).	89
79	View of the packing of (16-Eu) along the c-axis highlighting the threefold axis with a lattice MeCN molecule lying on it as well as the hydrogen bonds (green). Other lattice solvent molecules were omitted for clarity.	91
80	PXRD (left) and excerpt of the IR spectrum of (16-Eu) highlighting the asymmetric CO stretch vibration of the multidentate bridging carbonate ligand (right).	92
81	The molecular structure of (17-Dy) (left) with two views on its core structure (right). The vacant site is highlighted with a green arrow.	93
82	Packing of (17-Dy) highlighting the intermolecular HBs in green.	94
83	Two views of the packing of the cores of (17-Dy), along the a-axis (left) and along the c-axis (right) showing the orientation of the cores towards in the lattice.	94
84	PXRD (left) and IR spectrum of (17-Dy) (right).	95

85	Molecular structure of (21-Dy) representative for the other Ln_8 compounds (left) and two views on the carbonate bridged core structure (right).	96
86	Packing of the triclinic structure of (21-Dy), view along the a-axis highlighting the intermolecular HBs in green.	97
87	Packing of the monoclinic structure type using the measurement of (23-Er). View along the b-axis with the intermolecular HBs shown in green.	97
88	Comparison of the PXRDs of the Ln_8 complexes with the predicted powder pattern of the monoclinic crystal structure of (23-Er). The inset highlights the peak characteristic for the triclinic crystal structure obtained for larger Ln^{III} ions with a black arrow.	98
89	Identification of the side product of the reaction towards (20-Tb) as a Tb_5 complex, isostructural to (16-Eu).	99
90	Appearance of the vials containing the same reaction mixture once using $\text{Ho}(\text{NO}_3)_3 \cdot 5\text{H}_2\text{O}$ (left) and once using $\text{Er}(\text{NO}_3)_3 \cdot 5\text{H}_2\text{O}$ as lanthanide source (right). Picture courtesy of Daniel Seufert.	100
91	Solid state absorption spectra in the spectral range between 200 and 800 nm comparing the H_2opch ligand (black) with the different structure types obtained using the same reaction conditions only changing the lanthanide ion. At the top the visual appearance of the samples prepared of (14-La) and (15-Ce) highlighting the colour difference.	101
92	Absorption spectra of different structure types discussed in this chapter.	103
93	Absorption spectra of (15-Ce) in DMF solution. The first three samples were measured directly after dilution of the freshly prepared stock solution (black, red and blue). The same stock solution was used after 24 hours and after 5d resulting in the green and purple spectra.	104
94	Magnetic measurement of (15-Ce) performed at an applied dc field of 0.1 T at temperatures between 1.8 and 300 K. $\chi_M T$ vs T curve in black, χ_M^{-1} vs T curve in red and Curie-Weiss fit of the latter in the temperature range between 130 and 300 K in blue.	106
95	Magnetisation (left) and reduced magnetisation plots (right) of (15-Ce) at dc fields between 0 and 7 T at 1.8, 3 and 5 K.	107
96	$\chi_M T$ vs T plots for (19-Gd) in red, (20-Tb) in green, (21-Dy) in black and (22-Ho) in blue at temperatures between 2 and 300 K measured with an applied dc field of 0.1 T.	108
97	Curie-Weiss plots and fits for (19-Gd) in red, (20-Tb) in green, (21-Dy) in black and (22-Ho) in blue confirming weak to very weak antiferromagnetic interactions to be present.	109
98	Magnetisation measurements at dc fields between 0 and 7 T (left) and reduced magnetisation plot (right) for (19-Gd) (top), (21-Dy) (middle) and (22-Ho) (bottom). Lines are a guide to the eye.	110
99	Ac magnetic data for (20-Tb) with an applied dc field of 3000 Oe. Out-of-phase magnetic susceptibility (left) and in-phase magnetic susceptibility (right) against frequency at temperatures between 2.0 K and 4.8 K. Points are the experimental data and solid lines are best fits to these using the Debye model.	111
100	In- and out-of-phase ac magnetic susceptibilities of (21-Dy) measured between 1.8 and 5 K and frequencies between 0.1 and 1500 Hz showing	113

	slow relaxation of magnetisation. Solid lines are the best fit to experimental data using the Debye model (left) and Arrhenius plot of the first set of maxima (right, black dots) and the best fit to equation 13 (right, red line).	
101	MicroSQUID measurements on single crystals of (21-Dy) (top) and the literature known $\text{Dy}_8^{[200]}$ (bottom). On the left the temperature dependence is shown between 0.03 K and 5.5 K and on the right the sweep rate dependence between 0.5 T/s and 128 T/s.	114
102	Temperature dependence (left) and magnetic field dependence of the molar entropy change of (19-Gd) calculated using the Maxwell relation (equation 17). Lines are guide to the eyes.	115
103	Synthesis of further members of the H_2opch ligand family. In the last step functional groups can be introduced that can alter the ligand and therefore complex properties. R^1 = methyl or ethyl and R^2 = H, Br, I, NO_2 .	116
104	H_2opch and the five modified ligands that were used during this work.	116
105	^1H -NMR spectra of the ligand modifications recorded in DMSO-d_6 .	117
106	Solid state UVVis spectra of the modified H_2opch ligands between 200 and 800 nm.	118
107	Absorption spectra of the modified ligands in MeCN between 200 and 800 nm.	120
108	Molecular structure of (28-Er) showing the trigonal prismatic arrangement of Er^{III} ions (left) and a top and side view of the core structure (right).	124
109	Excerpt of the solid state ATR-IR spectrum of (27-Ho) highlighting the carbonate based vibration at 1444 cm^{-1} .	125
110	Packing view of (28-Er) along the b-axis highlighting intermolecular HBs in green.	125
111	Powder pattern (28-Er) compared to the simulation.	126
112	Molecular structure (left) and two views on the Er_6 core of (29-Er) (right). The disorder has been removed for clarity and the Cl ligand assigned to the site coordinating Er(2) for the graphics.	127
113	Powder pattern confirming the phase purity of (29-Er) (left) and excerpt of the IR spectrum of (29-Er) between 1600 and 1000 cm^{-1} with the carbonate peak highlighted at 1441 cm^{-1} (right).	127
114	Core structures of (28-Er) (left) and (29-Er) (right) highlighting the distortion of the trigonal prism and the high level of similarity between them.	128
115	Packing view along the fourfold axis (crystallographic c axis). Short bromine-bromine contacts are highlighted by the orange dotted lines.	129
116	Enlarged view of the halogen-halogen interactions dominating the packing of (29-Er) looking along the c axis (left) and from a different angle demonstrating the tetrahedral arrangement (right). The shortest distance between the tetrahedrally arranged bromine atoms (each $\text{Br}(1)$ of one Er_6 -cluster) is smaller than the combined VdW-radii indicating an attractive interaction. The angles highlighted in blue classify the interaction as a type II halogen interaction also known as a halogen bond.	130

117	Result of the topological analysis on (29-Er) in collaboration with Dr. George Kostakis (University of Sussex). Orange dots each represent one Er_6 complex, blue lines indicate the pattern in which each cluster is halogen bonded to six others.	131
118	UVVis absorption spectra of (27-Ho) and (29-Er) in solid state and DMF solution.	132
119	Magnetic M vs T measurements performed on (28-Er) (blue) and (29-Er) (red) between 1.8 K and 300 K with an applied dc field of 0.1 T. Solid lines are a guide to the eye.	133
120	Curie-Weiss plots for (28-Er) and (29-Er) in blue and red, respectively. Linear fits between 30 and 300 K reveal a negative Weiss constant indicating antiferromagnetic interactions.	134
121	Magnetisation measurements were performed with applied dc fields between 0 and 7 T at 2, 3 and 5 K. Both compounds (28-Er) and (29-Er) do not reach saturation at 7 T (top). Reduced magnetisation plots (bottom) showing the anisotropy of the system. Lines are guide to the eye.	135
122	Anisotropy axes (in light blue) of (26-Dy) calculated using MAGELLAN. ^[297]	137
123	Molecular structure (left) and two views on the core of (30-Er) (right).	138
124	Powder pattern confirming the phase purity of (30-Er) (left) and excerpt of the IR spectrum that highlights the carbonate related vibration at 1452 cm^{-1} (right).	138
125	Proposed mechanism for the self-assembly of (28-30-Er).	140
126	View along all three crystallographic axes of the packing of (30-Er). Intermolecular interactions between the lone electron pair of the pyrazine-N and the σ -hole of the iodine are highlighted in green.	142
127	Visual appearance of the reactions with the goal to produce modified Ce_4 clusters.	143
128	Molecular structure (left) and two views on the core of (31-Ce) (right).	143
129	Comparison of the angles and distances of the essentially square core structures of (15-Ce) (left) and (31-Ce) (right).	144
130	Packing of (31-Ce) highlighting the hydrogen bonded stacks. View along the crystallographic b axis.	145
131	Solid state UVVis absorption spectra of (15-Ce), (31-Ce) and (32-Ce) compared between 200 and 800 nm.	146
132	Molecular structure of (34-Nd) (left) and a top and side view on the heptanuclear core (right).	147
133	Core structure of (34-Nd) showing the essentially perfect hexagon around the central Nd(1).	148
134	Packing of (34-Nd), view along the crystallographic a axis with the hydrogen bonds highlighted in green.	148
135	PXRD confirming the phase purity of (34-Nd) (left) and IR spectrum of (34-Nd) (right) showing the OH-vibrations at around 3300 cm^{-1} .	149
136	Solid state UVVis absorption spectrum of (34-Nd) between 200 and 1000 nm. The states of the f-f transitions from the $^4\text{I}_{9/2}$ ground state.	149

137	MicroSQUID measurements performed on single crystals of (34-Nd). Temperature dependence measured between 30 mK and 4.5 K (left) and sweep rate dependence measured for sweep rates between 0.5 mT/s and 128 mT/s (right).	150
138	Molecular structure (left) and two views on the core structure (right) of (35-Gd B) as a representative for the Ln_7 clusters obtained using $\text{H}_2\text{opch-}\text{I}$.	151
139	Packing of (35-Gd A) showing the supramolecular dimer formed by halogen-halogen bonds as indicated by the highlighted I-I distance as well as C-I...I angles.	154
140	Packing of (35-Gd B) showing the supramolecular chain formation also found in (36-Dy). Halogen-halogen interactions are of type I as indicated by the highlighted I-I distance as well as C-I...I angles.	155
141	$\chi_M T$ vs T plot of (36-Dy) (red) and χ_M^{-1} vs T plot (hollow points) with the corresponding Curie-Weiss fit in blue.	156
142	M vs B plot (left) and reduced magnetisation (right) of (36-Dy) at 2, 3 and 5 K. Lines are a guide to the eye.	157
143	Anisotropy axes calculated using MAGELLAN ^[297] showing the poor alignment likely responsible for the absence of slow relaxation of magnetisation.	158
144	Molecular structure of (37-Tb) as an example for dimeric compounds with the original H_2opch ligand.	159
145	Packing of (37-Tb). Hydrogen bonding to lattice water molecules stabilising the crystal structure highlighted in green.	159
146	Molecular structure of (38-Dy).	160
147	Red and black hexagons highlight the overlap of π -systems resulting in π - π stacking responsible for the packing of (38-Dy).	161
148	View on the packing of (38-Dy) showing the zig-zag stacks.	161
149	PXRD of (38-Dy) confirming the phase purity of the crystals, while confirming the presence of another crystalline material in the bulk powder sample.	162
150	Molecular structure of (39-Dy).	163
151	Packing of (39-Dy) along the c axis showing that all molecules are oriented in the same direction as for crystallisation in $P\bar{1}$ with $Z = 1$.	163
152	Powder pattern of (39-Dy) showing the phase purity of the compound.	164
153	The two different coordination modes displayed by the opch-family ligands in (38-40-Dy).	165
154	Molecular structure of (40-Dy).	166
155	View on the packing of (40-Dy) along the c-axis highlighting the high symmetry of the crystal structure and the disorder of the lattice CCl_4 molecules. Hydrogen bonds can be seen in yellow.	167
156	Halogen-halogen bonds in (40-Dy) between coordinated chlorides and lattice CCl_4 shown as green dotted lines. Relevant distances and angles are given in red.	168
157	Two views on the anisotropy axes in (38-40-Dy) calculated using MAGELLAN ^[297] showing that the axes are essentially parallel to the Dy-Dy vector in (38/39-Dy) and essentially orthogonal to the Dy-Dy vector in	169

	(39-Dy), highlighting the difference the coordination mode makes to the anisotropy in dimers.	
158	$\chi_M T$ vs T plots for (39-Dy) (red) and (40-Dy) (blue) revealing ferromagnetic interaction between the Dy ^{III} centres in (38-Dy) and a potential antiferromagnetic interaction in (40-Dy).	170
159	Inverse magnetic susceptibility plots and Curie-Weiss fits for (39-Dy) and (40-Dy) showing the sign of the magnetic interaction in the respective dimer.	171
160	Magnetisation at applied dc fields between 0 and 7 T (top) and reduced magnetisation (bottom) of (39-Dy) (left) and (40-Dy) (right).	175
161	Magnetic ac out-of-phase susceptibility data for (40-Dy) showing the poor intensity. Lines are guide to the eye.	176
162	MicroSQUID measurements performed on single crystals of (40-Dy) between 30 mK and 5.5 K at a sweep rate of 128mT/s (top) as well as sweep rates between 0.5 mT/s and 128 mT/s at 0.03 K (bottom).	177
163	In-phase (left) and out-of-phase (right) ac susceptibility measurements on (38-Dy) in the range between 0.1 and 1500 Hz at 2-6 K and between 1 and 1500 Hz at 7-14 K. Lines are the best fit to the acquired data points using the Debye model.	178
164	Arrhenius plot of (39-Dy) using the τ values extracted from the Debye fit (black dots). Linear fit corresponding to the Orbach relaxation process (blue) and fit of the relaxation data to equation 13 proposed by Lunghi <i>et al.</i> ^[142] (red).	179
165	Molecular structures of (41-Dy) (top) and (42-Dy) (bottom).	180
166	View along the a axis on the packing of (41-Dy) highlighting the weak halogen interactions in green.	182
167	View along the a-axis on the packing of (42-Dy). Strong intermolecular halogen bonds are highlighted in green.	182
168	Anisotropy axes calculated with MAGELLAN ^[297] for (41-Dy) (top) and (42-Dy) (bottom).	183
169	$\chi_M T$ vs T plot (red) and Curie Weiss plot plus fit (blue) of (41-Dy). The $\chi_M T$ vs T plot reveals a ferromagnetic interaction which is confirmed by the linear fit to the χ_M^{-1} vs T plot resulting in a Weiss constant of +19.4K.	184
170	Magnetisation measurements on (41-Dy) at variable fields between 0 and 7 T at 2, 3 and 5 K (left) and reduced magnetisation (right). Lines are guide to the eyes.	185
171	In-phase and out-of-phase ac susceptibility measurements of (41-Dy) between 2 and 20 K and 1 and 1500 Hz. Lines are the best fits to the data points using the Debye model.	185
172	Arrhenius plot (left) (black dots) showing the relaxation dynamics in (41-Dy) between 2 and 15K. Linear fit to the Orbach process shown in blue and the best fit using the more sophisticated fitting method proposed by Lunghi <i>et al.</i> ^[142] taking other relaxation processes into account shown in red. Hysteresis plot at 2 K for (41-Dy) (right) between -5 and 5 T with the inset showing the very slight hysteresis near zero field. Lines in the inset are guides to the eye.	187

173	Redox activity of 9,10-phenanthrenequinone (left) showing two possible reversible one-electron reductions to the seqmiquinone radical anion (middle) and the diol form (right).	194
174	UVVis absorption spectra of 9,10-phenanthrenequinone (red arrow) before irradiation with visible light, after short irradiation with light leading to the blue-green radical intermediate that is stabilised by metal ions (blue arrow), after completed photoreduction to the diol (golden arrow) and after re-oxidation to the 9,10-phenanthrenequinone <i>via</i> aerial oxygen (green arrow). Adapted with permission from reference ^[338] [John Wiley & Sons] copyright [2008].	195
175	Molecular structure of the archetype complex $[\text{Dy}_2(\text{phsq})_4(\text{NO}_3)_2(\text{MeOH})_2]$.	196
176	MicroSQUID measurements performed on single crystals of the archetype Dy ^{III} dimer (left) as well as on the Y-doped sample (right) prepared by Dr. Anthony Blue Carter ^[32] showing the quenching of ZFQTM in the former and the presence of ZFQTM in the latter.	198
177	$\chi_M T$ vs T plot of (45-Eu) (left) showing thermal population of the 7F_1 state and Curie-Weiss plot and fit of (45-Eu) (right).	200
178	$\chi_M T$ vs T plot of (47-Tb) (left) and Curie-Weiss plot and fit (right).	201
179	In-phase (top) and out-of-phase (bottom) ac susceptibility vs frequency measured on (47-Tb) at temperatures between 1.8 K and 5.2 K with an applied dc field of 0.28 T. Lines are the best fit to the Debye model accounting for two sets of maxima.	202
180	Reaction vials showing the reaction mixture before heating (left), the dark green colour of the methanolic reaction solution after completion of the reaction (middle) as well as the discolouration of the dark solution in air (right). ^[31-32]	203
181	UVVis absorption spectrum of a 10 μM MeCN solution of the commercially obtained starting material 9,10-phenanthrenequinone.	203
182	Simulated and experimental EPR spectra confirming the synthesis of $[\text{CoCp}_2](\text{phsq})$.	204
183	UVVis absorption spectrum of a 10 μM solution of $[\text{CoCp}_2](\text{phsq})$ in MeCN between 200 and 800 nm.	205
184	Decomposition of $[\text{CoCp}_2](\text{phsq})$ in air as shown by successive UVVis absorption spectroscopy measurements. After about 15 minutes the spectrum of the dione-starting material is reproduced.	206
185	Comparison of the UVVis spectra of (48-Dy) and (49-Ho) in 10 μM MeCN solutions.	207
186	Comparison of the UVVis absorption spectra of (48-Dy) and (49-Ho) in MeCN (blue and red solid lines) to the respective solid state spectra (blue and red dashed lines) as well as the MeCN solution spectra of 9,10-phenanthrenequinone and the cobaltocenium salt of the phenanthrenesemiquinonate radical (green and orange lines, respectively).	208
187	Oxidation of the MeCN solution of (49-Ho) within ten minutes when opened to air.	209

188	UVVis absorption spectra of the same sample of (45-Eu) measured immediately after preparation (blue) and after storage under inert atmosphere (black).	210
189	Emission spectra of the same sample of (45-Eu) measured immediately after preparation (blue) and after storage under inert atmosphere for three days (black). The corresponding states of the transitions are shown in red.	210
190	Two views on the molecular structure of (60-Dy) as a representative for the $[\text{Ln}_2(\text{phsq})_4(\text{NO}_3)_2(\text{EtOH})_2]$ complexes.	213
191	View along the b axis on the packing of (60-Dy).	214
192	PXRDs of EtOH dimers suggesting the easy loss of lattice solvent potentially leading to the presence of at least one more unexplored crystal structure.	215
193	IR and UVVis suggesting identical molecular structures of different members of the $[\text{Ln}_2(\text{phsq})_4(\text{NO}_3)_2(\text{EtOH})_2]$ series.	215
194	Solid state and solution UVVis absorption spectra in MeCN of (60-Dy) compared to the spectra of the MeOH version (48-Dy) as well as the ligand reference spectra established above.	217
195	Anisotropy axes of the Dy^{III} ions in (60-Dy) calculated using MAGELLAN. ^[297]	217
196	$\chi_M T$ vs T (left) and χ_M^{-1} plot of (60-Dy) (right) obtained from susceptibility measurements at temperatures between 1.8 and 300 K and an applied magnetic dc field of 0.1 T.	218
197	Magnetisation of (60-Dy) measured at 1.8, 3 and 5 K and fields between 0 and 7 T (left) and reduced magnetisation plots (right).	219
198	In- and out-of-phase susceptibility at ac field frequencies between 1 and 1000 Hz and temperatures between 1.8 and 20 K (left and right, respectively).	219
199	Arrhenius plot of (60-Dy) (black dots) using the τ values extracted from the Debye fit to the ac susceptibility data fitted using a linear fit taking the thermal Orbach relaxation mechanism into account (blue) as well as using equation 13 by Lunghi <i>et al.</i> (red). ^[142]	221
200	Narrow hysteresis shown by (60-Dy) at 1.8 K between fields of -0.6 and -0.3 T as well as 0.3 and 0.6 T indicating SMM behaviour at this temperature.	221
201	MicroSQUID performed on single crystals of (60-Dy). Temperature dependence at temperatures between 0.03 and 4.5 K (left) and sweep rate dependence between 1 mT/s and 128 mT/s was investigated (right). Derivative plots of the respective measurements show the predominant level crossing at +/- 0.27 T (bottom).	223
202	Side and top view on the molecular structure of (74-Tm) as representative for the series of $[\text{Ln}_2(\text{phsq})_4(\text{NO}_3)_2(\text{iPrOH})_2]$ complexes.	224
203	Packing of (74-Tm) viewed along the c axis.	225
204	PXRD measurements compared to the simulated pattern using the SC-XRD dataset of (74-Tm) confirming the series of $[\text{Ln}_2(\text{phsq})_4(\text{NO}_3)_2(\text{iPrOH})_2]$ complexes to be isostructural from Eu^{III} to Lu^{III} as well as the Y and Dy-Y-doped versions.	226
205	Solid state UVVis absorption spectra of (65-Pr)-(78-DyY).	227

206	Anisotropy axes calculated using MAGELLAN on the crystal structure of (74-Tm) pretending the Tm ^{III} ions are Dy ^{III} ions based on the fact that (74-Tm) and (71-Dy) are isostructural. ^[297]	228
207	$\chi_M T$ vs T plot (left) and χ_M^{-1} vs T plot (right) obtained from susceptibility measurements performed on an immobilised powder sample of (71-Dy) at temperatures between 1.8 and 300 K with an applied dc field of 0.1 T.	228
208	Magnetisation (left) and reduced magnetisation plots of (71-Dy) (right) at 1.8, 3 and 5 K and fields between 0 and 7 T.	229
209	In- and out-of phase susceptibility vs frequency plots (left and right, respectively) obtained from ac susceptibility measurements on (71-Dy).	230
210	Relaxation processes fitted using equation 13 (red line) as well as using a linear fit to the high temperature region (blue).	231
211	MicroSQUID measurements performed on single crystals of (71-Dy). Temperature dependence between 0.03 and 5 K (left) and sweep rate dependence between 1 and 128 mT/s (right). Derivative plots for both dependencies highlighting the switching field of the level crossing from the essentially non-magnetic ground state at 0.41 T (bottom).	232
212	Top and side view on the molecular structure of (84-Dy) as a representative for the $[\text{Ln}_2(\text{phsq})_4(\text{Cl})_2(\text{MeOH})_2]$ series.	234
213	View along the crystallographic c axis on the packing of (84-Dy) showing the zig-zag chains formed by intermolecular π - π interactions which are held together by non-classical HBs.	235
214	Comparison of the PXRDs of the isostructural series of $[\text{Ln}_2(\text{phsq})_4(\text{Cl})_2(\text{MeOH})_2]$ compounds to the simulated powder pattern of (84-Dy).	235
215	Solid state UVVis absorption spectra of (83-Tb) and (84-Dy) as representatives for the $[\text{Ln}_2(\text{phsq})_4(\text{Cl})_2(\text{MeOH})_2]$ series between 200 and 800 nm.	236
216	Comparison of the UVVis absorption spectrum of (84-Dy) in 10 μ M MeCN solution to the solid state spectrum as well as the solution and solid state spectra of (48-Dy) and (60-Dy).	237
217	Side and top view on the molecular structure of (84-Dy) with the anisotropy axes calculated using MAGELLAN shown in cyan. ^[297]	237
218	$\chi_M T$ vs T plot (left) and χ_M^{-1} vs T plot with Curie-Weiss fit (right) of (84-Dy) at temperatures between 1.8 and 300 K with an applied dc field of 0.1 T.	238
219	In- and out-of-phase susceptibility of (84-Dy) (left and right, respectively) plotted vs the frequency of the applied ac field revealing slow relaxation of magnetisation up to around 30 K within the measured frequency range.	239
220	Relaxation processes in (84-Dy) fitted using equation 13.	240
221	Two views on the molecular structure of (90-Ce). A top view (top) highlighting the similarities to the previously described dimers and a side view showing the new 5 th and 6 th phenanthrenesemiquinonate radical ligand.	242
222	Views on the packing of (90-Ce) along the crystallographic b and c axes showing the alternating angled stacks of complexes.	243
223	¹ H-NMR and UVVis absorption spectrum of the modified precursor for a radical ligand pyrene-4,5-dione in 10 μ M MeCN solution.	244

224	The pyrene-4,5-dione (pydi) starting material as well as the <i>in-situ</i> generated radical ligand.	244
225	Top and side view on the molecular structure of (94-Er) as a representative of the series of $[\text{Ln}_2(\text{pysq})_4(\text{NO}_3)_2(\text{MeOH})_2]$ complexes (91-Tb)-(b)- 95-Y).	245
226	Two views on the packing of (94-Er) showing the stacks of clusters formed by π - π stacking between the pysq radicals coordinating to the Er ^{III} ions and the co-crystallising pydi ligands.	246
227	Close-up on the intermolecular π - π interactions around an individual $[\text{Er}_2(\text{pysq})_4(\text{NO}_3)_2(\text{MeOH})_2]$ cluster determining the packing in (94-Er).	247
228	PXRD of (93-Ho) compared to the simulated pattern using the crystal structure of (94-Er) confirming isostructural complexes.	247
229	Solid state absorption spectroscopy of (93-Ho) and (95-Y) as representatives for the series of $[\text{Ln}_2(\text{pysq})_4(\text{NO}_3)_2(\text{MeOH})_2]$.	248
230	Anisotropy axes of (92-Dy) calculated using MAGELLAN. ^[297]	249
231	$\chi_M T$ vs T (left) and χ_M^{-1} vs T plot (right) of (92-Dy) fitted to the Curie-Weiss law.	249
232	In- and out-of-phase susceptibility vs frequency plots of (92-Dy) obtained from ac measurements.	250
233	Arrhenius plot (92-Dy) using the τ values extracted from the Debye fit to the ac data (black dots) fitted using equation 13 (red line).	251
234	MicroSQUID measurements performed on single crystals of (92-Dy). The temperature dependence between 0.03 and 5 K is shown on the left and the sweep rate dependence between 1 and 128 mT/s shown on the right. The derivatives of either measurement are shown in the bottom.	252
235	Other diones used as starting material in attempts to produce complexes employing their <i>in-situ</i> generated semiquinone radical anions as ligand to form Ln_2Rad_4 clusters.	253
236	Solid state UVVis absorption spectra of (48-Dy), (60-Dy), (71-Dy), (84-Dy) and (93-Ho) in the spectral range between 200 and 800 nm.	254
237	Derivative plots of the temperature dependence in microSQUID measurements on (60-Dy), (71-Dy) and (92-Dy) as well as the previously obtained (48-Dy) that was mentioned in the preliminary results section. ^[339]	256
238	The biquinonen system with two easily modifiable positions (left) and two adducts that could not be satisfactorily characterised yet with R^1 = benzyl and R^2 = ⁿ SBu (middle) and an N-based compound with R^1 = methyl and R^2 likely = piperidine.	263
239	Visualisation of the σ -hole on the iodine atom of the ligand used for the synthesis of (42-Dy) as one of the preliminary results of the theoretical description of the halogen bonds in (42-Dy) in collaboration with Christian Pachl from the groups of Prof. Dr. Karin Fink and Prof. Dr. Annie Powell. Areas of low electron localisation are coloured in blue while areas of high electron localisation are shown in red.	267

13.2 Table of Tables

Table	Table caption	Page
1	Energy barriers, Cp-Dy-Cp angles and Dy-Cp _{centroid} distances for the six dysprosocenium SMMs mentioned above.	32
2	Deviation from planarity analysed for the luminescent methylbiquinoxen adducts.	48
3	Comparison of extinction coefficients of compounds (1-6).	56
4	Tuning of the emission wavelength in (1-6).	58
5	Quantum yields of DMF solutions of (1) after different times after sample preparation. ^[189]	60
6	Disorder on O(1) in (8/9-Co, 10/11-Cu and 12-Zn A and B).	62
7	Important distances and angles in (8/9-Co, 10/11-Cu as well as 12-Zn A and B).	64
8	Parameters used for and the results of the BVS analyses. ^[191-194]	65
9	Parameters used for the BVS analysis on (15-Ce).	86
10	Results of the BVS analysis highlighting the closest result for each of the four cerium ions in (15-Ce).	86
11	Type and number of ligands forming the coordination spheres around Eu(1)-Eu(5) in (16-Eu). Opch-N stands for the hydrazine-N, O-CH ₃ for the methoxy-O, phen-O for the phenoxy-O, carb for the carbonyl-O and pyz for the pyrazine-N of the H ₂ opch ligand. The number of strokes indicates the number each Eu ^{III} ion is coordinated to each type of ligand site.	90
12	Weiss constants θ, Curie constants C extracted from the linear fit and the temperature ranges in which the curves follow the Curie-Weiss law for (19-Gd), (20-Tb), (21-Dy) and (22-Ho).	109
13	Fitting parameters of the best fit to the relaxation processes relevant in (21-Dy) using equation 13.	112
14	Overview of the complexes presented in this chapter and their classification into the three different structure types.	121
15	BVS analysis on the cerium ions in (31-Ce) using the same parameters as for the BVS analysis on (15-Ce) described in section 5.2.1.2. The best results are highlighted in red. ^[191, 254-255]	144
16	Comparison of the six Ln-Ln bond lengths and the internal Ln-Ln-Ln angles (labelled with the central Ln ^{III} ion of the angle) forming the outer hexagon as well as the distance of the central Ln ^{III} ion from a mean plane through the outer six in (34-Nd), (35-Gd A), (35-Gd B) and (36-Dy).	152
17	Comparison of compounds (38-40-Dy) with complexes from the literature with Schiff base ligands with similar coordination spheres (both variations, enolate-bridged as well as phenoxy-bridged). In the “sample” column the compound identifiers for compounds produced in this work or molecular formulae for compounds from the literature are listed. Angles are given in degrees and distances in Angstrom with standard deviations if given in the corresponding reference. For compounds in which the direction of the anisotropy axes (abbreviated as AA) was investigated either by MAGELLAN ^[297] or <i>ab initio</i> methods, the direction is indicated	172

	as either “o” for axes (near) orthogonal to the Dy-Dy-vector or as “p” for axes (near) parallel to the Dy-O _{phenoxy} bonds. Additionally, the sign of the experimentally observed overall magnetic interaction is given as either “F” for ferromagnetic interactions or “AF” for antiferromagnetic ones as well as the references of the respective compounds.	
18	Comparison of <i>ab initio</i> calculations on four compounds representative for both bridging modes shown in scheme xxx as indicated by the bridging oxygen atom in the second column. The related directions of anisotropy axes are also indicated in the same column by “p” for anisotropy axes parallel to the Dy-O _{phenoxy} bond or “o” for axes orthogonal to the Dy-Dy vector.	174
19	Fitting parameters using equation 13 to fit the lifetime values extracted using the Debye model to fit the ac data of (39-Dy).	179
20	Fitting parameters using equation 13 to fit the relaxation processes in (41-Dy).	187
21	Fitting parameters using the equation introduced by Lunghi <i>et al.</i> ^[142] used to obtain the red fit to the relaxation processes in (60-Dy) in figure 199.	220
22	Fitting parameters used to fit the relaxation processes present in (71-Dy) using equation 13.	230
23	Fitting parameters used to fit the relaxation data of (84-Dy) to equation 13.	239
24	C-O bond lengths of the ligand confirming the radical oxidation state of the ligand. The other three ligands are the same per inversion symmetry.	241
25	BVS analysis for the cerium ion in (90-Ce) using the parameters $B = 0.37$ and $R_0 = 2.121 \text{ \AA}$ for the 3+ oxidation state and 2.068 \AA for the 4+ oxidation state. ^[254] As (90-Ce) is a dimer and therefore centrosymmetric with $Z' = 0.5$ the two cerium ions are identical, therefore only one calculation had to be performed per oxidation state. The Ce-O bond lengths are listed below as well as the results of the two calculations highlighting the best result in red.	242
26	Fitting parameters to fit the relaxation data of (92-Dy) to equation 13.	251
27	Comparison of the parameters used to fit the relaxation data of the different variations of dimers to equation 13. The specific tuning handle of the respective compounds are given in the second column.	256
28	Switching fields corresponding to the predominant level crossing in the different variations of the Ln_2Rad_4 dimers.	257

13.3 Crystallographic Tables

Compound	(1)	(2)
Empirical formula	C ₂₄ H ₃₀ N ₄ O ₂	C ₂₆ H ₃₄ N ₄ O ₂
Formula weight (g/mol)	406.52	434.57
Temperature (K)	180.00	150
Crystal system	triclinic	monoclinic
Space group	P-1	P2 ₁ /c
a (Å)	9.2870(3)	9.1279(5)
b (Å)	10.6054(3)	11.5688(6)
c (Å)	11.8298(3)	22.0877(12)
α (°)	98.896(2)	90
β (°)	90.332(2)	93.047(4)
γ (°)	110.925(2)	90
Volume (Å³)	1072.86(6)	2329.1(2)
Z	2	4
ρ_{calc} (g/cm³)	1.258	1.239
μ (mm⁻¹)	0.417	0.404
F(000)	436.0	936.0
Crystal size (mm³)	0.1 × 0.08 × 0.03	0.12 × 0.1 × 0.02
Radiation	GaKα (λ = 1.34143)	1.3401270, 1.34 Kα (λ = 1.34143)
2Θ range for data collection (°)	6.594 to 128.41	6.974 to 114.988
Index ranges	-12 ≤ h ≤ 12, -13 ≤ k ≤ 14, -15 ≤ l ≤ 5	-8 ≤ h ≤ 11, -14 ≤ k ≤ 7, -27 ≤ l ≤ 25
Reflections collected	15238	16867
Independent reflections	5211 [R _{int} = 0.0144, R _{sigma} = 0.0176]	4800 [R _{int} = 0.0262, R _{sigma} = 0.0213]
Data/restraints/parameters	5211/0/392	4800/0/426
Goodness-of-fit on F²	1.048	1.147
Final R indexes [I>=2σ (I)]	R ₁ = 0.0372, wR ₂ = 0.0979	R ₁ = 0.0398, wR ₂ = 0.1201
Final R indexes [all data]	R ₁ = 0.0451, wR ₂ = 0.1010	R ₁ = 0.0489, wR ₂ = 0.1269
Largest diff. peak/hole / e Å⁻³	0.29/-0.19	0.25/-0.20

Compound	(3)	(6)
Empirical formula	C ₂₄ H ₃₀ N ₄ S ₂	C ₃₀ H ₄₂ N ₄ O ₂
Formula weight (g/mol)	438.64	490.67
Temperature (K)	293(2)	180.0
Crystal system	monoclinic	monoclinic
Space group	P2 ₁ /c	P2 ₁ /n
a (Å)	10.6835(11)	9.6925(7)
b (Å)	11.7694(12)	11.6760(6)
c (Å)	9.3090(9)	24.890(2)
α (°)	90	90
β (°)	94.629(8)	94.535(6)
γ (°)	90	90
Volume (Å³)	1166.7(2)	2808.0(3)
Z	2	4
ρ_{calc} (g/cm³)	1.249	1.161
μ (mm⁻¹)	0.246	0.369
F(000)	468.0	1064.0
Crystal size (mm³)	? × ? × ?	0.12 × 0.07 × 0.02
Radiation	MoKα (λ = 0.71073)	GaKα (λ = 1.34143)
2Θ range for data collection (°)	3.824 to 55.752	6.198 to 99.976
Index ranges	-14 ≤ h ≤ 13, -14 ≤ k ≤ 15, -9 ≤ l ≤ 12	-9 ≤ h ≤ 11, -5 ≤ k ≤ 13, -28 ≤ l ≤ 27
Reflections collected	6610	15186
Independent reflections	2764 [R _{int} = 0.1105, R _{sigma} = 0.0971]	4331 [R _{int} = 0.0637, R _{sigma} = 0.0715]
Data/restraints/parameters	2764/0/139	4331/0/333
Goodness-of-fit on F²	1.285	2.811
Final R indexes [I>=2σ (I)]	R ₁ = 0.1311, wR ₂ = 0.3206	R ₁ = 0.1996, wR ₂ = 0.5770
Final R indexes [all data]	R ₁ = 0.1564, wR ₂ = 0.3478	R ₁ = 0.2432, wR ₂ = 0.5832
Largest diff. peak/hole / e Å⁻³	0.87/-1.06	0.90/-0.54

Compound	(7)	(10-Cu)
Empirical formula	C ₂₄ H ₂₆ N ₄ O ₂	C ₁₈ H ₁₅ Cl ₂ CuN ₄ O
Formula weight (g/mol)	402.49	437.78
Temperature (K)	180.0	180.00
Crystal system	monoclinic	monoclinic
Space group	P2 ₁ /n	P2 ₁ /c
a (Å)	8.0271(4)	13.4398(4)
b (Å)	8.8950(4)	7.8086(3)
c (Å)	14.4670(8)	16.2480(4)
α (°)	90	90
β (°)	93.209(4)	101.519(2)
γ (°)	90	90
Volume (Å³)	1031.34(9)	1670.82(9)
Z	2	4
ρ_{calc} (g/cm³)	1.296	1.740
μ (mm⁻¹)	0.433	1.643
F(000)	428.0	888.0
Crystal size (mm³)	0.26 × 0.24 × 0.2	0.16 × 0.14 × 0.12
Radiation	Ga Kα (λ = 1.34143)	Mo Kα (λ = 0.71073)
2Θ range for data collection (°)	10.16 to 123.964	5.118 to 66.276
Index ranges	-10 ≤ h ≤ 9, -8 ≤ k ≤ 11, -16 ≤ l ≤ 19	-20 ≤ h ≤ 20, -12 ≤ k ≤ 12, -21 ≤ l ≤ 24
Reflections collected	7115	29842
Independent reflections	2401 [R _{int} = 0.0106, R _{sigma} = 0.0075]	6356 [R _{int} = 0.0309, R _{sigma} = 0.0319]
Data/restraints/parameters	2401/0/188	6356/1/247
Goodness-of-fit on F²	1.037	1.045
Final R indexes [I>=2σ (I)]	R ₁ = 0.0428, wR ₂ = 0.1174	R ₁ = 0.0383, wR ₂ = 0.0936
Final R indexes [all data]	R ₁ = 0.0450, wR ₂ = 0.1189	R ₁ = 0.0570, wR ₂ = 0.1000
Largest diff. peak/hole / e Å⁻³	0.30/-0.24	0.46/-0.44

Compound	(11-Cu)	(12-Zn A)
Empirical formula	C ₁₈ H ₁₅ Br ₂ CuN ₄ O	C ₁₈ H ₁₅ Cl ₂ N ₄ OZn
Formula weight (g/mol)	526.70	439.61
Temperature (K)	180	170
Crystal system	monoclinic	monoclinic
Space group	P2 ₁ /c	P2 ₁ /c
a (Å)	14.0992(6)	13.4372(8)
b (Å)	7.8107(5)	8.0886(3)
c (Å)	16.1742(8)	16.1358(11)
α (°)	90	90
β (°)	101.516(4)	100.631(5)
γ (°)	90	90
Volume (Å³)	1745.32(16)	1723.67(17)
Z	4	4
ρ_{calc} (g/cm³)	2.004	1.694
μ (mm⁻¹)	5.846	3.291
F(000)	1032.0	892.0
Crystal size (mm³)	0.32 × 0.21 × 0.05	0.14 × 0.12 × 0.03
Radiation	Mo Kα (λ = 0.71073)	Ga Kα (λ = 1.34143)
2Θ range for data collection (°)	5.14 to 56.562	9.704 to 124.968
Index ranges	-14 ≤ h ≤ 18, -10 ≤ k ≤ 10, -21 ≤ l ≤ 21	-17 ≤ h ≤ 17, -8 ≤ k ≤ 10, -15 ≤ l ≤ 21
Reflections collected	11528	10103
Independent reflections	4311 [R _{int} = 0.0279, R _{sigma} = 0.0414]	4038 [R _{int} = 0.0142, R _{sigma} = 0.0123]
Data/restraints/parameters	4311/0/242	4038/0/247
Goodness-of-fit on F²	1.016	1.055
Final R indexes [I>=2σ (I)]	R ₁ = 0.0384, wR ₂ = 0.0840	R ₁ = 0.0271, wR ₂ = 0.0820
Final R indexes [all data]	R ₁ = 0.0639, wR ₂ = 0.0929	R ₁ = 0.0317, wR ₂ = 0.0870
Largest diff. peak/hole / e Å⁻³	0.59/-0.51	0.32/-0.35

Compound	(12-Zn B)	(14-La)
Empirical formula	C ₁₈ H ₁₅ Cl ₂ N ₄ OZn	C ₇₂ H _{77.5} La ₅ N _{25.5} O ₂₈
Formula weight (g/mol)	439.61	2442.64
Temperature (K)	293(2)	180.15
Crystal system	monoclinic	triclinic
Space group	P2 ₁ /n	P-1
a (Å)	9.2305(4)	14.7042(7)
b (Å)	14.3251(6)	16.2377(5)
c (Å)	13.6905(7)	19.1380(11)
α (°)	90	100.118(4)
β (°)	106.283(5)	91.686(4)
γ (°)	90	95.207(3)
Volume (Å³)	1737.65(14)	4475.0(4)
Z	4	2
ρ_{calc} (g/cm³)	1.680	1.813
μ (mm⁻¹)	4.925	12.925
F(000)	892.0	2394.0
Crystal size (mm³)	0.13 × 0.11 × 0.1	? × ? × ?
Radiation	CuKα (λ = 1.54184)	GaKα (λ = 1.34143)
2Θ range for data collection (°)	9.132 to 141.884	4.084 to 125.21
Index ranges	-9 ≤ h ≤ 11, -12 ≤ k ≤ 17, -16 ≤ l ≤ 9	-19 ≤ h ≤ 19, -21 ≤ k ≤ 17, -14 ≤ l ≤ 25
Reflections collected	9780	51941
Independent reflections	3304 [R _{int} = 0.0272, R _{sigma} = 0.0300]	20787 [R _{int} = 0.0337, R _{sigma} = 0.0460]
Data/restraints/parameters	3304/0/240	20787/42/1148
Goodness-of-fit on F²	1.034	0.946
Final R indexes [I>=2σ (I)]	R ₁ = 0.0366, wR ₂ = 0.0893	R ₁ = 0.0398, wR ₂ = 0.0990
Final R indexes [all data]	R ₁ = 0.0531, wR ₂ = 0.0999	R ₁ = 0.0565, wR ₂ = 0.1041
Largest diff. peak/hole / e Å⁻³	0.32/-0.40	2.59/-1.03

Compound	(15-Ce)	(16-Eu)
Empirical formula	C ₆₀ H ₆₅ Ce ₄ N ₂₂ O ₂₆	C _{110.67} H ₁₃₀ Eu ₅ N _{40.33} O ₂₉
Formula weight (g/mol)	2070.82	3249.01
Temperature (K)	180	180
Crystal system	monoclinic	trigonal
Space group	P2 ₁ /n	P-3
a (Å)	16.6925(6)	32.0835(4)
b (Å)	26.1270(10)	32.0835(4)
c (Å)	19.1392(11)	25.7765(3)
α (°)	90	90
β (°)	114.860(3)	90
γ (°)	90	120
Volume (Å³)	7573.6(6)	22978.3(6)
Z	4	6
ρ_{calc} (g/cm³)	1.816	1.409
μ (mm⁻¹)	12.509	2.091
F(000)	4076.0	9740.0
Crystal size (mm³)	? × ? × ?	0.26 × 0.2 × 0.16
Radiation	1.3401270, 1.34 Kα (λ = 1.34143)	Mo Kα (λ = 0.71073)
2Θ range for data collection (°)	5.316 to 125.072	3.878 to 51.362
Index ranges	-18 ≤ h ≤ 22, -34 ≤ k ≤ 18, -22 ≤ l ≤ 25	-39 ≤ h ≤ 39, -39 ≤ k ≤ 39, -21 ≤ l ≤ 31
Reflections collected	43483	130164
Independent reflections	17695 [R _{int} = 0.0313, R _{sigma} = 0.0276]	29076 [R _{int} = 0.0678, R _{sigma} = 0.0639]
Data/restraints/parameters	17695/17/1043	29076/67/1343
Goodness-of-fit on F²	1.052	0.982
Final R indexes [I>=2σ (I)]	R ₁ = 0.0425, wR ₂ = 0.1211	R ₁ = 0.0437, wR ₂ = 0.1102
Final R indexes [all data]	R ₁ = 0.0476, wR ₂ = 0.1244	R ₁ = 0.0742, wR ₂ = 0.1191
Largest diff. peak/hole / e Å⁻³	1.95/-2.23	0.90/-0.98

Compound	(17-Dy)	(18-Sm)
Empirical formula	C ₉₁ H ₁₀₈ Dy ₆ N ₃₂ O ₃₂	C ₁₃₂ H ₁₄₀ N ₄₄ O ₄₈ Sm ₈
Formula weight (g/mol)	3137.09	4313.67
Temperature (K)	180.15	180
Crystal system	triclinic	triclinic
Space group	P-1	P-1
a (Å)	18.4408(8)	18.1493(2)
b (Å)	18.7612(7)	18.5612(2)
c (Å)	19.2293(9)	28.3525(3)
α (°)	76.764(3)	72.8270(10)
β (°)	76.403(4)	77.4670(10)
γ (°)	60.463(3)	61.3850(10)
Volume (Å³)	5575.4(5)	7978.17(17)
Z	2	2
ρ_{calc} (g/cm³)	1.869	1.796
μ (mm⁻¹)	4.060	2.989
F(000)	3060.0	4240.0
Crystal size (mm³)	0.18 × 0.12 × 0.03	0.28 × 0.26 × 0.2
Radiation	MoKα (λ = 0.71073)	Mo Kα (λ = 0.71073)
2Θ range for data collection (°)	4.35 to 50.7	4.136 to 59.144
Index ranges	-22 ≤ h ≤ 22, -22 ≤ k ≤ 22, -23 ≤ l ≤ 23	-24 ≤ h ≤ 23, -25 ≤ k ≤ 25, -39 ≤ l ≤ 30
Reflections collected	38433	71829
Independent reflections	20094 [R _{int} = 0.0935, R _{sigma} = 0.1062]	40957 [R _{int} = 0.0311, R _{sigma} = 0.0329]
Data/restraints/parameters	20094/159/1339	40957/22/2156
Goodness-of-fit on F²	0.997	1.080
Final R indexes [I>=2σ (I)]	R ₁ = 0.0937, wR ₂ = 0.2468	R ₁ = 0.0505, wR ₂ = 0.1326
Final R indexes [all data]	R ₁ = 0.1214, wR ₂ = 0.2703	R ₁ = 0.0583, wR ₂ = 0.1367
Largest diff. peak/hole / e Å⁻³	6.79/-4.06	3.88/-3.09

Compound	(19-Gd)	(20-Tb)
Empirical formula	C ₁₂₈ H ₁₃₅ Gd ₈ N ₄₂ O ₄₈	C ₁₂₂ H ₁₀₁ N ₃₉ O ₄₄ Tb ₈
Formula weight (g/mol)	4287.77	4088.77
Temperature (K)	180	150
Crystal system	triclinic	monoclinic
Space group	P-1	C2/c
a (Å)	18.0662(6)	30.6281(17)
b (Å)	18.3969(6)	18.2659(4)
c (Å)	28.2356(10)	28.4471(12)
α (°)	72.485(3)	90
β (°)	77.273(3)	116.953(3)
γ (°)	61.037(2)	90
Volume (Å³)	7798.8(5)	14186.0(11)
Z	2	4
ρ_{calc} (g/cm³)	1.826	1.914
μ (mm⁻¹)	3.445	21.363
F(000)	4186.0	7912.0
Crystal size (mm³)	0.16 × 0.14 × 0.12	0.12 × 0.11 × 0.1
Radiation	Mo Kα (λ = 0.71073)	1.3401270, 1.34 Kα (λ = 1.34143)
2Θ range for data collection (°)	3.81 to 52.044	5.206 to 96.36
Index ranges	-22 ≤ h ≤ 22, -22 ≤ k ≤ 22, -34 ≤ l ≤ 34	-32 ≤ h ≤ 34, -14 ≤ k ≤ 20, -31 ≤ l ≤ 28
Reflections collected	54635	33714
Independent reflections	29573 [R _{int} = 0.0428, R _{sigma} = 0.0888]	9983 [R _{int} = 0.0571, R _{sigma} = 0.0635]
Data/restraints/parameters	29573/288/2099	9983/0/873
Goodness-of-fit on F²	0.970	1.168
Final R indexes [I>=2σ (I)]	R ₁ = 0.0438, wR ₂ = 0.0890	R ₁ = 0.0858, wR ₂ = 0.2488
Final R indexes [all data]	R ₁ = 0.0825, wR ₂ = 0.0973	R ₁ = 0.1290, wR ₂ = 0.2712
Largest diff. peak/hole / e Å⁻³	1.90/-1.21	2.32/-1.98

Compound	(21-Dy)	(22-Ho)
Empirical formula	C ₁₃₀ H ₁₃₁ Dy ₈ N ₄₄ O ₄₇	C ₁₂₂ H ₁₀₁ Ho ₈ N ₃₉ O ₄₄
Formula weight (g/mol)	4361.78	4136.85
Temperature (K)	180	273.15
Crystal system	triclinic	monoclinic
Space group	P-1	C2/c
a (Å)	18.0547(5)	31.4540(8)
b (Å)	18.4130(5)	18.2274(3)
c (Å)	28.1573(11)	28.5809(7)
α (°)	72.716(3)	90
β (°)	77.295(3)	117.543(2)
γ (°)	60.889(2)	90
Volume (Å³)	7777.0(5)	14529.0(6)
Z	2	4
ρ_{calc} (g/cm³)	1.863	1.891
μ (mm⁻¹)	20.145	4.396
F(000)	4246.0	7976.0
Crystal size (mm³)	? × ? × ?	0.16 × 0.14 × 0.12
Radiation	Ga-Kα (λ = 1.34143)	Mo-Kα (λ = 0.71073)
2Θ range for data collection (°)	4.894 to 125.132	2.67 to 50.706
Index ranges	-22 ≤ h ≤ 23, -24 ≤ k ≤ 23, -37 ≤ l ≤ 20	-37 ≤ h ≤ 37, -12 ≤ k ≤ 21, -34 ≤ l ≤ 31
Reflections collected	86126	40225
Independent reflections	36056 [R _{int} = 0.0366, R _{sigma} = 0.0404]	13058 [R _{int} = 0.0413, R _{sigma} = 0.0471]
Data/restraints/parameters	36056/47/2117	13058/234/865
Goodness-of-fit on F²	0.993	1.027
Final R indexes [I>=2σ (I)]	R ₁ = 0.0532, wR ₂ = 0.1395	R ₁ = 0.0627, wR ₂ = 0.1452
Final R indexes [all data]	R ₁ = 0.0670, wR ₂ = 0.1484	R ₁ = 0.0918, wR ₂ = 0.1582
Largest diff. peak/hole / e Å⁻³	3.82/-2.73	1.72/-3.12

Compound	(23-Er)	(24-Y)
Empirical formula	C ₁₂₂ H ₁₀₁ Er ₈ N ₃₉ O ₄₄	C ₈₀ H ₈₀ N ₂₀ O ₂₀ Y ₄
Formula weight (g/mol)	4155.49	1997.28
Temperature (K)	273.15	180
Crystal system	monoclinic	monoclinic
Space group	C2/c	C2/c
a (Å)	31.2914(5)	31.6698(16)
b (Å)	18.2141(3)	18.2460(4)
c (Å)	28.4812(6)	31.2023(15)
α (°)	90	90
β (°)	117.6360(10)	126.314(3)
γ (°)	90	90
Volume (Å³)	14380.8(5)	14528.4(12)
Z	4	8
ρ_{calc} (g/cm³)	1.919	1.826
μ (mm⁻¹)	4.708	3.260
F(000)	8008.0	8128.0
Crystal size (mm³)	0.18 × 0.16 × 0.14	0.16 × 0.14 × 0.12
Radiation	MoKα (λ = 0.71073)	Mo Kα (λ = 0.71073)
2Θ range for data collection (°)	2.75 to 54.966	4.464 to 63.062
Index ranges	-29 ≤ h ≤ 40, -21 ≤ k ≤ 23, -36 ≤ l ≤ 36	-43 ≤ h ≤ 43, -26 ≤ k ≤ 16, -39 ≤ l ≤ 44
Reflections collected	44203	35474
Independent reflections	16123 [R _{int} = 0.0479, R _{sigma} = 0.0497]	19530 [R _{int} = 0.1179, R _{sigma} = 0.2485]
Data/restraints/parameters	16123/52/891	19530/0/385
Goodness-of-fit on F²	1.062	1.365
Final R indexes [I>=2σ (I)]	R ₁ = 0.0714, wR ₂ = 0.2002	R ₁ = 0.1877, wR ₂ = 0.4288
Final R indexes [all data]	R ₁ = 0.0945, wR ₂ = 0.2156	R ₁ = 0.3558, wR ₂ = 0.5067
Largest diff. peak/hole / e Å⁻³	2.76/-2.05	7.12/-3.58

Compound	(26-Dy)	(28-Er)
Empirical formula	C ₉₉ H ₁₃₀ Cl ₂ Dy ₆ N ₂₄ O ₄₀	C ₉₈ H ₁₂₆ Cl ₂ Er ₆ N ₂₄ O ₃₉
Formula weight (g/mol)	3342.16	3338.68
Temperature (K)	180	180
Crystal system	triclinic	triclinic
Space group	P-1	P-1
a (Å)	14.8753(5)	14.7811(5)
b (Å)	18.6119(6)	18.5462(5)
c (Å)	23.2645(10)	23.0864(8)
α (°)	103.985(3)	104.257(2)
β (°)	92.525(3)	92.410(3)
γ (°)	104.587(2)	105.124(2)
Volume (Å³)	6010.7(4)	5883.0(3)
Z	2	2
ρ_{calc} (g/cm³)	1.847	1.885
μ (mm⁻¹)	3.818	14.566
F(000)	3284.0	3272.0
Crystal size (mm³)	0.18 × 0.12 × 0.06	0.14 × 0.12 × 0.1
Radiation	Mo Kα (λ = 0.71073)	1.3401270, 1.34 Kα (λ = 1.34143)
2Θ range for data collection (°)	4.148 to 56.564	5.424 to 109.758
Index ranges	-19 ≤ h ≤ 19, -24 ≤ k ≤ 18, -29 ≤ l ≤ 31	-18 ≤ h ≤ 10, -18 ≤ k ≤ 22, -28 ≤ l ≤ 28
Reflections collected	53226	62900
Independent reflections	28336 [R _{int} = 0.0759, R _{sigma} = 0.1022]	21808 [R _{int} = 0.0818, R _{sigma} = 0.1324]
Data/restraints/parameters	28336/26/1406	21808/23/1406
Goodness-of-fit on F²	0.988	0.944
Final R indexes [I>=2σ (I)]	R ₁ = 0.0828, wR ₂ = 0.2142	R ₁ = 0.0426, wR ₂ = 0.0923
Final R indexes [all data]	R ₁ = 0.1214, wR ₂ = 0.2324	R ₁ = 0.0958, wR ₂ = 0.1008
Largest diff. peak/hole / e Å⁻³	4.80/-5.07	1.46/-0.84

Compound	(29-Er)	(30-Er)
Empirical formula	C ₈₃ H ₆₈ Br ₆ Cl ₂ Er ₆ N ₂₄ O ₃₀	C ₈₄ H ₁₀₄ Er ₄ I ₄ N ₁₆ O ₃₂
Formula weight (g/mol)	3435.53	3026.47
Temperature (K)	293(2)	180
Crystal system	tetragonal	orthorhombic
Space group	P-42 ₁ C	Fdd2
a (Å)	30.4283(4)	49.8935(11)
b (Å)	30.4283(4)	20.3426(4)
c (Å)	27.2210(4)	20.7397(6)
α (°)	90	90
β (°)	90	90
γ (°)	90	90
Volume (Å³)	25203.4(8)	21050.0(9)
Z	8	8
ρ_{calc} (g/cm³)	1.811	1.910
μ (mm⁻¹)	5.967	17.077
F(000)	13008.0	11680.0
Crystal size (mm³)	? × ? × ?	0.14 × 0.12 × 0.1
Radiation	MoKα (λ = 0.71073)	1.3401270, 1.34 Kα (λ = 1.34143)
2Θ range for data collection (°)	5.184 to 52.044	5.514 to 109.76
Index ranges	-37 ≤ h ≤ 21, -25 ≤ k ≤ 36, -32 ≤ l ≤ 33	-52 ≤ h ≤ 60, -18 ≤ k ≤ 24, -25 ≤ l ≤ 25
Reflections collected	46293	63357
Independent reflections	23896 [R _{int} = 0.0351, R _{sigma} = 0.0575]	9853 [R _{int} = 0.1302, R _{sigma} = 0.1161]
Data/restraints/parameters	23896/263/1316	9853/16/480
Goodness-of-fit on F²	0.991	0.854
Final R indexes [I>=2σ (I)]	R ₁ = 0.0442, wR ₂ = 0.1006	R ₁ = 0.0438, wR ₂ = 0.0913
Final R indexes [all data]	R ₁ = 0.0695, wR ₂ = 0.1096	R ₁ = 0.0768, wR ₂ = 0.0967
Largest diff. peak/hole / e Å⁻³	1.04/-1.14	0.99/-0.68

Compound	(31-Ce)	(34-Nd)
Empirical formula	C ₇₂ H ₈₀ Ce ₄ N ₂₆ O ₂₄	C ₉₈ H ₁₀₃ N ₃₄ Nd ₇ O ₃₅
Formula weight (g/mol)	2254.10	3326.82
Temperature (K)	180.00	180
Crystal system	triclinic	monoclinic
Space group	P-1	P2 ₁ /n
a (Å)	17.0172(10)	18.3632(3)
b (Å)	17.0538(9)	22.6238(4)
c (Å)	18.9972(12)	29.8565(5)
α (°)	104.487(5)	90
β (°)	100.998(5)	103.6820(10)
γ (°)	114.656(4)	90
Volume (Å³)	4570.2(5)	12051.8(4)
Z	2	4
ρ_{calc} (g/cm³)	1.638	1.834
μ (mm⁻¹)	2.038	3.050
F(000)	2236.0	6516.0
Crystal size (mm³)	0.2 × 0.18 × 0.16	0.28 × 0.26 × 0.24
Radiation	MoKα (λ = 0.71073)	Mo Kα (λ = 0.71073)
2Θ range for data collection (°)	2.934 to 54.206	7.312 to 61.996
Index ranges	-21 ≤ h ≤ 20, -21 ≤ k ≤ 21, -24 ≤ l ≤ 24	-12 ≤ h ≤ 26, -32 ≤ k ≤ 16, -42 ≤ l ≤ 33
Reflections collected	38279	69949
Independent reflections	19546 [R _{int} = 0.0578, R _{sigma} = 0.0713]	37252 [R _{int} = 0.0261, R _{sigma} = 0.0286]
Data/restraints/parameters	19546/19/995	37252/52/1526
Goodness-of-fit on F²	0.881	1.019
Final R indexes [I>=2σ (I)]	R ₁ = 0.0394, wR ₂ = 0.0901	R ₁ = 0.0409, wR ₂ = 0.1018
Final R indexes [all data]	R ₁ = 0.0681, wR ₂ = 0.0971	R ₁ = 0.0508, wR ₂ = 0.1064
Largest diff. peak/hole / e Å⁻³	1.21/-1.42	2.55/-1.41

Compound	(35-Gd A)	(35-Gd B)
Empirical formula	C ₉₉ H ₁₀₃ Gd ₇ I ₆ N ₂₈ O ₄₃	C ₁₁₄ H ₁₃₃ Gd ₇ I ₆ N ₂₈ O ₄₈
Formula weight (g/mol)	4235.24	4525.63
Temperature (K)	150	180
Crystal system	triclinic	triclinic
Space group	P-1	P-1
a (Å)	15.7505(5)	15.7498(4)
b (Å)	18.7129(7)	20.1100(5)
c (Å)	24.9310(7)	24.5300(7)
α (°)	108.546(3)	92.311(2)
β (°)	98.831(2)	98.748(2)
γ (°)	92.782(3)	92.601(2)
Volume (Å³)	6846.6(4)	7662.3(4)
Z	2	2
ρ_{calc} (g/cm³)	2.054	1.962
μ (mm⁻¹)	25.231	22.593
F(000)	4006.0	4326.0
Crystal size (mm³)	0.2 × 0.173 × 0.14	0.22 × 0.2 × 0.18
Radiation	1.3401270, 1.34 Kα (λ = 1.34143)	1.3401270, 1.34 Kα (λ = 1.34143)
2Θ range for data collection (°)	6.44 to 100.876	5.45 to 107.82
Index ranges	-18 ≤ h ≤ 17, -21 ≤ k ≤ 21, -14 ≤ l ≤ 28	-7 ≤ h ≤ 18, -24 ≤ k ≤ 24, -29 ≤ l ≤ 29
Reflections collected	63552	100697
Independent reflections	21300 [R _{int} = 0.0857, R _{sigma} = 0.0801]	27608 [R _{int} = 0.1186, R _{sigma} = 0.1359]
Data/restraints/parameters	21300/198/1432	27608/140/1501
Goodness-of-fit on F²	0.969	0.904
Final R indexes [I>=2σ (I)]	R ₁ = 0.0682, wR ₂ = 0.1860	R ₁ = 0.0638, wR ₂ = 0.1465
Final R indexes [all data]	R ₁ = 0.1181, wR ₂ = 0.2013	R ₁ = 0.1091, wR ₂ = 0.1558
Largest diff. peak/hole / e Å⁻³	3.82/-1.50	1.77/-2.10

Compound	(36-Dy)	(37-Tb)
Empirical formula	C ₁₁₄ H ₁₃₃ Dy ₇ I ₆ N ₂₈ O ₄₈	C ₃₀ H ₃₄ N ₈ O ₁₄ Tb ₂
Formula weight (g/mol)	4562.38	1048.49
Temperature (K)	180.00	180
Crystal system	triclinic	monoclinic
Space group	P-1	P2 ₁ /n
a (Å)	15.6369(11)	8.8236(3)
b (Å)	20.0265(14)	15.2808(4)
c (Å)	24.3457(16)	13.4820(6)
α (°)	92.517(6)	90
β (°)	98.153(5)	104.464(2)
γ (°)	92.766(6)	90
Volume (Å³)	7528.1(9)	1760.18(11)
Z	2	2
ρ_{calc} (g/cm³)	2.013	1.978
μ (mm⁻¹)	4.747	4.065
F(000)	4354.0	1024.0
Crystal size (mm³)	0.2 × 0.19 × 0.18	0.16 × 0.14 × 0.12
Radiation	MoK α (λ = 0.71073)	MoK α (λ = 0.71073)
2Θ range for data collection (°)	2.92 to 53.466	5.332 to 59.148
Index ranges	-19 ≤ h ≤ 18, -25 ≤ k ≤ 25, -26 ≤ l ≤ 30	-12 ≤ h ≤ 6, -20 ≤ k ≤ 20, -18 ≤ l ≤ 18
Reflections collected	51253	9613
Independent reflections	29808 [R _{int} = 0.0642, R _{sigma} = 0.0779]	4597 [R _{int} = 0.0657, R _{sigma} = 0.0579]
Data/restraints/parameters	29808/4/1507	4597/8/262
Goodness-of-fit on F²	0.878	1.075
Final R indexes [I>=2σ (I)]	R ₁ = 0.0506, wR ₂ = 0.1224	R ₁ = 0.0572, wR ₂ = 0.1387
Final R indexes [all data]	R ₁ = 0.0776, wR ₂ = 0.1328	R ₁ = 0.0718, wR ₂ = 0.1457
Largest diff. peak/hole / e Å⁻³	2.00/-2.85	3.58/-1.93

Compound	(38-Dy)	(39-Dy)
Empirical formula	C ₃₂ H ₃₂ Br ₂ Dy ₂ N ₈ O ₁₂	C ₃₈ H ₄₆ Dy ₂ N ₁₆ O ₂₀
Formula weight (g/mol)	1205.47	1371.91
Temperature (K)	180	180.0
Crystal system	monoclinic	triclinic
Space group	P2 ₁ /n	P-1
a (Å)	13.7340(9)	9.7649(3)
b (Å)	8.6025(3)	10.7782(4)
c (Å)	17.1665(10)	12.7771(4)
α (°)	90	106.587(3)
β (°)	100.961(5)	100.331(3)
γ (°)	90	99.037(3)
Volume (Å³)	1991.17(19)	1236.59(8)
Z	2	1
ρ_{calc} (g/cm³)	2.011	1.842
μ (mm⁻¹)	5.799	16.264
F(000)	1156.0	678.0
Crystal size (mm³)	0.24 × 0.097 × 0.02	0.15 × 0.14 × 0.13
Radiation	Mo Kα (λ = 0.71073)	GaKα (λ = 1.34143)
2Θ range for data collection (°)	4.834 to 59.15	6.464 to 127.892
Index ranges	-18 ≤ h ≤ 18, -11 ≤ k ≤ 7, -14 ≤ l ≤ 23	-11 ≤ h ≤ 13, -14 ≤ k ≤ 13, -11 ≤ l ≤ 17
Reflections collected	10603	14034
Independent reflections	5488 [R _{int} = 0.0382, R _{sigma} = 0.0648]	5930 [R _{int} = 0.0229, R _{sigma} = 0.0173]
Data/restraints/parameters	5488/1/259	5930/0/349
Goodness-of-fit on F²	0.935	1.053
Final R indexes [I>=2σ (I)]	R ₁ = 0.0378, wR ₂ = 0.0753	R ₁ = 0.0284, wR ₂ = 0.0743
Final R indexes [all data]	R ₁ = 0.0662, wR ₂ = 0.0822	R ₁ = 0.0287, wR ₂ = 0.0746
Largest diff. peak/hole / e Å⁻³	1.73/-1.58	2.29/-1.69

Compound	(40-Dy)	(41-Dy)
Empirical formula	C ₂₇ H ₂₀ Br ₂ Cl ₈ Dy ₂ N ₈ O ₆	C ₃₂ H ₃₀ Br ₂ Dy ₂ N ₁₀ O ₁₄
Formula weight (g/mol)	1320.93	1263.48
Temperature (K)	180	180.00
Crystal system	tetragonal	monoclinic
Space group	P4/n	P2 ₁ /c
a (Å)	20.9056(4)	8.4229(5)
b (Å)	20.9056(4)	9.1407(4)
c (Å)	9.1595(2)	26.4480(14)
α (°)	90	90
β (°)	90	92.073(5)
γ (°)	90	90
Volume (Å³)	4003.11(18)	2034.93(18)
Z	4	2
ρ_{calc} (g/cm³)	2.192	2.062
μ (mm⁻¹)	24.286	5.684
F(000)	2496.0	1212.0
Crystal size (mm³)	0.12 × 0.09 × 0.05	0.16 × 0.14 × 0.12
Radiation	1.3401270, 1.34 Kα (λ = 1.34143)	MoKα (λ = 0.71073)
2Θ range for data collection (°)	8.398 to 128.31	4.716 to 66.69
Index ranges	-27 ≤ h ≤ 20, -20 ≤ k ≤ 25, -7 ≤ l ≤ 12	-11 ≤ h ≤ 12, -13 ≤ k ≤ 7, -39 ≤ l ≤ 38
Reflections collected	12934	11484
Independent reflections	4746 [R _{int} = 0.0340, R _{sigma} = 0.0311]	6754 [R _{int} = 0.0925, R _{sigma} = 0.0815]
Data/restraints/parameters	4746/37/281	6754/0/274
Goodness-of-fit on F²	1.125	1.463
Final R indexes [I>=2σ (I)]	R ₁ = 0.0490, wR ₂ = 0.1417	R ₁ = 0.1356, wR ₂ = 0.3480
Final R indexes [all data]	R ₁ = 0.0605, wR ₂ = 0.1485	R ₁ = 0.1557, wR ₂ = 0.3633
Largest diff. peak/hole / e Å⁻³	1.74/-1.63	11.21/-17.04

Compound	(42-Dy)	(60-Dy)
Empirical formula	C ₃₂ H ₃₀ Dy ₂ I ₂ N ₁₀ O ₁₄	C ₆₈ H ₆₈ Dy ₂ N ₂ O ₂₀
Formula weight (g/mol)	1357.46	1558.24
Temperature (K)	150	180(2)
Crystal system	monoclinic	monoclinic
Space group	P2 ₁ /c	P2 ₁ /n
a (Å)	8.2803(4)	11.6579(5)
b (Å)	28.0217(10)	18.4992(5)
c (Å)	9.1873(4)	14.5998(6)
α (°)	90	90
β (°)	95.062(4)	94.545(3)
γ (°)	90	90
Volume (Å³)	2123.40(16)	3138.7(2)
Z	2	2
ρ_{calc} (g/cm³)	2.123	1.649
μ (mm⁻¹)	26.339	2.441
F(000)	1284.0	1564.0
Crystal size (mm³)	0.22 × 0.173 × 0.14	0.160 × 0.155 × 0.150
Radiation	1.3401270, 1.34 Kα (λ = 1.34143)	MoKα (λ = 0.71073)
2Θ range for data collection (°)	8.844 to 128.198	4.14 to 56.56
Index ranges	-10 ≤ h ≤ 7, -31 ≤ k ≤ 37, -11 ≤ l ≤ 12	-14 ≤ h ≤ 15, -15 ≤ k ≤ 24, -19 ≤ l ≤ 19
Reflections collected	13465	15826
Independent reflections	5105 [R _{int} = 0.0308, R _{sigma} = 0.0295]	7688 [R _{int} = 0.0777, R _{sigma} = 0.0910]
Data/restraints/parameters	5105/0/274	7688/2/423
Goodness-of-fit on F²	1.097	0.959
Final R indexes [I>=2σ (I)]	R ₁ = 0.0408, wR ₂ = 0.1145	R ₁ = 0.0543, wR ₂ = 0.1277
Final R indexes [all data]	R ₁ = 0.0495, wR ₂ = 0.1202	R ₁ = 0.0881, wR ₂ = 0.1421
Largest diff. peak/hole / e Å⁻³	1.93/-0.77	2.90/-2.43

Compound	(74-Tm)	(78-DyY)
Empirical formula	C ₆₈ H ₆₄ N ₂ O ₁₈ Tm ₂	C ₆₈ H ₆₄ Dy _{0.58} N ₂ O ₁₈ Y _{1.42}
Formula weight (g/mol)	1535.07	1417.71
Temperature (K)	180.0	180
Crystal system	monoclinic	monoclinic
Space group	P2 ₁ /n	P2 ₁ /n
a (Å)	12.8549(4)	12.8440(3)
b (Å)	17.7648(4)	17.7484(4)
c (Å)	13.3236(4)	13.3983(4)
α (°)	90	90
β (°)	93.486(2)	93.324(2)
γ (°)	90	90
Volume (Å³)	3037.01(15)	3049.14(13)
Z	2	2
ρ_{calc} (g/cm³)	1.679	1.544
μ (mm⁻¹)	9.944	5.273
F(000)	1536.0	1447.0
Crystal size (mm³)	0.14 × 0.12 × 0.1	? × ? × ?
Radiation	GaKα (λ = 1.34143)	1.3401270, 1.34 Kα (λ = 1.34143)
2Θ range for data collection (°)	7.224 to 124.98	7.2 to 125.06
Index ranges	-9 ≤ h ≤ 16, -23 ≤ k ≤ 21, -17 ≤ l ≤ 15	-16 ≤ h ≤ 13, -22 ≤ k ≤ 23, -17 ≤ l ≤ 10
Reflections collected	19632	32027
Independent reflections	7151 [R _{int} = 0.0219, R _{sigma} = 0.0301]	7311 [R _{int} = 0.0152, R _{sigma} = 0.0103]
Data/restraints/parameters	7151/11/424	7311/17/432
Goodness-of-fit on F²	1.016	1.029
Final R indexes [I>=2σ (I)]	R ₁ = 0.0261, wR ₂ = 0.0631	R ₁ = 0.0222, wR ₂ = 0.0560
Final R indexes [all data]	R ₁ = 0.0387, wR ₂ = 0.0658	R ₁ = 0.0242, wR ₂ = 0.0570
Largest diff. peak/hole / e Å⁻³	0.59/-0.64	0.34/-0.54

Compound	(82-Gd)	(84-Dy)
Empirical formula	C ₅₈ H ₄₀ Cl ₂ Gd ₂ O ₁₀	C ₅₈ H ₄₀ Cl ₂ Dy ₂ O ₁₀
Formula weight (g/mol)	1282.30	1292.80
Temperature (K)	180	180
Crystal system	monoclinic	monoclinic
Space group	P2 ₁ /c	P2 ₁ /c
a (Å)	9.2625(3)	9.2078(2)
b (Å)	16.4397(6)	16.3944(3)
c (Å)	15.2753(5)	15.3029(4)
α (°)	90	90
β (°)	100.939(2)	100.981(2)
γ (°)	90	90
Volume (Å³)	2283.75(14)	2267.77(9)
Z	2	2
ρ_{calc} (g/cm³)	1.865	1.893
μ (mm⁻¹)	16.106	18.233
F(000)	1260.0	1268.0
Crystal size (mm³)	0.11 × 0.1 × 0.09	? × ? × ?
Radiation	Ga-Kα (λ = 1.34143)	Ga-Kα (λ = 1.34143)
2Θ range for data collection (°)	8.46 to 128.39	8.51 to 124.932
Index ranges	-12 ≤ h ≤ 10, -21 ≤ k ≤ 20, -20 ≤ l ≤ 14	-10 ≤ h ≤ 12, -21 ≤ k ≤ 20, -20 ≤ l ≤ 12
Reflections collected	14909	13809
Independent reflections	5469 [R _{int} = 0.0276, R _{sigma} = 0.0292]	5280 [R _{int} = 0.0249, R _{sigma} = 0.0289]
Data/restraints/parameters	5469/1/330	5280/1/329
Goodness-of-fit on F²	0.990	1.077
Final R indexes [I>=2σ (I)]	R ₁ = 0.0356, wR ₂ = 0.0885	R ₁ = 0.0322, wR ₂ = 0.0822
Final R indexes [all data]	R ₁ = 0.0439, wR ₂ = 0.0926	R ₁ = 0.0394, wR ₂ = 0.0841
Largest diff. peak/hole / e Å⁻³	2.05/-0.90	2.28/-2.18

Compound	(85-Ho)	(86-Er)
Empirical formula	C ₅₈ H ₄₀ Cl ₂ Ho ₂ O ₁₀	C ₅₈ H ₄₀ Cl ₂ Er ₂ O ₁₀
Formula weight (g/mol)	1297.66	1302.32
Temperature (K)	180	180
Crystal system	monoclinic	monoclinic
Space group	P2 ₁ /c	P2 ₁ /c
a (Å)	9.1885(4)	9.1772(6)
b (Å)	16.4120(6)	16.3704(6)
c (Å)	15.3229(7)	15.3322(10)
α (°)	90	90
β (°)	101.115(3)	101.206(5)
γ (°)	90	90
Volume (Å³)	2267.38(17)	2259.5(2)
Z	2	2
ρ_{calc} (g/cm³)	1.901	1.914
μ (mm⁻¹)	3.649	3.875
F(000)	1272.0	1276.0
Crystal size (mm³)	0.22 × 0.2 × 0.18	0.18 × 0.16 × 0.14
Radiation	Mo Kα (λ = 0.71073)	Mo Kα (λ = 0.71073)
2Θ range for data collection (°)	4.964 to 54.968	4.524 to 56.562
Index ranges	-11 ≤ h ≤ 7, -21 ≤ k ≤ 20, -19 ≤ l ≤ 19	-10 ≤ h ≤ 12, -21 ≤ k ≤ 16, -20 ≤ l ≤ 20
Reflections collected	11276	11174
Independent reflections	5113 [R _{int} = 0.1066, R _{sigma} = 0.0710]	5528 [R _{int} = 0.0874, R _{sigma} = 0.1024]
Data/restraints/parameters	5113/1/329	5528/1/329
Goodness-of-fit on F²	1.031	0.982
Final R indexes [I>=2σ (I)]	R ₁ = 0.0560, wR ₂ = 0.1465	R ₁ = 0.0757, wR ₂ = 0.1903
Final R indexes [all data]	R ₁ = 0.0600, wR ₂ = 0.1514	R ₁ = 0.1123, wR ₂ = 0.2176
Largest diff. peak/hole / e Å⁻³	2.75/-2.10	4.34/-5.29

Compound	(88-Y)	(90-Ce)
Empirical formula	C ₅₈ H ₄₀ Cl ₂ O ₁₀ Y ₂	C ₉₅ H ₉₄ Ce ₂ O ₂₄
Formula weight (g/mol)	1145.62	1899.94
Temperature (K)	180	180
Crystal system	monoclinic	monoclinic
Space group	P2 ₁ /c	P2 ₁ /n
a (Å)	9.1968(4)	17.3653(17)
b (Å)	16.3971(9)	15.2064(9)
c (Å)	15.3154(7)	17.1838(15)
α (°)	90	90
β (°)	100.933(4)	112.508(7)
γ (°)	90	90
Volume (Å³)	2267.66(19)	4192.0(6)
Z	2	2
ρ_{calc} (g/cm³)	1.678	1.505
μ (mm⁻¹)	2.732	6.132
F(000)	1160.0	1944.0
Crystal size (mm³)	0.28 × 0.26 × 0.24	0.12 × 0.11 × 0.1
Radiation	Mo Kα (λ = 0.71073)	1.3401270, 1.34 Kα (λ = 1.34143)
2Θ range for data collection (°)	4.968 to 63.026	5.354 to 92.292
Index ranges	-12 ≤ h ≤ 10, -22 ≤ k ≤ 23, -14 ≤ l ≤ 22	-18 ≤ h ≤ 17, -16 ≤ k ≤ 12, -18 ≤ l ≤ 16
Reflections collected	10833	17130
Independent reflections	6212 [R _{int} = 0.0266, R _{sigma} = 0.0360]	5298 [R _{int} = 0.0899, R _{sigma} = 0.0693]
Data/restraints/parameters	6212/1/329	5298/10/458
Goodness-of-fit on F²	1.011	1.146
Final R indexes [I>=2σ (I)]	R ₁ = 0.0379, wR ₂ = 0.0833	R ₁ = 0.1101, wR ₂ = 0.2897
Final R indexes [all data]	R ₁ = 0.0561, wR ₂ = 0.0910	R ₁ = 0.1357, wR ₂ = 0.3023
Largest diff. peak/hole / e Å⁻³	0.88/-0.66	2.17/-1.67

Compound	(92-Dy)	(94-Er)
Empirical formula	C _{96.5} H ₅₅ Dy ₂ N ₂ O ₂₁	C ₉₇ H ₅₆ Er ₂ N ₂ O ₂₁
Formula weight (g/mol)	1903.42	1919.95
Temperature (K)	293(2)	180
Crystal system	orthorhombic	orthorhombic
Space group	Pbca	Pbca
a (Å)	18.3532(2)	18.3067(7)
b (Å)	18.4489(2)	18.4019(5)
c (Å)	22.1516(5)	22.0921(7)
α (°)	90	90
β (°)	90	90
γ (°)	90	90
Volume (Å³)	7500.5(2)	7442.3(4)
Z	4	4
ρ_{calc} (g/cm³)	1.686	1.714
μ (mm⁻¹)	11.244	7.777
F(000)	3792.0	3824.0
Crystal size (mm³)	? × ? × ?	0.18 × 0.16 × 0.14
Radiation	Cu K α (λ = 1.54184)	1.3401270, 1.34 K α (λ = 1.34143)
2θ range for data collection (°)	7.88 to 141.984	6.872 to 118.606
Index ranges	-22 ≤ h ≤ 14, -21 ≤ k ≤ 22, -27 ≤ l ≤ 26	-17 ≤ h ≤ 22, -19 ≤ k ≤ 23, -28 ≤ l ≤ 9
Reflections collected	21108	24987
Independent reflections	7080 [R _{int} = 0.0256, R _{sigma} = 0.0287]	7806 [R _{int} = 0.0355, R _{sigma} = 0.0409]
Data/restraints/parameters	7080/6/560	7806/117/558
Goodness-of-fit on F²	1.059	1.009
Final R indexes [I>=2σ (I)]	R ₁ = 0.0402, wR ₂ = 0.1105	R ₁ = 0.0479, wR ₂ = 0.1454
Final R indexes [all data]	R ₁ = 0.0636, wR ₂ = 0.1295	R ₁ = 0.0896, wR ₂ = 0.1640
Largest diff. peak/hole / e Å⁻³	0.68/-0.87	0.88/-0.81